MEASUREMENTS WITHIN SELF-AERATED FLOW ON A LARGE SPILLWAY

A thesis presented for the degree of
Doctor of Philosophy in Civil Engineering
at the University of Canterbury,
Christchurch, New Zealand.

by

PAUL CAIN

April 1978

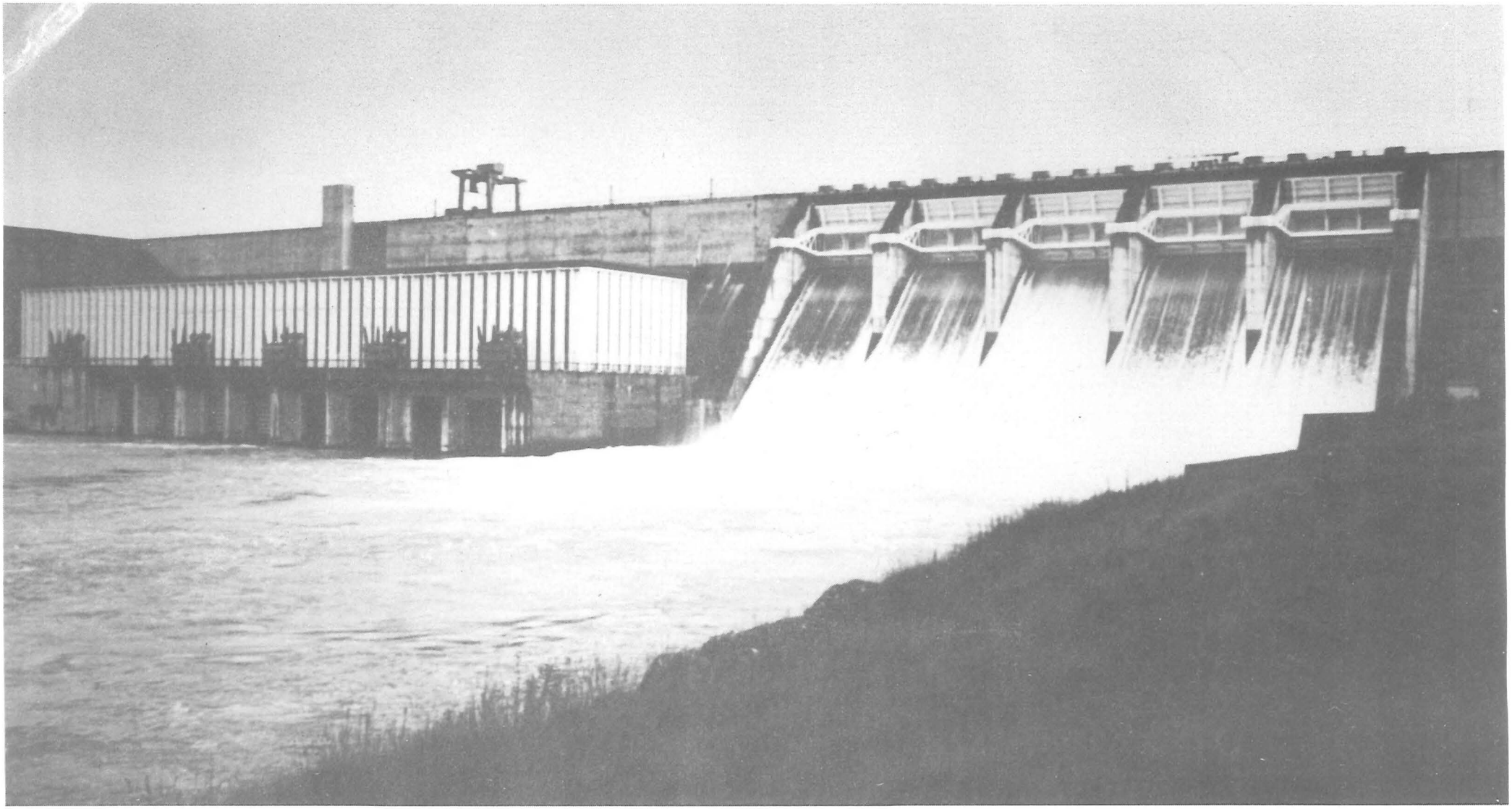

FRONTISPIECE : Self-Aerated Flow on the Spillway of Aviemore Dam, Waitaki River, New Zealand.

Spillway gates open 600 mm except central gate open 300 mm.

ABSTRACT

Instruments were developed and were used to obtain measurements of the most important flow parameters within self-aerated flows on the spillway of Aviemore dam.

Compressibility effects within self-aerated flows are examined. It is shown that Mach numbers as large as 2 will occur in localised aerated regions on large structures.

A probe was developed which measured stagnation pressure and air concentration. The compressible nature of self-aerated flows is taken into consideration in formulating a relationship between these measurements and the velocity of the water. This expression is found to overestimate the velocity by about 7% over a wide range of flow conditions.

A velocity probe was also developed, based on a cross-correlation technique. This latter probe was the more successful and is recommended for future measurements within self-aerated flows.

Profiles of stagnation pressure, air concentration and velocity were measured at each of five positions down the spillway for each of two discharges. These are the most comprehensive and detailed measurements yet obtained on a large structure.

The regions of non-aerated, partially aerated and fully aerated flow down a spillway are distinguished. A dimensional analysis is used to indicate the important variables effecting the distribution of air downstream of the point of inception. This forms the basis for plotting the measurements from Aviemore plus the available measurements from laboratory flumes.

The shear stress on the spillway surface at Aviemore is calculated from the measurements.

ACKNOWLEDGEMENTS

The writer gratefully acknowledges the opportunity to undertake research within the Civil Engineering Department, University of Canterbury, and expresses his sincere thanks to the following persons:

Professor I. R. Wood who supervised this research, providing inspiration, guidance and encouragement.

Mr. A. Stokes who constructed much of the test equipment and assisted with the field tests.

Messrs. C. Rowe and D. Chambers of DAVCO who developed the electronics for the field tests. Mr. C. Rowe also provided invaluable assistance throughout all phases of the research.

Mr. P. J. Robinson who constructed electrical equipment and assisted with the field tests.

Messrs. K. D. McCool, L. Newbury and G. Symes of the New Zealand Electricity Department for their co-operation that made the field tests possible. Also, the staff at Aviemore who assisted with the measurements.

Messrs. S. M. J. Smith and J. Crawford of the Ministry of Works and Development who provided the equipment for access onto the spillway. Also, Dr. R. J. Keller who assisted with the field tests.

Mr. W. K. Kennedy of the Electrical Engineering Department who generously assisted with data analysis.

Those University staff, technicians and post-graduate students, too numerous to mention individually, whose interest and help is appreciated.

My friends, family and Lynnie for their moral support.

This study was financially supported by the University Grants Committee.

CONTENTS

LIST OF SYMBOLS

Each symbol is defined where it first appears in the text. In general, only those symbols which appear in more than one Chapter have been listed below.

A	Area
C	Air concentration
f	Frequency
L	Length
P	Static pressure
P_o	Atmospheric pressure
P_s	Stagnation pressure
t	Time
T	Intermittency parameter
V	Water velocity
y	Normal distance from spillway surface
Z	Relative response
ρ_w	Density of water
τ	Time delay

CHAPTER 1

INTRODUCTION

1.1 SUMMARY

Self-aerated flow is described in detail, and previous research is briefly surveyed. The existing test facilities at Aviemore and the conditions for their use are discussed. Initial instrument and test design considerations are also described.

1.2 INTRODUCTION

Self-aeration in open channel flow is the natural phenomenon whereby atmospheric air is drawn into and mixed with the water, creating a characteristic white appearance. This condition is possible only in high velocity flows and can frequently be observed on spillways. As air is drawn into the flow, the mixture increases in volume, or "bulks". The lack of information on the bulking effect on large structures has meant that spillways have been designed assuming non-aerated flow, and allowing a conservative margin for the height of the side walls.

1.3 FLOW DESCRIPTION

For flow over a large spillway, self-aeration commences at the point where the turbulent boundary layer (A, Fig.1.1) intersects the free surface. This point (B) is referred to as the point of inception. Downstream of the point of inception, an aerated region (C) develops which increases in thickness until the entire depth of flow is aerated. The flow in this region (F) is termed partially aerated.

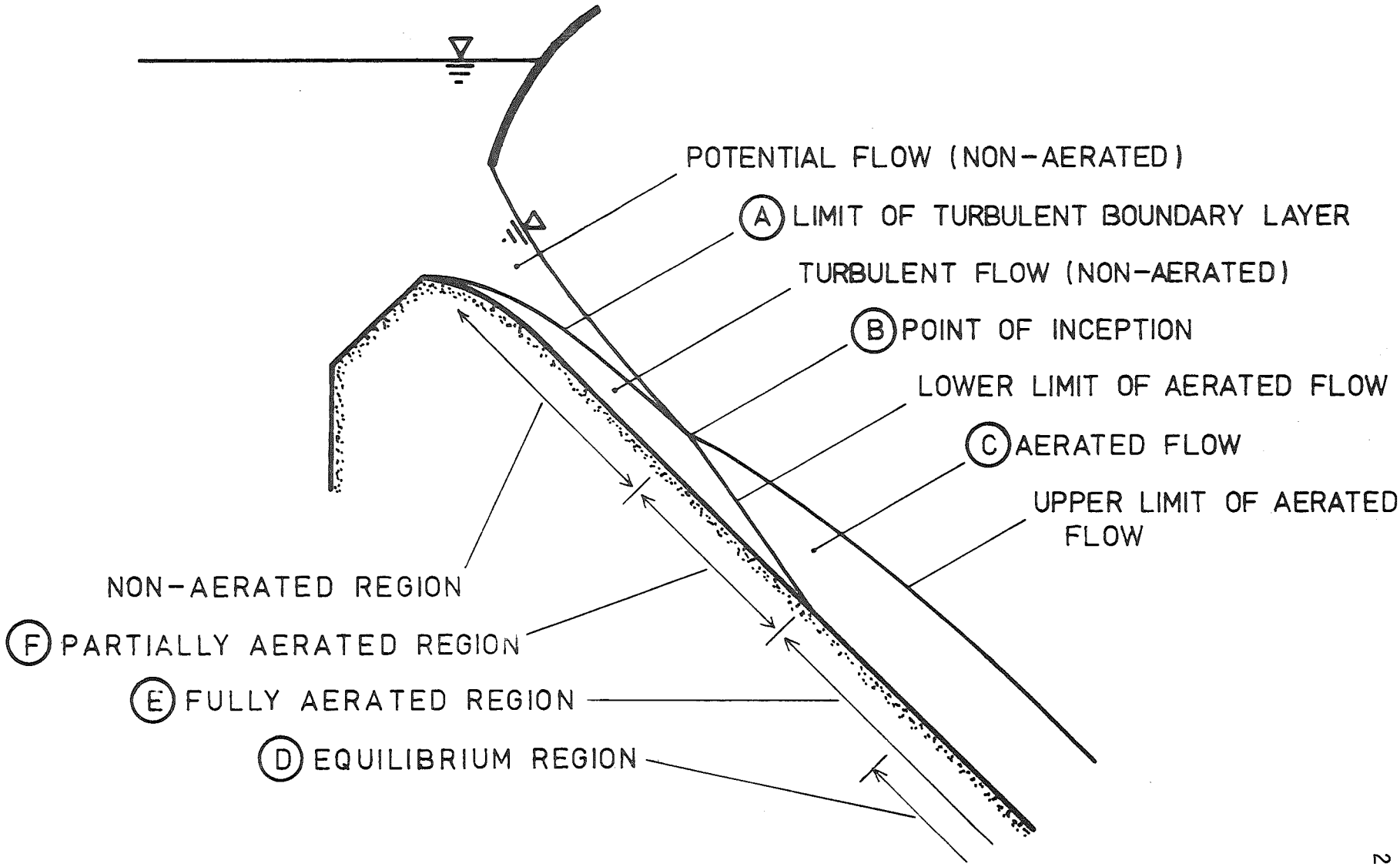

Fig. 1.1 Schematic of Longitudinal Flow Profile Down a Spillway (Flow depth exaggerated).

It has previously been speculated that further downstream still, the fully aerated flow (E) approaches a uniform or equilibrium situation (D) in which the time averaged air concentration and velocity profiles remain constant. The expression "developing aerated flow" is used to refer to the region of partially aerated flow (F) plus the region of fully aerated flow which is upstream of the uniform flow.

The growth of the turbulent boundary layer (A) is almost independent of the water discharge. The point of inception therefore moves downstream as the discharge increases. (Compare the different gate openings in the frontispiece and in Fig.1.2). The small rate of growth of the boundary layer means that self-aeration will only occur on relatively long spillways or with relatively small discharges. The aerated region also grows slowly so that fully aerated flow would only be possible for particularly long spillways or particularly small discharges.

Although the mechanism of air entrainment is not fully understood, the initial development of the aerated region is known to be dependent primarily on the intensity of the turbulence within the flow.

Aeration appears to commence when the transverse turbulent velocities are sufficiently strong near the water surface to cause clumps of water to burst through the surface into the air. These fall back by gravity into the main stream, breaking into spray and entraining air. This action intensifies until further downstream the surface has developed into a highly irregular and turbulent wave system bounded by a continuous air-water interface. The dimensions of the surface waves (spacing and amplitude) are of the same order as the depth of flow. Overturning waves are continuously entraining air beneath the water surface. This is broken into bubbles which are dispersed by the intense turbulence. The spray

Fig. 1.2 Self-Aerated Flow on the Spillway of Aviemore Dam. Spillway gates open 900, 600, 900, 600, 900 mm respectively.

projected from the violently agitated water surface may extend a considerable height above the main flow, although it contributes little to the total water discharge.

Fig. 1.3 shows the initial bursts of whiteness A-B at the onset of self-aeration. (The white streaks upstream of these are caused by vortices and are discussed later).

Fig. 1.4 illustrates the wavy nature of the surface. This was taken by panning a 35 mm camera in the direction of the flow. The flow direction and dimensions are only approximate. (These are based on the dexion just visible in the lower right hand corner. This dexion is described in Appendix A which details an unsuccessful attempt to obtain a photographic record of the flow surface). The spacing of the waves is similar in magnitude to the 300 mm depth of flow. Spray is visible over the entire photograph.

Measurements in very aerated regions of flow on the spillway of Aviemore dam indicate the distribution of air bubbles illustrated in Fig. 1.5. The flow near the water surface (A) is very aerated with air concentrations frequently in the range 0.5 - 0.9. The largest bubbles within this surface region are about 10 - 20 mm dimension. Away from the surface (B) the flow is less aerated, and the bubbles have been sheared down to about 0.5 - 3 mm dimension. This range is thought to result from an equilibrium between the agitation of the flow and a bubble's resistance to deformation due to surface tension.

Similar observations are reported by Straub and Lamb (1953) and Killen (1968) of self-aerated flow on the flume at the St. Anthony Falls Hydraulic Laboratory, Minnesota, U.S.A. High speed photographs showed that below the surface region, the bubbles were spherical and in the range 1 - 3 mm.

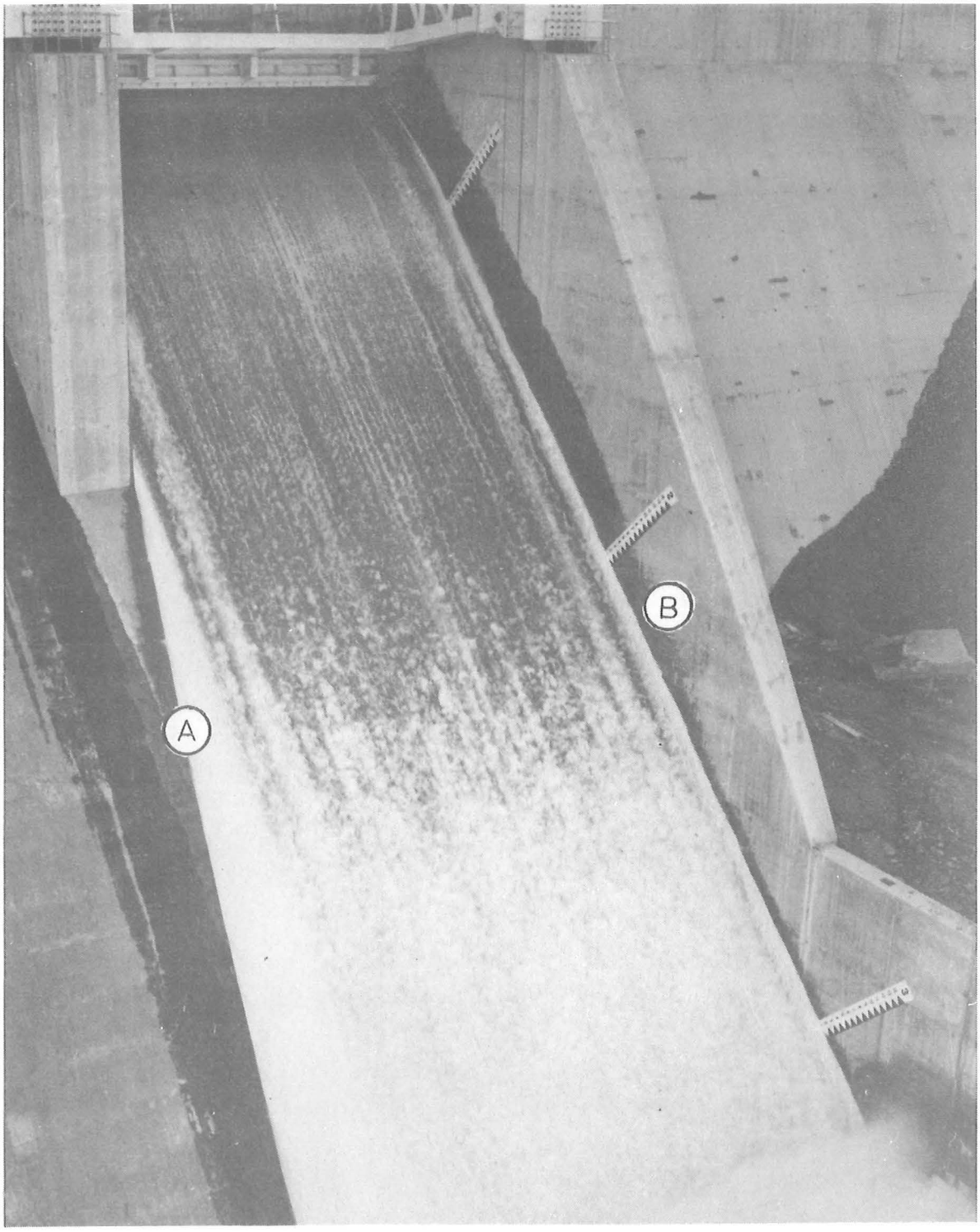

Fig. 1.3 Spillway Gate Open 600 mm.

Fig. 1.4 Surface of Self-Aerated Flow.

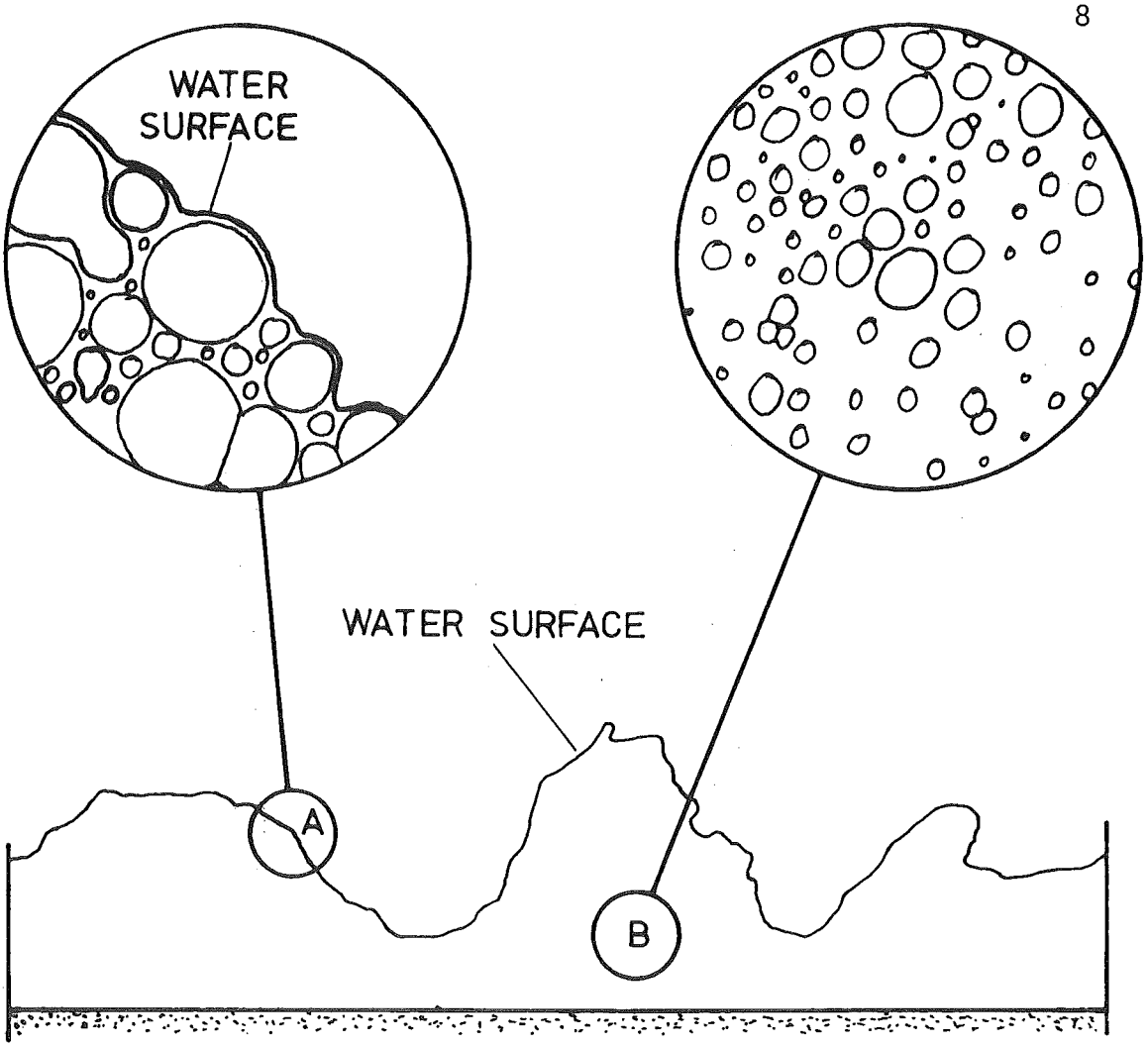

A — Largest bubbles 10 - 20 mm dimension. Air concentration within water surface as large as 0.5 - 0.9.

B — Bubble size about 0.5 - 3 mm. Air concentration less than 0.5.

Fig. 1.5 Schematic of Section Through Self-Aerated Flow (Spray not shown).

It is possible that the buoyancy of entrained bubbles will cause slip between them and the surrounding water. No information is available on this aspect.

An unrelated source of aeration on large spillways is caused by vortices originating upstream of the spillway gate. This appears as white "lines" in the direction of flow, visible between the spillway gates and the point of inception on the frontispiece and in Figs. 1.2 and 1.3. The measurements reported here show that upstream of the point of inception, vortex induced aeration is restricted to the surface region of the flow.

Each vortex lasts in the order of minutes. Their transient nature is illustrated in Fig. 1.6. This shows two photographs of the flow under the spillway gate taken within 30 seconds of each other. The position of the arrows A, B, C, D is identical in each photograph. The extent of the aeration downstream of these is different in each instance, and has moved sideways from B and C in the lower photograph. The aeration downstream of E is always present. This is caused by a gate lifting mechanism on the upstream face of the gate.

1.4 LITERATURE SURVEY

There is an extensive volume of published material on which the present knowledge of air entrainment is based. Much of this is of little relevance to this investigation. This survey is therefore restricted to those publications most relevant to self-aeration on large spillways.

It has been well established that for large spillways, the point of inception is at the interception of the turbulent boundary layer and the water surface. Bauer (1956) investigated the development of the turbulent boundary layer on a model overflow spillway. He proposed an

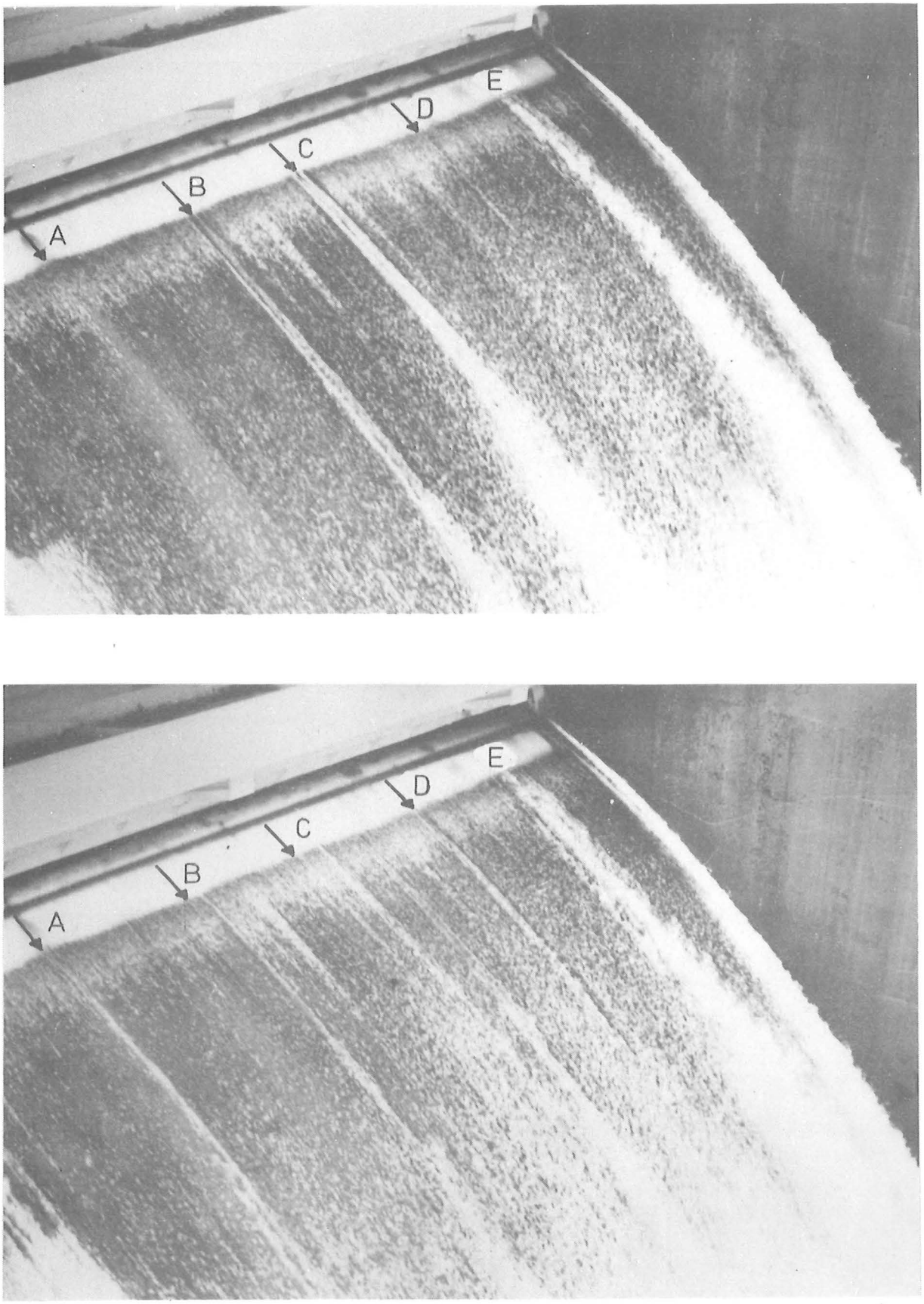

Fig. 1.6 Flow at Top of Spillway. Gate Open 300 mm

Scale : 8.2 m of gate seal visible.

approximate but practical method of calculating the longitudinal boundary layer and water surface profiles so that the point of inception can be determined. More recently, Keller and Rastogi (1975, 14) developed a computer program that predicts the velocity distribution within the boundary layer. This allows the boundary layer and water surface profiles to be determined.

On channels or flumes with low velocities (typically less than 5 m/s) the emergence of the turbulent boundary layer may result in roughening of the water surface but without any air entrainment occurring. Gangadharaiah et al. (1970) have developed a criterion for air entrainment to occur, based on the ratio of the kinetic energy of the turbulent eddies to the surface tension energy of an eddy.

Self-aerated flows on large spillways are poorly represented in hydraulic models because surface tension and resistance effects cannot be correctly modelled. In spite of this, almost all research to date has been on laboratory flumes. The main reasons for the lack of research on large structures are:

(i) problems with instrumentation and the necessary remote control,

(ii) lack of suitable test facilities plus the small range of test conditions that can be tested on any one structure,

(iii) the large expense of such research.

The development of suitable instrumentation for measurement of air concentration and velocity within aerated flows presents formidable problems even today. In the past, this has severely limited the accuracy of most measurements.

A major advance in instrumentation was the development by Lamb and Killen (1950) of an electrical resistance method for measuring the air concentration between two electrodes. This was followed by a sophisticated velocity instrument developed by Straub, Killen and Lamb (1954). This measured the time for a small slug of salt solution to travel the known distance between two pairs of electrodes aligned with the flow.

Using these two instruments, Straub and Anderson (1958) conducted a series of experiments at the St. Anthony Falls Hydraulic Laboratory. They obtained measurements near the end of a 15 m long flume for a wide range of flume slopes and water discharges. In each case, they adjusted the inlet flow conditions to achieve what they considered was uniform flow at the measurement section. It is shown in Chapter 11 that this procedure complicates the interpretation of their measurements.

Prior to, and even since the development of these instruments, most researchers have predicted the velocity from measurements of air concentration and stagnation pressure. This method has the disadvantage that at high air concentrations, the relationship used is very sensitive to errors in either measurement.

Keller (1972) used this approach to obtain measurements on the spillway of Aviemore dam. He used an electrical method to measure air concentration, based on Lamb and Killen's (1950) method. His results are of limited use, mainly because of the large probe spacing.

The writer considers that the only useful measurements published to date are those of Rao et al. (1970) and Lai (1971) on laboratory flumes. Both measured the air concentration by sampling the aerated flow through a tube and separating the air and water phases to measure their relative proportions. The tube was then used to measure the stagnation pressure

in order to predict the velocity.

One aspect of self-aerated flows that has received little attention is the aeration at the side walls caused by the growth of a boundary layer along the wall, (see Fig. 1.7). The bulking of the flow at the side wall is in fact likely to govern the minimum wall height required. This was considered beyond the scope of the investigation reported here.

Another aspect that has received little if any attention until now is the compressible nature of self-aerated flows. It has been well established for instance that at atmospheric pressures, the speed of sound in two-phase homogeneous air-water mixtures with air concentrations from 0.2 - 0.8 is about 25 m/s. On large spillways, velocities are well in excess of this. The effects of compressibility and the possible formation of shock waves must therefore be considered when interpreting measurements.

1.5 EXISTING TEST FACILITIES AT AVIEMORE

The spillway of Aviemore Dam had some unique test facilities incorporated into it during construction. These facilities make it a suitable site for obtaining measurements in self-aerated flows. Spillway bays 4 and 5 each have five test stations located at 6.10 m intervals down the spillway as shown in Fig. 1.8. These have been designated N01 for the top test station to N05 for the bottom one where N is the spillway bay number, 4 or 5. Each test station is a steel box 460 x 460 x 460 mm set into the concrete, with a removable steel cover plate 610 x 610 x 25 mm. The cover plate is recessed flush with the spillway surface and secured to the box with countersunk stainless steel screws. These test stations are

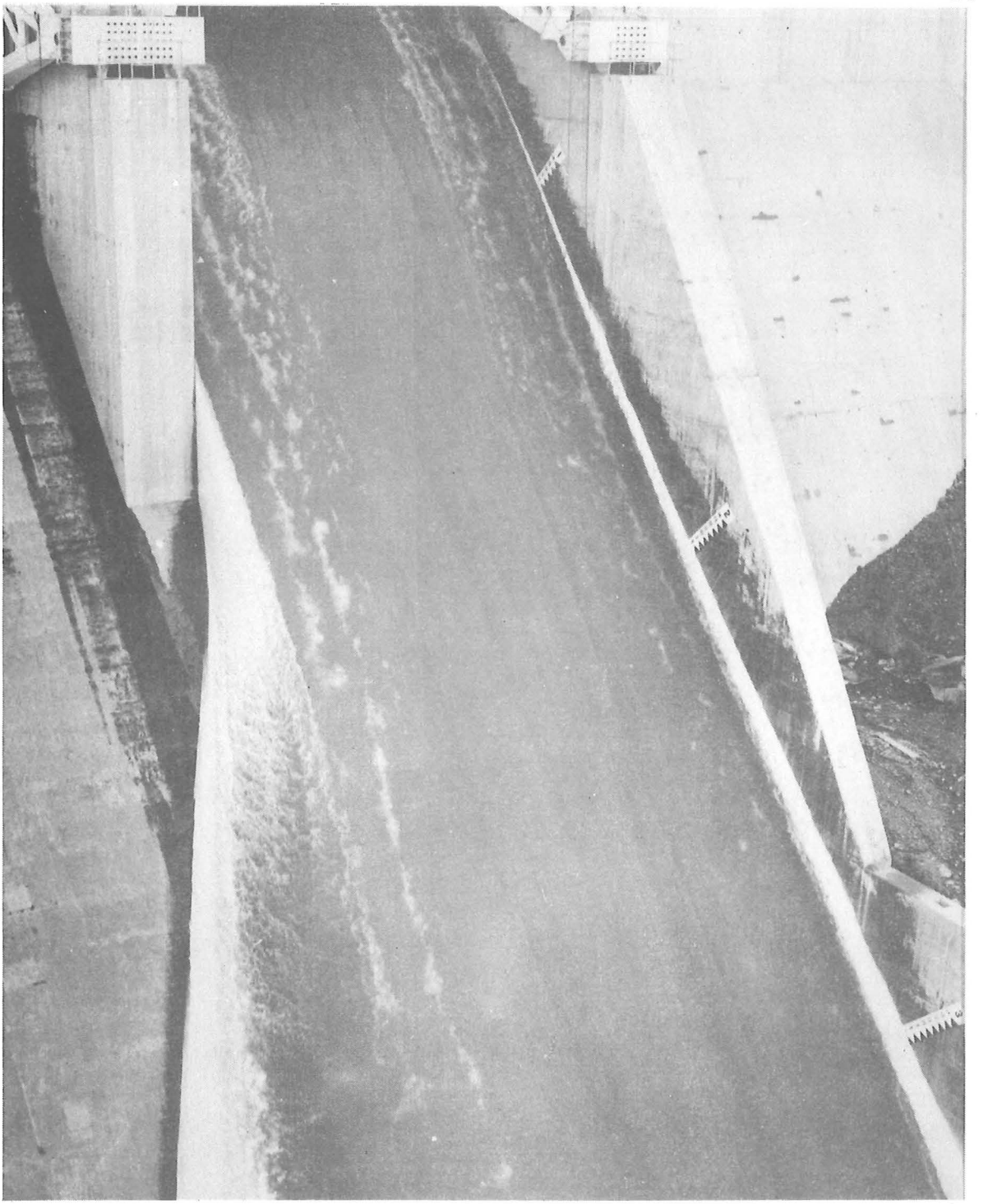

Fig. 1.7 Side Wall Induced Aeration.

Spillway gate fully open.

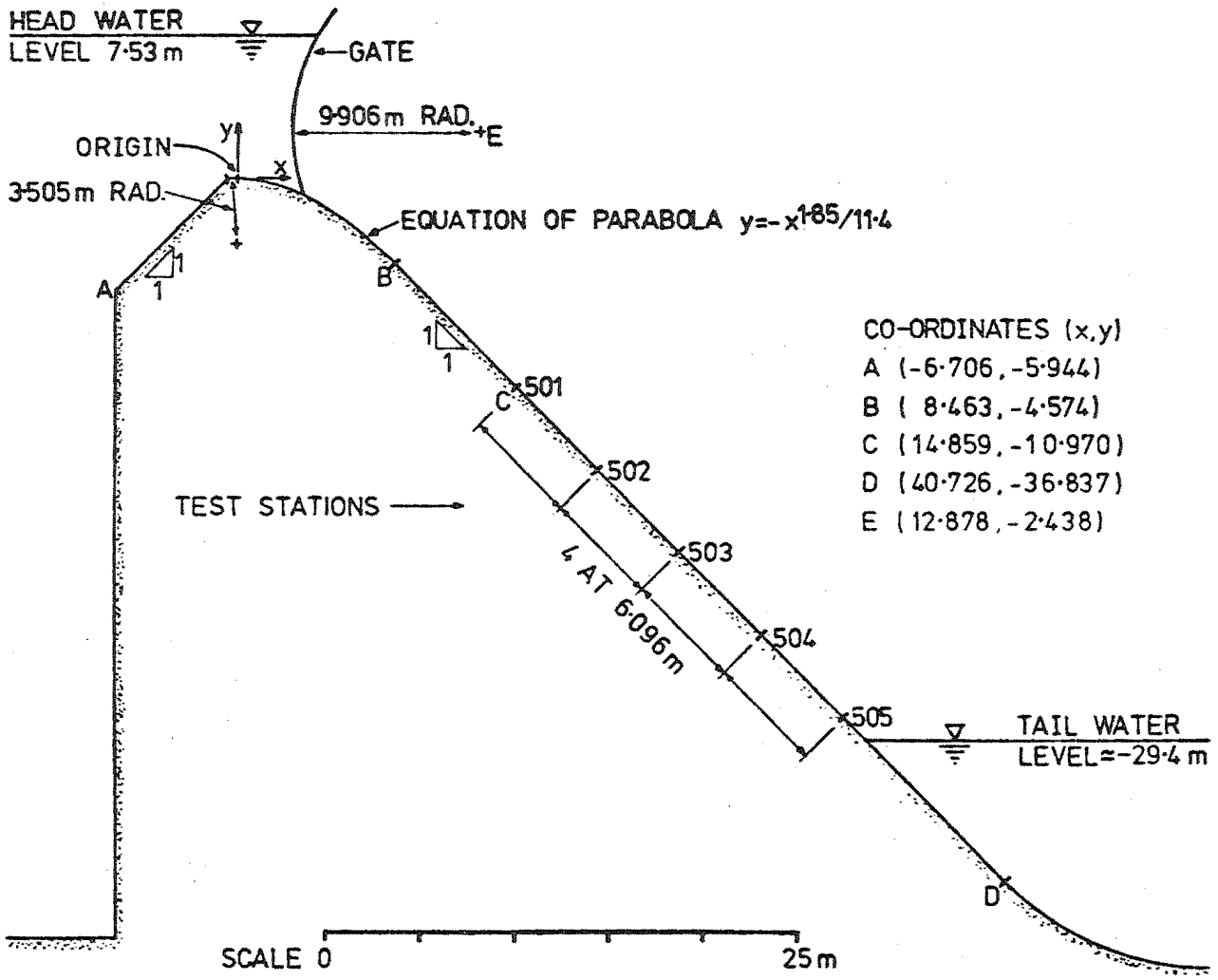

Fig. 1.8 Dimension Sketch of Spillway and Test Stations.

visible in Fig. 7.5. The stations are interconnected with 150 mm diameter pipe embedded 300 mm below the spillway surface. Each is served via these pipes by a separate cable which terminates at the spillway side wall, adjacent to a recording hut. Access to the test stations is by a "skip" which is lowered from the top of the dam by a crane. This was modified specially for the tests reported here and is shown in Fig. 7.5.

1.6 TEST CONDITIONS

A serious limitation in using thest test facilities was the condition imposed for the controlled release of water; namely that there was excess water available that could not be used for electricity generation and therefore had to be spilled. Such forced spills are infrequent and unpredictable. In fact, no spillage occurred at Aviemore for about three years prior to the initial field tests at Aviemore in April 1975.

1.7 INITIAL INSTRUMENT AND TEST DESIGN CONSIDERATIONS

The principal object of this research as initially envisaged was to obtain detailed measurements of stagnation pressure, air concentration and velocity within the developing region of self-aerated flow on the spillway of Aviemore Dam. As Keller (1972) had previously attempted to obtain the same data, his recommendations strongly influenced the initial direction of this research. It was initially, and incorrectly, believed that the measurement principles he employed could be successfully adapted to allow accurate data to be obtained.

His field test equipment is shown fixed on the spillway in Fig. 1.9. This consisted of two columns of instruments, 305 mm apart. The first had twelve total pressure probes at 50.8 mm intervals, and the second had twelve air concentration probes. The output signals were recorded digitally on paper tape at a rate of 2 samples per second. Each probe was sampled for about 1 minute.

This project therefore involved modifying and improving his instrumentation and measuring techniques to overcome their serious limitations, and to design test equipment to utilise the existing test facilities at Aviemore. The major modifications considered necessary were:-

(i) the design of an instrument that measured the stagnation pressure and air concentration at the same point in the flow,

(ii) the recording of both measurements simultaneously,

(iii) reduction of the probe size so that it was small compared with the depth of flow,

(iv) the use of only one probe that could be remotely traversed through the depth of flow.

Keller's results indicated that the aerated region was a significant proportion of the flow only for gate openings less than 600 mm. For openings smaller than about 150 mm, the shape of the spillway gate seal causes the water to leave the spillway surface, as shown in Fig. 1.10. The tests were therefore planned for 300 and 450 mm gate openings. Keller's results indicated the maximum depth of flow at any test station would be in the range 200 - 350 mm.

Note: These gate openings are taken from a dial on top of the dam and are used throughout this report. The actual distance between the gate is not accurately recorded by the dial (ref. section 9.4).

Fig. 1.9 Keller's (1972) Field Test Equipment in Aerated Flow, Viewed from the Top of the Dam.

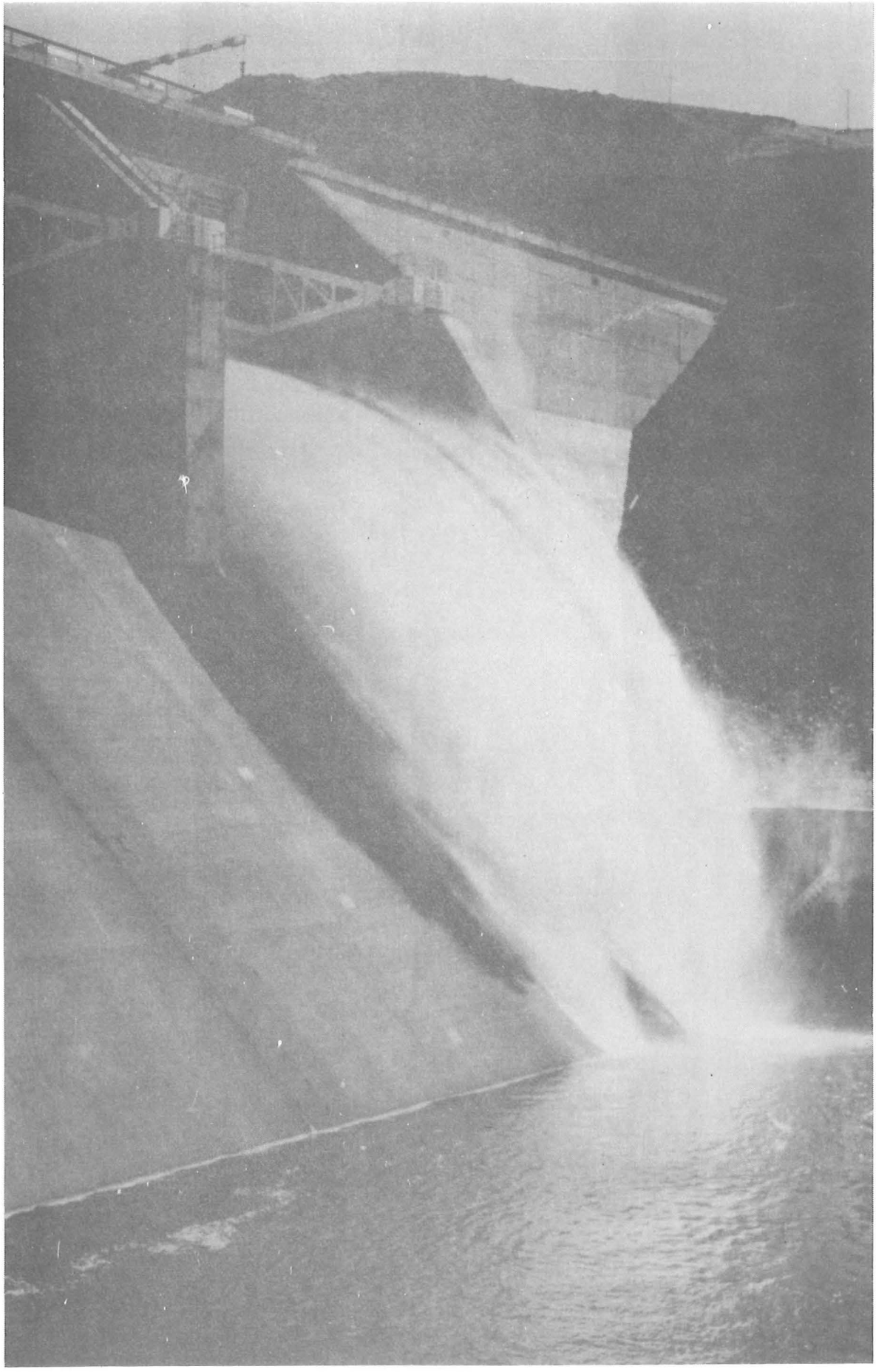

Fig. 1.10 Spillway Gate Being Opened.

CHAPTER 2

VELOCITY PREDICTION FROM AIR CONCENTRATION AND STAGNATION PRESSURE

2.1 SUMMARY

An expression is developed which relates the velocity in self-aerated flows to measurements of stagnation pressure and air concentration. This takes into consideration the non-homogeneous and compressible nature of bubbly flows approaching a stagnation point, plus the effects of large air gaps in wavy regions of flow.

2.2 INTRODUCTION

The initial aim of this research was to obtain profiles of stagnation pressure, air concentration and velocity within self-aerated flows on the spillway of Aviemore Dam. Based on Keller's (1972) research it was decided to develop an instrument that could simultaneously measure stagnation pressure and air concentration at the same point. It was expected that these measurements could be accurately related to the velocity.

It will be shown in Chapter 3 that the air concentration can be successfully measured with minimal disturbance to the flow. However the stagnation pressure measured with a total pressure probe will in general be different from the total pressure of the undisturbed flow. This difference is caused primarily by the large pressure gradients in the vicinity of the stagnation point.

The possible formation of shock waves in front of a total pressure probe further complicates the situation. It has been well established that the speed of sound in homogeneous air-water mixtures at atmospheric pressures is approximately 25 m/s for air concentrations from 0.2 - 0.8. Velocities well in excess of this can be expected on large spillways. In spite of this, little if any consideration has previously been given to compressibility effects within self-aerated flows.

Any relationship between velocity, stagnation pressure and air concentration should also take into account the wide range of flow conditions expected within self-aerated flows.

An expression for the velocity within self-aerated flows is developed in this chapter. The expressions presented here are evaluated in Chapter 10 with the measurements obtained on the Aviemore spillway.

2.3 FLOW RELATIONSHIPS

2.3.1 Speed of Sound

The speed of sound within an aerated flow depends on the nature of the air-water mixture. In self-aerated flows, the distribution of air is continuously changing so that the speed of sound will vary continuously. To derive an expression for the speed of sound in self-aerated flows, consider firstly a homogeneous mixture of air bubbles in water.

Eddington (1967) has shown that over a wide range of conditions, such a mixture can be treated as an isothermal continuum for the propagation of pressure (or sound) waves provided the bubbles are less than 0.1 mm diameter and the distance between bubble centres is less than half the wave length. This latter restriction limits the maximum frequency

of the pressure wave. If the bubbles' diameter is increased, the heat generated within them during the passage of a pressure wave takes longer to dissipate to the surrounding water. For high frequency pressure waves in self-aerated flows, the larger bubbles (0.5 - 20 mm) will therefore tend to behave adiabatically rather than isothermally. Gouse and Brown (1963) have shown that the adiabatic and isothermal speeds of sound are in fact identical providing the air concentration is less than 0.99. This will always be the case in self-aerated flows.

It seems possible that in self-aerated flows a slip velocity will exist between entrained air bubbles and the water surrounding them (ref. Section 1.3). Gouse and Brown have derived an expression for the speed of sound which takes slip into account. For bubble velocities as small as half the water velocity, the speed of sound is almost identical to that with no slip. The effect of slip on the speed of sound in self-aerated flows is therefore considered insignificant.

It is shown in Appendix B that for a homogeneous bubbly air-water mixture that can be considered an isothermal continuum, the speed of sound S in the continuum is given by

$$S = \left[\frac{P}{\rho_w C\ (1-C)}\right]^{\frac{1}{2}} \qquad 2.1$$

where P = static pressure (abs)

ρ_w = water density

C = air concentration

This is plotted in Fig. 2.1 for a static pressure equal to atmospheric pressure (102 kN/m^2 abs). This is a representative value for all spillways at sea level because of the relatively small range of flow depths expected (ref. Appendix C). This illustrates the remarkably low speed

of sound possible within an aerated flow compared with an all water or all air flow.

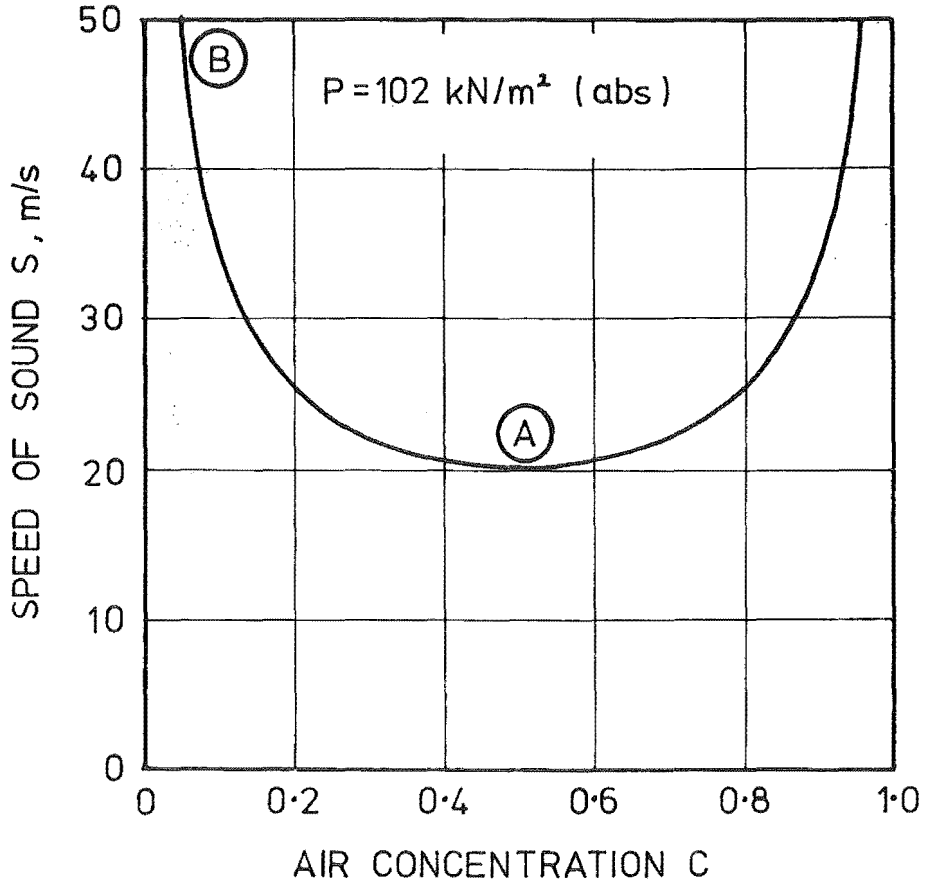

Fig. 2.1 Isothermal Speed of Sound.

The Mach number M for a flow is defined as

$$M = \frac{V}{S} \qquad 2.2$$

where V = velocity.

The maximum flow velocities on large spillways will often be in the range 25 - 50 m/s (ref. Appendix C). In localised regions within self-

aerated flows, supersonic velocities would therefore appear possible with Mach numbers as large as 1 - 2.

2.3.2. Shock Structure

The shock structure in a homogeneous bubbly air-water mixture is determined by the dynamic and thermal behaviour of the bubbles. A bubble entering a shock will be compressed, overshooting and oscillating about its equilibrium size. These subsequent oscillations are thought to be highly damped. During this compression, the air temperature within the bubble can increase significantly, depending upon the bubble size, the pressure increase and how rapidly compression is accomplished. The bubble will approach its final equilibrium size as the air cools to the water temperature. The cooling time is much longer than that involved with bubble dynamics.

For self-aerated flow on spillways, the shock structure will be dependent mainly on the bubble size. The "characteristic times" for the initial compression of a bubble t_c and the subsequent cooling of the air to reach 10% and 90% of its thermal equilibrium t_{10} and t_{90} are shown in Fig. 2.2, adapted from Eddington (1967).

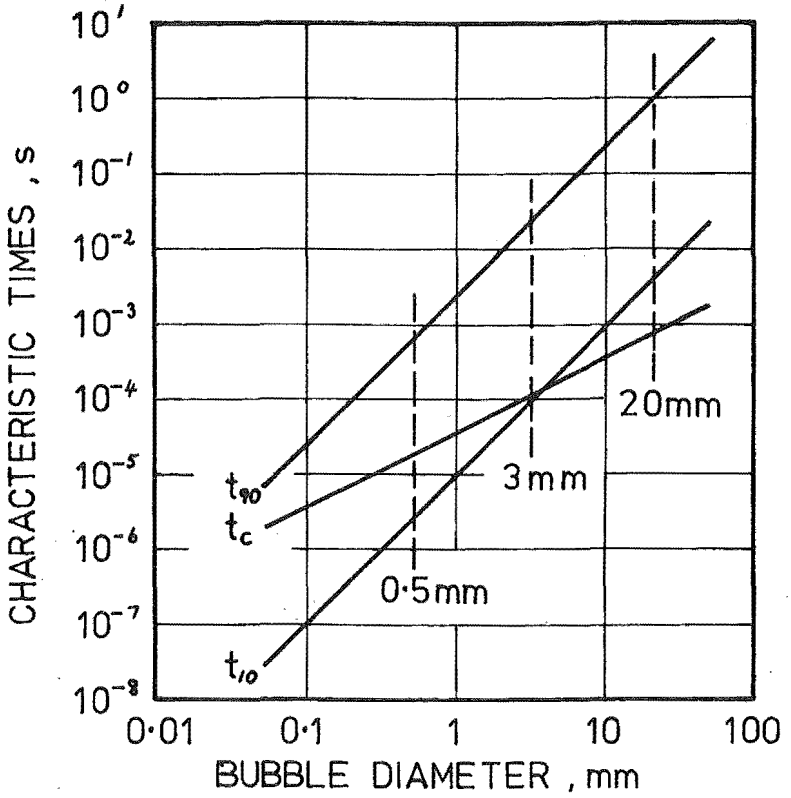

Fig. 2.2 Initial Compression and Cooling Times for Bubbles (following Eddington, 1967)
P = 102 kN/m^2 (abs), T = 20^{o}C.

Expressions for the flow parameters downstream of a normal shock structure are given in the next section. Subscript 1 is used to denote the region upstream of the shock, subscript 2 the region downstream.

Using the expression for the velocity downstream of a shock, it has been possible to estimate the shock thickness for self-aerated flows representative of those on large spillways. These are shown in Table 2.1. Three bubble sizes were chosen 0.5, 3 and 20 mm. The upstream velocities V_1 = 23.3 and 46.7 m/s were chosen to correspond with Mach numbers equal to 1 and 2 respectively.

Table 2.1 Shock Thickness in Self-Aerated Flows

Thickness evaluated for 0.5, 3, 20 mm diameter bubbles using Eqs 2.1, 2.2 and 2.5 and taking $C_1 = 0.25$ and $P_1 = 102$ kN/m^2 (abs). t_c, t_{10} and t_{90} are taken from Fig. 2.2.

	Bubble Diameter mm	Velocity V_1 m/s	
		23.3	46.7
Distance for initial bubble compression = $V_1 t_c$, mm	0.5	0.5	0.9
	3	2.3	4.7
	20	16	33
Distance for 10% thermal equilibrium = $V_2 t_{10}$, mm	0.5	0.1	0.1
	3	2.3	3.8
	20	92	150
Distance for 90% thermal equilibrium = $V_2 t_{90}$, mm	0.5	19	30
	3	610	990
	20	23×10^3	38×10^3

The shock thickness associated with bubble dynamics is seen to be similar in size to the bubble diameter. For the bubbles 0.5 - 3 mm dimension, the thermal relaxation process extends the shock thickness by hundreds of millimetres. For the 20 mm diameter bubbles, the thermal relaxation process extends the shock thickness by 20 - 40 m.

2.3.3 Shock Relationships

For a homogeneous bubbly air-water mixture flowing through a normal shock structure the most important flow parameters can be derived from the conservation of mass and momentum and the isothermal equation of state. Following Eddington (1967) the relaxation processes within the shock can be ignored and the above equations can be applied to both sides of the shock structure. If subscript 1 denotes the region upstream of the shock and subscript 2 the region downstream, then

$$P_2 = M_1^2 P_1 \qquad 2.3$$

$$C_2 = \left[1 + \frac{1 - C_1}{C_1} M_1^2 \right]^{-1} \qquad 2.4$$

$$V_2 = V_1 \left[1 - C_1 + \frac{C_1}{M_1^2} \right] \qquad 2.5$$

$$M_1 M_2 = 1 \qquad 2.6$$

These relationships have been derived in Appendix B. Eddington has confirmed them for $C_1 \simeq 0.5$ and $V_1 = 40 - 100$ m/s and has extended the analysis to oblique shock waves.

2.4 VELOCITY PREDICTION IN AERATED FLOWS

2.4.1 Introduction

Consider now the behaviour of a homogeneous bubbly air-water flow as it approaches the stagnation point of a total pressure probe.

Eddington (1967) has observed that if the flow is supersonic it is possible for a detached shock wave to form in front of the probe. This is clearly shown in Fig. 2.3, taken from Eddington. The distinguishable portion of the shock is that which is associated with the initial

collapse and rebound of the bubbles. The distance required for completion of the relaxation processes was much larger than the distance between the shock leading edge and the probe inlet. His probe was therefore sampling within the shock structure.

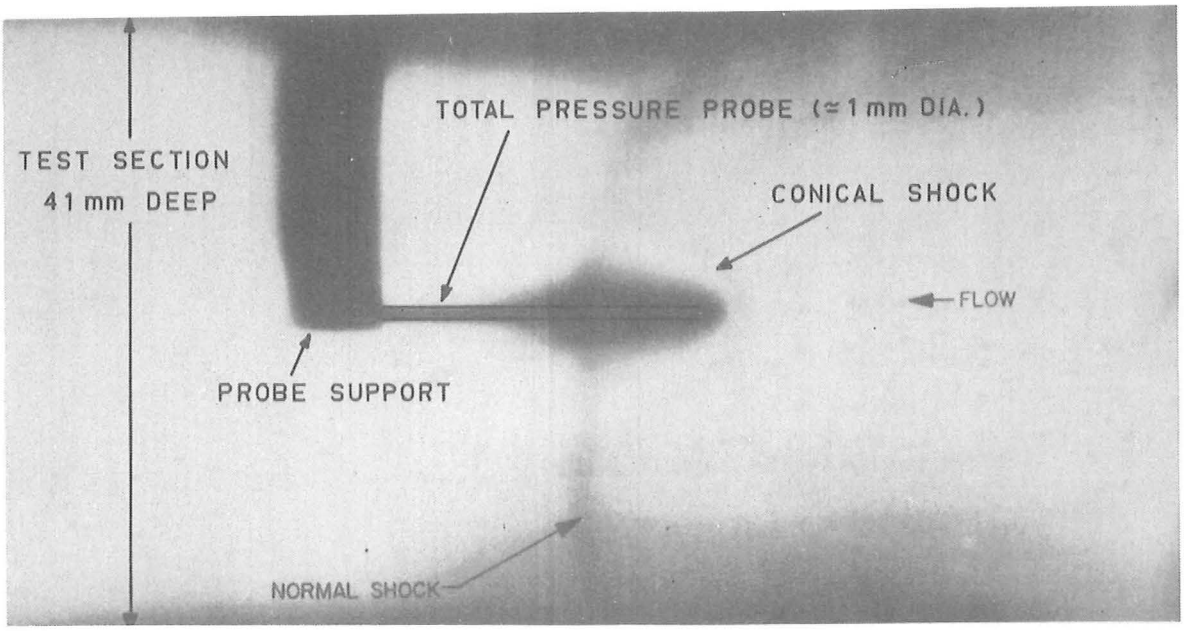

Fig. 2.3 Shock Wave in Front of Probe

(From Eddington 1967).

Upstream flow conditions : V = 84 m/s, C ≃ 0.48, M ≃ 4.

Several factors reduce the likelihood of shock formation in front of a probe:

(i) It seems likely a shock will not occur except in homogeneous flow in which the probe is much larger than the bubble size and spacing.

High speed photographs of Eddington's (1967, p.55) flows upstream of a shock showed a "bubble structure of two basic size groups in a water matrix. These bubble sizes were about 0.1 - 0.5 mm and 0.5 - 1.5 mm and were generally formed into chain-like groups oriented in the direction of flow". The entrance of these chains into the shock front compressed the bubbles and destroyed their connecting chain structure. By comparison with this range of bubble sizes, his total pressure probe was about 1 mm diameter.

(ii) Sterlini and Trotignon (1971) have used a combination of theory and experiment to show that the very high pressure gradients surrounding a stagnation point cause the bubbles to "slip" or "migrate" as they approach it. The air concentration decreases to zero along the streamline leading to the stagnation point causing the speed of sound to increase (A to B in Fig. 2.1). The flow can therefore change from supersonic to subsonic without the formation of a shock wave in front of the probe.

(iii) In self-aerated flows the proximity of the free surface might prevent shock formation.

Sterlini and Trotignon's results also indicated that:

(i) Bubbles larger than 0.1 mm diameter will be compressed almost adiabatically when approaching a stagnation point.

(ii) The stagnation pressure measured in a bubbly flow will increase as the probe diameter is decreased. This is caused by the slip between the bubbles and the water in the vicinity of the stagnation point.

Some laboratory tests (ref. Section 6.5.3) were conducted to investigate this latter observation. Probes 1.1, 6 and 19 mm diameter were tested in an aerated flow which simulated conditions within self-aerated flows. In these tests, the measured stagnation pressure was insensitive to the probe diameter.

2.4.2 Velocity Prediction in Homogeneous Flows

An expression for velocity that could accurately describe the behaviour of bubbly air-water flows approaching a total pressure probe would necessarily be very complex (see for instance Sterlini and Trotignon, 1971). The only suitable expressions developed to date assume that the flow appears homogeneous to the probe. This assumption requires that the air-water structure is small compared with the dimensions of the probe's measurement region. If the air-water structure is large compared with the probe's measurement region, the flow will appear non-homogeneous to the probe.

Four expressions are presented below, each based on a different simplified flow behaviour. They all assume a homogeneous flow with no friction losses and no slip between the bubbles and the water.

(i) In subsonic flow in which the Mach number is much less than 1.0, the air-water mixture can be considered incompressible with density $\rho_w(1-C)$. From Bernoulli's equation

$$V = \left[\frac{2}{\rho_w}\left[\frac{P_s-P}{1-C}\right]\right]^{\frac{1}{2}} \qquad 2.7$$

where P_s = stagnation pressure.

(ii) For isothermal flow which is either subsonic or supersonic with shock-free deceleration to the stagnation point

$$V = \left[\frac{2}{\rho_w}\left[P_s-P + \frac{C}{1-C}\,P\,\ln\left[\frac{P_s}{P}\right]\right]\right]^{\frac{1}{2}} \qquad 2.8$$

This is derived in Appendix B.

(iii) In subsonic or supersonic flow with shock-free deceleration to the stagnation point, and for which the compression of the bubbles is adiabatic

$$V = \left[\frac{2}{\rho_w} \left[P_s - P + \frac{C}{1-C} P \frac{\gamma}{\gamma-1} \left[\left[\frac{P_s}{P} \right]^{\frac{\gamma-1}{\gamma}} - 1 \right] \right] \right]^{\frac{1}{2}} \qquad 2.9$$

where $\gamma = 1.4$, the ratio of specific heats for air.

(iv) For supersonic flow in which a detached shock wave forms in front of the probe as in Fig. 2.4 the normal shock relations Eqs. 2.3 - 2.6 can be applied from 1-2 (Fig. 2.4) and the expression for stagnation pressure recovery Eq. 2.8 can be applied from 2-3. This assumes that the shock relaxation processes are completed at 2 before the flow decelerates to the stagnation point and that the flow is isothermal. It is shown in Appendix B that

$$V = \frac{\left[\frac{2}{\rho_w} \left[P_s - M^2 P + \frac{C}{1-C} P \ln \left[\frac{P_s}{M^2 P} \right] \right] \right]^{\frac{1}{2}}}{\left[1-C + \frac{C}{M^2} \right]} \qquad 2.10$$

where $M^2 = \frac{V^2 \rho_w C(1-C)}{P}$

and where V, P, C, M refer to the undisturbed flow upstream of the normal shock.

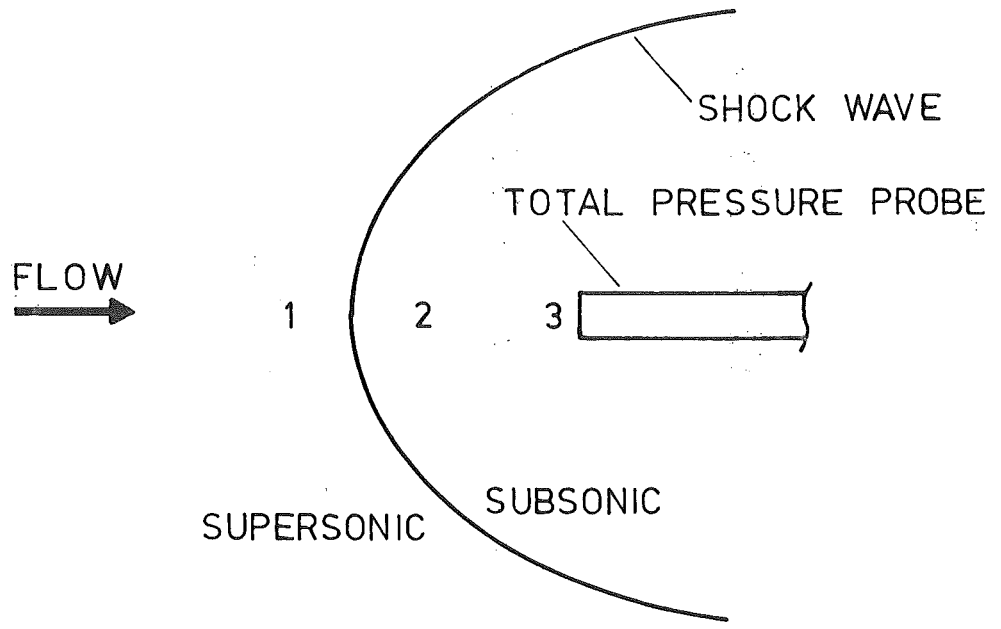

Fig. 2.4 Schematic of Shock Wave in Front of Pressure Probe.

The only published experimental data known to the writer that is suitable for comparison of these expressions was obtained by Eddington (1967) who used a total pressure tube to measure the stagnation pressure for each of five flow conditions. His measurements are shown in Fig. 2.5 together with the corresponding velocities predicted by Eqs. 2.7 to 2.10. This data has been listed in Table 2.2 for clarity. The velocities range from 45 - 102 m/s, much larger than the 12 - 22 m/s later measured at Aviemore.

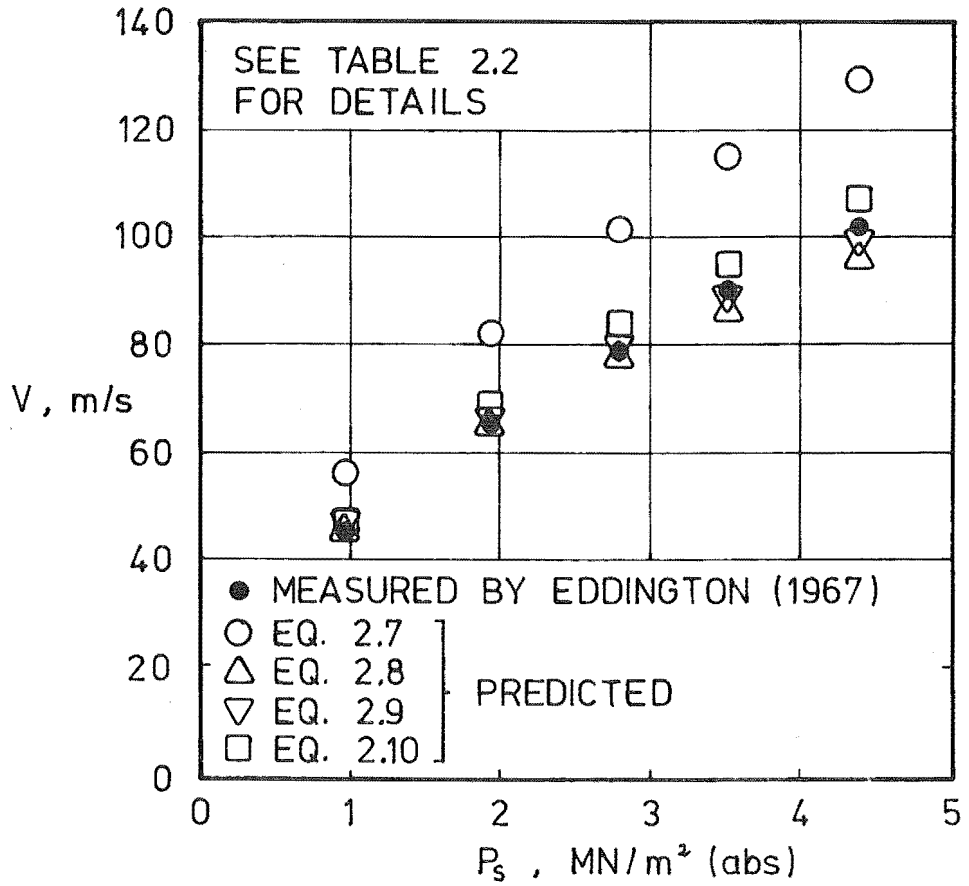

Fig. 2.5 Comparison of Measured and Predicted Velocity (P = 98 kN/m^2 (abs))

Table 2.2 Comparison of Measured and Predicted Velocity

($P = 98\ kN/m^2$ (abs))

Measured by Eddington (1967)	Stagnation Pressure P_s, MN/m^2 (abs)	0.99	1.95	2.8	3.5	4.4
	Air Concentration C	0.435	0.46	0.475	0.485	0.49
	Velocity V, m/s	45	65	79	90	102
Predicted	Velocity Eq. 2.7	56	83	101	115	130
	Velocity Eq. 2.8	46	65	77	87	97
	Velocity Eq. 2.9	48	67	80	89	100
	Velocity Eq. 2.10	48	69	84	95	107

Sterlini and Trotignon (1971) have reported similar measurements at velocities from 10 - 25 m/s and 40 - 60 m/s for air concentrations from 0.5 - 0.55 and 0.8 - 0.85 respectively. They stated that their results indicated Eq. 2.8 overestimated the velocity by about 5% and underestimated by 2 - 3.5% in each of the range of flows.

These discrepancies between the measured and predicted velocities can be attributed to the phenomenon of slip and thermal exchanges between the bubbles and water.

The maximum velocities to be expected on the spillways of large structures will be about 25 - 50 m/s so that although not strictly applicable, Eq. 2.8 provides the best estimate of velocity. Eq. 2.8 has therefore been used as the basis for deriving an expression which is applicable within the non-homogeneous wavy regions of self-aerated flows. This expression was developed to improve the accuracy of velocity predictions on the Aviemore spillway.

2.4.3 Application to Self-Aerated Flows

Consider an instrument which can measure stagnation pressure and air concentration at a "point". If this point is large relative to the bubble size and spacing within a self-aerated flow, the bubbly mixture within the water surface will appear homogeneous. In wavy regions of flow, the measurement region is sometimes in large air gaps (BC and DE, Fig. 2.6) and sometimes in the homogeneous bubbly flow within the water surface (AB and CD).

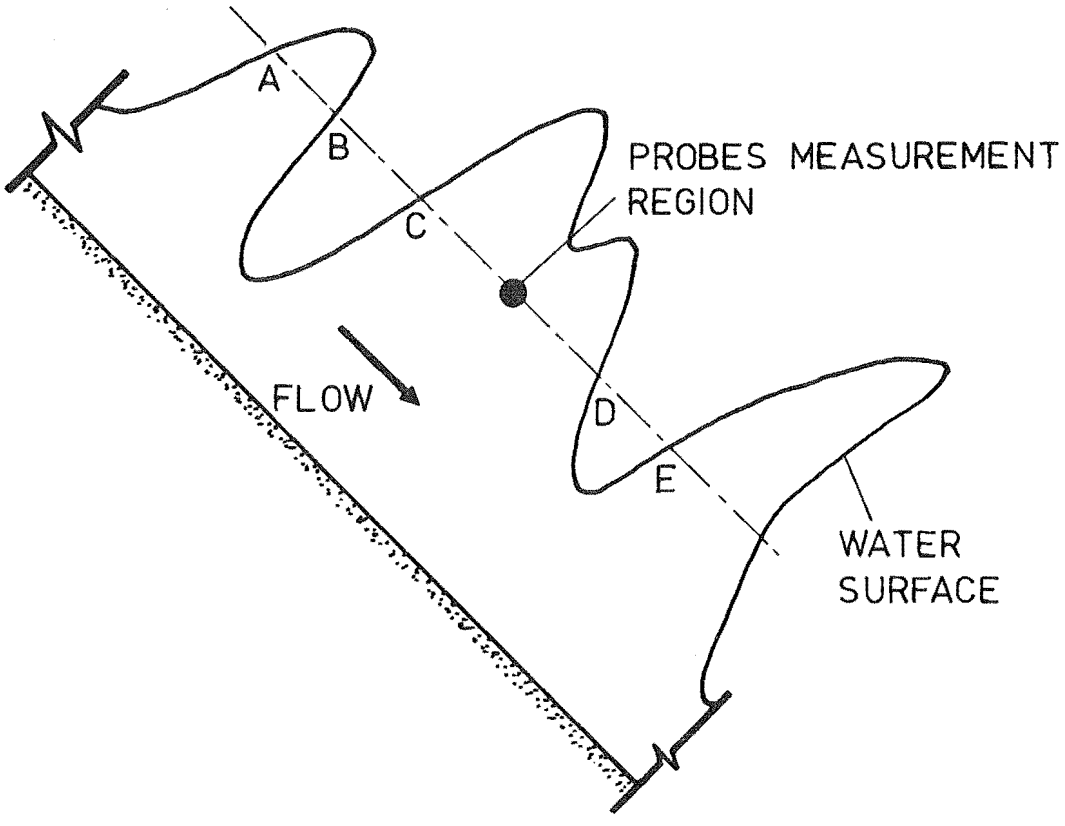

Fig. 2.6 Schematic of Probe in Self-Aerated Flow.

Eq. 2.8 can only be applied when the measurement region is in the homogeneous bubbly flow (AB and CD). In a wavy region of flow, this would require fast response instruments plus sophisticated analysis techniques.

It would be much simpler if the mean velocity could be calculated from mean values of stagnation pressure $\overline{P_s}$ and air concentration $\overline{C}$, each measured over a long time interval during which both large air gaps and homogeneous bubbly flow passed the probe.

In order to derive an expression for the mean velocity, an "intermittency parameter" T will be introduced. Initially, this will be simply defined as the proportion of time that the probe's measurement region is within the water surface. (This definition will later be modified because at Aviemore, it was found that the largest bubbles were larger than the probe's measurement region. Such bubbly flow does not appear homogeneous to the probe).

The expression for the mean velocity can be derived with reference to the simplified model shown in Fig. 2.7. During the interval $T < t \leq 1.0$, the probe is assumed to be in a large air gap. During the interval $0 \leq t < T$, the probe is assumed to be in a homogeneous bubbly flow within the water surface. The air concentration C' and velocity V' are assumed constant over this interval (C' and V' can be considered mean values over this time interval because they will not usually be constant).

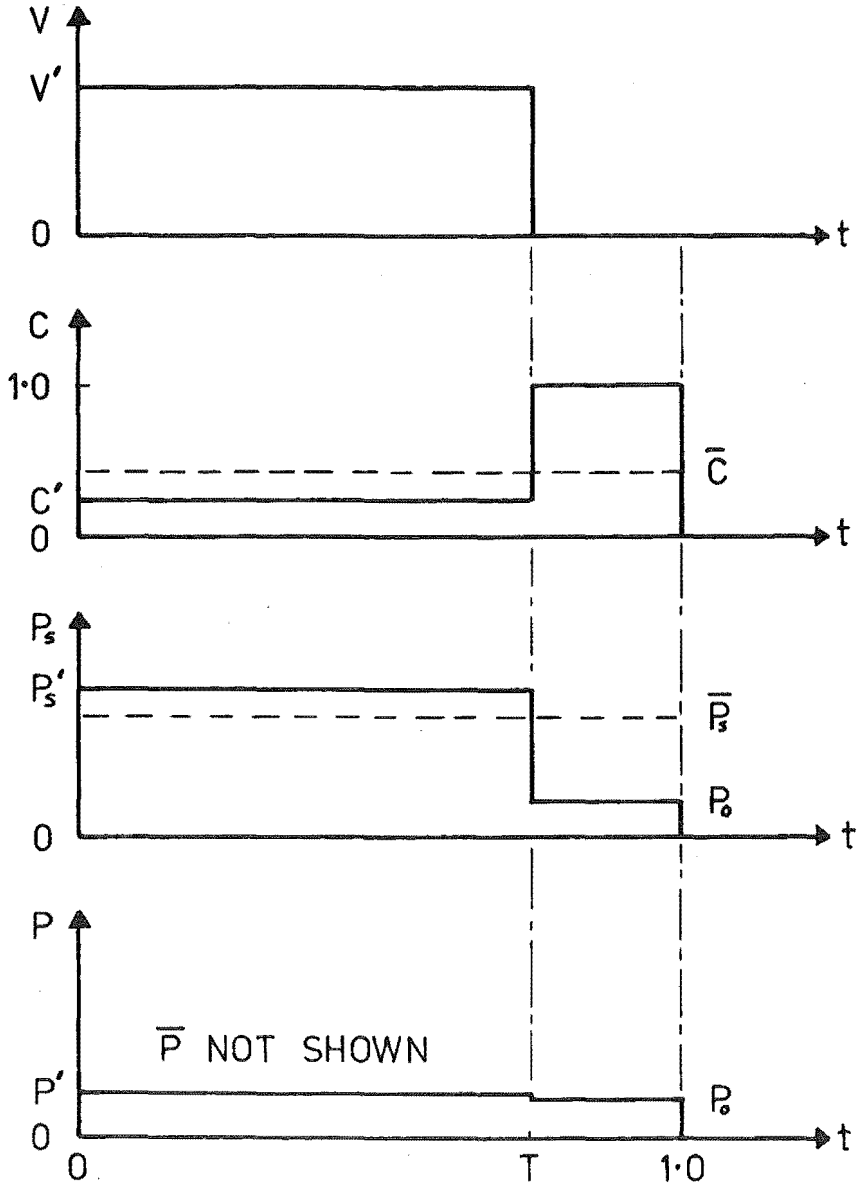

Fig. 2.7 Simplified Aerated Flow Model.

Primed values refer to the interval $0 \leqslant t < T$.

Pressures are absolute. P_o = atmospheric pressure.

From Fig. 2.7, we see that

$\bar{C} = C'T + (1-T)$ so that

$$T = \frac{1-\bar{C}}{1-C'} \qquad 2.11$$

$$C' = \frac{\bar{C} - (1-T)}{T} \qquad 2.12$$

Similarly

$P_s = P_s' T + P_o(1-T)$ and

$$\overline{P} = P'T + P_o(1-T)$$

where P_o = atmospheric presure, so that

$$\left.\begin{aligned} P_s' &= \frac{\overline{P_s} - P_o}{T} + P_o \\ P' &= \frac{\overline{P} - P_o}{T} + P_o \end{aligned}\right\} \quad 2.13$$

Eq. 2.8 can be evaluated over the portion of time T for which C ≠ 1.0 as

$$V' = \left[\frac{2}{\rho_w}\left[P_s' - P' + \frac{C'}{1-C'} P' \ln\left[\frac{P_s'}{P'}\right]\right]\right]^{\frac{1}{2}}$$

Substituting Eqs. 2.12 and 2.13 into this gives

$$V' = \left[\frac{2}{\rho_w}\left[\frac{(\overline{P}_s-\overline{P})}{T} + \left[\frac{T-(1-\overline{C})}{1-\overline{C}}\right]\left[\frac{(\overline{P}-P_o)}{T} + P_o\right] \ln\left[\frac{\frac{\overline{P}_s-P_o}{T} + P_o}{\frac{\overline{P}-P_o}{T} + P_o}\right]\right]\right]^{\frac{1}{2}}$$

As the depth of self-aerated flows is usually relatively small, $P' \simeq P_o$ and so this simplifies to the required expression for the mean water velocity,

$$V' = \left[\frac{2}{\rho_w}\left[\frac{(\overline{P}_s-P_o)}{T} + \left[\frac{T-(1-\overline{C})}{1-\overline{C}}\right] P_o \ln\left[\frac{\frac{(\overline{P}_s-P_o)}{T} + P_o}{P_o}\right]\right]\right]^{\frac{1}{2}} \quad 2.14$$

It is worth noting that this equation could equally well have been expressed in terms of C' rather than T.

Two special cases of this equation are of interest:

(i) Measurements in a completely homogeneous air-water mixture for which T = 1.0. Eq. 2.14 then reduces to Eq. 2.8, in which P_s and C are now mean values, and the static pressure is P_o.

(ii) Measurements in a wavy region with no bubbles within the interface so that C' = 0.0 and from Eq. 2.11, $T = 1-\overline{C}$. Eq. 2.14 thus reduces to Eq. 2.7 in which P_s and C are again mean values, and the static pressure equals P_o.

Two instruments were used in the final tests at Aviemore. One measured the stagnation pressure and air concentration simultaneously at the same "point" in the flow, and is described in Chapters 3 and 4. The measurement region was made about 6 - 12 mm dimension, larger than the 1 - 3 mm bubble size initially expected at Aviemore. It was later found that near the surface, the air bubbles were as large as 10 - 20 mm (ref. Section 10.3.3). To the probe, these large bubbles will appear as small air gaps in wavy flow.

In order to use Eq. 2.14 to calculate the mean velocity using the measurements from this probe, it is therefore necessary to redefine the intermittency parameter T. This will henceforth be defined as the proportion of time the probe's measurement region is within a bubbly (or non-aerated) flow which appears homogeneous to the probe.

The large bubbles are not expected to limit the validity of Eq. 2.14. However, they do complicate the measurement of the intermittency parameter T. (T is estimated from probability density functions of the air concentration signal as described in Section 10.3.4).

The other instrument used in the final tests at Aviemore measured the velocity by a cross-correlation technique, (ref. Section 5.3). This was considerably more reliable than the velocities predicted by Eq. 2.14.

The analysis of the measurements in self-aerated flow at Aviemore are reported in Section 10.4. It was found that Eq. 2.14 overestimated the velocity by about 7% for mean air concentrations from 0.2 - 0.7. This difference increased to about 10 - 20% at mean air concentrations equal to 0.9, and decreased to about 0% in non-aerated flow, (ref. Fig. 10.42).

For mean air concentrations less than 0.7, the above differences are in good agreement with Sterlini and Trotignon's (1971) observations. They found that in aerated flows with similar velocities and with mean air concentration from 0.5 - 0.55, Eq. 2.8 (from which Eq. 2.14 was derived) overestimated the velocity by about 5%.

The larger 10 - 20% overestimation of velocity at high air concentrations is most likely due to the sensitivity of Eq. 2.14. This is discussed below.

2.4.4 Sensitivity of Velocity Equations

It is found that all the equations for predicting velocity (Eqs. 2.7 to 2.10 and 2.14) are sensitive to errors in either stagnation pressure or air concentration when the air concentration tends to 1.0. This can be shown most simply by differentiating Eq. 2.7 and rearranging as below:

$$V = \left[\frac{2}{\rho_w}\left[\frac{P_s-P}{1-C}\right]\right]^{\frac{1}{2}} \qquad 2.7$$

$$dV = \frac{1}{2}\left[\frac{2}{\rho_w}\left[\frac{P_s-P}{1-C}\right]\right]^{-\frac{1}{2}}\left[\frac{2\ dP_s}{\rho_w(1-C)} + \frac{2(P_s-P)dC}{\rho_w(1-C)^2}\right]$$

$$\frac{dV}{V} = \frac{dP_s}{2(P_s-P)} + \frac{dc}{2(1-C)}$$

$$\frac{dV}{V} = \frac{dP_s}{V^2\rho_w(1-C)} + \frac{dC}{2(1-C)} \qquad 2.15$$

It is apparent from Eq. 2.15 that when C tends to 1.0, even small errors in stagnation pressure dP_s or air concentration dC will cause large errors in velocity dV.

It can be similarly shown that the other velocity prediction equations are also sensitive to errors at high air concentrations.

2.5 PRESSURE SCALES

All equations in this Chapter have been expressed for pressures measured in absolute units. The pressure transducers used in this research were all gauge (relative to atmospheric pressure) devices. It has therefore been convenient to express stagnation pressures as gauge pressures in all subsequent Chapters, and to modify Eqs. 2.7 to 2.10 and 2.14 accordingly. Atmospheric and static pressures will still be expressed in absolute units. As in this Chapter, this is indicated by the suffix (abs). For example, the atmospheric pressure at sea level is taken as $P_o = 102\ kN/m^2$ (abs).

CHAPTER 3

AIR CONCENTRATION MEASUREMENT

3.1 SUMMARY

The design of the combined pressure air concentration probe used at Aviemore is discussed. The method used to measure air concentration is described and the electronic measuring circuit is analysed.

3.2 INTRODUCTION

Numerous techniques have been reported for the measurement of air concentration in two-phase air-water mixtures.

Lamb and Killen (1950), Rao et al (1970) and Lai (1971) have reported the use of mechanical samplers in model studies of self-aerated flows. Lamb and Killen developed an electrical resistance method which measured the mean air concentration of a bubbly mixture between two electrodes. This was later used in a pioneering series of model studies of self-aerated flow, reported by Straub and Anderson (1958). Keller (1972) adapted this technique for use in field tests.

Resistivity probes have recently been developed to a very high standard by Serizawa et al. (1975) and by Herringe and Davis (1974). These detect the passage of individual air bubbles because they indicate the air concentration at a point.

Other methods used in air-water mixtures are: hot wire, hot film, optical, radiation absorption, and capacitive. These methods are discussed in the above references and by Hewitt (1971).

Lamb and Killen's resistance method was chosen for this research for two reasons:

(i) It was the method most suitable for remote operation and for which the instrument was sufficiently small, accurate and rugged.

(ii) It had been used successfully in self-aerated flows in the past.

The subsequent developments of resistivity probes indicate these would be more suitable for future measurements in self-aerated flows. These probes are discussed in detail in Chapter 5.

This Chapter describes the resistance method of air concentration measurement, the probe design, the relationship between the output signal and the air concentration, and the electronics used. The instrument was tested in aerated flows within the laboratory as described in the calibration tests in Section 6.5.

3.3 RESISTANCE METHOD OF AIR CONCENTRATION MEASUREMENT

Resistance and capacitance methods are known generally as impedance methods. These use the different electrical conductivities and dielectric constants of liquids and gases to measure the void fraction in a liquid-gas mixture.

Lamb and Killen (1950) developed a resistance method suitable for use in self-aerated flows. This was based on an equation derived by Maxwell (1873) for the specific resistivity of a suspension of spheres. Maxwell's derivation assumed the spheres to be the same diameter, and their spacing large compared with this diameter. By taking the conductivity of air as zero, Lamb and Killen showed Maxwell's equation could be reduced to an expression for the air concentration of a suspension of air bubbles

in water

$$C = \frac{\frac{R_E}{R_{EO}} - 1}{\frac{R_E}{R_{EO}} + 1} \qquad 3.1$$

where R_E is the resistance of the air-water mixture between two electrodes. R_{EO} is the resistance of the water alone, measured between the same electrodes.

Experiments have shown that even if the distance separating the spheres is small compared with their diameter, this has little effect on the accuracy of Maxwell's equation.

In a series of tests in self-aerated flows, Lamb and Killen obtained excellent agreement between an instrument utilising this method and a mechanical sampler. These tests are discussed below because they remain the best verification of Eq. 3.1, yet obtained in self-aerated flows.

The mechanical sampler used a hollow sharpened tube aligned with the flow as shown in Fig. 3.1. Aerated flow was sucked through this at the same velocity as would occur if the tube was not present. In this way the flow was sampled without being disturbed by the tube. To achieve this, they assumed that because the flow depth was so small, the static pressure in the flow was equal to the atmospheric pressure. The suction was then adjusted with the aid of the two pressure tappings until the pressure at the entrance of the tube was atmospheric. The air and water in the tube were then separated and their flow rates measured. This apparatus took about 30 minutes per reading.

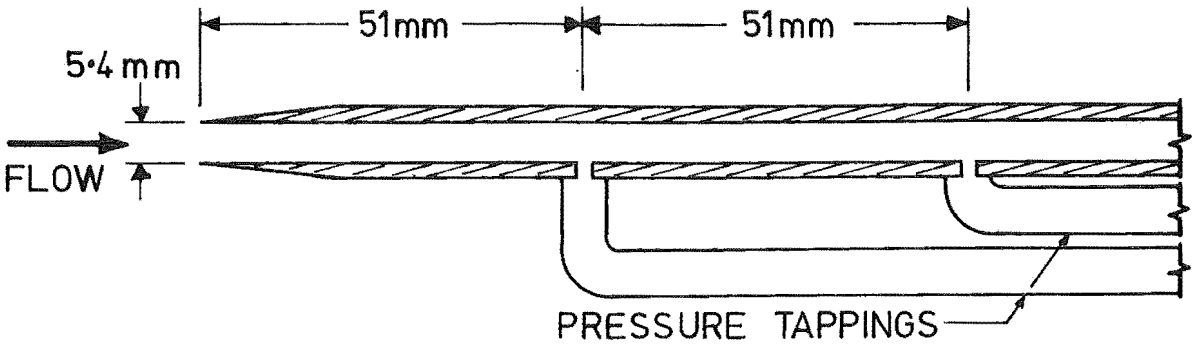

Fig. 3.1 Mechanical Sampler Inlet Tube.

The probe they developed for the resistance method is shown in Fig. 3.2. This consisted of two stainless steel electrodes fixed to a non-conducting rod. The electrodes were insulated except on the inner surfaces. They were bent slightly outward to prevent separation occurring on the inner surfaces should they be misaligned with the flow. The resulting contraction did not effect the indicated air concentration.

The electrical circuit they developed is shown in Fig. 3.3. For reasons explained later, the impedance between the electrodes was effectively resistive. The potential difference over the electrodes can therefore be simply related to the air concentration by using Eq. 3.1. They adjusted the reference resistor, as explained later, to get a linear relationship.

Air concentration profiles were measured by both instruments in self-aerated flows in a large laboratory flume. A sample profile is reproduced in Fig. 3.4 and illustrates the excellent agreement between the two instruments.

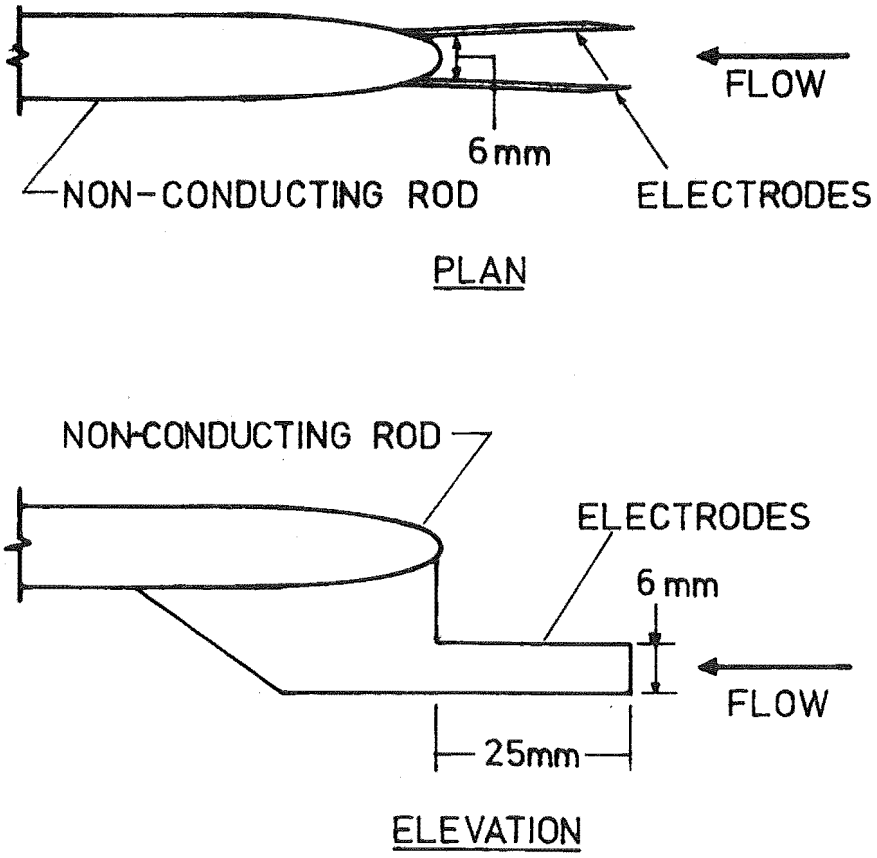

Fig. 3.2 Resistivity Probe.

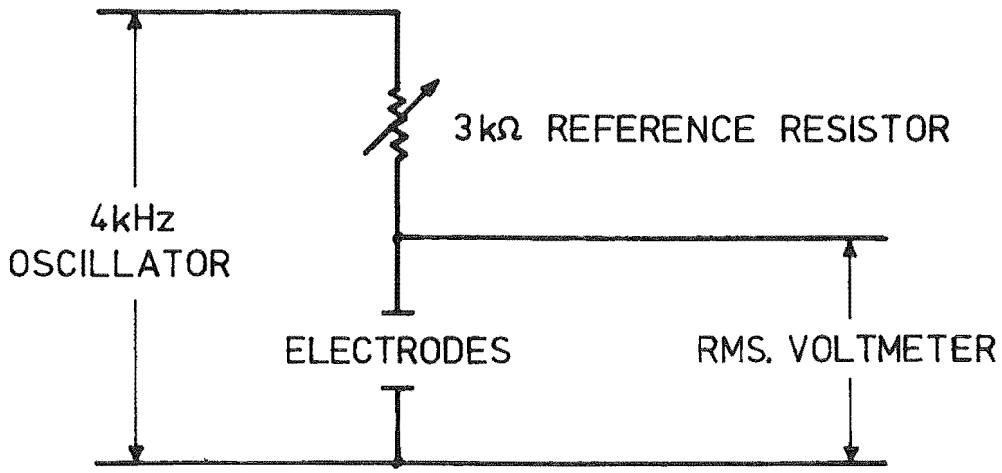

Fig. 3.3 Electrical Circuit.

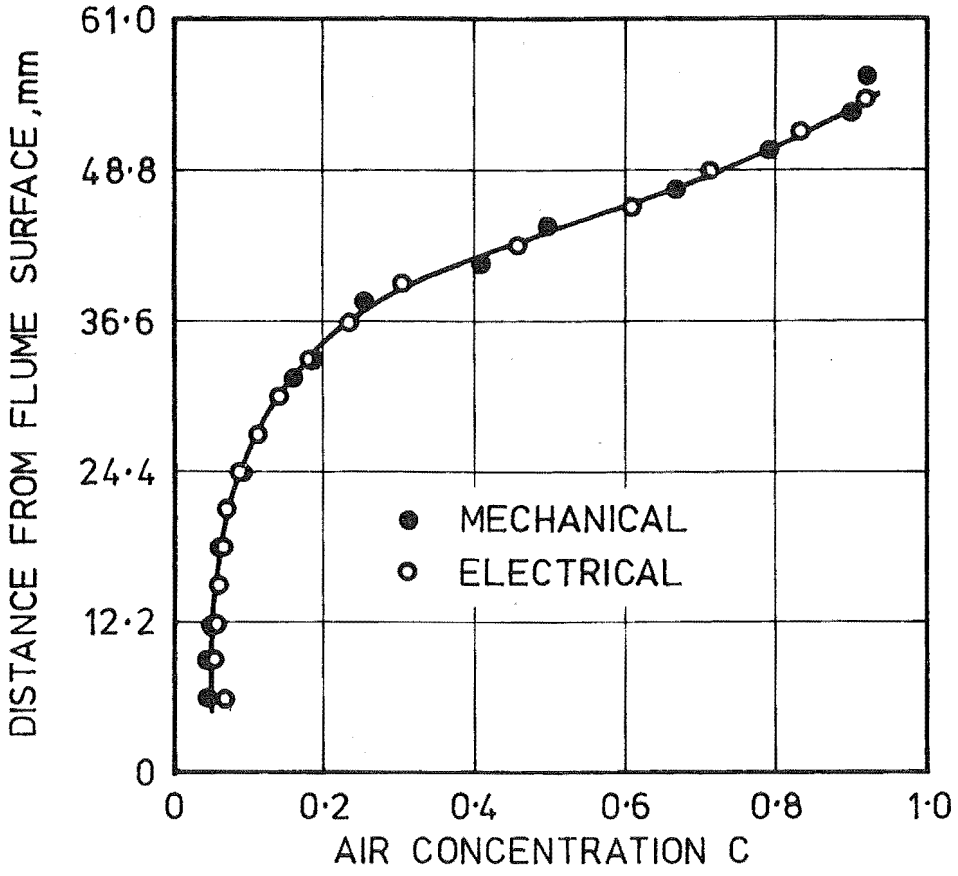

Fig. 3.4 Sample Air Concentration Profile

(from Lamb and Killen, 1950).

Although this is not an absolute verification of Eq. 3.1, its validity is further supported by the calibration tests reported in Section 6.5.

3.4 MEASUREMENT OF RESISTANCE

Resistances are usually measured in a bridge circuit with a d.c. (direct current) source of e.m.f. (electro motive force). However, in measuring the resistance between two electrodes immersed in an air-water mixture, an additional resistance would occur due to polarisation and electrolysis.

It is therefore necessary to use an a.c. (alternating current) source. The a.c. carrier is amplitude modulated according to the impedance (not resistance) between the electrodes, then demodulated and filtered to remove all the carrier. By using a high frequency low voltage source with stainless steel or platinum electrodes, the effects of polarisation and electrolysis will then be minimised.

The use of an a.c. source complicates the measurement of resistance. This is because the reactive component of the impedance can be important. The reactance associated with a capacitance C_E is given by $-\frac{1}{wC_E}$ where w is the angular frequency of the a.c. source ($w = 2\pi f$ where f = frequency, Hz). Two types of capacitance can be distinguished here:

(i) A variable component, the capacitance between the electrodes which will vary with the air concentration because of the difference between the dielectric constants of water and air.

(ii) A constant component, the capacitance of the leads to the electrodes and between adjacent components of the electronic measuring circuit.

Resistance measuring instruments using a.c. sources normally have provision for balancing out any constant reactance. However, the elimination of a rapidly varying reactance is much more difficult, and must be approached by either:

(i) Ensuring w and C_E are sufficiently small that the impedance is effectively resistive, (the capacitance between the electrodes can be reduced by increasing their spacing and decreasing their size), or

(ii) Designing a special circuit to continuously balance the capacitance.

Two requirements must be met in choosing the frequency of the a.c. source:

(i) It must be more than twice the output signal's maximum required frequency in order to remove all the a.c. carrier with a low pass filter.

(ii) It must be larger than the maximum input frequency so that errors are not caused by the two "beating".

Both the resistance and the reactance between the electrodes will depend not only on the air concentration but also on the concentration of electrolyte dissolved in the water and the water temperature. Neither of these would vary significantly during tests at Aviemore because the spillway outlet is about 8 m below the surface of a large lake.

3.5 PROBE DESIGN

3.5.1 Description

The design of a combined probe to measure both stagnation pressure and air concentration was first suggested by Keller (1972) to improve the accuracy of velocity predictions. Such a design is necessarily a compromise between the various design criteria. As a result, the writer spent much time constructing and testing the first two designs. Both of these were rejected because they did not perform satisfactorily. They will not be discussed further.

It is expedient to present the design which was finally adopted and then to discuss the design criteria in turn. This probe is shown in Figs. 3.5 and 3.6 and will be referred to as the "combined pressure air concentration probe". It will be noted that the air concentration electrodes are very similar to Lamb and Killen's (1950) successful probe shown in Fig. 3.2.

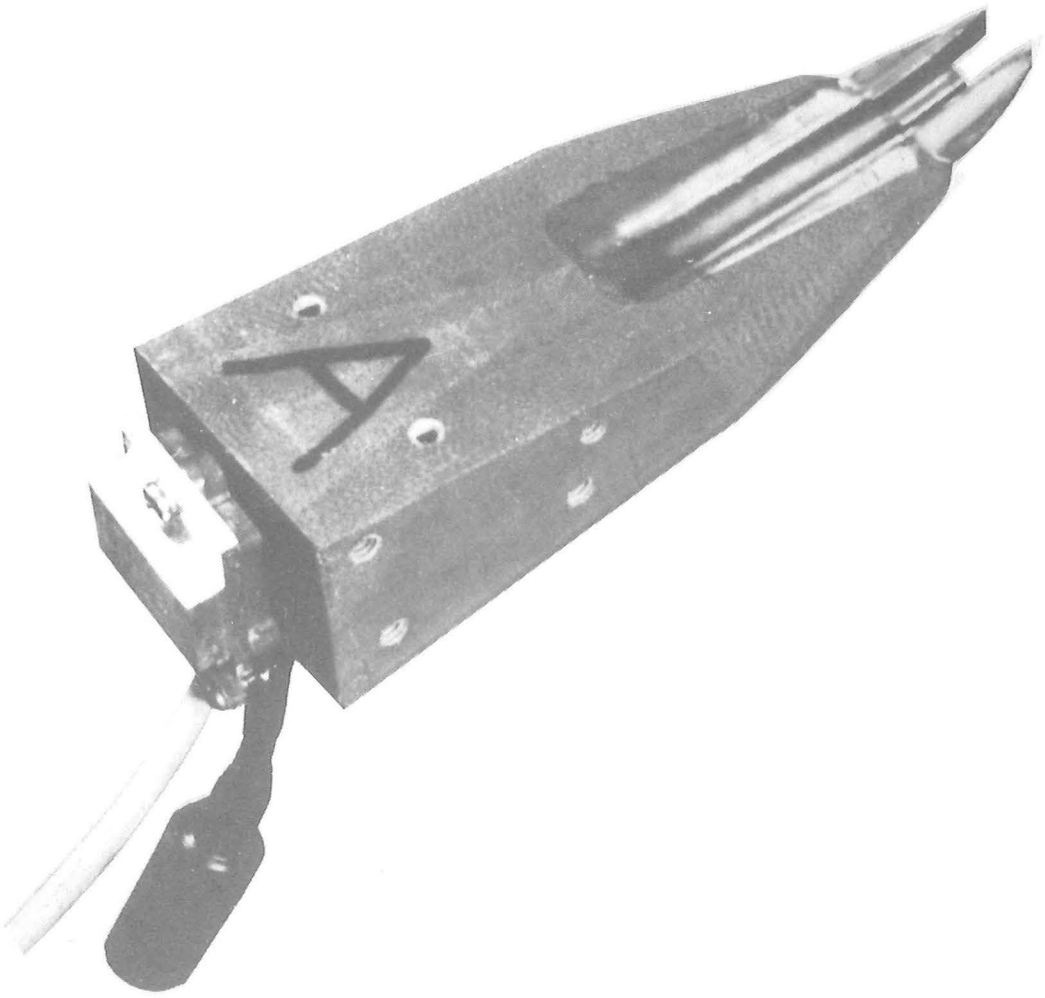

Fig. 3.5 Combined Pressure Air Concentration Probe, National Semiconductor pressure transducer connected.

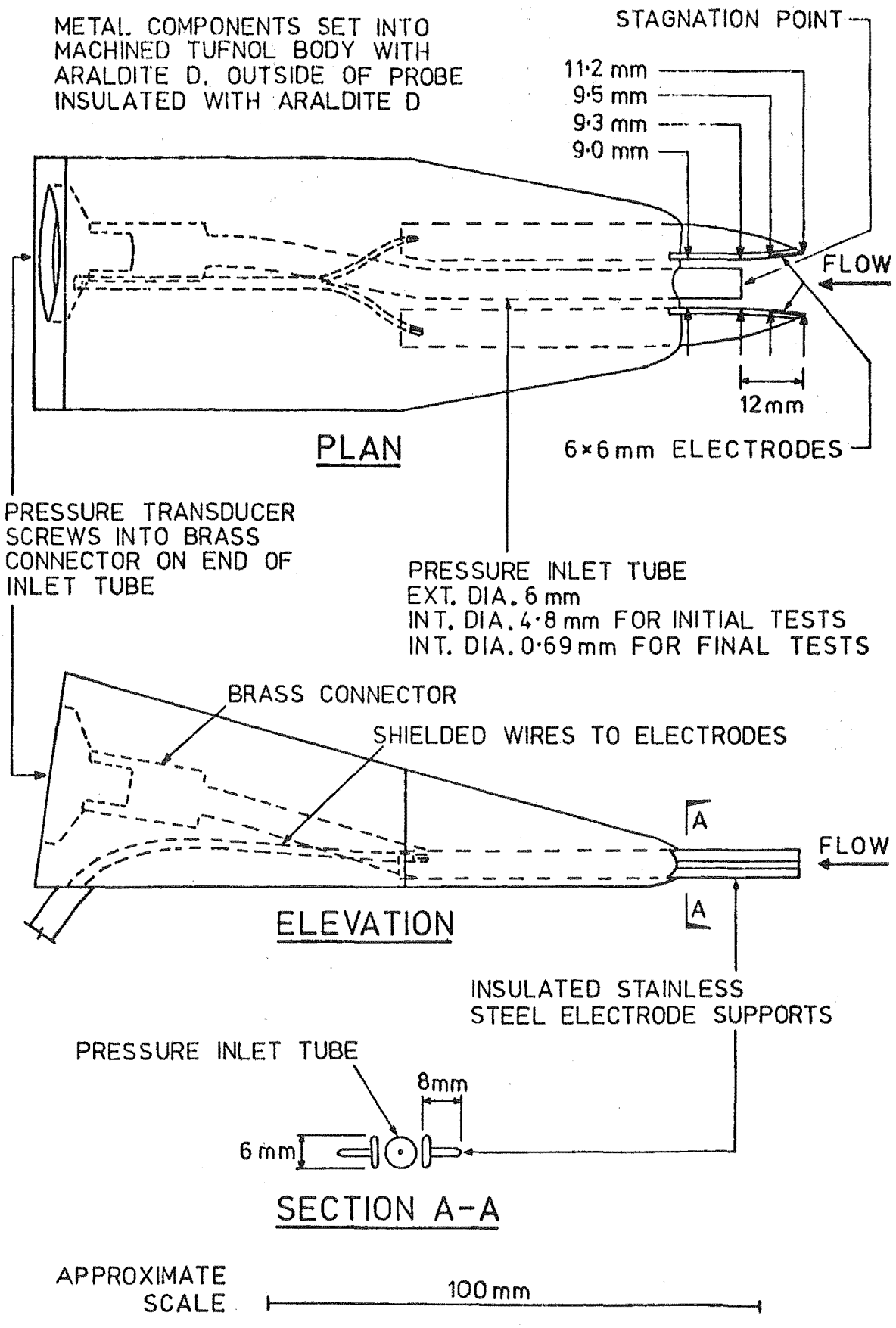

Fig. 3.6 Combined Pressure Air Concentration Probe.

3.5.2 Design Criteria

This section discussed the design criteria for the combined pressure air concentration probe. The criteria related only to the pressure transducer and inlet tube are left until Section 4.2.

(i) The initial design aim called for a probe that would allow simultaneous measurement of stagnation pressure and air concentration at the same point in the flow. The air concentration is measured in the electric field set up between the two electrodes (Fig. 3.7). The dimensions of this field are large relative to the electrodes' size but its strength is greatly reduced at small distances from them. The measurement region is therefore mainly within the volume indicated (about 12 mm diameter).

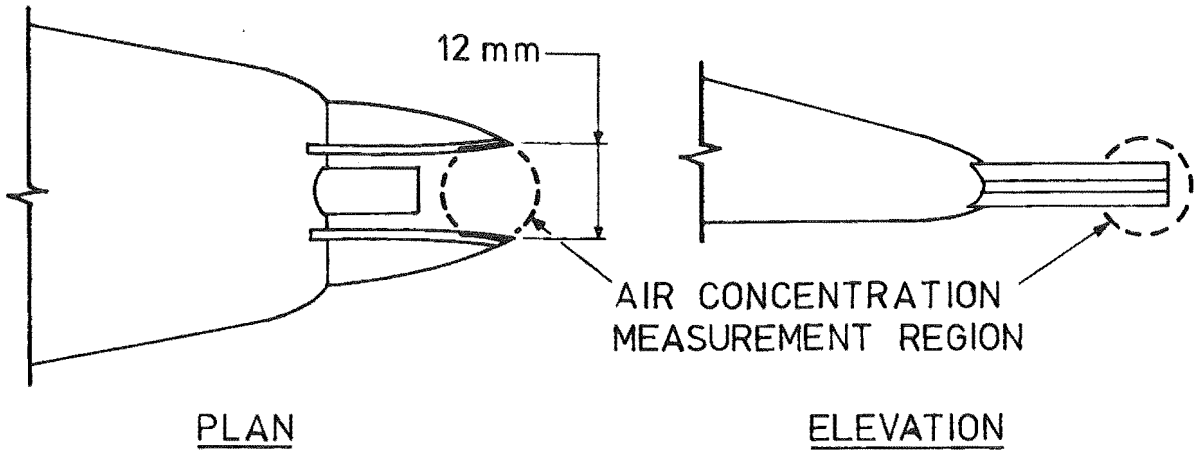

Fig. 3.7 Measurement Region.

The region of stagnation pressure measurement is limited to the cross-section area of the pressure inlet tube which is 6 mm diameter.

Both measurements refer to almost the same stream tube. Their separation in the flow direction causes a phase difference which is discussed later.

(ii) The concept of measurements at a "point" is important. The dimensions of the measurement regions were made small compared with the velocity, stagnation pressure and air concentration gradients expected in the 200 - 350 mm depths of flow. It was initially expected that the bubbles would be in the range 1 - 3 mm dimension, as reported by Straub and Lamb (1953) and Killen (1968). In this case, the flow beneath the water surface would all appear homogeneous to the probe. It was not until the final field tests that bubbles as large as 20 mm were measured near the water surface (ref. Section 10.3.3). Such large bubbles in fact appear non-homogeneous to the probe, and complicated the interpretation of the air concentration signals measured at Aviemore.

(iii) Because of the extreme difficulties encountered in calibrating instruments in aerated flows, it is best that neither probe effects the flow measured by the other. The air concentration electrodes were placed upstream of the pressure inlet tube entrance for this reason. The distance upstream was chosen by consideration of the streamlines around a pressure inlet tube in a homogeneous compressible fluid.

Bryer and Pankhurst (2) indicate that for a 6 mm diameter pitot tube 1.5 mm from a solid boundary, the pressure will be overestimated by 1.2%. The two electrode supports can therefore be expected to cause an error of this magnitude in the measurement of stagnation pressure.

(iv) To prevent separation from the leading edge of the electrodes from obscuring them, they were tapered as shown in Fig. 3.6. This allows the instrument to be misaligned from the flow direction by about 10^{o}. As mentioned, Lamb and Killen (1950) tapered their electrodes for the same reason without affecting the probes performance.

(v) The probe must be strong because of the severe flow conditions. The electrode supports were made particularly rigid to prevent vibration.

(vi) To minimise the likelihood of normal shocks forming ahead of the probe, it was made as sharp as possible.

(vii) It was initially intended that turbulent velocity parameters be calculated for frequencies to 1 kHz. This requires that both the stagnation pressure and air concentration signals have a frequency response to 1 kHz.

The maximum frequency response possible (for both stagnation pressure and air concentration) is limited by the dimensions of the measurement region relative to the dimensions of the fluctuations being measured. For example, variations in air concentration whose dimensions are much smaller than the measurement region between the electrodes will be damped. It has been possible to derive an expression (Appendix D) which describes the response of the air concentration probe to the frequency of air concentration variations. This analysis assumes a uniform electric field between the electrodes, and air concentration variations in the direction of flow only. The frequency response is then given by

$$Z = \frac{V}{\pi fL} \; Sin\left[\frac{\pi fL}{V}\right] \qquad 3.2$$

where Z = relative amplitude,

f = frequency of the air concentration at the central point between the electrodes,

V = velocity,

L = length of the measurement region.

Eq. 3.2 has been evaluated by assuming a conservative value of 12 mm for L, and is plotted in Fig. 3.8 for V = 12, 22 m/s. This shows a flat frequency response up to 100 - 200 Hz, less than the 1 kHz of the electronics developed for this probe (ref. Appendix E).

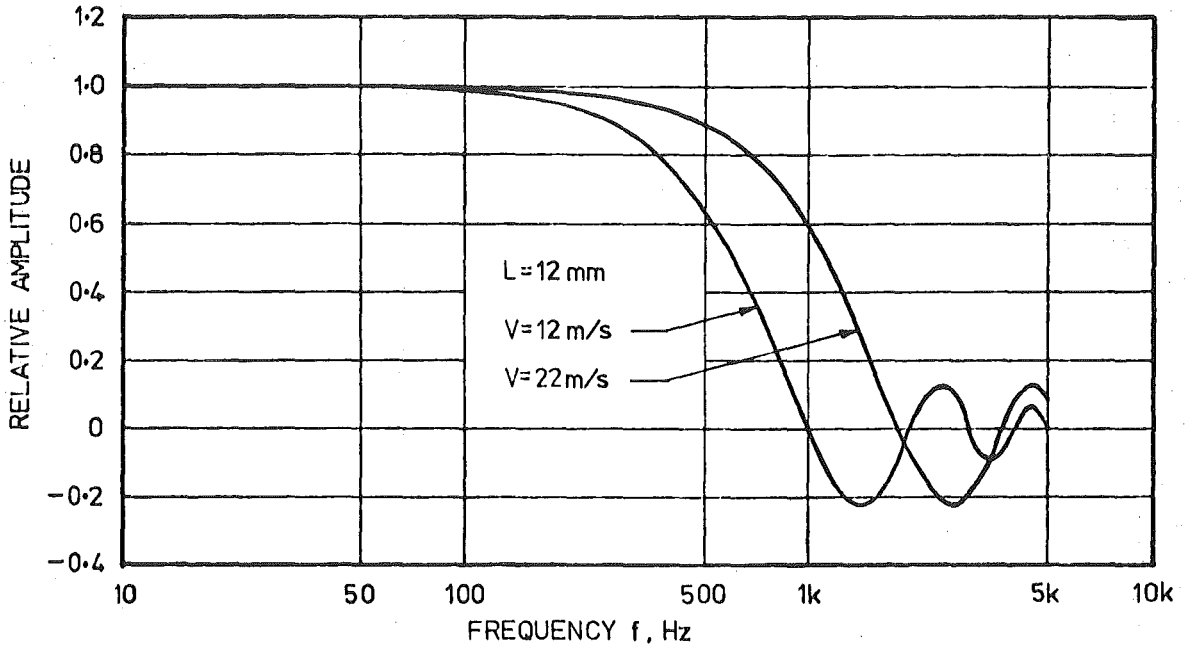

Fig. 3.8 Response of the Air Concentration Probe to the Frequency of Air Concentration Variations.

In section 4.8.4 it is shown that the frequency response of the pressure transducer and inlet tube, as used for the final tests, was limited to about 1 Hz. This is much less than the response of the air concentration probe, and prevented any useful turbulence measurements.

(viii) To calculate instantaneous velocities, the stagnation pressure and air concentration signals must have identical phase response as well as frequency response.

The spacing of the two measurement regions causes a phase difference between the two signals which is related to the water velocity. This was simply corrected during analysis as described in Section 10.4.1.

3.6 INPUT-OUTPUT RELATIONSHIP

3.6.1 Introduction

There are three basic steps in relating the air concentration to the output voltage of the electronic measuring circuit used here:

(i) The relationship between the air concentration and the resistance between the electrodes is assumed to be given by Eq. 3.1. This is supported by the excellent agreement Lamb and Killen (1950) obtained between their instrument and the mechanical sampler discussed earlier, and the similarity between their probe and the electrodes of the probe developed here. It is further supported by the calibration tests with this probe in the laboratory flow simulator, reported in Section 6.5.

(ii) The electrical circuit for this probe is analysed in the following section, and the resistance between the electrodes is related to the potential difference over them.

The results of a series of laboratory tests allow this expression to be considerably simplified. It is then possible to combine this with Eq. 3.1 to give an expression relating the air concentration to the potential difference over the electrodes.

(iii) The third step relates this potential difference to the output voltage of the electronic measuring circuit used here.

3.6.2. Electrical Circuit

The electrical circuit used to measure air concentration can be represented by Fig. 3.9 in which the impedance between the electrodes Z_E is simulated by a capacitor C_E and a resistor R_E in parallel. The a.c. source was an electrical circuit which supplied approximately 2 volts RMS, with angular frequency $w = 126 \times 10^3$ rad/s. The potential difference V_E over the electrodes gives a measure of the air concentration.

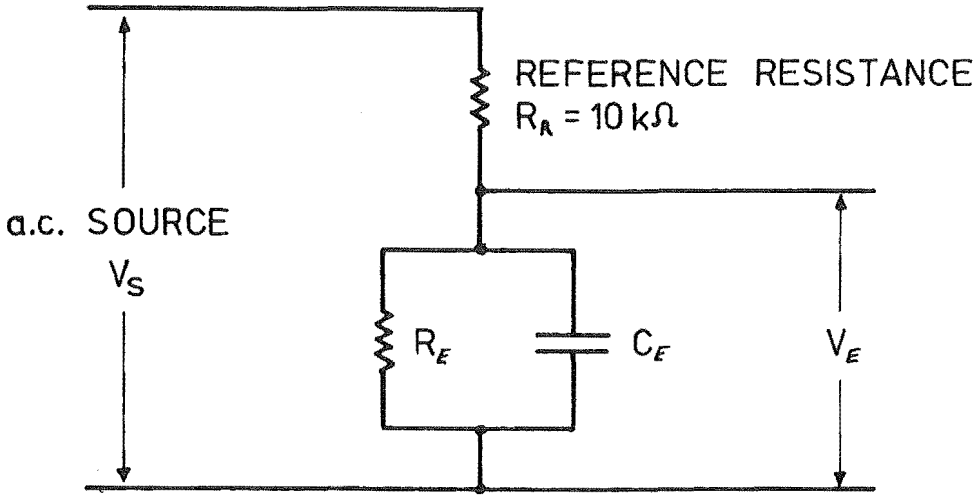

Fig. 3.9 Electrical Circuit.

Although Lamb and Killen (1950) and Keller's (1972) electrical circuits were effectively identical to the one used here, they analysed the simpler circuit of Fig. 3.10. In this circuit, the impedance between the electrodes has been assumed to be purely resistive. This is strictly valid only for the special case w = 0 (i.e. a d.c. source) for the circuit in Fig. 3.9.

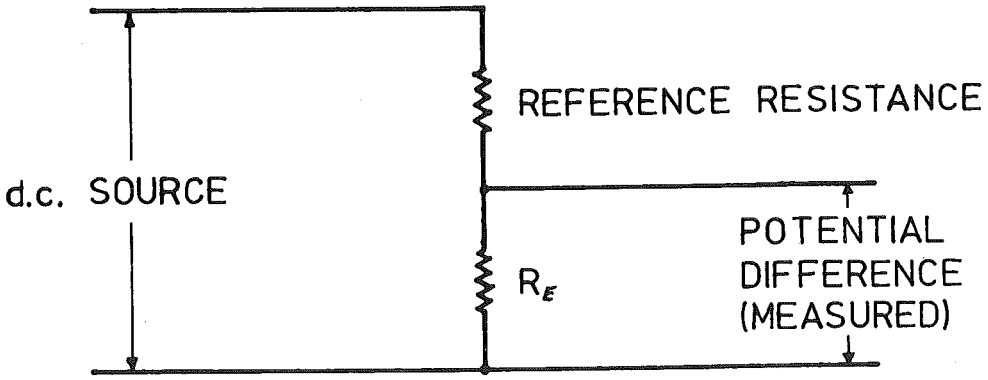

Fig. 3.10 Electrical Circuit when w=o.

3.6.3 Circuit Analysis

For the electrical circuit in Fig. 3.9

$$\frac{V_E}{V_S} = \frac{1}{1 + \frac{R_R}{Z_E}}$$

where Z_E is given by

$$Z_E = \frac{1}{\frac{1}{R_E} + jwC_E}$$

where j is the complex operator.

Combining these two equations gives:

$$\frac{V_E}{V_S} = \frac{1}{\left[1 + \frac{R_R}{R_E}\right] + j\ (wC_E\ R_R)}$$

This is illustrated in the complex diagram in Fig. 3.11.

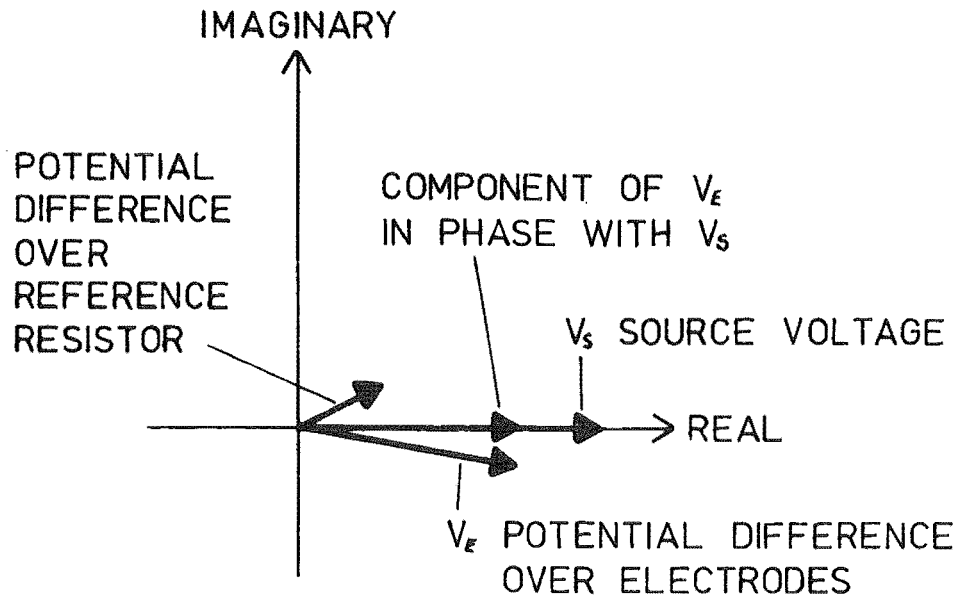

Fig. 3.11 Potential Difference over the Electrodes, V_E.

The magnitude of $\frac{V_E}{V_S}$ is given by

$$\left|\frac{V_E}{V_S}\right| = \frac{1}{\left[\left[1 + \frac{R_R}{R_E}\right]^2 + (w\ C_E\ R_R)^2\right]^{\frac{1}{2}}} \qquad 3.3$$

It is convenient to scale this so that it varies between 0.0 and 1.0 corresponding to C = 0.0 and 1.0 respectively.

If when C = 0.0, the variables R_E , C_E and V_E are denoted R_{EO} , C_{EO} and V_{EO} then Eq. 3.3 becomes

$$\left|\frac{V_{EO}}{V_S}\right| = \frac{1}{\left[\left[1 + \frac{R_R}{R_{EO}}\right]^2 + (wC_{EO}R_R)^2\right]^{\frac{1}{2}}} \qquad 3.4$$

If we denote the scaled magnitude of $\left|\frac{V_E}{V_S}\right|$ by $||V_E||$ then

$$||V_E|| = \frac{\left|\frac{V_E}{V_S}\right| - \left|\frac{V_{EO}}{V_S}\right|}{1 - \left|\frac{V_{EO}}{V_S}\right|} \qquad 3.5$$

Substituting Eqs. 3.3 and 3.4 into Eq. 3.5 gives

$$||V_E|| = \frac{\frac{1}{\left[\left[1 + \frac{R_R}{R_E}\right]^2 + (wC_ER_R)^2\right]^{\frac{1}{2}}} - \frac{1}{\left[\left[1 + \frac{R_R}{R_{EO}}\right]^2 + (wC_{EO}R_R)^2\right]^{\frac{1}{2}}}}{1 - \frac{1}{\left[\left[1 + \frac{R_R}{R_{EO}}\right]^2 + (wC_{EO}R_R)^2\right]^{\frac{1}{2}}}} \qquad 3.6$$

In order to relate $||V_E||$ to R_E for the general case $w \neq 0$, it is necessary to establish the relationship between air concentration and C_E (see for example Cimorelli and Evangelisti, 1966).

Instead, consider the special case w = 0. Eq. 3.6 reduces to

$$||V_E||_{w=0} = \frac{\frac{1}{\left[1 + \frac{R_R}{R_E}\right]} - \frac{1}{\left[1 + \frac{R_R}{R_{EO}}\right]}}{1 - \frac{1}{\left[1 + \frac{R_R}{R_{EO}}\right]}} \qquad 3.7$$

This equation could have been obtained by analysing the electrical circuit of Fig. 3.10, as Lamb and Killen (1950) and Keller (1972) have done.

As Eq. 3.7 can be simply related to the air concentration, it is of interest to evaluate the difference

$$\delta = ||V_E|| - ||V_E||_{w=0} \qquad 3.8$$

It is shown in the next section that for the tests at Aviemore, the values of w, C_E and R_E were such that $\delta < 0.01$. We therefore have the very

important result

$$||V_E|| = ||V_E||_{w=0} \qquad 3.9$$

It is shown in Appendix F that the magnitude of δ decreases rapidly with decreasing source frequency. As Lamb and Killen (1950) and Keller (1972) used much lower source frequencies (4 kHz and 800 Hz respectively) it seems likely that Eq. 3.9 would also be valid for their probes. This justifies their analysis of the simplified electrical circuit of Fig. 3.10 instead of the circuit of Fig. 3.9 which was analysed above.

The relationship between $||V_E||$ and the air concentration can be expressed in terms of a single parameter α defined as

$$\alpha = 1 + \frac{R_{EO}}{R_R} \qquad 3.10$$

The measurement and control of α is discussed in Section 3.7.

The relationship between the air concentration and resistance is

$$C = \frac{\frac{R_E}{R_{EO}} - 1}{\frac{R_E}{R_{EO}} + \frac{1}{2}} \qquad 3.1$$

The required expression is obtained by combining Eq's 3.1, 3.7, 3.9 and 3.10

$$||V_E|| = \frac{3C(\alpha-1)}{2\alpha - C(3-\alpha)} \qquad 3.11$$

or on rearranging

$$C = \frac{2\alpha\,||V_E||}{3(\alpha-1) + (3-\alpha)\,||V_E||} \qquad 3.12$$

Equations 3.11 and 3.12 are similar to the expressions derived by Lamb and Killen (1950) and Keller (1972) for the electrical circuit of Fig. 3.10. The main difference in the expressions derived here is the introduction of a scaled voltage $||V_E||$. Plotting $||V_E||$ against C (Fig. 3.12) allows the effect of α to be readily seen. When $\alpha = 3$, Eq. 3.10 gives

$R_R = \frac{R_{EO}}{2}$, and Eq. 3.12 gives $C = ||V_E||$ i.e. a linear relationship between the air concentration and the potential difference over the electrodes.

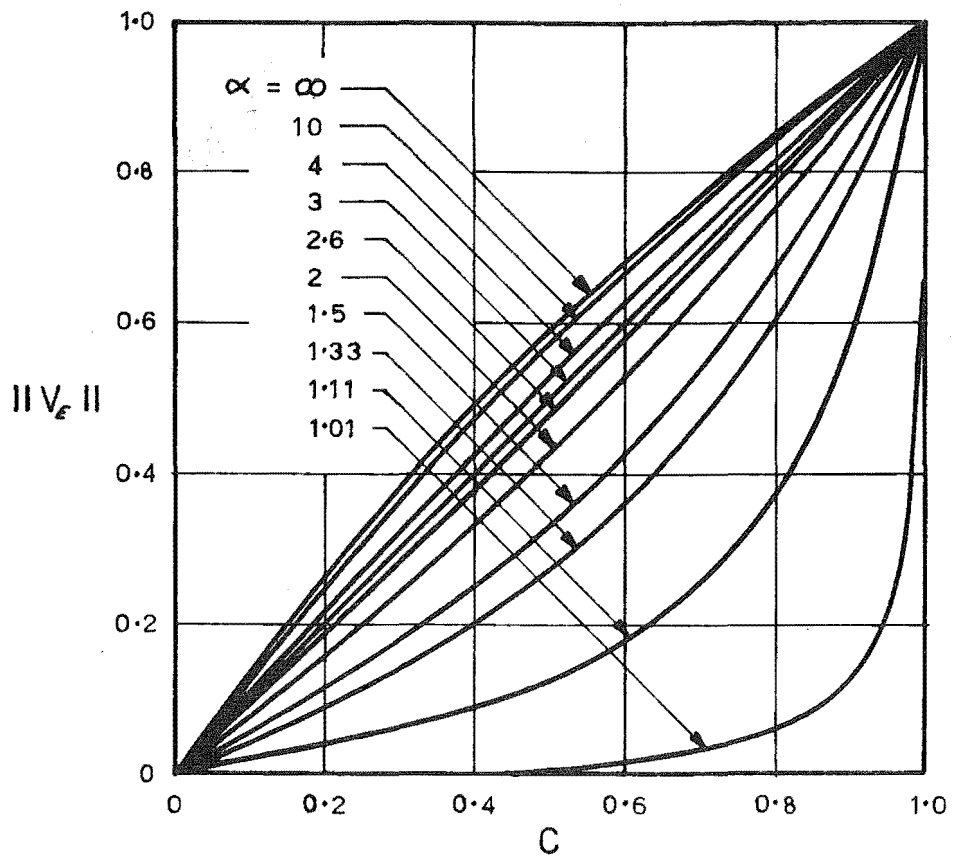

Fig. 3.12 Plot of Eq. 3.11.

For the second test series at Aviemore, α was determined from laboratory measurements of R_{EO} in a sample of Aviemore water. These measurements, discussed in detail in the next section, showed R_{EO} to be in the range 15.8 - 16.1 kΩ. As the reference resistance R_R = 10 kΩ, we have from Eq. 3.10 that α = 2.6. This gives an almost linear relationship between C and $||V_E||$ (Fig. 3.12) which from Eq. 3.12 is given by

$$C = \frac{13\,||V_E||}{12 + ||V_E||} \qquad 3.13$$

3.6.4 Evaluation of Eq. 3.8

The variables C_E and R_E (the capacitance and resistance between the electrodes) were measured in the laboratory, independent of the electrical circuit, for a range of simulated air concentrations for each of three different water salinities. These were then used to calculate the corresponding values of $||V_E||$ (Eq. 3.6) and $||V_E||_{w=0}$ (Eq. 3.7) that would have occurred had the probe actually been in the electrical measuring circuit of Fig. 3.9. δ was then calculated from Eq. 3.8.

C_E and R_E were measured by connecting the probe to a "Wayne Kerr Auto Balance Universal Bridge B641" (0.1% accuracy).

The first test used water obtained from Aviemore; the second used three solutions of salt dissolved in distilled water, with salt concentrations of 12.3, 24.5 and 49.0 g/m^3. The values of R_E and C_E were almost identical in the Aviemore water and the 24.5 g/m^3 salt solution.

For each of the test solutions, variations in air concentration were simulated by:

(i) Partially submerging the electrodes (Fig. 3.13a), as would occur during the passage of a large air-water interface.

(ii) By inserting perspex plates of various shapes between the submerged electrodes to simulate air bubbles (see Fig. 3.13b). (It must be realised that because the electric field between the electrodes is non-uniform, the dimensions of a perspex plate can not be directly related to an "air concentration".)

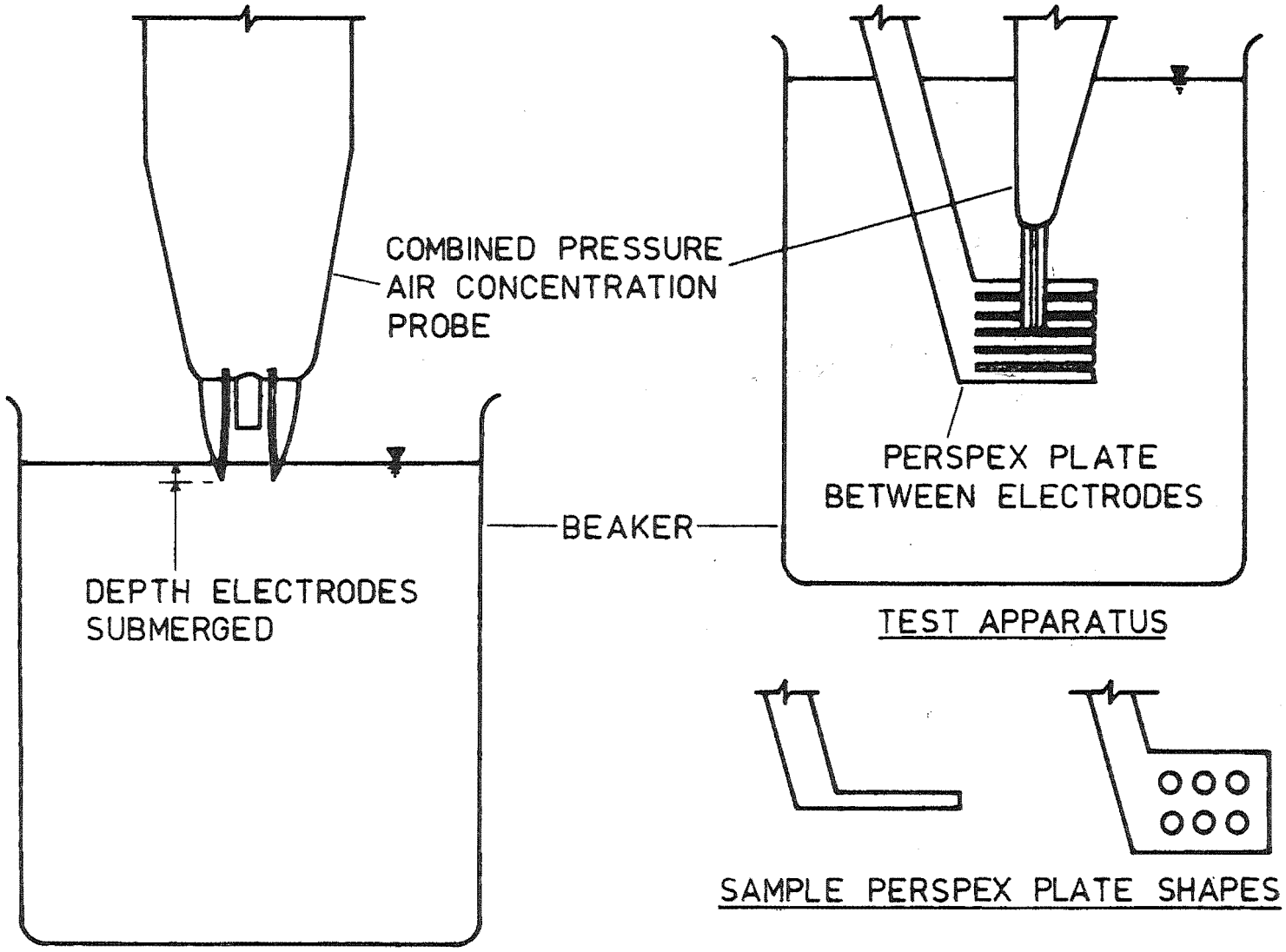

Fig. 3.13 (a) Partially Submerged Electrodes (b) Simulated Air Concentration Apparatus

Sample results are presented in Table 3.1 for the electrodes partially submerged in the water from Aviemore. The first line corresponds to C = 0.0 so that:

$$R_E = R_{EO} = 15.8\ k\Omega \text{ and}$$

$$C_E = C_{EO} = 351\ pF.$$

That $\delta \simeq 0$ for all test solutions is apparent from the last column of Table 3.1 and also from the plots of $||V_E||$ plotted against $||V_E||_{w=0}$ in Fig. 3.14.

Table 3.1 Evaluation of δ

$w = 126 \times 10^3$ rad/s, $R_R = 10\ k\Omega$.

Depth Electrodes Submerged (approx.)* mm	Measured Data		Calculated Data		
	R_E kΩ	C_E pF	$\|\|V_E\|\|$ Eq.3.6	$\|\|V_E\|\|_{w=0}$ Eq.3.7	δ Eq.3.8
75	15.8	351	0.0	0.0	0.0
10	16.1	311	0.021	0.011	0.010
6.4	18.1	265	0.094	0.082	0.012
4.8	22.6	233	0.216	0.209	0.007
3.2	28.9	195	0.342	0.337	0.005
1.6	41.0	157	0.496	0.494	0.002
just touching	62.5	135	0.640	0.644	-0.004
in air	63700	13.3	0.999	1.000	-0.001

*This "depth" is explained in Fig. 3.13a.

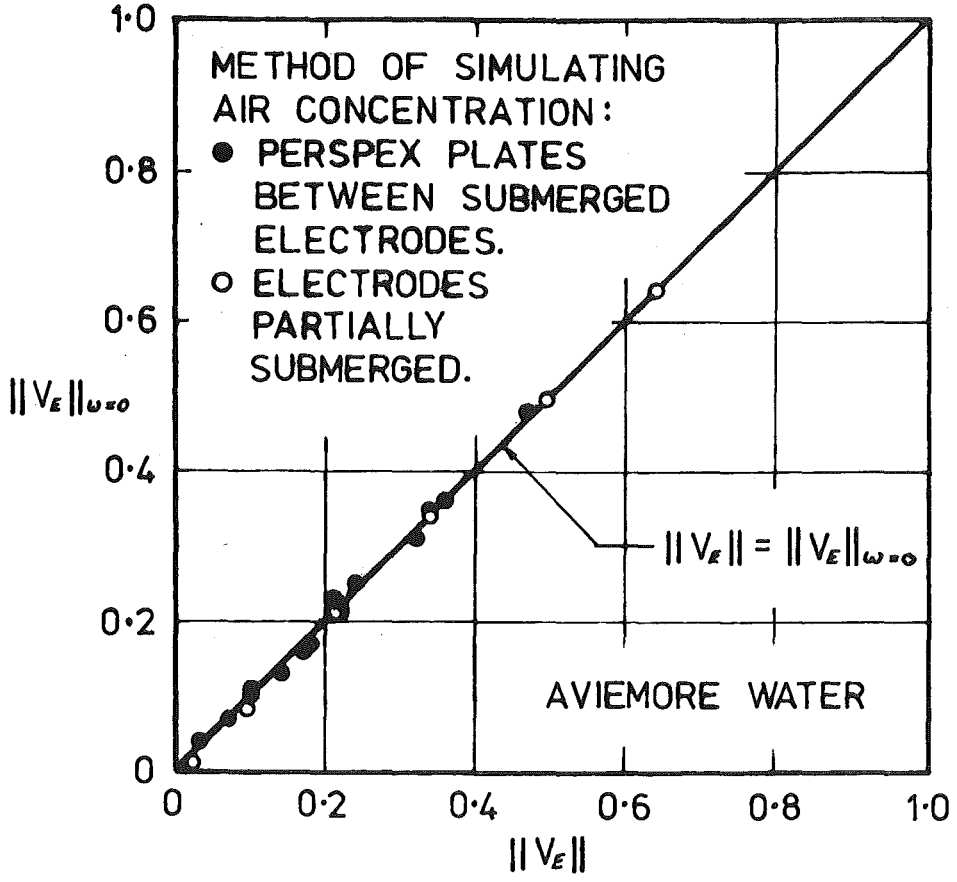

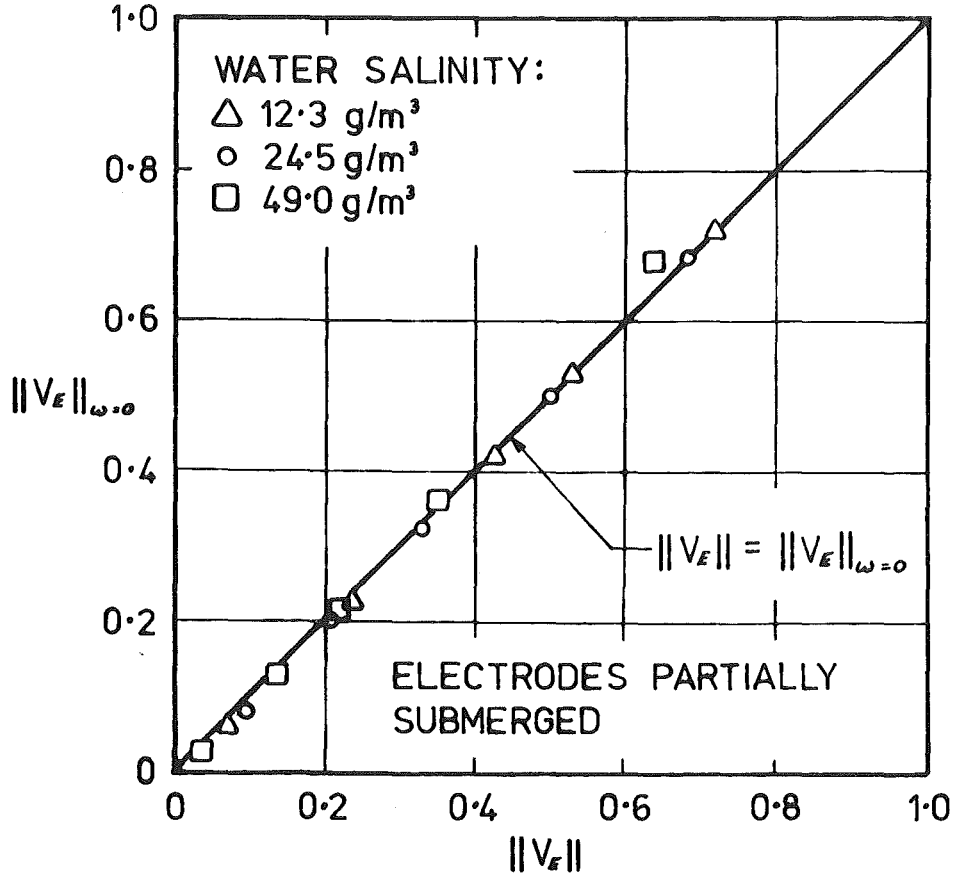

Fig. 3.14 Comparisons of Eq's 3.6 and 3.7.

3.6.5 Electronic Measuring Circuit

The electronic measuring circuit was designed in consultation with DAVCO (Electronics firm) and is shown in Fig. 3.15. It does not in fact measure the potential difference V_E over the electrodes, only the component of V_E in phase with the source V_S (i.e. the real component of V_E in Fig. 3.11)

This approach was chosen because of concern over the validity of Lamb and Killen's (1950) circuit analysis, and thus their relationship between V_E and the air concentration. Their analysis was applicable for their measurements because the impedance between their electrodes was effectively resistive. For the instrument used here, the source frequency was so much larger than Lamb and Killen's that the reactance $-\frac{1}{wC_E}$ and the resistance R_E were similar in magnitude. It was therefore initially thought that δ (Eq. 3.8) would not be zero and that Lamb and Killen's analysis would not be applicable. (δ has since been evaluated for various source frequencies using the measured data in Table 3.1, (see Appendix F). The magnitude of δ is shown to increase with increasing frequency. These results would allow optimum choice of frequency for any future designs).

The electronic measuring circuit used here was chosen because it was thought that the air concentration could be simply related to the component of V_E in phase with V_S, regardless of the magnitude of the reactance $-\frac{1}{wC_E}$. In fact, it was not possible to formulate a simple relationship between the air concentration and the output voltage of this measuring circuit. It was therefore necessary to experimentally relate the output from this electronic measuring circuit to the potential difference V_E measured independently with an RMS voltmeter.

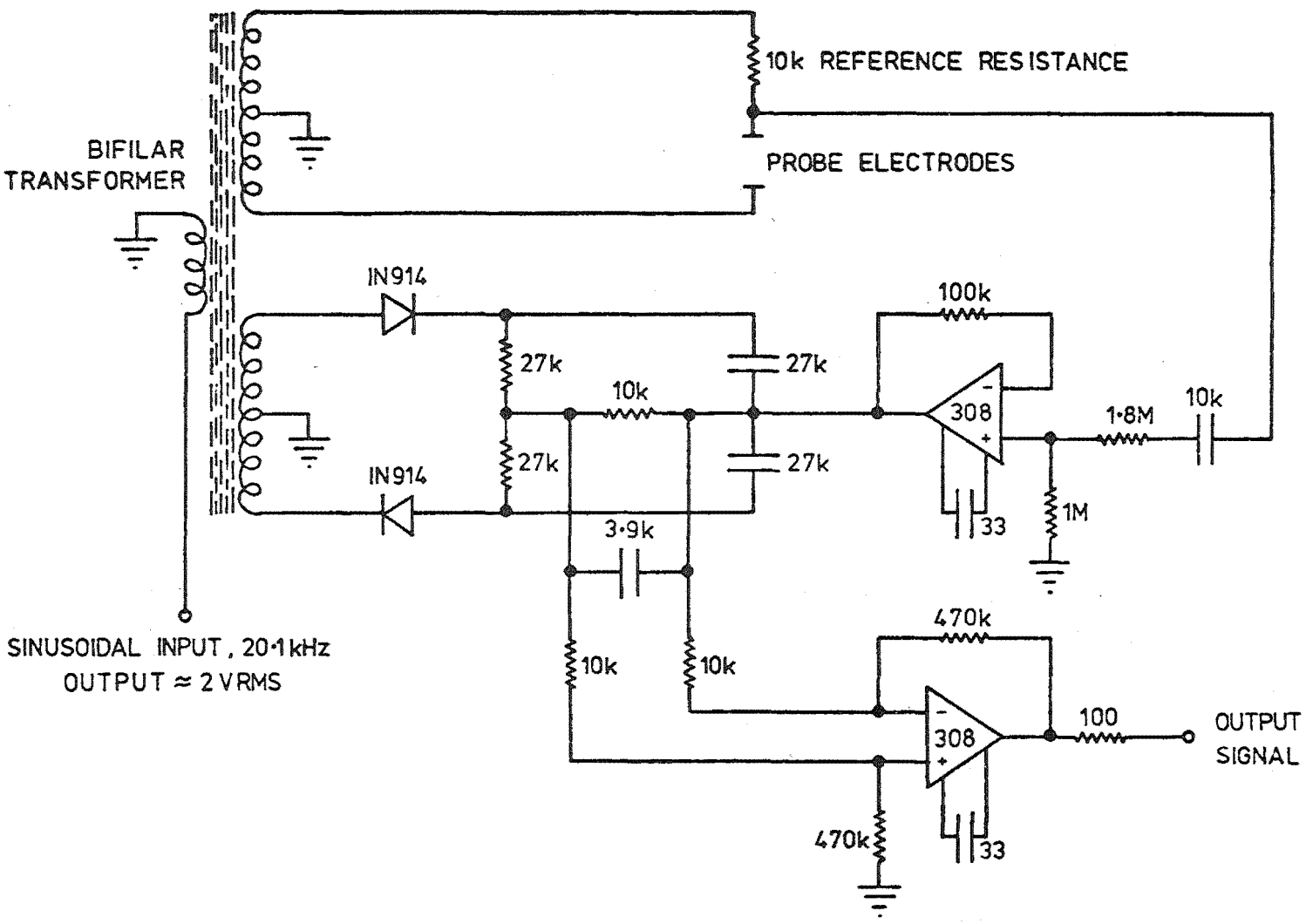

Fig. 3.15 Electronic Measuring Circuit.

The measuring circuit and an RMS voltmeter (Hewlett-Packard 3400A RMS voltmeter; 10MΩ, 17-30pF input impedance; 1% FS accuracy) were both connected to the probe. Variations in air concentration were simulated by slowly lowering the electrodes into each of three salt solutions, with salinities as used in the previous tests. The output signals were recorded on the X and Y axes of an XY plotter.

The curves for each saline solution have been scaled between 0.0 and 1.0 and plotted in Fig. 3.16. These are seen to be non-linear, and salinity dependent. It will be recalled that the probe's output was almost identical in the Aviemore water and the 24.5 g/m^3 salt solution.

The input-output relationship for the probe and its electronic measuring circuit can now be formulated for Aviemore water. The scaled output from the electronic measuring circuit $||V||$ is related to $||V_E||$ by the curve for 24.5 g/m^3 salinity in Fig. 3.16, and this is related to the air concentration by Eq. 3.13. Combining these, we get the curve shown in Fig. 3.17. This curve is described by the equation

$$C = 1.0 - 1.008\ (1.0 - ||V||)^{0.741} \qquad 3.14$$

which was subsequently used to analyse the data measured at Aviemore.

The frequency response of the electronic measuring circuit was flat to 1 kHz (see Appendix E). As previously mentioned, this was much better than the frequency response of the air concentration output signal from the probe.

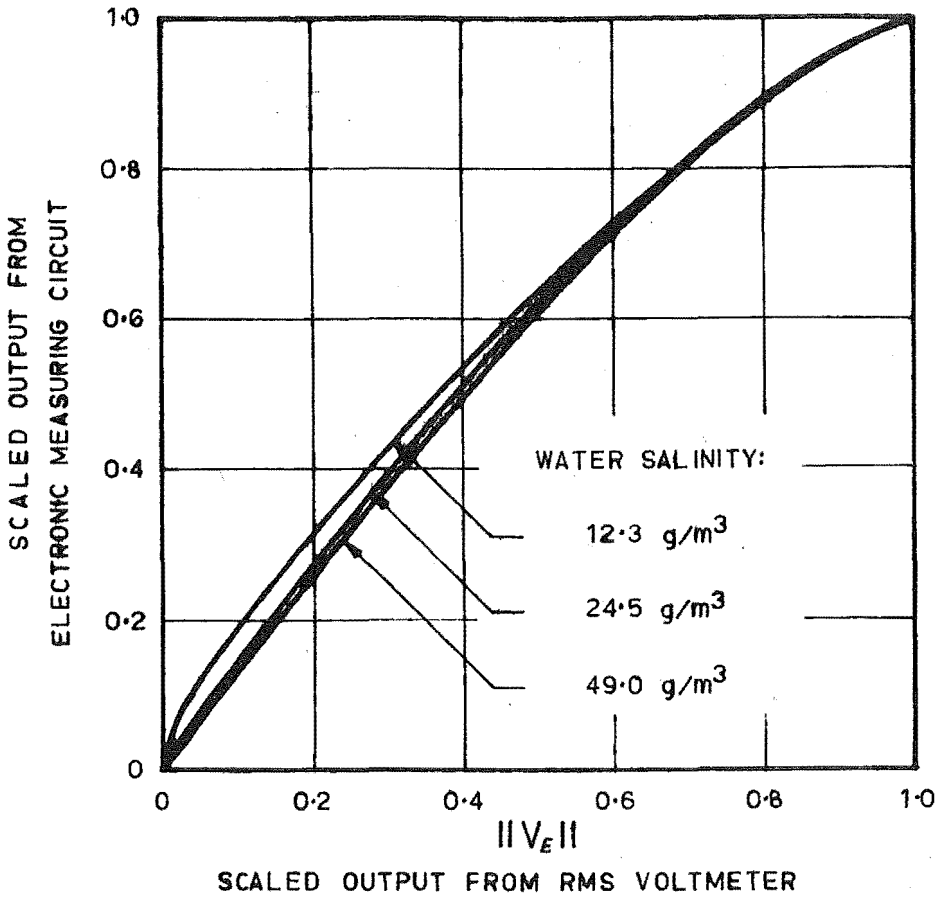

Fig. 3.16 Electronics Calibration.

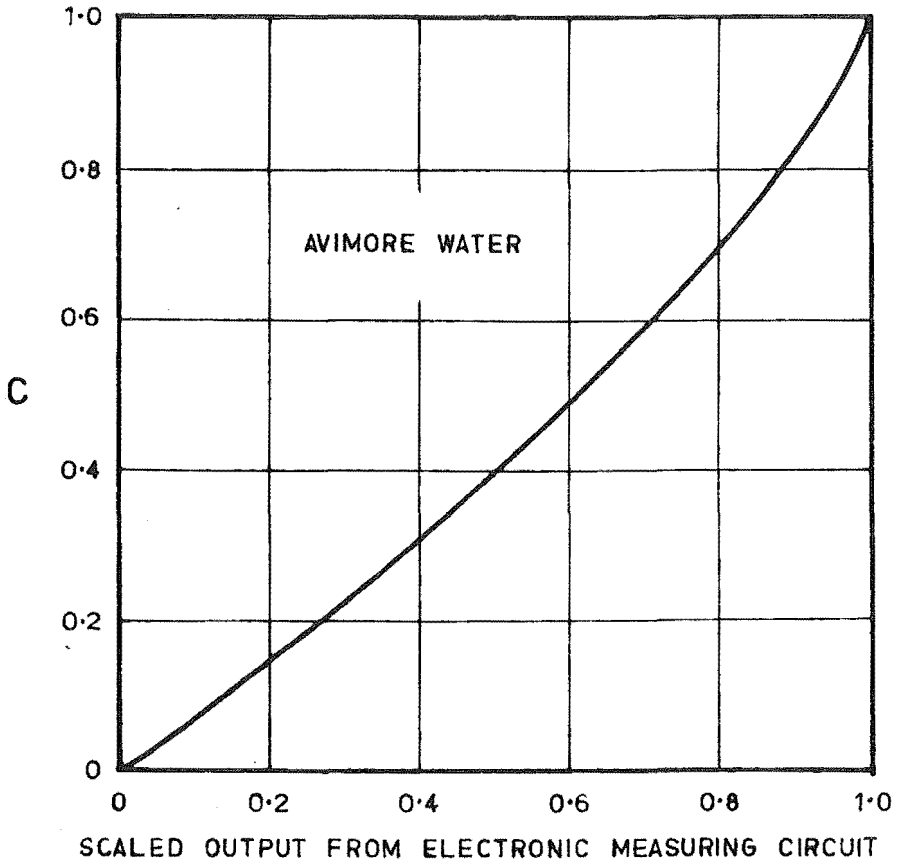

Fig. 3.17 Input-Output Relationship.

3.7 CHOICE OF REFERENCE RESISTANCE

This section discusses the control of α in a circuit which is described by Eq. 3.7 and for which the measured voltage is V_E (RMS).

It is most desirable to set $\alpha = 3$ to obtain a linear input-output relationship. It can be simply shown that if the electrodes are submerged in water and R_R is chosen such that $V_{EO} = \frac{2}{3}V_S$ then $\alpha = 3$. V_S can be simply measured by setting $R_R = 0$ so that $V_E = V_S$.

The value of α will vary with the salinity of the water. However, if the reference resistance is replaced with two electrodes submerged in water of the same salinity, it can be shown that α will be independent of variations in water salinity. This principle was employed by Keller (1972) and in the first test series at Aviemore reported here.

The apparatus is shown in Fig. 3.18. A sample of aerated water (J) was continuously tapped from the flow, de-aerated (K), and then circulated past the reference electrodes (L). This device was fixed within the wet compartment of the spillway instrument assembly (ref. Section 7.3).

α could be adjusted by changing the spacing of the two electrodes (L). For the final field tests at Aviemore, this device was abandoned in favour of a simple resistor because of the difficulty in determining α with the electrical measuring circuit used here.

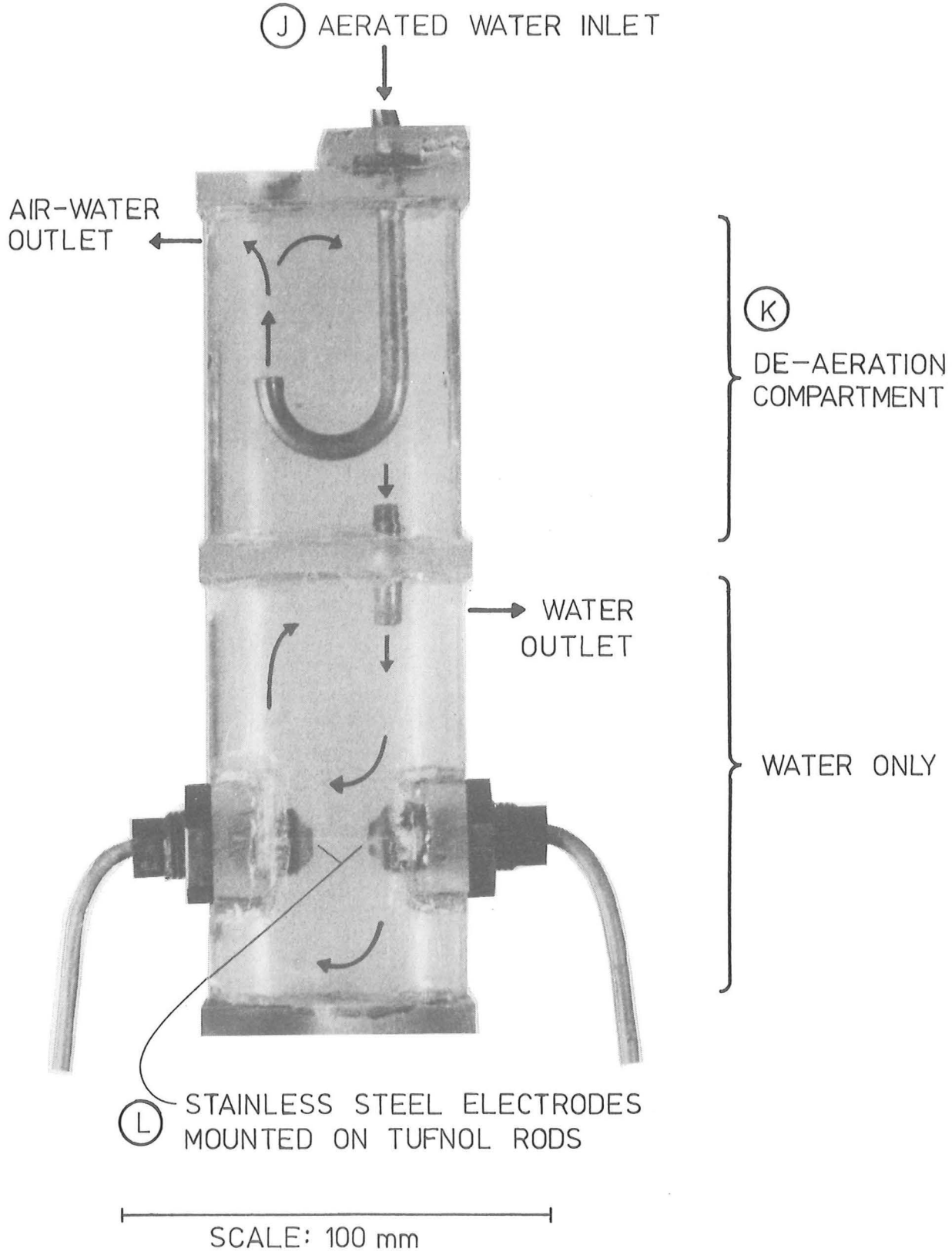

Fig. 3.18 Reference Electrodes.

3.8 PARTIALLY SUBMERGED ELECTRODES

When the electrodes are partially submerged, as would occur in the passage of a large air-water interface, the distortion of the electric field between the electrodes will cause the mean air concentration to be under-estimated.

This is illustrated in Fig. 3.19 using the experimental data from Table 3.1. At each depth the electrodes were submerged, the air concentration was calculated with Eq. 3.13. For example, when the electrodes are just touching the water, from Table 3.1 $\|V_E\| = 0.640$ and from Eq. 3.13, $C = 0.66$. This is shown as the point U in Fig. 3.19. Similarly, when the electrodes were submerged 3.2 mm, we get $C = 0.36$, the point R in Fig. 3.19.

This shows an unexpectedly rapid transition from S to U when the electrodes first enter (or leave) the water. This is caused by the distortion of the electric field. For the velocities at Aviemore, an air-water interface takes only about 0.3 ms to pass the electrodes. The rapid transition from S to U was not apparent in the output signal because the frequency response of the electronic measuring circuit was limited to about 5 kHz maximum.

Because the area $A_1 > A_2$ the mean air concentration will be underestimated. This will in turn cause underestimation of the mean velocity calculated from measurement of stagnation pressure and air concentration. The error introduced depends on the number of air-water interfaces passing the electrodes. This could not be determined. The results in Section 10.4 indicate this error is not important.

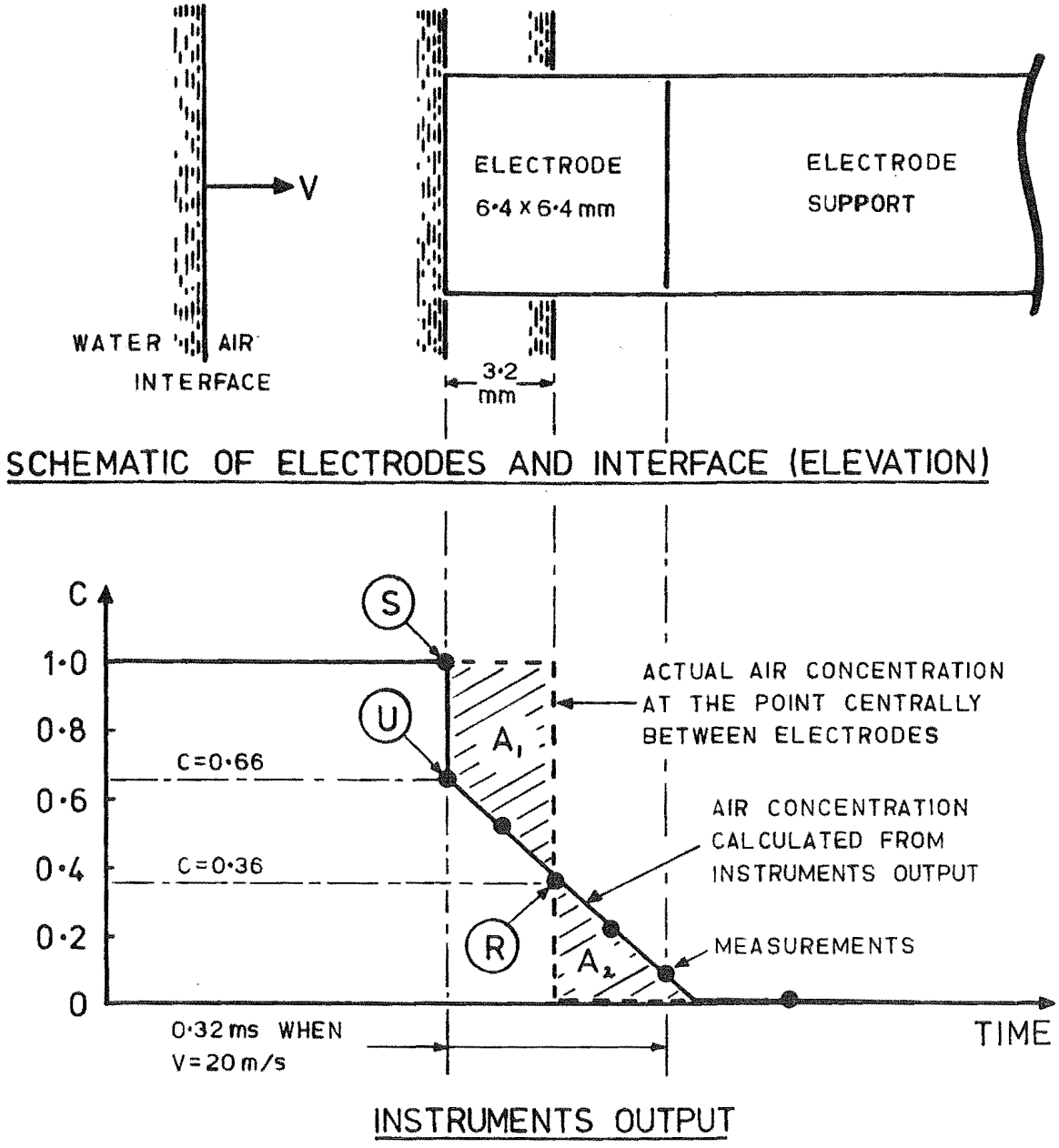

Fig. 3.19 Passage of an Air-Water Interface.

CHAPTER 4

STAGNATION PRESSURE MEASUREMENT

4.1 SUMMARY

The design and the development of the pressure inlet tube for the combined pressure air concentration probe is discussed. A theoretical analysis is developed which predicts the dynamic response of a pressure transducer plus pressure inlet tube. This is shown to be in reasonable agreement with the measured response.

Calibration tests with this probe in the A flow simulator are described in Section 6.5.

4.2 PROBE DESIGN CRITERIA

The design adopted for the combined stagnation pressure air concentration probe was shown in Figs. 3.5 and 3.6, and the design criteria were discussed in Section 3.5. Further points relating specifically to the measurement of stagnation pressure are described below:

(i) As discussed in Section 3.5 it was desired to measure stagnation pressure at a point 6 mm diameter and to make the probe as sharp as possible. Because of the geometry and the relatively large size of the available transducers, it was necessary to place the transducer about 130 mm from the stagnation point (ref. Figs. 3.5 and 3.6). The transducer was connected to the stagnation point with a fluid filled pressure inlet tube.

(ii) The pressure transducer and the fluid within the inlet tube should be readily replaceable. The transducers were screwed into a brass connector fixed to the end of the inlet tube. This was done submerged

in a container of the fluid to ensure the inlet tube was de-aerated

(iii) It was initially desired to obtain a frequency response to 1 kHz. The maximum frequency response possible is limited by the dimensions of the stagnation point relative to the dimensions of the pressure fluctuations. Very small dimension fluctuations will be "damped", a situation analogous to the damping of small dimension variations in air-concentration by the size of the electrodes, (ref. Section 3.5). The frequency response will therefore also be given by Eq. 3.2.

$$Z = \frac{V}{\pi fL} \text{ Sin} \left[\frac{\pi fL}{V}\right] \qquad 3.2$$

where Z = relative amplitude,

V = velocity,

L = length of measurement region,

f = frequency of pressure fluctuations at the stagnation point.

In this case, it is not obvious what the length of the measurement region L will be. Consideration of the streamlines around a total head tube in a homogeneous incompressible fluid suggest a value L = 6 mm, the same as the diameter, would be a reasonable estimate. Evaluating Eq. 3.2 and plotting as in Fig. 3.8 shows the maximum possible flat frequency response will be limited to about 200 - 400 Hz, depending on the velocity.

The frequency response of the stagnation pressure output signal is also limited by:

(i) The frequency response of its electronics. This is not a limiting factor.

(ii) The frequency response of the pressure transducer and its inlet tube. This is discussed in the rest of this Chapter.

4.3 PRESSURE TRANSDUCER RESPONSE

The linearity, hysteresis (or repeatability) temperature and vibration response characteristics of pressure transducers are relatively simple to determine and are usually provided by manufacturers. Each introduces errors of order 1% FS.

The dynamic response of a pressure transducer with or without a pressure inlet tube will in general be described by the linear second order differential equation (ref. Neubert, 20):

$$M \frac{d^2y}{dt^2} + D \frac{dy}{dt} + Ky = F \qquad 4.1$$

where y = output

M = moving mass

D = viscous damper

K = restoring force

F = input.

(Expressions for M, D and K in terms of the pressure transducer and inlet tube parameters are developed in Section 4.4).

The solutions of Eq. 4.1 are fully defined by two parameters: the resonant frequency f_o, and the damping ratio h where

$$f_o = \frac{1}{2\pi} \left[\frac{K}{M} \right]^{\frac{1}{2}} \qquad 4.2$$

$$h = \frac{D}{2 \left[KM \right]^{\frac{1}{2}}} \qquad 4.3$$

Solutions of Eq. 4.1 have been well documented (e.g. Neubert, 20). The response to sinusoidal, step and impulse inputs are illustrated in Fig. 4.1. Two solutions which will be used within this Chapter are given below:

(i) For a sinusoidal input of frequency f, the relative amplitude response Z is defined as the ratio of the amplitude (RMS or peak-to-peak)

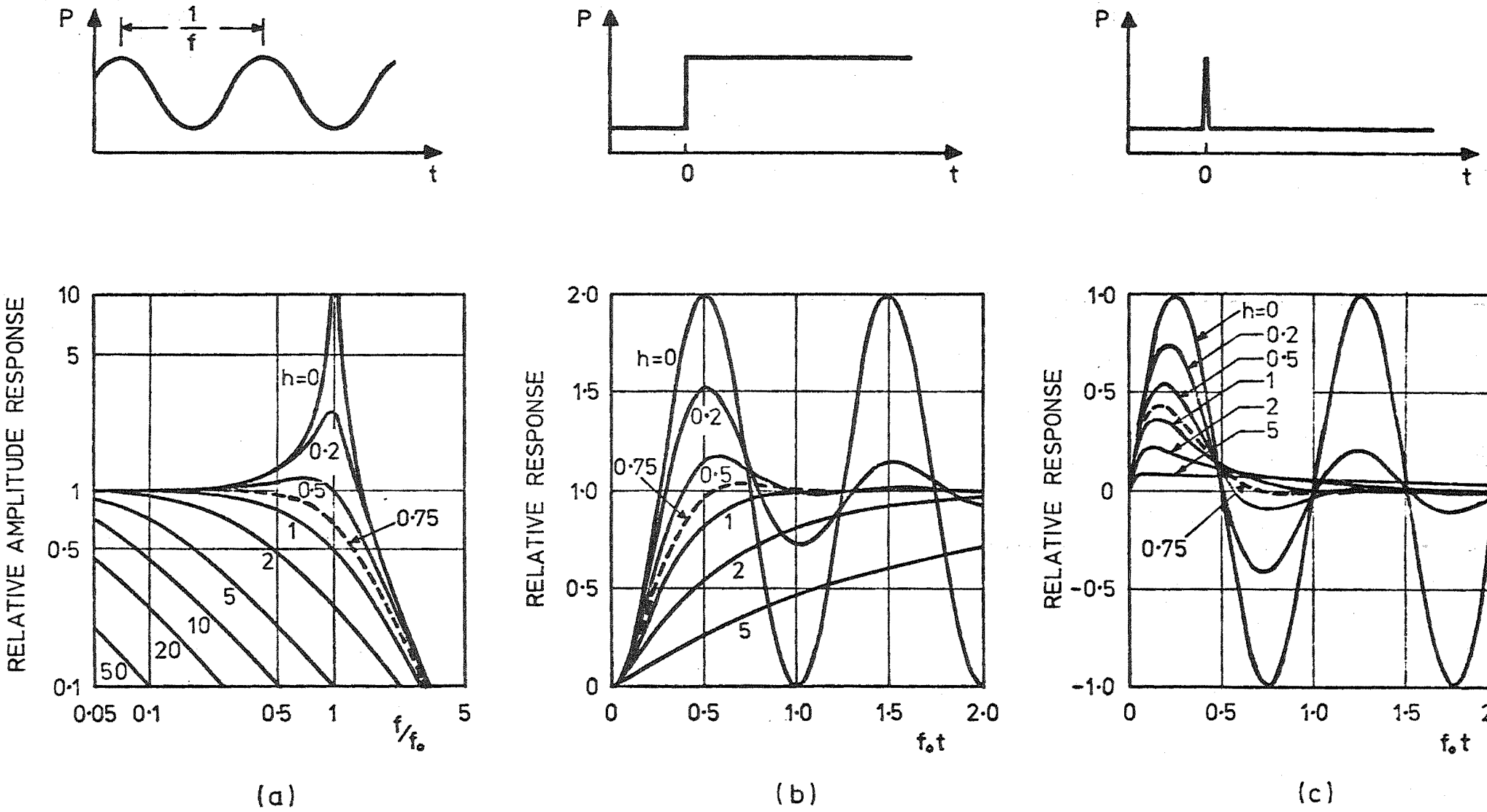

Fig. 4.1 Solutions to Eq. 4.1.

of the output signal to the amplitude of the input signal. This is given by Eq. 4.4 and is plotted in Fig. 4.1a.

$$Z = \left[\left[1 - \left[\frac{f}{f_o} \right]^2 \right]^2 + \left[2h \frac{f}{f_o} \right]^2 \right]^{-\frac{1}{2}} \qquad 4.4$$

(ii) At time t after a step change in pressure, the relative response Z is defined as the ratio of the change in the pressure output signal to the initial step change in input pressure. This is plotted in Fig. 4.1b. For the case $h < 1$, Z is given by:

$$Z = 1 - \frac{1}{2(h^2-1)^{\frac{1}{2}}} \left[\frac{1}{h-(h^2-1)^{\frac{1}{2}}} \cdot e^{-(h-(h^2-1)^{\frac{1}{2}})2\pi f_o t} - \frac{1}{h+(h^2-1)^{\frac{1}{2}}} \cdot e^{-(h+(h^2-1)^{\frac{1}{2}})2\pi f_o t} \right] \qquad 4.5$$

For a given resonant frequency the optimum dynamic response is obtained when $h \simeq 0.75$. This is shown in Fig. 4.1 as a broken line. From Fig. 4.1a, $h = 0.75$ gives the maximum flat frequency response with no resonance at the resonant frequency. From Fig. 4.1b $h = 0.75$ gives the quickest rise time to a step input without resonating.

For damping ratios $h < 0.75$, the transducer (with or without a pressure inlet tube) will resonate when excited at its resonant frequency (Fig. 4.1a) or when subjected to step or impulse inputs (Figs. 4.1b and 4.1c). In this case, the output signal can be electronically filtered to obtain a response similar to that for $h = 0.75$.

For damping ratios $h > 0.75$ the dynamic response is similar to that for $h = 0.75$ but with a reduced resonant frequency.

The magnitude of h is particularly important in self-aerated flows. From the flow description in Section 1.3 it is apparent the transducer (with or without a pressure inlet tube) will be continually subjected to:

(i) High frequency variations in pressure caused by both turbulence and air bubbles within the water.

(ii) Step inputs in pressure when the probe enters or leaves a wave.

(iii) Impulse inputs when the probe intercepts spray, large air bubbles, or the crests or troughs of waves. Most transducers are undamped ($h \simeq 0$) so that they would resonate continually in self-aerated flows. The resultant high pressures could easily damage a transducer.

It is therefore most desirable to increase the damping ratio to $h = 0.75$. The only practical way to do this is by connecting it to the measurement (stagnation) point with a fluid filled pressure inlet tube. Variations in pressure will cause movement of this fluid so that it acts as a viscous damper.

The dynamic response of a transducer plus inlet tube will be different from that of the transducer alone. It will depend on transducer parameters, inlet tube dimensions and the inlet tube fluid. The dynamic response is best determined directly from tests with sinusoidal and step inputs. Alternatively a theoretical analysis can be used to estimate the parameters f_o and h from which the dynamic response can be calculated.

4.4 THEORETICAL ANALYSIS OF DYNAMIC RESPONSE

4.4.1 Introduction

Wad (1969) has developed an approximate analysis of the dynamic response of a pressure transducer connected to a pressure inlet tube. This is the only theoretical analysis known to the writer. It expresses M, D and K (ref. Eq. 4.1) in terms of transducer and inlet tube parameters. The resonant frequency and damping ratio can then be calculated from Eqs. 4.2 and 4.3.

It must be emphasized that this analysis is based on some questionable assumptions, as indicated in the following sections. In spite of these faults, Wad (1969) found it predicted results in reasonable agreement with his experimental measurements, (see Fig. 4.2). The analysis was therefore adapted with no attempt made to improve on it.

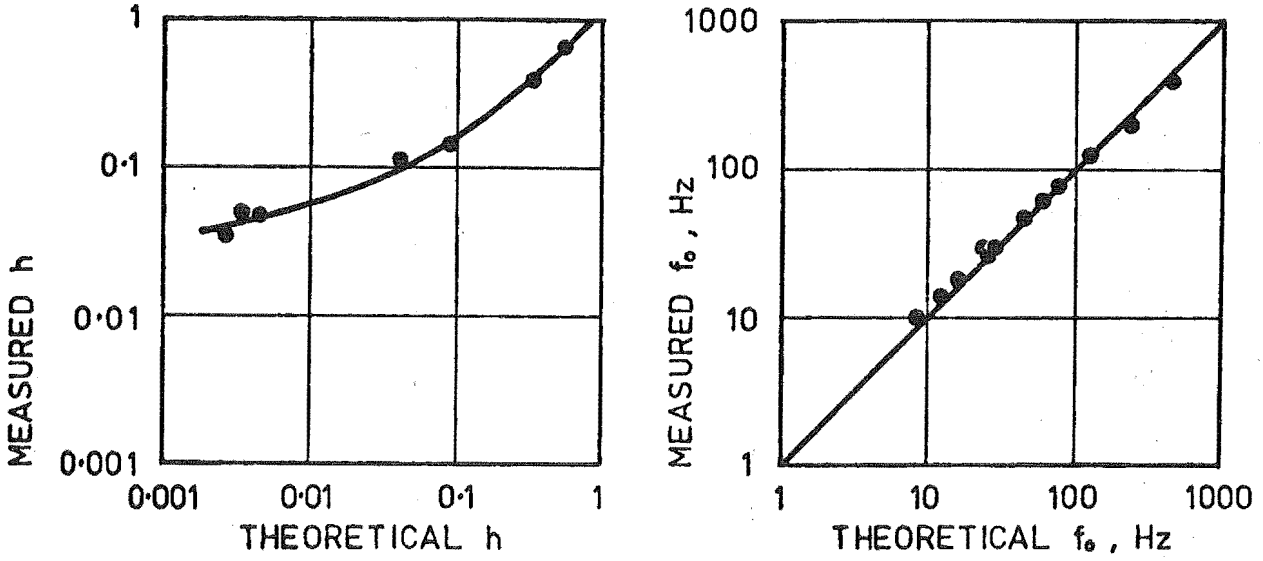

Fig. 4.2 Comparison of Theory with Measurements (From Wad, 1969).

The probes used here can be represented schematically as in Fig. 4.3. A pressure increase at the inlet tube entrance will be transmitted to the pressure transducer via the column of fluid in the inlet tube. This column will move towards the transducer because:

(i) deflection of the pressure sensing diaphragm (F),

(ii) deflection of the cover on the back of the transducer (E),

(iii) compression of any air bubbles not purged during assembly,

(iv) compression of a rubber "sock" within the transducer (H),

(v) compression of an O-ring seal at the transducer (G).

The analysis assumes the column of fluid in the inlet tube will act as a moving mass M. The movement of the fluid will provide viscous damping D. The restoring force K will be provided by the stiffness of those components whose deflection (or compression) allows the column of fluid to move.

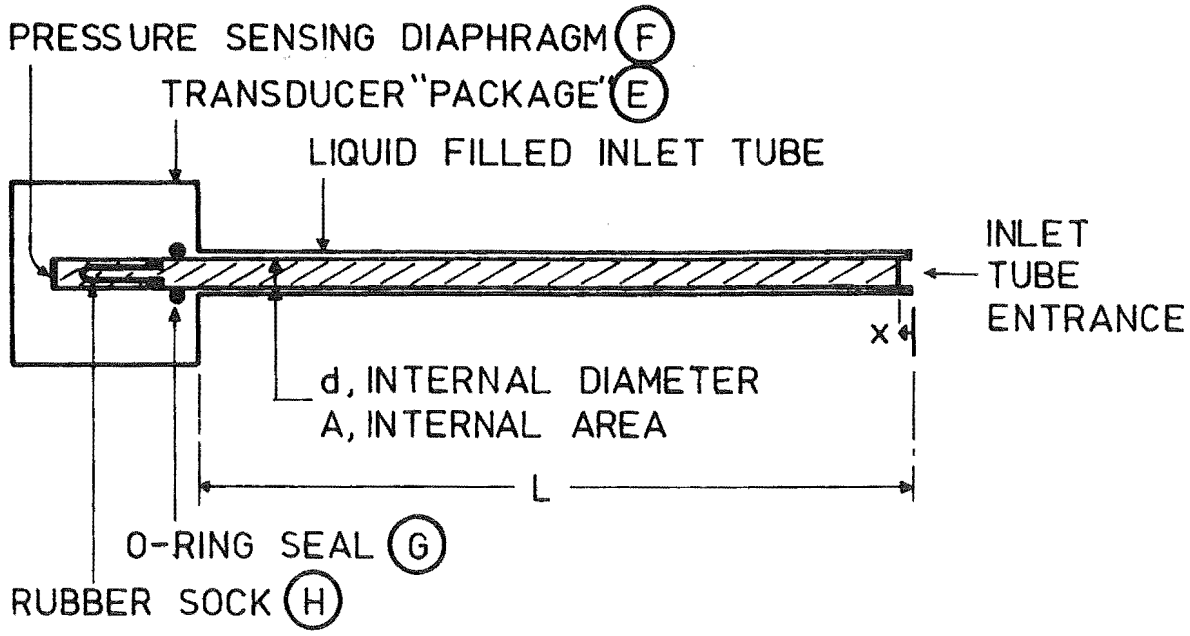

Fig. 4.3 Schematic of Pressure Transducer and Inlet Tube.

4.4.2 Spring Constant K.

Consider a small increase in pressure δP for which the column of fluid moves δx. The spring constant K is given by the force per unit displacement

$$K = \frac{A\delta P}{\delta x}$$

It is convenient to express δx in terms of the volume $\delta \forall$ where

$$\forall = A\delta x.$$

Combining these two equations

$$K = A^2 \frac{\delta P}{\delta \forall} \qquad 4.6$$

For a given transducer the ratio $\frac{\delta V}{\delta P}$ may be determined from static measurements.

4.4.3 Equivalent Mass M

Wad (1969) assumed that for the small movements of the fluid in the inlet tube, the flow could be considered laminar with a parabolic velocity distribution given by

$$V = 2\bar{V}\left[1 - \left[\frac{2r}{d}\right]^2\right] \qquad 4.7$$

where V is the velocity at a distance

r from the centre of the tube,

$\bar{V}$ is the mean velocity.

In fact, the parabolic velocity distribution could only develop with large movements of the fluid. Accepting this discrepancy the kinetic energy of a ring shaped element of radius r is

$$dE = \frac{1}{2}(\rho L 2\pi r.dr)V^2$$

Substituting Eq. 4.7 into this and integrating, we get the total kinetic energy of the moving fluid.

$$E = \frac{2}{3} LA\rho\bar{V}^2$$

but $$\bar{V} = \frac{dx}{dt}$$

so $$E = \frac{1}{2}\left[\frac{4}{3}LA\rho\right]\left[\frac{dx}{dt}\right]^2$$

Now if the fluid were moving as one solid column at the velocity $\frac{dx}{dt}$, the total kinetic energy would be

$$E = \frac{1}{2} M \left[\frac{dx}{dt}\right]^2$$

Thus we have an equivalent mass

$$M = \frac{4}{3} LA\rho \qquad 4.8$$

4.4.4 Damping D

Wad (1969) again assumed the small fluid movements to have a parabolic velocity distribution. He was therefore able to relate the damping to the pressure drop along the inlet tube

$$D\,\bar{V} = A\left[\frac{32\mu l\bar{V}}{d^2}\right]$$

where μ = dynamic viscosity,

so $D = 8\pi\mu L$ 4.9

4.4.5 Resonant Frequency and Damping Ratio

Substituting Eqs. 4.6, 4.8 and 4.9 into Eqs. 4.2 and 4.3 gives

$$f_o = \frac{1}{4\pi}\left[\frac{3A}{\rho L}\cdot\frac{\delta P}{\delta \Psi}\right]^{\frac{1}{2}} \qquad 4.10$$

$$h = 2\pi\mu\left[\frac{3L}{\rho A^3}\cdot\frac{\delta \Psi}{\delta P}\right]^{\frac{1}{2}} \qquad 4.11$$

Assuming the highest possible resonant frequency is determined by the wavelength of the sound waves in the liquid in the inlet tube, then f_o predicted by Eq. 4.10 should not exceed $\frac{C}{4L}$ where C is the velocity of sound in the liquid. (For the inlet tubes used at Aviemore, this limiting value was about 2.7 kHz).

Eqs. 4.10 and 4.11 can be used for:

(i) Predicting the dynamic response of a pressure transducer and inlet tube (see Sections 4.7.3 and 4.8.5).

(ii) Designing an inlet tube for optimum dynamic response (see Appendix G)

In both cases, it must be realised that the results are only approximate because of the assumptions in the analysis.

4.5 TEST METHODS FOR DETERMINING THE DYNAMIC RESPONSE OF PRESSURE TRANSDUCERS PLUS PRESSURE TRANSDUCERS AND INLET TUBES

4.5.1 Introduction

Sinusoidal and step inputs are both used in dynamic testing of pressure systems. Except for very small amplitudes, the necessary sinusoidal input can only be obtained at low frequencies. For higher frequencies, the frequency response must be obtained from the response to a step (or impulse) input by either graphical or analogue computer techniques.

Step inputs require the change from one known pressure level to a second known level in a time sufficiently short to shock-excite the instrument at its resonant frequency. These can be provided by: opening a valve. Minimum rise times are about 10 ms; burst diaphragm shock tubes. Minimum rise times are about 100 μs; while high pressure explosive shocks have rise times of about 1 μs.

So little information has been published on the design of sinusoidal or step input devices that it was necessary to develop the two devices used here. The first was similar to a burst diaphragm shock tube except that it used water instead of a gas. It produced step inputs with rise times of about 1 ms. This can be used to shock a transducer into oscillation when its resonant frequency is less than 2 kHz. The second used an MTS machine to produce sinusoidal pressure fluctuations in a small container. The fluctuations were limited to about 100 Hz maximum.

4.5.2 Step Input Test Apparatus

This was designed to create step pressure inputs in the range 0 - 250 N/m^2, with a 20 ms test duration. The apparatus, shown in Fig. 4.4, consists of 2 cylindrical steel pressure vessels 320 x 380 mm diameter, interconnected by a copper pipe 12.4 m x 17.1 mm diameter. To operate, a thin plastic membrane (B) is inserted between one cylinder and the pipe and the system is filled with water and bled. A slowly increasing differential pressure is applied across the membrane until it bursts. Pressure waves (water hammer) then travel through the water in the pipe and in the tank at 1.24×10^3 and 1.08×10^3 m/s respectively, (ref. Appendix H).

The transmission and reflection factors for pressure waves in both the cylinders and in the pipe are calculated in Appendix H. These show that the pressure wave entering the cylinder is very much smaller than that in the pipe. This very small wave is reflected back and forth within the cylinder, with a very small wave transmitted into the pipe each time. Simultaneously, the pressure wave in the pipe travels to the other cylinder where it is reflected back, returning to the first cylinder 20 ms later. Pressure waves will continue to travel throughout the system until it reaches an equilibrium pressure, many seconds later.

Most tests were at a point in the pipe 100 mm from the membrane. After the initial pressure change, the pressure at this point remains almost constant for 20 ms, as illustrated in Fig. 4.4.

Less than 5% of the tests with this apparatus were successful. The other tests resulted in high amplitude oscillations of random frequency, as shown in Fig. 4.5. The writer considers the most likely explanation

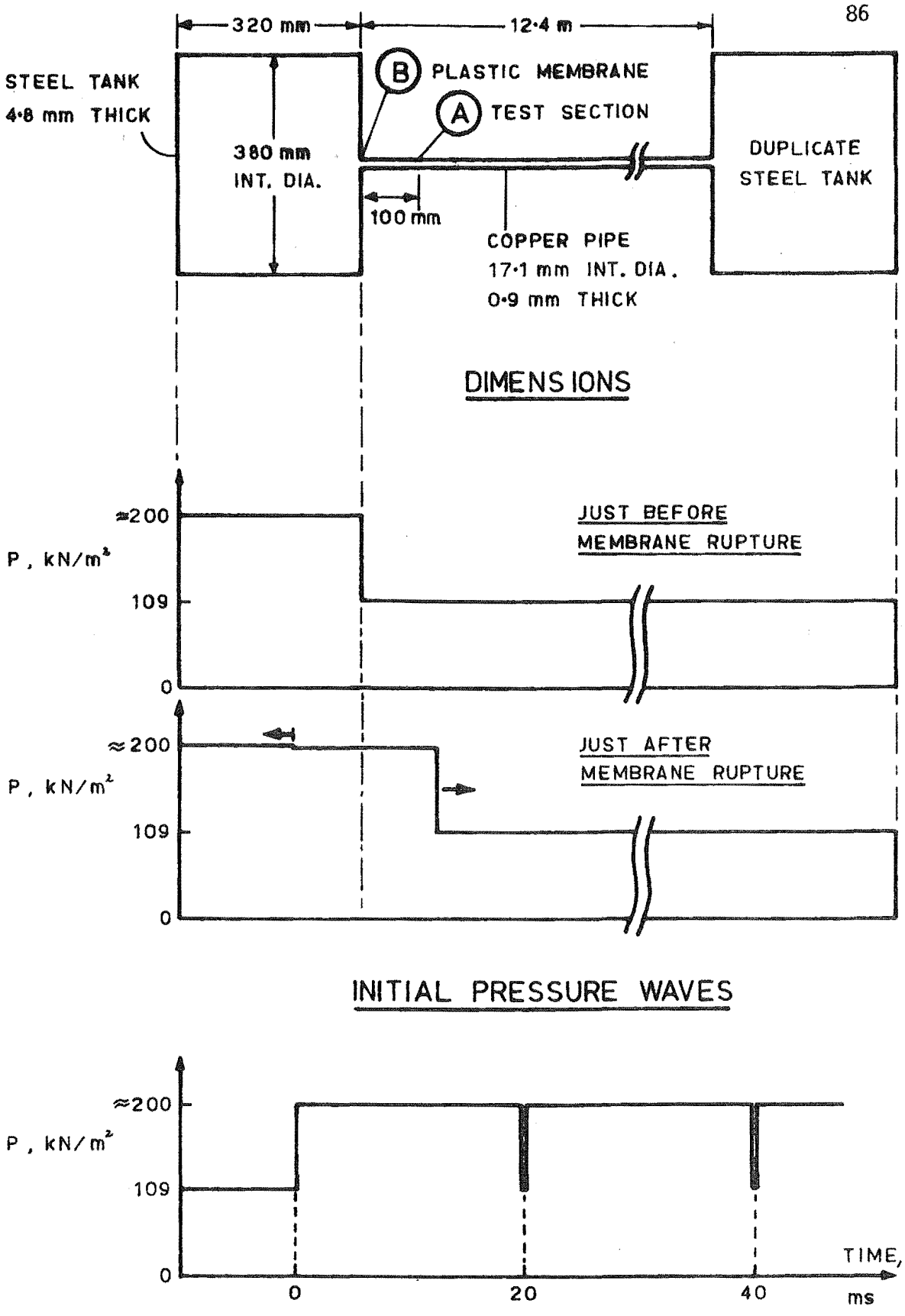

Fig. 4.4 Step Input Apparatus.

for this inconsistent behaviour is that variations in the plastic membranes caused them to rupture differently.

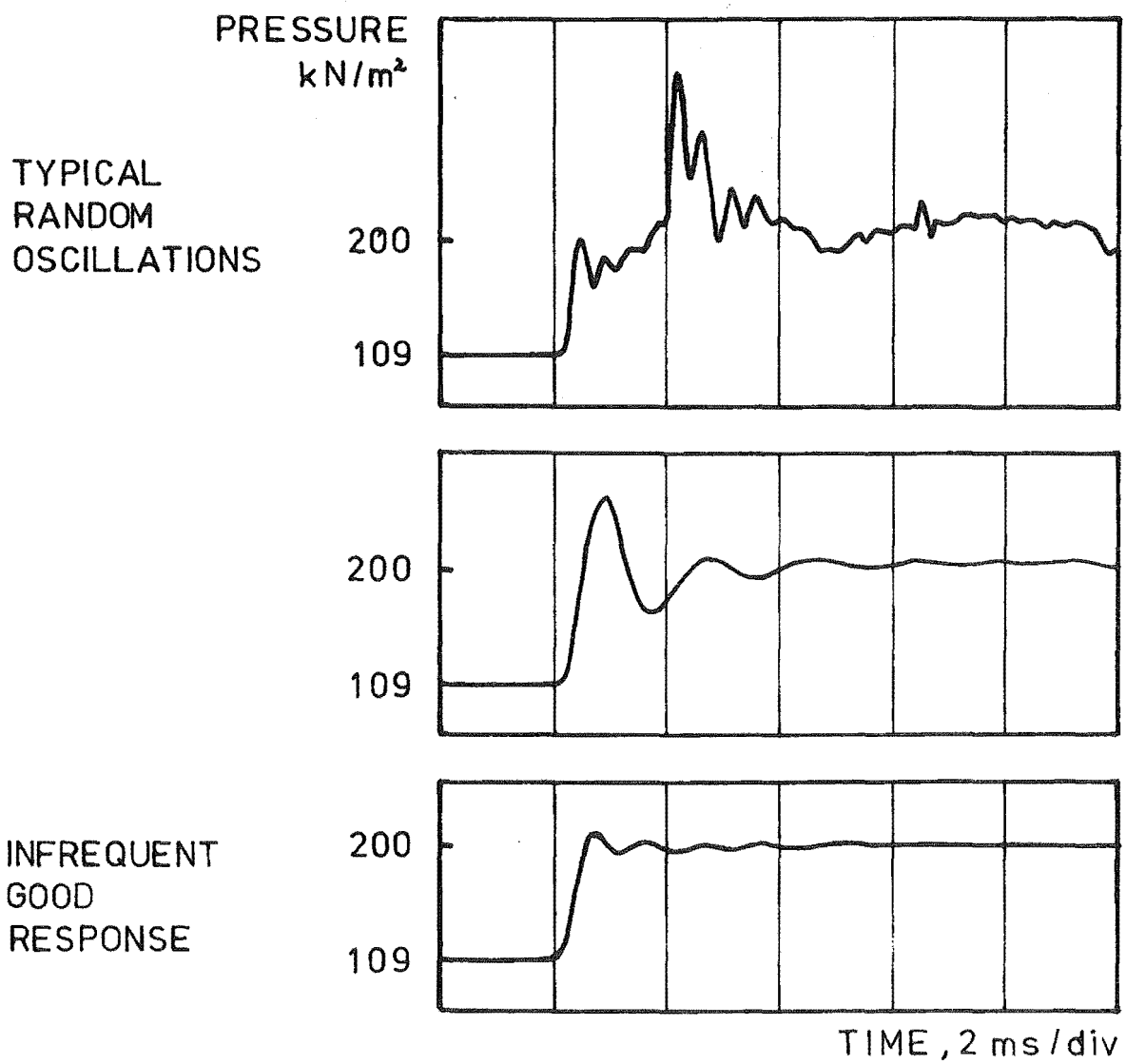

Fig. 4.5 Sample Results from Step Input Apparatus. (National Semiconductor pressure transducer with water filled pressure inlet tube about 20 mm long and 4.8 mm internal diameter).

The best results were measured at A (Fig. 4.4) with the pipe thoroughly bled but with the cylinder adjoining the membrane full of air. The fastest step pressure changes occurred in 0.5 - 1 ms, (Fig. 4.5). This apparatus can therefore be used to shock a transducer into oscillation when its resonant frequency is less than 2 kHz. Because of the low test success rate, it was necessary to also use a reference transducer whose resonant frequency was much larger than 2 kHz. By connecting them both at A, the reference transducer would indicate whether the input was in fact a step pressure change.

4.5.3 Sinusoidal Input Test Apparatus

To measure the frequency response of a probe, it was connected to one end of a short length of high pressure rubber hose as shown in Fig. 4.6. A transducer with a much higher frequency response was also connected to provide a reference. A valve at the other end of the hose allowed it to be filled with water and sealed.

Pressure fluctuations were generated by compressing the hose with the hydraulic ram of an MTS machine. A sinusoidal ram motion caused pressure fluctuations that were almost sinusoidal. The maximum input frequency was limited to about 100 Hz by the MTS machine.

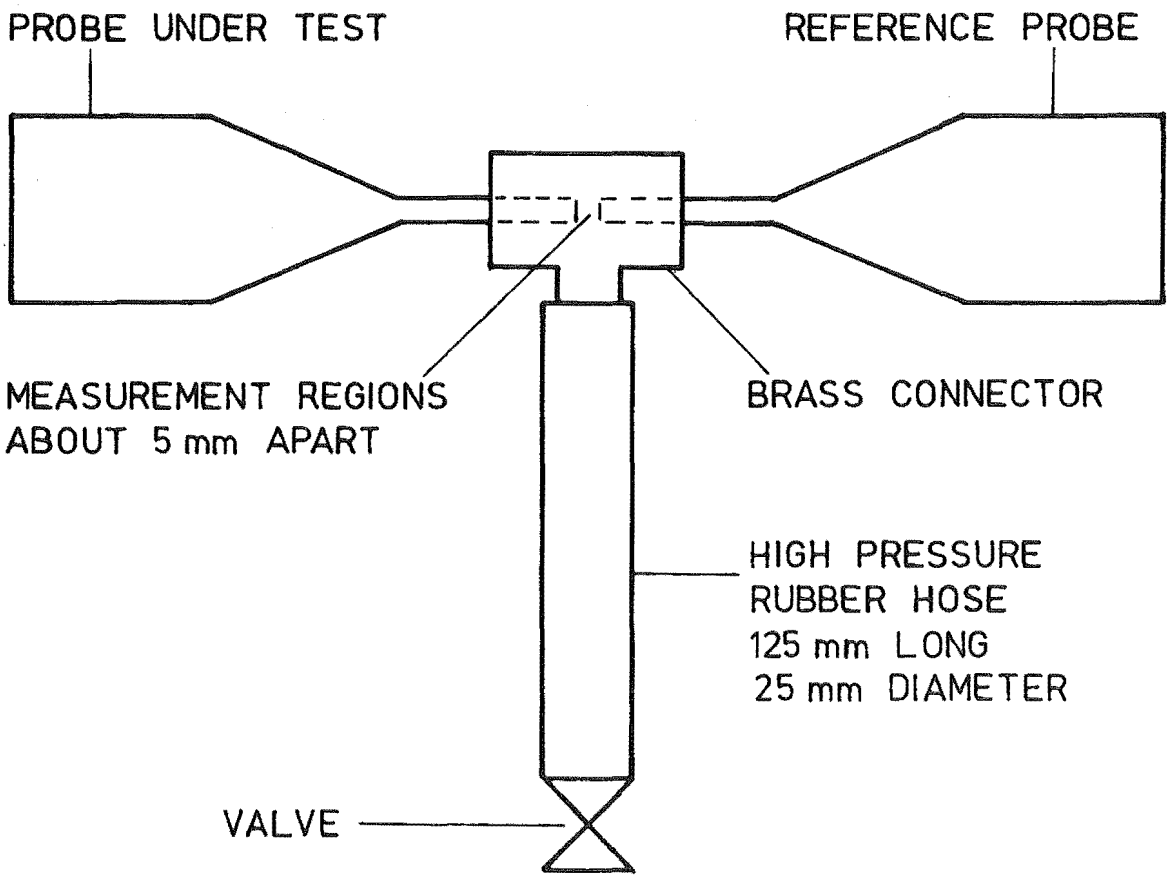

Fig. 4.6 Schematic of Sinusoidal Test Apparatus.

4.6 PRESSURE TRANSDUCER SELECTION

Only 2 commercial pressure transducers were initially available, a Celesco capacitive type transducer (model KP15), and a National Semiconductor piezo resistive type transducer (LX1610G). 20 Shinkoh strain gauges (FD108) were also available. A number of transducers were made in the laboratory by bonding these to metal diaphragms about 9 mm diameter and about 0.2 mm thick. Some of these transducers are shown in Fig. 4.7.

As their dynamic response was unknown, they were tested in the step input apparatus previously described, each connected with a water filled inlet tube about 20 mm long and 4.8 mm internal diameter. The Celesco was found to resonate at frequencies from 250 - 650 Hz, depending on the diaphragm used. The other transducers could not be shock excited, suggesting their resonant frequencies were higher than 2 kHz.

The bonded strain gauge devices could be incorporated into very small probes, one preliminary design using 2 mm diameter inlet tubes only 21 mm long (ref. A, Fig. 4.7). However, these dimensions were considered too small compared with the bubble size, (see Section 3.5).

The National Semiconductor transducers were finally selected and the probe was designed to suit them. They offered good static response specifications, simple electronic requirements, and most importantly were "readily" available.

Their poor design complicated the inlet tube connections and the water proofing of electrical connections, and made them susceptible to accidental damage. Seven transducers were purchased altogether, although one was unsuitable, having been acquired because of misleading

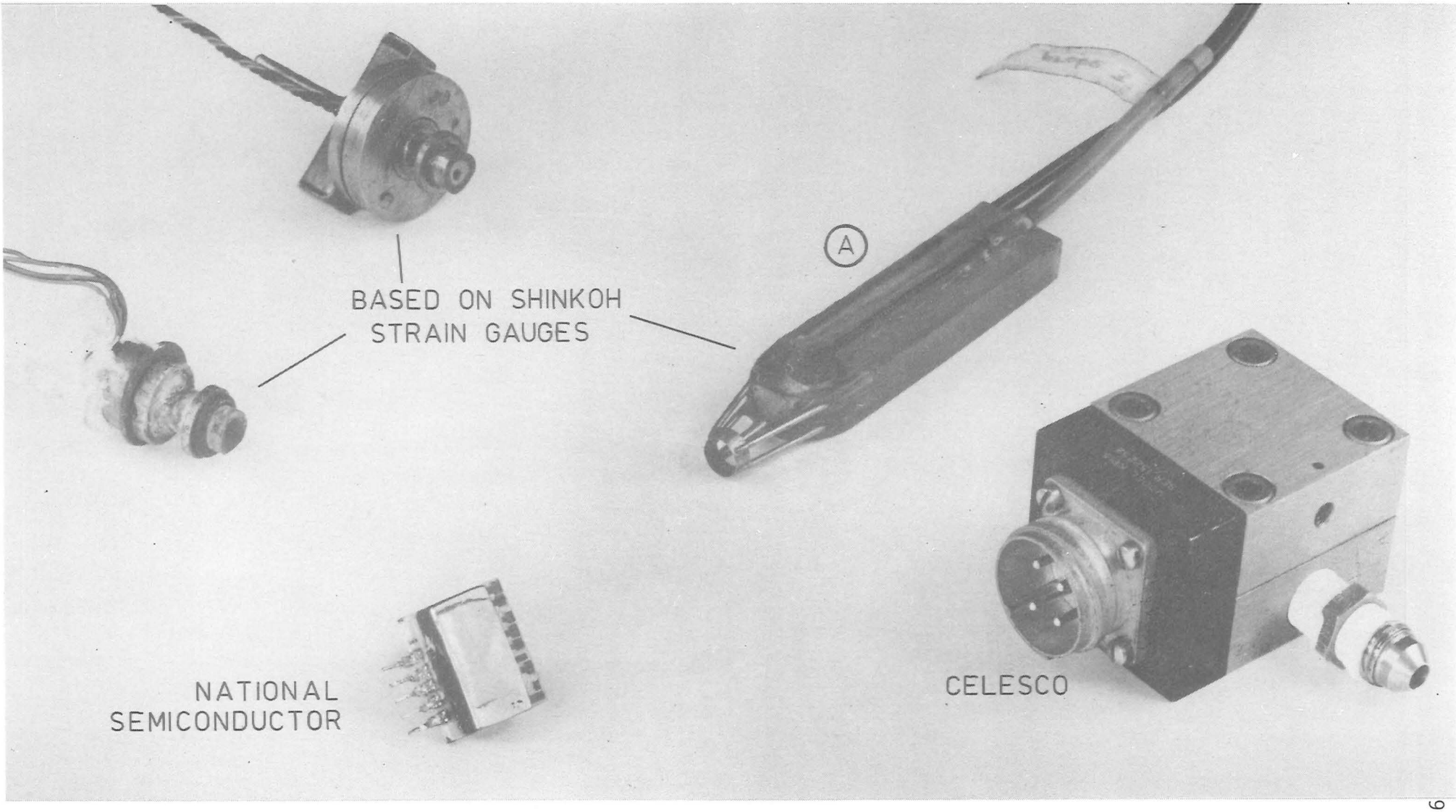

Fig. 4.7 Pressure Transducers.

advertising. Two ruptured at low pressures. The backs of all subsequent transducers were spring loaded to prevent this problem recurring. Three other transducers were damaged because of their bad packaging.

Two other types of commercial transducers later became available: (i) A Bell and Howell unbonded strain gauge device which had excellent static response specifications, (about 0.1% FS). This was mounted so that it could be interchanged with the National Semiconductor devices, although it was rarely used because it was the wrong pressure range. (ii) Four Kyowa miniature bonded strain gauge devices, only 6 mm diameter and 2 mm thick. These had the highest resonant frequency of all the transducers used (about 20 kHz) and would have been ideal had they been available initially. These were mounted without inlet tubes as shown in Fig. 4.8, and were used as a reference in the tests reported here.

Manufacturers specifications for the National Semiconductor and Kyowa transducers are contained in Appendix E.

For the National Semiconductor transducers chosen, it was necessary to measure the ratio $\frac{\delta \Psi}{\delta P}$ for the theoretical analyses, (Section 4.4.2). To do this a transducer was fixed to one end of a glass tube, and the other end was connected to a variable pressure air supply as shown in Fig. 4.9. The internal diameter of the glass tube tapered from the transducer to a constant value, about 0.59 mm. The tube was water filled from the transducer to about 30 mm from the other end. The position of the air-water interface (A) indicated the variation in the internal volume of the transducer with variations in air pressure. The measurements from several tests are plotted in Fig. 4.10. This

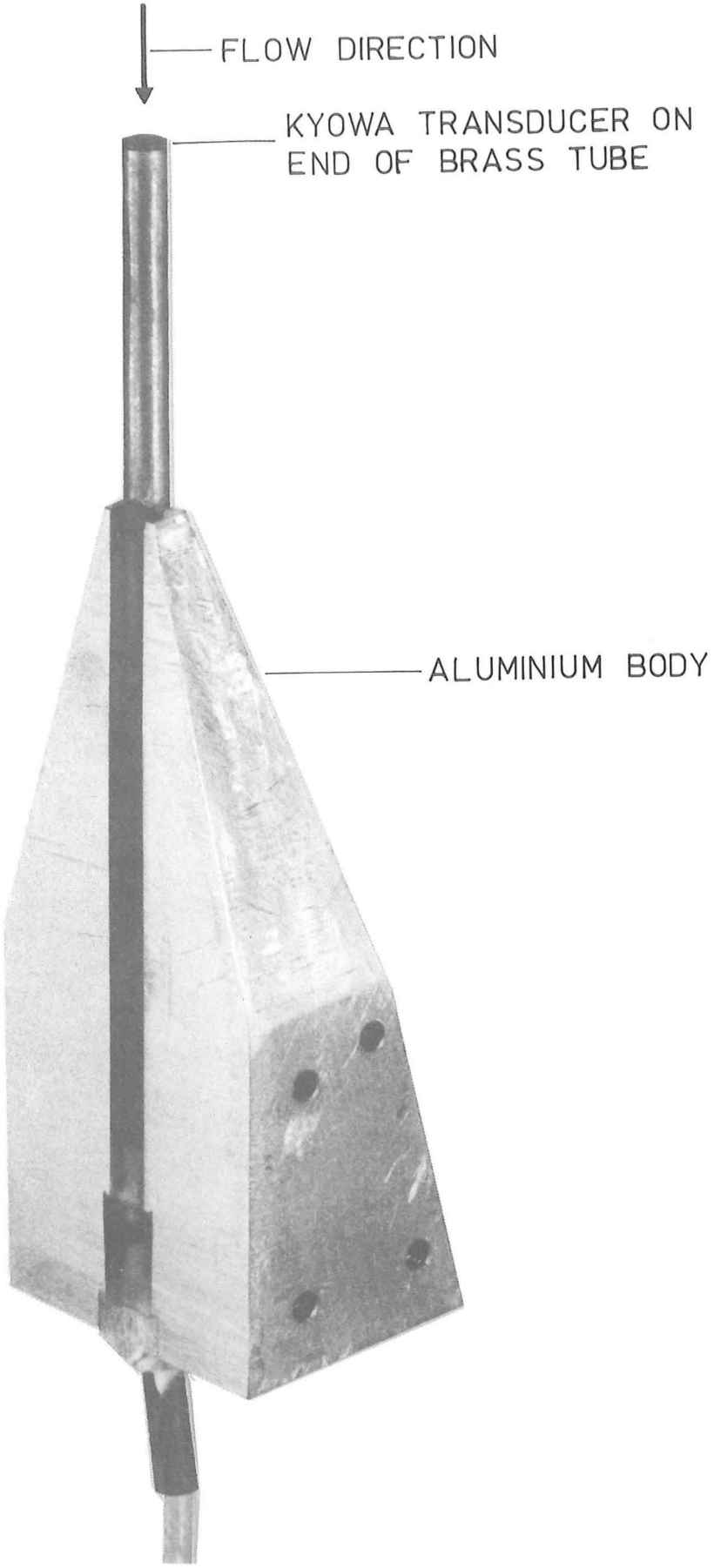

Fig. 4.8 Kyowa Pressure Probe.

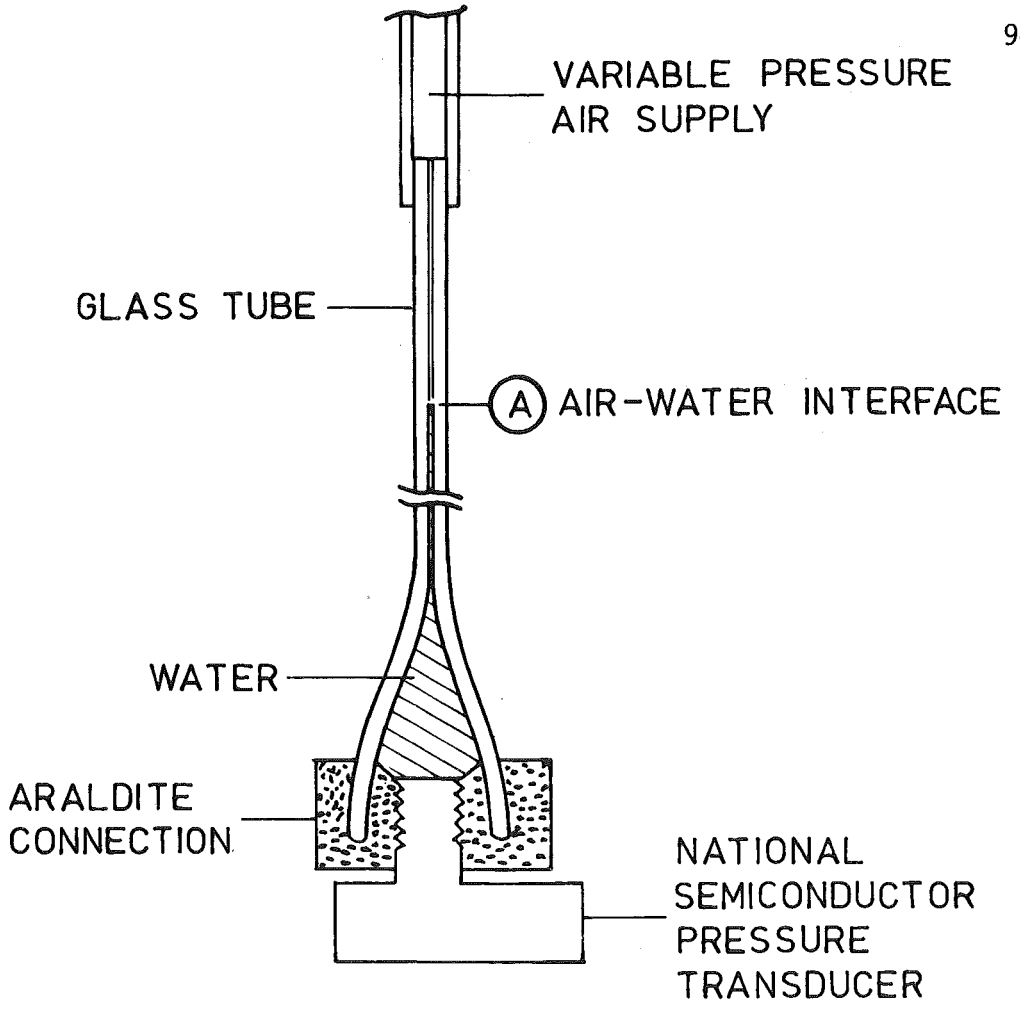

Fig. 4.9 Schematic of Transducer Test Apparatus.

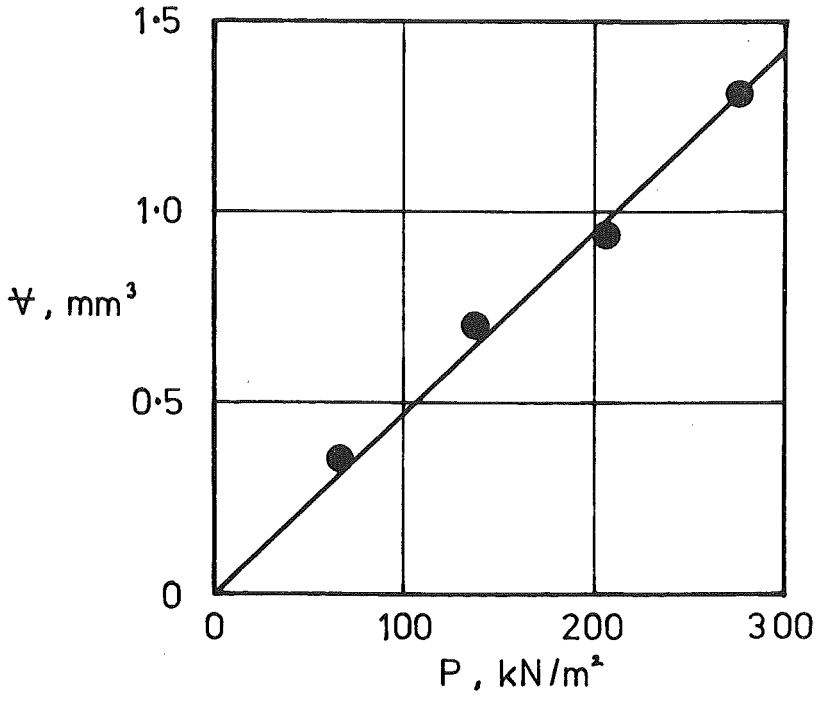

Fig. 4.10 Results of Transducer Test.

shows a linear relationship for which

$$\frac{\delta \Psi}{\delta P} = 4.8 \times 10^{-15} \ m^5/N.$$

For the pressure changes expected at Aviemore, the volume change within the transducer is about 1 mm^3. If the total volume of any bubbles in the fluid in the inlet tube is about 1 mm^3 or larger, the ratio $\frac{\delta \Psi}{\delta P}$ will be significantly increased. The effect of such an increase on the dynamic response of the probe is discussed in Section 4.8.5.

4.7 PRESSURE INLET TUBE USED IN INITIAL FIELD TESTS

4.7.1 Development of Inlet Tube

No theoretical analysis was available to assist in the optimum design of an inlet tube for the initial field tests. The initial designs were influenced primarily by the construction requirements of a combined pressure air concentration probe that could meet the design criteria previously discussed. These resulted in tentative inlet tube dimensions of 6 mm external diameter, 4.8 mm internal diameter and 130 mm long.

A series of qualitative tests followed to assess this design. These were conducted in aerated flow in the A flow simulator. (This simulator is described in Section 6.3). The results of these tests are described below:

(1) Inlet tubes with internal diameters as large as 4.8 mm had to be water filled as any other liquid was quickly displaced by water.

(ii) Inlet tubes ranging in length from 50 - 150 mm were tested under a range of flow conditions. Each was 6 mm external diameter and 4.8 mm internal diameter and was water filled. The output signals were displayed on a storage oscilloscope and the screen was photographed. Comparison

of these photographs showed no apparent differences, with maximum frequences about 1-2 kHz.

(iii) An air pocket always formed at the entrance to the pressure transducer. This was observed by disconnecting the pressure transducer from the inlet tube under water. A bubble about 3-5 mm diameter would rise to the surface regardless of the duration of the test. It was not until after the initial field tests that this air was found to adversely effect the dynamic response.

(iv) Inlet tubes with smaller internal diameters were to be tested also. This was prevented by the failure of both of the National Semiconductor transducers.

The replacement transducers took three months to arrive. In this time, the combined pressure air concentration probe was constructed using a pressure inlet tube similar to those tested in the laboratory flow simulator. Its construction and design was such as to allow modifications to the inlet tube if subsequent dynamic response tests indicated these were necessary.

By the time the transducers arrived, it was anticipated that water would become available for field tests within weeks. This left insufficient time to complete the qualitative tests in the flow simulator or to test any inlet tubes in the step input test apparatus. (The sinusoidal test apparatus was not developed at this stage).

Because the qualitative tests in the flow simulator had not indicated any faults with the inlet tube design, it was not modified at all for these field tests.

4.7.2 Initial Field Tests

The initial field tests at Aviemore are described in Chapter 8. Measurements of stagnation pressure through the aerated flow were obtained at only one spillway station before the tests were cancelled.

As expected, the upper regions of the flow produced input pressures that approximated step changes and impulses. It is therefore possible to predict the dynamic response characteristics f_o and h of the pressure instrument without using the laboratory test apparatus (step or sinusoidal input).

Fig. 4.11 shows two particularly interesting records of stagnation pressure and air concentration recorded in these tests. Fig. 4.11a shows the response to an impulse input caused by the crest of a wave or a large water droplet. Comparison of Figs. 4.1c and 4.11a shows the pressure signal is different from all the theoretical ones. These differences are explained in the next section in terms of non-linear response. Approximate values of the resonant frequency and damping ratio from Figs. 4.1c and 4.11a are $f_o \simeq 70$ Hz and $h \simeq 0.1 - 0.2$.

Fig. 4.11b shows the output signals in very aerated flow. The air concentration signal indicates the probe is intercepting a series of "waves". This would appear as a series of step pressure inputs. Comparison of the pressure signal with Fig. 4.1b again shows differences between the observed and theoretical responses. The transducer has "clipped" the pressure signal in Fig. 4.11b at its maximum value of 345 kN/m^2. This is about twice the pressure expected at this velocity. This is caused by the small damping ratio $h \simeq 0.1 - 0.2$ as shown in Fig. 4.1b.

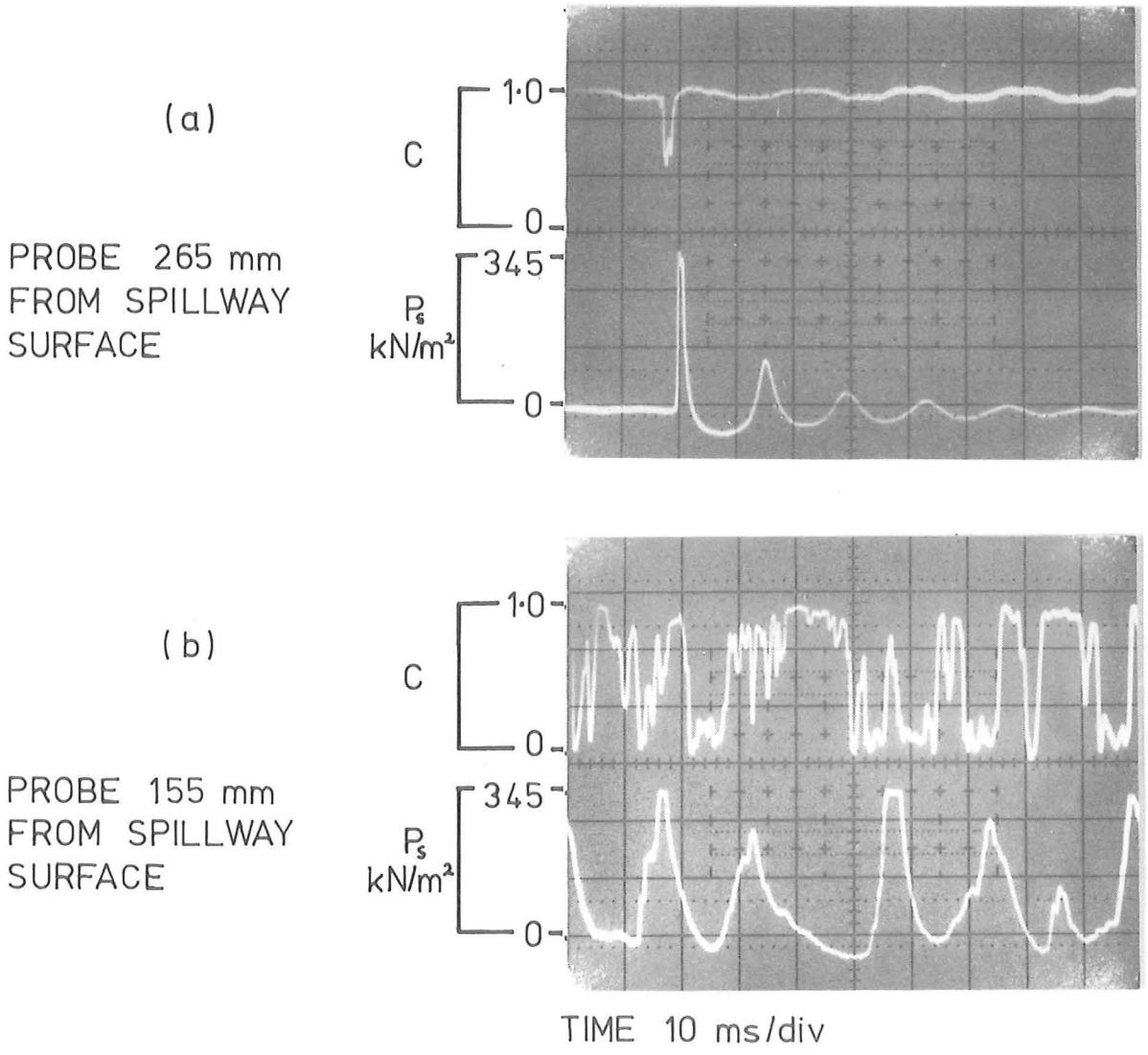

Fig. 4.11 Probe Response.

Station 401, gate open 300 mm

(50 Hz mains hum on the C signal in (a)).

4.7.3 Theoretical Analysis of Inlet Tube for Initial Field Tests

The writer first read Wad's (1969) theoretical analysis of the dynamic response of pressure inlet tubes shortly after the initial field tests. It is shown below that this analysis predicts and explains the observed dynamic response reasonably well.

It is necessary to modify Wad's (1969) analysis because the ratio $\frac{\delta \forall}{\delta P}$ (see section 4.4.2) will now be dependent almost entirely on the volume of the air pocket that was observed to form at the entrance to the transducer. Compression of this air pocket will cause the movement of the column of water in the inlet tube. The pressure within the air pocket will provide the restoring force.

Consider an air pocket of volume $\forall$ at pressure P. A small increase in pressure δP will cause a small decrease in volume $\delta \forall$. The air will be compressed isothermally so that

$$P \forall = \text{const.} \qquad 4.12$$

Differentiating gives

$$P \delta \forall + \forall \delta P = 0$$

$$\frac{\delta \forall}{\delta P} \simeq - \frac{\forall}{P}$$

Combining this with Eq. 4.12 gives

$$\frac{\delta \forall}{\delta P} = \frac{\text{const}}{P^2} \qquad 4.13$$

The new expressions for f_o and h can now be obtained by substituting Eq. 4.13 into Eqs. 4.10 and 4.11

$$f_o = \frac{P}{4\pi} \left[\frac{3A}{\rho L . \text{const}} \right]^{\frac{1}{2}} \qquad 4.14$$

$$h = \frac{2\pi\mu}{P} \left[\frac{3L . \text{const}}{\rho A^3} \right]^{\frac{1}{2}} \qquad 4.15$$

Eq. 4.14 shows that the resonant frequency is proportional to the pressure. This explains the non-linear (pressure dependent) behaviour of the signal in Fig. 4.11a.

Substituting Eq. 4.13 into Eq. 4.6 gives the new expression for the spring constant K

$$K = \left[\frac{A^2}{\text{const}}\right] P^2$$

It is apparent that for a given inlet tube and quantity of air at the transducer, K is not in fact constant but proportional to the square of the pressure. The dynamic response will therefore not be described exactly by the theoretical analysis. In spite of this, satisfactory results can be obtained by evaluating fo and h (Eqs. 4.14 and 4.15) at the minimum pressure P_o (atmospheric) and the maximum pressure P_1 expected at Aviemore. If the volume of the pocket of air is V_o at atmospheric pressures then the value of the constant in Eqs 4.14 and 4.15 can be evaluated using Eq. 4.12 as

$$\text{const} = P_o V_o$$

Table 4.1 lists the values of f_o and h calculated with Eqs. 4.14 and 4.15. These were evaluated for various sized air pockets which are for convenience considered to be spheres of diameter $\emptyset_o$ at atmospheric pressure. For $\emptyset_o$ = 3 - 5 mm as observed in the laboratory tests, Table 4.1 indicates:

$f_o \simeq$ 50 - 160 Hz when P is a minimum

$f_o \simeq$ 170 - 530 Hz when P is a maximum

and h $\simeq$ 0 for all P.

This compares well with the mean values $f_o \simeq 70$ Hz and h $\simeq$ 0.1 - 0.2 observed from the measurements at Aviemore, (Fig. 4.11a).

Table 4.1 Prediction of f_o and h

where : L = 130 mm, A = 17.8 mm^2, $\rho = 10^3$ kg/m^3, $\mu = 1.13 \times 10^{-3}$ Ns/m^2, $P_o = 102 \times 10^3$ N/m^2 (abs), $P_1 = 329 \times 10^3$ N/m^2 (abs).

Bubble Diameter $\emptyset_o$ (mm)	Resonant Frequency f_o, Hz		Damping Ratio h	
	$P = P_o$	$P = P_1$	$P = P_o$	$P = P_1$
12.4	16.2	52.8	5.87×10^{-3}	1.80×10^{-3}
5.76	51.3	167	1.86×10^{-3}	570×10^{-6}
2.67	162	528	587×10^{-6}	180×10^{-6}
1.24	513	1670	186×10^{-6}	57×10^{-6}

The dynamic response of this inlet tube and transducer was considered unacceptable because:

(i) Fig. 4.1a indicates that for $f_o \simeq 70$ Hz and $h \simeq 0.1$, the flat frequency response would be limited to about 20 Hz.

(ii) Even if the output signal was filtered (electronically) to 20 Hz, the instantaneous and mean values of pressure could be incorrect because of the non-linear response.

(iii) The large pressures, observed in Fig. 4.11b and predicted by Fig. 4.1b for h ≃ 0, could easily destroy the transducers.

4.8 PRESSURE INLET TUBE USED IN FINAL FIELD TESTS

4.8.1 Development of Inlet Tube

It was considered necessary to modify the inlet tube to improve its dynamic response. The theoretical analysis indicated that preventing air from entering the inlet tube would result in the following improvements:

(i) The resonant frequency, and thus the frequency response, would increase significantly.

(ii) The spring constant K would be a constant, so that the response would be linear.

A series of qualitative tests followed, aimed at preventing air from entering the inlet tube and increasing the damping ratio. Nine different inlet tubes (Fig. 4.12) were tested in the A flow simulator. These were filled with water and oils (SAE 20 to SAE 90). The output signals were displayed on an oscilloscope and the screen was photographed for comparisons, as shown in Fig. 4.13.

The results of these tests are summarised below:

(i) If even a small volume of air entered an inlet tube during a test, the dynamic response would alter, often dramatically.

(ii) No practical construction method could be devised for fixing flexible membranes to the entrance of the inlet tubes to prevent the entry of air, (see inlet tube C, Fig. 4.12).

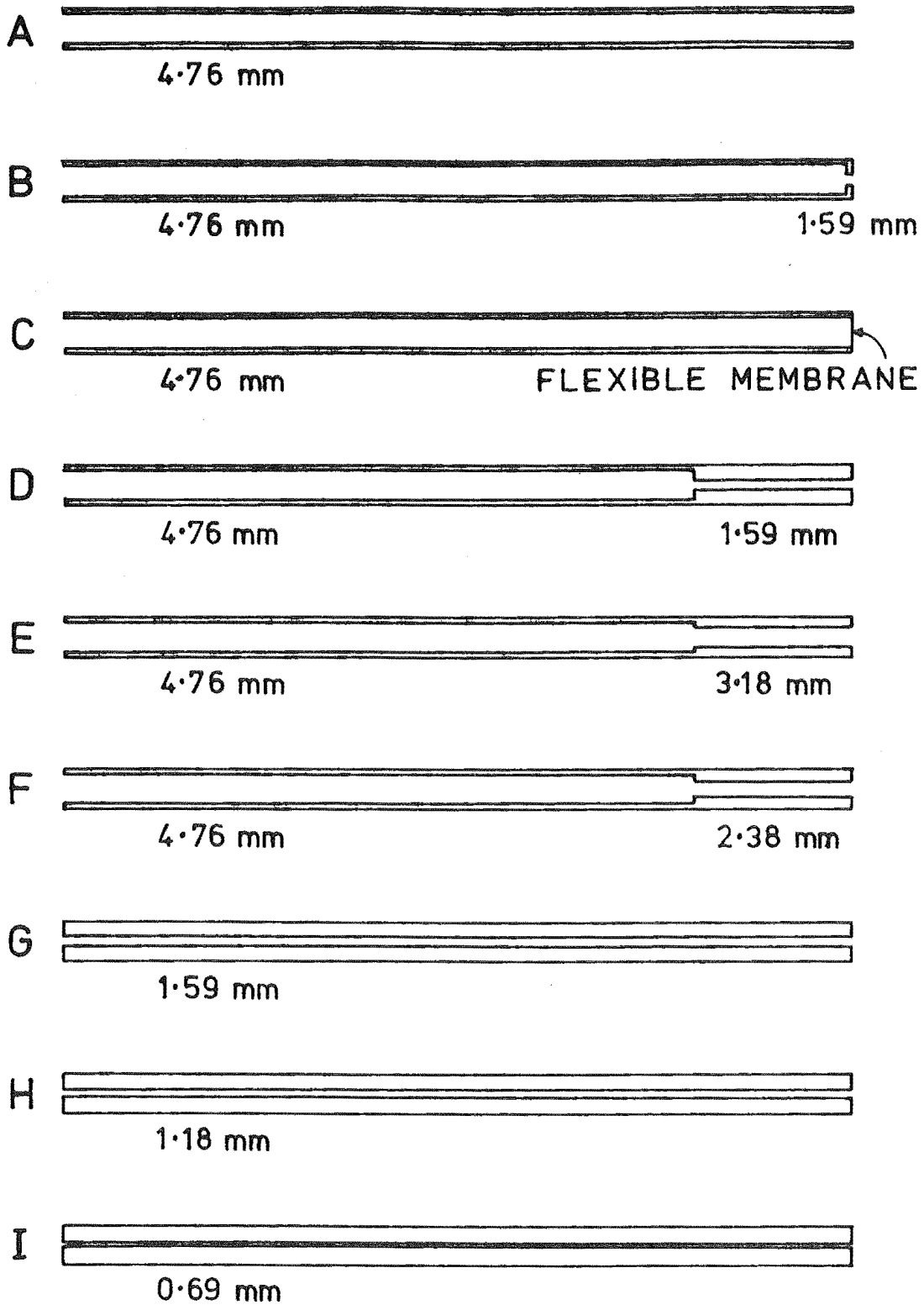

All inlet tubes 6.4 mm external diameter. Internal diameters as indicated at that section. Nominal length 125 mm.

Pressure transducers connected to left hand ends.

Fig. 4.12 Inlet Tube Configurations.

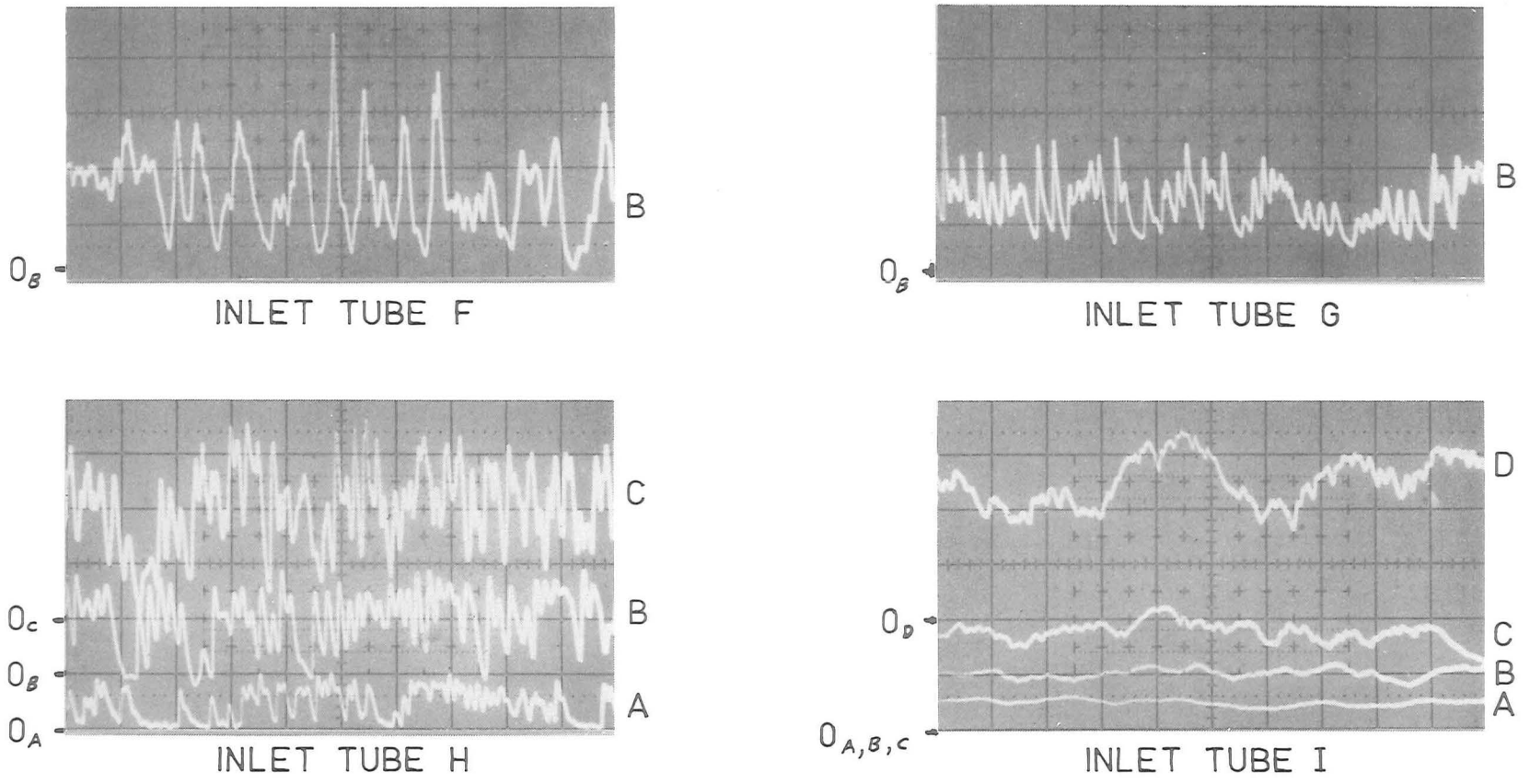

A, B, C & D INDICATE 4 DIFFERENT VELOCITIES.
0_x INDICATES ZERO PRESSURE FOR VELOCITY X

HORIZONTAL SCALE 10 ms/div
VERTICAL SCALE 68 kN/m²/div

Fig. 4.13 Sample Pressure Signals.

(iii) Only inlet tube I, filled with oil, prevented air entering in all tests.

(iv) The theoretical analysis predicted qualitatively the effect on the frequency response of the inlet tube geometries and liquid viscosities. Difficulties in measuring the ratio $\frac{\delta\Psi}{\delta P}$ (Section 4.6) for the pressure transducer prevented quantitative theoretical predictions of the frequency response until much later.

4.8.2 Final Field Tests

Anticipated availability of water for further field tests forced the writer to adopt an inlet tube design and modify the combined pressure air concentration instrument. There was insufficient time to first measure the dynamic response of the various inlet tubes in the step input test device. This would have allowed choice of an inlet tube with best performance.

Inlet tube design I filled with SAE 30 oil was chosen because only this design had consistently excluded the entry of air. The qualitative tests in the A flow simulator showed this inlet tube had the lowest frequency response of all the inlet tubes tested. Theoretical predictions of the frequency response, based on estimates of $\frac{\delta\Psi}{\delta P}$ for the pressure transducer, indicated only that the response would be overdamped.

The internal diameter of the inlet tube of the combined pressure air concentration instrument was modified by aralditing a 0.69 mm internal diameter stainless steel tube within the existing copper inlet tube.

All measurements were successfully obtained in these field tests, which are described in Chapter 9. Comparison of the pressure and air concentration signals showed that the pressure instrument was overdamped

and had a very low frequency response. Because it was overdamped, it was not possible to estimate the resonant frequency and damping ratio from its response to step or impulse inputs caused by the aerated flow.

It was therefore necessary to measure the dynamic response in the laboratory.

4.8.3 Laboratory Measurement of Step Input Response

The pressure inlet tube used in the final field tests was tested in the step pressure input device previously described. This and a fast response Kyowa pressure transducer (ref. Section 4.6) were mounted directly opposite each other at A (Fig. 4.4).

As mentioned earlier, most tests resulted in random oscillations which were attributed to variations in the plastic membranes. The Kyowa transducer provided a reference allowing such tests to be rejected.

More than 100 tests were recorded on the FM tape recorder before two satisfactory step inputs were obtained. The two signals of each were originally transferred to a chart recorder (using the technique described in Appendix E) but have been traced and superimposed here for comparison. They are shown in Fig. 4.14. As expected, the response to both increasing and decreasing step pressure inputs is almost identical.

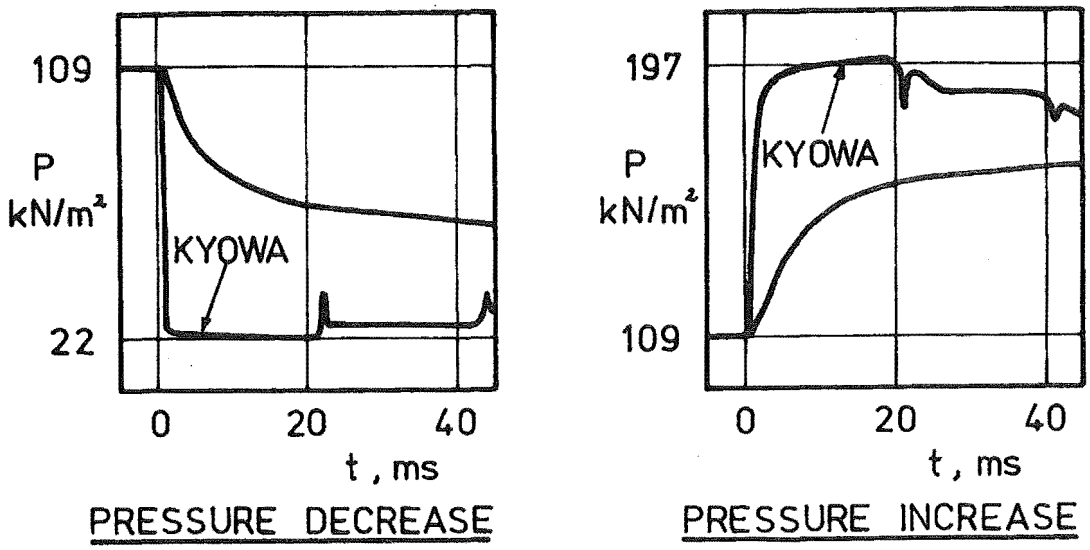

Fig. 4.14 Probe Response to Step Input.

4.8.4 Laboratory Measurement of Frequency Response

The frequency response was measured using the sinusoidal test apparatus previously described. The fast response Kyowa Pressure transducer was again used as a reference. Five input frequencies were used from 1 - 20 Hz. In each case, the input pressure range was about $20 \times 10^3 - 150 \times 10^3$ N/m^2. The output signals from both transducers were recorded on a chart recorder, as shown in Fig. 4.15.

The attenuation of the amplitude was measured from these recordings and used to plot the frequency response (Fig. 4.16). This is flat to less than 1 Hz, much less than the 1 kHz initially sought. This effectively prevented any turbulent velocity calculations with the data measured in the final field tests at Aviemore.

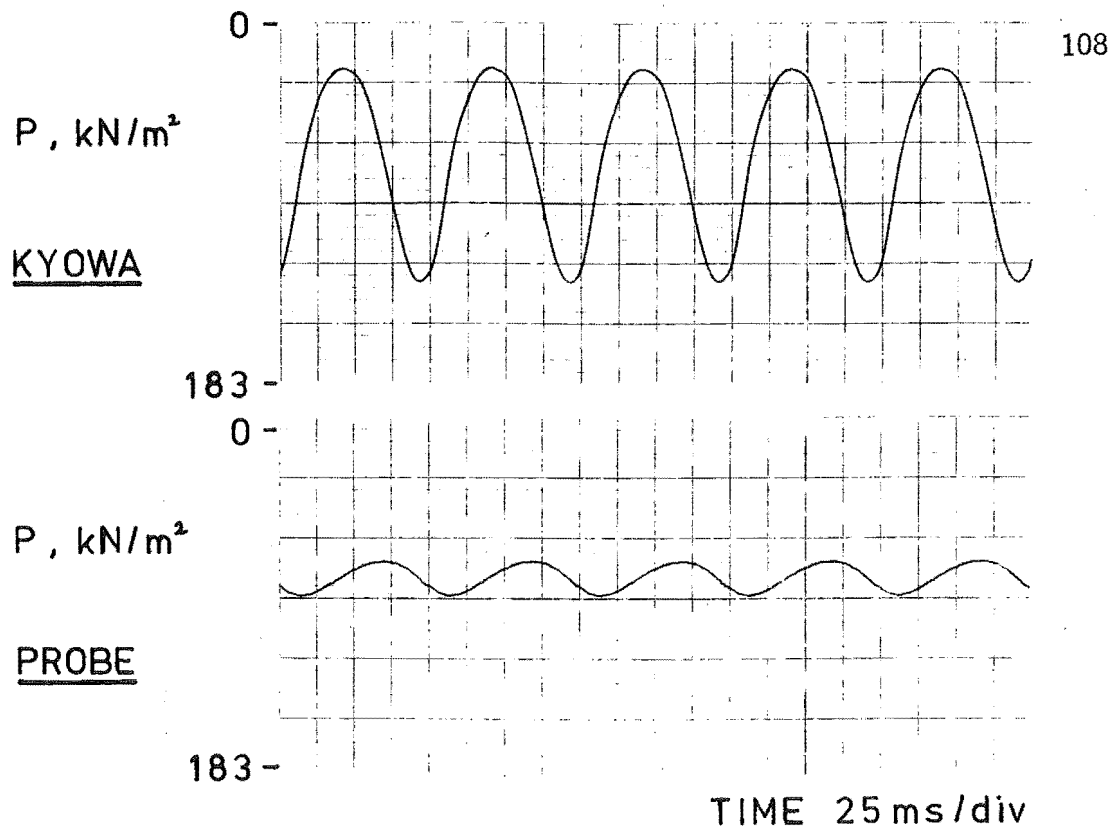

Fig. 4.15 Sample Output from Sinusoidal

Test Apparatus. f = 10 Hz.

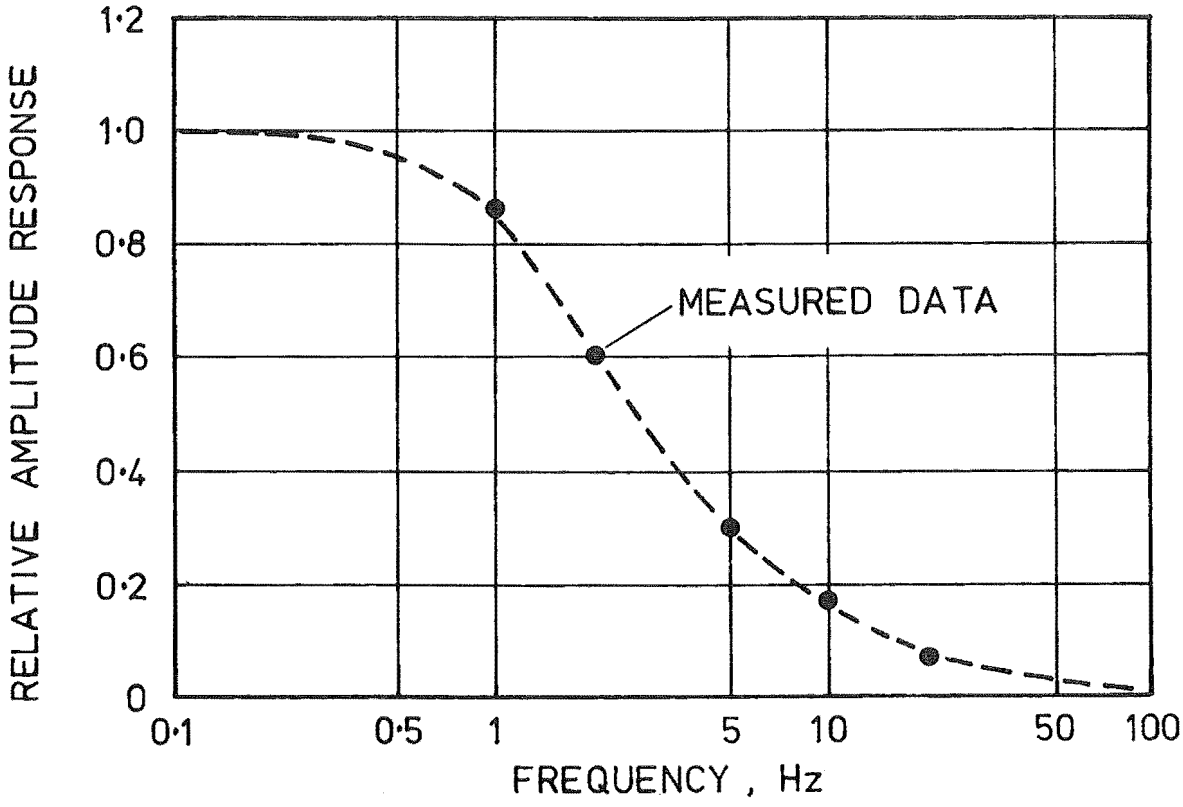

Fig. 4.16 Measured Frequency Response.

Fig. 4.15 also shows a phase difference between the two signals. This ranged from 18 ms at 20 Hz to 90 ms at 1 Hz.

4.8.5 Theoretical Response of Inlet Tube Used in Final Field Tests

A reasonably accurate measurement of the ratio $\frac{\delta\Psi}{\delta P}$ for the National Semiconductor pressure transducers (ref. Section 4.6) allowed the theoretical dynamic response to be calculated using Eqs. 4.10 and 4.11 as:

resonant frequency f_o = 107 Hz

damping ratio h = 18

where : L = 140 mm, A = 0.37 mm^2, ρ = 920 kg/m^3 (SAE 30 oil), μ = 0.44 Ns/m^2 (SAE 30 oil), $\frac{\delta\Psi}{\delta P}$ = 4.8 x 10^{-15} m^5/N.

The theoretical response to sinusoidal and step inputs were then calculated with these values of f_o and h using Eqs. 4.4 and 4.5 respectively. These are shown in Figs 4.17 and 4.18. The measured response (Figs 4.14 and 4.16) has been superimposed as a broken line. The theoretical analysis overestimates the frequency response (Fig. 4.17) and underestimates the response to a step input (Fig. 4.18).

Consider the effect on the theoretical response of a value $\frac{\delta\Psi}{\delta P}$ = 9.0 x 10^{-15} m^5/N instead of the measured value $\frac{\delta\Psi}{\delta P}$ = 4.8 x 10^{-15} m^5/N. Such an increase could be caused by a very small air bubble, about 1 mm^3 at the entrance to the transducer (ref. Section 4.6). Substituting this new value of $\frac{\delta\Psi}{\delta P}$ into Eqs 4.10 and 4.11 gives theoretical values of:

f_o = 78 Hz compared with 107 Hz

h = 25 compared with 18.

The new theoretical frequency response, calculated with Eq. 4.4, is now identical to the measured one in Fig. 4.17. However, the new theoretical response to a step input, calculated with Eq. 4.5, underestimates the measured response of Fig. 4.18 even more than before. It was found that

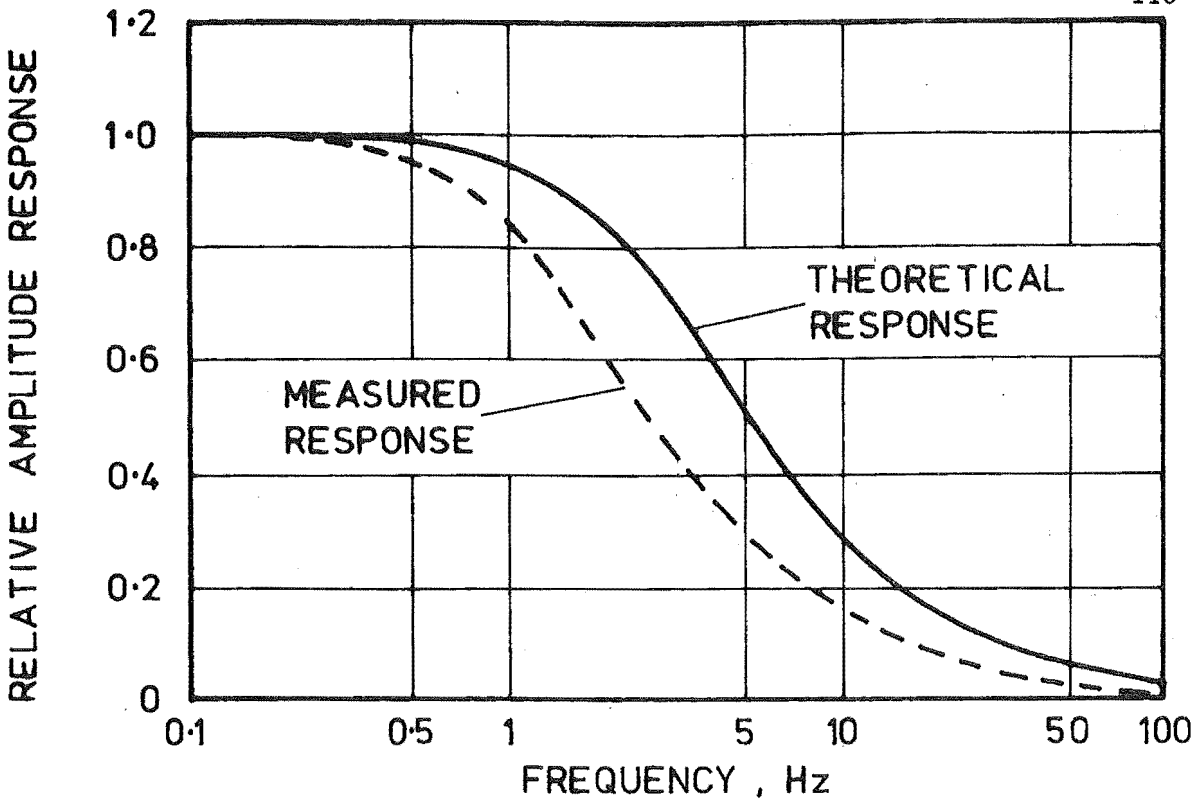

Fig. 4.17 Frequency Response.

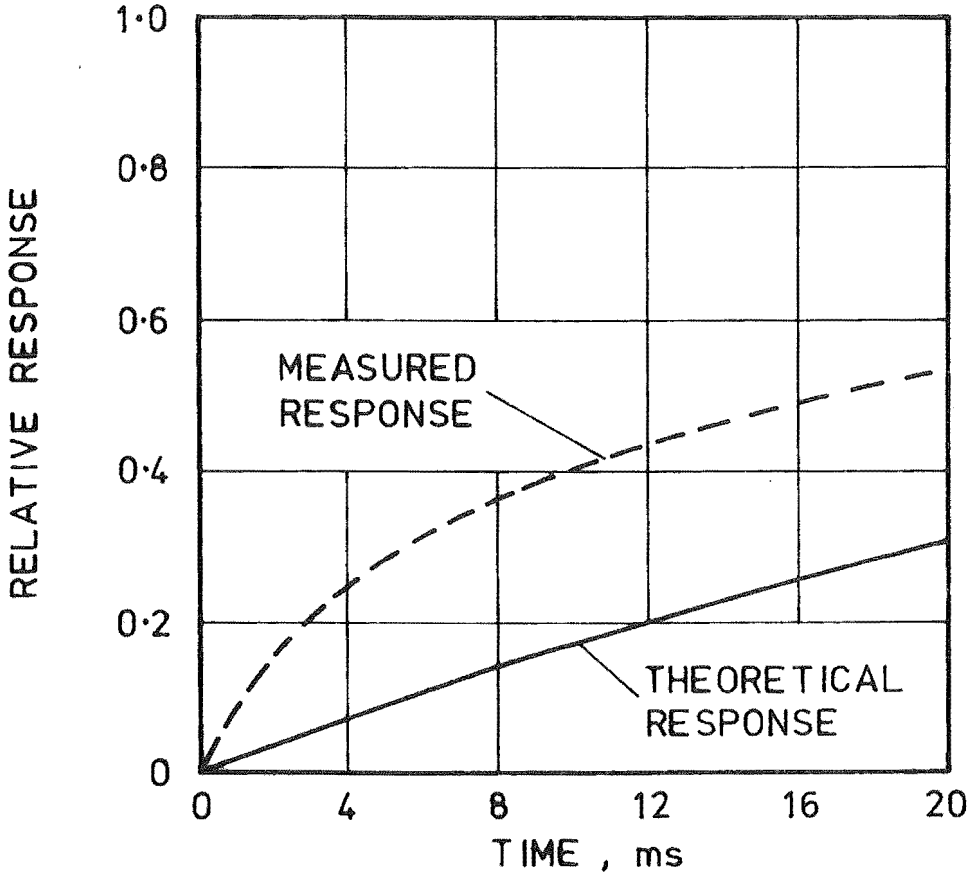

Fig. 4.18 Response to Step Input.

whatever the value of $\frac{\delta\Psi}{\delta P}$ chosen, the theoretical response does not agree with the measured response for both step and sinusoidal inputs. This suggests a fault with Wad's (1969) analysis.

It was also found that whatever the values of f_o and h chosen, the theoretical response to a step input is a different shape to the measured one. This suggests that the response of the pressure probe is not described exactly by a linear second order differential equation, as was initially assumed, (Section 4.3).

CHAPTER 5

BUBBLE AND VELOCITY PROBES

5.1 SUMMARY

This Chapter describes the development of two instruments employing "resistivity probes". The first was used to measure the bubble size at Aviemore and in the laboratory flow simulators. The second was used to measure the velocity at Aviemore. This incorporates two resistivity probes and utilises a cross-correlation technique to calculate the velocity. The cross-correlation analyses are described in detail.

5.2 BUBBLE PROBE

5.2.1 Operating Principle

Fig. 5.1a shows a resistivity probe and a simple electrical circuit, suitable for use in an air-water mixture. The probe is a sharpened rod which is insulated except for it's tip and set into a metal supporting tube. The electrical circuit applies a constant voltage over the probe and a series resistance. When the probe tip is in contact with water, current will flow between the tip and the supporting metal tube; when it is in contact with air, no current will flow.

The output is the potential difference over the resistor. This will vary between two values corresponding to air and water, as shown in Fig. 5.1b. This signal is in fact oversimplified because the poor wettability of the probe tip will result in an output as in Fig. 5.1c. The bubble size and spacing can then be calculated providing the velocity is known.

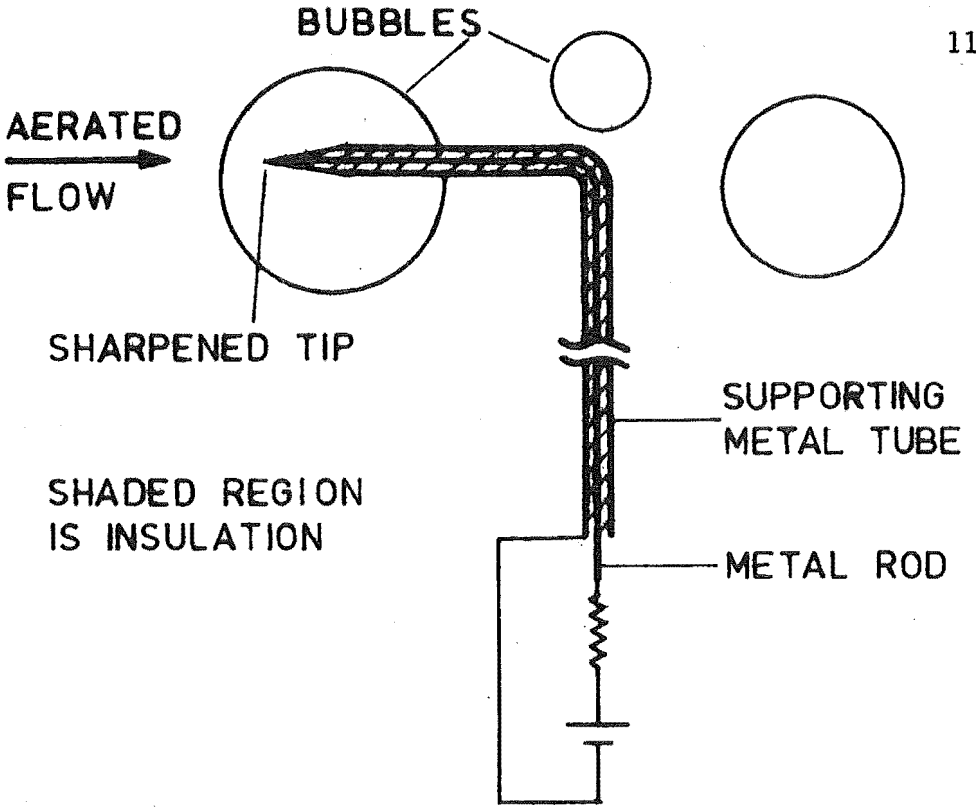

(a) RESISTIVITY PROBE

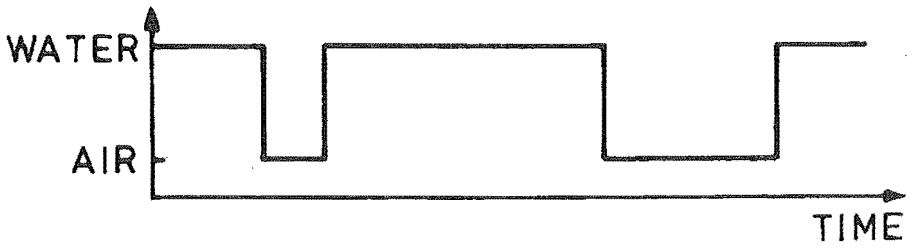

(b) IDEAL OUTPUT SIGNAL

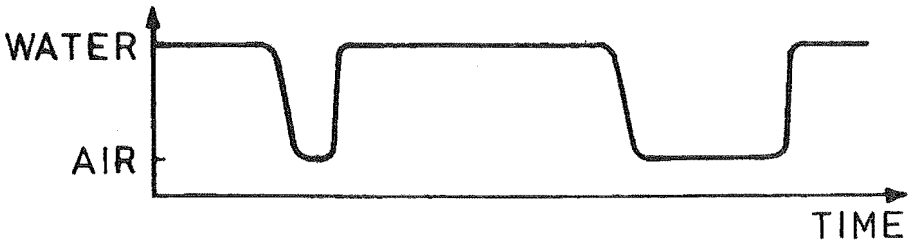

(c) ACTUAL OUTPUT SIGNAL

Fig. 5.1 Principle of Resistivity Probes.

5.2.2 Probe Design

Resistivity probes were first reported by Neale and Bankoff (1963) for measuring local parameters in mercury-nitrogen flows. A resistivity probe was constructed and was used at Aviemore only three months after the writer located this article.

The first probe utilised 0.08 mm diameter platinum wire which was encased in glass for insulation and support. The tip was ground to a point, about 0.5 mm diameter. Smaller tips were not practical because of the brittle nature of the glass. This performed so well in the A flow simulator that a probe was designed for field use.

This is shown in Fig. 5.2 and will be referred to as a "bubble probe". This utilised a chrome plated steel needle with a tip ≃ 0.05 mm diameter. This was insulated with Araldite D except for about 0.25 mm at the tip.

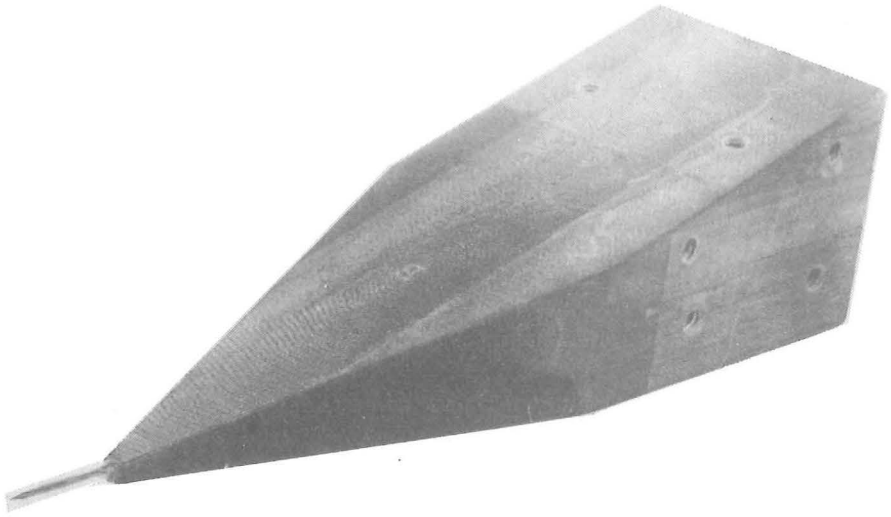

Fig. 5.2 Bubble Probe.

The electrical circuit was similar to Fig. 5.1b, using a 10 kΩ resistance and 9V battery. However the circuit between the probe tip and the negative battery terminal was via the metal probe supporting assembly. The current therefore had to travel about 100 mm through an irregular water path. For field measurements the output was buffered with a high input impedance amplifier because of the long distance (about 50 m) between the instrument and the recording hut.

5.2.3 Probe Performance

The bubble probe was only just constructed when it became apparent water would be made available at Aviemore. It was therefore practically untested when used in the initial field tests at Aviemore (see Chapter 8).

In these tests, the output signal was displayed on the storage oscilloscope and recorded on film. Sample photographs are shown in Fig. 5.3. Bubbles can be readily identified close to the spillway surface (y = 6, 45 and 85 mm where y is the normal distance from the spillway surface). In the very aerated flow at large distances from the surface, these photographs are difficult to interpret (y = 205 mm).

This is caused by the large distance between the probe tip and the metal probe supporting assembly. The electrical circuit between them will be very irregular and will depend on the distribution of water around the probe (see Fig. 5.4). Thus even when there is water at the probe tip, the output level of the signal will vary as the resistance of the electrical circuit through the water changes. This problem was not recognised until after the Aviemore tests. It could have been corrected simply by placing an uninsulated needle adjacent to the probe and

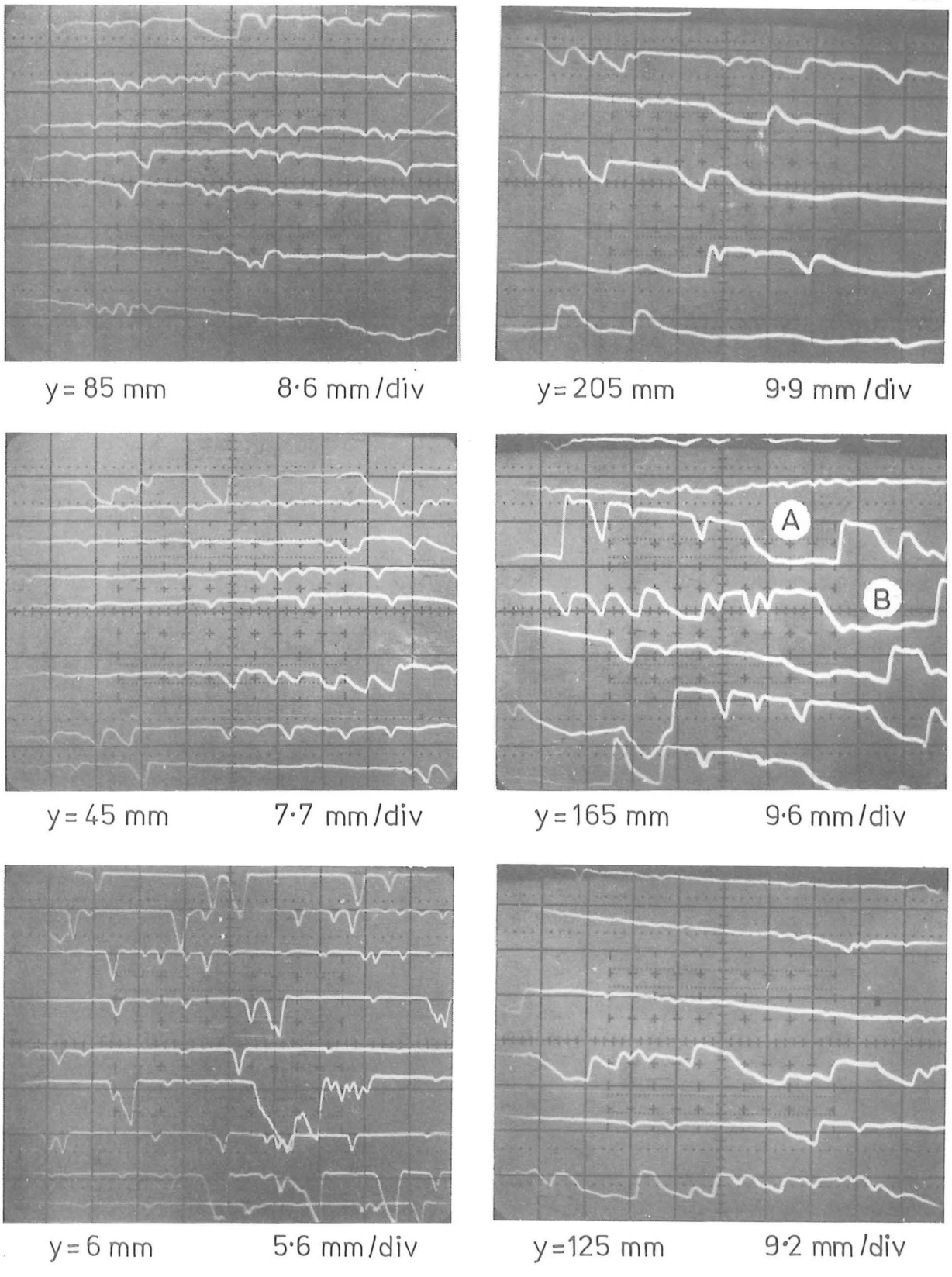

Fig. 5.3 Sample Bubble Probe Signals Measured at Aviemore Station 402, Gate Open 450 mm.

connecting this directly to the negative battery terminal. This modification would also allow spray to be detected.

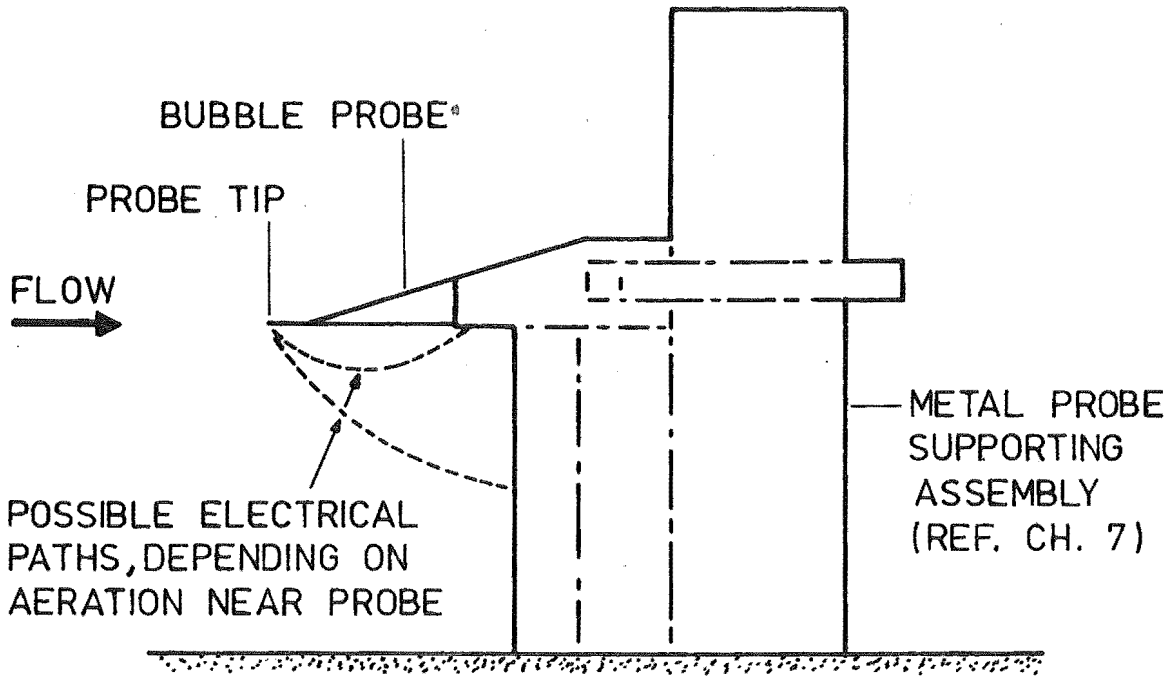

Fig. 5.4 Schematic of Electrical Paths.

The horizontal (length) scale is indicated below each photograph in Fig. 5.3. This was calculated from the corresponding flow velocity, measured independently as described in Section 10.3.3. Close to the spillway (y = 6, 45 and 85 mm) the bubbles are about 0.5 - 3 mm dimension. The mean air concentration in these flows is about 0.07, 0.16 and 0.21 respectively, (ref. Section 10.3.2).

At y = 165 mm, the mean air concentration is about 0.54. This photograph shows some small bubbles about 0.5 - 3 mm. The signals at A and B (y = 165 mm) were initially attributed to the previously mentioned

problem, i.e. the large distance between the probe tip and the probe supporting assembly. This view was supported by the difficulty in interpreting the signals recorded in very aerated flows. See for example the signals at y = 125, 165 and 205 mm for which the mean air concentrations were about 0.28, 0.54 and 0.81 respectively.

It is now considered that the signals at A and B (y = 165 mm) may have been caused by bubbles about 20 mm dimension. This view is supported by measurements reported in Section 10.3.

It must be emphasized that the probe tip was uninsulated for about 0.25 mm. This probe could therefore not detect bubbles smaller than 0.5 mm dimension.

In retrospect, the performance of the bubble probe could have been significantly improved to allow it to detect smaller bubbles, and to allow it to operate in very aerated flows. Recent publications describing such probes and improved electronic circuits which measure the air concentration are referenced in Section 12.2.2.

5.3 VELOCITY PROBE

5.3.1 Introduction

The use of a correlation technique to measure the velocity between two transducers aligned in the direction of flow was suggested to the writer by Elliott (5) (private correspondence) just before the initial field tests. Many difficulties were encountered in predicting velocity from the measurements of stagnation pressure and air concentration obtained in these tests. It was therefore decided to develop a velocity probe based on a correlation technique, and using resistivity probes. These

were the logical choice for transducers because of their simplicity, small size, high frequency response and because of the experience with them in the initial field tests.

The probe described here was developed independently of similar probes which have been reported since then. These similar probes were used to measure bubble velocities and are referenced in Section 12.2.3.

5.3.2 Principle of Velocity Measurement

If the tips of two resistivity probes are aligned in the direction of flow (see Fig. 5.5a) then the water velocity can be calculated from the time of travel of an air-water interface between the probe tips. Ideally the two signals would be identical but separated by a time delay τ_o (Fig. 5.5b). In practice they will differ because the upstream probe will disturb the flow. In this case the probable time delay can be found by cross-correlating the two signals. If the measured cross-correlation function is plotted against time delay, then τ_o will correspond to the maximum correlation as shown in Fig. 5.5c. This plot is called a cross-correlogram.

This method assumes firstly that the upstream probe does not alter the velocity of the air-water interfaces between the probes, and secondly that this velocity is the same as the water velocity.

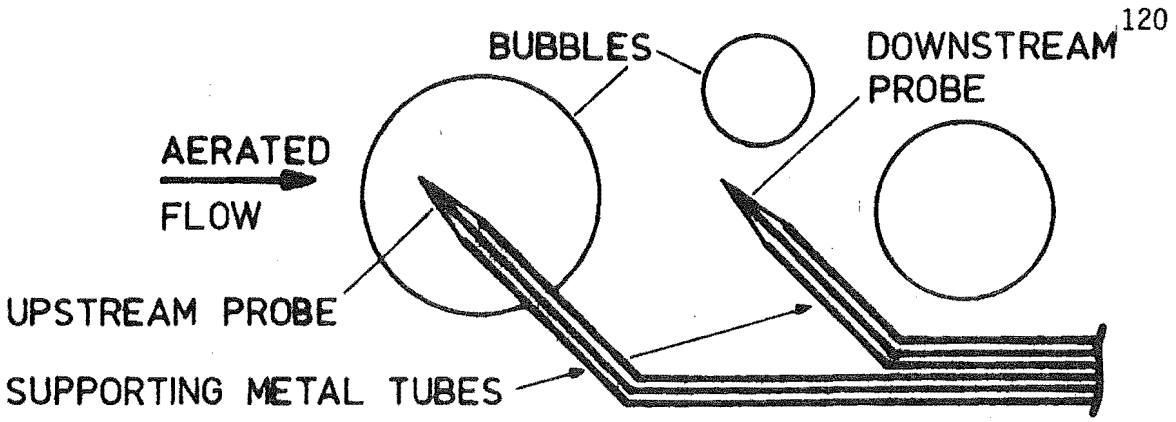

(a) VELOCITY PROBE

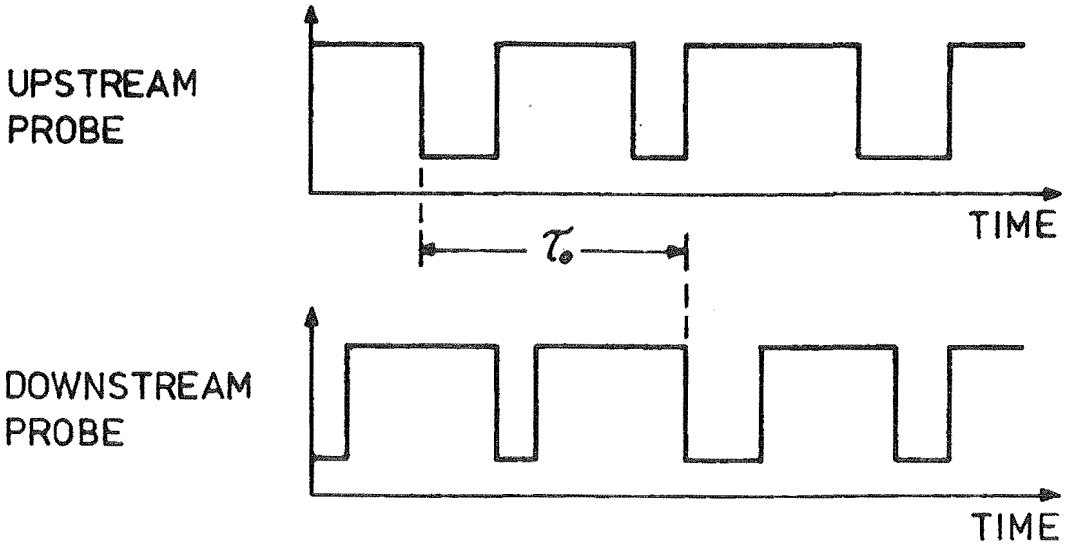

(b) IDEAL OUTPUT SIGNALS

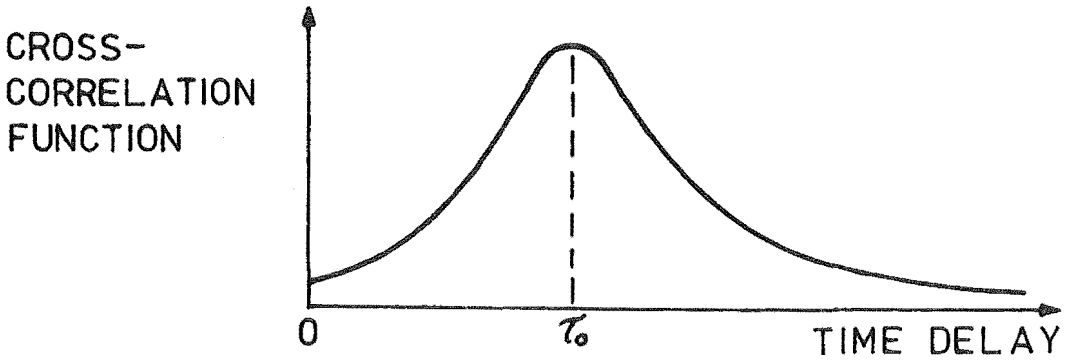

(c) TYPICAL CROSS-CORRELOGRAM

Fig. 5.5 Velocity Measurement by Cross-Correlation.

5.3.3 Cross-Correlation Functions

Consider the two signals x(t), y(t) in Fig. 5.6. The cross-correlation function for these two signals is defined as

$$R_{xy}(\tau) = \lim_{T\to\infty} \frac{1}{T} \int_0^T x'(t)y'(t+\tau)dt \qquad 5.1$$

where primes denote variations from the mean values, defined for x(t) as

$$x'(t) = x(t) - \bar{x}$$

$$\bar{x} = \lim_{T\to\infty} \frac{1}{T} \int_0^T x\,(t)\,dt \qquad 5.2$$

and similarly for y(t). In order to calculate $R_{xy}(\tau)$ for the general case $\bar{x}$, $\bar{y} \neq 0$, Eq. 5.1 may be more conveniently expressed as

$$R_{xy}(\tau) = \lim_{T\to\infty} \frac{1}{T} \int_0^T x(t)y(t+\tau)dt - \bar{x}\,\bar{y} \qquad 5.3$$

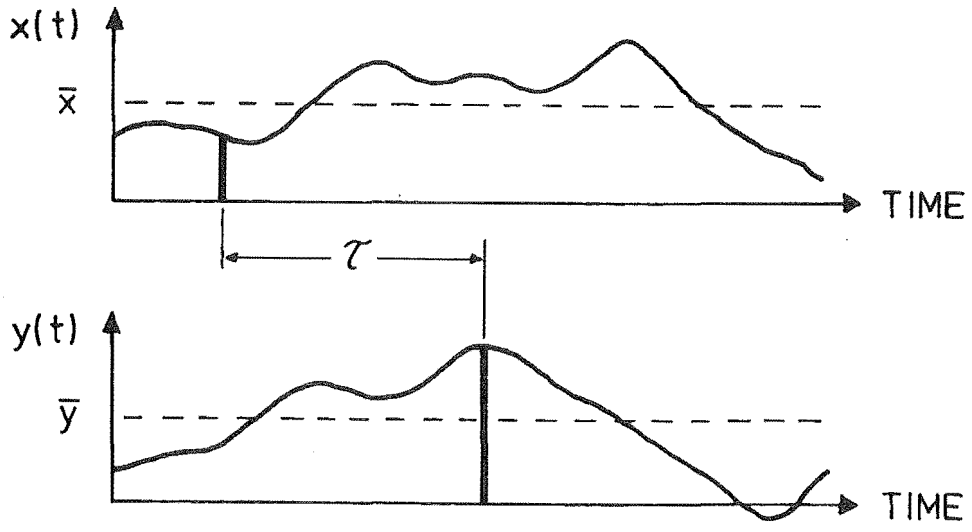

Fig. 5.6 Cross-Correlation of Two Signals.

Alternatively, a normalised cross-correlation function may be defined as

$$\rho_{xy}(\tau) = \frac{R_{xy}(\tau)}{R_x \; R_y} \qquad 5.4$$

where $-1 \leq \rho_{xy} \leq 1$ and where R_x is the RMS of the variations, i.e.

$$R_x = \left[\lim_{T\to\infty} \frac{1}{T} \int_o^T (x'(t))^2 \, dt \right]^{\frac{1}{2}} \qquad 5.5$$

In order to calculate $\rho_{xy}(\tau)$ for the general case $\bar{x}$, $\bar{y} \neq 0$, Eq. 5.5 may be expressed as

$$R_x = \left[\lim_{T\to\infty} \frac{1}{T} \int_o^T (x(t))^2 \, dt - \bar{x}^2 \right]^{\frac{1}{2}} \qquad 5.6$$

The normalised cross-correlation function can then be calculated by substituting Eqs. 5.2, 5.3 and 5.6 into Eq. 5.4.

For the data obtained at Aviemore, the cross-correlation analyses were performed on a digital computer as described later. The first programs developed formed the normalised cross-correlation function as indicated above. As the magnitude of this is of little interest in this application, subsequent analyses merely evaluated the function

$$R_{xy}(\tau) = \lim_{T\to\infty} \frac{1}{T} \int_o^T x(t)y(t+\tau)dt$$

This was then scaled to fill the plot.

5.3.4 Design Criteria

In designing a probe to use this principle, it is apparent the tip dimensions and spacing must be related to the dimensions of the air-water interface to be measured. For instance, if it was intended to operate in a bubbly flow with a uniform bubble size, say 1 mm diameter, then:

(i) The probe tips must be much less than 1 mm diameter to minimise the distortion and deflection of bubbles.

(ii) The tip spacing must not be greater than about 10 mm if bubbles intercepting the upstream tip are to intercept the downstream one.

Considering the nature of self-aerated flows (Section 1.3) it is apparent that a much larger probe will operate successfully by measuring the passage time not of small bubbles but of the large bubbles and air-water interfaces. (See Fig. 5.7). This difference is important because the velocity of the large interfaces will be the same as the water within them, whereas a "slip" velocity could exist between bubbles and the water, (ref. Section 1.3). For this reason, the probe constructed was of this latter type, with probe tips uninsulated over a 1 mm length and spaced 101.6 mm apart.

A large probe also has the advantages of being easier to construct and is more robust, an important consideration for field use.

A large probe does have disadvantages. Because of the large spacing between the probe tips, bubbles smaller than about 5 mm are unlikely to intercept them both. The large probe tips will not detect bubbles smaller than about 2 mm.

5.3.5 Probe Design

The velocity probe is shown in Fig. 5.8. An upstream probe (B) and an in-line downstream probe (D) form the basic instrument (compare with Fig. 5.5a). A second downstream probe (E) was also incorporated, displaced 6.4 mm from the first. The cross-correlation analysis could therefore be performed with either downstream probe, and the effect of the upstream probe on the flow directly behind it could be determined in the

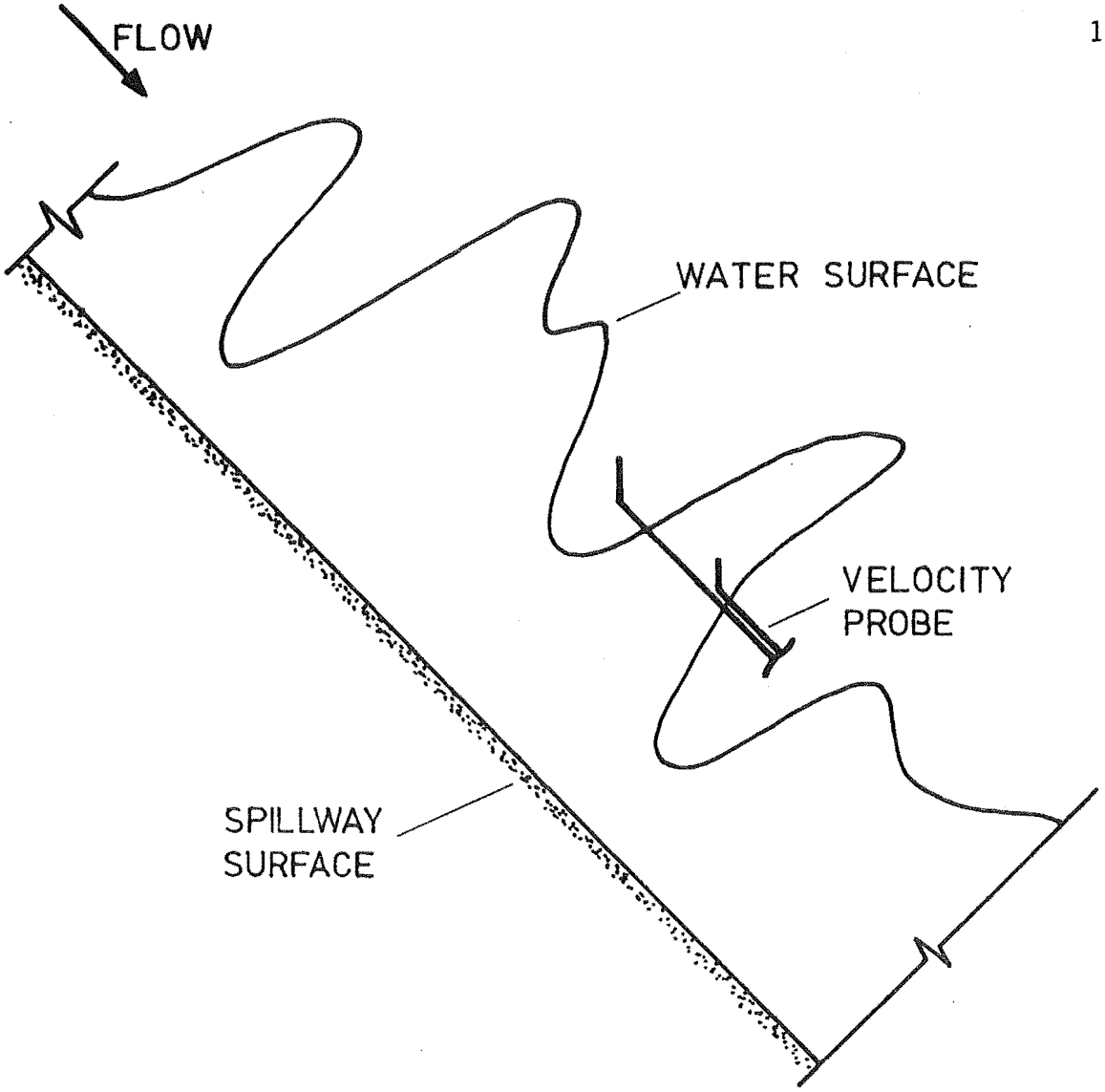

Fig. 5.7 Schematic of Aerated Flow.

laboratory. The probes are 1 mm diameter stainless steel rods insulated with araldite and set into stainless steel tubes, (C and G). These tubes and the sharpened rods (A and F) are all connected directly to the battery. This ensures a short electrical path through the water to the probe tips even in very aerated flows.

The upstream and downstream probes are 101.6 mm apart so that for velocities from 12 - 22 m/s the time delay between the two signals will be 4.6 - 8.5 ms. This spacing is therefore suitable for the 0 - 10 ms delay range on commercial correlators.

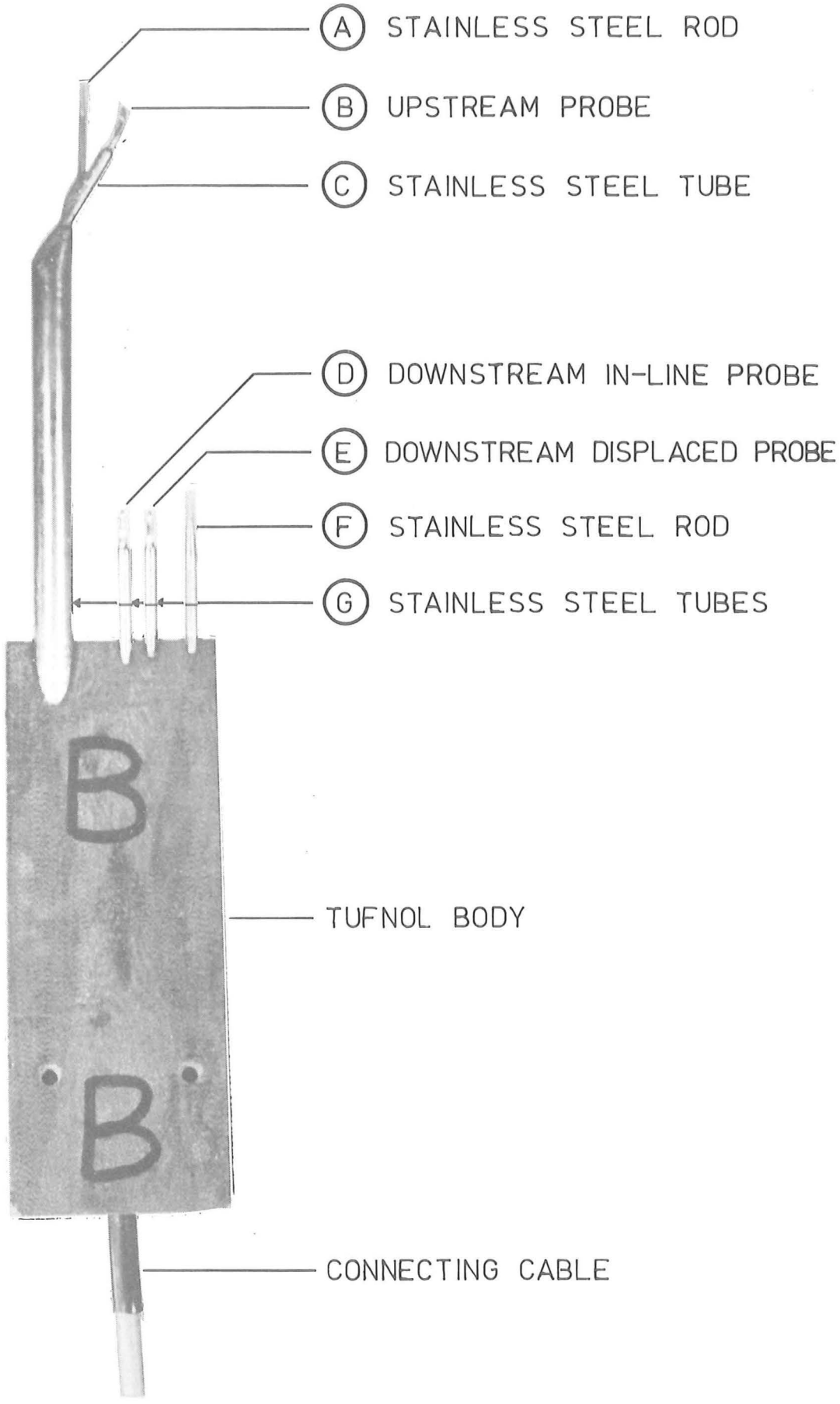

Fig. 5.8 Plan View of Velocity Probe.

For 0.1 ms resolution of the time delay (1% of the 10 ms delay range) it is desirable to have a signal frequency response from 0 - 10 kHz. The uninsulated probe tips tapered to a point over a distance of 1 mm. For velocities from 12 - 22 m/s, the maximum signal frequency will therefore be limited to about 10 kHz.

As no high speed cross-correlators were available for on-line analysis of the field measurements, these had to be recorded on the F M tape recorder for computer analysis within the laboratory (ref. Section 5.4). At a tape speed of 381 mm/s this limits the maximum frequency response to 8 kHz. Slight misalignment of the record and playback heads causes a small phase difference between any two tracks. This was 70 x 10^{-6} s for the tracks used at Aviemore and can be taken into account when calculating velocity.

A simple electronic circuit was used successfully in laboratory tests and at Aviemore and is shown in Appendix I.

5.3.6 Laboratory Tests

The velocity probe was initially tested in the A flow simulator using a DISA correlator (see Fig. 5.9). This is a slow speed analogue device, which took about 25 minutes to form a reliable cross-correlogram.

While it was not possible to measure the velocity independently, it was possible to establish the following points:

(i) In this flow it is difficult to see the correlation between the two signals when they are displayed on a storage oscilloscope. (Sample displays of the data measured at Aviemore are shown in Fig. 10.13). In spite of this, the cross-correlograms do have well defined peaks.

Fig. 5.9 Cross-Correlation Test Equipment.

(ii) There is better correlation for the in-line downstream probe than the displaced one, (see Fig. 5.10).

(iii) The in-line and displaced probes predicted the same time delay to within about 0.1 ms (this is the claimed accuracy of the correlator, i.e. 1% of the 10 ms delay range).

As a result of these tests, the downstream in-line probe was used in the final field tests at Aviemore.

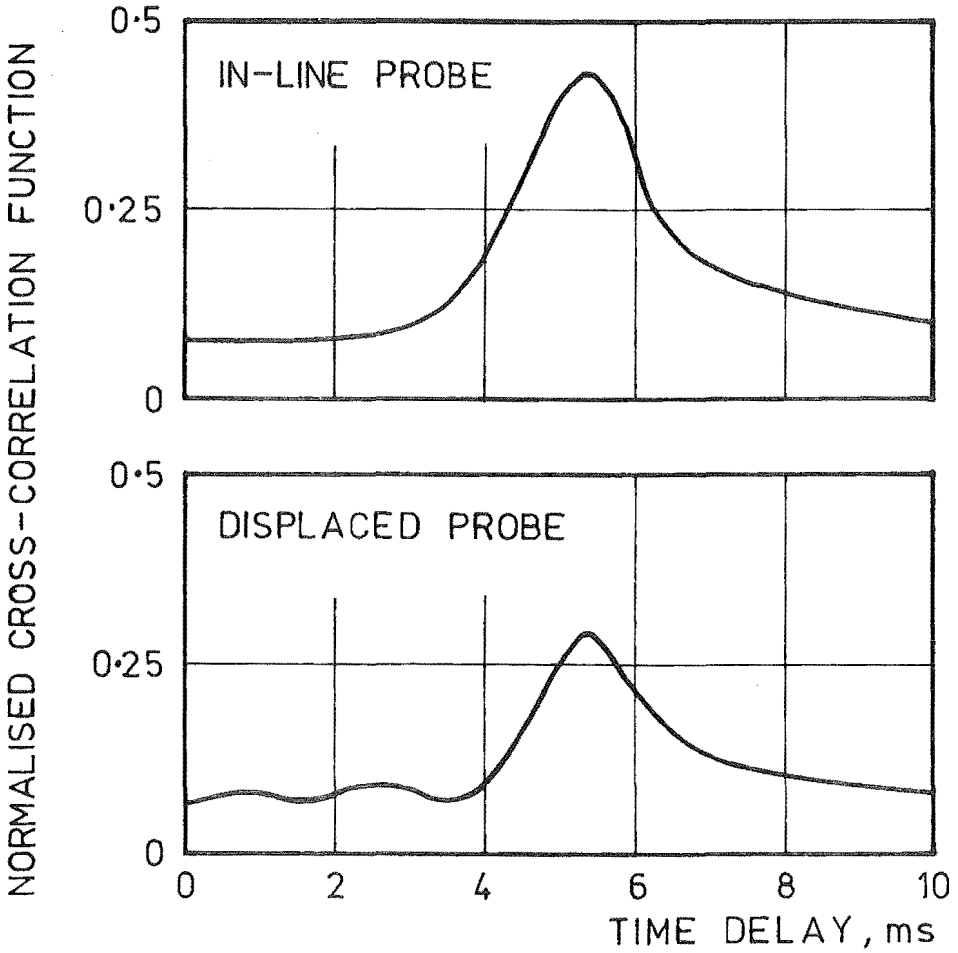

Fig. 5.10 Comparison of Downstream Probes.

5.3.7 Accuracy

It was not possible to calibrate the velocity probe within the laboratory. Attempts to compare the velocity predicted by this and by the combined pressure air concentration probe in the laboratory flow simulators were unsuccessful for reasons explained in Section 6.5.

The following observations suggest the velocity predicted with this probe is accurate to within about 3%.

(i) Profiles of velocity measured at Aviemore (Section 10.3.3) showed about 3% scatter about smooth curves drawn through them.

(ii) Recent articles describing similar instruments using the same technique to measure bubble velocities claim 3 - 5% accuracy (ref. Section 12.2.3).

5.4 ANALYSIS OF AVIEMORE VELOCITY DATA

5.4.1 Introduction

The DISA correlator took about 25 minutes to form a reliable cross-correlogram when the velocity probe was in the A flow simulator. By comparison a very fast digital cross correlator could form a comparable cross-correlogram in about 0.12 s. Records of 15 and 60 s duration were therefore considered adequate for the measurements at Aviemore, which were to be analysed on an EAI 590 hybrid computer.

This computer is described in Appendix J. Its limited storage meant that the data had to be analysed "on-line" from the FM tape recorder. Its relatively slow speed resulted in many programs being developed. These were refined, each faster but more complex than the previous, until the cross-correlograms had well defined peaks in most flow conditions.

5.4.2 Program Description

Four almost identical programs were developed to form cross-correlograms with 10 and 20 ms delay ranges, and for 15 and 60 s data records. These evaluated the cross-correlation function

$$R_{xy}(\tau) = \sum_{n=1}^{N} x(n)\, y(n+\tau)$$

with details of the cross-correlograms shown in Table 5.1

Table 5.1 Cross-Correlogram Details

Nominal Delay Range	Data Length	Actual Delay Range	Number of Points Formed	Interval Between Points	Number of Cycles N
10 ms	15 s	0.4 - 10.0 ms	97	0.1 ms	5120
	60 s				20480
20 ms	15 s	2.2 - 20.0 ms	90	0.2 ms	7040
	60 s				28160

The cross-correlation functions were calculated by a sophisticated assembler subroutine. This controlled the multiplexor and the timing interrupts which initiated the analogue to digital conversions. Various operations were performed with each sample when it arrived. The computer then paused for about 5×10^{-6} s to await the next interrupt. The frequency of these interrupts, and thus the time delay axis of the cross-correlograms, were accurate to within 0.2%.

A major difficulty with assembler is that it utilises scaled integer notation; there are no decimal points. The data was therefore scaled to prevent any registers overflowing during multiplication and addition operations. By careful scaling, the magnitude of the cross-correlation functions (the vertical axis of the cross-correlograms) were accurate to within 0.8% FS.

The main programs, written in FORTRAN, controlled the computer between analyses and also scaled the data for plotting. A FORTRAN subroutine plotted the cross-correlograms on a visual display unit, as in Fig. 5.11.

This is in fact the autocorrelation of a 200 Hz square wave, which was connected to both analogue input terminals. This method was used to check that the software and timing were working correctly. The top curve is as calculated; the middle and bottom ones have been smoothed by 5 and 9 point moving averages respectively. These were found to be helpful for estimating τ_o in regions of poor correlation.

The program for a 10 ms delay range and 15 s of data has been listed in Appendix K to illustrate in particular the complexity of the assembler subroutine. This is the only program listed in this thesis, even though this and another computer were used extensively.

In practice, the tape speed was actually slowed from 381 to 190 mm/s to effectively increase the computer speed by 2 times. Thus the 10 and 20 ms delay ranges for instance were actually 20 and 40 ms.

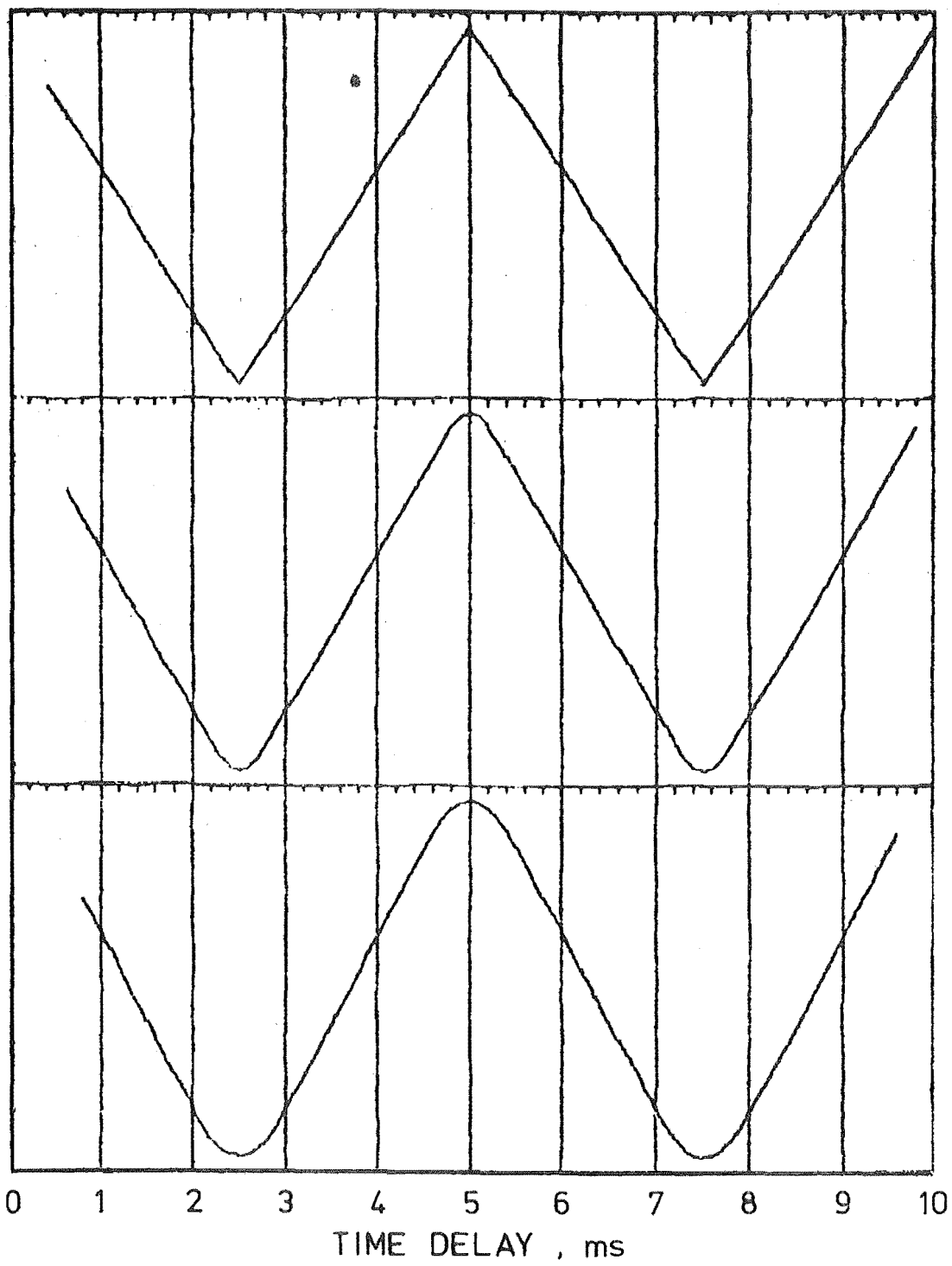

Fig. 5.11 Auto-Correlation Test.

CHAPTER 6

LABORATORY CALIBRATION TESTS

6.1 SUMMARY

The two flow simulators used to produce aerated flows within the laboratory are described. These were used for the development and calibration of the instruments used at Aviemore. The calibration tests are described in detail.

6.2 INTRODUCTION

Measurements of stagnation pressure with the combined pressure air concentration probe are likely to be overestimated because of the proximity of the electrode supports to the stagnation point (ref. Section 3.5). A more important source of error discussed in Section 2.4 is the validity of using total head tubes to measure stagnation pressures in aerated flows. It was therefore considered necessary to calibrate this instrument to determine the accuracy of the stagnation pressure measurements.

It was also considered desirable to check the accuracy of the air concentration and velocity measurements, although this was considered less important. The velocity instrument should be accurate because of its simple direct measurement principle. The air concentration instrument should be accurate because of its similarity with Lamb and Killen's (1950) instrument.

Aerated flows were produced in the laboratory in two flow simulators, A and B. The A flow simulator was used for the development and initial testing of all the instrments used at Aviemore. It produced an unsteady non-uniform flow which was unsuitable for calibration tests. The B flow

simulator produced a steady uniform flow and was used for the calibration tests.

This Chapter describes the two flow simulators and the calibration tests in the B flow simulator.

6.3 A FLOW SIMULATOR

The A flow simulator, shown in Fig. 6.1 was initially designed and used by Keller (1972) for testing his instruments. It was intended to produce flows with the range of turbulence, air concentration and velocities found on spillways.

The aerator (Fig. 6.2) utilises a high velocity jet of water (H) to suck air (J) into a chamber (K) in which the air and water combine by turbulent mixing. This aerated flow passes through a perspex pipe then discharges into a calibrated pit. Valves were provided in the water and air inlet pipes to control the velocity and air concentration.

It was found that when the air inlet valve (L) is closed, the pressure in the mixing section (K) decreases until some water vaporises. The water velocity from the orifice (M) to the outlet is almost constant regardless of the position of the air inlet valve (L) so that the resultant flow must be a mixture of water, water vapour and air.

It seems likely that both the electrical conductivity and dielectric constant of water vapour will be different to those of water or air. This could adversely affect the performance of the air concentration and velocity probes. The air inlet valve was therefore left fully open and the air concentration was varied by changing the orifice diameter.

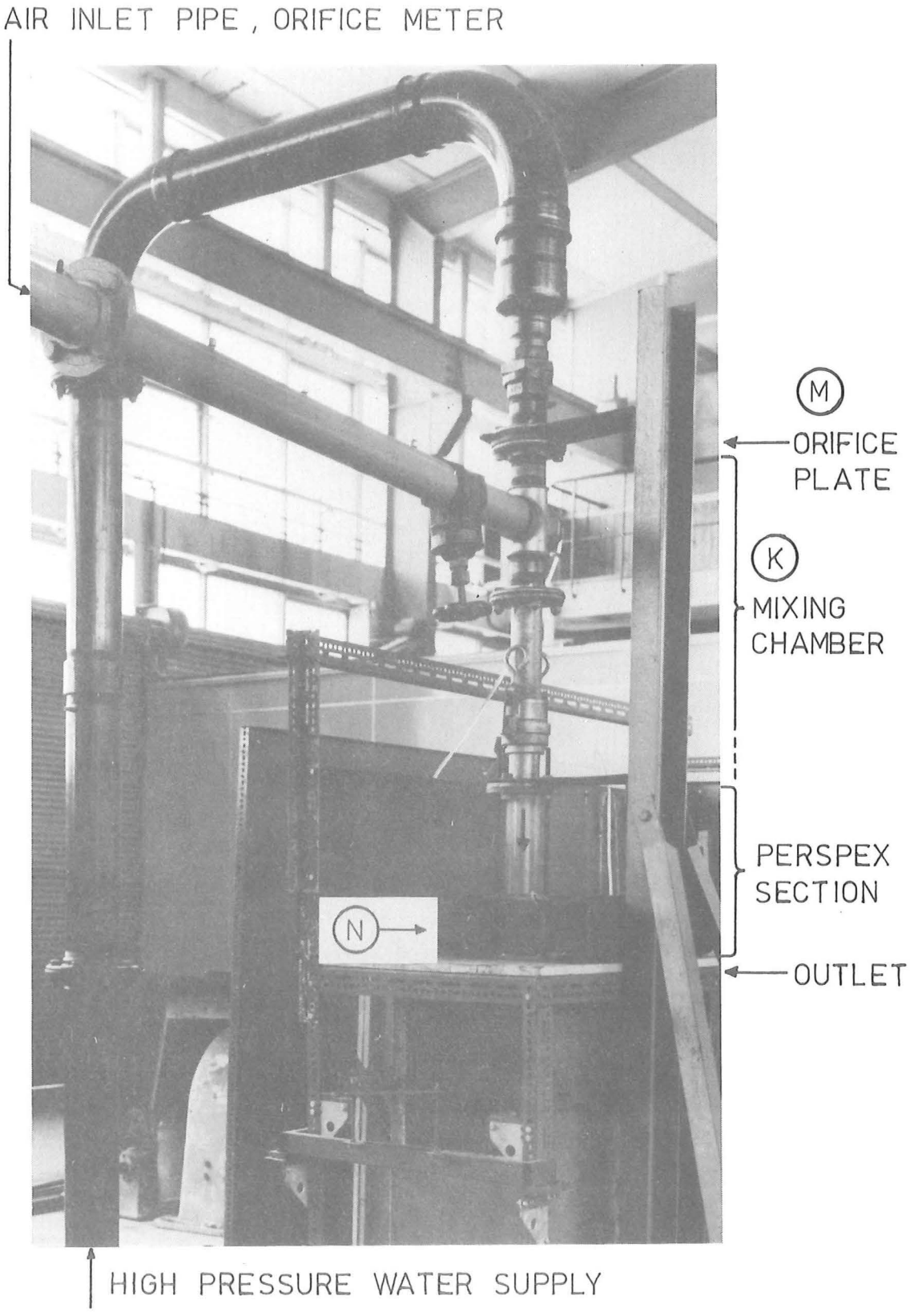

Fig. 6.1 A Flow Simulator.

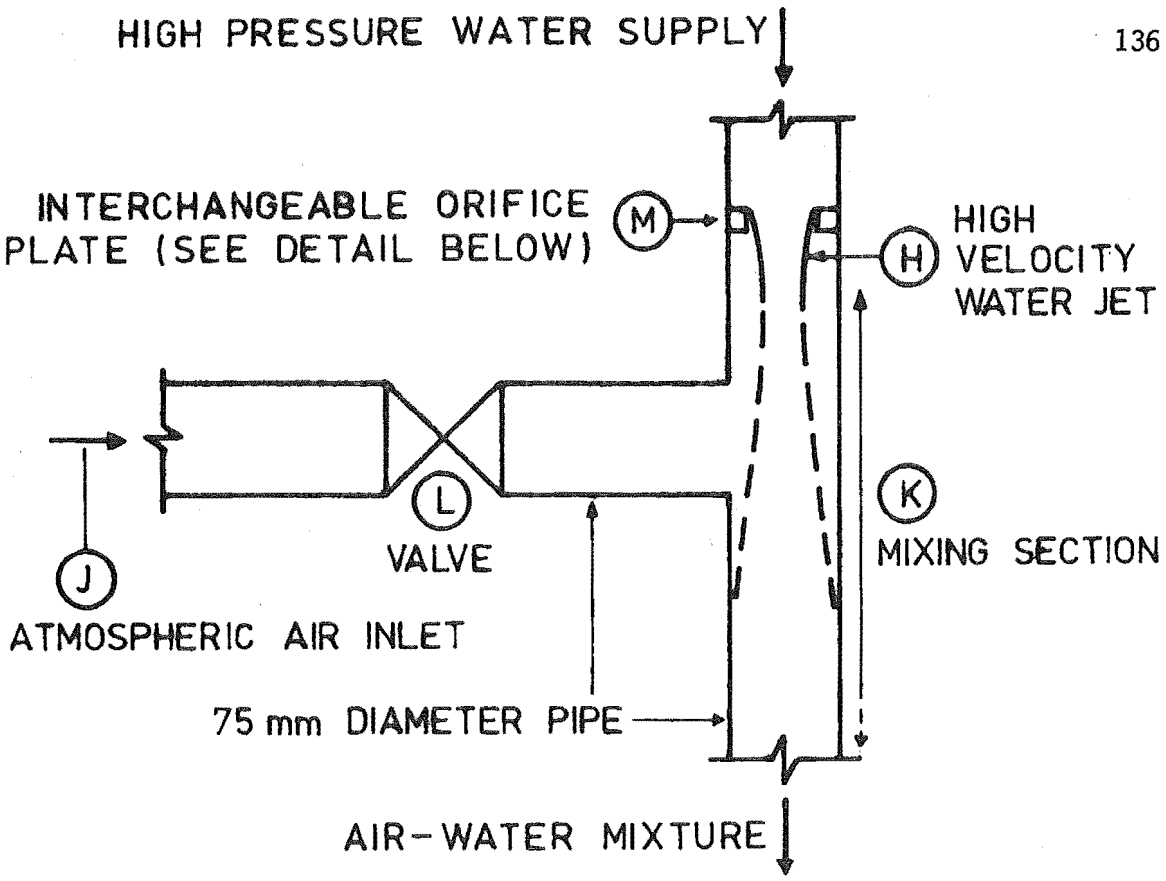

(a) AERATOR SCHEMATIC

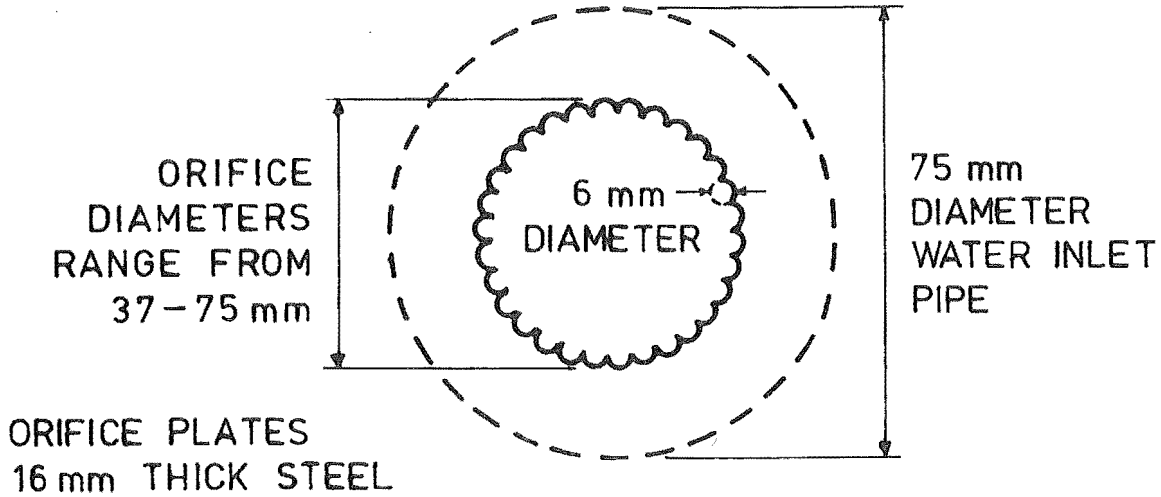

(b) ORIFICE PLATE DETAILS

Fig. 6.2 A Flow Simulator.

In this way the simulator could produce flows with mean air concentrations up to about 0.8. The maximum water discharge (about 0.05 m^3/s) and the outlet pipe diameter (about 75 mm) limited the minimum air concentrations to 0.2 - 0.5 for velocities from 14 - 22 m/s.

Bubble probe measurements indicated a non-uniform distribution of air bubbles and "pockets" of water vapour. Stagnation pressure and air concentration measurements showed the flow to be very unsteady and non-uniform.

The A flow simulator was used extensively for initial testing and development of all instruments. The large air bubbles and water vapour pockets enabled the velocity probe to perform satisfactorily, and produced transient variations in stagnation pressure which were particularly suitable for qualitative comparisons of different pressure inlet tubes. These tests are described in Chapters 4 and 5.

The A flow simulator was not used in the calibration tests reported in this Chapter because accurate measurements required a steady uniform flow without any water vapour pockets.

6.4 B FLOW SIMULATOR

6.4.1 Introduction

The B flow simulator was constructed specifically for the calibration tests reported in this Chapter. It was designed to produce a steady uniform bubbly flow with velocities the same as at Aviemore and with a mean air concentration about 0.13.

This one air concentration was considered adequate because:

(i) It was representative of the range of air concentrations initially expected in the bubbly flow beneath the water surface. It was not until the results from the final field tests at Aviemore were analysed that it was realised that air concentrations in the bubbly flow near the surface were much larger, often in the range 0.5 - 0.9.

(ii) The large (mean) air concentrations measured in wavy regions of self-aerated flow are simply the integration of the large air gaps between adjacent waves and the air (bubbles) within the water surface.

(iii) The spray is thought to represent only a small portion of the total water discharge and can therefore be ignored.

It was intended that the air bubbles be 1 - 3 mm dimension, the same as expected at Aviemore. As mentioned earlier, it was not until after the final field tests at Aviemore that bubbles as large as 20 mm were measured near the water surface.

The air concentration and bubble size for which the B flow simulator was designed were therefore representative of the flows measured at Aviemore except for the very aerated region near the water surface.

6.4.2 Description

The B flow simulator is shown operating in Fig. 6.3 with the air inlet device in Fig. 6.4. This device consists of three hollow aerofoil shaped tubes (K. Fig. 6.4) each vented to the atmosphere. To these are connected eighteen tubes (L, Fig. 6.4) each 4.7 mm external diameter, which terminate in a uniformly spaced pattern across the entrance to the perspex mixing section (M, Fig. 6.3). The tubes were made from stainless steel and rigidly braced after a vibration fatigue failure of the prototype. The perspex section is 610 x 50 x 50 mm internal dimension.

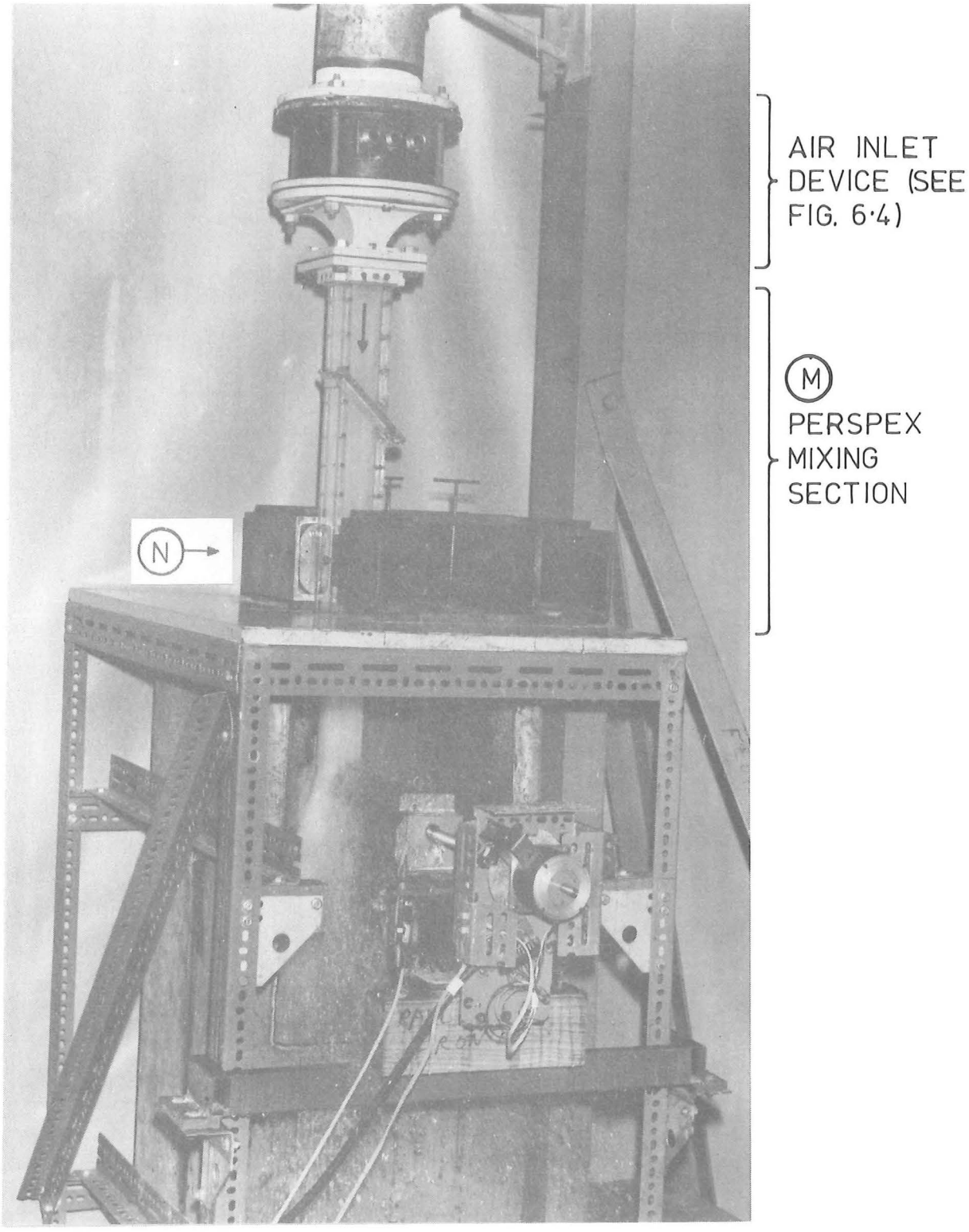

Fig. 6.3 B Flow Simulator in Operation.

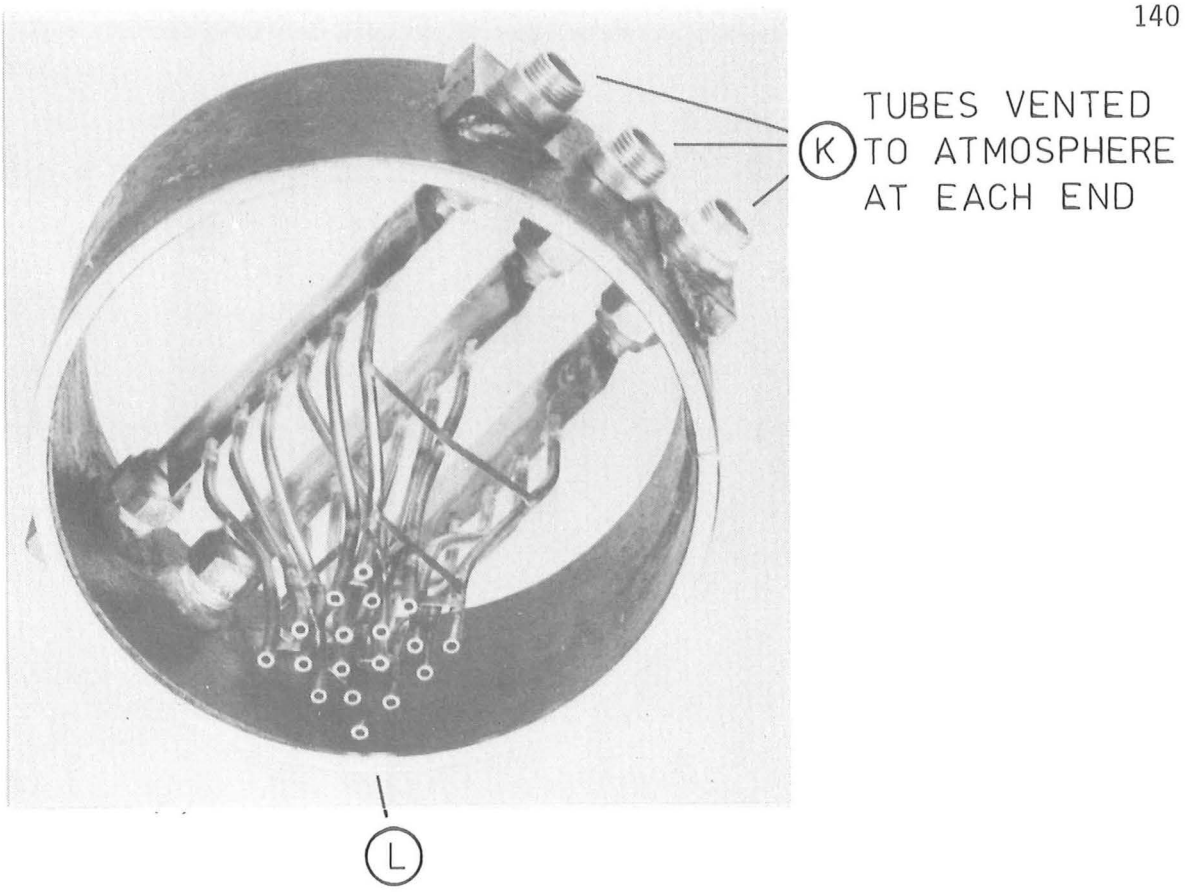

Fig. 6.4 Downstream View of Air Inlet Device.

(Disconnected from the simulator).

The operating principle is similar to the A flow simulator; the high velocity water sucks air down the tubes into the water where it is dispersed by the turbulence.

The design was based on the following considerations:

(i) The eighteen air inlet tubes reduce the cross section area of the perspex tube by about 13% so that the mean air concentration will be about 0.13. To produce a non-aerated flow the air inlet device was simply replaced with a section without inlet tubes.

(ii) The diameter of the tubes should be similar to the bubble size required. Measurements with a very sharp bubble probe showed the bubbles were in fact in the range 0.25 - 1.5 mm, much smaller than the 4.7 mm diameter of the inlet tubes. (This probe was irreparably damaged by a piece of wood in the flow before any signals were recorded).
(iii) The cross-section of the perspex tube was chosen so that the maximum water velocities are about 20 and 23 m/s for C = 0 and 0.13, compared with the 22 m/s maximum velocity later measured at Aviemore.

6.4.3 Test Equipment

The probe under test was mounted on a sliding carriage and support as shown in Fig. 6.5 and in position in Fig. 6.3. The sliding carriage was usually aligned with the centre of the flow although it could be simply offset. The top of a probe was always positioned at a level 10 mm below the downstream end of the perspex pipe.

A stepper motor and infra-red light position indicating device was attached to the threaded drive shaft. These were connected via electrical cables to a remote control unit. This mechanism was part of the test equipment used at Aviemore (ref. Section 7.3) but was modified to allow the following test procedures:
(i) A probe could be driven to within 1 mm of any predetermined position in the flow. This allowed comparison of different probes at the same point in the flow.
(ii) A probe could be traversed through the flow at a constant speed from 0 - 10 mm/s, while simultaneously recording the probe's output. The profiles obtained by different probes could then be compared.

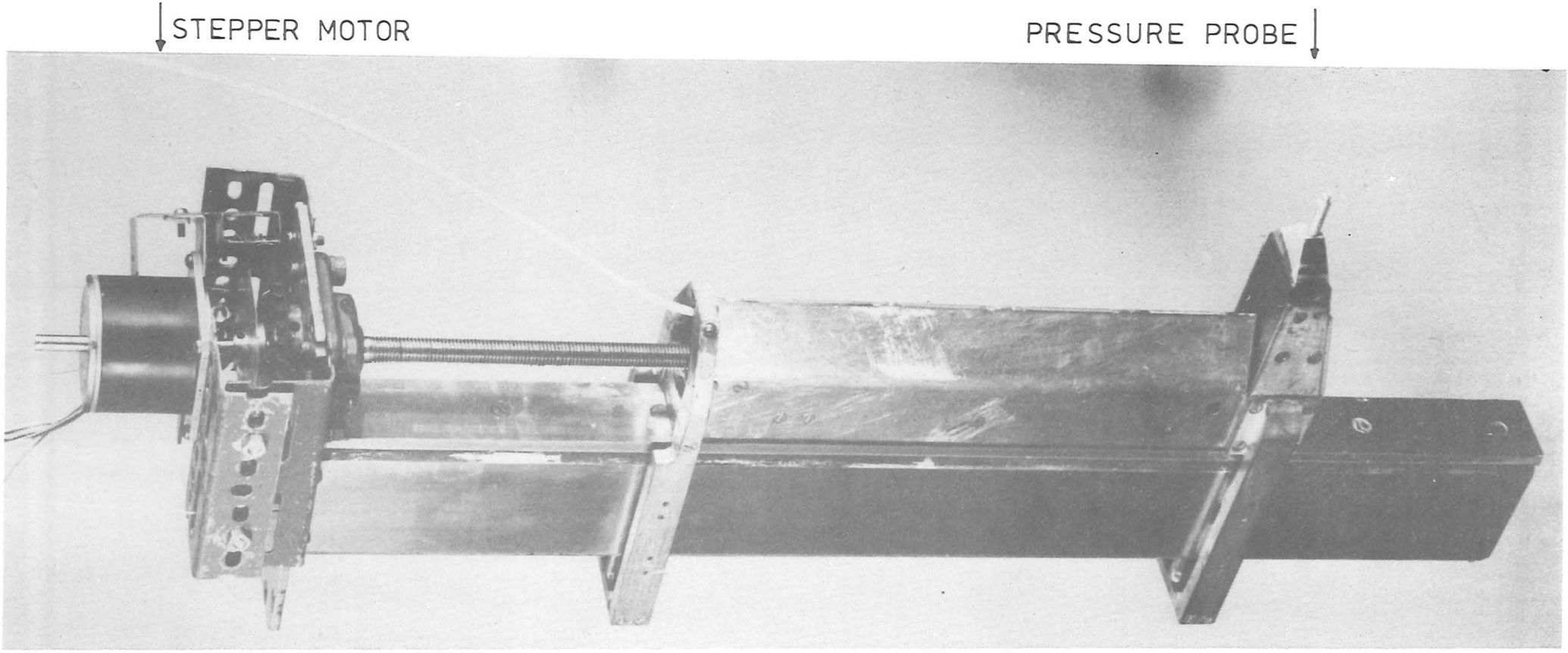

Fig. 6.5 Support and Sliding Carriage for Use in Laboratory Tests.

In order to interchange two probes for comparison, it was in fact necessary to stop the flow. The water flow rate was then accurately reset with the aid of a calibrated pit which was accurate to within 1%.

6.5 CALIBRATION TESTS

6.5.1 Introduction

One of the few methods of calibrating velocity and air concentration probes in aerated flows is to traverse them through the entire cross-section of the flow. The integrated water and air flow rates can then be compared with those measured in the air and water inlet pipes.

This method was not attempted here because it was thought that "edge effects" would limit its accuracy to about 10%. These edge effects arise because the 50 x 50 mm cross section of the B flow simulator is not sufficiently large compared with the probe's size. This is clearly illustrated later by the discrepancies between the stagnation pressure and air concentration signals when the combined pressure air concentration probe is traversed into and out of the flow.

The B flow simulator was used for the following calibration tests:

(i) Comparison of stagnation pressure measured by the combined pressure air concentration probe and by a pressure probe with no air concentration electrodes.

(ii) Comparison of stagnation pressure measured with different pressure inlet tube diameters.

(iii) Comparison of air concentration measured by the combined pressure air concentration probe and by a gamma radiation technique.

(iv) Effect of velocity on air concentration measurement.

No velocity comparisons were possible because of the edge effects and also because the velocity instrument would not operate in the bubbly flow of the B flow simulator. The results from the final field tests at Aviemore do allow the accuracy of the velocity predictions to be assessed. This is discussed in Section 10.4.

In the last section of this Chapter, profiles of velocity and Mach number are calculated from the measurements of stagnation pressure and air concentration. These are similar to those later measured at Aviemore.

6.5.2 Stagnation Pressure Comparisons

These tests were designed to assess the effect of the electrode supports on the stagnation pressure measured by the combined pressure air concentration probe.

The pressure measured by this probe was compared with that measured by a probe referred to as the Kyowa probe. The Kyowa probe is discussed in Section 4.6 and is shown in Fig. 4.8.

Measurements were obtained for six different test conditions, three in non-aerated flows (A - C) and three in aerated flows (D - F). The two probes were traversed through each of these at 5.0 mm/s. Their output signals were recorded on a Hewlett-Packard chart recorder at a chart speed also 5.0 mm/s.

These profiles of stagnation pressure are shown in Figs. 6.6 and 6.7. The profiles from each probe do not align exactly with each other because as explained, the flow was stopped to interchange probes. The accuracy with which the flow was reset is shown in Table 6.1; less than 1% difference in water discharge in all but one test.

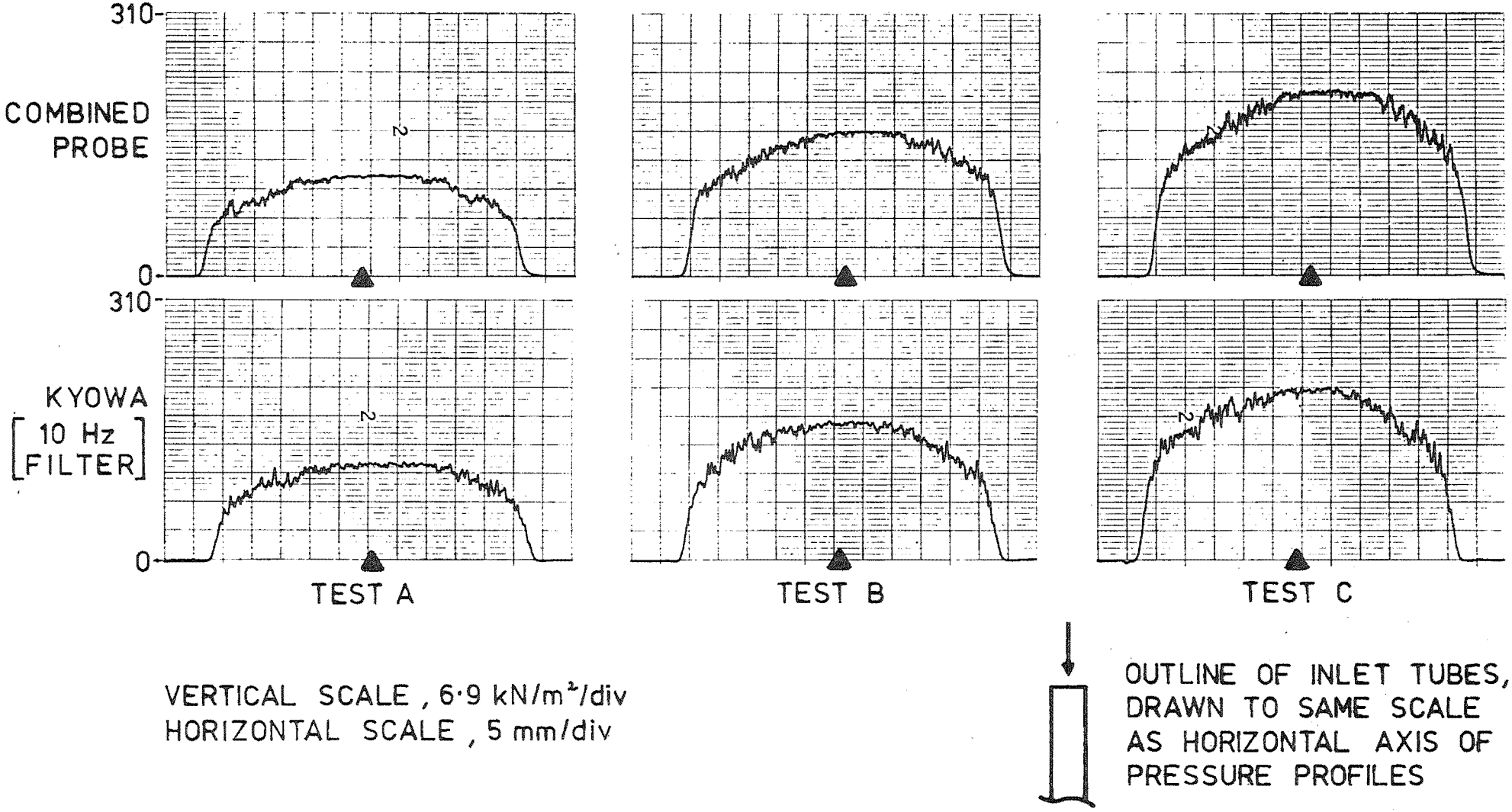

Fig. 6.6 Stagnation Pressure Profiles in Non-Aerated Flow.

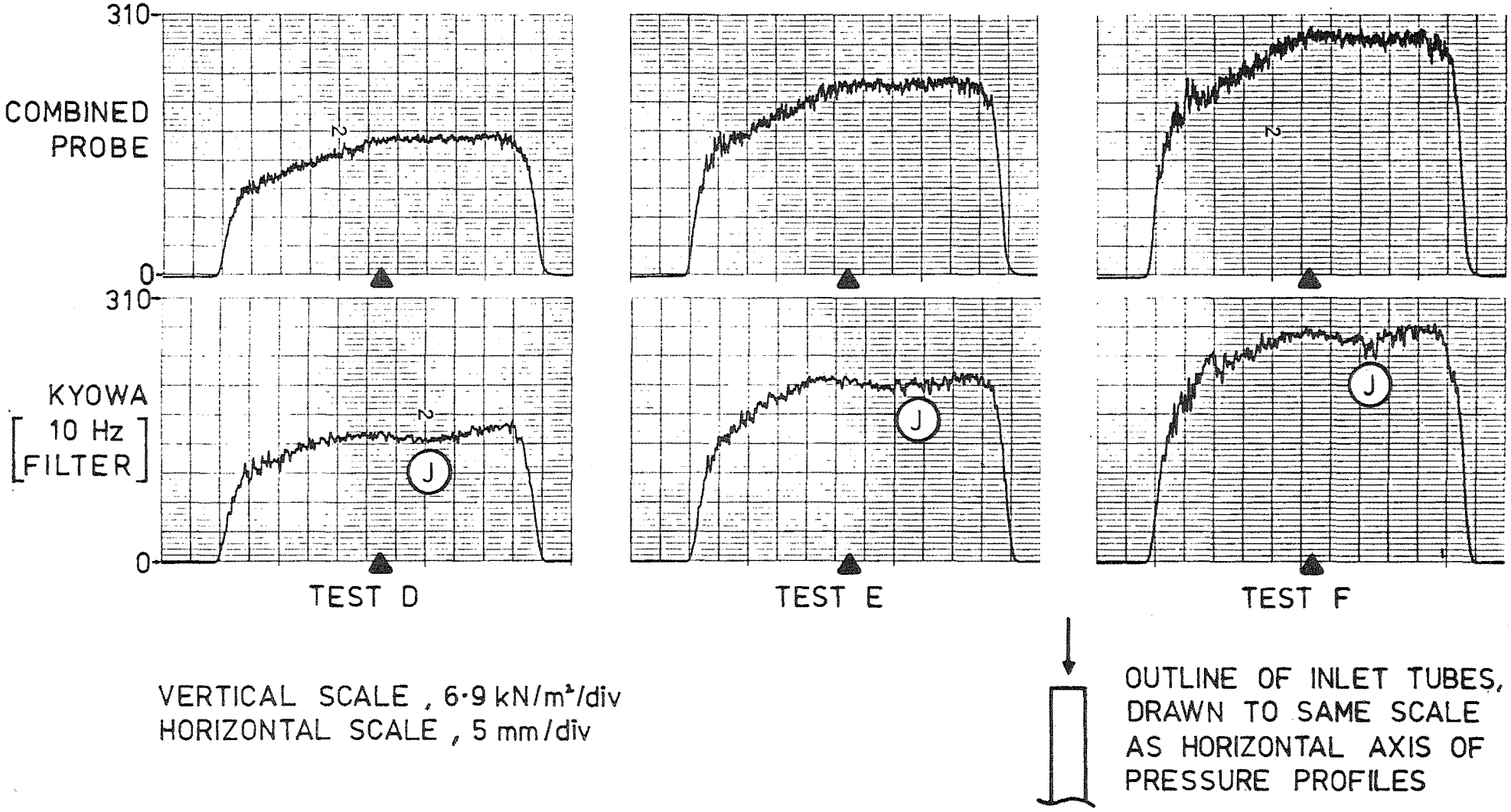

Fig. 6.7 Stagnation Pressure Profiles in Aerated Flow.

Table 6.1 Water Discharge x 10^{3} m^{3}/s

	Non-aerated Flow			Aerated Flow		
	A	B	C	D	E	F
Combined Probe	34.2	40.7	45.8	32.8	38.7	43.2
Kyowa Probe	34.4	41.3	45.8	32.6	38.5	43.2
% Difference	-0.4	-1.5	-0.1	0.7	0.4	-0.2

In the non-aerated flows (Fig. 6.6) the pressure profiles measured by each probe are similar in shape. In the aerated flows (Fig. 6.7) the profiles measured by the Kyowa probe show a dip at (J) which is not present in the profiles measured with the combined probe. It was not possible to account for this in terms of different test conditions. Indeed, similar irregularities occur in the profiles of Fig. 6.9 all of which were obtained within five minutes under identical flow conditions. It must therefore be assumed this is an unsteady flow phenomenon.

The differences between the two pressure profiles for a given test was calculated by dividing the central portion of each profile into nine 5 mm intervals. (The small triangle below each profile indicates the centre of it). The mean pressure was measured for each interval and the pressure difference calculated. The differences for all intervals for all six tests are summarised in Table 6.2. This shows the mean and extreme differences, expressed as a pressure and as a percentage of the measured pressure.

Table 6.2 Pressure Difference for all Tests

P_c denotes values for combined Probe.

P_k denotes values for Kyowa Probe.

Test	$P_c - P_k$ (kN/m^2)		$(P_c - P_k)/P_k$ (%)	
	A - C	D - F	A - C	D - F
Mean Difference	7	9	5	5
Max. Positive Difference	23	24	13	12
Max. Negative Difference	-1	-5	-1	-2

Before assessing these values, it is important to appreciate their accuracy. If the two transducers are assumed to be accurate to 1% FS., this corresponds to 4 kN/m^2 for the combined probe and 5 kN/m^2 for the Kyowa probe. Also, the scale of Figs. 6.6 and 6.7 and the signal fluctuations will limit their accuracy to about 4 kN/m^2. These are very significant pressures compared with the pressure differences $P_c - P_k$ in Table 6.2.

Table 6.2 indicates that the combined probe overestimates the stagnation pressure by about 5% in both the non-aerated and aerated flows. An error of this magnitude could well be caused by the proximity of the air concentration electrodes to the stagnation point, and the contraction of the flow between them. However, the limited accuracy of these measurements and the unsteady nature of the flow may have contributed to this overestimation.

6.5.3 Effect of Pressure Inlet Tube Diameter on Stagnation Pressure

These tests were designed to see whether the ratio of bubble size to pressure inlet tube diameter effects the stagnation pressure. It is known that in some circumstances, the behaviour of bubbles approaching a total head tube is dependent on their relative size (ref. Section 2.4).

For these tests a probe was constructed which used the same pressure transducer as was used with the combined pressure air concentration probe. The inlet tube was identical except that the end of it was modified to accept two cylindrical caps as shown in Fig. 6.8. (This probe is shown on the sliding carriage in Fig. 6.5). The diameters of these three configurations were 1.1, 6 and 19 mm compared with the 6 mm diameter inlet tube of the combined pressure air concentration probe.

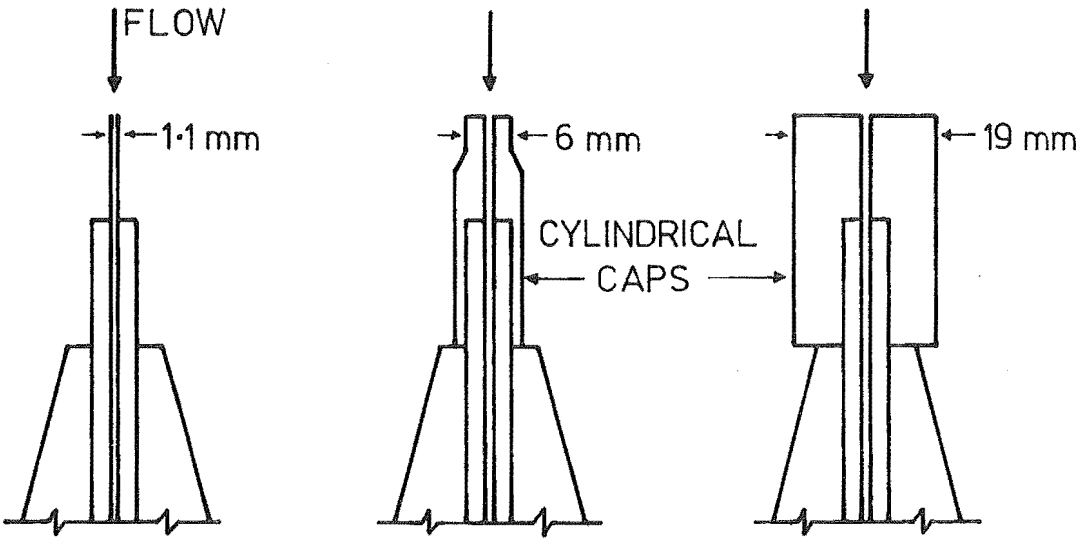

Fig. 6.8 Cross-Section of Inlet Tubes.

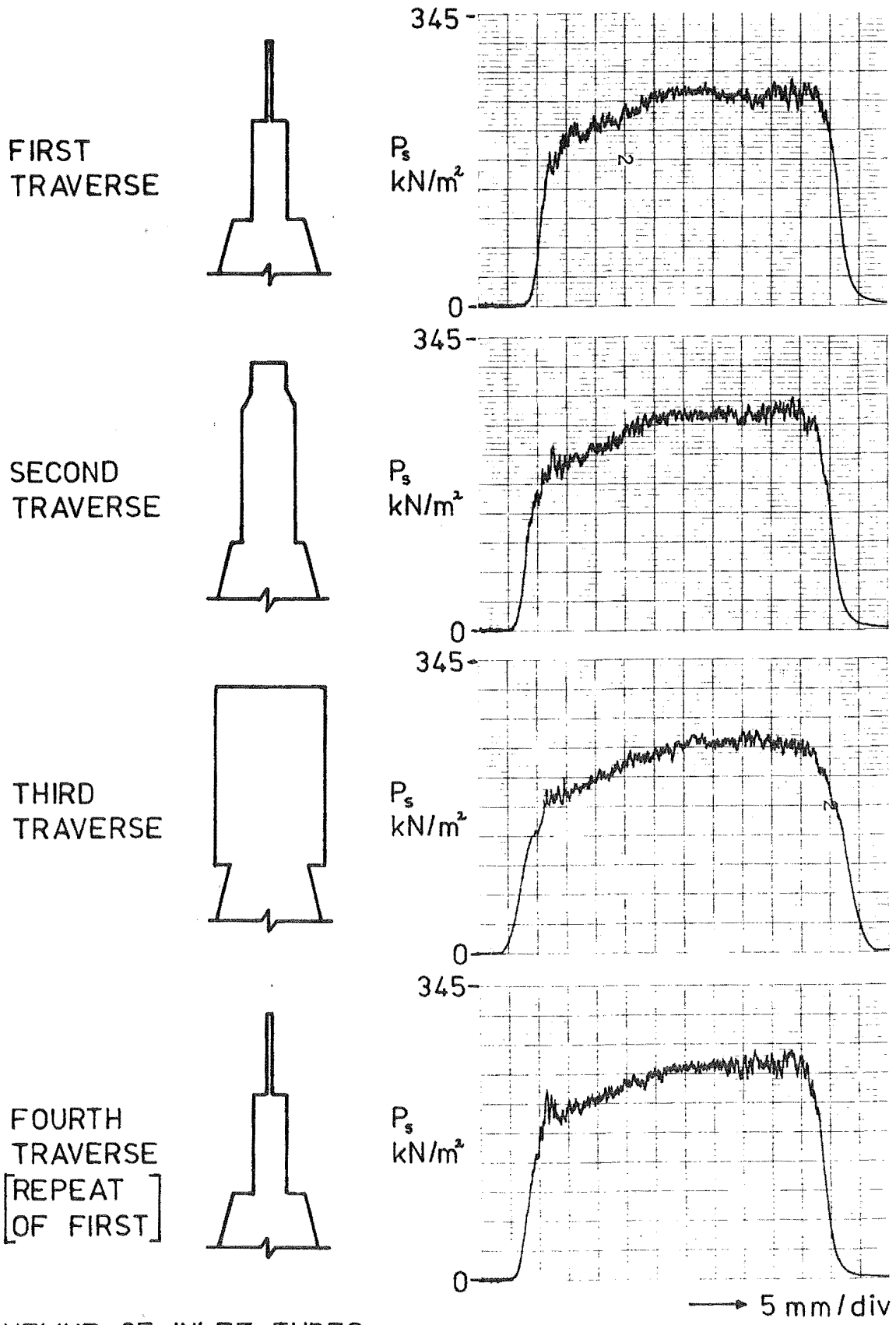

Fig. 6.9 Pressure Inlet Tube Comparison.

The three configurations were all traversed through the same aerated flow in quick succession merely by changing the caps. The output signals were recorded on a chart recorder as in the previous tests and are shown in Fig. 6.9. It is shown in Section 6.5.6. that for this (water) discharge (44.1×10^{-3} m^3/s) the velocity was about 24 m/s, the air concentration about 0.15 and the Mach number about 0.85.

In the central portion of the profiles where there are no edge effects the only differences are due to the unsteady nature of the flow. For these flow conditions the measured stagnation pressure is therefore insensitive to the diameter of the pressure inlet tube.

6.5.4 Air Concentration Comparisons

Two methods were considered suitable for checking the accuracy of the air concentration instrument; namely a mechanical sampler as used by Lamb and Killen (1950), (ref. Section 3.3) or a gamma radiation technique as used by Keller (1972). This latter technique was chosen because Keller's apparatus was available and because the accuracy of this method is well established.

The gamma radiation technique depends on the attenuation of a beam of γ-rays (photons) in an air-water mixture. It is shown in Appendix L that for a monoenergetic collimated beam of γ-rays the air concentration is given by

$$C = \frac{\ln\left[\frac{I}{I_o}\right]}{\ln\left[\frac{I_1}{I_o}\right]}$$

where I is the intensity of the emergent radiation beam.

I_o is the intensity when C = 0.0

I_1 is the intensity when C = 1.0.

The radiation source and a detector are each encased in lead within a steel frame, and securely positioned on opposite sides of the perspex outlet pipe, (see N, Fig. 6.3 and also Figs. 6.1 and L.1, Appendix L). The radiation beam is about 12 x 12 mm (cross-section) and is about 100 mm from the downstream end of the perspex pipe.

Keller's (1972) apparatus was extensively modified by the writer until the air concentration measurements were accurate to within 1%. Details of the apparatus and the accuracy checks are in Appendix L.

The gamma radiation apparatus measures the mean air concentration in the path of the beam. The air concentration probe therefore had to be traversed through the flow directly downstream of the beam. The mean air concentration could then be calculated from the air concentration profile which was recorded on a chart recorder.

Three air concentration comparisons were obtained in this way. These were in fact recorded simultaneously with the stagnation pressure measurement when the combined pressure air concentration probe was traversed through the three aerated flows D, E and F. The air concentration profiles are shown in Fig. 6.10. The irregularities when $C \simeq 1.0$ are caused by spray hitting the electrodes.

Because of the edge effects it was again considered best to measure the mean air concentration over the central 45 mm portion of the flow only, by dividing the profiles into nine 5 mm intervals. The input-output relationship for the air concentration instrument was derived by the method described in Section 3.6 and detailed below.

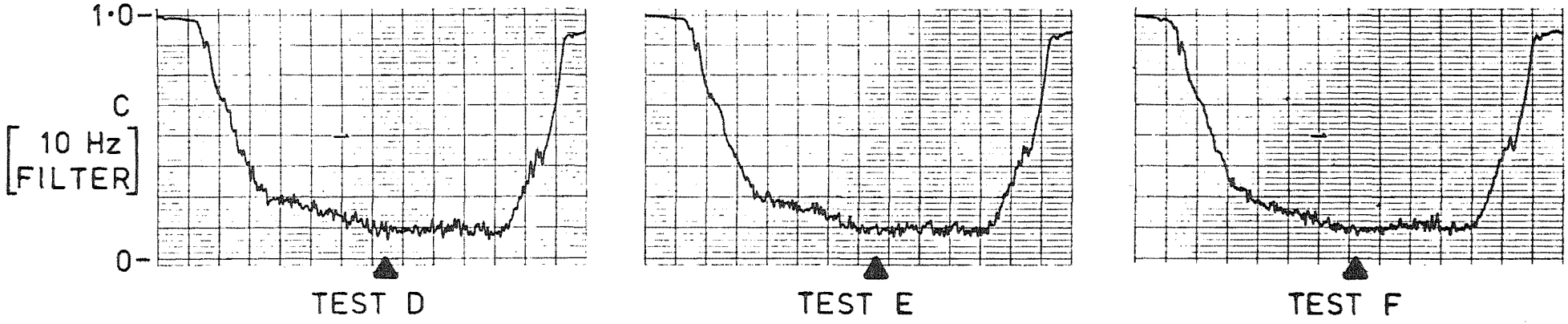

Fig. 6.10 Air Concentration Profiles in Aerated Flow.

The instrument's response in the laboratory water and in a salt solution of concentration 49.0 g/m^3 was almost identical. (This concentration is twice the equivalent salinity of the Aviemore water during the final field tests). For this salinity R_{EO} = 9.4kΩ (measured with the Wayne Kerr Autobalance Universal Bridge) and so α = 1.94. From Eq. 3.11 the air concentration is therefore given by:

$$C = \frac{3.66 \, || V_E ||}{2.66 + || V_E ||}$$

Combining this with the electronics calibration curve of Fig. 3.17 for 49.0 g/m^3 salinity gives the input-output relationship for these tests, shown in Fig. 6.11. This was used to calculate the mean air concentration in the profiles of Fig. 6.10, which are listed in Table 6.3

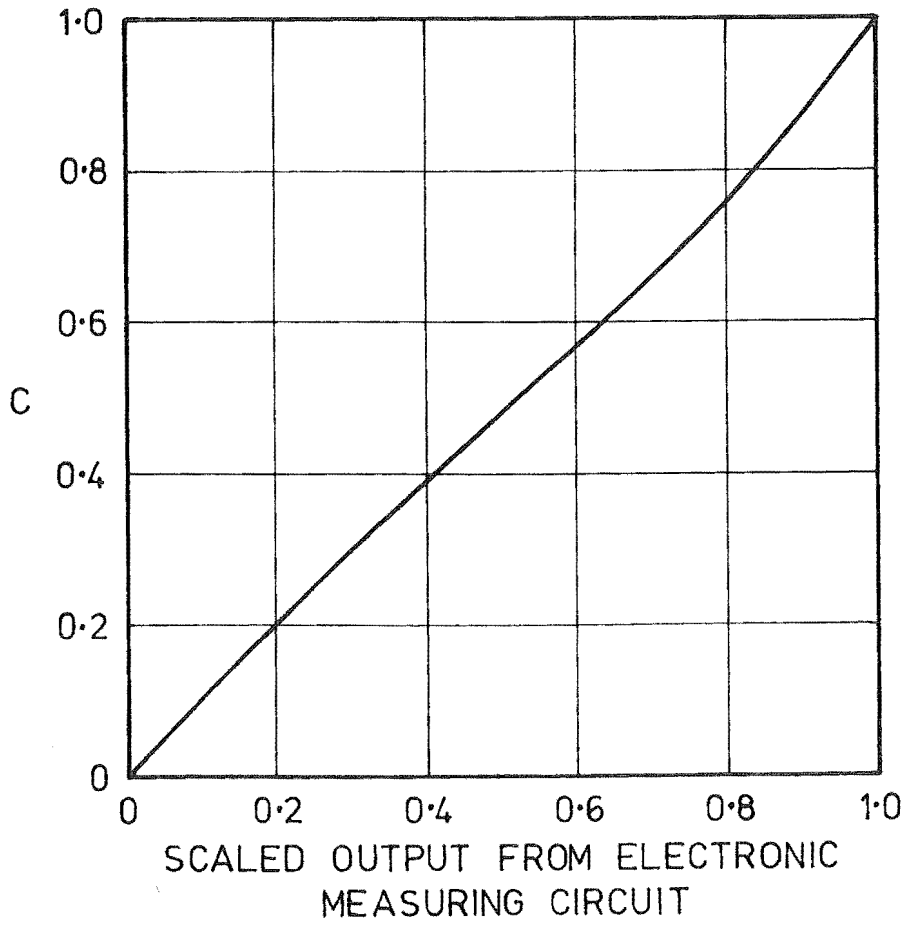

Fig. 6.11 Input-Output Relationship for the Air Concentration Instrument in the Laboratory Tests.

Table 6.3 also lists the air concentration calculated with the gamma radiation apparatus. These calculations are described in detail in Appendix L where it is shown that the statistical uncertainty of each air concentration is less than 0.006.

The mean air concentrations from the two methods are in excellent agreement; the difference between them is on average only about 0.01. Once again, it is important to realise the accuracy of this comparison. The scale of Fig. 6.10 and the signal fluctuations will limit their accuracy to about 0.01. The use of only the central portion of each profile will also introduce an error which cannot be assessed with any confidence.

Table 6.3 Comparison of Mean Air Concentration Measurements

	Test		
	D	E	F
Gamma Radiation	0.164	0.154	0.149
Combined Probe	0.16	0.16	0.17
Difference	0	0.01	0.02

6.5.5 Effect of Velocity on Air Concentration Measurement

Until now it has been assumed that the air concentration predicted by the combined pressure air concentration probe is independent of the water velocity. (Neither Lamb and Killen (1950) nor Keller (1972) questioned this).

This assumption was simply verified for the special case C = 0.0. The probe was positioned in the centre of a non-aerated flow and the water velocity was decreased from about 25 - 0 m/s. The velocity had no effect on the air concentration signal.

This simple test is not possible in aerated flows because any signal variation could be caused by either a velocity effect or a variation in air concentration.

6.5.6 Velocity and Mach Number in Tests

It is desirable to show that the flow velocities in these tests were in fact identical to those at Aviemore. In the tests A - F, the stagnation pressure and air concentration were recorded simultaneously as the combined probe was traversed through the flow. It is therefore possible to predict velocity and Mach number profiles using Eq. 2.8 and Eqs. 2.1 and 2.2 namely,

$$V = \left[\frac{2}{\rho_w}\left[P_s + \frac{C}{1-C} P_o \ln\left[\frac{P_s + P_o}{P_o}\right]\right]\right]^{\frac{1}{2}} \qquad 2.8$$

$$M = V\left[\frac{\rho_w C(1-C)}{P_o}\right]^{\frac{1}{2}} \qquad 2.1, 2.2$$

These have been rewritten so that the stagnation pressures are expressed in gauge units (ref. Section 2.5). Also, the static pressure P is assumed equal to the atmospheric pressure P_o (ref. Appendix C) which can be taken as $P_o = 102\ kN/m^2$ (abs).

These equations (2.8 and 2.1, 2) were evaluated over the central 45 mm of the flow only, for each of the nine 5 mm intervals that the stagnation pressure and air concentration had been calculated.

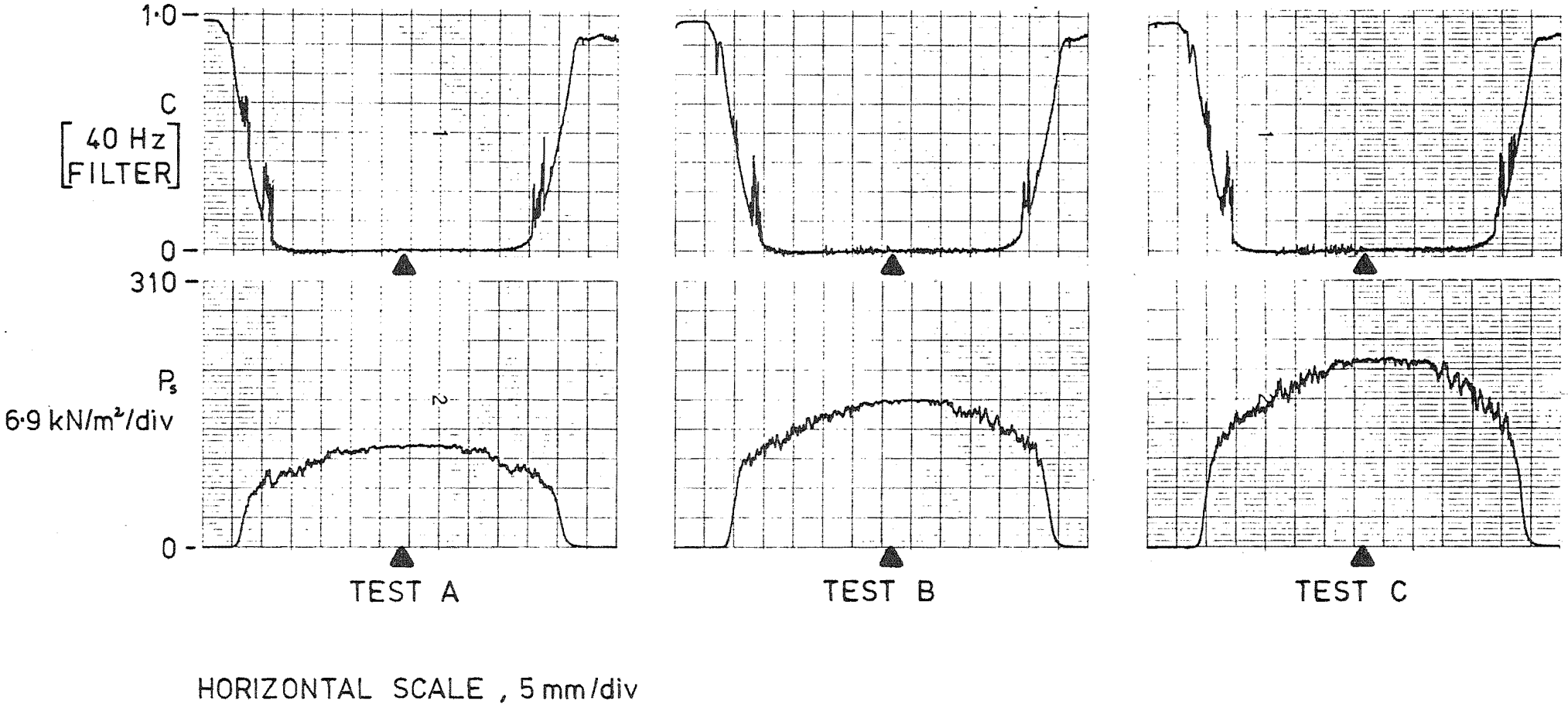

Fig. 6.12 Air Concentration and Stagnation Pressure Profiles in Aerated Flow.

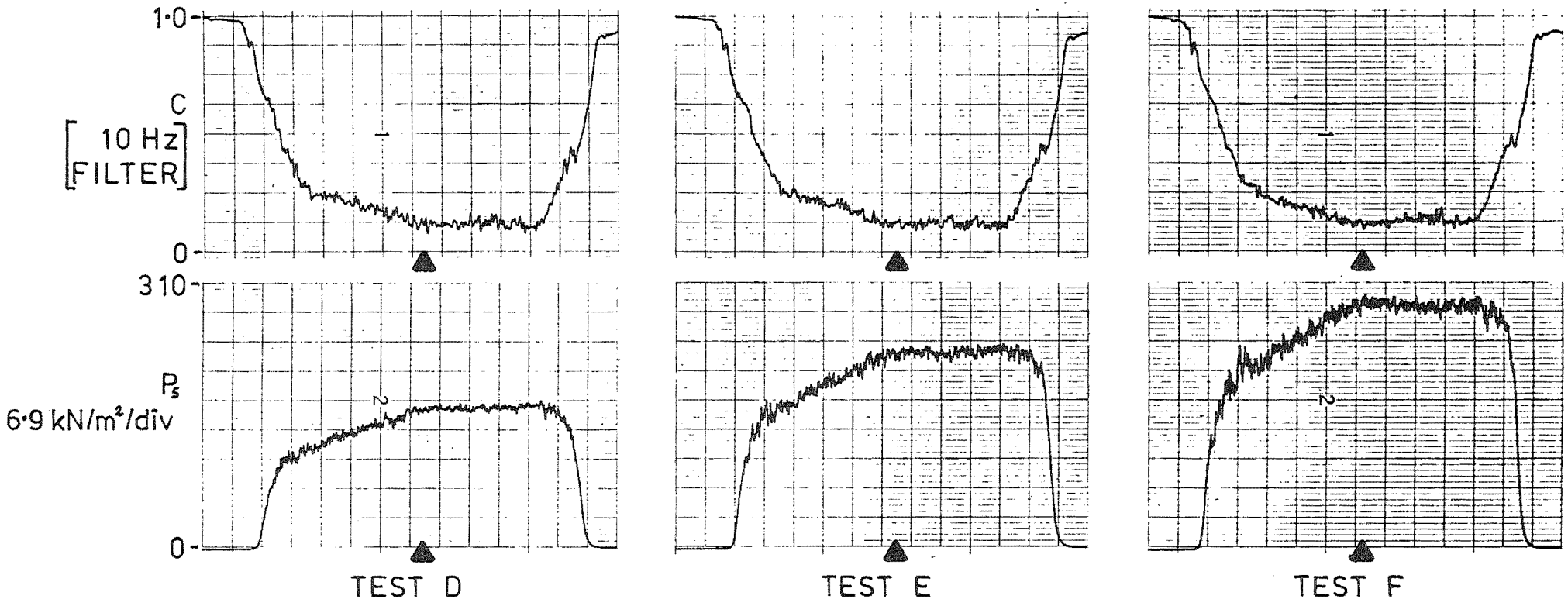

Fig. 6.13 Air Concentration and Stagnation Pressure Profiles in Non-Aerated Flow.

The combined profiles of stagnation pressure and air concentration are shown in Figs. 6.12 and 6.13, with superimposed profiles of velocity and Mach number in Fig. 6.14. In all tests, the flow was subsonic, with velocities ranging from 13 - 25 m/s, very similar to the 12 - 22 m/s range measured at Aviemore. The Mach numbers ranged from 0.4 - 1.0.

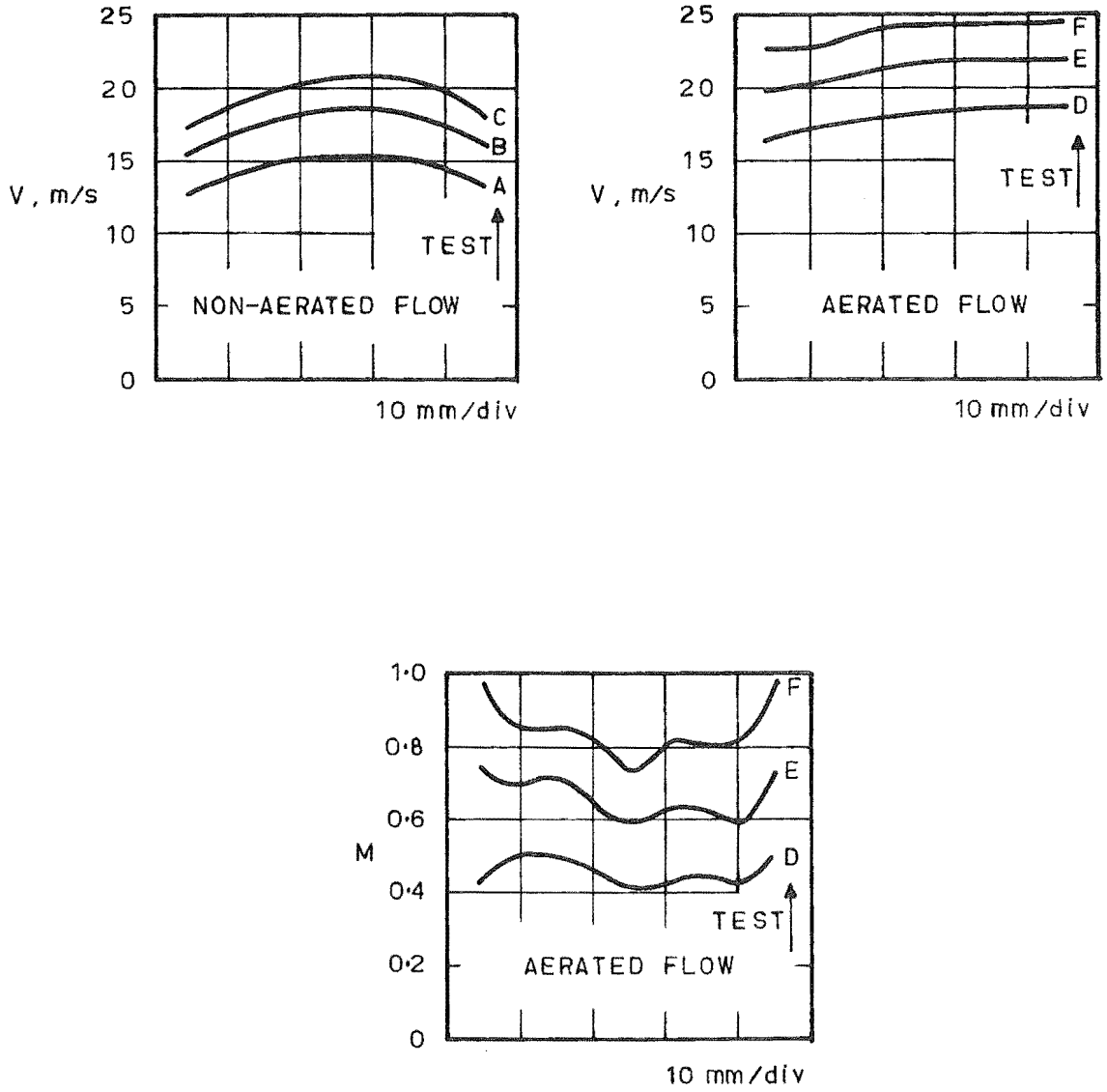

Fig. 6.14 Velocity and Mach. Number Profiles.

CHAPTER 7

FIELD TEST EQUIPMENT

7.1 SUMMARY

The equipment used in the field tests at Aviemore is described. This comprised the mechanical and electrical equipment for remotely traversing probes through the flow on the spillway, plus the equipment for recording the instrument's output signals.

7.2 INTRODUCTION

For the measurements on Aviemore spillway, the test equipment was designed to use the existing test stations, spillway cable and recording hut described in Section 1.5. A single instrument assembly was constructed which could be fixed to any of the spillway test stations. A probe mounted on this could be remotely traversed through the flow. The probe could be accurately positioned to a maximum depth of 352 mm. The probe's output signals were recorded on a tape recorder within the recording hut.

7.3 SPILLWAY INSTRUMENT ASSEMBLY

7.3.1 Description

The spillway instrument assembly is shown in Figs. 7.1 - 7.4. The steel plate (A, Fig. 7.4) was made to fit flush with the spillway surface in place of the test station cover plates. The steel box (C) beneath this plate is divided into two main compartments, one of which is kept dry (U) while the other is able to fill with water (B).

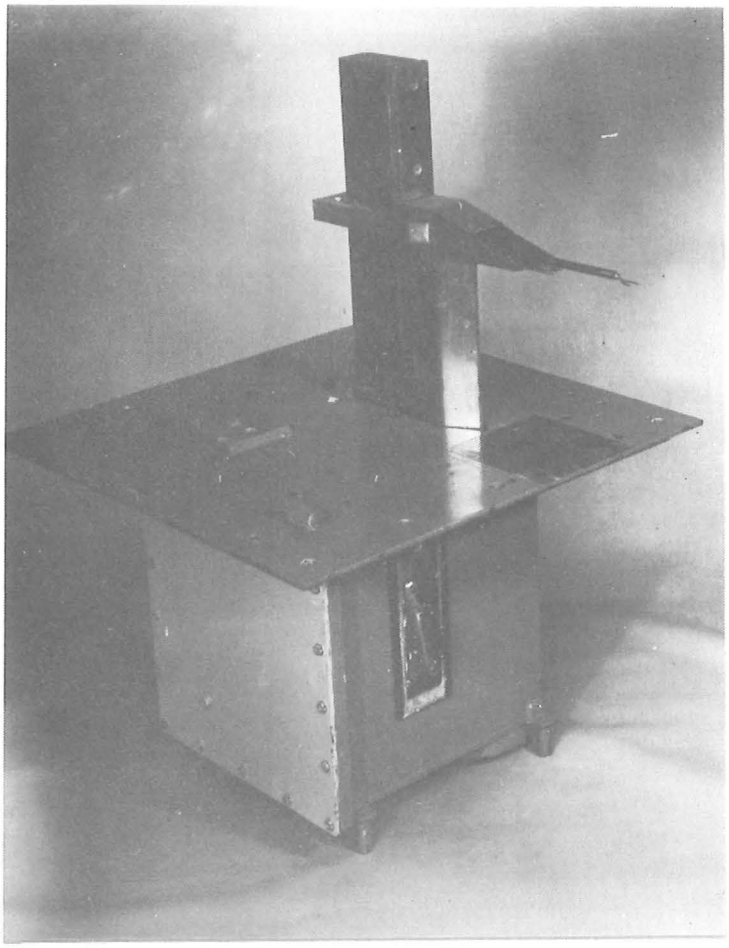

Fig. 7.1 Spillway Instrument Assembly.

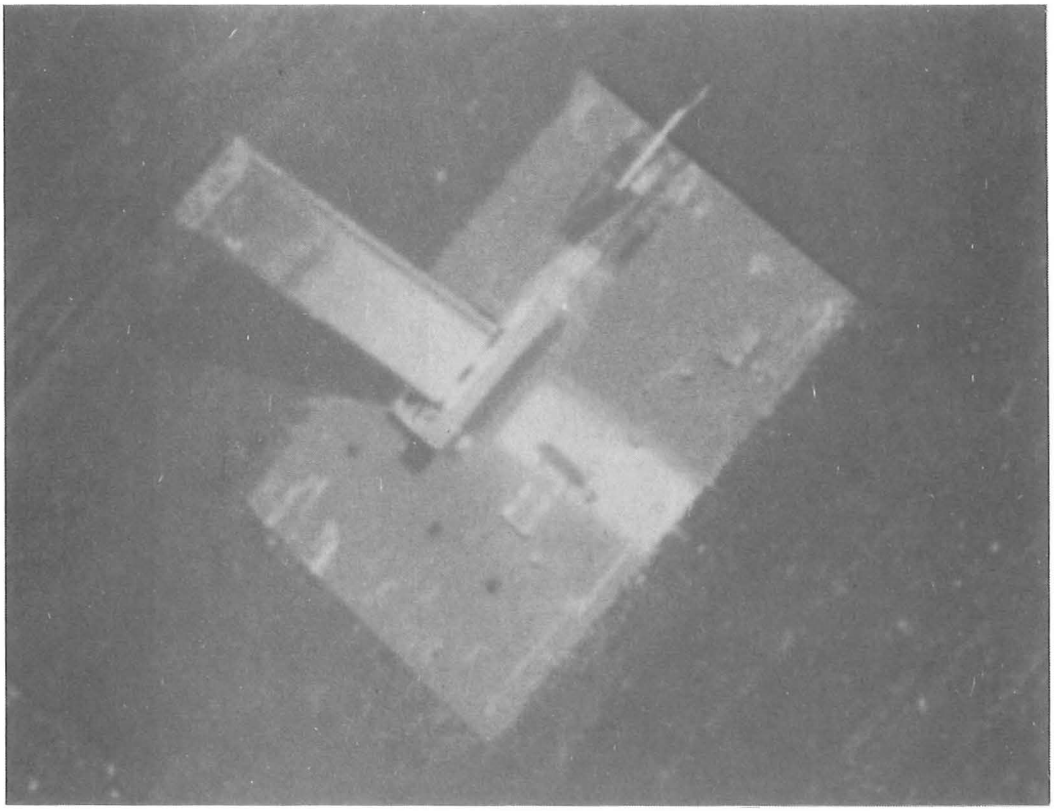

Fig. 7.2 Spillway Instrument Assembly on the Spillway

(The velocity probe is at the spillway surface).

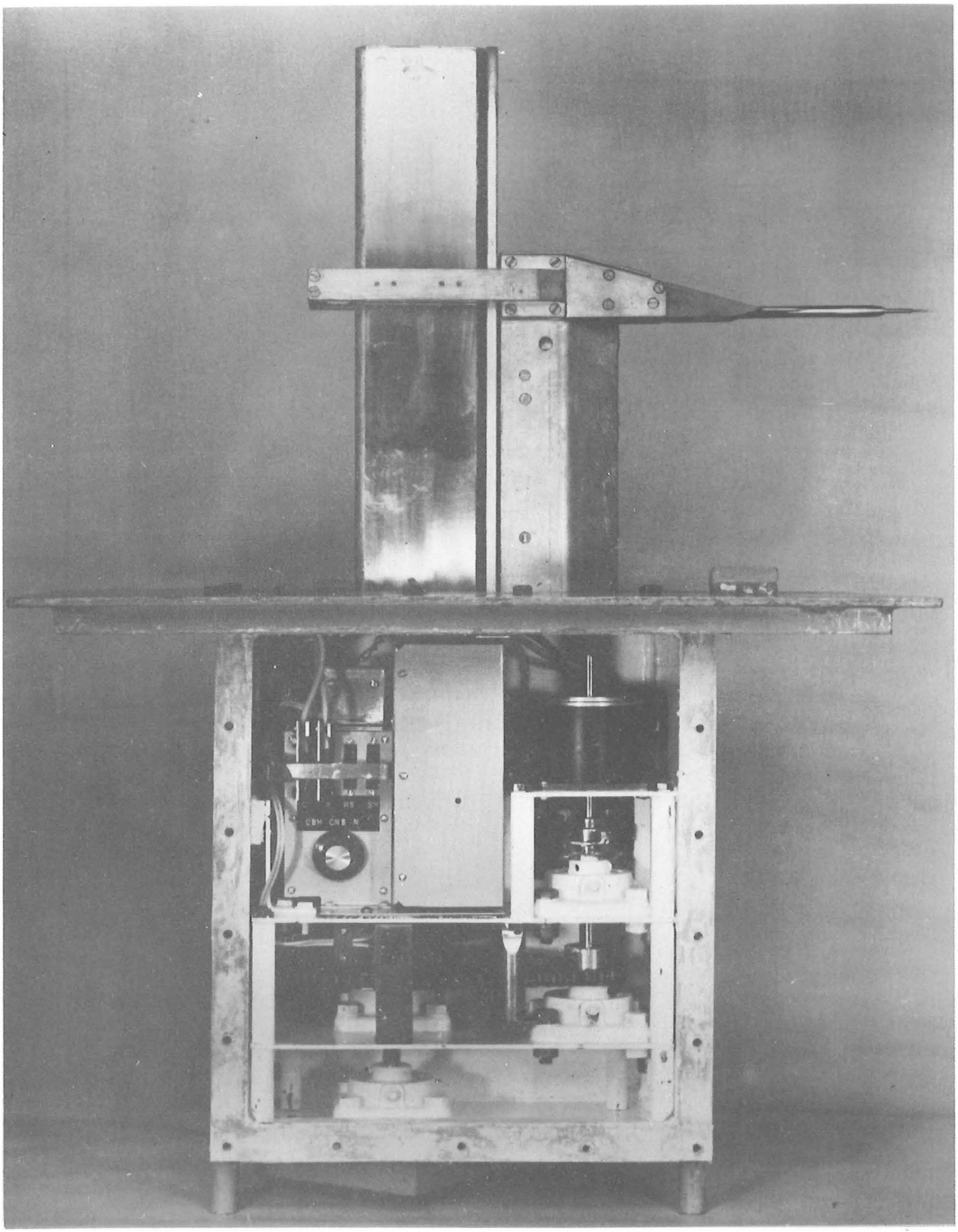

Fig. 7.3 Spillway Instrument Assembly with the Side Cover Removed.

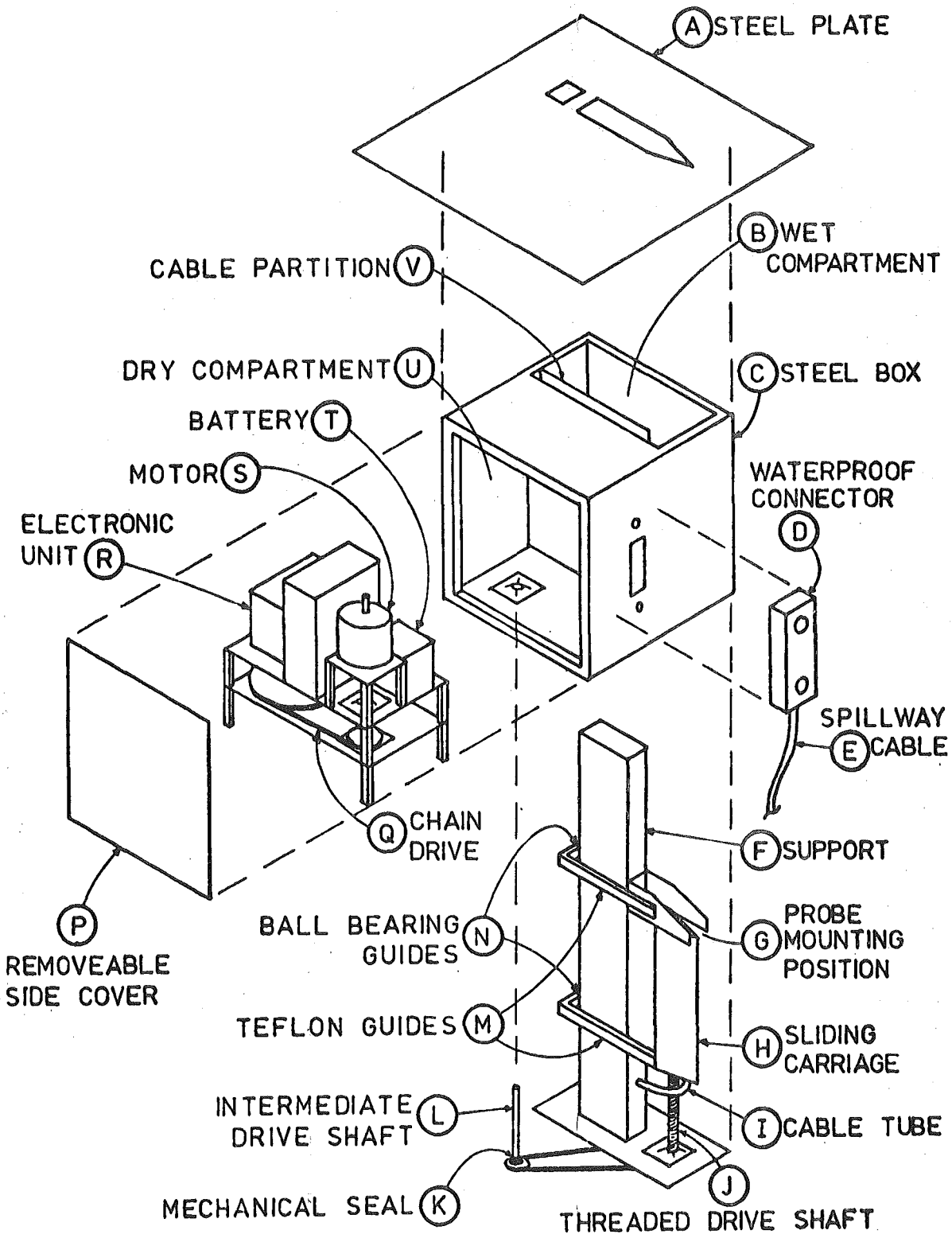

Fig. 7.4 Schematic of Spillway Instrument Assembly.

The dry compartment contains a stepper motor (S), chains, cogs and drive shafts (Q , K) plus a battery (T) and an electronic unit (R). The spillway cable (E) was connected to the spillway instrument assembly by a water proofed connector (D).

The wet compartment contained the sliding carriage (H) and its support (F). The upper half of this support plus part of the sliding carriage protrude above the plate (A). Probes were attached to the top of the sliding carriage (G) which was driven by the stepper motor.

Seals were provided at all entrances to the dry compartment. In the event of a seal leaking, any water entering the dry compartment would be absorbed by a hydroscopic material in the bottom of this compartment.

Most components were made from mild steel, which was either painted, cadmium plated or chromed to prevent rust.

7.3.2 Drive Mechanism

An available stepper motor was used to drive the sliding carriage This could be driven in either direction in increments of $\frac{1}{200}$th of a revolution.

The motor was connected via a series of reduction cogs and chains to a threaded drive shaft (J, Fig. 7.4). This drove through a phosphor bronze nut fixed within the sliding carriage.

A mechanical seal (K) connected to an intermediate drive shaft (L) on the outside of the dry compartment. This prevented water entering at this point.

Four sealed ball bearing races within the sliding carriage contacted the upstream face of the support. The sliding carriage was constrained to move up and down the support by teflon guides at the side (M) and by ball bearing races at the rear (N). In tests in the A flow simulator, these guides prevented vibration yet provided little resistance to sliding,even when the support and sliding carriage were inclined at 10^{o} to the direction of flow.

As all the drive shafts were mounted on ball bearing races, the power losses from the motor were caused mainly by the mechanical seal and the friction between the threaded drive shaft and the phosphor bronze nut. These friction forces were simply measured.

To determine the cog ratios, it was necessary to predict the worst case of water loading on the sliding carriage. The load was calculated for the instrument assembly at the bottom test station,with the sliding carriage in a range of positions,and for the support partially and completely submerged in water. All approximations erred on the conservative side.

The cog reduction ratios (9:1 overall) were then chosen so that at its minimum speed of 50 rpm , the motor would have sufficient torque to overcome the power losses plus drive the sliding carriage against the worst case water loading. For the smaller water loading predicted in aerated flows, the motor speed could then be increased up to its maximum of 500 rpm At this speed its torque was only one third of the torque at 50 rpm.

7.3.3 Structural Design

The worst case of water loading on the various structural components was calculated once again conservatively. For these loads the maximum steel stresses were less than 0.25 times the yield stress so that the actual stresses in aerated flows would be much less than this.

This conservative approach reduced the likelihood of adverse deflections and vibrations, but did result in a very heavy unit, about 80 kg.

7.3.4 Installation

The spillway instrument assembly was moved from station to station with the aid of a skip, (Fig. 7.5). This was lowered from the top of the dam by a crane (Fig. 7.6) and slid down the spillway face on runners fixed to the underside of it. In Fig. 7.5 the spillway instrument assembly is suspended from a boom with a lifting device. Station 505 is visible just below it with the cover plate removed, and station 504 is visible at the top of the photograph. The two persons required on the skip were in radio contact with a person at the top of the dam who directed the crane driver.

Fig. 7.5 Spillway Skip at Station 505. Station 504 is visible at the top.

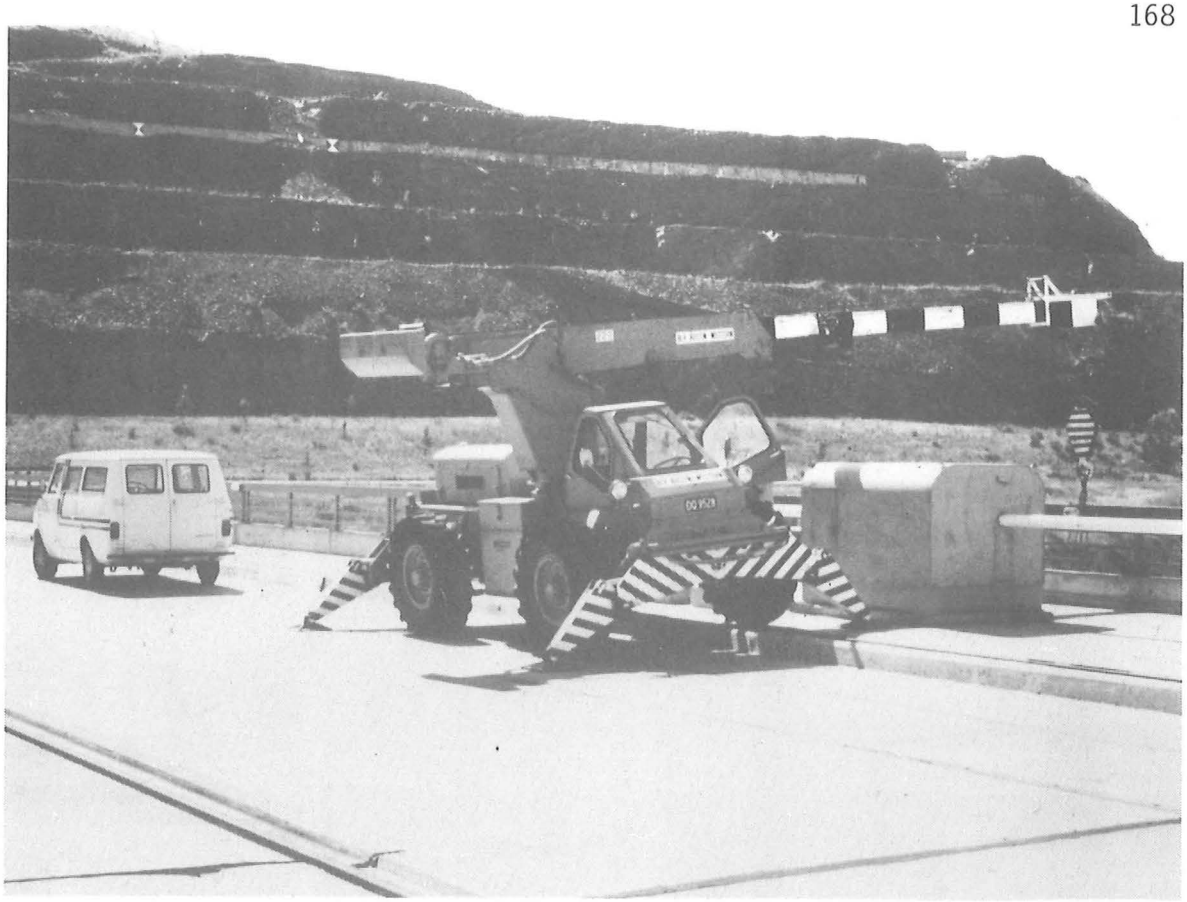

Fig. 7.6 Crane at Top of Dam.

7.4 ELECTRICAL SYSTEM

7.4.1 Introduction

The electrical system was initially designed and constructed by DAVCO (electronics firm). In spite of preliminary laboratory testing, various electrical problems occurred in the initial field tests at Aviemore. These problems and the extensive modifications necessary are discussed in Chapter 8. The modifications to the electrical system were designed by the writer and were constructed within the University. The following discussion refers only to the modified electronics which were used in the final field tests at Aviemore.

7.4.2 Description

The electrical system performed two separate functions, firstly controlling the probe's position and secondly getting signals from the instruments into the tape recorder.

The cables between the recording hut and the spillway instrument assembly were so long (about 50 m) that it was necessary to construct two different electrical units. One was a control unit which was placed inside the recording hut (see Fig. 7.8). This contained the motor drive logic, a digital display indicating the probe position and signal conditioning for the output signals. The other unit was contained within the dry compartment of the spillway instrument assembly. (See Fig. 7.7 and also R, Fig. 7.4). This contained the instrument's electronics and the electronic circuit for a device which indicated the probe's positions.

7.4.3 Probe Position

The probe's position was determined from the rotation of the intermediate drive shaft (L, Fig. 7.4). A metal disc attached to this shaft rotated between the emitter and detector of an infra-red light module. The disc had two large slots 180° apart through which the emitter was visible to the detector.

An electrical circuit within the spillway instrument assembly provided the power supply for this light module, and generated an electrical pulse each time a slot in the disc aligned with the light module. Each pulse was transmitted via the spillway cable to the control unit.

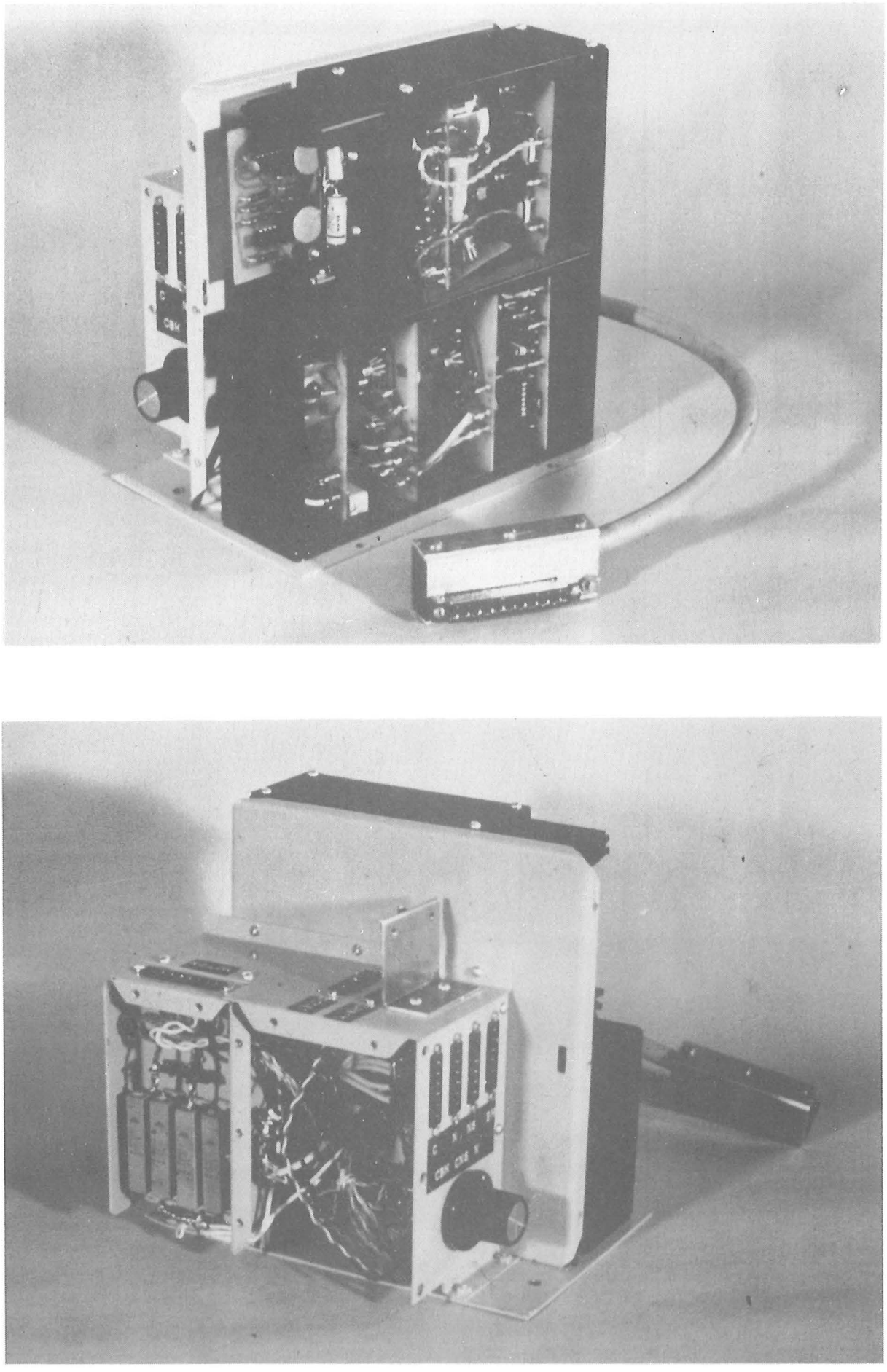

Fig. 7.7 Electronics Unit from Spillway

Instrument Assembly. (Side covers removed).

As the sliding carriage was driven up the support, the pulses were counted within the control unit, the total number being displayed on the front panel of the control unit. When the sliding carriage was lowered, the number displayed was automatically decremented rather than incremented. By zeroing the display when the sliding carriage was in its lowest position, the probe position was indicated as a number from 0 - 705 corresponding to the 352 mm of travel.

7.4.4 Motor Drive Logic

The motor's power supply and speed control plus the drive logic were contained within the control unit. The drive logic allowed the probe to be driven to any predetermined position. This position was first selected on three thumbwheel switches. When the motor was activated, the probe would be driven until its displayed position was identical to that on the thumbwheel switches. In this way, a probe could be traversed through the flow with measurements recorded at regular increments.

7.4.5 Instrument Electronics

Because the spillway cable was so long, it was necessary to provide electrical circuits for each probe within the spillway instrument assembly.

Electrical circuits were provided for the combined pressure air concentration probe and the velocity probe. The circuit diagram for the air concentration instrument is shown in Fig. 3.15. The circuit providing the 20.1 kHz sine wave input for these electronics has been omitted from this figure.

Two pressure transducer circuits were provided. One was simply a unity gain operational amplifier for the National Semiconductor transducers. This prevents the recording circuit from loading the transducer, and protects it from short circuits. The other circuit was for a Bell and Howell transducer. This provided a 5 volt floating earth power supply, derived from an 18 volt battery within the spillway instrument assembly. It also included a 470 times gain differential amplifier to increase the signal level to within the tape recorder's input range.

The circuit diagram for the velocity probe is shown in Fig. I.1. This also employed a unity gain operational amplifier.

The electrical circuits were powered by a ±12.5 volt d.c. power supply within the spillway assembly. This was derived from a ±15 volt d.c. power supply in the control unit.

The electronic circuits for either instrument (and either pressure transducer) were selected with a rotary switch within the spillway instrument assembly. This connected the power supplies and output leads for each circuit. It had a total of 64 gold plated connections which were connected in pairs to minimise the possibility of failure due to dirty contacts or excessive vibration.

The electronic circuit boards within the spillway instrument assembly were designed to prevent vibration problems. They were foam rubber mounted, did not use preset potentiometers, and all wires connected to them through securely mounted "pins". Coaxial cables were used extensively to minimise inductive noise. All circuits were sprayed with a silicone oil to waterproof them.

7.4.6 Electrical Connections to Probes

Two 4-core individually shielded cables were used to connect the probes to the electronic circuits within the dry compartment. In order to interchange probes, it was necessary to provide water proof electrical connectors within the sliding carriage. Because no commercial water proof connectors were available, DIN plugs were used which were covered with rubber sleeves and sprayed with a silicone oil.

The two cables passed through a tube (I, Fig. 7.4) on the bottom of the sliding carriage and then behind a partition (V) in the wet compartment. They were in a loop behind the partition, so that the sliding carriage could move without damaging or being restricted by them.

The cables entered the dry compartment through holes which were sealed with O-ring fittings. McMurdo connectors were fitted to their ends. These could be locked into various sockets on the electronic unit, depending on which instrument was in use.

7.4.7 Spillway Cable

The spillway cables (between the spillway instrument assembly and the control unit in the measuring hut) each had seven cores. A minimum of ten was required for the motor to be driven and measurements to be recorded simultaneously. It was therefore necessary to have two distinct modes of operation; drive or measure. The mode was selected by a switch on the front panel of the control unit. This activated four relays in both the control unit and the spillway instrument assembly electronic unit. In this way, four cable cores were used alternatively by the stepper motor and by the instruments.

7.5 RECORDING EQUIPMENT

The recording hut was adjacent to spillway bay 5 where the spillway cables terminated. This housed the control unit, tape recorder and ancillary equipment as shown in Fig. 7.8 and the block diagram in Fig. 7.9.

Before the two output signals from an instrument could be recorded, they had to be adjusted to suit the input range of the tape recorder. This signal conditioning was provided by d.c. offset and attenuation facilities incorporated into the control unit. These were necessary because the signal level of all instruments except for the pressure transducers were dependent on the conductivity of the water.

The tape recorder was a CEC Datatape VR-3300 analogue magnetic tape recorder. This was a 7 track 6 speed device with 2 FM (Frequency Modulated) amplifiers. An eighth channel was available for voice logging. The important performance specifications are listed in Appendix E.

When the control unit was in the drive mode, the input leads to the tape recorder were shorted to ground. This zero volt signal served as an inter-record gap and also as a check on the tape recorder amplifier's drift.

Calibration signals were also recorded before and after any measurements so that the input-output relationship could be determined when the data was taken from the tape. These were +1, 0, -1V signals from which drift and linearity could also be calculated.

The output signals from the tape recorder were continuously monitored on an oscilloscope. As indicated in Fig. 7.9, a digital voltmeter could also monitor either output signal.

Also shown in Fig. 7.8 is some electronic test equipment. This was present in case on site repairs were necessary.

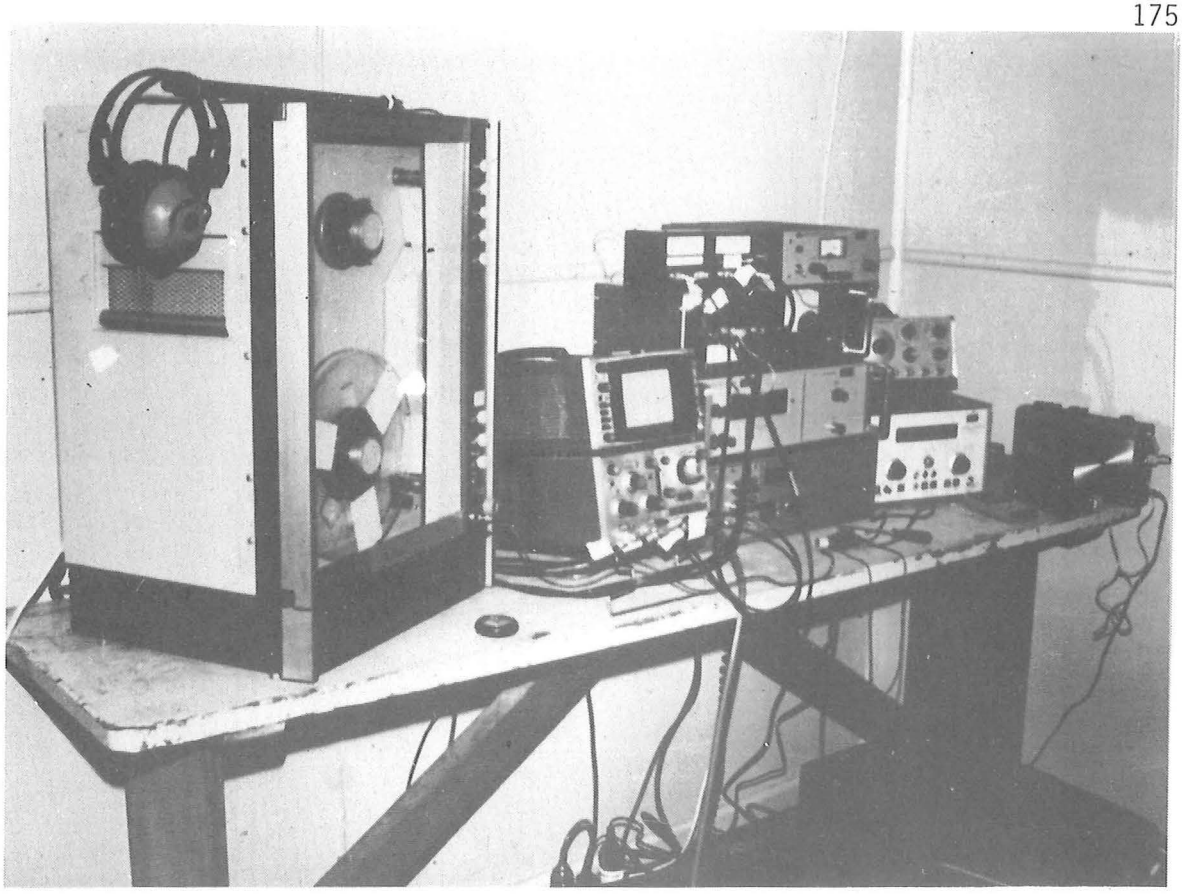

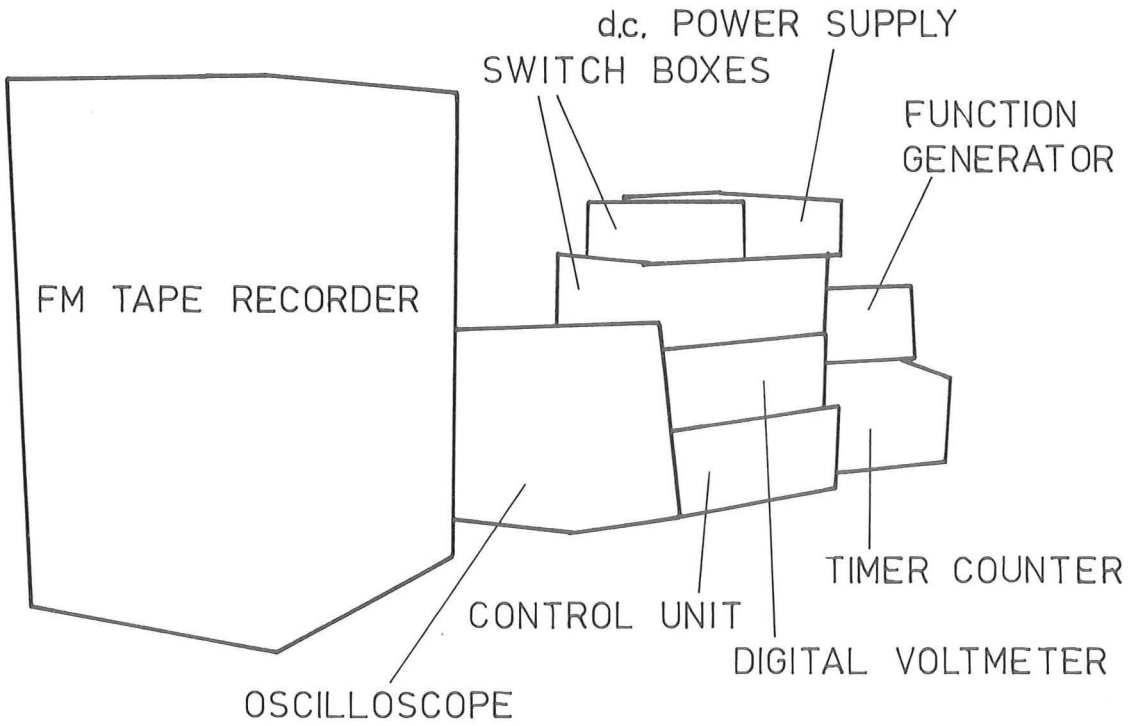

Fig. 7.8 Recording Equipment.

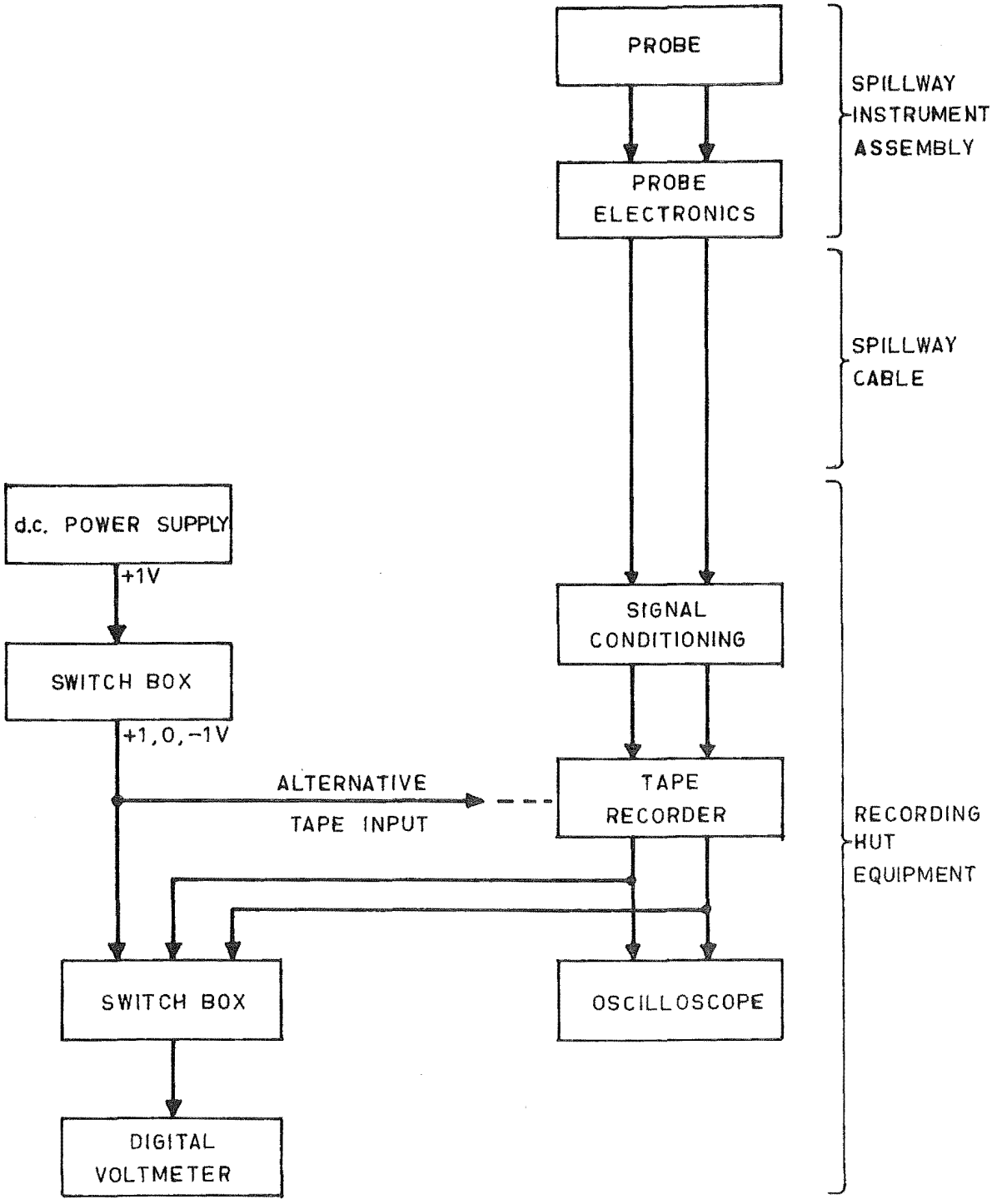

Fig. 7.9 Recording Equipment Connections for Final Field Tests at Aviemore.

CHAPTER 8

INITIAL FIELD TESTS

8.1 SUMMARY

The first of the two field tests at Aviemore is described These tests were cancelled because of various problems. The test program and the results obtained are described, plus the faults that occurred and the subsequent modifications.

8.2 INTRODUCTION

This Chapter describes the first of two series of tests at Aviemore. This series took place in April 1975 when the flooding of the Waitaki River first made water available for tests.

At this stage, all the equipment necessary for field tests (refer to Chapter 7) had been constructed and tested in the laboratory. The two instruments though had only been partially tested.

The combined pressure air concentration probe was used with the pressure inlet tubes internal diameter equal to 4.8 mm (ref. Section 4.7). At this stage, it was thought the velocity could be accurately calculated from the measurements of stagnation pressure and air concentration from this probe. A bubble probe (refer to Section 5.2) was also used to measure the range of bubble sizes as this was considered an important factor in the design of the previous probe.

The tests were unsuccessful because of the many problems that arose with the probes and the associated electronics. In spite of this some data was obtained and the problems recognised allowed significant and

often essential modifications to be made prior to the final field tests.

The tests were finally cancelled because of a mechanical failure of the crane used for access to the spillway. This in fact left the instrument assembly stranded on the spillway for many weeks.

8.3 TEST PROGRAM

These tests were conducted on spillway bay number 4, the same as used by Keller (1972). Measurements were obtained firstly with the combined pressure air concentration probe at station 401 with a 300 mm gate opening.

The probe was traversed through the flow starting at the spillway surface. Readings were taken at 5 mm intervals through the flow. This corresponds to the minimum resolution of this probe.

The data records were each 15 seconds duration. This was estimated to be much longer than the time scale associated with the largest eddies or with the intermittency of the flow. The length scale of both of these is likely to be of the order of the flow depth. At these velocities, this corresponds to a time scale of about 20 ms.

When the probe was out of the flow, the gate was opened a further 150 mm to 450 mm. The same measurement procedure was then repeated with the instrument starting at the limit of its travel and traversing through the flow towards the spillway surface.

Instrumentation failures (discussed later in this Chapter) prevented these measurements being completed and caused the cancellation of the measurements planned for stations 402 - 405.

The bubble probe was then installed and the corresponding electronics within the instrument assembly were connected. This was installed at station 402 and the spillway gate was opened to 300 mm. Measurements were obtained at 10 mm intervals through the flow. The signal was recorded by displaying it on a storage oscilloscope and photographing the screen.

It was considered these measurements plus similar measurements at station 404 would be sufficient. However the mechanical failure of the crane prevented the spillway instrument assembly being installed at station 404.

8.4 RESULTS

The only results obtained with the combined pressure air concentration instrument were for station 401 with a 300 mm gate opening. Mean values of stagnation pressure and air concentration were later calculated in the laboratory by filtering the signals with a 0.3 Hz low pass filter; recording them on the Y axis of an X-Y recorder for which the X axis was time; and integrating the area under the signals with a planimeter.

The profiles of mean values were plotted but have not been presented here because they have been superceded by the more accurate results from the final field tests. A profile of mean velocity was also obtained from this data, but is not shown either. Like Keller's (1972) velocity measurements within aerated flow, these velocities were larger than the maximum possible from energy considerations. This was caused primarily by the errors in the stagnation pressure and air concentration measurements, and the sensitivity of the velocity equations at high air concentrations (ref. Section 2.4.4).

Four significant conclusions were drawn from these measurements:

(i) Samples of 15 s duration were sufficiently long.

(ii) 10 mm intervals between measurements would be adequate to accurately describe the profiles.

(iii) The pressure instrument resonated with almost zero damping (ref. Section 4.7).

(iv) Velocity predictions are unreliable in highly aerated flows.

Measurements with the bubble probe were obtained at station 402 only, with sample results shown in Fig. 5.3. These indicated that in the lower regions of flow for which the mean air concentration was less than about 0.2, the bubbles were about 0.5 - 3 mm dimension. In the highly aerated regions of flow, the instrument did not perform very well for reasons explained in Section 5.2.3.

8.5 MAJOR FAULTS

The major faults that arose during these tests are listed below:

(i) The first pressure transducer failed within minutes for reasons unknown.

(ii) A preset potentiometer in the air concentration electronics was found to have rotated suggesting strong vibrations in the instrument assembly.

(iii) The long spillway cables accentuated a fault in the probe position counting circuit within the control unit.

(iv) A faulty relay put 80 volt motor drive "spikes" onto the wrong lines causing the second pressure transducer and the air concentration electronics to both fail at the end of the first set of measurements.

8.6 MODIFICATIONS FOR FINAL FIELD TESTS

The following list of major modifications were all a direct result of the initial field tests.

(i) The pressure transducer inlet tube was modified to prevent the resonant fluctuations observed in the stagnation pressure signal (ref. Section 4.8).

(ii) The spillway instrument assembly electronics originally designed by DAVCO were redesigned. All relays were replaced and connected differently, no preset potentiometers were used, and extra protection was provided against vibration.

(iii) To facilitate adjustment of the salinity dependent output signals, the signal conditioning was incorporated into the control unit instead of the spillway instrument assembly electronics.

(iv) Quick release electrical connectors were installed on both ends of each spillway cable to facilitate changing to different test stations.

(v) It was realised that the gate opening indicated by the dial on top of the dam was too inaccurate and so a new mechanism was devised (ref. Section 9.4).

(vi) Spillway bay 5 would be used in future because the shorter cables would reduce the likelihood of any further problems with the instrument position circuitry.

(vii) The difficulties in predicting velocity from stagnation pressure and air concentration, plus the simplicity and success of the bubble probe prompted the development of a velocity instrument based on a cross-correlation technique (ref. Section 5.3).

CHAPTER 9

FINAL FIELD TESTS

9.1 SUMMARY

This Chapter describes the final field tests at Aviemore and the two major faults that occurred during them. The data analyses and results from these tests are presented in Chapter 10.

9.2 DESCRIPTION

The final field tests at Aviemore took place in January 1976 following flooding of the catchment. This was the first time water had become available for testing since the initial field tests in April 1975. Measurements were successfully obtained over 2½ days at each of stations 501 - 505 and for both 300 and 450 mm gate openings.

Figs. 9.1 and 9.2 show the flow at each gate opening. In these photographs, the spillway instrument assembly is installed at station 503, and the probe is at the spillway surface. The spray from the spillway instrument assembly is clearly visible in both photographs. The crane and spillway skip are just visible at the top of the dam.

Two instruments were used, the combined pressure air concentration instrument and the velocity instrument. Fig. 9.3 shows the velocity probe in aerated flow at station 504. In this photograph, the gate is open 450 mm and the probe is 352 mm from the spillway surface.

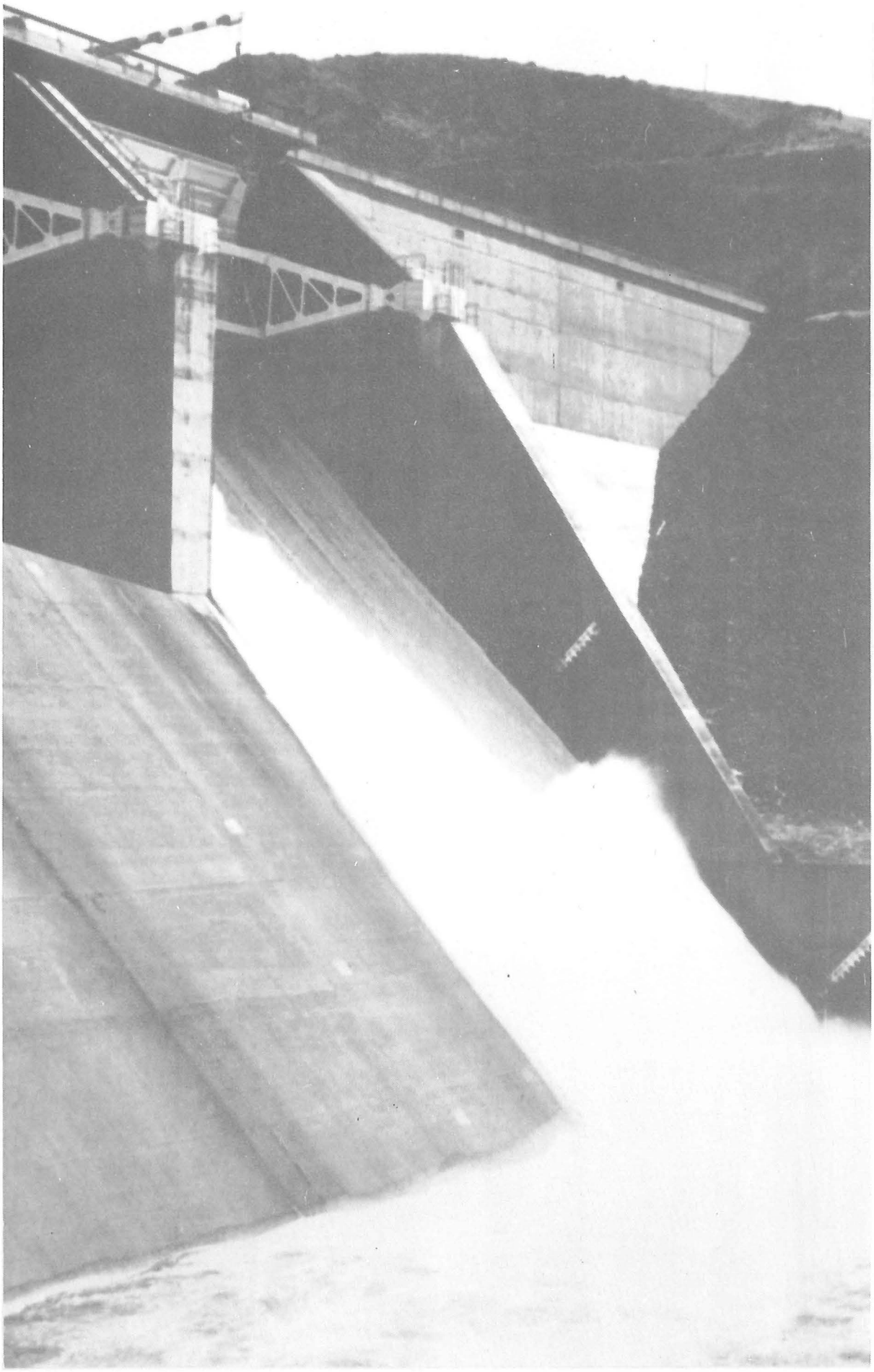

Fig. 9.1 Spillway Gate Open 300 mm.

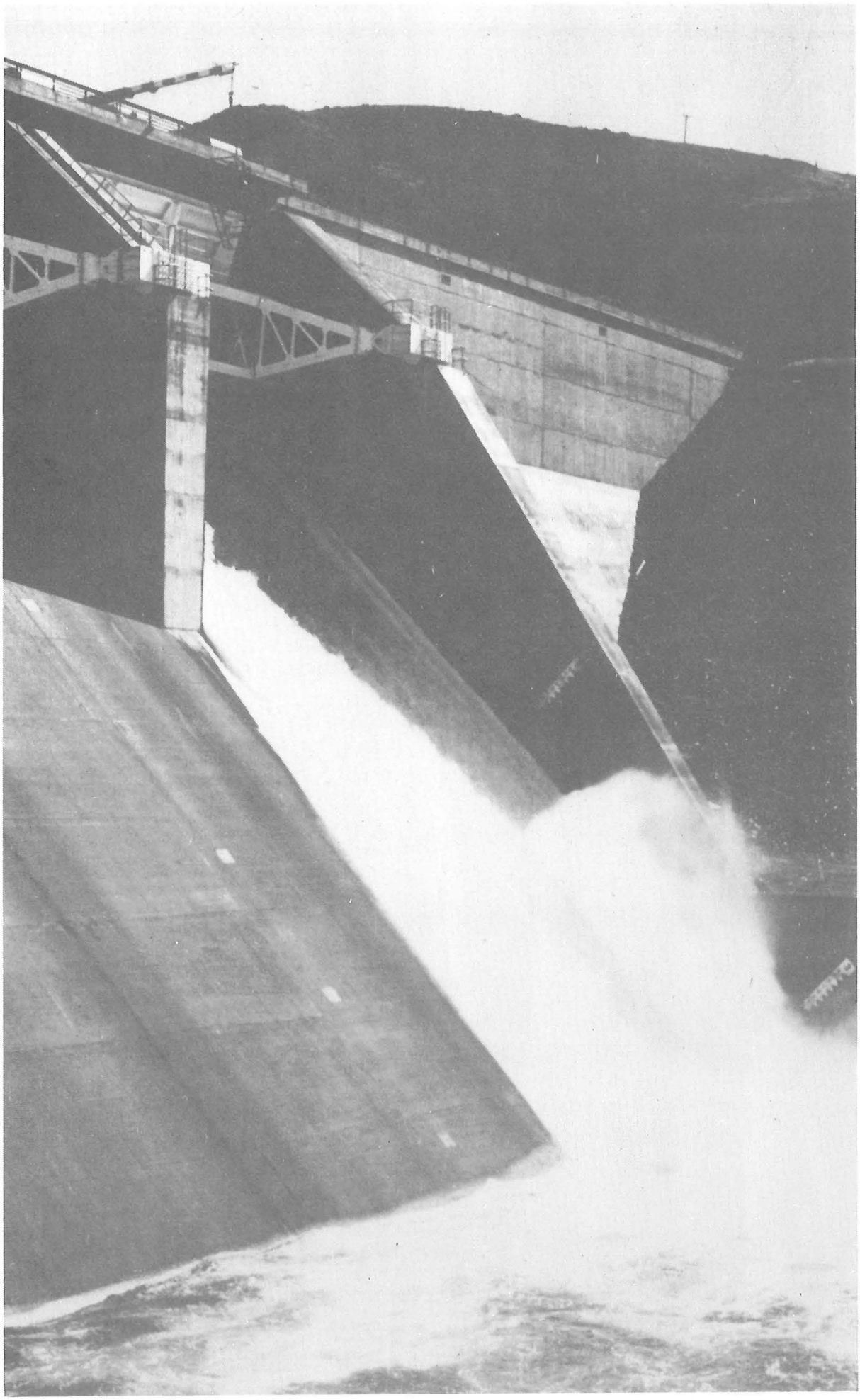

Fig. 9.2 Spillway Gate Open 450 mm

Fig. 9.3 Velocity Probe in Aerated Flow

The test program and measurement procedure were very similar to those in the initial field tests (refer to Chapters 7 and 8). In these final tests, the output signals from both instruments were recorded on the tape recorder. These were 15 second duration, recorded at 10 mm intervals through the flow. For the velocity instrument each fifth sample was 60 second duration in case 15 seconds was too short for the cross-correlation analyses. This precaution was taken because the velocity instrument had not been field tested and the cross-correlation analyses for the EAI computer had not been developed.

In spite of the large number of faults recognised and corrected following the initial field tests, some faults did remain undetected. Two major faults occurred during the final tests which were not recognised until many months later. These severely complicated the analyses and limited the accuracy of the results. It was not possible to correct these faults and repeat the measurements because no water became available for further tests.

9.3 MAINS FREQUENCY VARIATION

During preliminary analyses of the recorded data, the calibration signals were observed to fluctuate by up to 4% FS. The largest such fluctuation is shown in Fig. 9.4

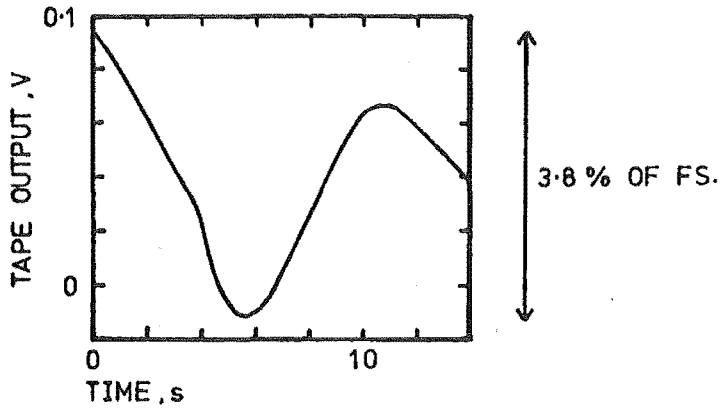

Fig. 9.4 Largest Calibration Signal Fluctuation.

These were further investigated by measuring the output voltage of all the 0.0 volt signals which were recorded between each sample of data. These were plotted as a function of time and a continuous line drawn through them for clarity. Only the curves for the 300 mm gate

opening are shown here (Fig. 9.5); the curves for the 450 mm gate opening being very similar. All but three of these curves vary significantly about the mean.

This problem was found to be caused by variations in the frequency of the mains power supply at Aviemore. In New Zealand the frequency of the national grid is maintained at 50.0 ± 0.1 Hz. However it was not realised at the time that the power provided at the recording hut was from an auxiliary generator which served only the power station and immediate locality. The dynamic response of the generator's governor causes the frequency to fluctuate within the range 49.5 - 51 Hz with a period of about 10s. The mean frequency over a duration of 15s will therefore approach 50.0 Hz.

In Appendix M the relationship between variations in the mains frequency and variations in the tape recorder output voltage are derived by considering the operating principles of the tape recorder. It is seen that the fluctuations in Fig. 9.2 are in fact almost always bounded by the broken lines which correspond to a ± 1% variation in mains frequency (49.5 - 50.5 Hz).

These variations complicated the measurement of:

(i) the + 1.0, 0, - 1.0 volt calibration signals,

(ii) the C = 0.0 and 1.0 air concentration signals.

These were required during the stagnation pressure and air concentration analyses in order to calculate the tape recorder input-output relationships. Errors in any of these would cause errors in complete sets of data. The problem was resolved by using the mean values of all relevant recordings. This is illustrated below for the calibration signals. The C = 0 and 1.0 air concentration signals were treated in an identical manner, not illustrated here.

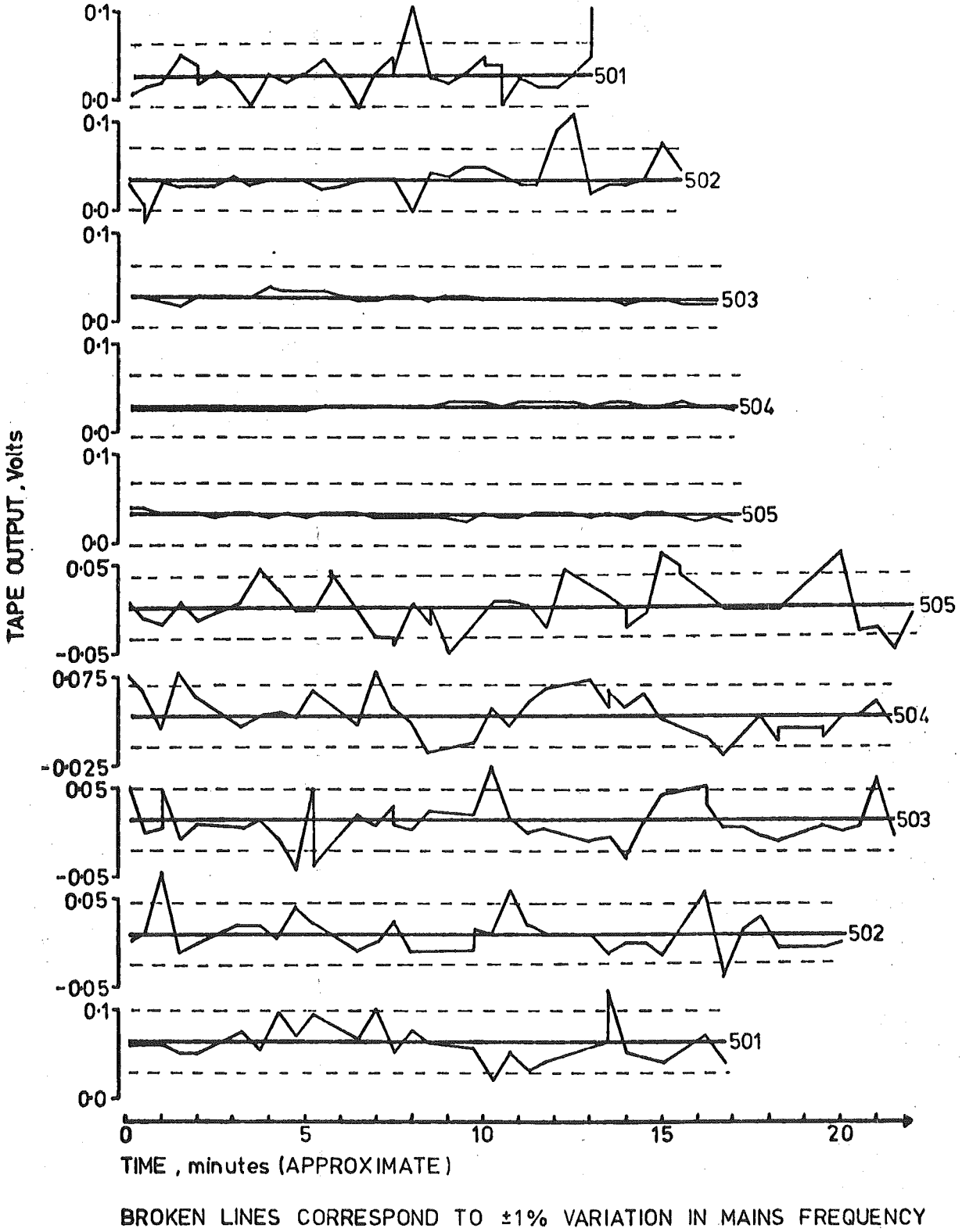

Fig. 9.5 Variation of 0 Volt Inter-Record Signals. Gate Open 300 mm.

Fig. 9.6 shows a sample of the pressure record for station 502 which includes the initial calibration signals (A, B, D and E) plus the final calibration signals (F, G and H). These were recorded from the FM tape recorder onto a chart recorder.

The mean output voltage for a 0 volt input was calculated from

(i) the 0 volt calibration signals (A, E and H),

(ii) the 0 volt inter-record signals (I). The variation of these inter-record signals was discussed previously and illustrated in Fig. 9.5. The differences between this mean output voltage and the mean voltage at A was defined as a correction factor for this set of data. Prior to an analysis, the mean output voltage for a 0 volt input could be calculated by sampling the signal A and adding the correction factor to it.

The mean output voltage for a 1.0 volt input was calculated from the calibration signals B and G. The difference between this mean output voltage and the mean voltage at B was again defined as a correction factor for this set of data. This allowed the mean output voltage for a 1.0 volt input to be calculated prior to an analysis by sampling the signal B and adding the correction factor to it.

The mean output voltage for a -1.0 volt input was treated in an identical manner to the 1.0 volt input.

This procedure was necessary for both the stagnation pressure and air concentration signals at each of the five spillway test stations. The correction factors were typically 0.010 volts (0.4% FS output).

The uncertainty associated with the various measurements has been calculated in Appendix M. It is shown that a ± 1% variation in mains frequency will cause:

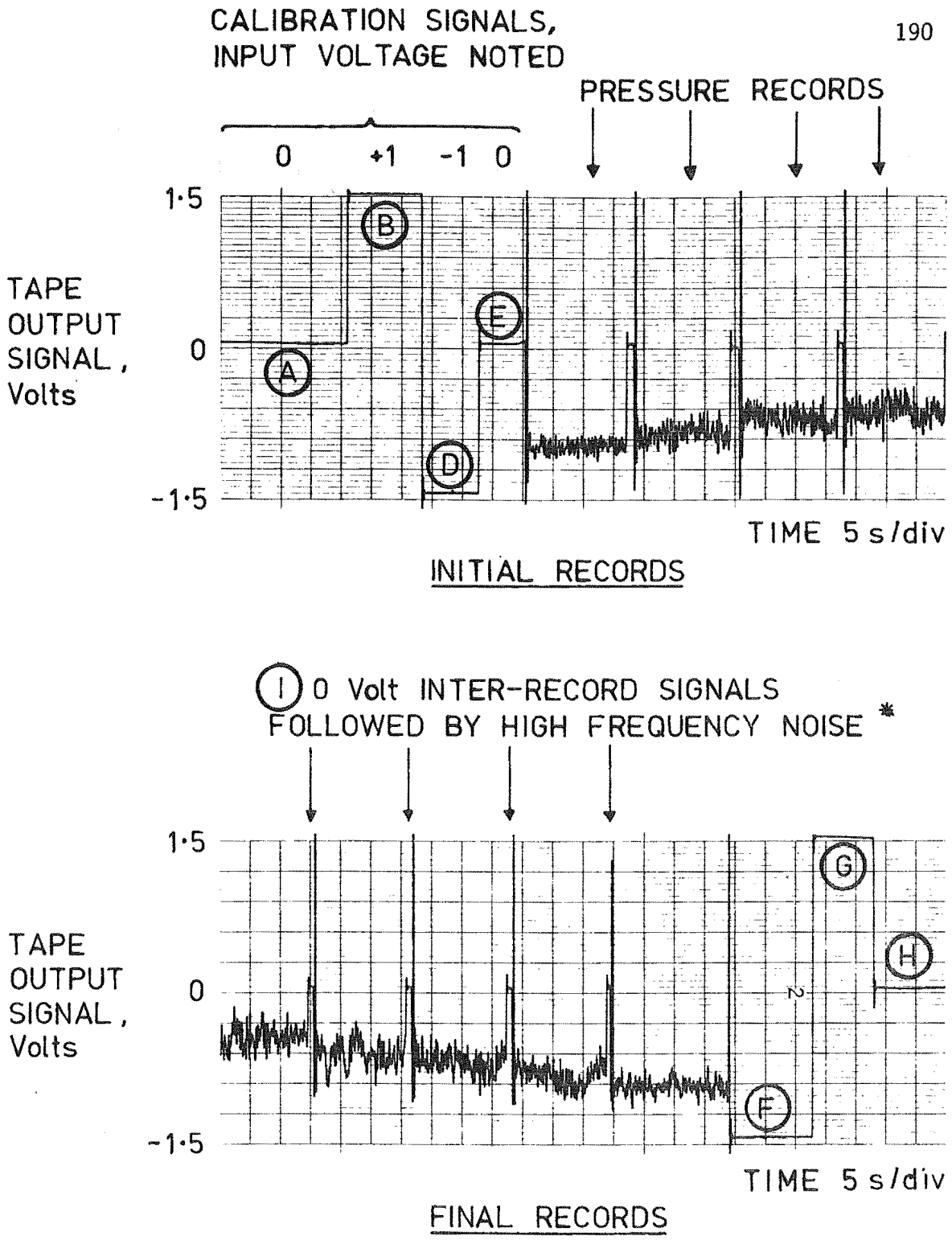

* NOISE OCCURS DURING RECORDING WHEN TAPE TRANSPORT IS STARTED. SIGNAL WAS FILTERED TO 5 Hz TO LIMIT NOISE BEFORE RECORDING ON CHART RECORDER

Fig. 9.6 Stagnation Pressure Signals as Recorded on Tape Station 502, Gate Open 450 mm.

(i) about ± 4 kN/m^2 uncertainty for any stagnation pressures measurement. This corresponds to ± 2% of the maximum mean stagnation pressure measured,

(ii) about ± 0.015 uncertainty for any air concentration measurement,

(iii) about ± 1% of the velocity calculated with the cross correlation technique.

9.4 SPILLWAY GATE OPENING VARIATIONS

In order to investigate the development of air entrainment down the spillway, it is desirable that the gate openings and therefore the water discharge is identical for the measurements at each spillway station.

The gate opening was indicated on a dial at the top of the dam, but its graduations are too coarse to allow the gate to be accurately reset. Therefore a mechanism was devised which would provide the necessary accuracy and also enable the exact distance from the spillway to the gate to be determined. It was clamped to the parapet near the gate opening controls on top of the dam, as shown in Fig. 9.7. A wire cable was suspended over two pulleys on this frame and fixed to the spillway gate 7 m below. The free end at the top of the dam was attached to a weight. This kept the wire taut and served as a pointer against a ruler fixed to the frame.

For the first measurements of the final test series the gate was opened according to the dial firstly to 300 mm and then a further 150 mm to 450 mm. These two openings were marked on the ruler as 196 and 280 mm respectively. For all subsequent measurements the gate was opened until the pointer was within 2 mm (<1% FS) of the marks on the ruler.

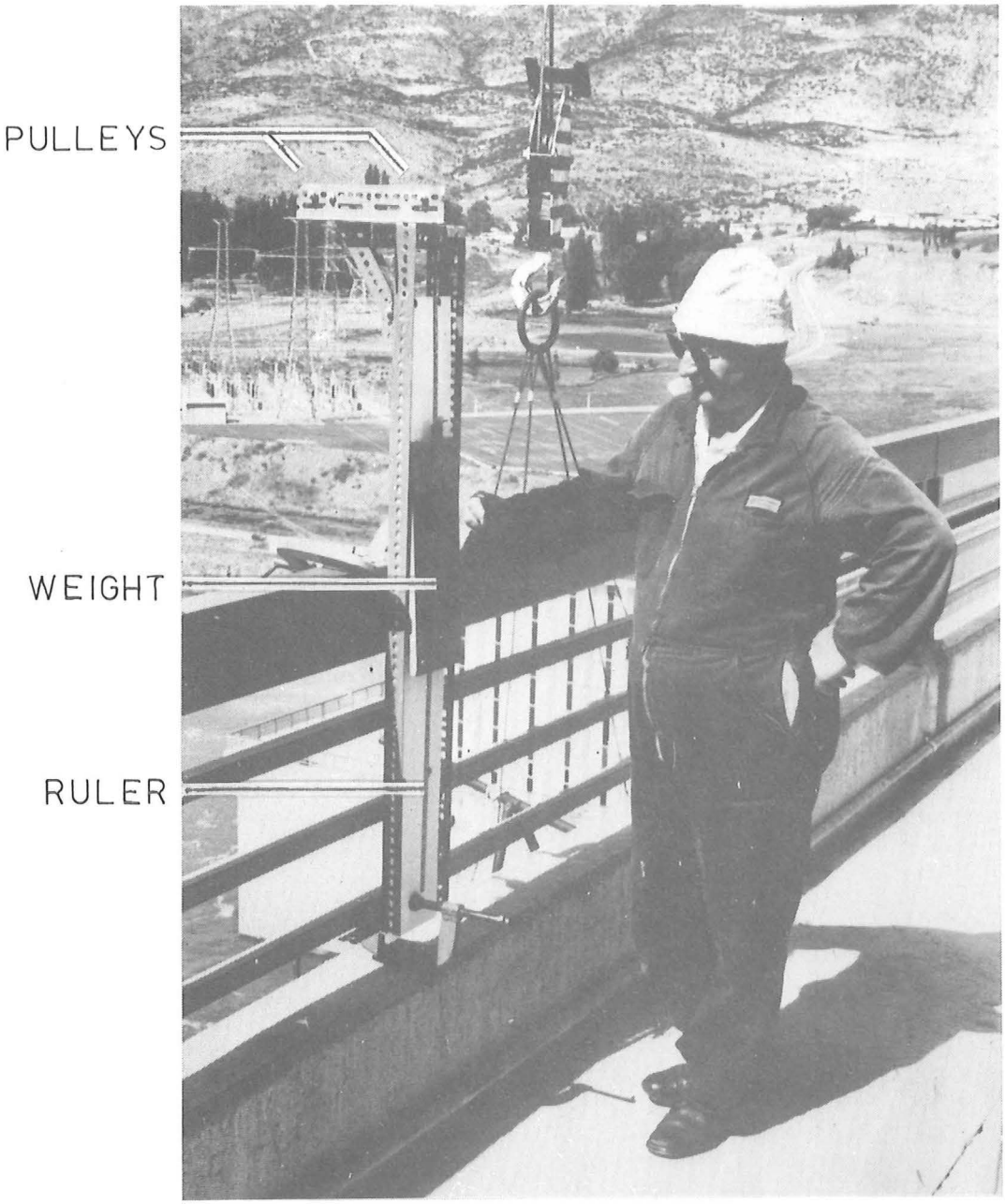

Fig. 9.7 Gate Opening Indicator.

Anomalies were encountered during analysis of the results which suggested that the gate had not in fact been accurately reset. This was most apparent in the variations in water discharge from station to station, as calculated from the profiles of air concentration and velocity. It is shown in Section 10.5 that these variations are in fact consistent with

a variable gate opening. To understand this it is necessary to consider in more detail firstly the gate opening procedure and secondly the spillway gate seal.

Prior to testing at any station, the ruler was zeroed if necessary, and the gate was opened relative to that zero. This practice was necessary on three occasions when the mechanism was removed from the parapet; once for alterations between two of the first tests, and twice over-night for security reasons. On other occasions, small variations were observed in the initial zero which at the time were attributed to the mechanism settling.

This zeroing practice would have been satisfactory except that the gates initial closed position could in fact vary. This is possible because of the type of seal, namely a strip of rubber set into the spillway (see Fig. 9.8). This rubber deforms under the weight of the gate, its compression increasing with time due to creep. The rubber will rebound when the gate is opened so that the rubber will again deform and start to creep when the gate is reclosed. As the gate had been closed for several weeks prior to the first measurements, the rubber was initially compressed more than for the subsequent ones. The distance between the spillway surface and the bottom of the gate was therefore smallest for the first measurements. This was reflected in the water discharges which were about 10% less than for the following ones.

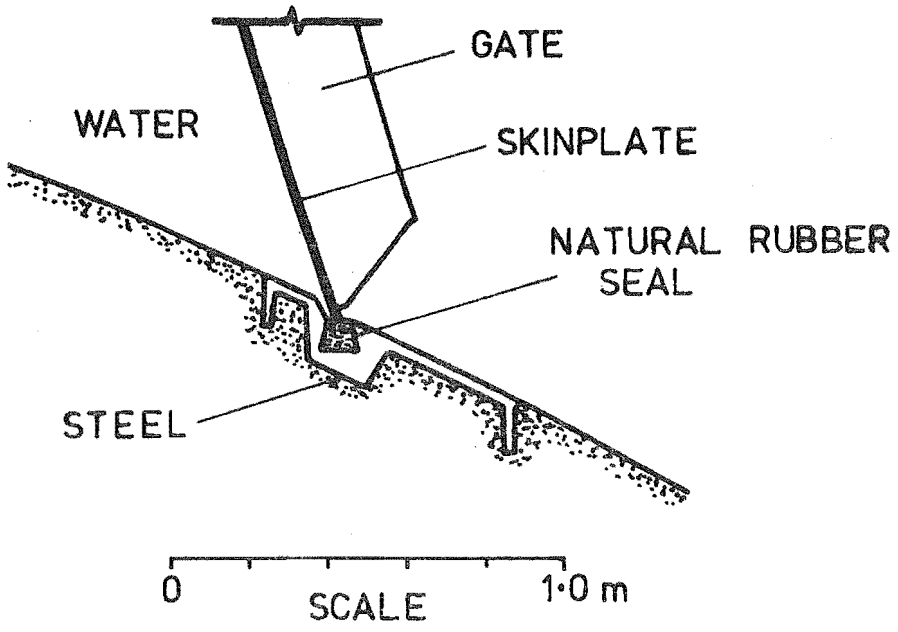

Fig. 9.8 Section Through the Spillway Gate Seal.

CHAPTER 10

RESULTS

10.1 SUMMARY

This Chapter describes the reduction of the data measured in the final field tests at Aviemore. The velocities predicted from measurements of stagnation pressure and air concentration are compared with the velocities measured with the correlation technique. Calculations of water discharge show the spillway gate was opened by a different amount for each test. The measured air concentration profiles are adjusted to compensate for the variations in gate opening.

10.2 INTRODUCTION

The measurements from the second test series at Aviemore were recorded on the FM tape recorder. These were initially digitised and analysed on an EAI 590 hybrid computer, described in Appendix J. This allowed the analogue signals to be accurately digitised at high sampling rates. More than ten different programs were developed for these analyses. Only one, a cross-correlation analysis, is listed (ref. Appendix K). The remainder are filed at the University of Canterbury.

For all these programs, information describing the probes position, spillway station and gate opening was obtained from the voice channel of the tape recorder and entered into the computer via either of two keyboards.

For the stagnation pressure and air concentration analyses, the +1, 0, -1 volt calibration signals recorded at Aviemore were sampled and corrected as described in Section 9.3. The tape recorder output signals

could then be simply converted to pressures and air concentrations. The errors in these due to the non-linearity of the tape recorder amplifiers were also calculated from the +1, 0, -1 volt calibration signals. In all cases, these were less than 0.5% FS.

The results of these initial data analyses were typed on a line printer and displayed on a visual display screen. The results were later punched on cards which were used in the final analyses performed on a Burroughs B6700 computer. About twenty programs were developed for this computer. Most involved straightforward calculations with the results plotted by the computer. These programs have also been filed at the University of Canterbury.

The results have been compared with Keller's (1972) results where applicable.

10.3 DATA REDUCTION

10.3.1 Stagnation Pressure Measurements

Fig. 10.1 shows sample stagnation pressure signals which were measured at station 501 with a 450 mm gate opening. They were recorded from the tape recorder onto a chart recorder. These are of interest because, as will be seen later, they cover the largest non-aerated region of flow in which measurements were obtained.

The flow is non-aerated up to 125 mm from the spillway surface. Variations in the mains frequency will have very little effect over the short time scale of these signals. The pressure fluctuations are therefore caused mainly by turbulent velocity fluctuations. The magnitude of the fluctuations indicates a decrease in turbulent intensity as the normal distance from the spillway surface y increases from 6 - 125 mm.

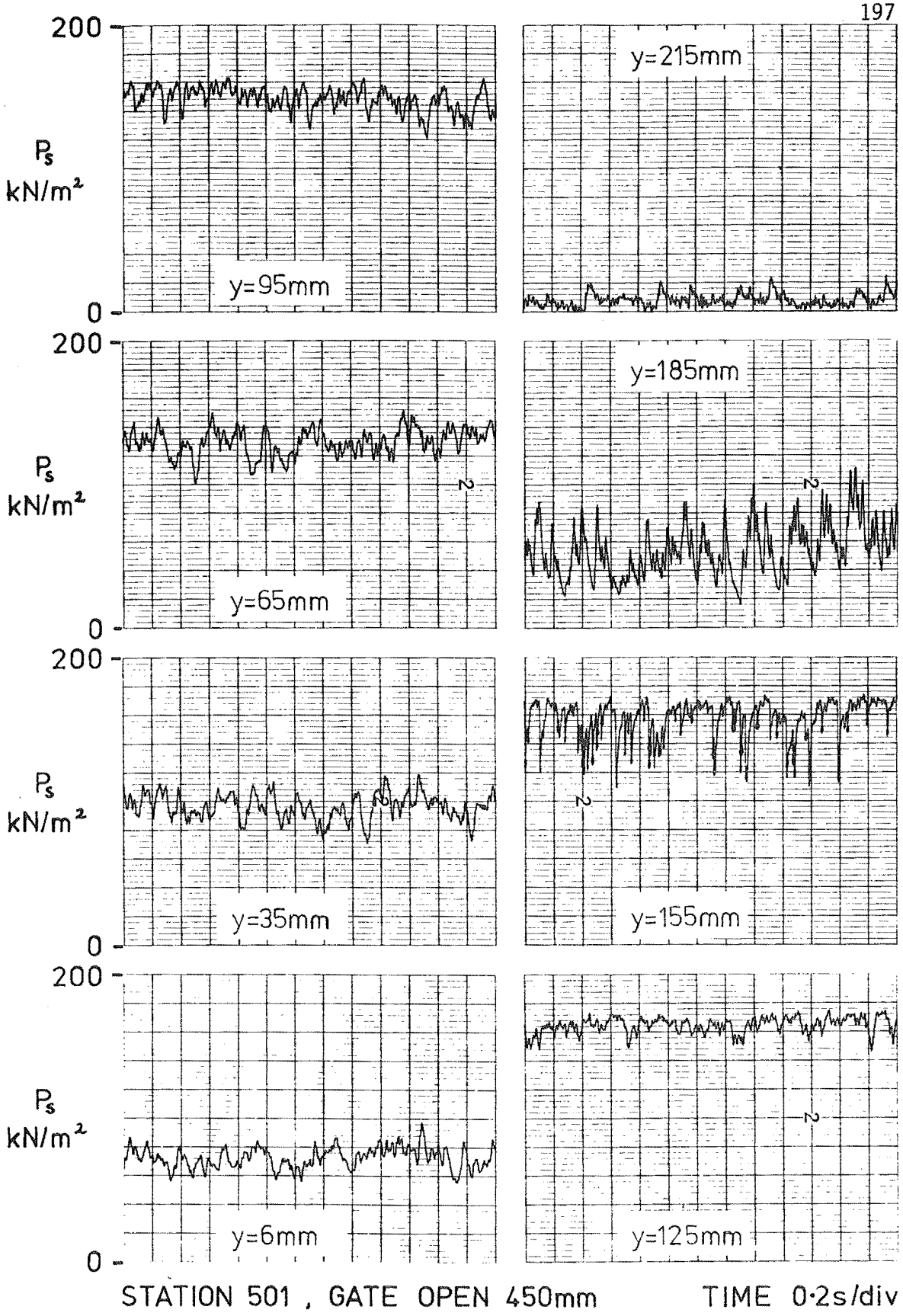

Fig. 10.1 Sample Stagnation Pressure Signals.

At distances larger than 155 mm, the flow is very aerated. The pressure fluctuations are therefore caused by turbulent velocity fluctuations and by variations in air concentration.

The stagnation pressure signals from the tape recorder were conditioned then digitised and analysed on the EAI computer. This analysis was only part of a complex analysis in which both the stagnation pressure and air concentration signals were analysed and velocities calculated simultaneously. A description of the analogue signal conditioning is therefore best left until Section 10.4.1 where the complete analysis is discussed. Suffice to say now that the pressure signal was filtered to 10 Hz maximum and sampled at 25 Hz for 14 seconds.

Each of the 350 samples was converted to a pressure and the mean value was calculated and typed on the line printer. Profiles of the mean values have been plotted in Figs. 10.2 and 10.3. Each mean value is at the centre of a symbol N where N indicates the station. For example, data for station 503 is plotted as a "3". The horizontal scale refers to the profiles for station 501. The profiles for stations 502 - 505 have been displaced by 40, 80, 120 and 160 kN/m^2 respectively.

The symbols inside ovals for the 300 mm gate opening were obtained by Keller (1972) on spillway bay 4 of Aviemore Dam. In each case, he opened the gate according to the dial on top of the dam. It is therefore not possible to comment on their accuracy because it is unlikely the spillway gate openings were identical to those used here. (Ref. Section 9.4).

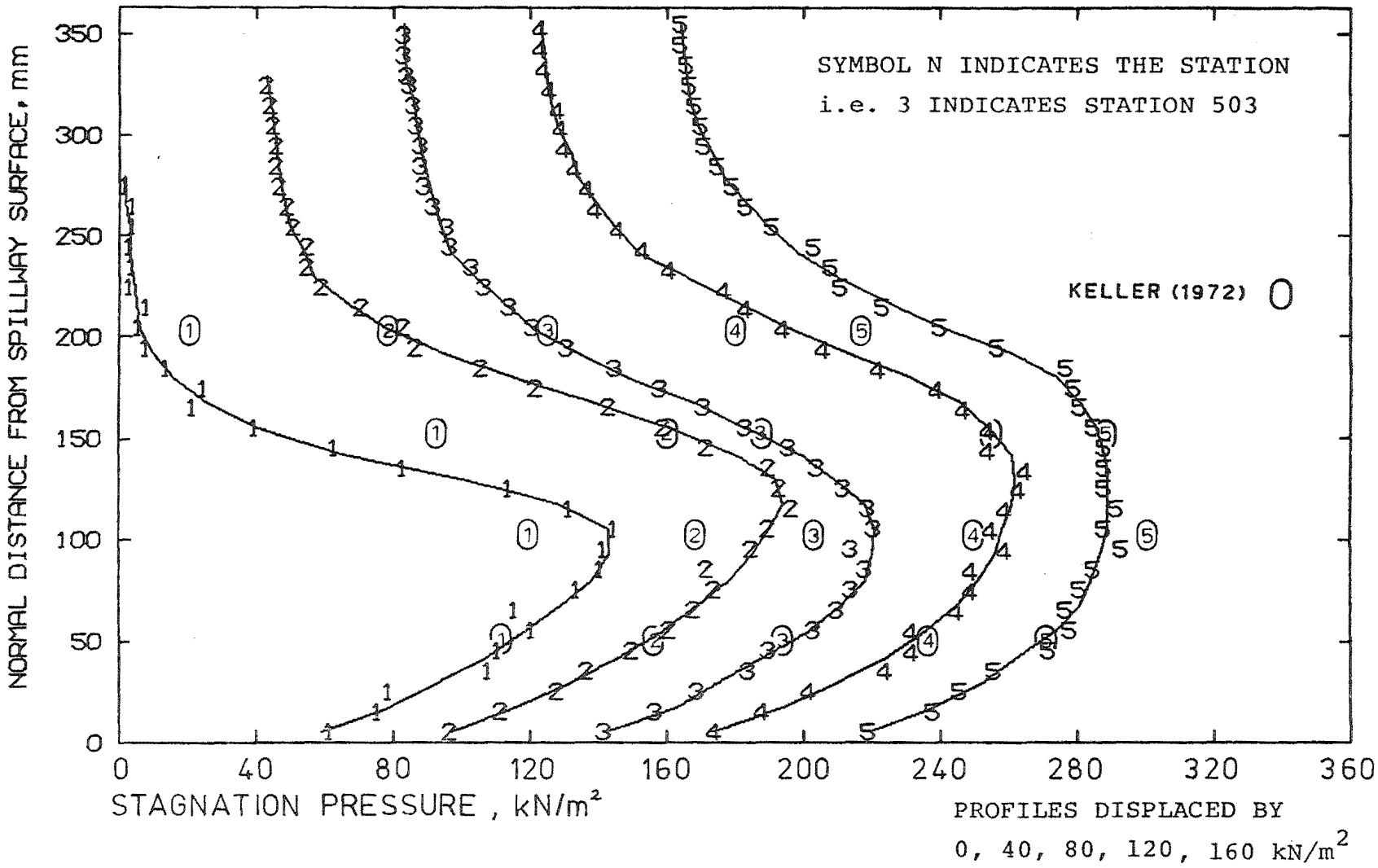

Fig. 10.2 Measured Stagnation Pressure Profiles, Gate Open 300 mm.

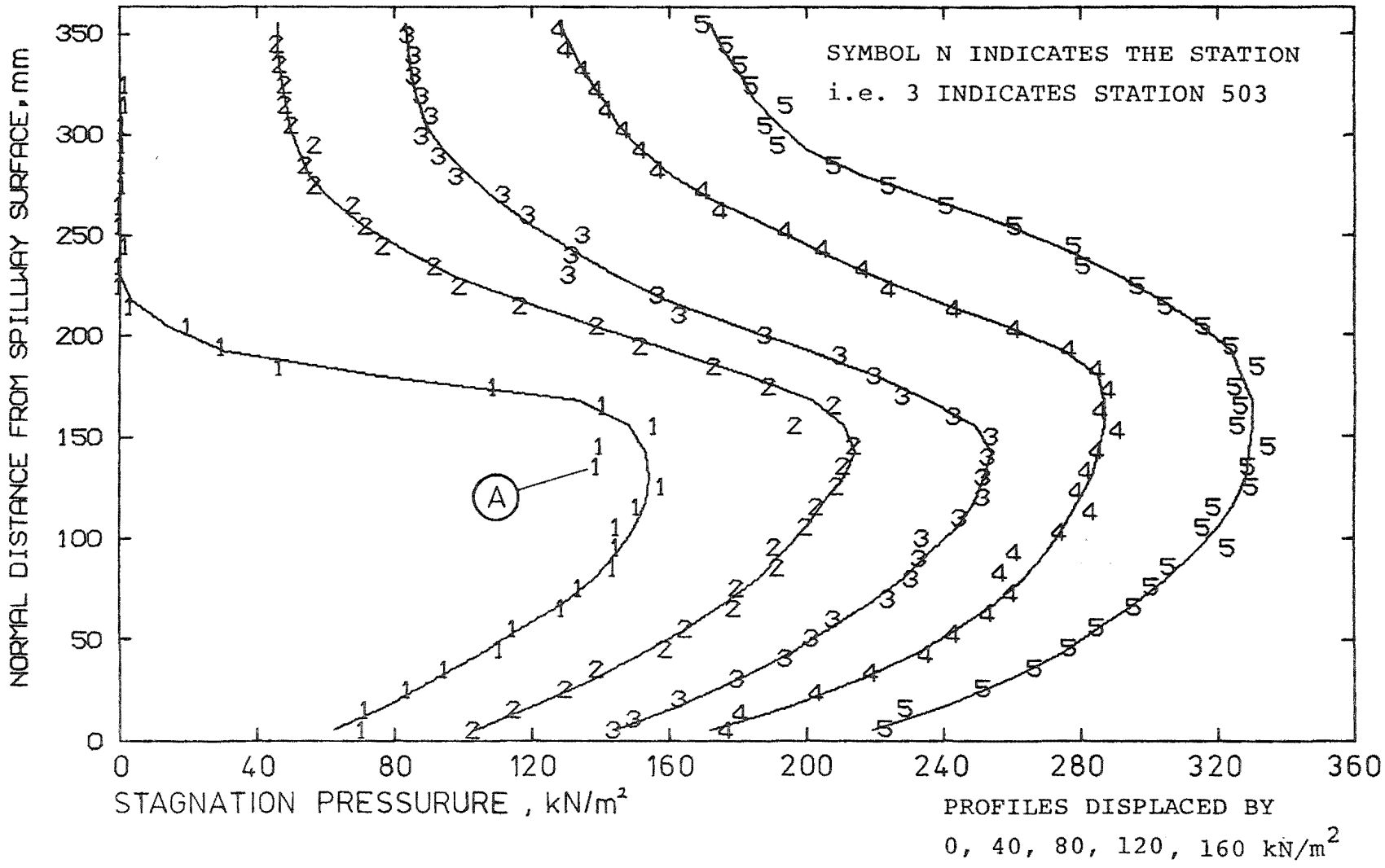

Fig. 10.3 Measured Stagnation Pressure Profiles, Gate Open 450 mm.

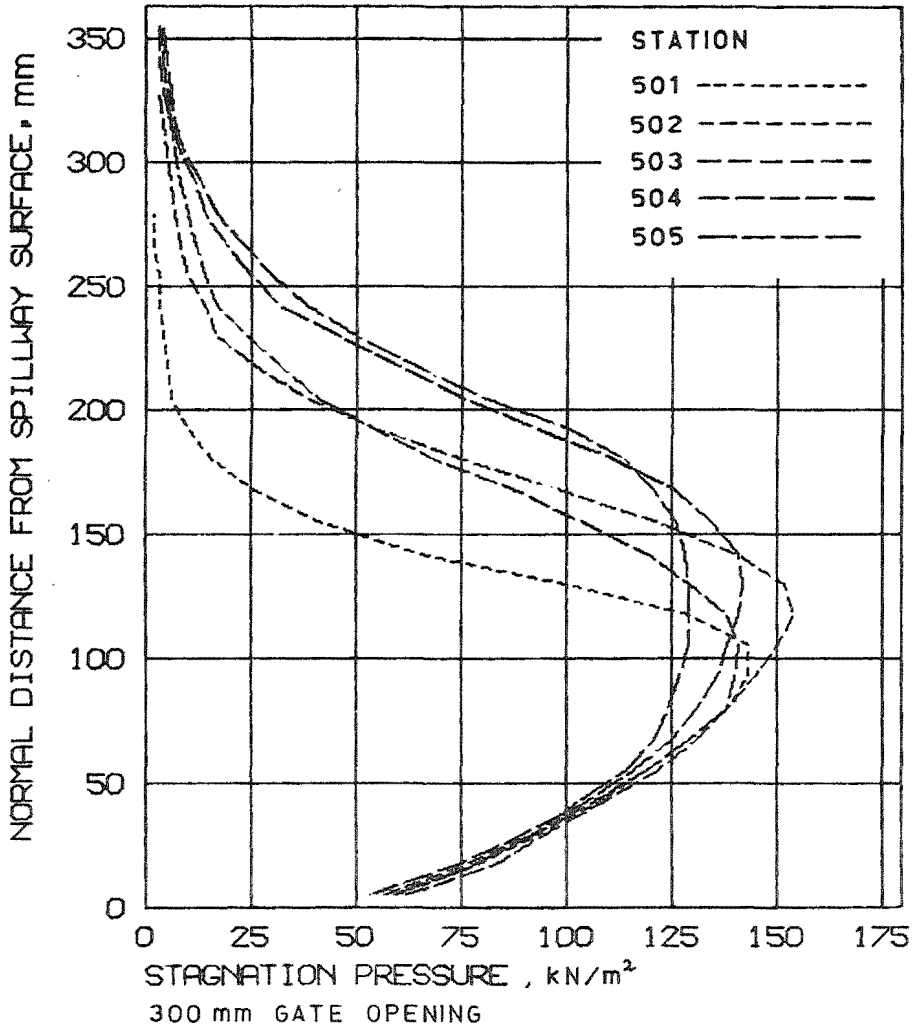

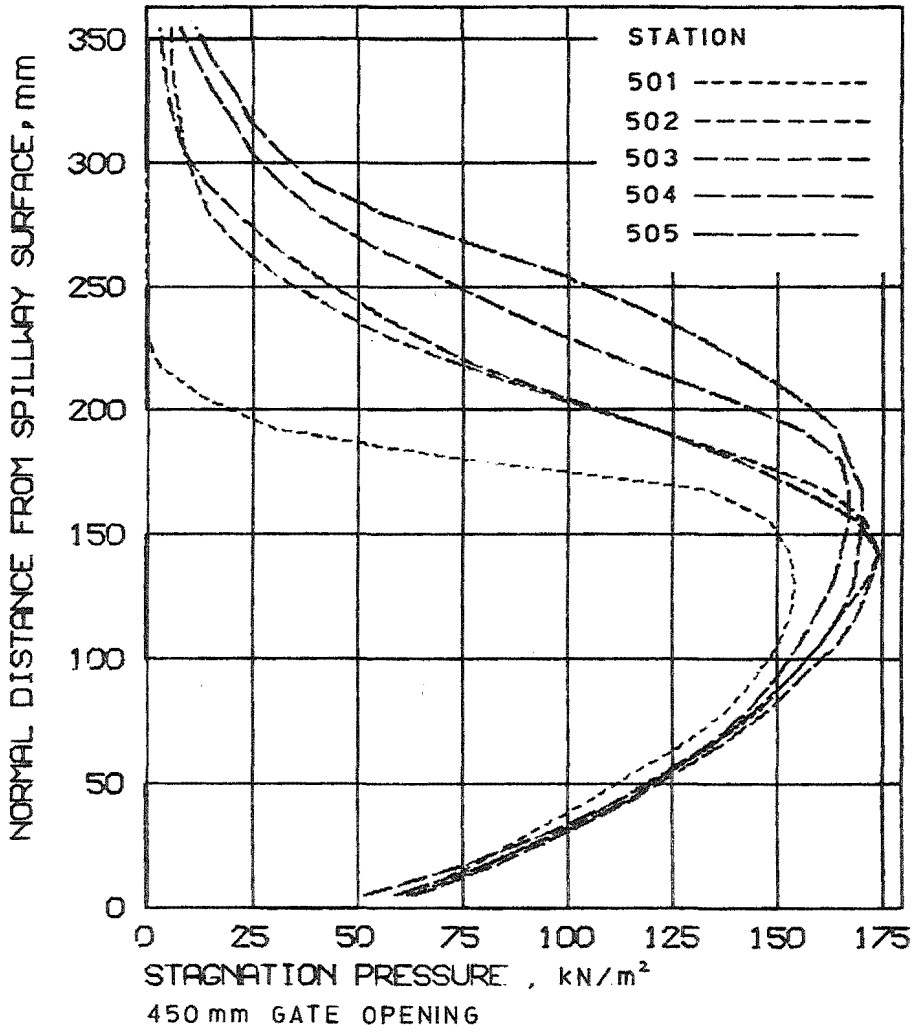

Fig. 10.4 Measured Stagnation Pressure Profiles.

The smooth curves drawn through the measured points were used for subsequent predictions of mean velocity profiles. Each is represented by an array of up to 29 points. The normal distance in millimeters of the I th point from the spillway surface is given by

$$y = 12.45 * I - 6.9 \qquad 10.1$$

For example, the fourth point is

$$12.45 * 4 - 6.9 = 43 \text{ mm}$$

from the spillway surface.

The smoothed profiles are superimposed in Fig. 10.4 for comparison. They have been drawn with broken lines to distinguish them, the smallest dash referring to station 501, the longest to station 505.

The data array for the smoothed profiles is listed in Appendix N.

10.3.2 Air Concentration Measurements

Samples of the air concentration signal as recorded on the tape recorder have been transferred to a chart recorder and are shown in Figs. 10.5 to 10.9. These were recorded by the technique described in Appendix E so that the chart recorders flat frequency response has been effectively extended to 500 Hz. The frequency response of the air concentration instrument is less than this (ref. Section 3.5), so that the signals on the tape recorder have been accurately transcribed.

It will be shown that the signal level varies almost linearly with air concentration between the upper limit, all air, (C = 1.0) and the lower limit, all water (C = 0.0). It will also be shown that in all cases, the velocity varies from about 12 m/s at the spillway surface to about 20 m/s in the upper regions. The 5 ms/division horizontal (time) scale of the signals can therefore be related to a length scale, i.e.

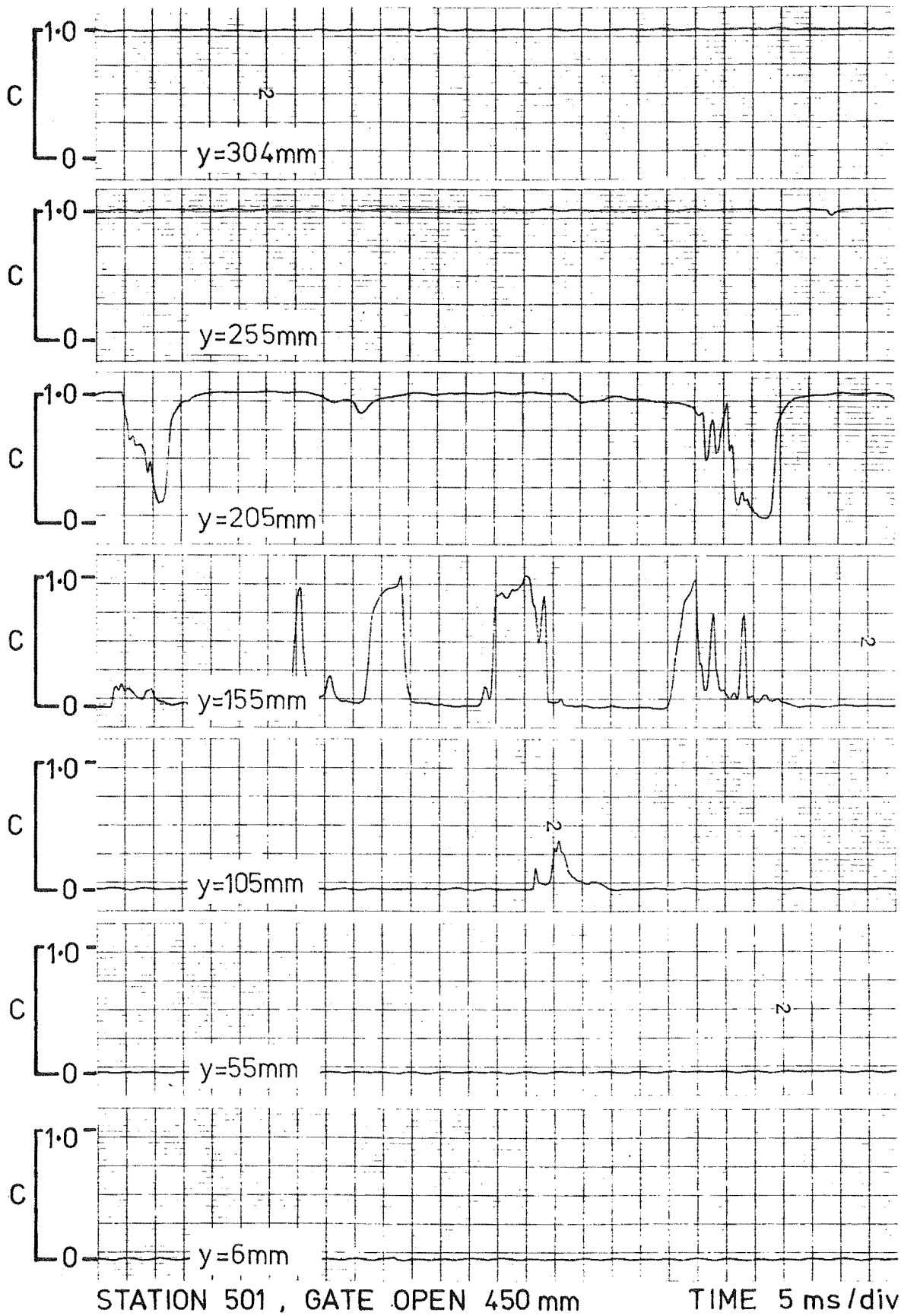

Fig. 10.5 Sample Air Concentration Signals.

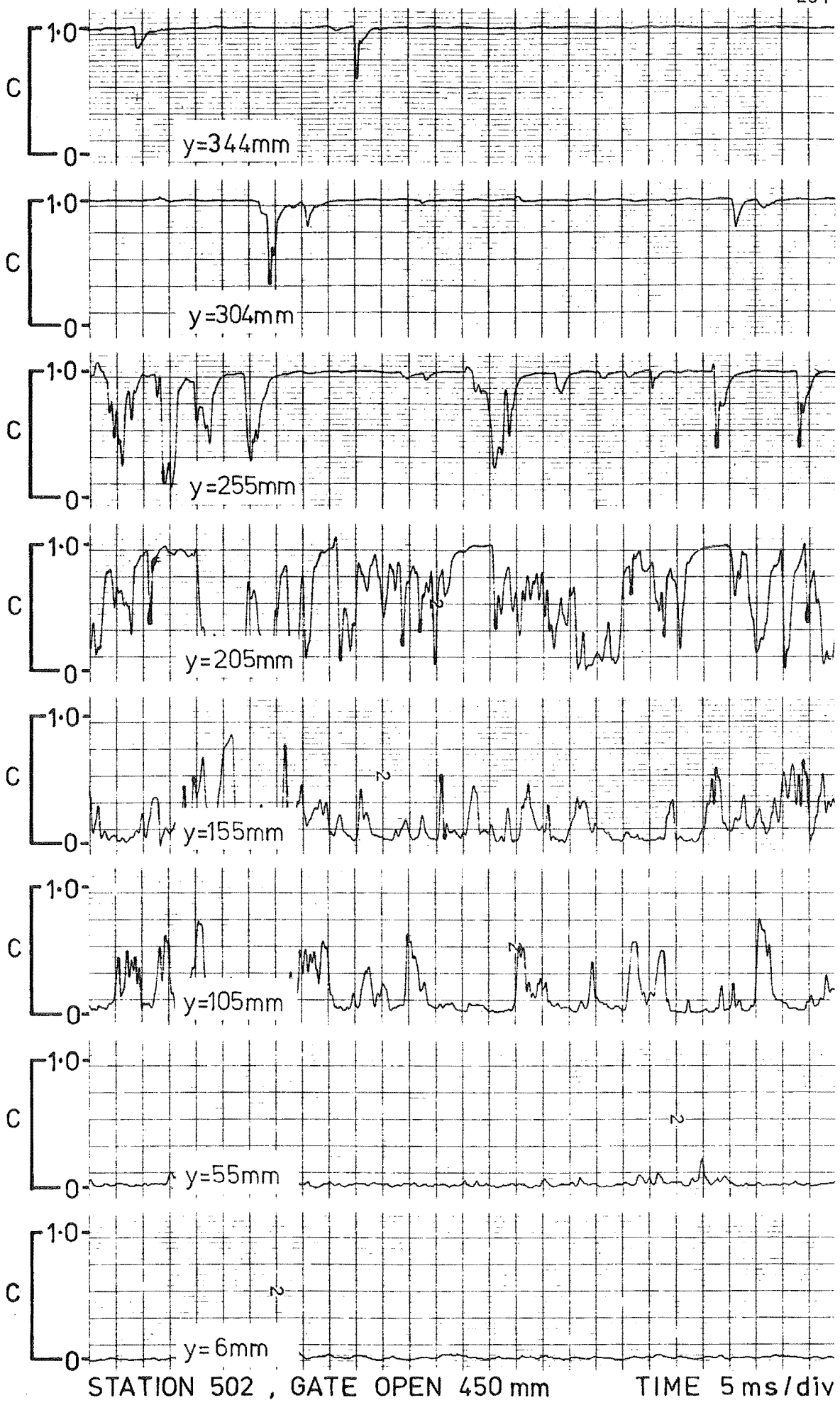

Fig. 10.6 Sample Air Concentration Signals.

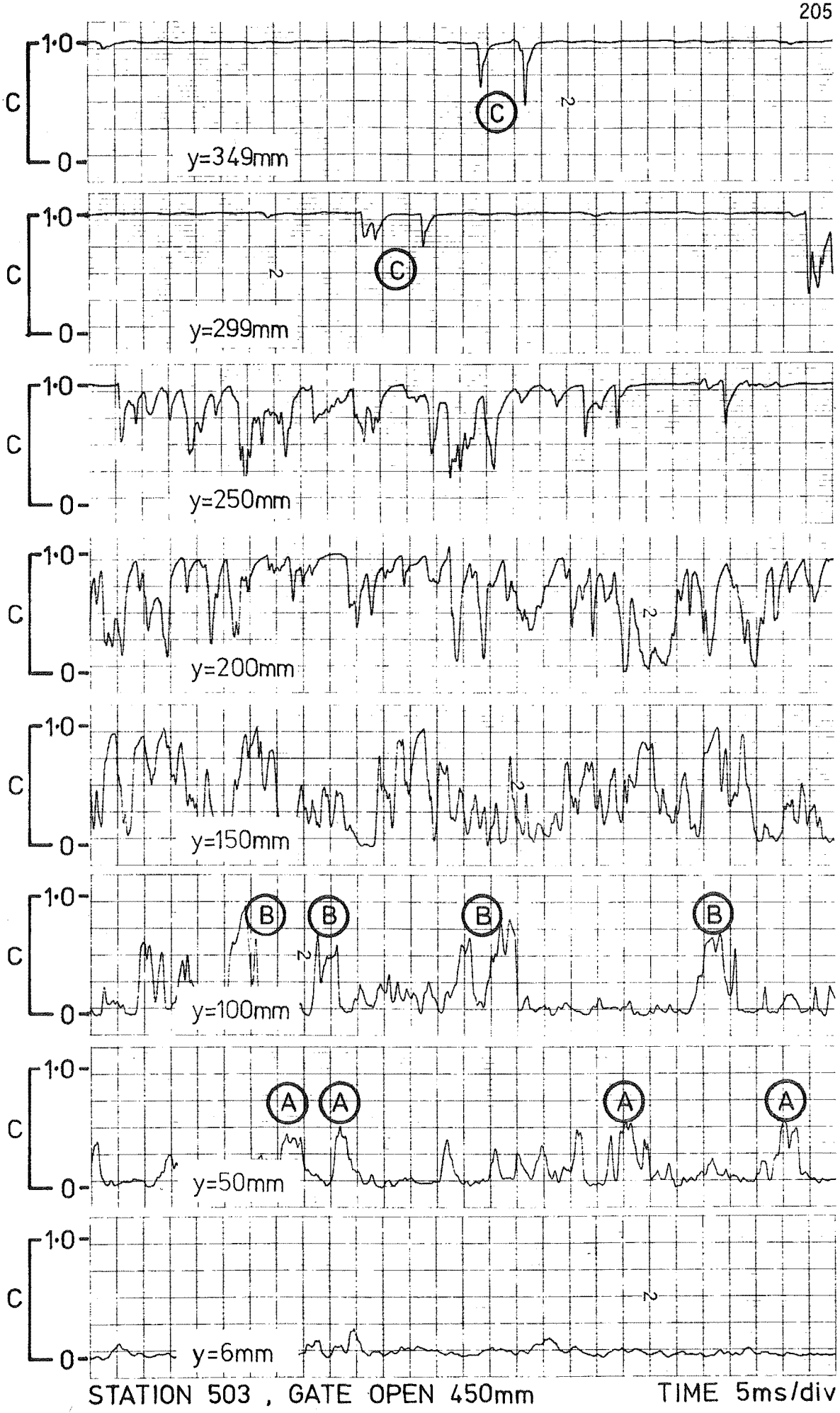

Fig. 10.7 Sample Air Concentration Signals.

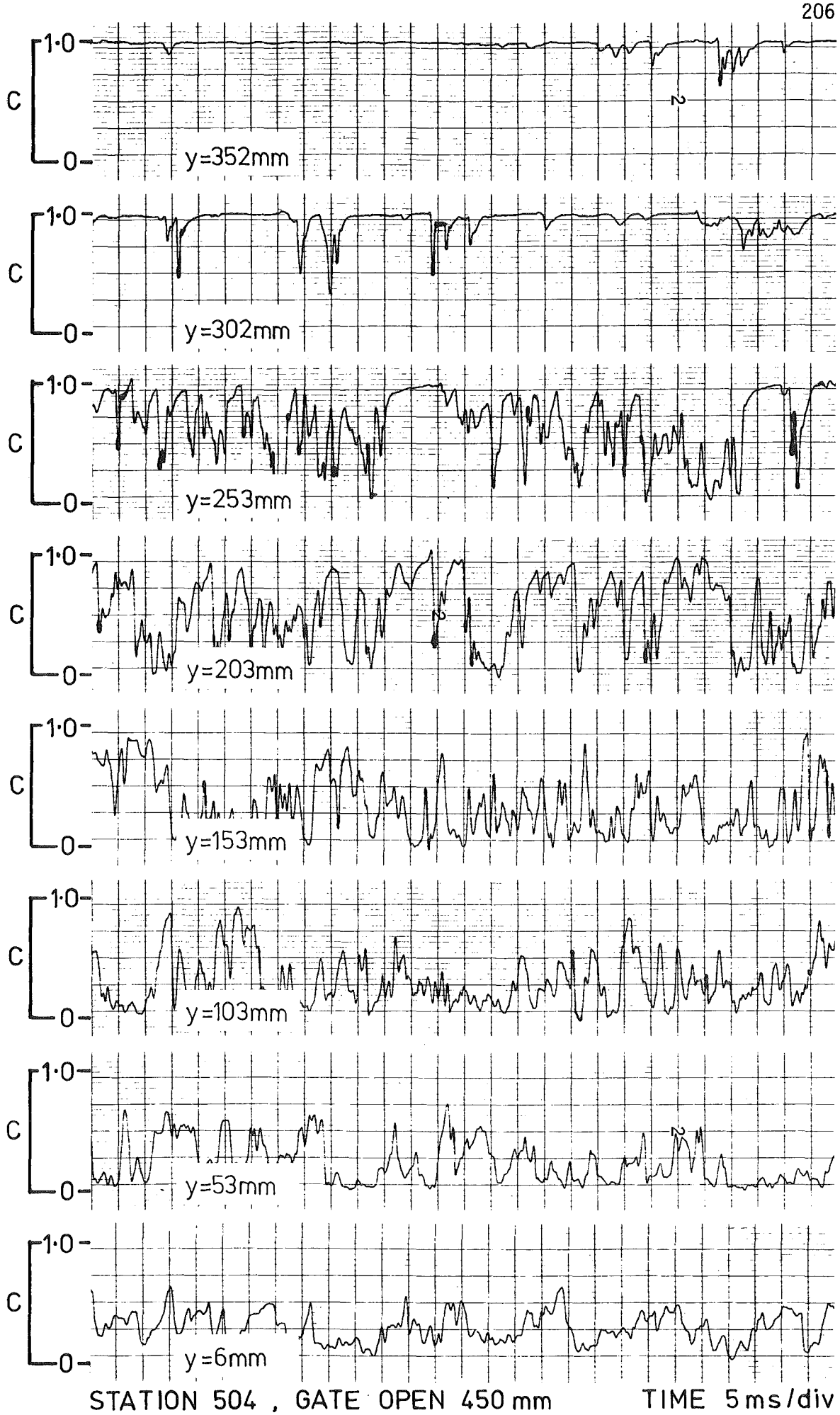

Fig. 10.8 Sample Air Concentration Signals.

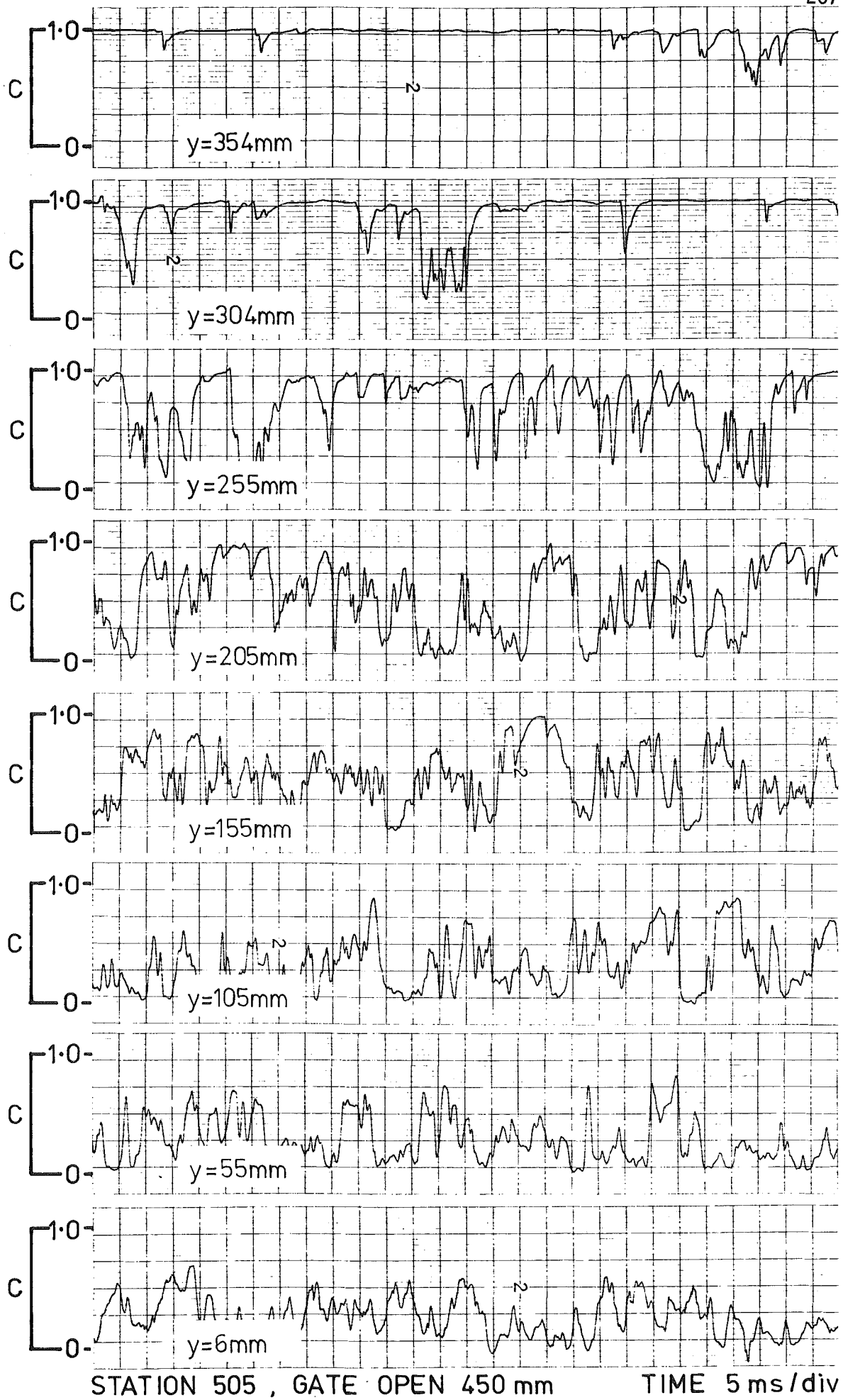

Fig. 10.9 Sample Air Concentration Signals.

about 60 mm/division at the spillway surface, and about 100 mm/division in the upper regions. The length of the measurement region between the air concentration electrodes is about 12 mm. For these signals, this length corresponds to about $\frac{1}{5}$ division at the spillway surface and about $\frac{1}{8}$ division in the upper regions.

The signals clearly show the increase in aeration with distance down the spillway, and the nature of self-aerated flows. Consider for example the signals at station 503 (Fig. 10.7). At 6 mm from the spillway surface, the flow is bubbly with small air concentrations. At 50 mm there are regions about 50 mm long in which the air concentration increases to about 0.5 (A). At 100 mm, these regions are a little longer and more aerated (B). At 150 and 200 mm, the flow is very aerated, ranging from all water to all air. At larger distances, the signals show the electrodes piercing waves which are very aerated (C).

The nature of this aeration is investigated in the next section with the smaller scale velocity probe. It is shown that in the regions of large air concentrations near the water surface, the air bubbles were as large as 20 mm dimension. The existence of such large bubbles and the large air concentrations (0.5 - 0.9) that are apparent in Figs. 10.5 to 10.9 were not envisaged when the probe was designed. However these should not limit its accuracy. Indeed, it was noted in Section 6.3 that the A flow simulator produced an aerated flow with large mean air concentrations ($\overline{C} > 0.5$) and with bubbles as large as 20 mm dimension, not unlike that observed in the surface regions at Aviemore. In a preliminary test traverse in this flow simulator (not reported in Chapter 6) the mean air concentrations measured with γ-rays and with the air concentration instrument were 0.61 and 0.59 respectively. This is excellent agreement considering the non-uniform unsteady nature of the flow.

The air concentration signals were analysed twice on the EAI computer. The first analysis incorrectly assumed that the signal level varied linearly with air concentration. This analysis is only mentioned because it resulted in some important qualitative conclusions. The analysis was part of a complex analysis in which air concentrations and stagnation pressures were simultaneously measured and velocity signals predicted from these. This is discussed in Section 10.4.1.

The remainder of this section discusses the correct non-linear analysis. In Section 3.6, it was shown that the electronic measuring circuit had a non-linear output. It was possible to correct for this with the non-linear curve in Fig. 3.17. This is applicable to instantaneous values of the output signal from the electronics.

The air concentration signals were therefore reanalysed, this time by themselves, with the low pass filter set at 2 kHz. This filtered any high frequency noise that might be present from the tape recorder without filtering the signal. Each digital sample was converted to an air concentration C_L using a linear input-output relationship as in the first analysis. This was then corrected for the non-linearity according to Eq. 3.14:

$$C = 1.0 - 1.008(1 - C_L)^{0.741} \qquad 3.14$$

Because of the slow speed of the computer in evaluating this equation, only 550 samples were obtained over the 14 seconds. Profiles of the mean values are shown in Figs. 10.10 and 10.11.

Again, the symbols within ovals were obtained by Keller (1972) under similar (but not identical) conditions.

The smooth curves drawn through the measured points have been superimposed in Fig. 10.12 for comparison. The data array for these is listed in Appendix N.

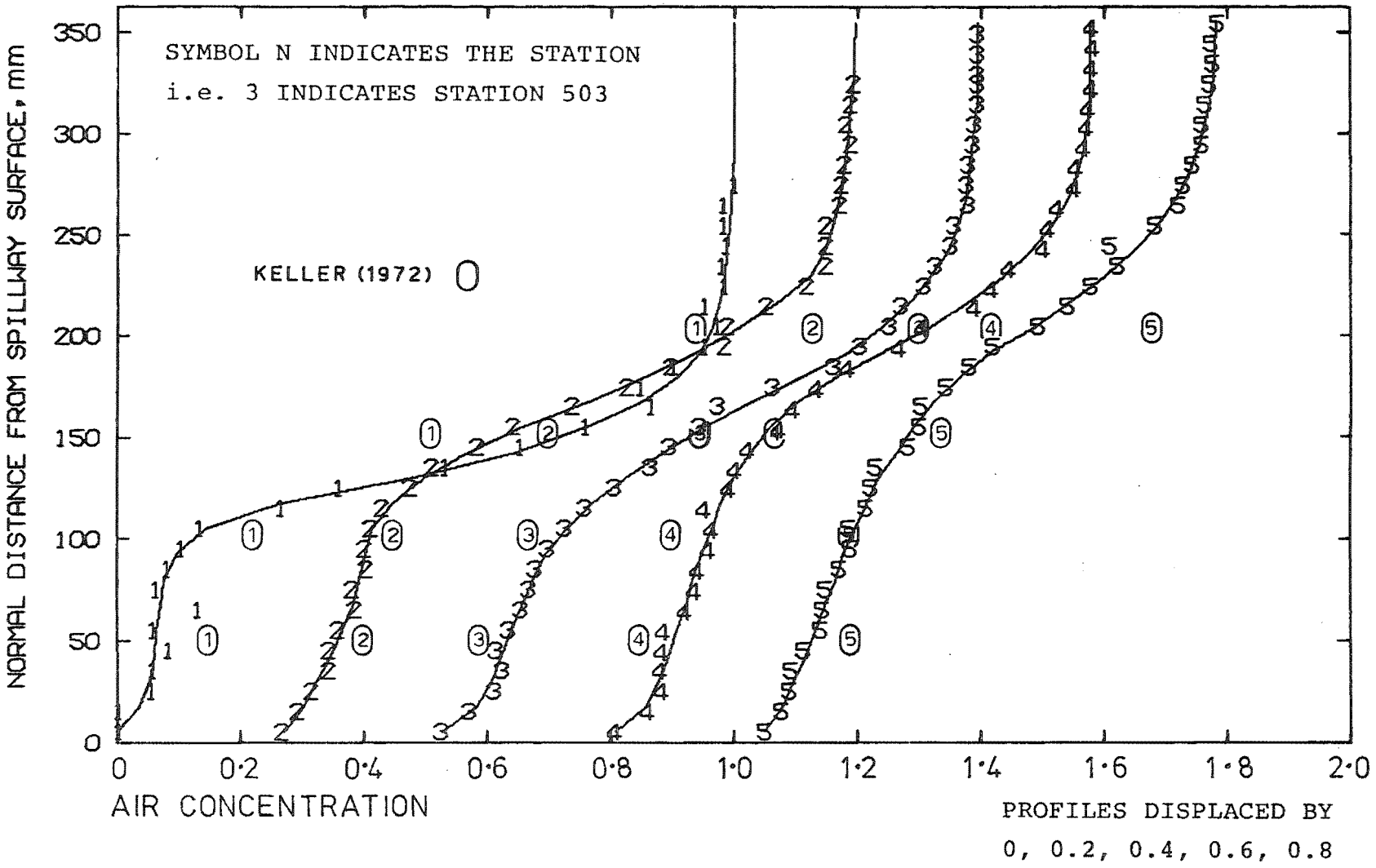

Fig. 10.10 Measured Air Concentration Profiles, Gate Open 300 mm.

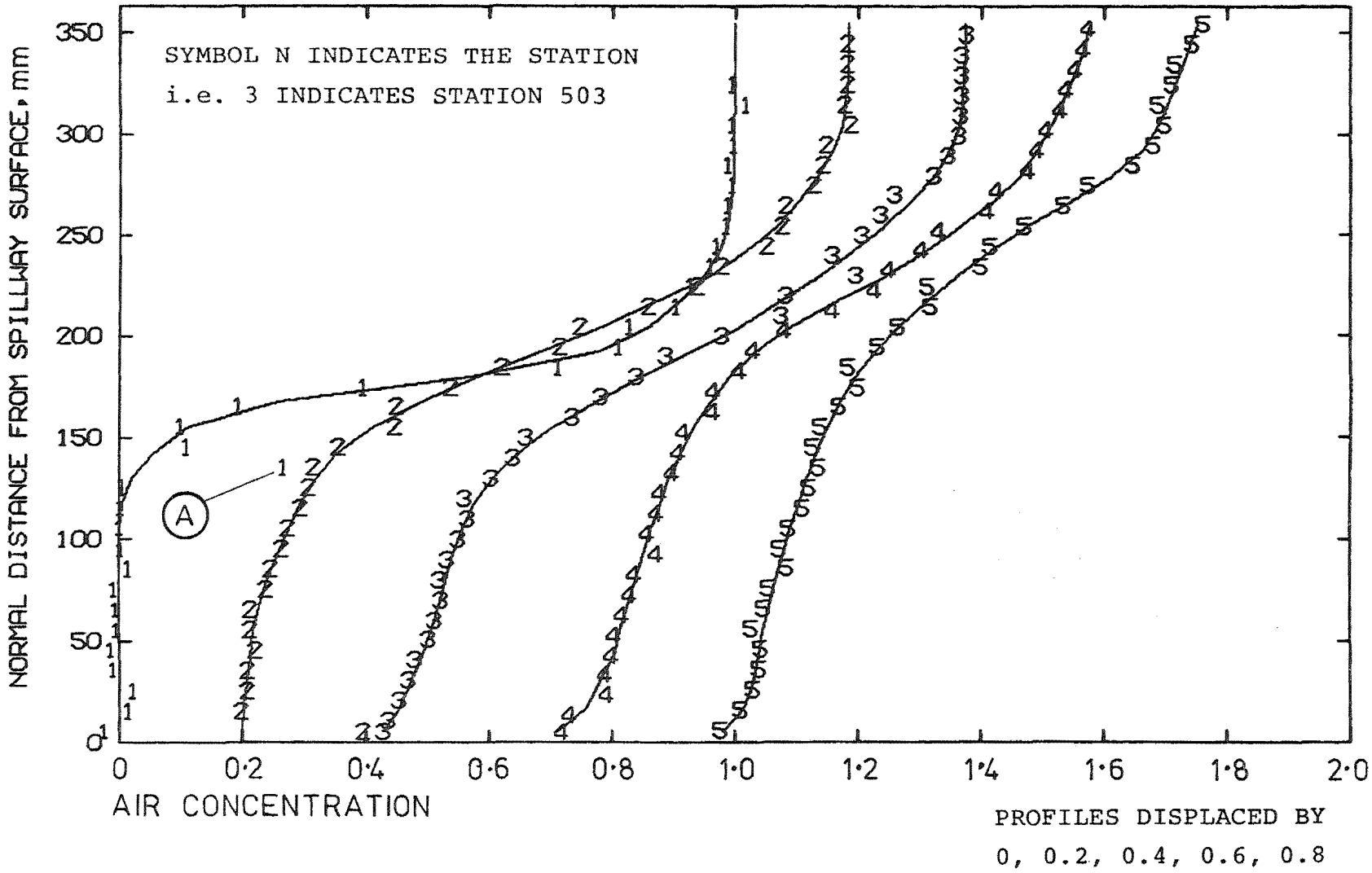

Fig. 10.11 Measured Air Concentration Profiles, Gate Open 450 mm.

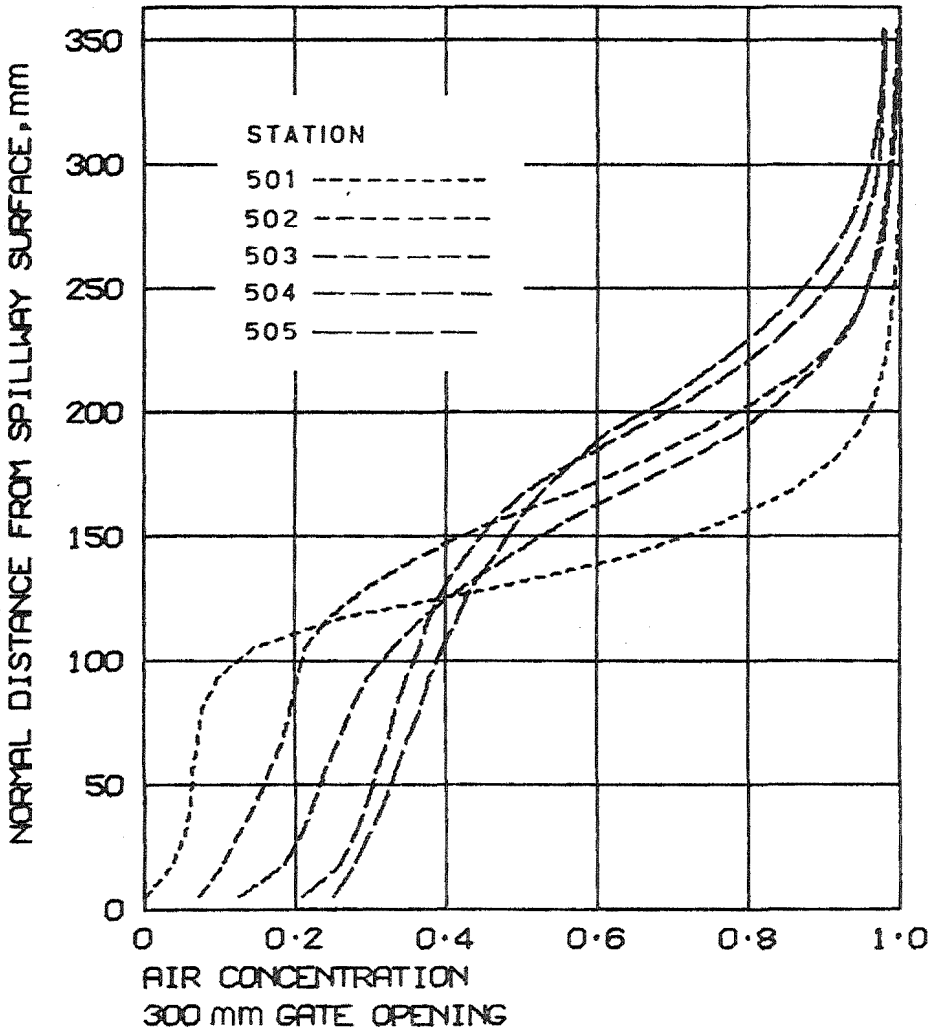

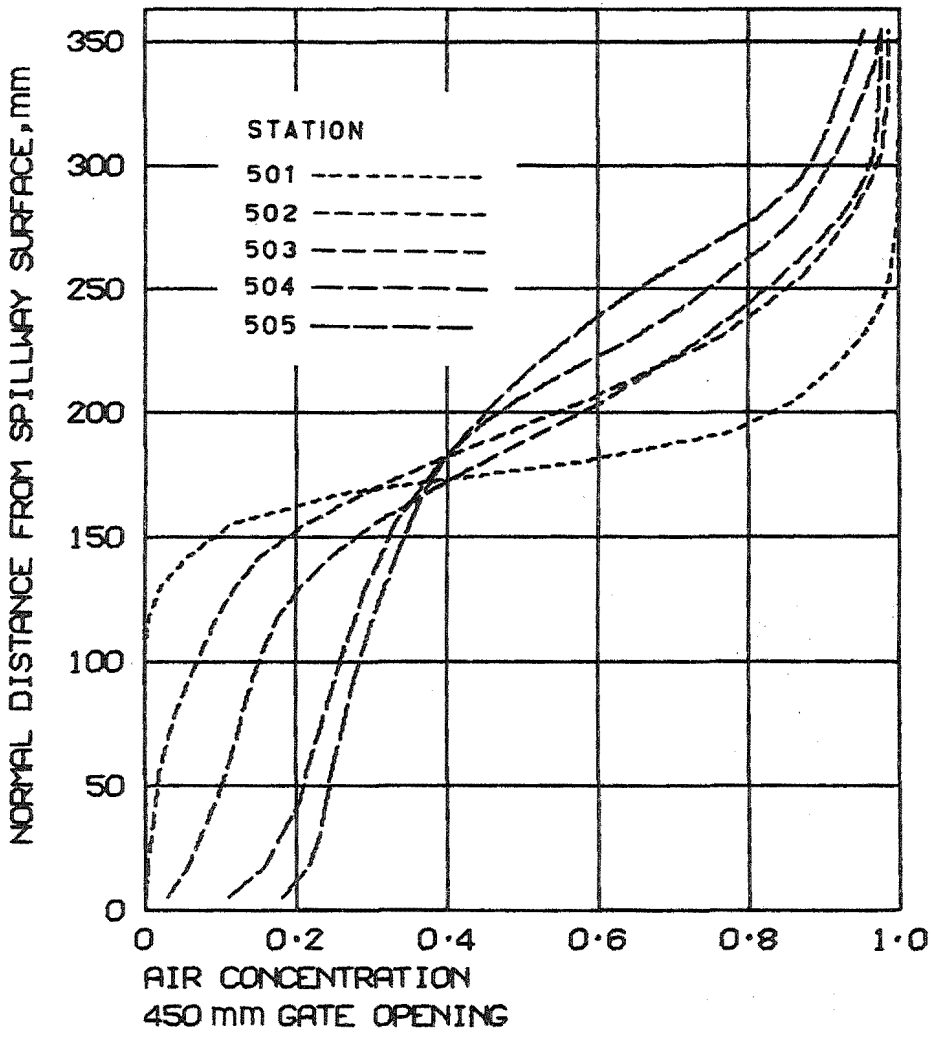

Fig. 10.12 Measured Air Concentration Profiles.

10.3.3 Velocity Measurements (Correlation Technique)

Sample output signals from the velocity instrument are shown in Fig. 10.13. These were taken from the tape recorder, displayed on a storage oscilloscope and photographed. The τ_o value noted on each photograph is the time delay for maximum correlation between the two signals. This is discussed within this section.

It will be shown that in all cases, the velocity varies from about 12 m/s at the spillway surface to 20 m/s in the upper regions. The 2 ms/division horizontal (time) scale of the signals can therefore be related to a length scale, i.e. about 25 mm/division at the spillway surface and about 40 mm/division in the upper regions. The length of each of the probes electrodes is about 1 mm. For these signals, this length corresponds to about $\frac{1}{25}$ division at the spillway surface and about $\frac{1}{40}$ division in the upper regions.

It is of interest to compare these signals with those in Fig. 10.7 obtained under almost identical conditions with the air concentration instrument. The signals from these two instruments are similar in that both indicate the variation in air concentration with time. The smaller electrodes of the velocity probe allow it to detect bubbles as small as 3 mm dimension, (ref. Section 5.3). The air concentration instrument will only indicate C = 1.0 for bubbles or air gaps larger than about 10 - 20 mm dimension.

The low air concentrations in Fig. 10.7 at 6 mm and 50 mm from the spillway are necessarily caused by bubbles less than about 3 mm as they are just too small for the velocity instrument to respond to (J). This is in agreement with the 0.5 - 3 mm bubble size measured with the bubble

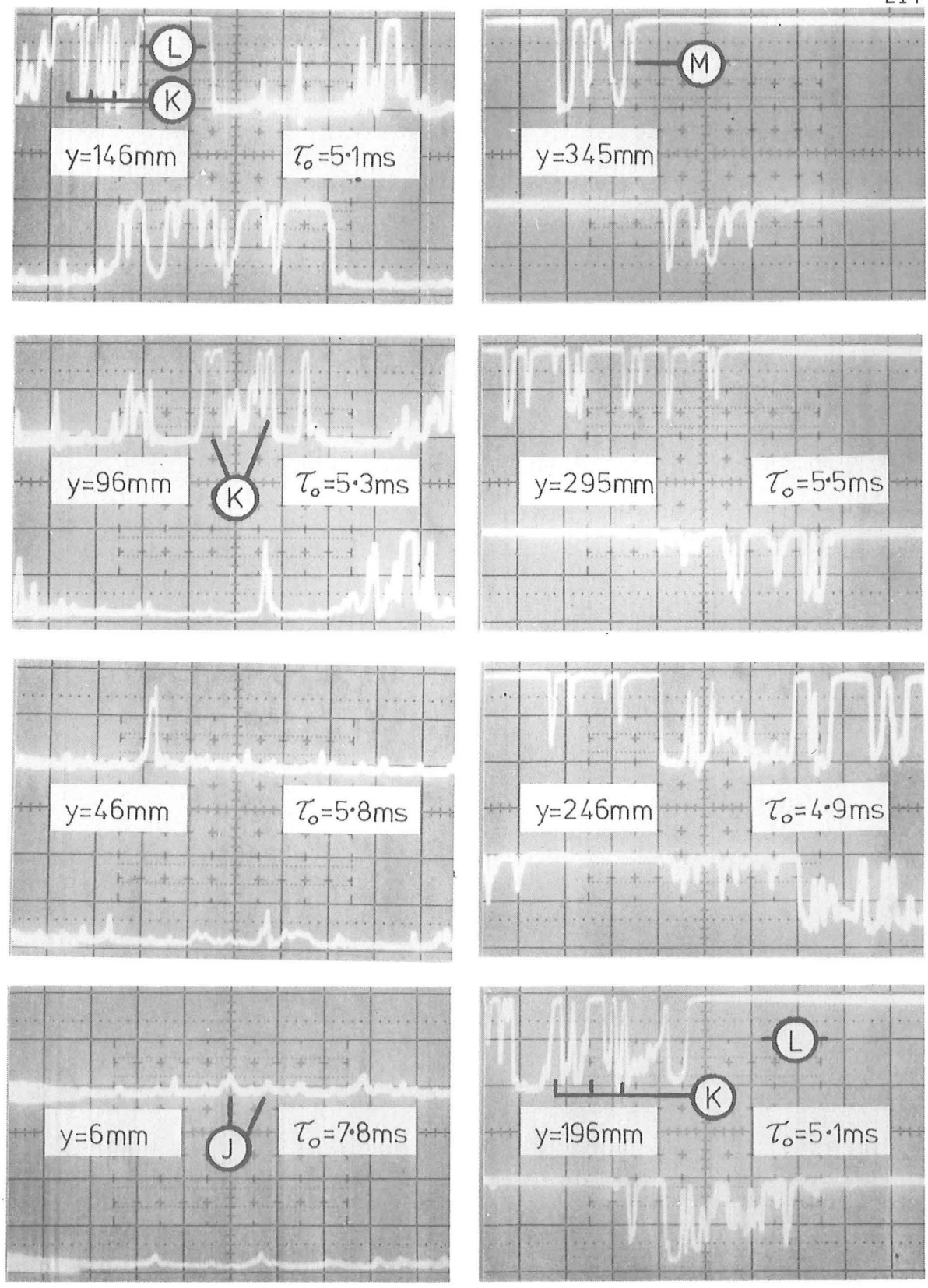

Upper trace, upstream probe; lower, downstream.
Signals upper limit, air; lower limit, water.
τ_o = time delay from cross-correlograms.

Fig. 10.13 Sample Velocity Instrument Signals.

probe in the lower region of flow at station 402 (ref. Section 5.2.3). It also agrees with the 1 - 3 mm that Killen (1968) observed in the St. Anthony Falls laboratory flume.

The very aerated flow from 100 - 250 mm in Fig. 10.7 appears in Fig. 10.13 as aerated water in which the bubbles are as large as 20 mm (½ division) (K). The longer periods of air (L) are the gaps between waves.

The crests of waves (C) at 299 and 349 mm in Fig. 10.7 are also shown in Fig. 10.13 (M). These are very aerated with bubbles as large as 10 - 20 mm.

It is speculated that air is entrained below the surface by a process of overturning waves. Very large air concentrations are possible in this surface region, with bubbles as large as 10 - 20 mm dimension. The intense turbulence deforms these large bubbles, shearing them to spheroids of uniform size from 0.5 - 3 mm. These are diffused towards the spillway surface against the buoyant forces. This description of the flow is consistent with that given in Section 1.3.

The velocity instruments signals were analysed on the EAI computer, the cross-correlation analyses being described in Section 5.4. The cross-correlograms were displayed on the visual display unit and recorded either on 35 mm film or in hard copy form. Representative plots for station 503 with a 450 mm gate opening are shown in Figs. 10.14 to 10.17. Well defined peaks were obtained when the mean air concentration was in the range about 0.3 - 0.9. In the regions of poorer correlation, the analyses using 60 second data samples often indicated peaks not discernable with only 15 second samples. Peaks were not discernable when the mean

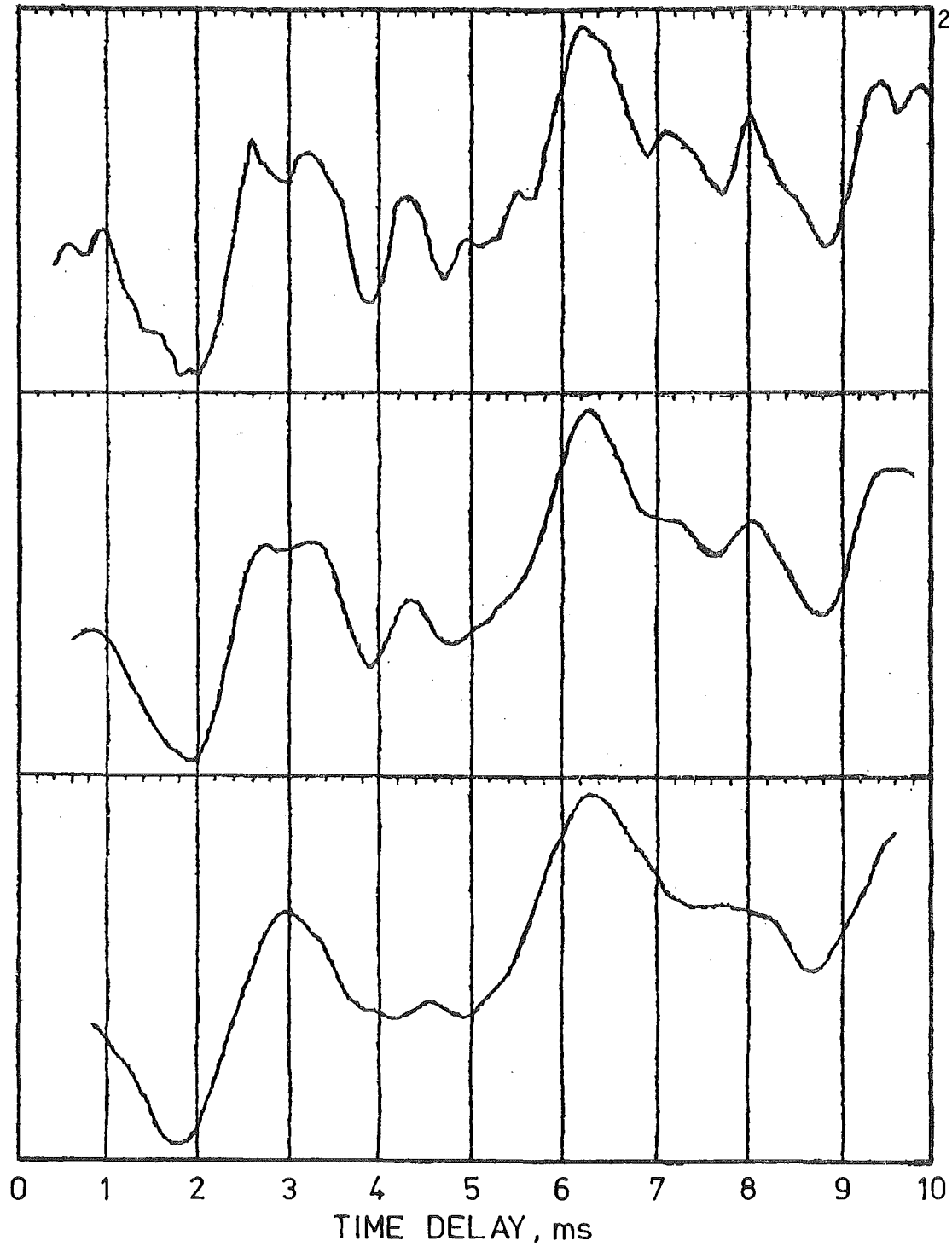

The cross-correlation functions are scaled to fit the vertical axes. The top curve is as calculated. The middle and lowest curves are smoothed with 5 and 9 point moving averages respectively.

Fig. 10.14 Cross-Correlograms at y = 36 mm.

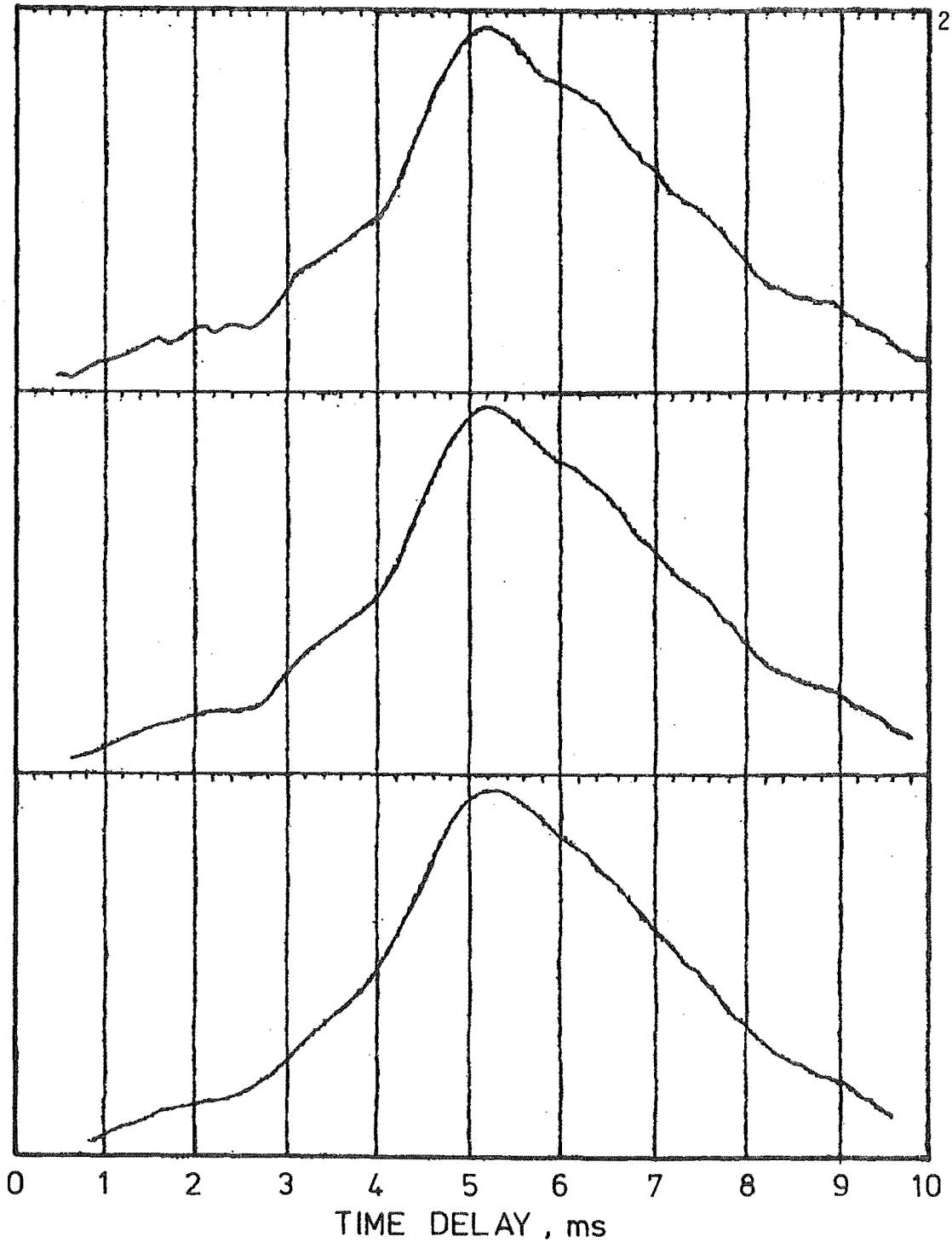

The cross-correlation functions are scaled to fit the vertical axes. The top curve is as calculated. The middle and lowest curves are smoothed with 5 and 9 point moving averages respectively.

Fig. 10.15 Cross-Correlograms at y = 136 mm.

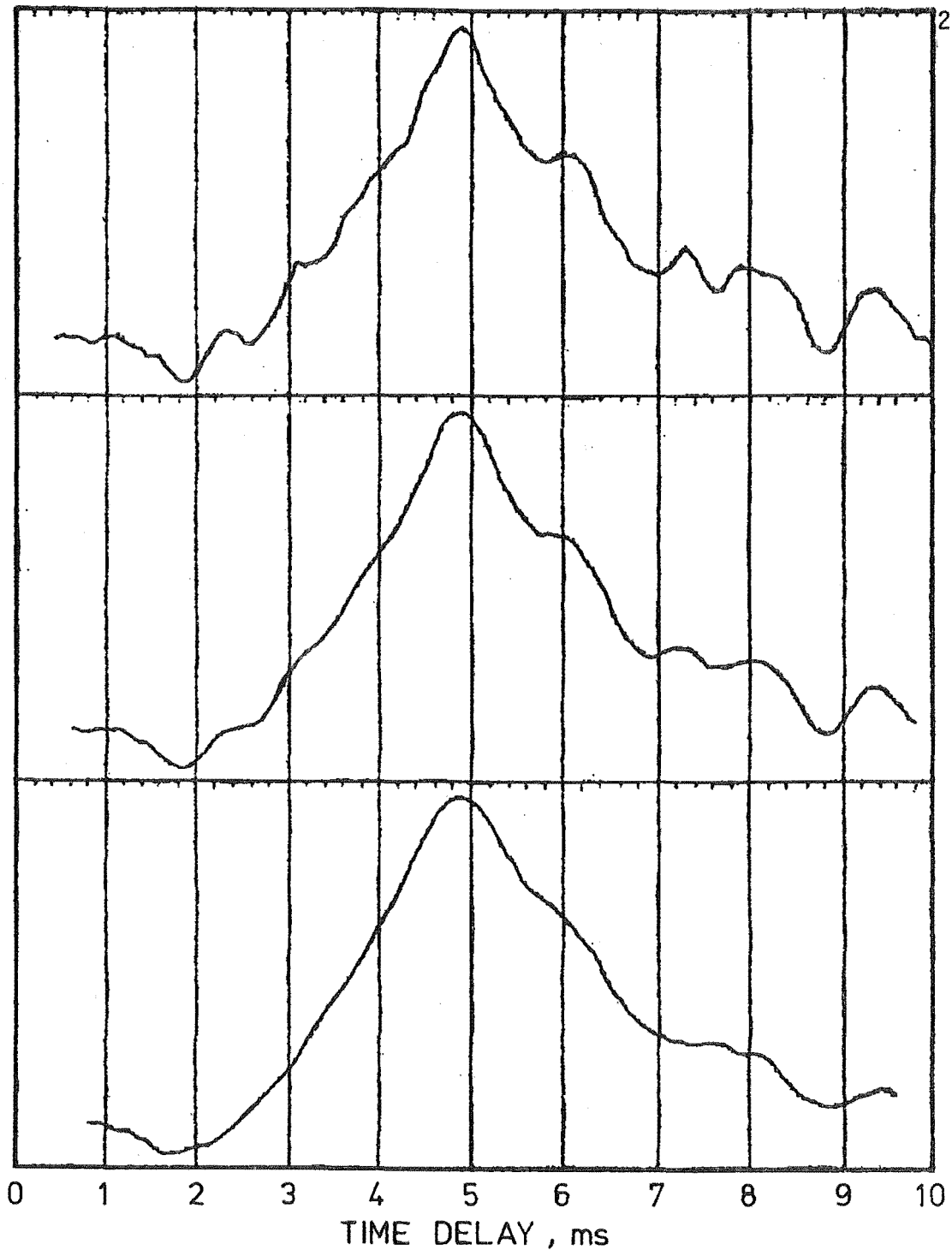

y = 236 mm , STATION 503 , GATE OPEN 450 mm , 15 s DATA
MEAN AIR CONCENTRATION ≃ 0·66

The cross-correlation functions are scaled to fit the vertical axes. The top curve is as calculated. The middle and lowest curves are smoothed with 5 and 9 point moving averages respectively.

Fig. 10.16 Cross-Correlograms at y = 236 mm

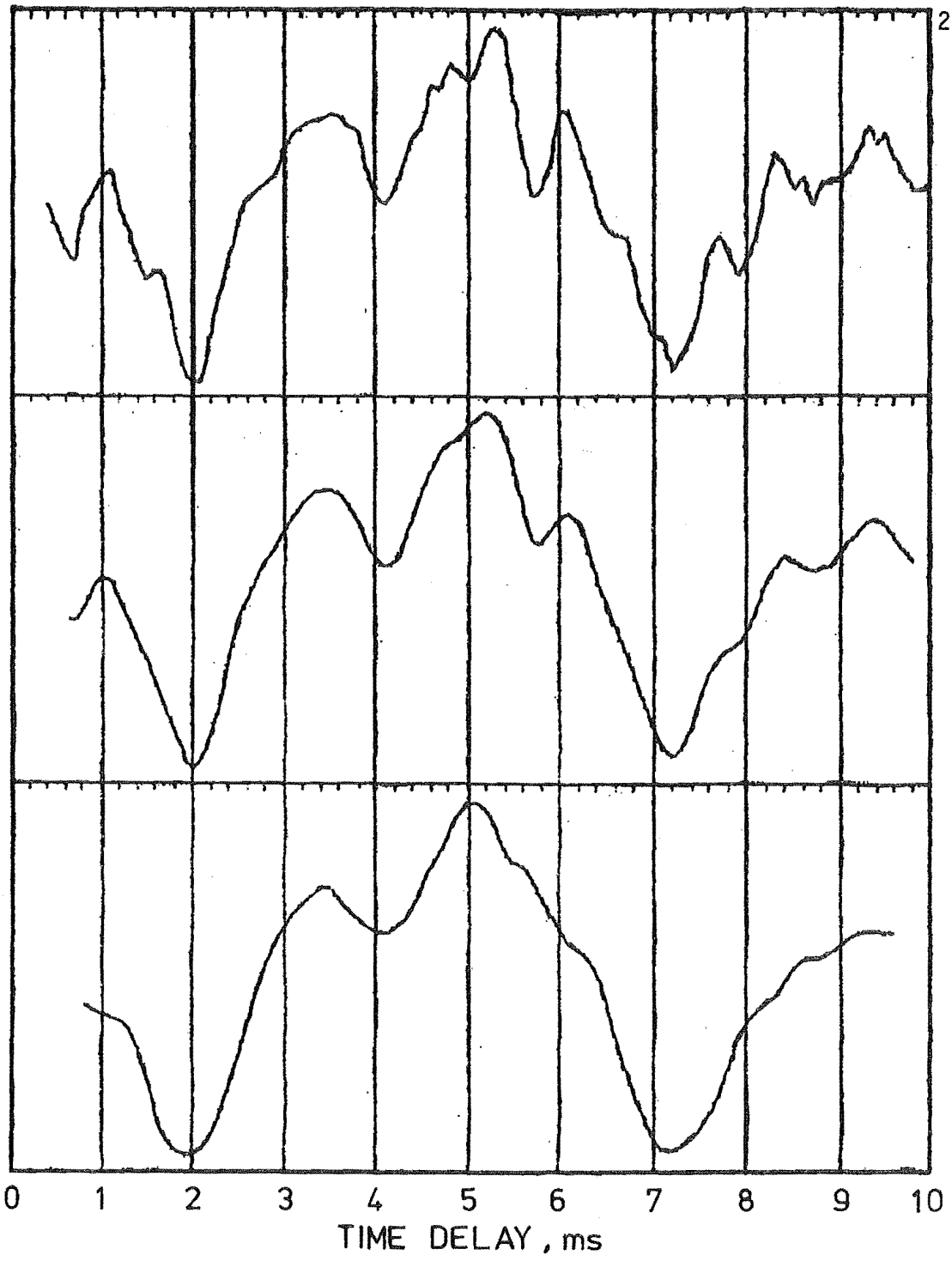

y = 335 mm, STATION 503, GATE OPEN 450 mm, 15 s DATA
MEAN AIR CONCENTRATION ≈ 0·97

The cross-correlation functions are scaled to fit the vertical axes. The top curve is as calculated. The middle and lowest curves are smoothed with 5 and 9 point moving averages respectively.

Fig. 10.17 Cross-Correlograms at y = 335 mm.

air concentration was outside the range about 0.05 - 0.98. As expected, no peaks were obtained for the almost non-aerated flow at station 501 with a 450 mm gate opening.

The magnitude of the normalised cross-correlation functions were obtained with one of the first programs developed (ref. Section 5.3.3). Although it is of no importance here, the magnitude of the peaks may be of interest for future instrument development. These were in the range 0.4 - 0.6 for mean air concentrations from about 0.35 - 0.8. Outside this range of air concentrations, the normalising scaling factors were too inaccurate and so the magnitude of these peaks was unreliable.

It is of interest to compare the signals in Fig. 10.13 with the time delay τ_o to the peak noted below each photograph. The two signals are so often so dissimilar that even knowing τ_o, it is difficult to see any correlation between them.

For each cross-correlation analysis τ_o was converted to a velocity V_X according to

$$V_X = \frac{d}{\tau_o - \delta t} \quad m/s$$

where d = 0.1016 m, distance between the upstream and downstream electrodes. $\delta t = 70 \times 10^{-6}$ s, phase shift between adjacent channels of the tape recorder due to misalignment of the heads.
These velocities have been plotted in Fig. 10.18 and 10.19.

The smooth curves drawn through these measurements have been extended to those regions in which the instrument did not perform well (including station 501 with a 450 mm gate opening). This was accomplished by comparison with the velocity profiles calculated from the measured profiles of stagnation pressure, air concentration and the intermittency parameter. These comparisons are discussed later.

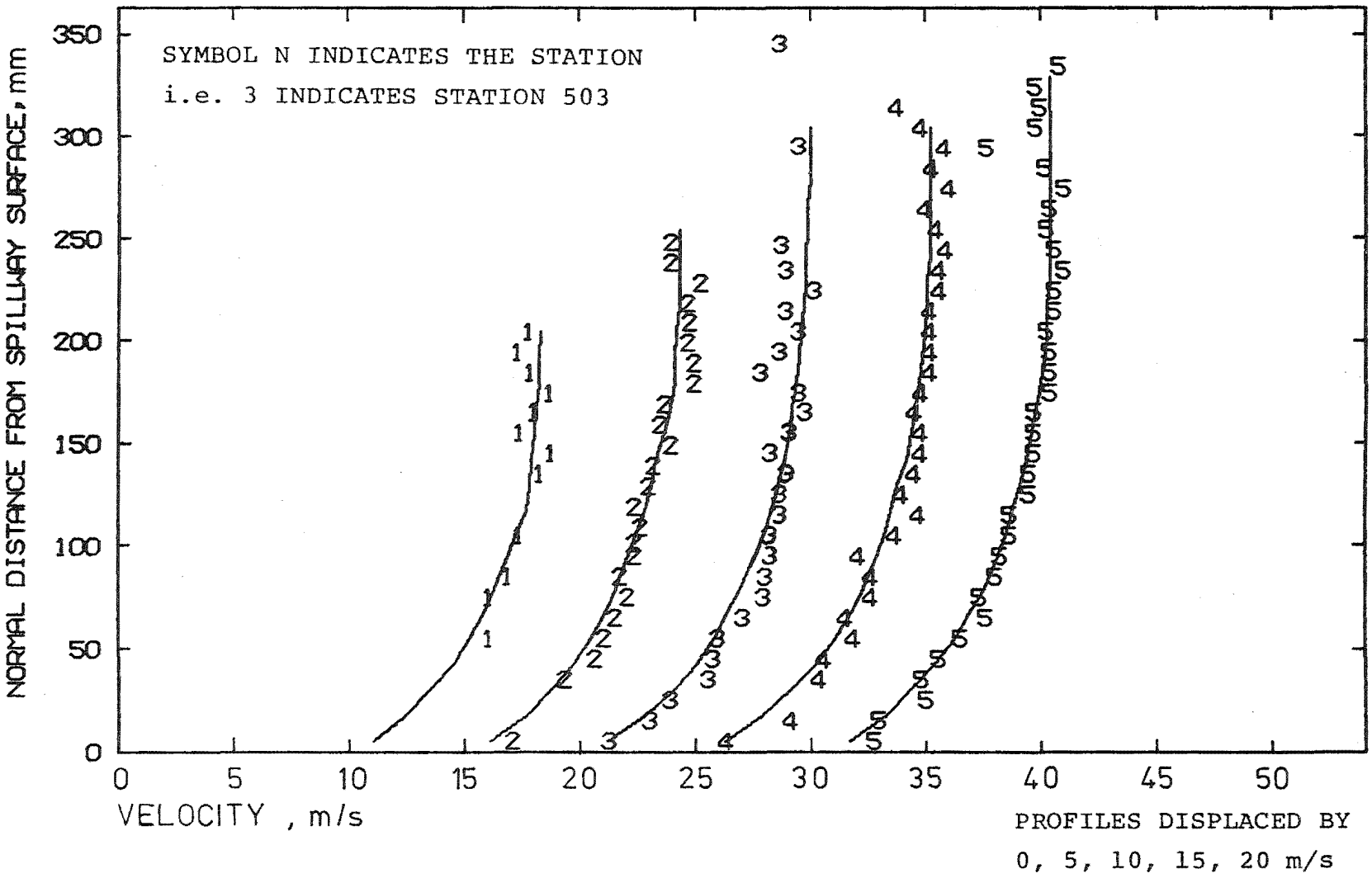

Fig. 10.18 Measured Velocity Profiles, Gate Open 300 mm.

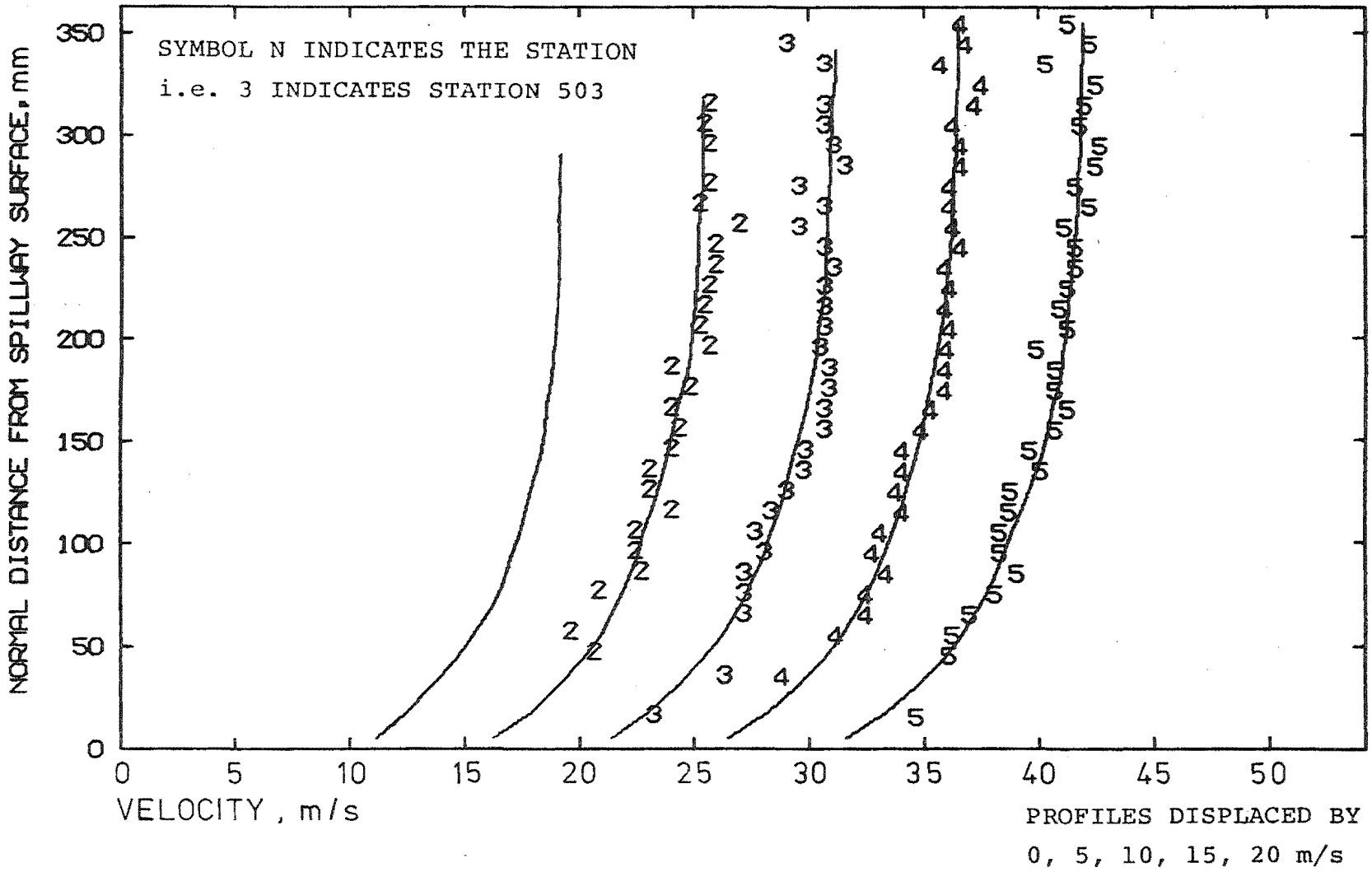

Fig. 10.19 Measured Velocity Profiles, Gate Open 450 mm.

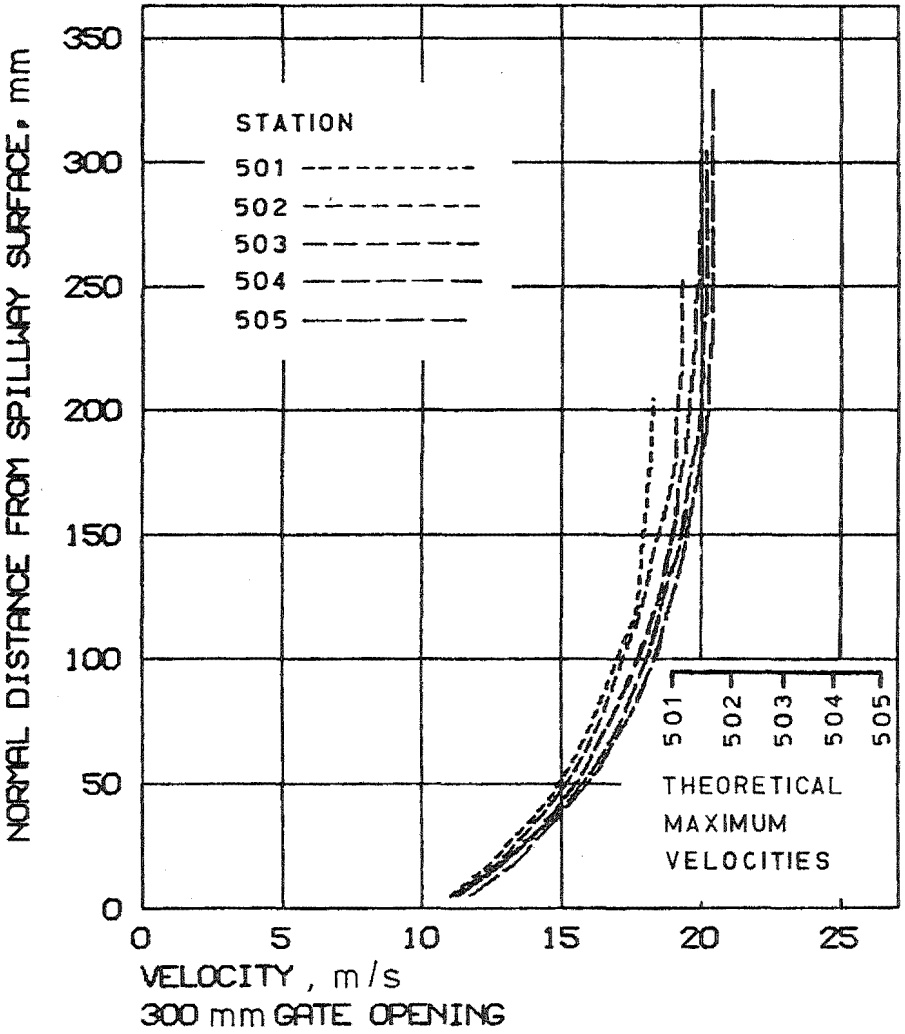

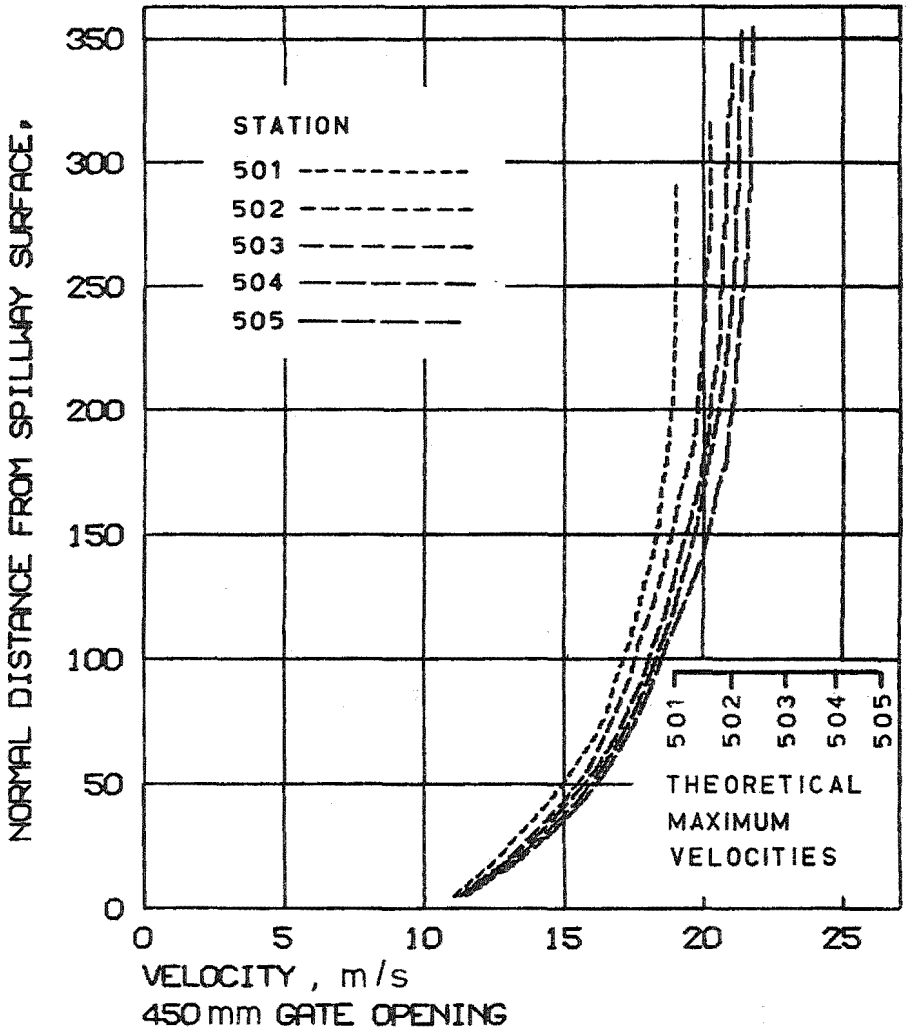

Fig. 10.20 Measured Velocity Profiles.

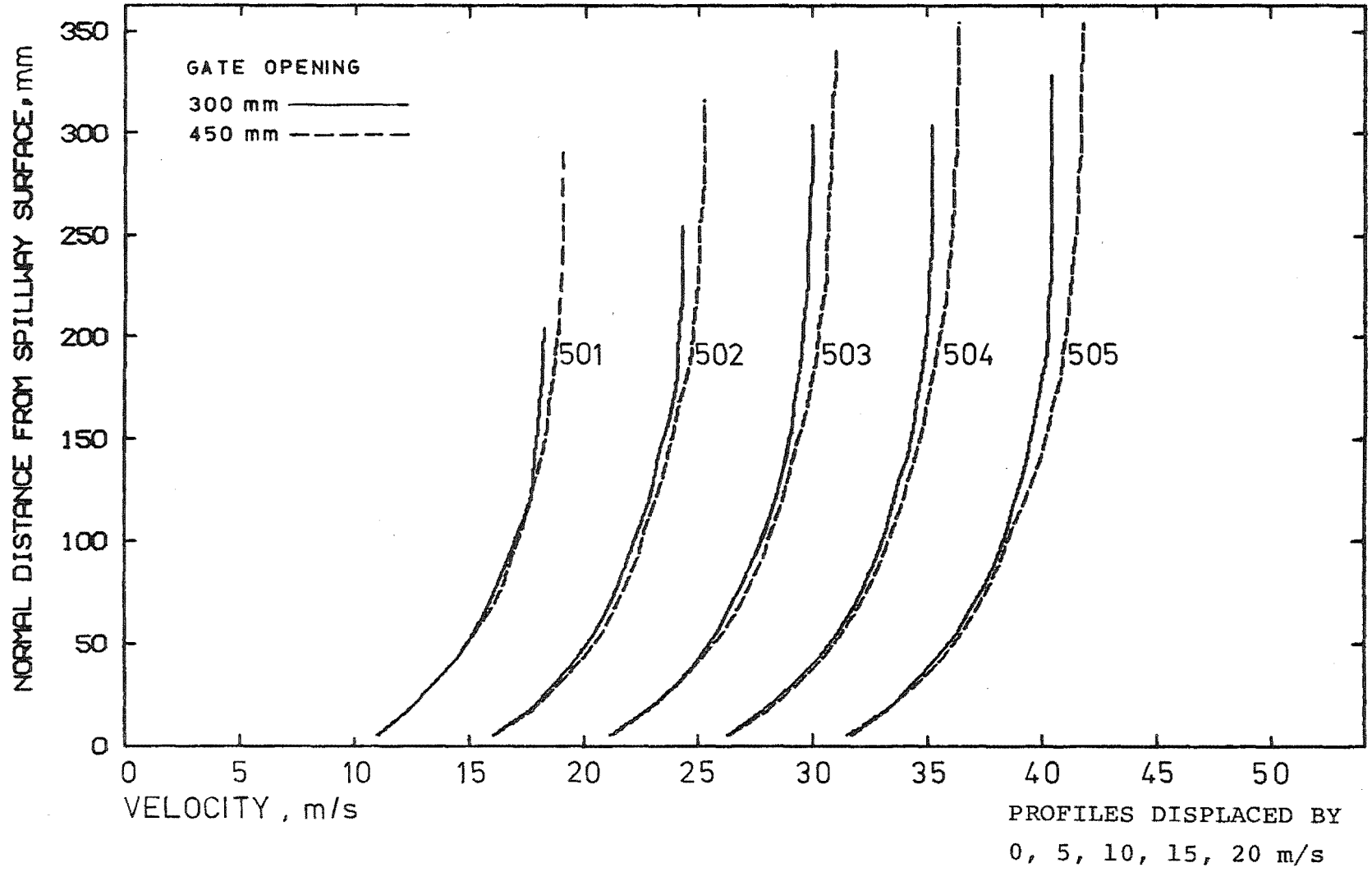

Fig. 10.21 Measured Velocity Profiles.

The smooth profiles have been superimposed in Fig. 10.20. The theoretical maximum velocities shown were calculated, assuming no friction losses, from

$$V = [2gH]^{\frac{1}{2}} \qquad 10.2$$

where H is the vertical distance from the spillway station to the head water level behind the dam (ref. Fig. 1.8).
Compared with the theoretical maximum velocities, the measured profiles show remarkably little increase in velocity with distance down the spillway.

The profiles at each station have been superimposed in Fig. 10.21. This shows a small increase in the velocity in the upper regions for the larger gate opening.

It was shown in Section 2.3.1 that the speed of sound is in the range 20 - 25 m/s for air concentrations from 0.2 - 0.8. The measured velocities ranged from about 12 - 22 m/s (Fig. 10.20). Mach numbers about 1.0 will therefore occur whenever the local air concentration is in the range 0.2 - 0.8.

The data arrays for the velocity profiles of Fig. 10.20 are listed in Appendix N.

10.3.4 Intermittency Parameter Measurements

The concept of an intermittency parameter T was introduced in Section 2.4.3 to improve the accuracy of mean velocity predictions from the stagnation pressure and air concentration measurements.

The intermittency parameter was initially defined as the proportion of time the measurement region of the combined pressure air concentration probe was within the water surface. The dimensions of the probe were

chosen so that the measurement region was larger than the 1 - 3 mm bubble size that was initially expected at Aviemore. If this was so, all the flow within the water surface would appear a homogeneous bubbly mixture to the probe.

This condition was not satisfied because as noted, the air bubbles near the water surface were as large as 20 mm. Such bubbly flow will not appear homogeneous to the probe; the bubbles will appear as small air gaps in wavy flow. It was therefore necessary to redefine the intermittency parameter as the proportion of time the probe's measurement region is within bubbly (or non-aerated) flow which appears homogeneous to the probe. As mentioned in Section 2.4.3 this should not limit the validity of the velocity expressions developed for self-aerated flows. However, it will be seen that the large bubbles do limit the accuracy of the intermittency parameter measurements.

The intermittency parameter was estimated from probability density functions of the air concentration signal. The basis of the analysis, performed on the EAI computer, is illustrated below.

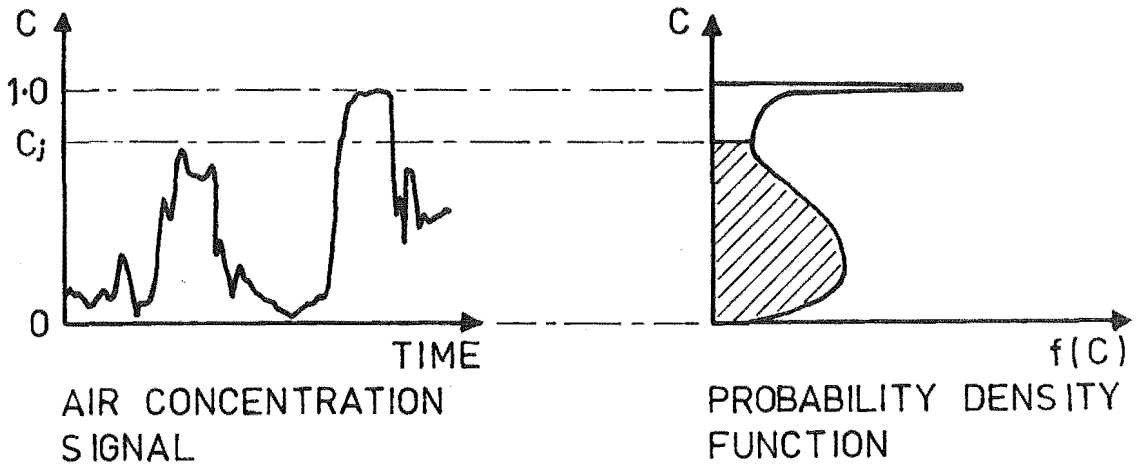

Fig. 10.22 Schematic of Probability Density Function in Self-Aerated Flow.

For a given air concentration C_j the probability density function $f(C_j)$ is the proportion of time that the air concentration signal is equal to C_j. The integral of the probability density function from $C = 0$ to $C = C_j$ represents the probability that at any instant, the air concentration will be less than or equal to C_j.

An intermittency analysis was incorporated into the non-linear air concentration data analysis previously described. The 550 air concentration samples from each 14 second data record were used to evaluate the probability density function at 100 points between C = 0 and 1.0. These were plotted on the visual display unit. The curves were not smooth because such a small number of samples were used to form them. Sample curves have been smoothed by eye and are shown in Fig. 10.23. The areas between each curve and the vertical axes are identical.

The plot of probability density function at 6 mm from the spillway surface shows the air concentration to be in the range 0 - 0.5. Such low values suggest the flow always appeared homogeneous to the probe.

The plots of probability density function at 205 and 255 mm from the spillway have peaks at C = 1.0. These are caused mainly by the large air gaps between waves. The largest bubbles could also contribute to these peaks.

If the frequency response of the air concentration instrument was infinite, any large air bubbles which obscured one or both of the electrodes would produce an output signal C = 1.0. Instead, the limited frequency response causes the output signal to fluctuate rapidly, frequently without attaining the level C = 1.0. This is apparent from the fluctuations of the sample signals, e.g. at 200 mm from the spillway surface in Fig. 10.7.

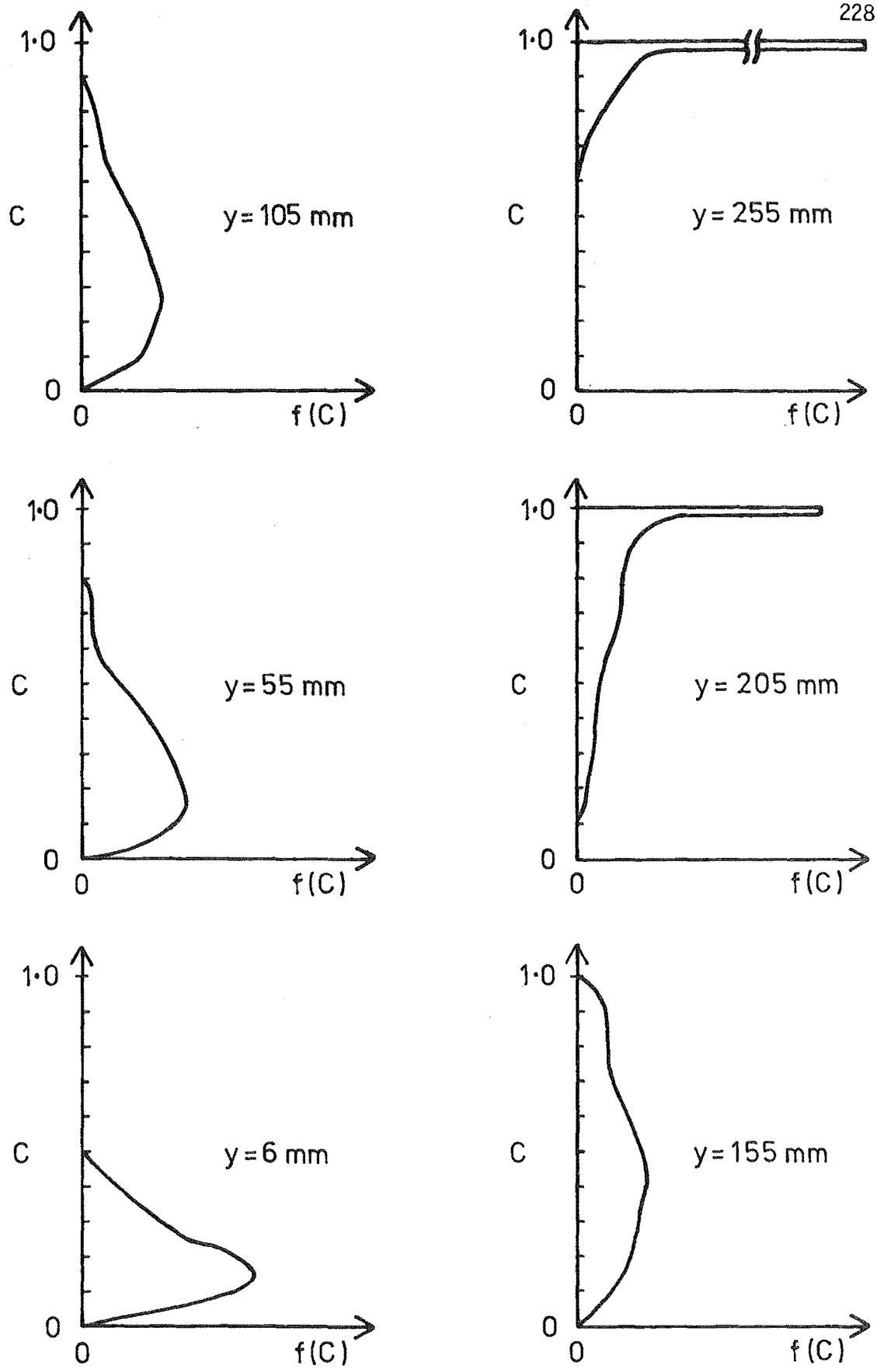

Fig. 10.23 Sample Probability Density Functions

Station 504, Gate open 300 mm.

This response complicates the interpretation of most of the plots of probability density function. Consider for example the plot at 155 mm from the spillway (Fig. 10.23). The value of f(C) at say C = 0.8 could be caused entirely by large bubbles which are inaccurately recorded. Alternatively, it could be caused entirely by a homogeneous mixture of small bubbles for which C = 0.8. In general, both sources will contribute to the value f(C). Their individual contributions cannot be distinguished.

Under these circumstances, it was thought the intermittency parameter could be estimated most accurately as the integral of f(C) from C = 0 - 0.7. This assumes that the air concentration within homogeneous mixtures of small bubbles will rarely exceed 0.7.

The choice of 0.7 is rather arbitrary and cannot be justified with experimental evidence. For this reason the velocity calculations using T have been repeated for values of T calculated as the integral from C = 0 - 0.6 and C = 0 - 0.8. These different values of T will be shown to have little effect on the calculated velocities. This is because the velocity equation (Eq. 2.14) is insensitive to small errors in T.

Profiles of the intermittency parameter T calculated as the integral of the probability density functions from C = 0 - 0.7 are plotted in Figs. 10.24 and 10.25. The smoothed profiles have been superimposed in Fig. 10.26 for comparison. The data arrays for these are listed in Appendix N.

The profiles calculated as the integral from C = 0 - 0.6 and C = 0 - 0.8 have been plotted in Appendix P.

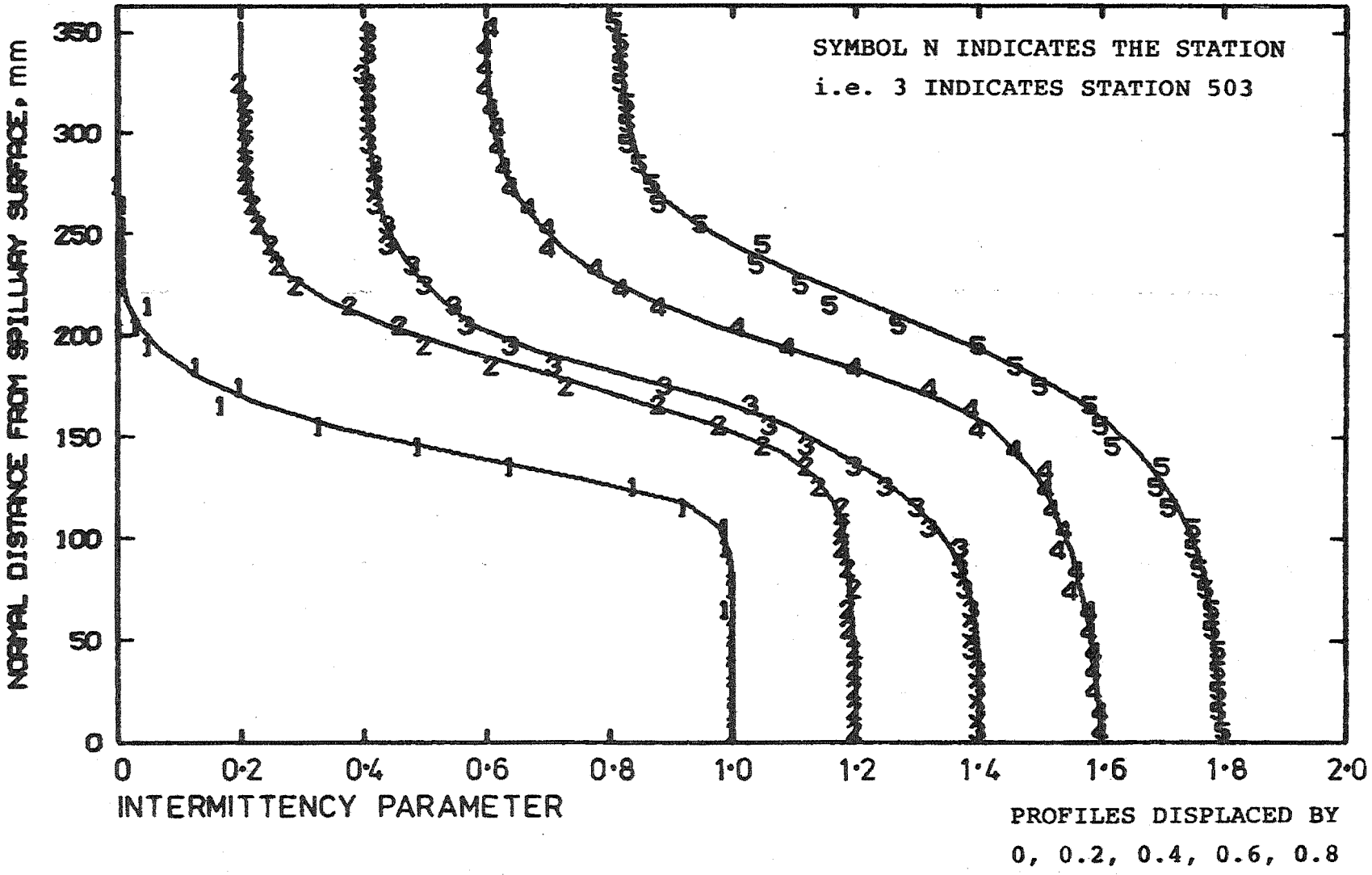

Fig. 10.24 Measured Intermittency Parameter Profiles, Gate Open 300 mm.

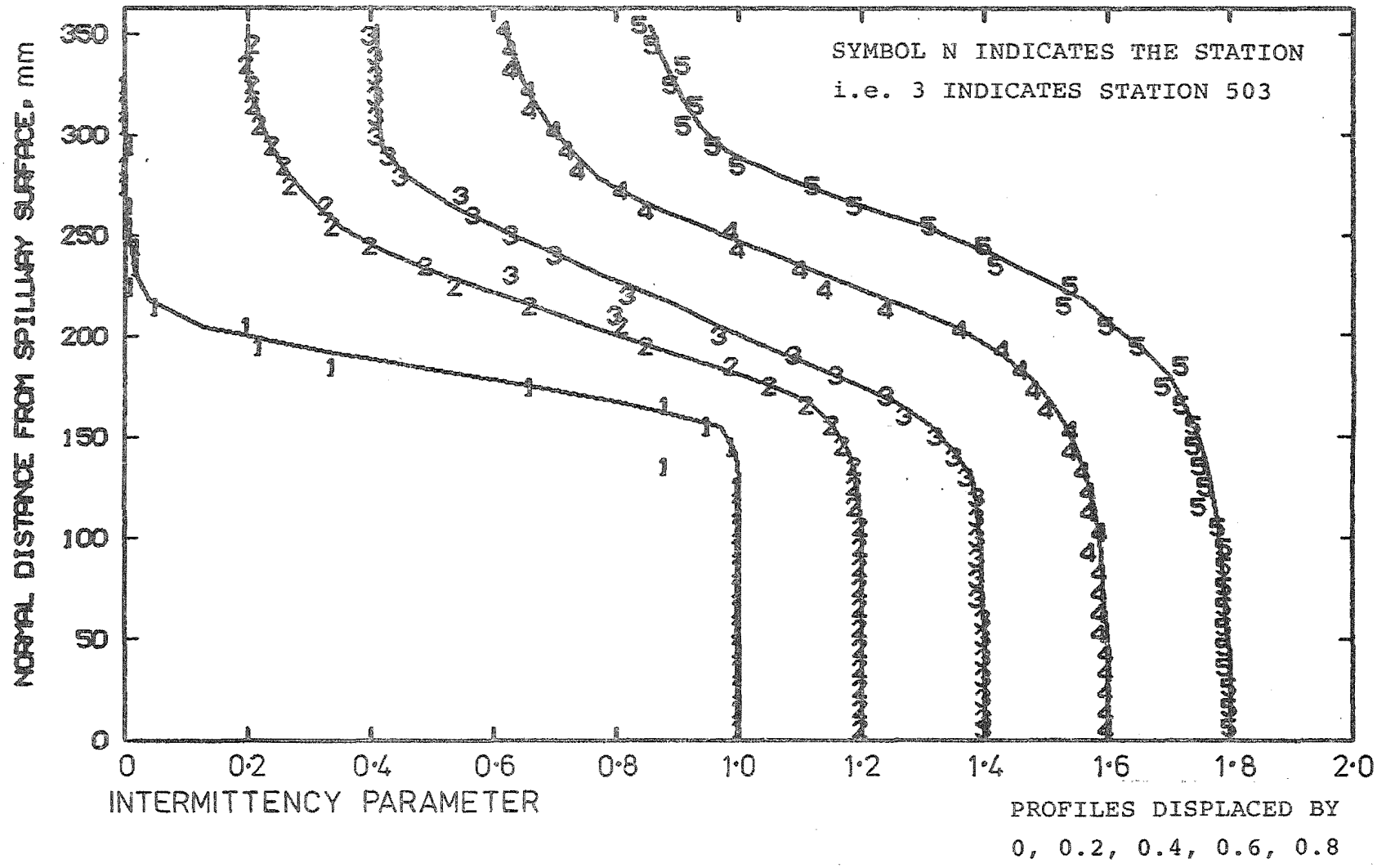

Fig. 10.25 Measured Intermittency Parameter Profiles, Gate Open 450 mm.

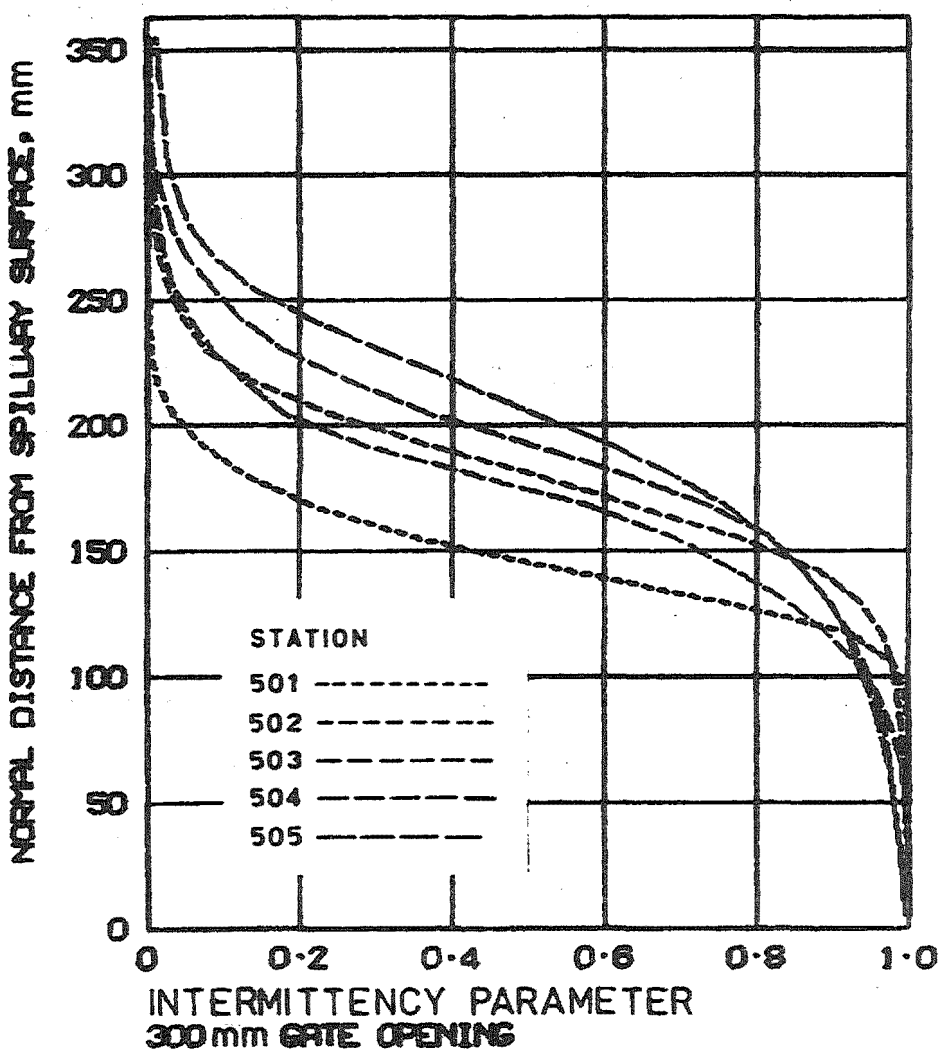

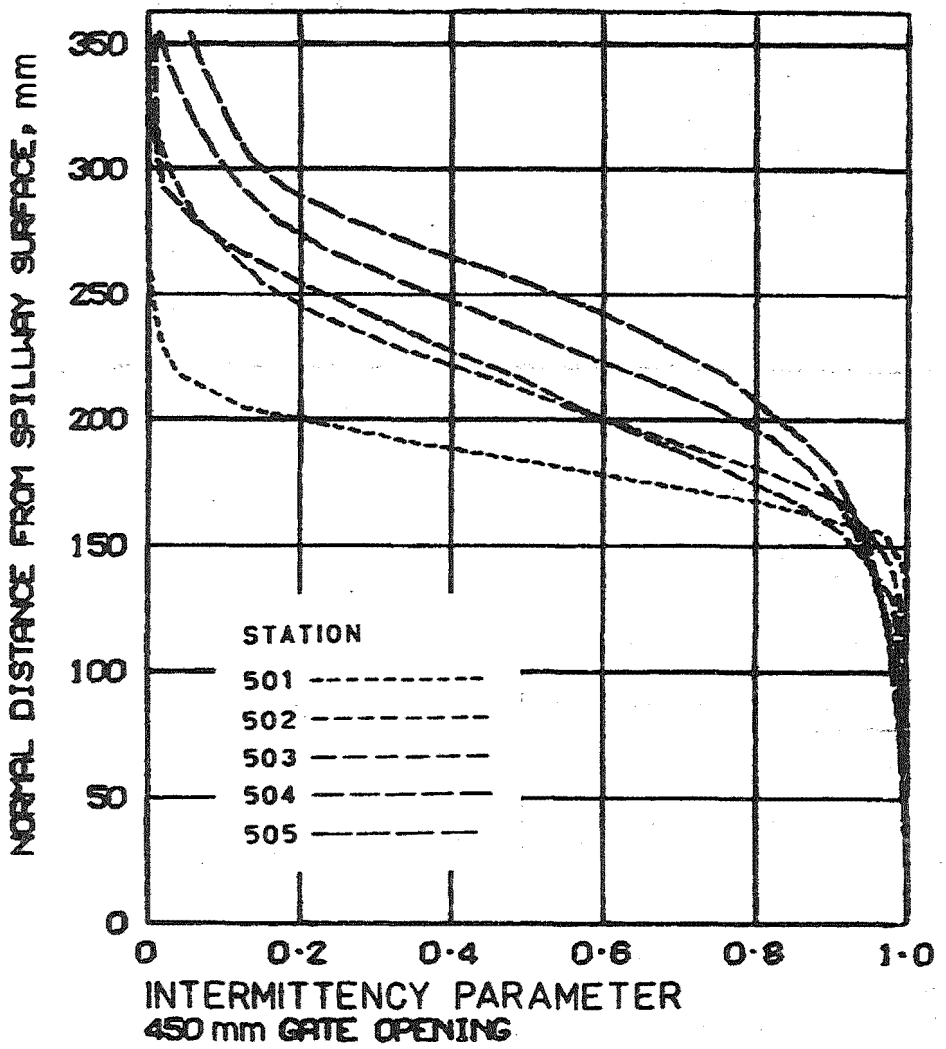

Fig. 10.26 Measured Intermittency Parameter Profiles.

10.4 VELOCITY PREDICTION

10.4.1 Velocity Signal Calculations

One of the initial aims of this research was to generate a velocity signal from the stagnation pressure and air concentration signals so that various turbulent parameters could be calculated. This was attempted during the simultaneous analyses of the stagnation pressure and air concentration signals on the EAI computer and is discussed below.

The velocity calculations in this section do not use the intermittency parameter. This was introduced to improve the accuracy of mean velocity predictions whereas this section is concerned primarily with generating velocity signals. Mean velocities are discussed here but are treated in detail in the following section where the intermittency parameter is used.

In this analysis the air concentration was calculated assuming, incorrectly, a linear relationship between C = 0.0 and 1.0 (see Section 10.3.2). The results of this analysis are therefore qualitative only but they are important. It was concluded from these results that it was unnecessary to repeat this analysis using the correct non-linear air concentration relationship.

A requirement for calculating velocity is that the stagnation pressure and air concentration instruments have identical frequency and phase responses. This was achieved by conditioning the analogue signals prior to sampling them with the computer, as shown in Fig. 10.27 and described below.

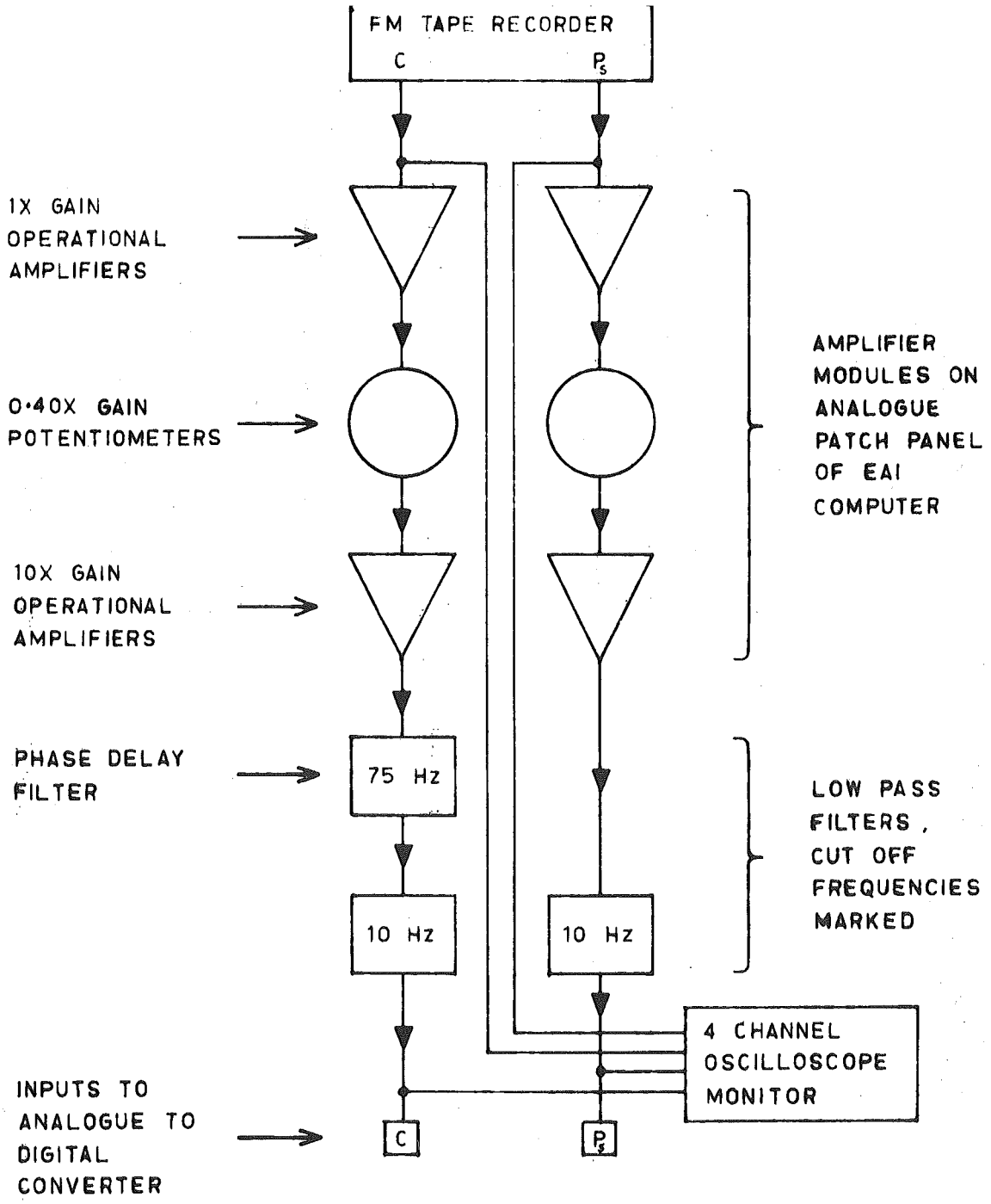

Fig. 10.27 Analogue Signal Conditioning.

The phase response of the pressure instrument varies with frequency (ref. Section 4.8.4) whereas the air concentration output signal is in phase with the input signal (ref. Section 3.5). It was observed that by filtering the air concentration signal to 75 Hz and thus delaying it by 13 ms, the phase difference between the two signals was largely eliminated.

The frequency response of the pressure instrument was flat to less than 1 Hz (ref. Section 4.8.4) so that both signals should be filtered to about 0.5 Hz.

The frequency of most signal fluctuations was greater than 0.5 Hz so that most transient information would then be lost. As a compromise, the signals were filtered to 10 Hz. This value was chosen after many trial analyses using filter cut off frequencies from 1 - 75 Hz.

The amplifiers in Fig. 10.27 amplified the signals 4.0 times so as to suit the input range of the filters and analogue to digital converters.

For each data record the two analogue signals were simultaneously sampled at 40 ms intervals for 14 seconds. This gives 350 pairs of samples with a sampling rate 2.5 times the maximum signal frequency. These samples were converted to stagnation pressures P_s and air concentrations C as previously described.

The velocity was then calculated for each pair of samples using the "incompressible" and "compressible" velocity equations,

$$V_I = \left[\frac{2}{\rho_w} \left[\frac{P_s}{1-C} \right] \right]^{\frac{1}{2}} \qquad 2.7$$

$$V_C = \left[\frac{2}{\rho_w} \left[P_s + \frac{C}{1-C} P_o \ln \left[\frac{P_s + P_o}{P_o} \right] \right] \right]^{\frac{1}{2}} \qquad 2.8$$

These have been rewritten so that the stagnation pressures are expressed in gauge units (ref. Section 2.5). Also, the static pressure P is assumed equal to the atmospheric pressure P_o which can be taken as $P_o = 102\ kN/m^2$ (abs).

The velocity was not calculated whenever:

(i) $C > 0.95$. This is because the above equations are too sensitive to errors in P or C as the mean air concentration $\overline{C}$ tends to 1.0 (ref. Section 2.4.4).

(ii) $P < 0.0$. This impossible situation is caused by variations in the mains frequency when the mean stagnation pressure $\overline{P} \simeq 0.0$. This occurs when $C \simeq 1.0$, so that the above criteria (i) usually prevented this arising.

(iii) $C < 0.0$. This impossible situation is also caused by variations in the mains frequency. This only occurred when the mean air concentration $\overline{C} < 0.1$. When $\overline{C} = 0.0$ this situation $C < 0.0$ occurred about 50% of the time as expected. This is discussed and illustrated later.

After each analysis, P, C, V_I and V_C were plotted on the visual display unit, with samples reproduced in Figs. 10.28 to 10.35. Each curve consists of 350 points except that the velocity curves are discontinuous when the velocity was not calculated.

Figs. 10.28 to 10.33 show a range of flow conditions for station 504 with a 450 mm gate opening. The larger amplitude of the velocity fluctuations in Figs 10.31 and 10.32 can be attributed primarily to the sensitivity of Eqs. 2.7 and 2.8 as C tends to 1.0.

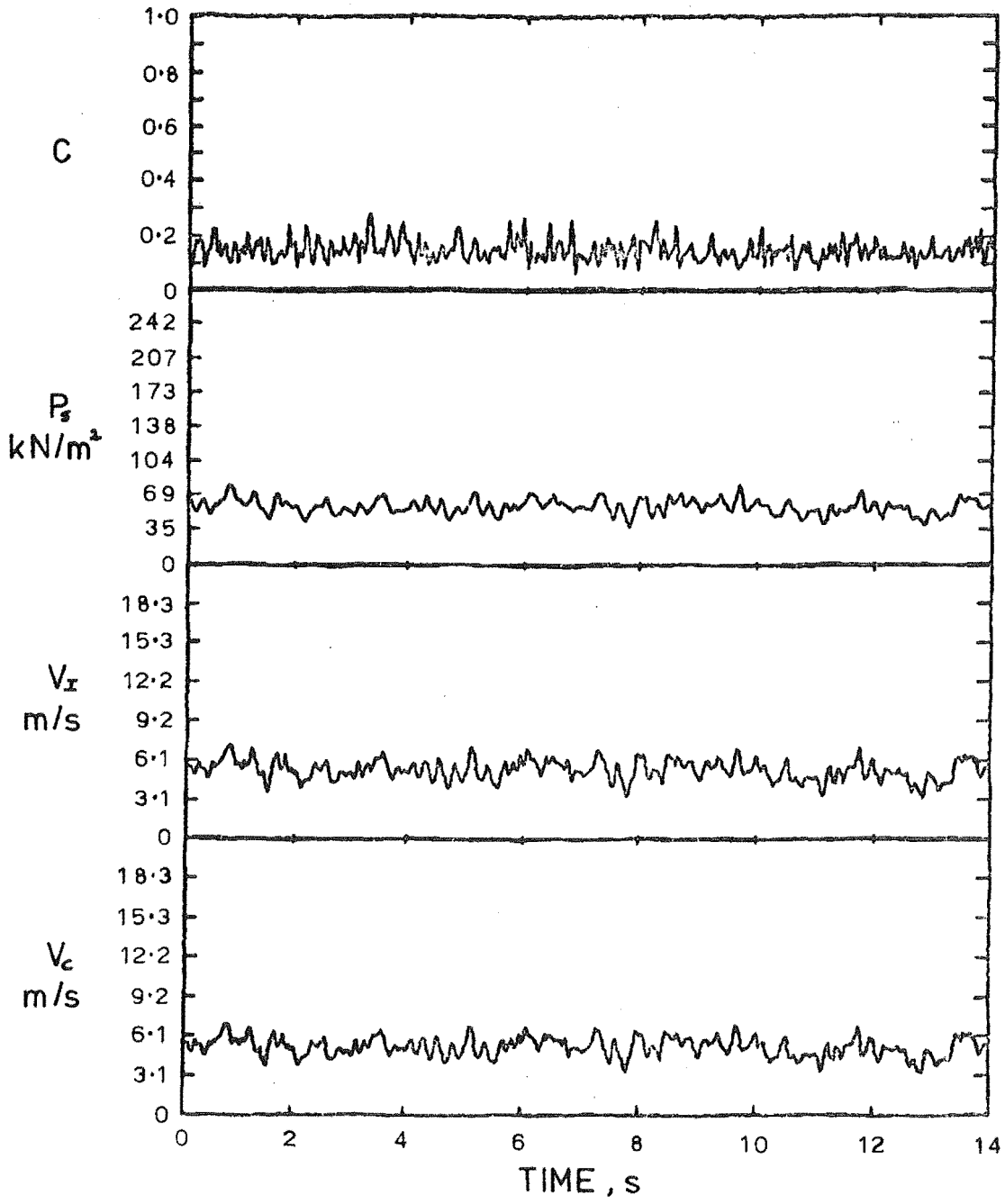

y=6 mm , STATION 504 , GATE OPEN 450 mm

Fig. 10.28 Output Signals at y = 6 mm.

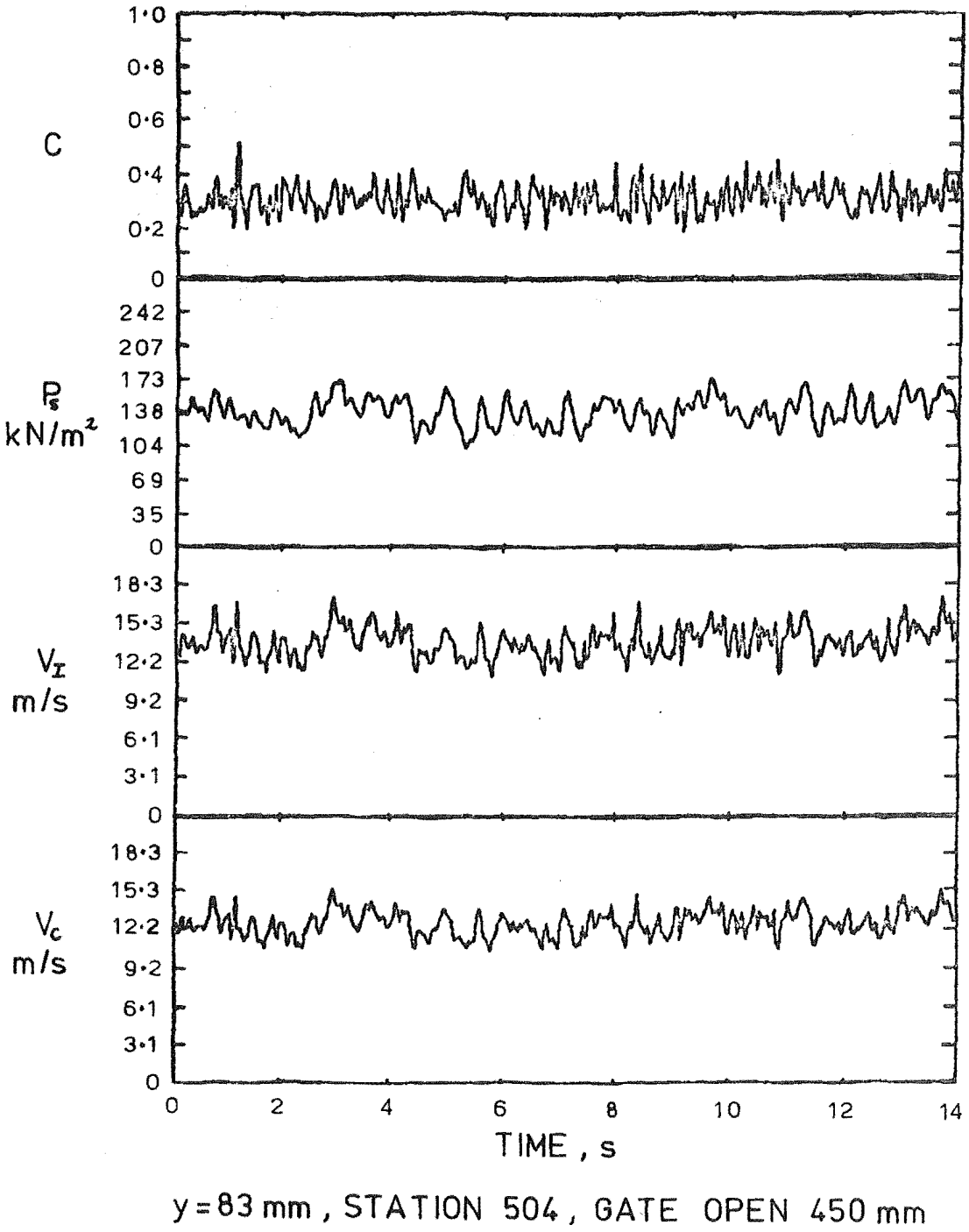

Fig. 10.29 Output Signals at y = 83 mm.

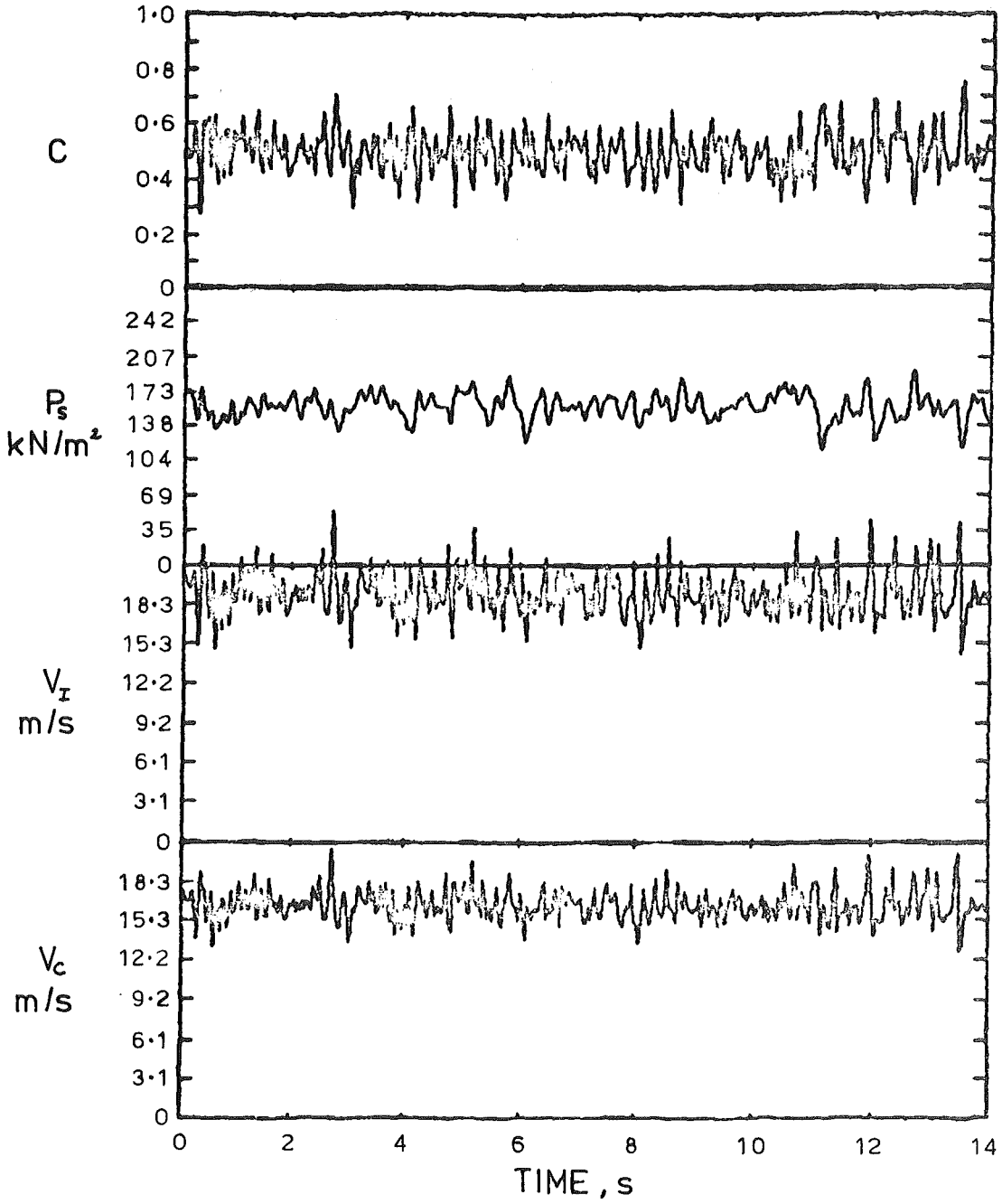

Fig. 10.30 Output Signals at y = 193 mm.

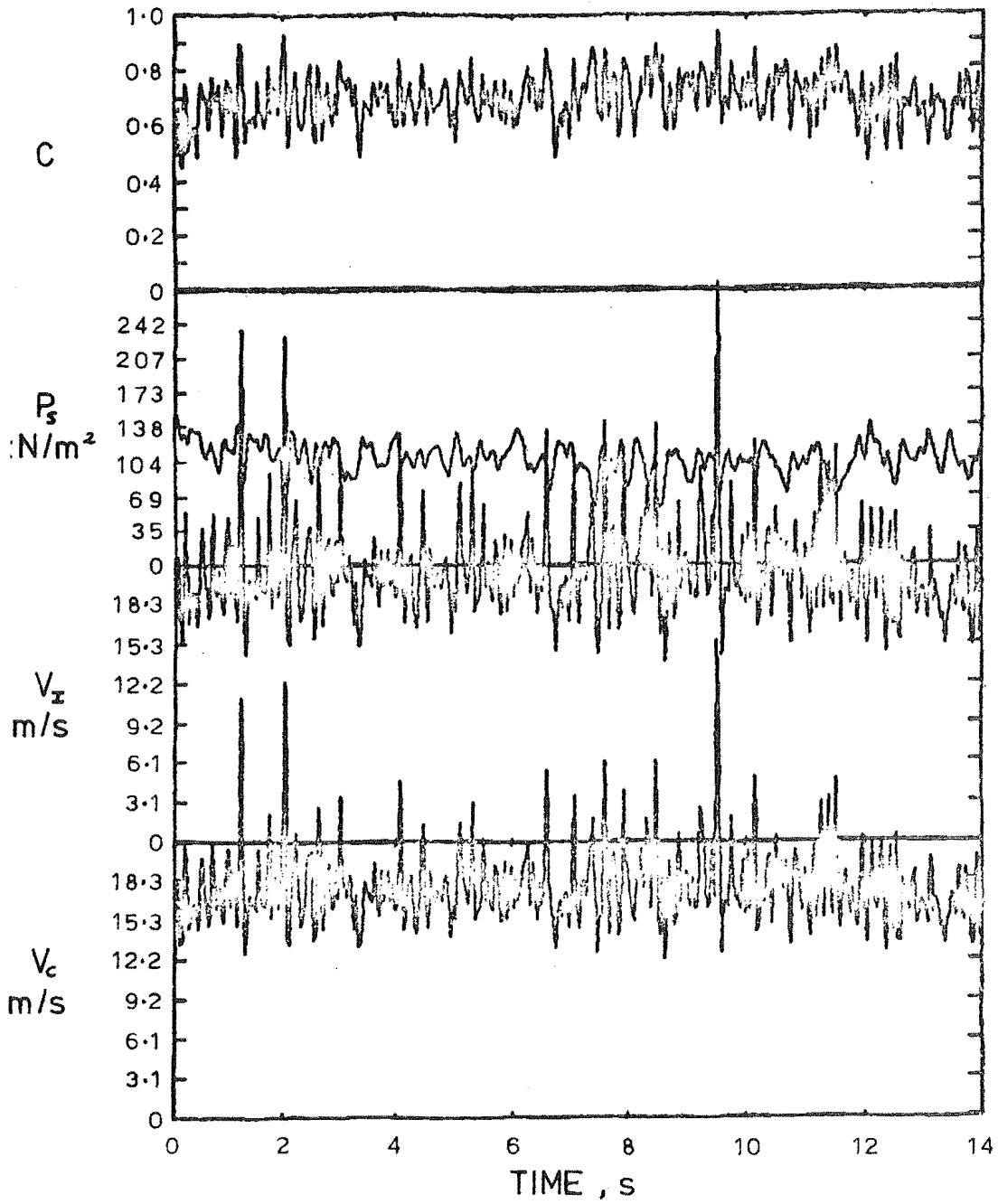

Fig. 10.31 Output Signals at y = 223 mm.

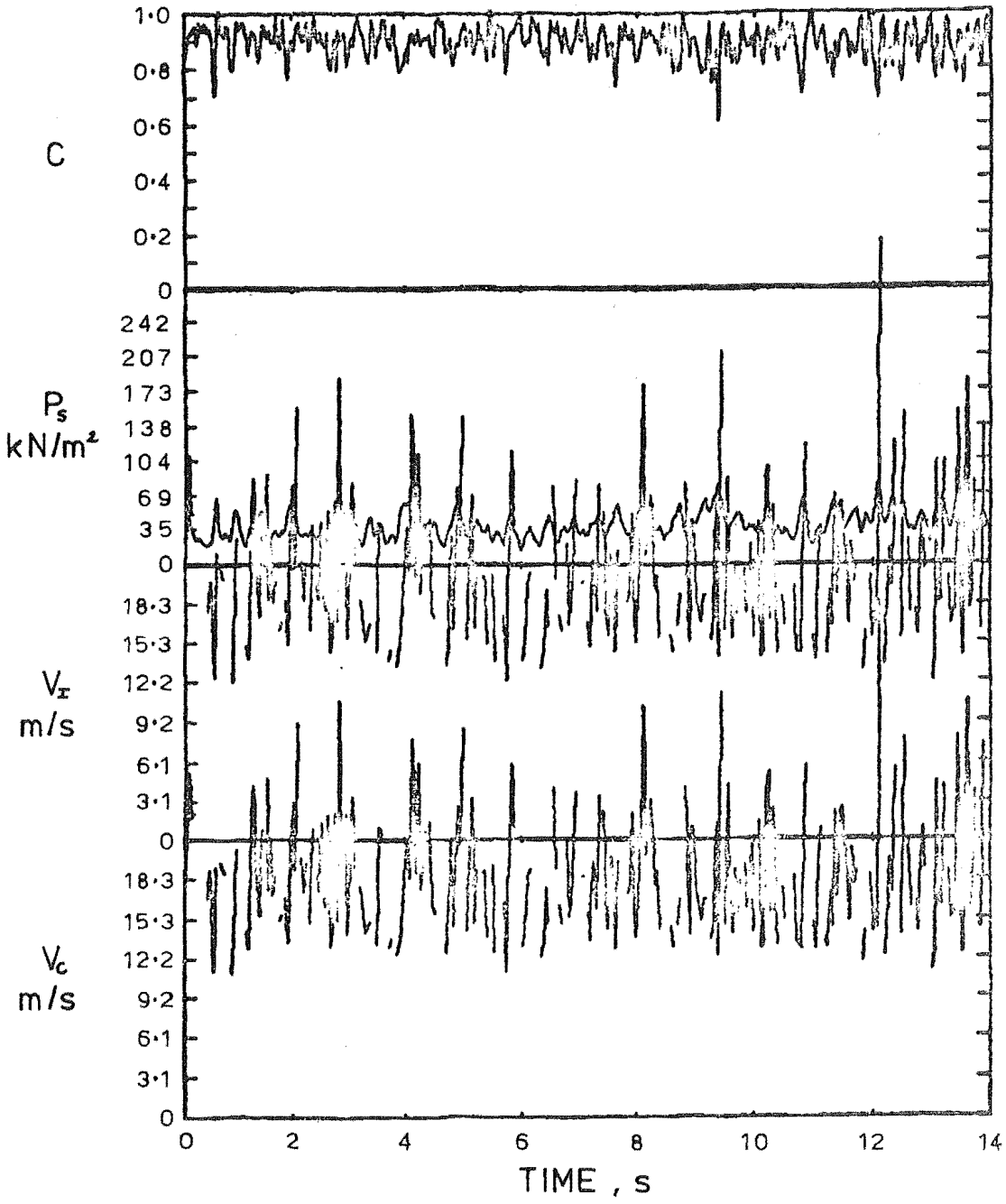

y= 282 mm , STATION 504 , GATE OPEN 450 mm

Fig. 10.32 Output Signals at y = 282 mm

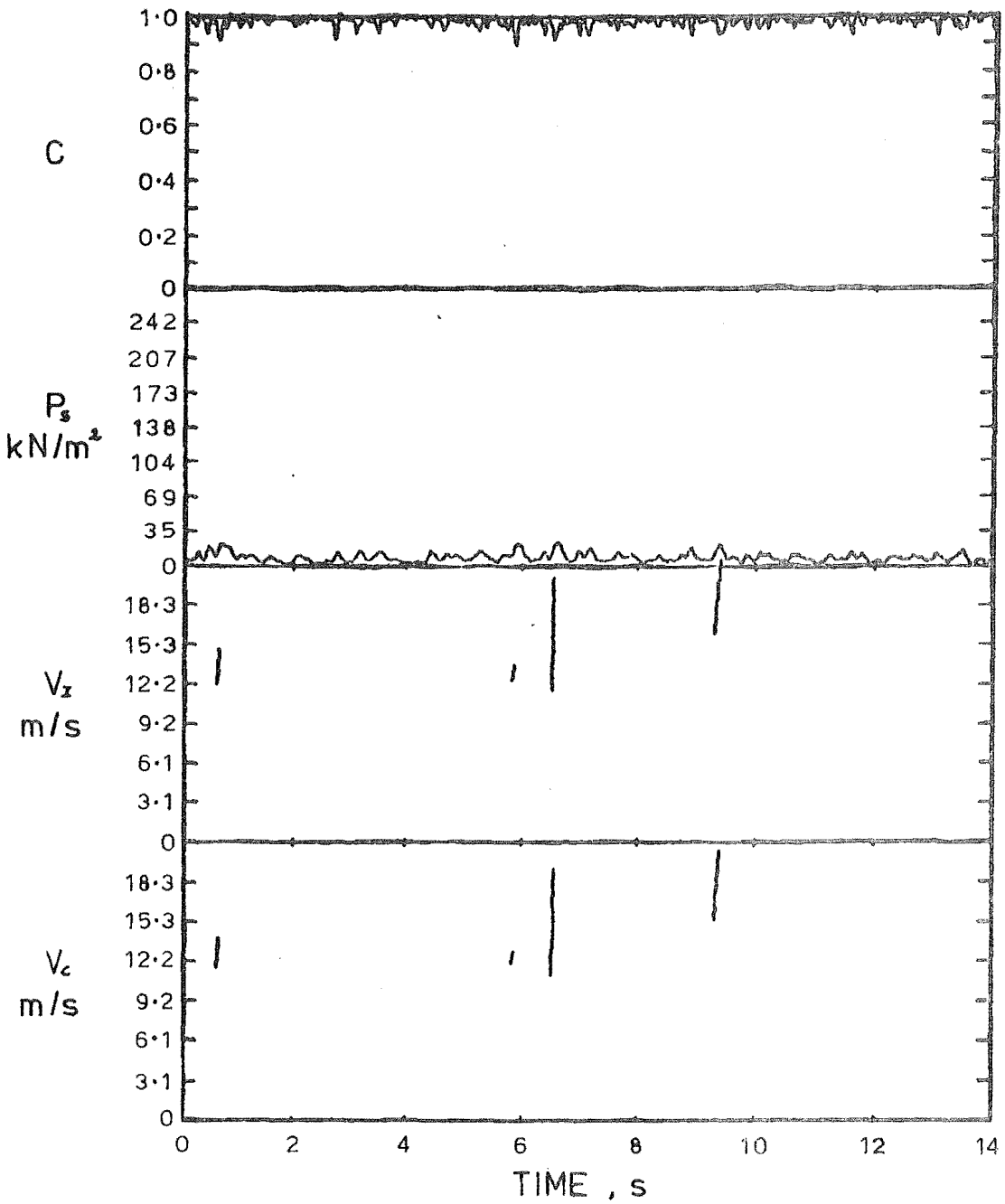

Fig. 10.33 Output Signals at y = 352 mm

They also show the difference in frequency response between the stagnation pressure and air concentration signals. This will cause fluctuations of the instantaneous velocity signals which are indistinguishable from turbulent velocity variations. The instantaneous velocity signals are therefore unreliable although the mean velocity was reliable (discussed later).

Fig. 10.34 shows the effect on the signals of a large variation in mains frequency. In this case, the air concentration signal was less than 0.0 for 65% of the time. During this period, the velocity was not calculated.

Fig. 10.35 is interesting because compared with Fig. 10.29 for instance, the stagnation pressure and air concentration signals indicate a particularly unsteady flow. It was speculated that such cases were caused by large vortices which form behind the spillway gate and appear as white lines on the flow surface, (ref. Section 1.3, Figs. 1.2 and 1.3). Such unsteady flows were rare and were only observed at station 501 with a 450 mm gate opening. It was in these cases that the mean values of stagnation pressure and air concentration differed significantly from the smooth profiles. The mean values for the data of Fig. 10.35, for instance, is indicated by the letter A in Figs. 10.3 and 10.11.

As well as the visual display unit output, various important parameters were printed on the line printer. These included the mean stagnation pressure $\bar{P}$, the mean air concentration $\bar{C}$ and the mean velocity.

The mean velocity was calculated by four different methods:

(i) As the mean values of the "incompressible" and "compressible" velocity signals (V_I and V_C) which had been generated from the stagnation

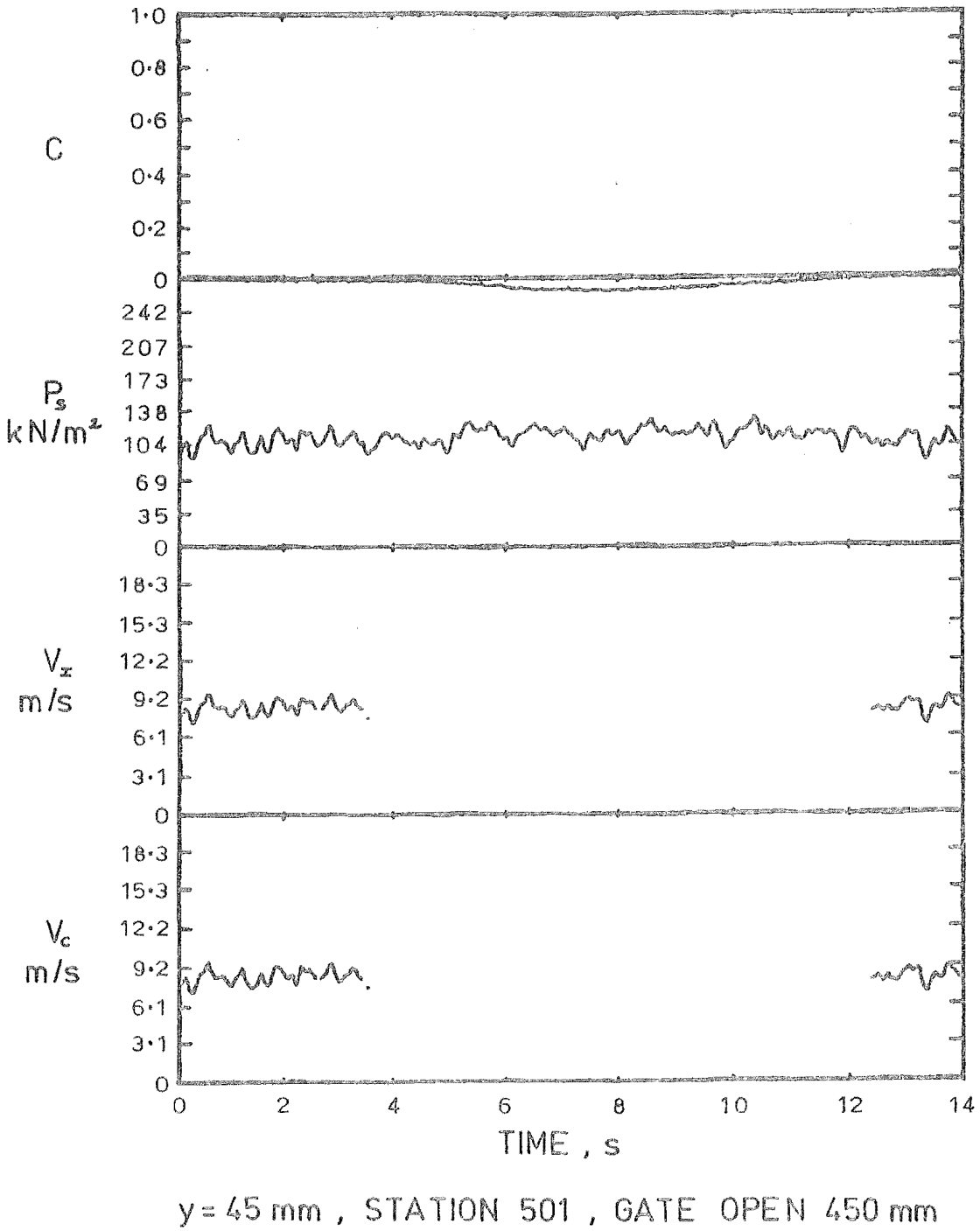

Fig. 10.34 Output Signals at y = 45 mm

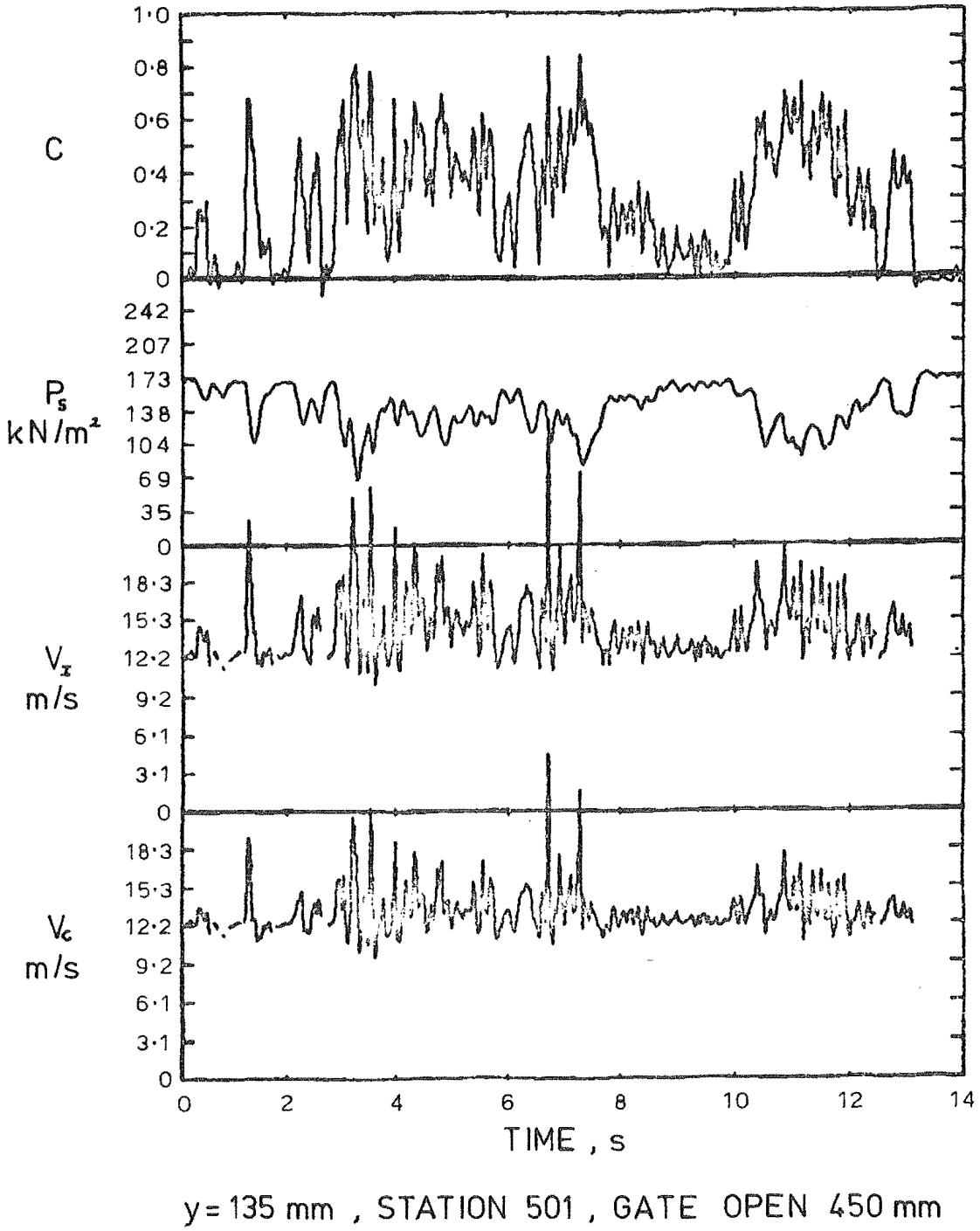

g. 10.35 Output Signals at y = 135 mm.

pressure and air concentration signals. These were denoted V_{IMEAN} and V_{CMEAN} respectively.

(ii) From the mean stagnation pressure $\overline{P}$ and air concentrations $\overline{C}$ using the "incompressible" and "compressible" velocity equations:

$$\overline{V}_I = \left[\frac{2}{\rho_w} \left[\frac{\overline{P}}{1-\overline{C}} \right] \right]^{\frac{1}{2}} \qquad 2.7$$

$$\overline{V}_C = \left[\frac{2}{\rho_w} \left[\overline{P} + \frac{\overline{C}}{1-\overline{C}} \; P_o \ln \left[\frac{\overline{P} + P_o}{P_o} \right] \right] \right]^{\frac{1}{2}} \qquad 2.8$$

If the dynamic response of the stagnation pressure and air concentration signals was identical and if there were no mains frequency variations then V_{IMEAN} should equal $\overline{V}_I$ and V_{CMEAN} should equal $\overline{V}_C$. It was found that they were almost identical at low air concentrations, differing by less than 0.5% for $\overline{C} < 0.5$. As $\overline{C}$ tends to 1.0, the differences increased because of the sensitivity of Eq's. 2.7 and 2.8. At $\overline{C} = 0.9$ for instance the differences were within 3% and on average 2%. The values $\overline{V}_I$ and $\overline{V}_C$ were considered most reliable because for these calculations, the stagnation pressure and air concentration signals have been averaged over the 14 seconds. The signals have therefore been digitally filtered to much less than 1 Hz so their dynamic response is identical.

The RMS velocity fluctuations and turbulent intensities were also calculated for the V_I and V_C signals. For mean air concentrations $\overline{C} < 0.5$, the turbulent intensities were usually in the range 0.04 - 0.10. For mean air concentrations $\overline{C} < 0.5$, these increased up to 0.18 maximum. This increase can be attributed primarily to the sensitivity of Eqs. 2.7 and 2.8. These values must be considered unreliable because of the inaccuracy of the V_I and V_C signals.

Even though the air concentration was incorrectly calculated during these analyses, it was not necessary to repeat them using the correct non-linear relationship. This is because:

(i) Velocity signals and turbulent velocity parameters could not be accurately calculated because of the poor frequency response of the pressure probe and because of the mains frequency variations. It will be recalled that the low frequency response of the pressure probe was a result of modifications necessary to prevent air entering the inlet tube.

(ii) Mean velocities were best calculated using mean values of stagnation pressure and air concentration.

It was therefore only necessary to re-analyse the air concentration data using the correct non-linear relationship as already described. The mean velocities could then be calculated as described in the following section.

10.4.2 Mean Velocity Calculations

The smoothed profiles of mean stagnation pressure $\overline{P}_s$ (Fig. 10.4) and air concentration $\overline{C}$ (Fig. 10.12) from the non-linear analysis plus the smoothed T profiles (Fig. 10.26) were used to calculate mean velocity profiles on the Burroughs computer using Eqs. 2.7, 2.8 and 2.14, i.e.

$$\overline{V}_I = \left[\frac{2}{\rho_w}\left[\frac{\overline{P}_s}{1-\overline{C}}\right]\right]^{\frac{1}{2}} \qquad 2.7$$

$$\overline{V}_C = \left[\frac{2}{\rho_w}\left[\overline{P}_s + \frac{\overline{C}}{1-\overline{C}}\, P_o \ln\left[\frac{\overline{P}_s + P_o}{P_o}\right]\right]\right]^{\frac{1}{2}} \qquad 2.8$$

$$\overline{V}_T = \left[\frac{2}{\rho_w}\left[\frac{\overline{P}_s}{T} + \left[\frac{T-(1-\overline{C})}{1-\overline{C}}\right] P_o \ln\left[\frac{\frac{\overline{P}_s}{T} + P_o}{P_o}\right]\right]\right]^{\frac{1}{2}} \qquad 2.14$$

These have again been written for stagnation pressures expressed in gauge units (ref. Section 2.5) and with the static pressure P assumed equal to the atmospheric pressure P_o = 102 kN/m^2 (abs).

The velocity profiles calculated have been plotted as broken lines in Figs. 10.36 to 10.40, the smallest dashes for $\overline{V}_I$, the next size for $\overline{V}_C$ and the largest for $\overline{V}_T$. The velocity profiles V_X (Fig. 10.20) measured by the cross-correlation technique have been superimposed for comparison, plotted as continuous lines.

Keller's (1972) results have been superimposed as circles. These were calculated using Eq. 2.7. At stations 502, 503 and 504 at 203 mm from the spillway, he predicted velocities of 33.1, 29.3 and 30.5 m/s. These are not shown here as they are too large for this scale.

Once again the velocities $\overline{V}_I$, $\overline{V}_C$ and $\overline{V}_T$ have only been calculated for $\overline{C} < 0.95$ because of the sensitivity to errors in the stagnation pressure or air concentration measurements as $\overline{C}$ tends to 1.0.

In the lower regions of the flow, T = 1.0 so that $\overline{V}_T = \overline{V}_C$ and the two profiles are superimposed. In the upper regions when $\overline{C}$ tends to 0.95, $\overline{V}_T$ is sometimes larger than either $\overline{V}_C$ or $\overline{V}_I$.

Of the three equations used here to calculate velocity, only Eq. 2.14 attempts to account for the compressibility of an air-water mixture and the wavy surface of self-aerated flows. Eqs. 2.7 and 2.8 are plotted in Figs. 10.36 to 10.40 simply for comparison with Eq. 2.14. The remainder of this section considers the $\overline{V}_T$ profiles and their accuracy.

The $\overline{V}_T$ profiles have been superimposed in Fig. 10.41 for comparison. In the lower depths these show a trend of increasing velocity with distance down the spillway, as expected. In the upper regions when $\overline{C}$ tends to 0.95, these profiles are less reliable because of the sensitivity of Eq. 2.14.

It is apparent that the calculated velocities $\overline{V}_T$ are usually larger than the velocities V_X measured with the correlation technique.

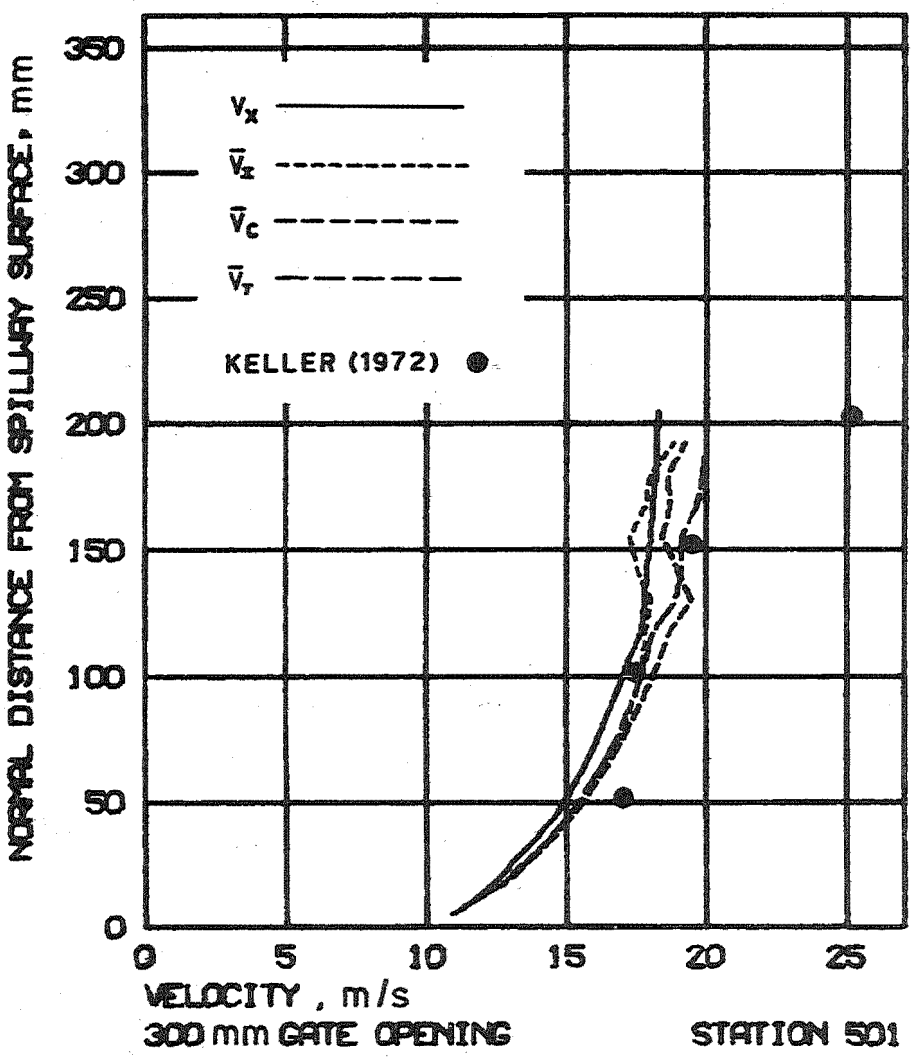

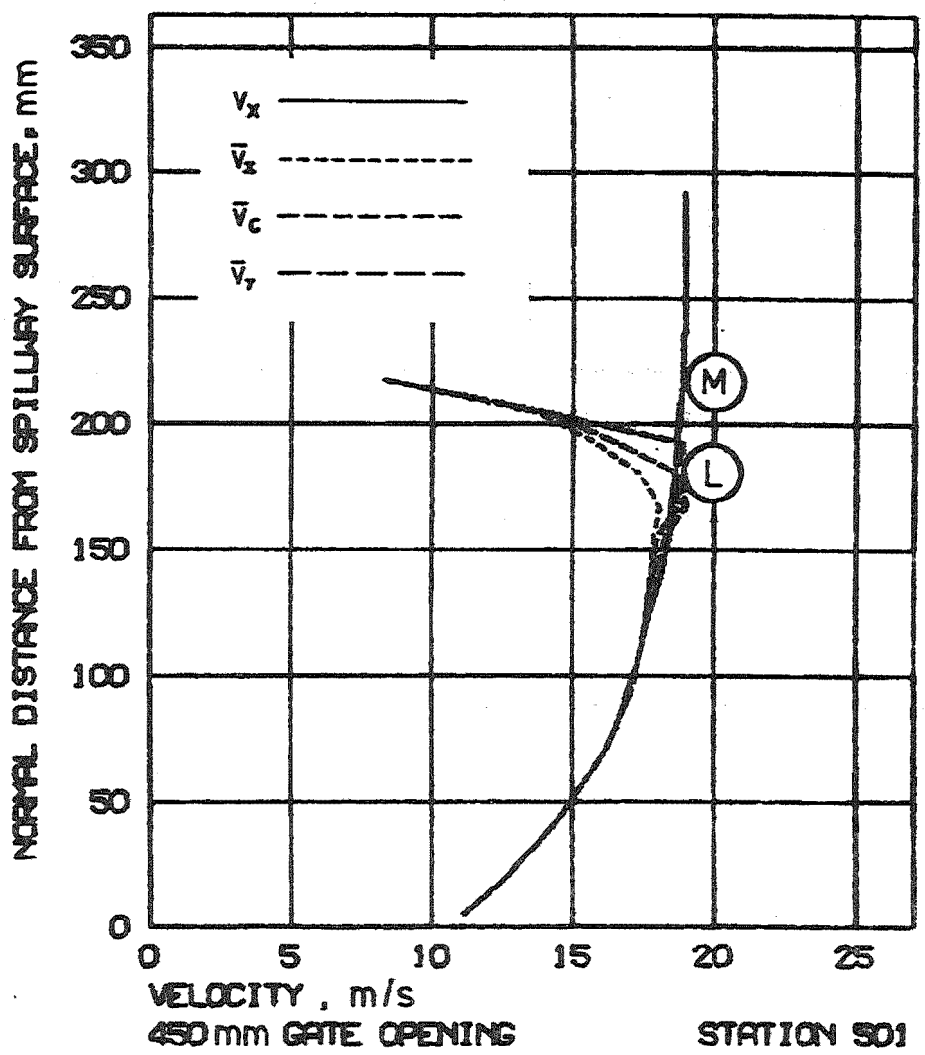

Fig. 10.36 Calculated Velocity Profiles.

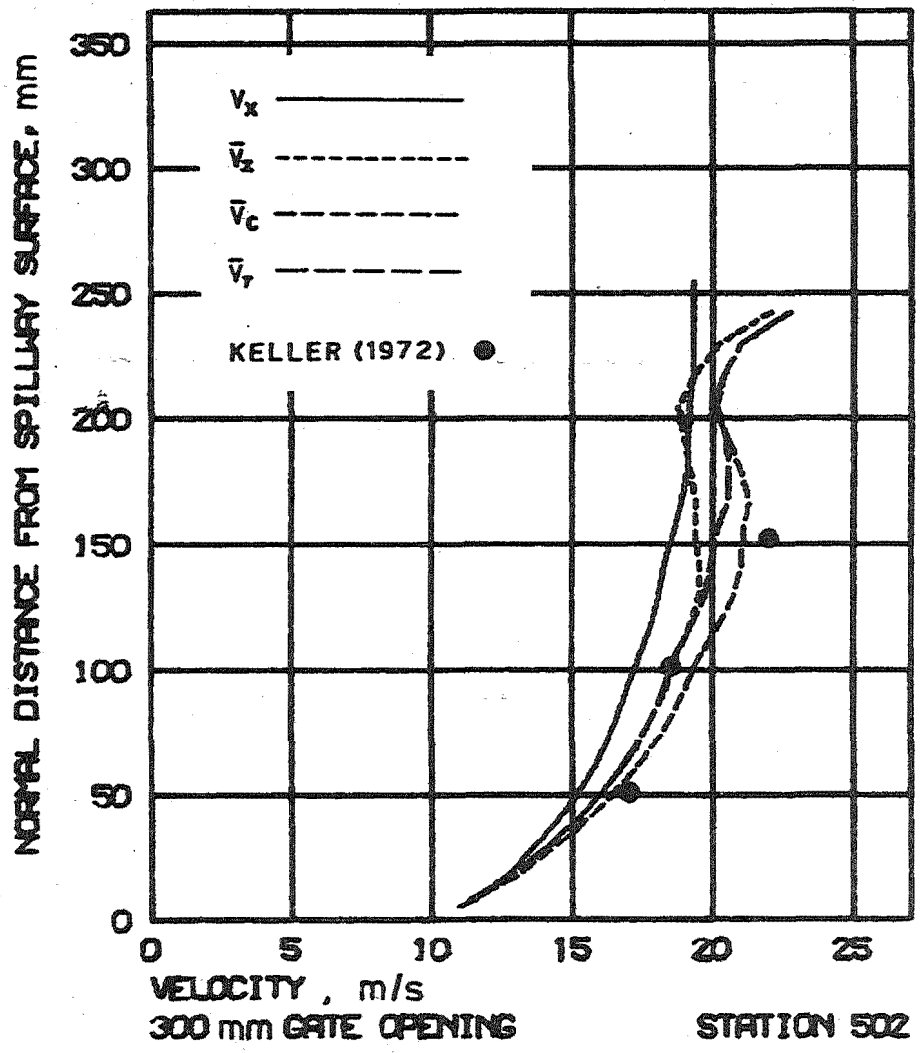

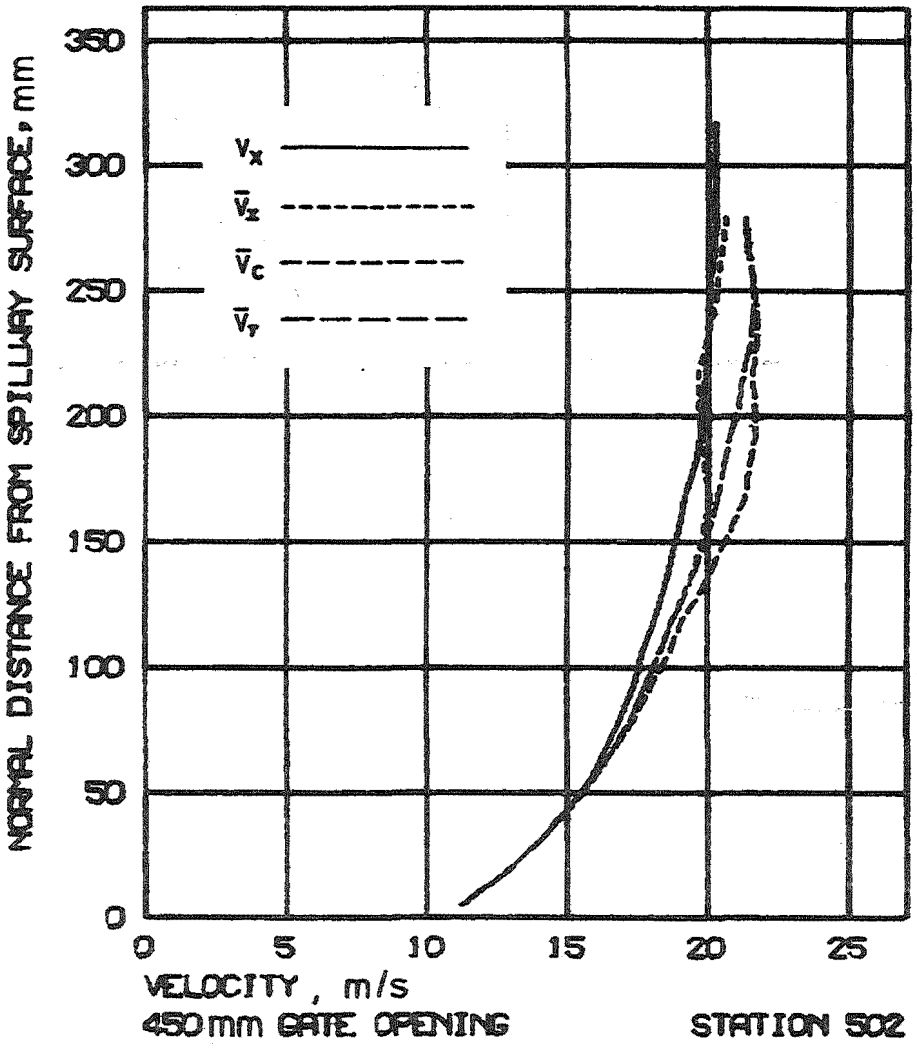

Fig. 10.37 Calculated Velocity Profiles.

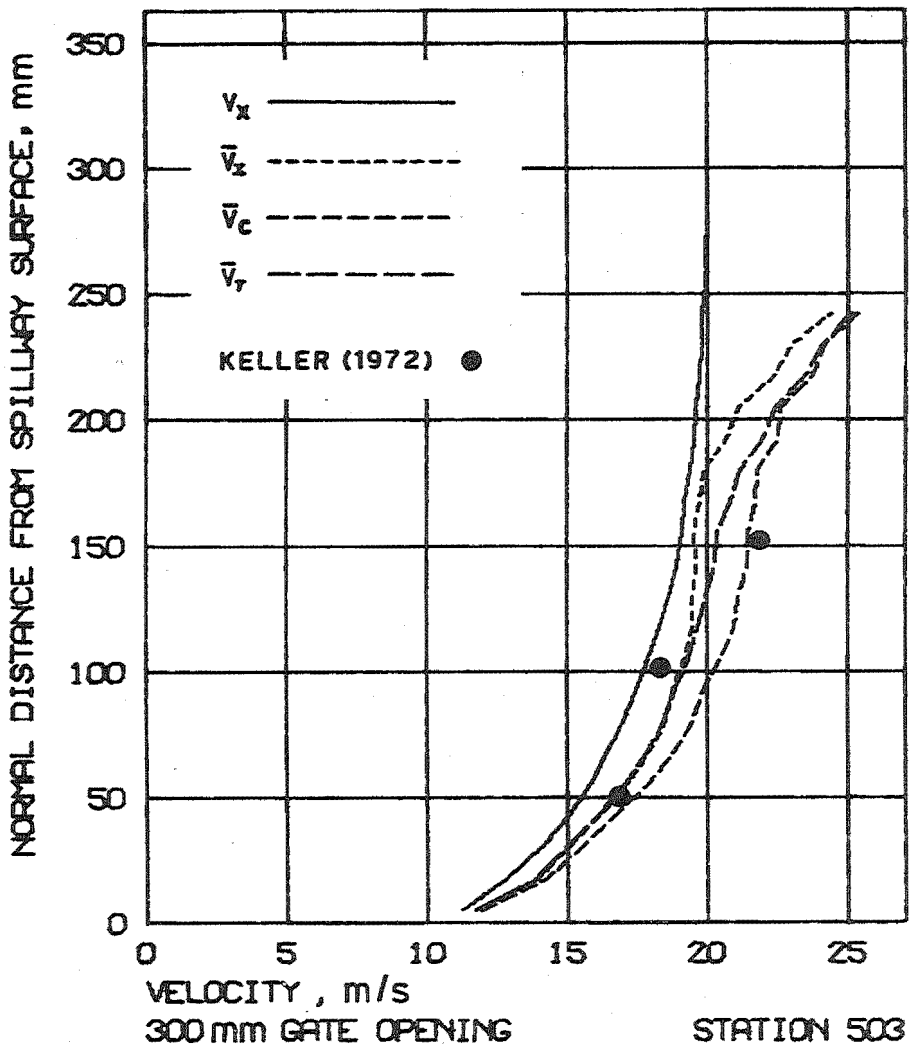

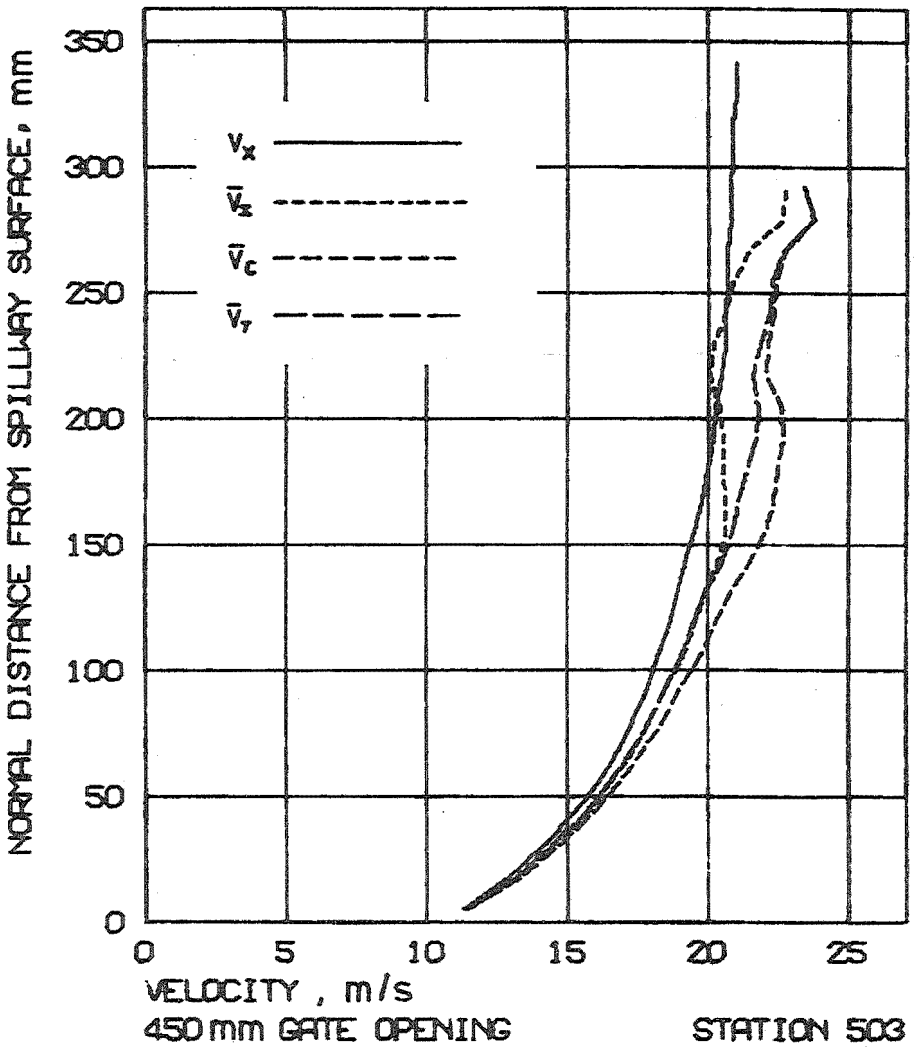

Fig. 10.38 Calculated Velocity Profiles.

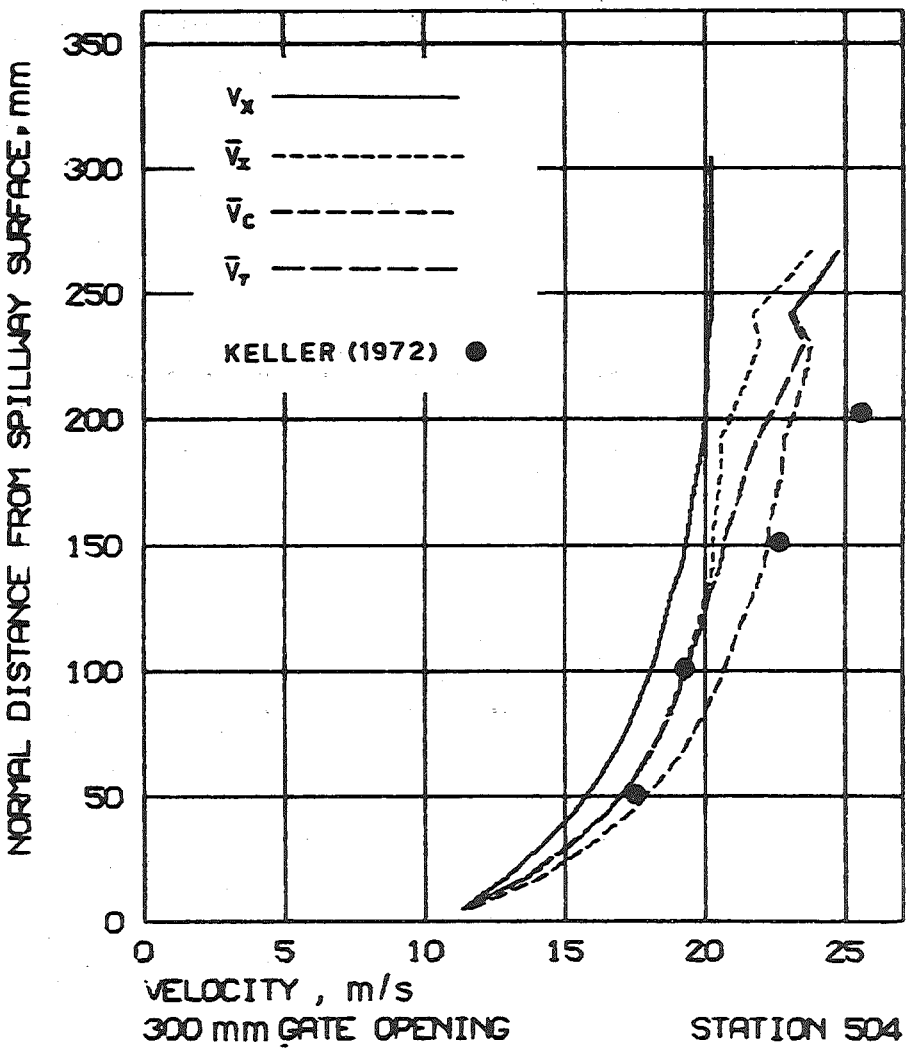

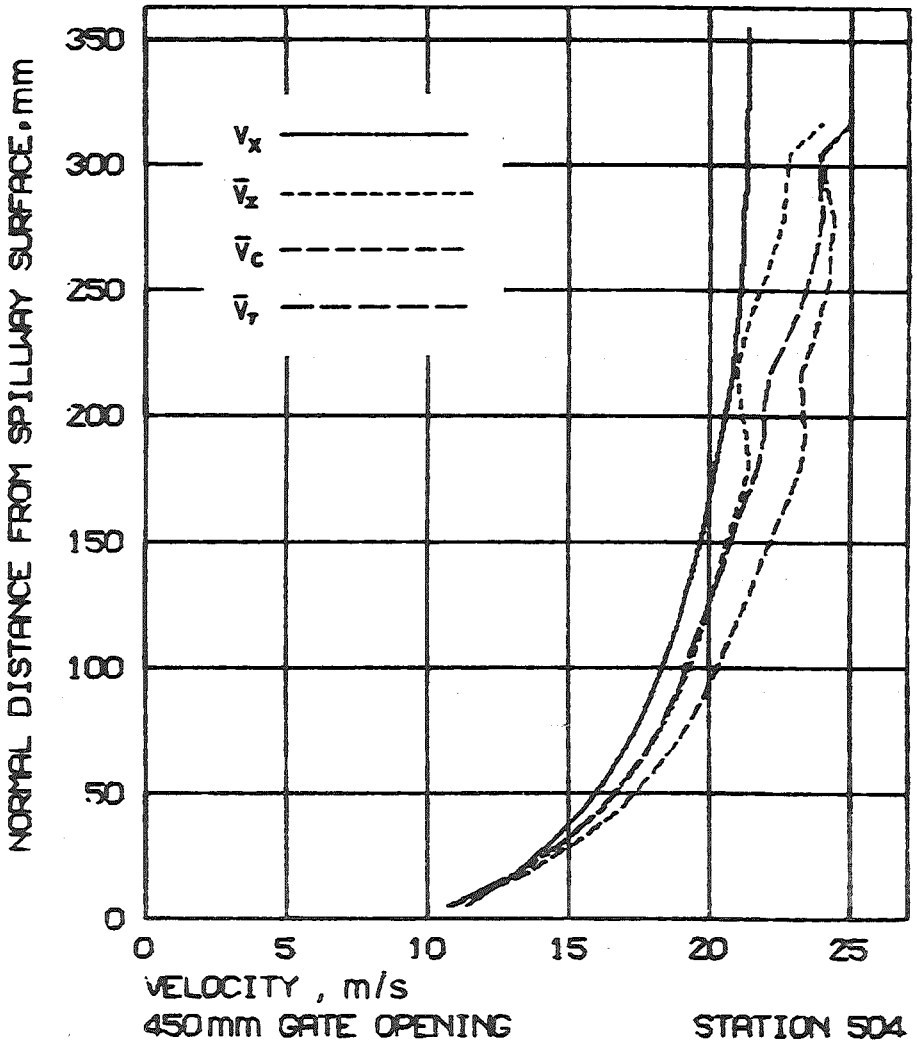

Fig. 10.39 Calculated Velocity Profiles.

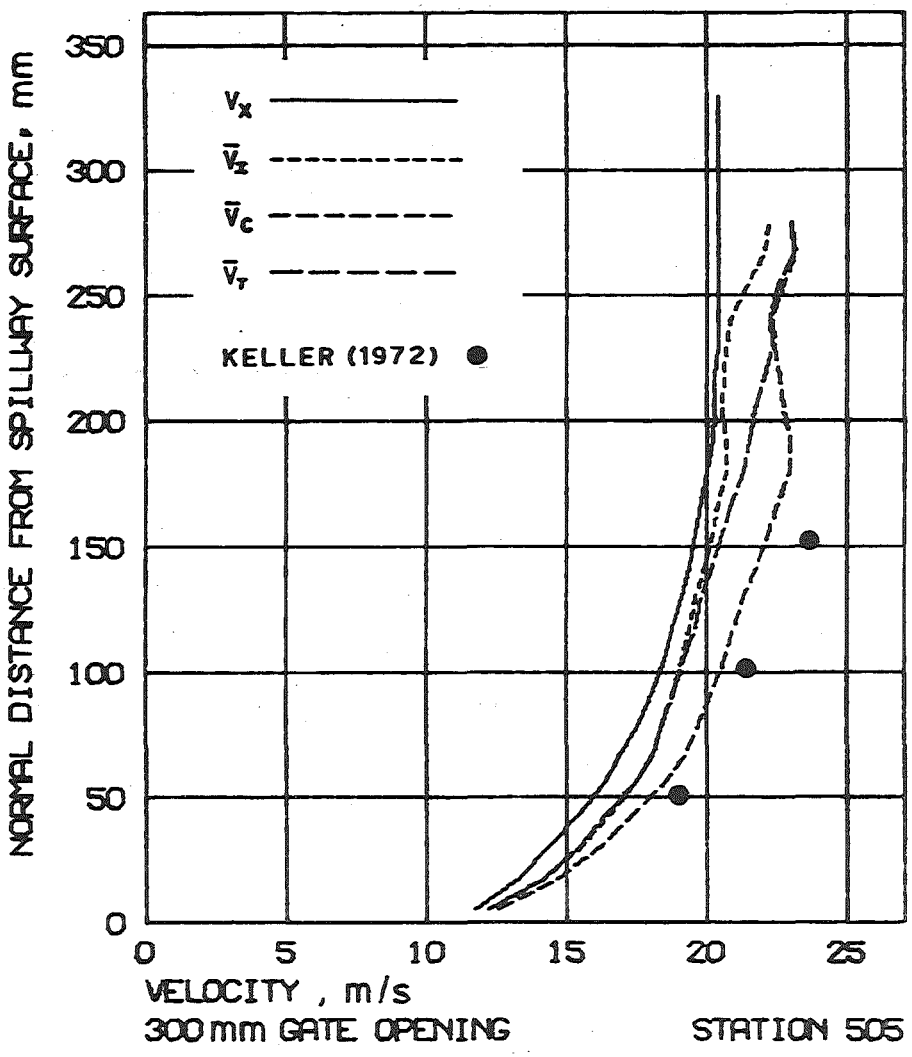

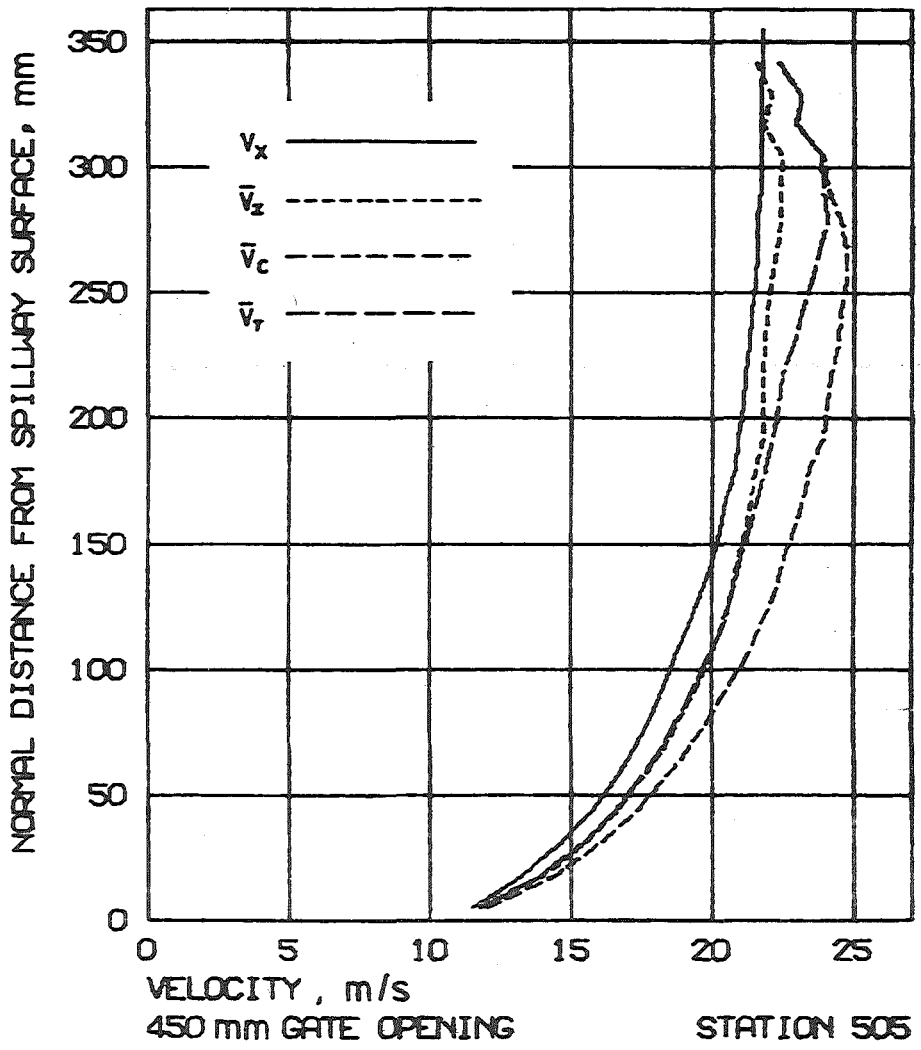

Fig. 10.40 Calculated Velocity Profiles.

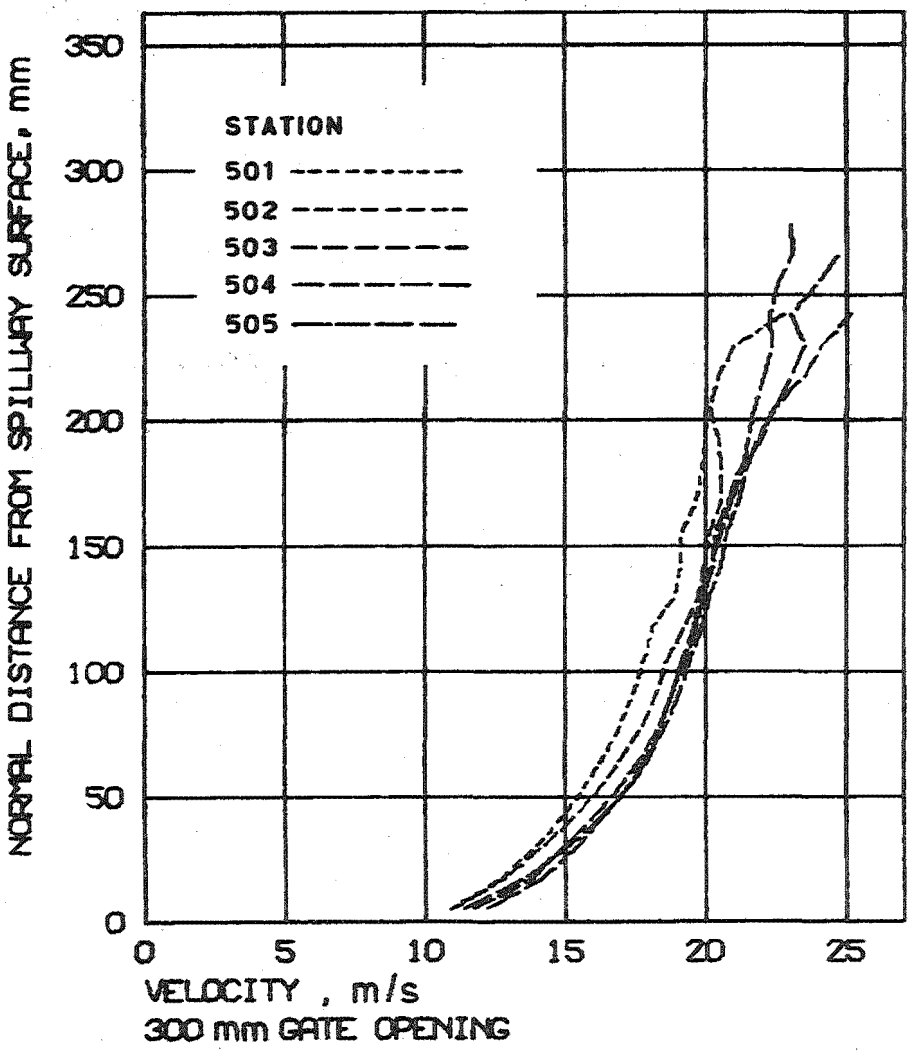

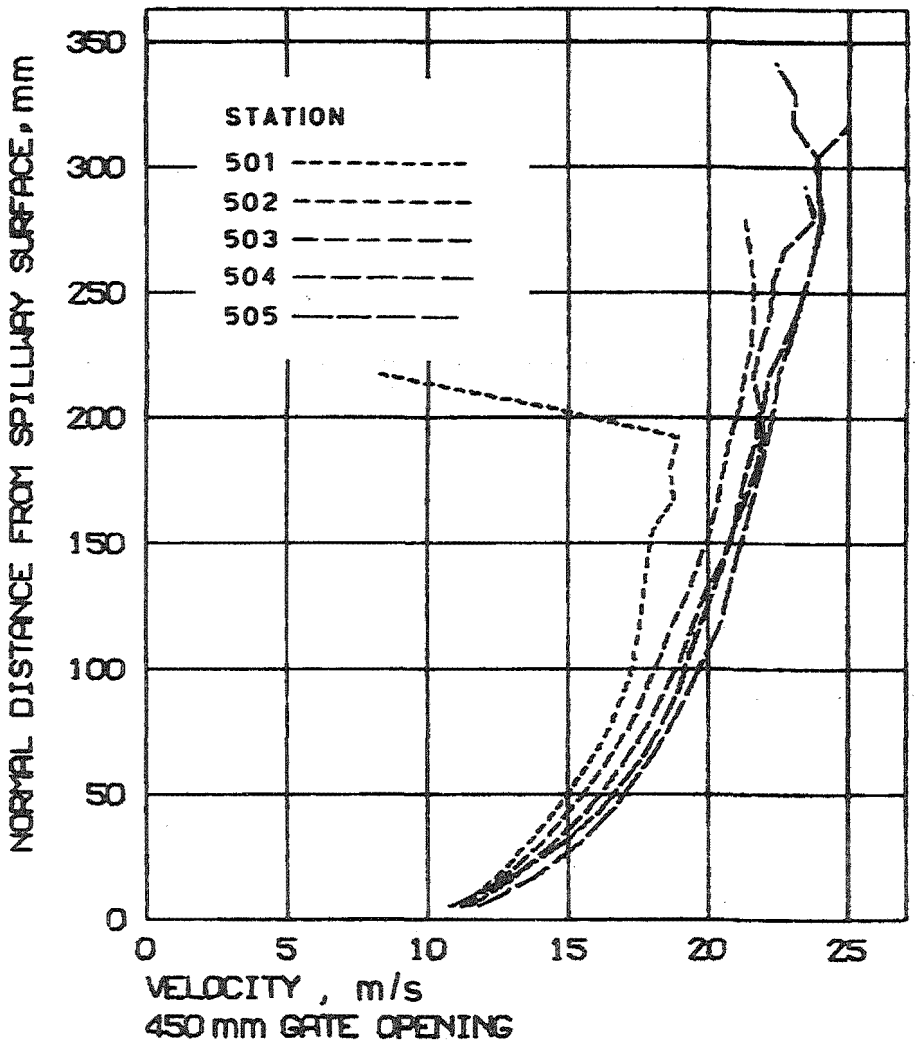

Fig. 10.41 Calculated Velocity Profiles.

In order to investigate this difference, it is convenient to henceforth assume that the measured profiles V_X are correct.

The percentage overestimation of the $\overline{V}_T$ profiles is plotted in Fig. 10.42 as a function of the mean air concentration $\overline{C}$. As $\overline{C}$ does not vary linearly with depth, the individual points have also been plotted.

Most curves show a similar trend, with about 7% overestimation for $0.2 < \overline{C} < 0.7$. This difference increases to about 10 - 20% at $\overline{C} = 0.9$ and decreases to about 0% at $\overline{C} = 0$. The exception is station 501 with a 450 mm gate opening. Referring to Fig. 10.36 it is only the relatively small aerated region L-M that shows most variation.

Fig. 10.42 is based on the measurements of intermittency parameter calculated as the integral of the probability density functions from C = 0 - 0.7. For the intermittency parameters calculated as the integral from C = 0 - 0.6 and C = 0 - 0.8, the corresponding plots have been presented in Appendix P (Figs. P.3 and P.4). In each case, the curves are very similar up to $\overline{C} = 0.7$. This is because the velocity equation (2.14) is insensitive to small variations or errors in T at low air concentrations. At air concentrations tending to 0.95, the differences between Figs. 10.42, P.3 and P.4 increases. This reflects the sensitivity of Eq. 2.14 to any errors, whether in stagnation pressure, air concentration or intermittency parameter measurements.

10.4.3 Validity of Eq. 2.14

It was stated in Section 2.4 that Eq. 2.14 was expected to overestimate the velocity. This is because Eq. 2.8, from which it was derived, did not account for the phenomenon of slip and thermal exchanges between the bubbles and water in the vicinity of the stagnation point.

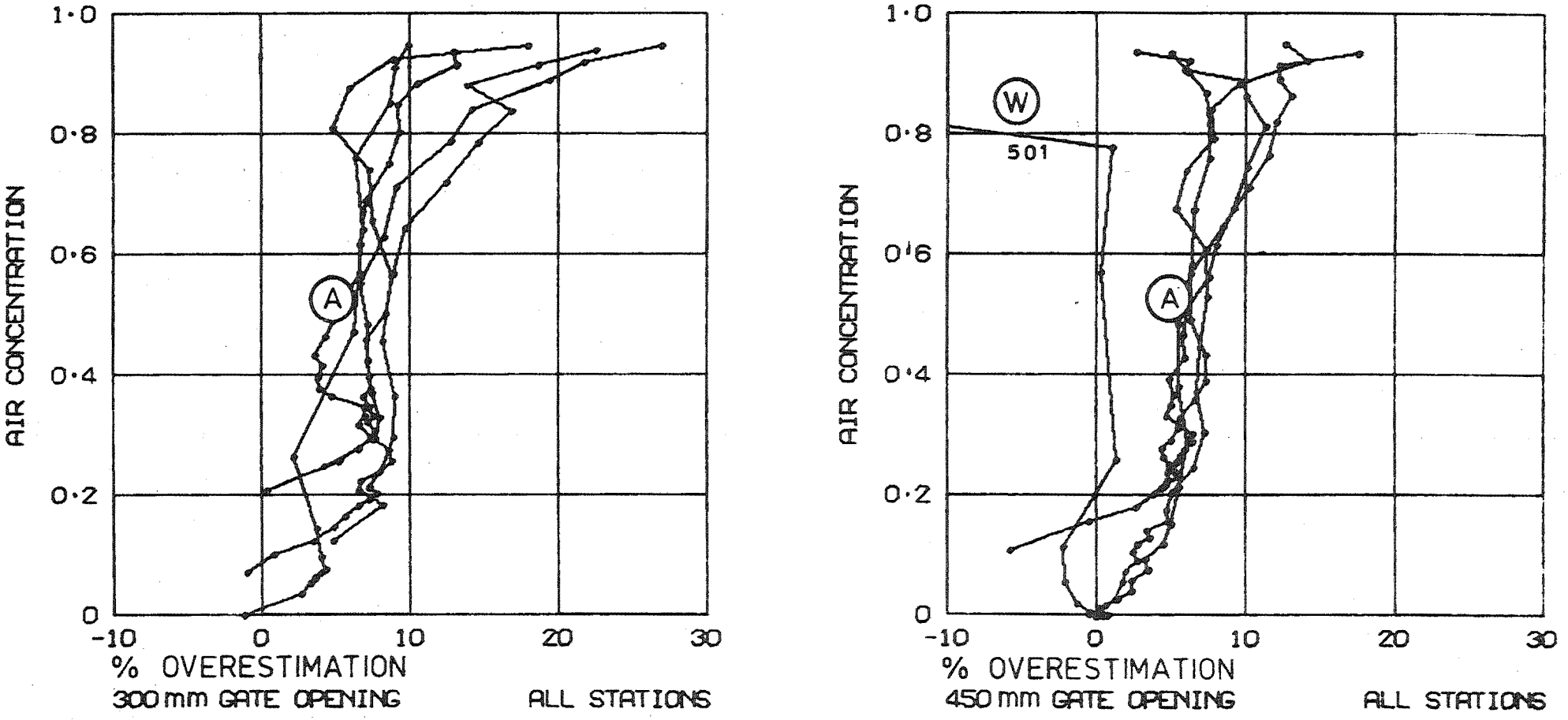

Fig. 10.42 Percentage Overestimation of Calculated Velocity.

Before investigating this further, consider first the possibility that errors in either $\overline{P_s}$, $\overline{C}$ or T have caused the overestimation of velocity in Fig. 10.42, and that Eq. 2.14 is in fact correct.

If only the $\overline{C}$ profiles are in error, the correct profiles can be obtained by substituting V_X, $\overline{P_s}$ and T into Eq. 2.14 and solving for $\overline{C}$. The difference between these is the "error". It has been found best to plot this against the measured air concentration, expressed as a percentage of its range (FS = 1.0). These errors are shown in Fig. 10.43. The error is a maximum of about 10% or 0.1 at $\overline{C} \simeq 0.3$ and decreases to about zero at $\overline{C} = 0.0$ and 1.0. That such small errors in $\overline{C}$ can cause such large errors in V_X as $\overline{C}$ tends to 1.0 is due to the sensitivity of Eq. 2.14. It is considered unlikely that an error as large as 0.1 would have occurred at $\overline{C} \simeq 0.3$. (See results of calibration tests, Section 6.5.4).

If only the $\overline{P_s}$ profiles are in error, a similar analysis yields the almost identical error curves shown in Fig. 10.44. These have also been plotted against the measured air concentration, expressed as a percentage of their range (FS = 175 kN/m^2). It is possible that the stagnation pressures, although measured correctly, have been overestimated because of the presence of the air concentration electrodes. This possibility is best investigated by replotting the above errors, this time expressed as a percentage of the mean pressure measured at the point under consideration. These are shown in Fig. 10.45. In the calibration tests of Section 6.5.2, it was found that the pressure was overestimated by about 5% at an air concentration approximately 0.15. This value is shown as the point B in Fig. 10.45. It seems possible then that an overestimation of stagnation pressure may have contributed to the overestimation of velocity in Fig. 10.42.

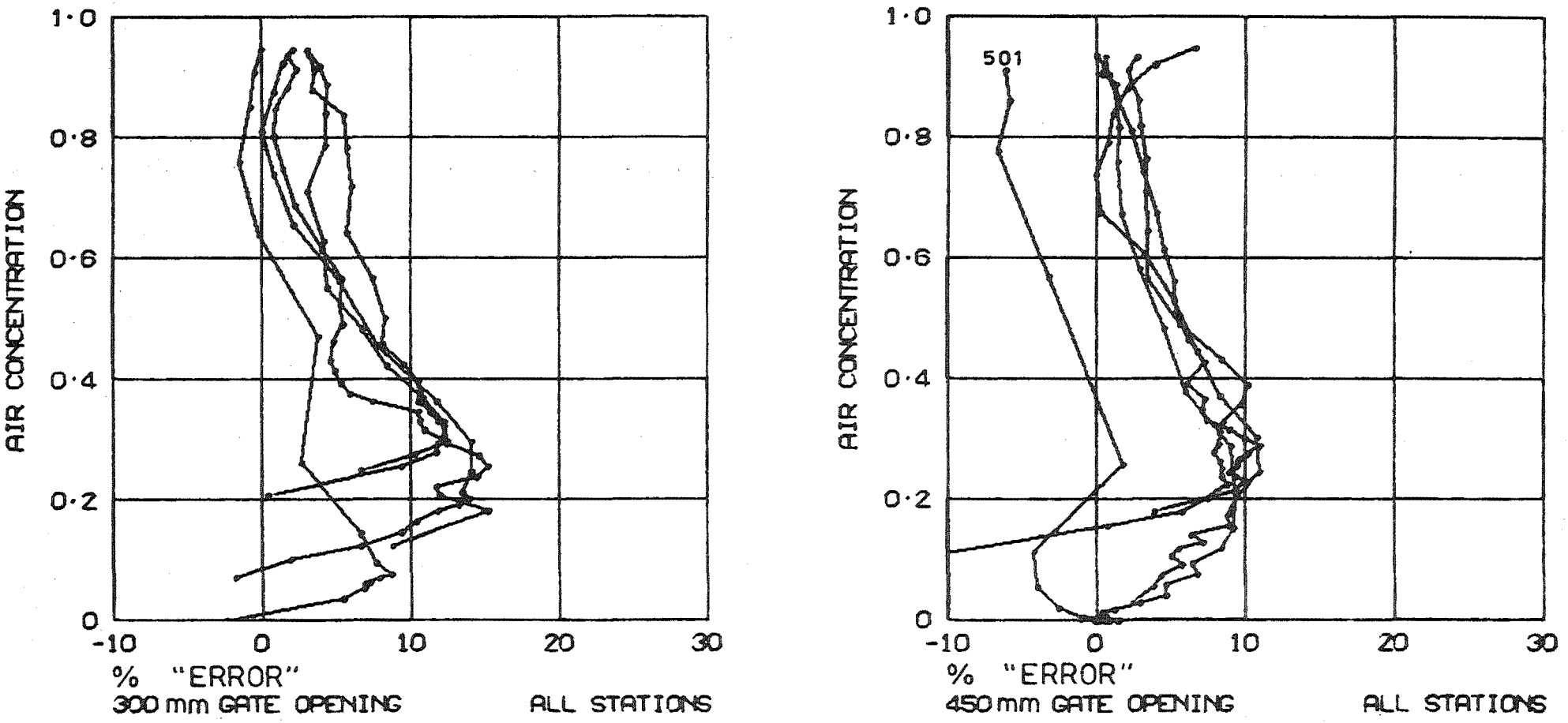

Fig. 10.43 Percentage "Error" of Measured Air Concentration, Expressed as a Percentage of FS = 1.0

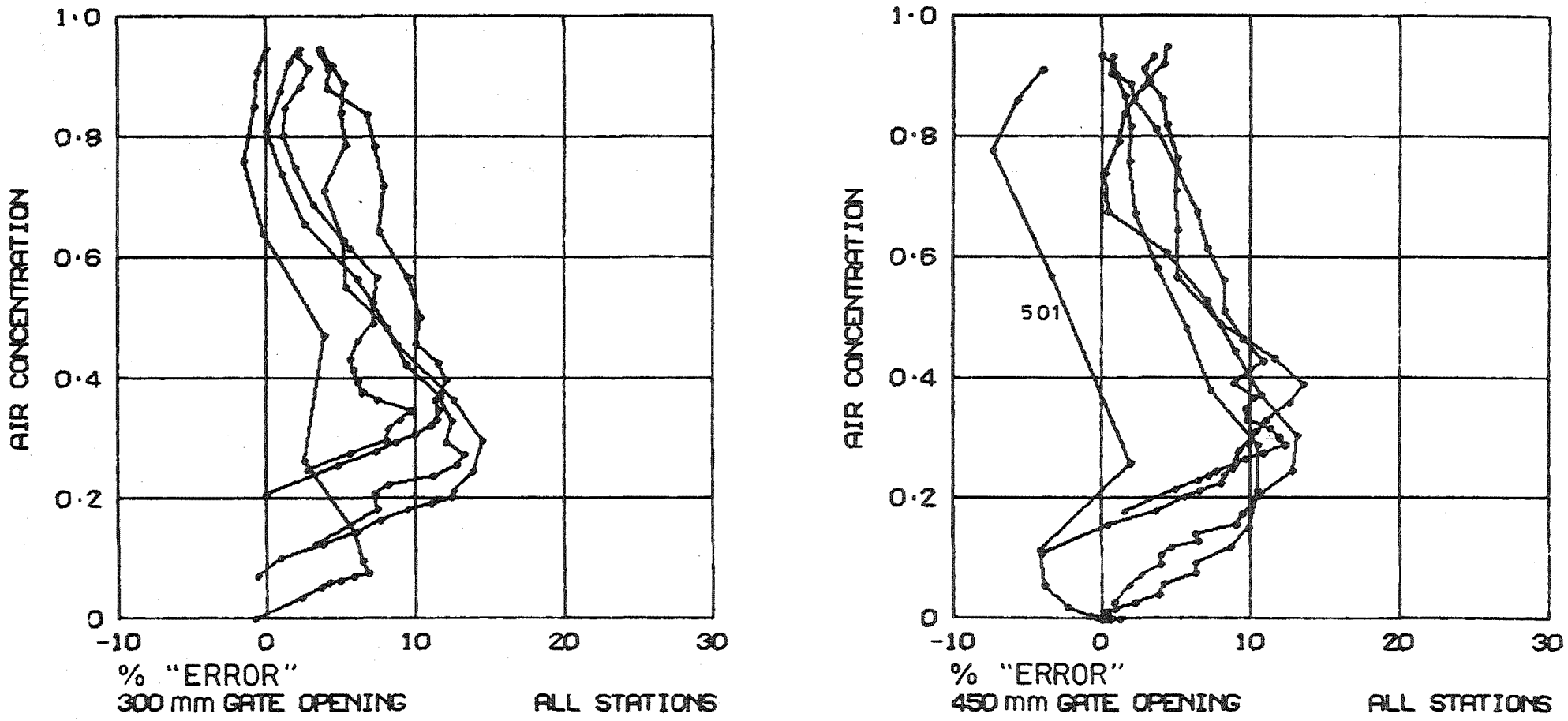

Fig. 10.44 Percentage "Error" of Measured Stagnation Pressure Expressed as a Percentage of FS = 175 kN/m^2

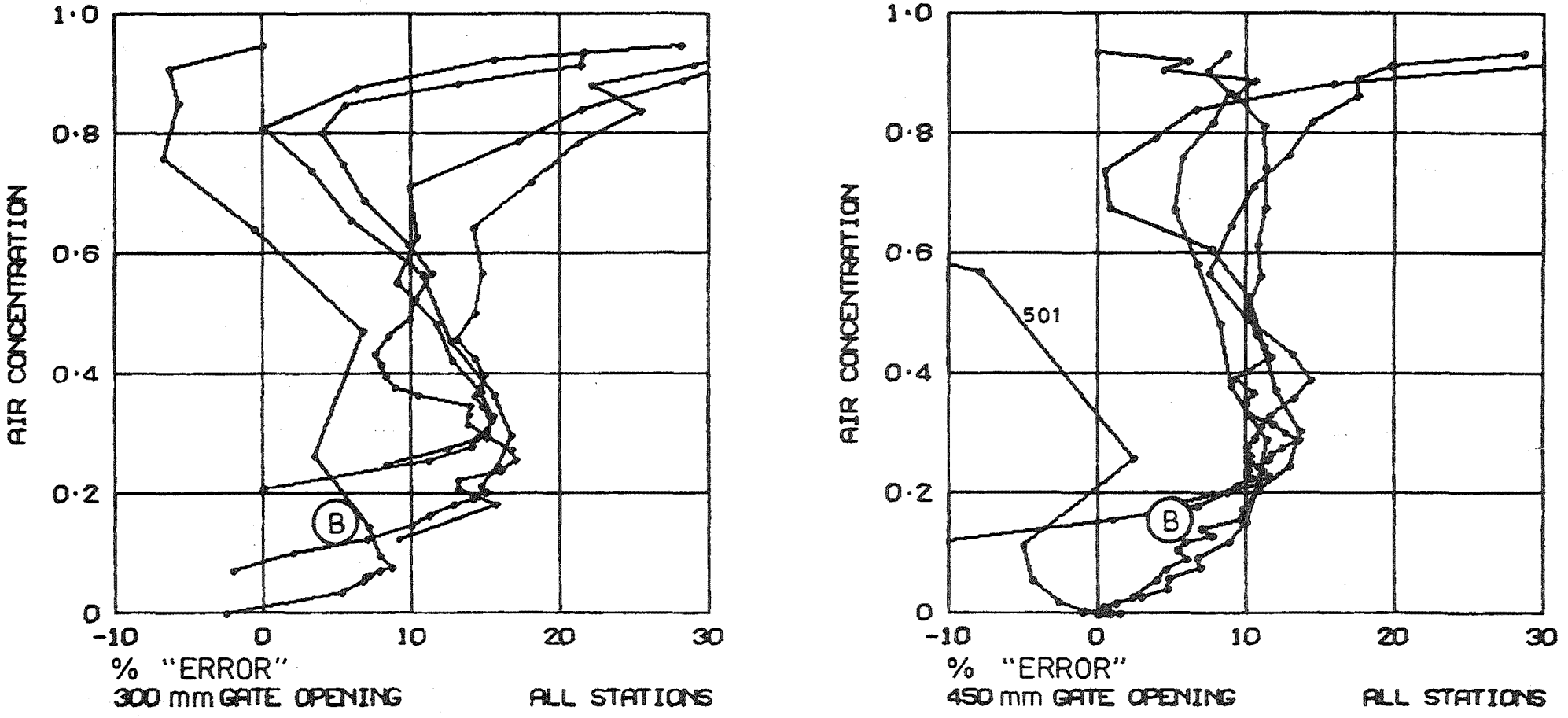

Fig. 10.45 Percentage "Error" of Measured Stagnation Pressure Expressed as a Percentage of the Measured Stagnation Pressure.

Inaccuracies in the intermittency factor T may have contributed also. Referring to Figs. 10.36 to 10.40, the $\overline{V}_C$ profile overestimates the velocity V_X in most instances. Errors in T alone could therefore not cause the overestimation of velocity.

While it is possible that errors in $\overline{P}_s$, $\overline{C}$ and T have contributed to the overestimation of velocity, it does seem likely that the basic Eq. 2.8 is also responsible. Sterlini and Trotignon (1971) found Eq. 2.8 (from which Eq. 2.14 was derived) overestimated the velocity by about 5% in aerated flows with mean velocities 10 - 25 m/s and mean air concentrations from 0.5 - 0.55. This is shown as the point A in Fig. 10.42 and is seen to be consistent with these results. This comparison is not strictly valid because in wavy regions of self-aerated flows, the mean air concentration will be larger than the mean air concentration within the water surface. This discrepancy is considered minor at these air concentrations.

10.5 ADJUSTED AIR CONCENTRATION PROFILES

10.5.1 Water Discharge

The water discharge was calculated for each station and each gate opening from the measured profiles of velocity V_X (Fig. 10.20) and air concentration $\overline{C}$ (Fig. 10.12). (It will be recalled that the V_X profiles of velocity measured by the correlation technique were considered more reliable than the $\overline{V}_T$ profiles calculated from $\overline{P}_s$, $\overline{C}$ and T). This provided a check on the accuracy both of these measurements and of the spillway gate opening. The discharge per unit width q was calculated as

$$q = 0.01245 \sum_{I=1}^{LIMIT} V_{XI}(1-\overline{C}_I) \qquad (m^2/s)$$

where I refers to the Ith point from the spillway surface (Eq. 10.1).

0.01254 m is the spacing between adjacent points

LIMIT is the value of I when $\overline{C}$ = 0.95.

The choice of $\overline{C}$ = 0.95 for LIMIT was dictated by the maximum air concentration for station 505 with a 450 mm gate opening. This choice is not critical for discharge calculations because there is so little water in this region. The proportion of water from this point to the highest measurement point was calculated as only 1% on average.

The results are shown in Table 10.1. The variations from the mean water discharge are relatively large, the maximum being for station 501. For the 300 and 450 mm gate openings, the variations at this station are 9.4 and 7.6% of the respective mean values. The variations in water discharge are caused by errors in the V_X and $\overline{C}$ profiles or by variations in the spillway gate opening for the measurements at different stations.

Table 10.1 Water Discharge q and Variation from Mean q

		Station					Mean
		501	502	503	504	505	q
300 mm Gate Opening	q, m^2/s	2.02	2.36	2.12	2.32	2.34	2.23
	Variation from mean	-0.21	0.13	-0.11	0.09	0.11	
450 mm Gate Opening	q, m^2/s	2.91	3.26	3.11	3.16	3.32	3.15
	Variation from mean	-0.24	0.11	-0.04	0.01	0.17	

In Section 9.4 it was stated that the mechanism indicating the gate opening ensured that it was opened by the same amount at each station, to within 1%; but that variations in its initial closed position were possible because of the spillway gate seal.

Ministry of Works measurements on model studies indicate an almost linear relationship between the gate opening and discharge, as would be expected. The difference in discharge δq between the discharge for the 300 and 450 mm gate openings should therefore be identical for all stations, regardless of the gate's initial closed position. It follows that any variations between the calculated values of δq can be attributed to errors in the measured V_x and $\bar{C}$ profiles. The calculated values of δq were simply obtained from Table 10.1 and are shown in Table 10.2.

Table 10.2 Differences in Water Discharge δq and Variations from Mean δq

	Station					Mean
	501	502	503	504	505	δq
$\delta q, m^2/s$	0.89	0.90	0.99	0.84	0.98	0.92
Variation from mean	-0.03	-0.02	0.07	-0.08	0.06	

The variations in δq (Table 10.2) are relatively small. The maximum value of 0.08 m^2/s for instance is only $\frac{1}{3}$ the maximum variation in q (Table 10.1) of 0.24 m^2/s. It can be shown that an error of 0.08 m^2/s can be caused by errors of only 1-2% in the measured V_x and $\bar{C}$ profiles.

Given the accuracy of the measured profiles, it seems almost certain that the relatively large variations in q (Table 10.1) are caused mainly by variations in the initial position of the spillway gate. That the discharge at station 501 (Table 10.1) is much less than at any other station is caused by a particularly large initial compression of the rubber gate seal. This can be expected since the spillway gate was closed for several weeks prior to the first test.

10.5.2 Development of Self-Aeration Down the Spillway

In order to investigate the development of air entrainment down the spillway, it is desirable that the spillway gate opening and thus the water discharge be identical for the tests at each station. It has in fact been possible to adjust the profiles of mean air concentration to compensate for the variations in the gate opening. This was only possible because at any station, there is almost no difference between the velocity profiles for the 300 and 450 mm gate openings, (see Fig. 10.21). These velocity profiles can therefore be considered correct in spite of the minor variations in the initial gate position during these tests.

Profiles of mean air concentration, adjusted for variations in the gate opening, are shown in Figs. 10.46 to 10.48 as broken lines. It will be shown that the water discharges calculated with these is within 1% of the mean values of Table 10.1. Their construction from the measured profiles, shown as solid lines in Figs. 10.46 to 10.48 is explained below.

At any station, contours of air concentration profiles can be envisaged, corresponding to different gate openings. Only two of these have been measured, corresponding to 300 and 450 mm gate openings. Others can be constructed from these if we assume the ratio of the

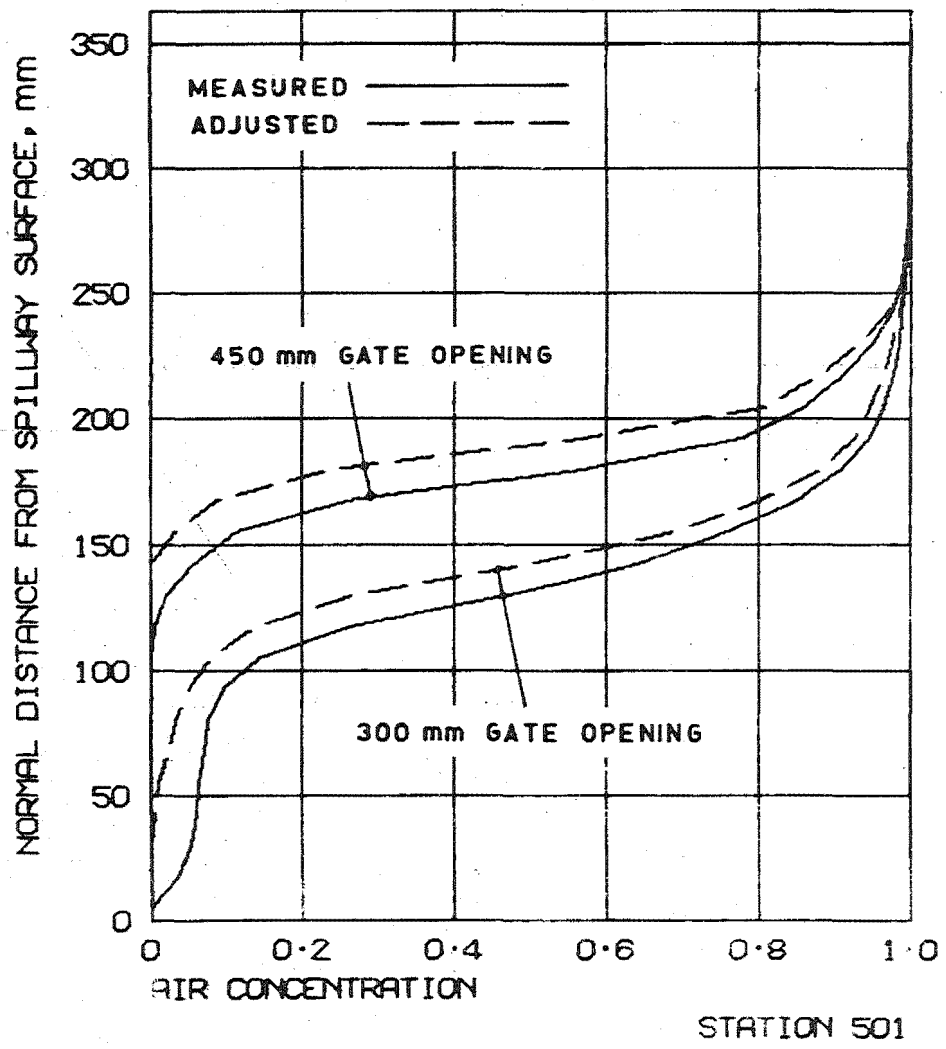

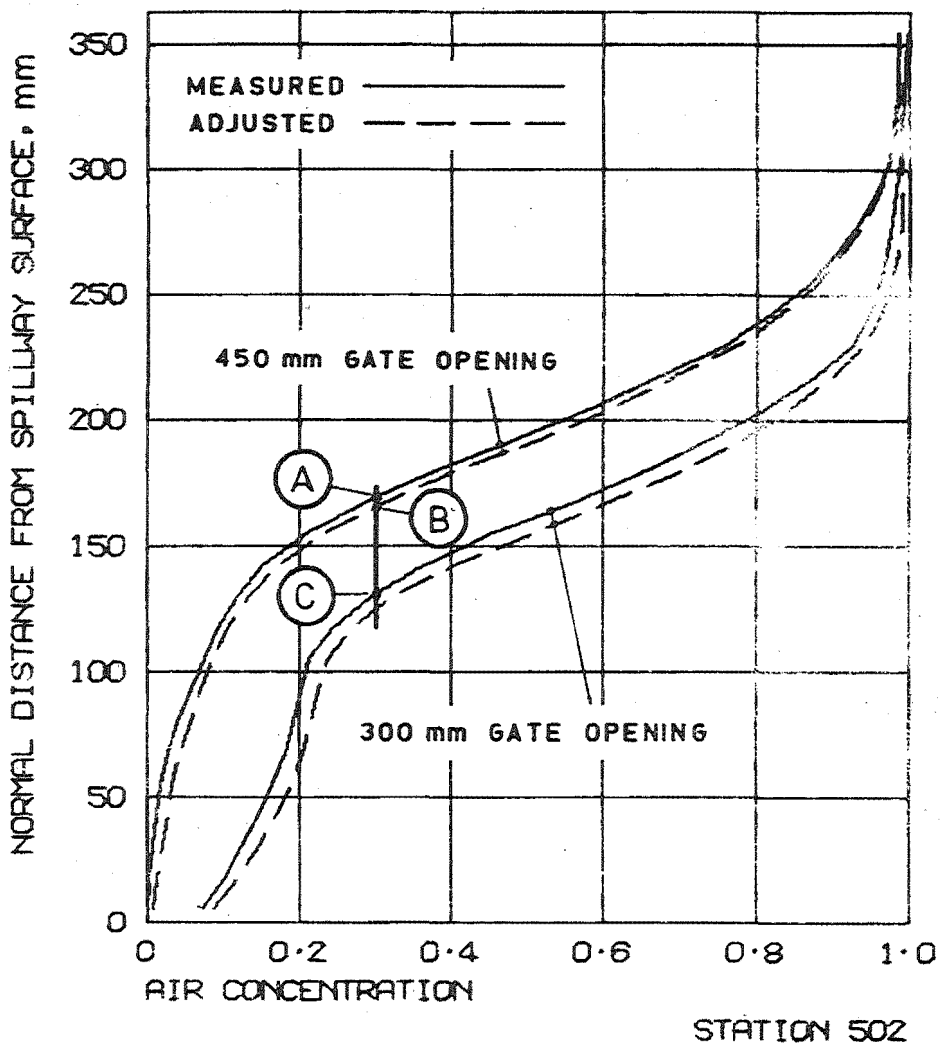

Fig. 10.46 Air Concentration Profiles.

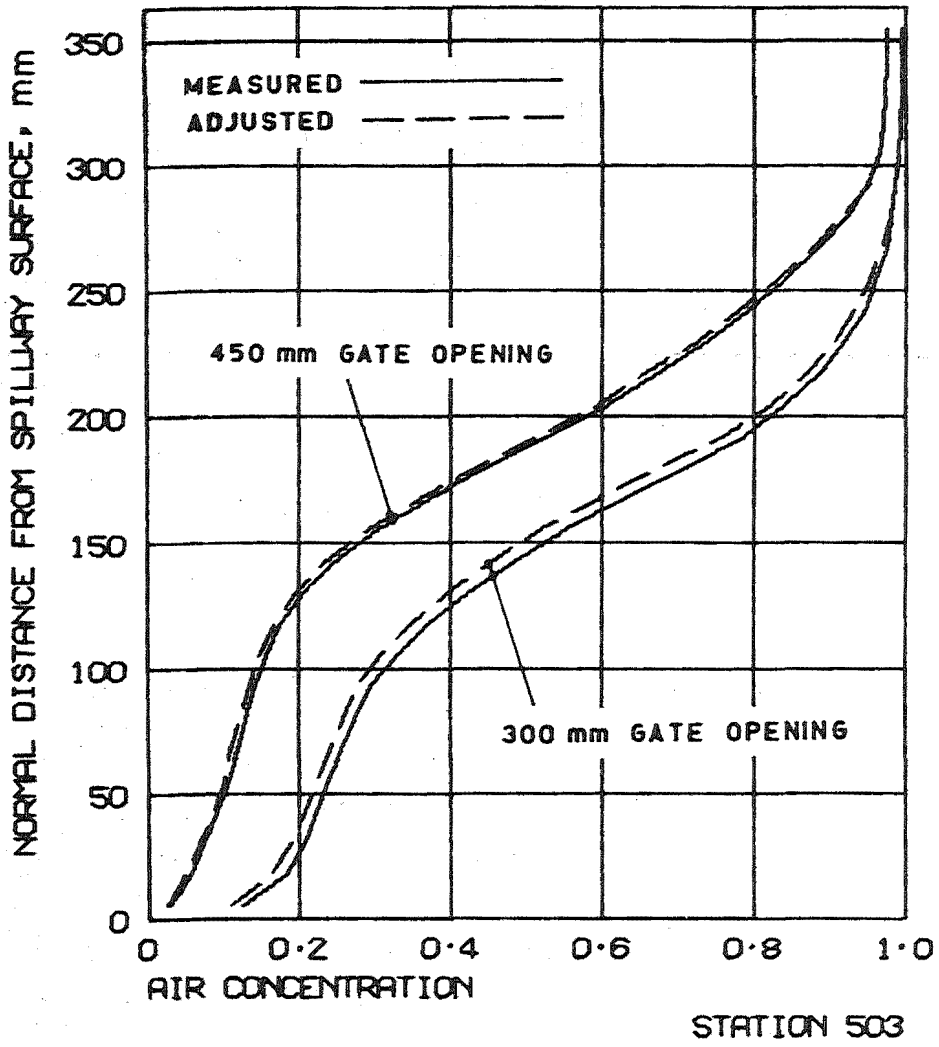

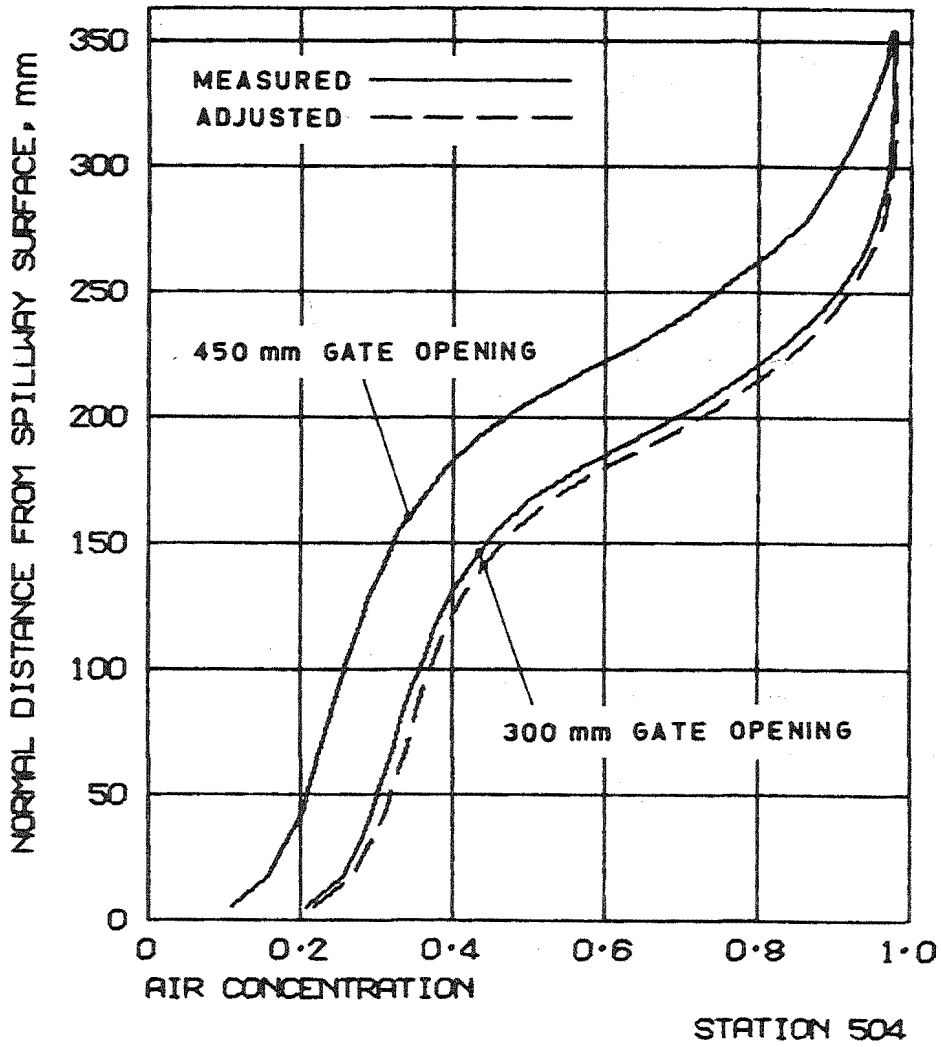

Fig. 10.47 Air Concentration Profiles.

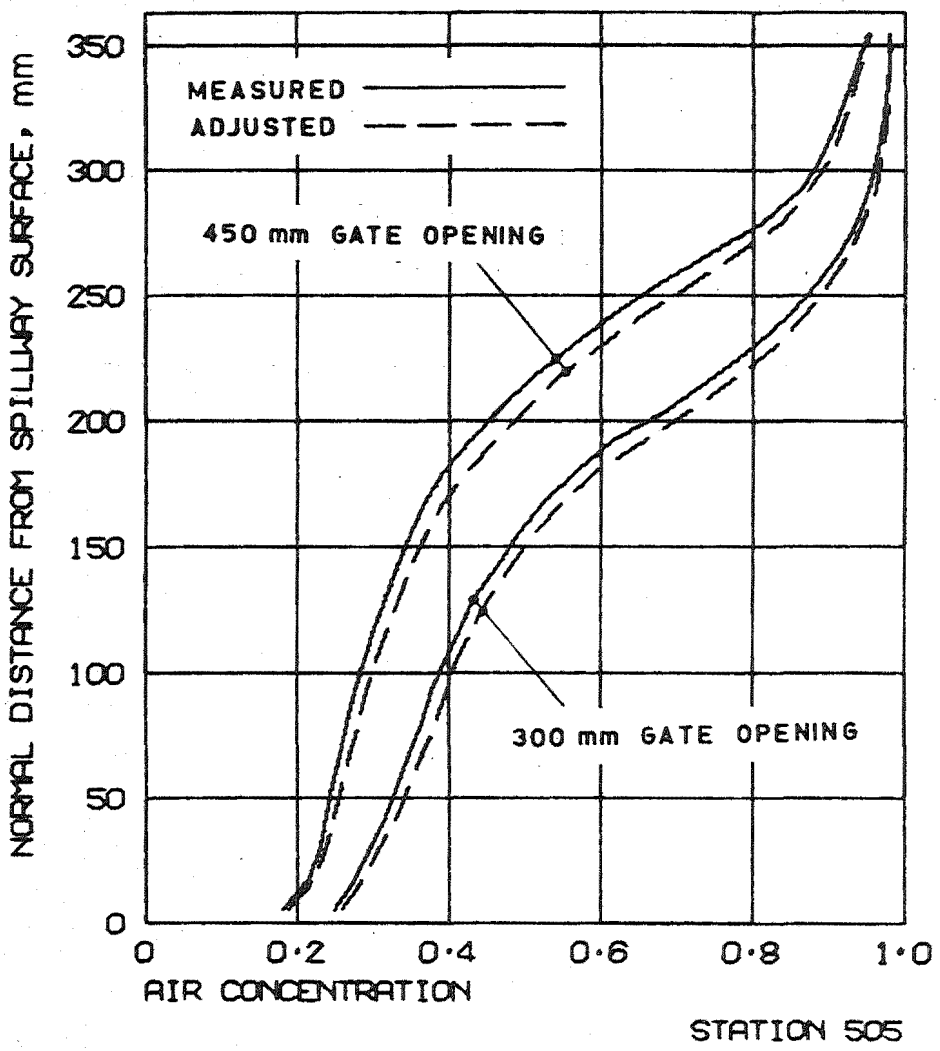

Fig. 10.48 Air Concentration Profiles.

distances separating adjacent profiles is constant. This is the ratio $\frac{AB}{AC}$ in Fig. 10.46 (station 502). This assumption is reasonable because the adjusted profiles, constructed in this way, are so similar to the measured ones. It makes little difference to their shape whether the line AC is vertical or normal to the measured profiles.

The water discharges calculated as previously but using the adjusted air concentration profiles are given in Table 10.3. In all cases, these are within 1% of the mean discharges.

Table 10.3 Water Discharge q' and Variation from Mean q'

(using adjusted profiles of mean air concentration)

		Station					Mean
		501	502	503	504	505	q'
300 mm Gate Opening	q', m^2/s	2.25	2.24	2.22	2.22	2.23	2.23
	Variation	0.02	0.01	0.01	-0.01	0	
450 mm Gate Opening	q', m^2/s	3.14	3.17	3.17	3.16	3.17	3.16
	Variation	-0.02	0.01	0.01	0	0.01	

These adjusted air concentration profiles are superimposed in Fig. 10.49 for comparison. They have also been used to generate the curves of constant air concentration in Fig. 10.50, showing the development of self-aeration down the spillway.

To illustrate the construction of Fig. 10.50, consider the points ABCDE in Fig. 10.49 for which the air concentration is 0.2. The distance from the spillway to each of these points has been used to plot the corresponding points ABCDE in Fig. 10.50. Because the profiles of Fig.

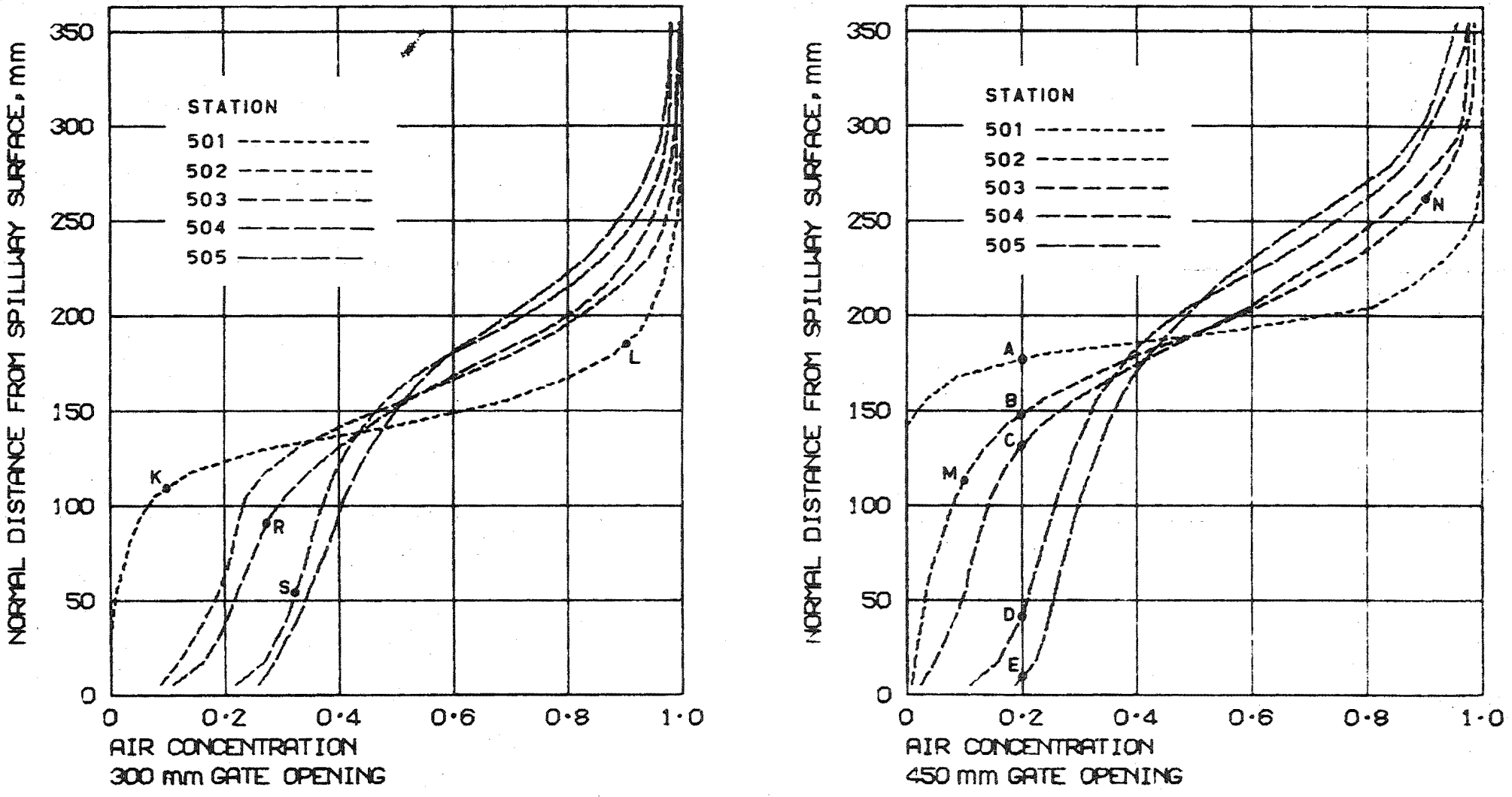

Fig. 10.49 Adjusted Air Concentration Profiles.

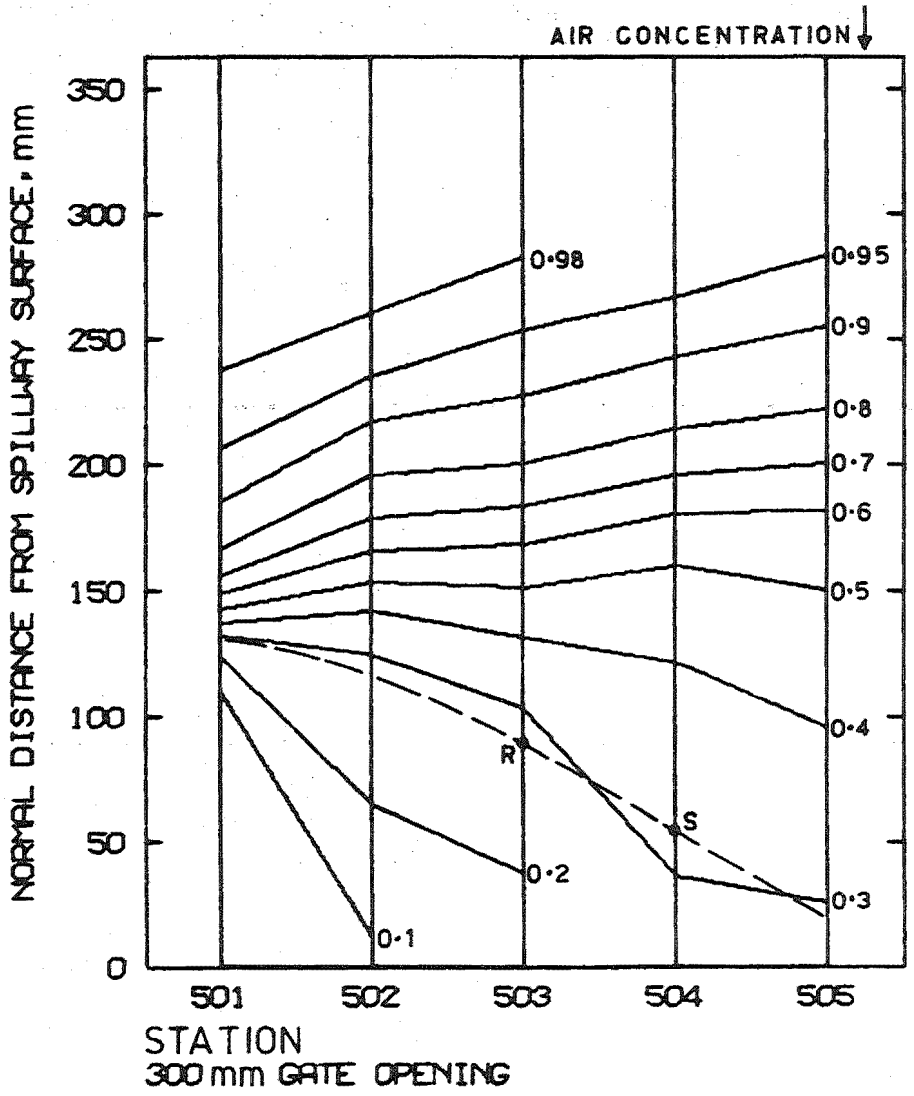

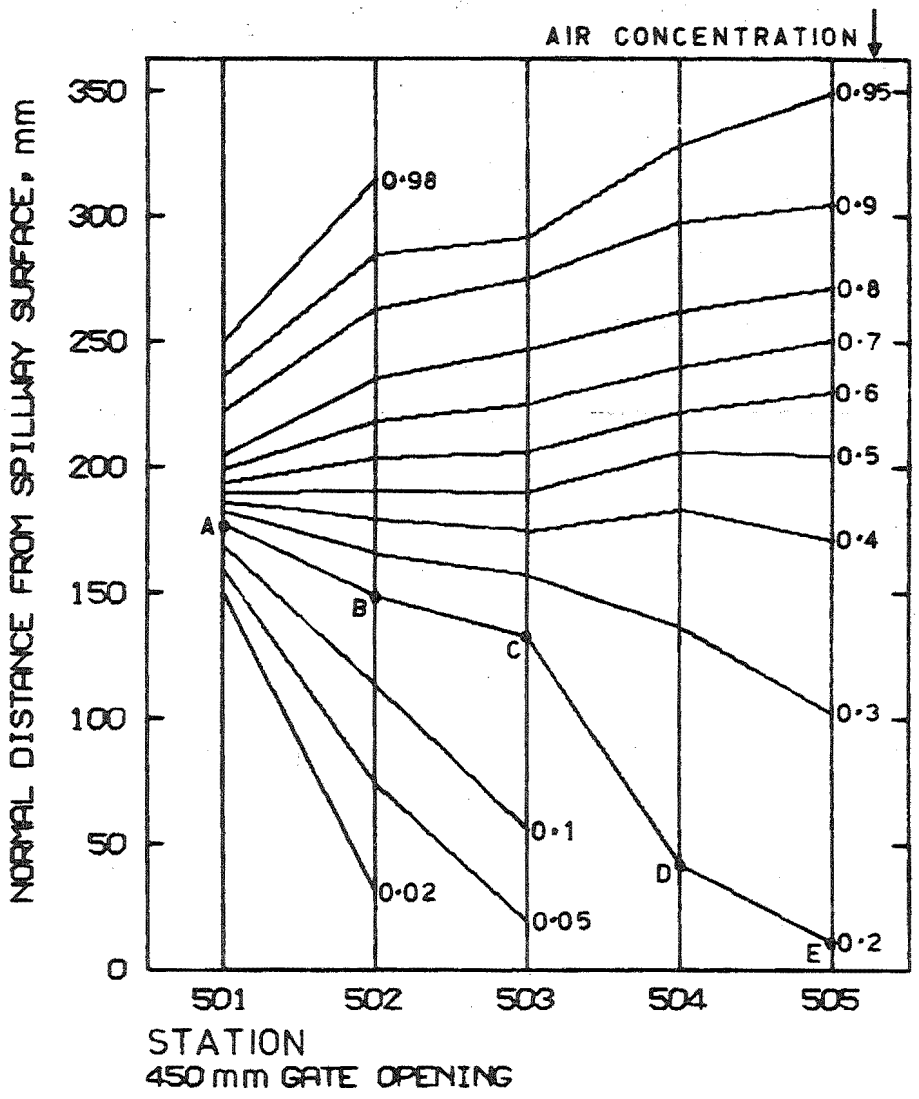

Fig. 10.50 Curves of Constant Air Concentration Down the Spillway.

10.49 are each formed from an array of only 29 points, the distances were found by linear interpolation. Consider for example point A in Fig. 10.49. The 14th and 15th points of the array for this profile were 0.086 and 0.235 for distances of 167 and 180 mm from the spillway. By linear interpolation, an air concentration of 0.2 will occur at a distance of 177 mm from the spillway surface. The point A in Fig. 10.50 was therefore plotted 177 mm from the spillway surface.

If smooth curves are drawn through these curves of constant air concentration, the differences between them at any station are about ± 0.03 maximum. Consider for example the smooth curve, drawn as a broken line, through $\overline{C}$ = 0.3 in Fig.10.50. The point R at station 503 is 91 mm from the spillway surface. The corresponding point is shown in Fig. 10.49, 91 mm from the spillway surface on the profile for station 503. The air concentration at this point is 0.27. Similarly, the air concentration at the point S is 0.32.

10.5.3 Bulking of Self-Aerated Flows

The bulking of self-aerated flows due to the entrained air is of practical importance in the economical design of spillway walls. The bulking can be visualised from the streamlines, constructed from the velocity profiles and the adjusted air concentration profiles.

The streamlines are shown in Fig. 10.51. The number at the end of each streamline indicates the proportion of water between it and the spillway surface. For instance, 90% of the water flows between the spillway surface and the streamline denoted 0.9. These show clearly the increasing depth or bulking of the flow with distance down the spillway. By comparison, non-aerated flow would decrease in depth.

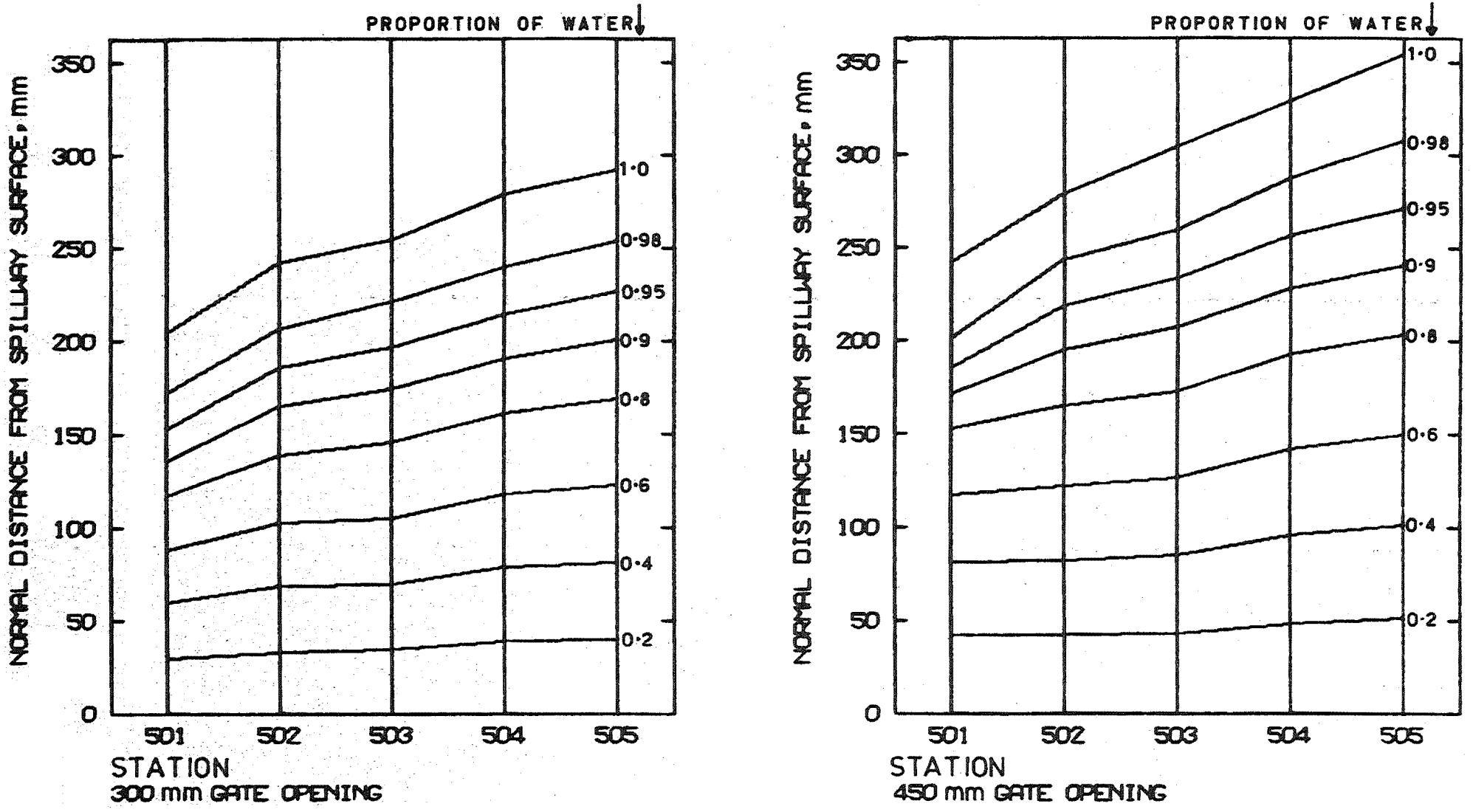

Fig. 10.51 Streamlines Down the Spillway.

To construct these curves, the proportion of water flowing between the spillway surface and every point above it was calculated. The normal distance from the spillway surface to a particular curve was then found by linear interpolation, as for the curves of constant air concentration. The maximum depth for the discharge calculations was again chosen to correspond with $\overline{C} = 0.95$ except for station 502 with a 450 mm gate opening. This was chosen to correspond to $\overline{C} = 0.94$ so as to produce a smooth upper curve. This irregularity has no effect on the other curves because there is so little water in this region.

If smooth curves are superimposed on these curves, the differences between them is found to be about ± 0.03 maximum.

The data from which the curves of Figs. 10.49 to 10.51 were plotted has been listed in Appendix N.

CHAPTER 11

DISCUSSION OF RESULTS

11.1 SUMMARY

Various regions are distinguished within flow down a spillway. The measured position of the point of inception and the important flow parameters at this point are compared with analytical predictions. Dimensional analysis is used to indicate the important variables effecting the distribution of air in the region downstream of the point of inception. This forms the basis for plotting the measurements from Aviemore plus the available measurements from laboratory flumes. Shear stresses on the spillway surface are calculated.

11.2 THE DIFFERENT FLOW REGIONS

It is possible to divide the flow into three separate regions as shown in Fig. 11.1, i.e.

(i) non-aerated flow (H) from the spillway gate to the point of inception (R) of air entrainment,

(ii) partially aerated flow (I) from the point of inception to the point where the aerated region reaches the spillway surface,

(iii) fully aerated flow (J) in which the flow is aerated at the spillway surface.

The growth of the turbulent boundary layer (Q) and the development of the aerated flow allows other regions to be distinguished. The lower limit of the aerated flow S is shown intercepting the spillway surface at W. The spillway surface will influence the aeration within the region

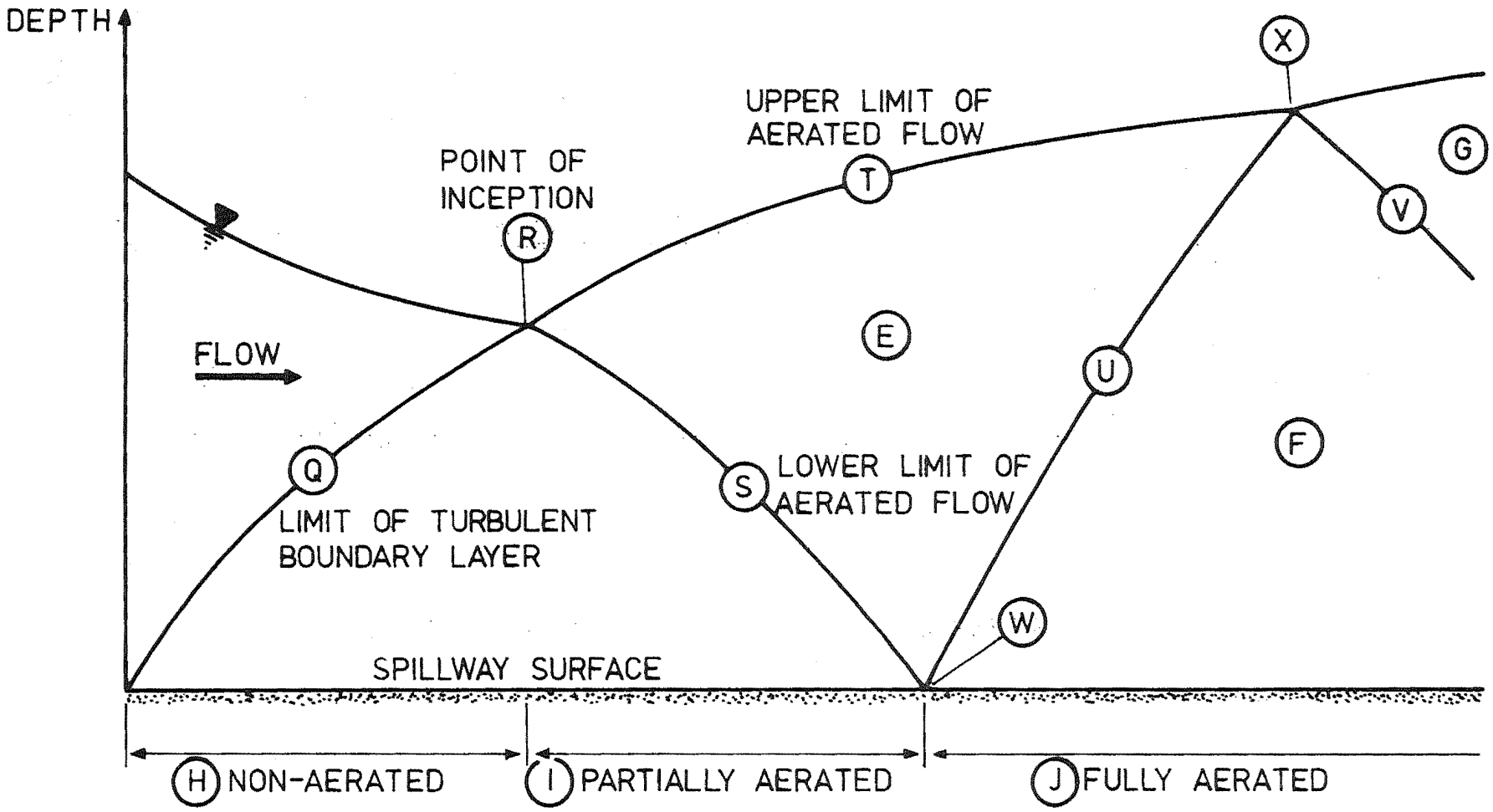

Fig. 11.1 Regions of Flow Down a Spillway (Flow Depth Exaggerated)

F, downstream of the point W. The upper limit of this region of influence is shown as the line U. Above and upstream of this line, the spillway surface has no direct effect on aeration.

The line U can be constructed by considering a mirror image of this diagram about the spillway surface. The mirror image satisfies the requirement that there should be no flow of air ($\frac{\partial C}{\partial y} = 0$) through the spillway surface. Line U is then the continuation of the mirror image of the line S.

It seems likely that another region G can be similarly distinguished. This is bounded by the line V which represents the limit of influence of the air above the flow on the region affected by the spillway. It is possible that any number of such regions could be distinguished.

The growth of the aerated region is in many ways analogous to the growth of the turbulent boundary layer in the non-aerated flow. Indeed, the growth rate of the turbulent boundary layer is found to be similar in magnitude to the growth rate of the partially aerated region of flow.

Most researchers have divided the flow into regions similar to those described above. The main difference here is the introduction of divisions based on the concept of mirror images.

It is now proposed to discuss details of the various regions of the flow.

11.3 NON-AERATED REGION OF FLOW

11.3.1 Point of Inception for Aviemore Measurements

Locating the exact position of the point of inception for the measurements at Aviemore was complicated by the presence of surface

aeration upstream of this point. This is caused by vortices originating behind the spillway gate. These vortices appear as white lines in the direction of flow (see Section 1.3). The point of inception is that at which additional whiteness appears.

The point of inception was determined from photographs of the flow surface. The first bursts of whiteness, caused by the emergence of the turbulent boundary layer, were about 7.7 and 2.3 m upstream of station 501 for the 300 and 450 mm gate openings respectively. (Refer to Thomas and Brown (1977) for a description of bursts within turbulent boundary layers).

The depth of flow at the point of inception y_I can be estimated from the air concentration curves of Fig. 10.50. These are necessarily estimates because of the vortex induced surface aeration at the point of inception. It would appear that the depths (y_I) can be taken as 152 mm and 194 mm for the 300 and 450 mm gate openings respectively.

Assuming potential flow in the region Q (Fig. 11.2) above the boundary layer, the velocity V_I at the point of inception is

$$V_I = [2gx_I \sin\theta]^{\frac{1}{2}} \qquad 11.1$$

where x_I and θ are defined in Fig. 11.2.
This has been calculated as 16.0 and 18.2 m/s for the 300 and 450 mm gate openings.

This data referring to the point of inception has been tabulated in Table 11.1 for reference.

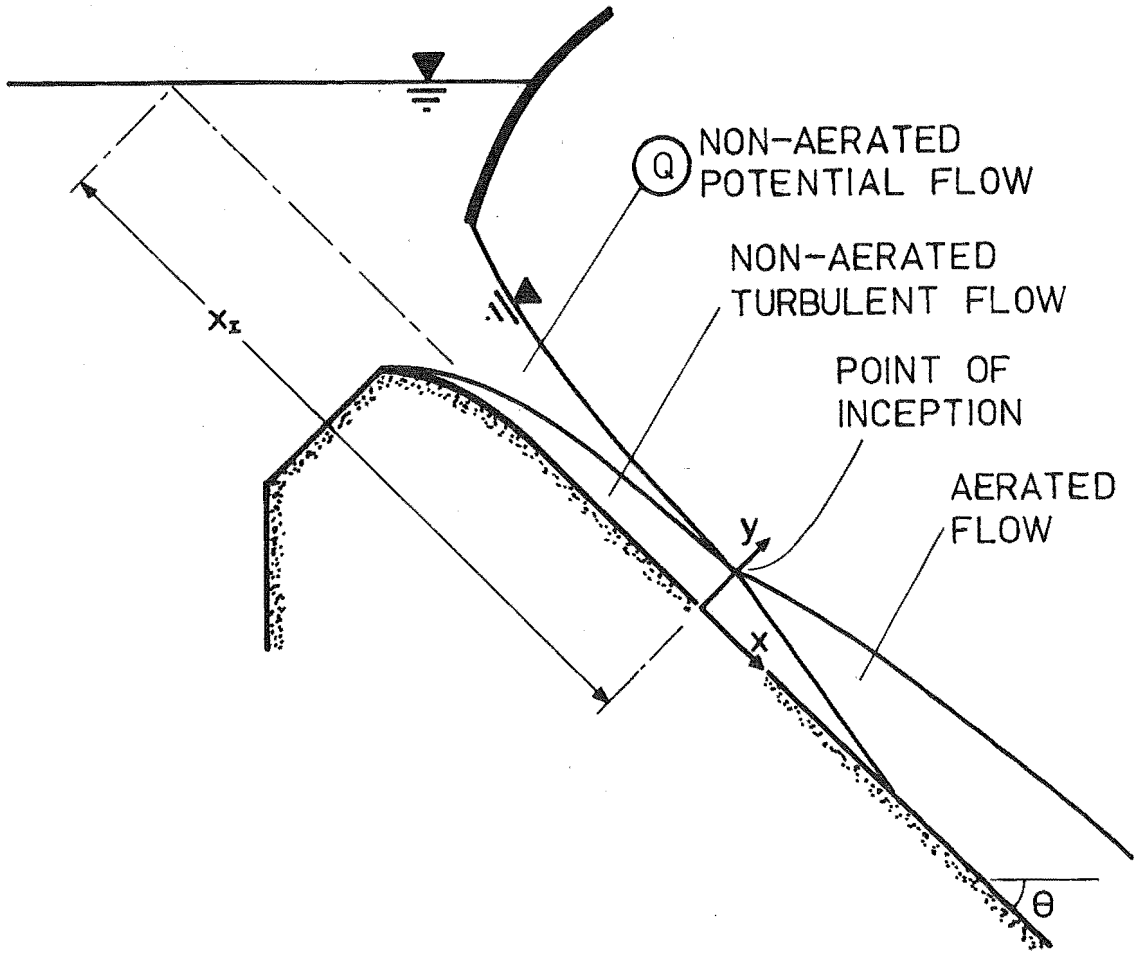

Fig. 11.2 Definition Sketch (Flow Depth Exaggerated)

Table 11.1 Point of Inception Data

Gate Opening mm	x_I m	y_I mm	V_I * m/s
300	18.4	152	16.0
450	23.8	194	18.2

* V_I is the velocity at the point of inception. It is not an average over the depth of flow.

11.3.2 Comparison With Theoretical Predictions

Two theoretical methods for predicting the location of the point of inception will be discussed here. The first, proposed by Bauer (1954) was based on the development of the turbulent boundary layer on a model overflow spillway.

The location of the point of inception is determined graphically by the interception of the boundary layer with the free surface. The boundary layer thickness is determined with reference to a design curve. The free surface is calculated as the depth of the potential flow plus the displacement thickness of the boundary layer. Following Bauer, the displacement thickness is assumed to be $\frac{1}{10}$ the boundary layer thickness.

In a discussion of this paper Halbronn (1954) proposed the following expression for the boundary layer thickness,

$$\delta = 0.0447 \quad \epsilon^{0.154} \, x^{0.846} \qquad 11.2$$

where δ = boundary layer thickness (m),

x = distance along spillway surface from water surface (m),

ϵ = the equivalent sand grain roughness.

He showed that the available prototype data was in fact intermediate between that predicted by using Eq. 11.2 and Bauer's design curve.

This is also the case for the Aviemore data as shown in Fig. 11.3. The observed critical point is intermediate between the points A and B predicted using Halbronn and Bauer's data respectively.

The second theoretical method of predicting the location of the point of inception is that of Keller and Rastogi (1975, 14). They developed a computer program that predicts the velocity distribution within the boundary layer. This enables both the boundary layer

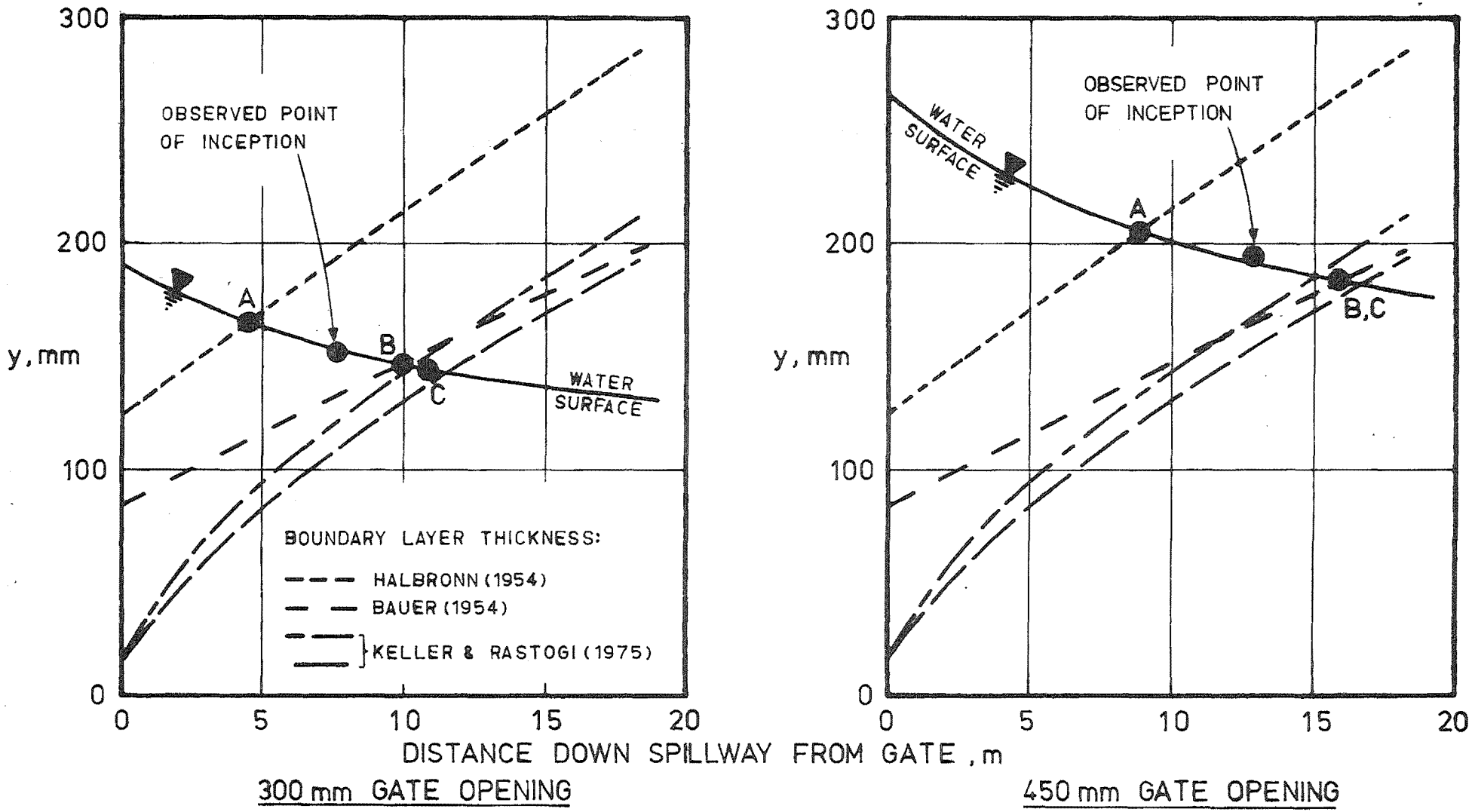

Fig. 11.3 Point of Inception Predictions, Aviemore.

thickness and the water depth to be calculated. Fig. 11.3 shows the boundary layer thickness which intercepts the free surface at C. For both gate openings, this is about 3 m downstream of the observed point of inception.

11.4 THE REGION DOWNSTREAM OF THE POINT OF INCEPTION

11.4.1 Introduction

The development of aeration within the partially and fully aerated regions will be discussed separately. However, the following dimensional analysis is common to both discussions. It provides the basis of a new approach to plotting and analysing measurements in self-aerated flows.

11.4.2 Dimensional Analysis

The air concentration downstream of the point of inception can be expressed in terms of the significant parameters as

$$C = f_1(V_I, y_I, x, y, g, \nu, S, \varepsilon)$$

where x = distance downstream from the point of inception,

y = distance normal to spillway,

g = gravitational constant,

S = Sinθ, channel slope,

ε = equivalent sand grain roughness of spillway surface,

ν = kinematic viscosity of water.

Dimensionless combinations of these parameters can be formed to give

$$C = f_2\left[\frac{x}{y_I}, \frac{y}{y_I}, \frac{V_I}{[gy_I S]^{\frac{1}{2}}}, \frac{V_I\, y_I}{\nu}, S, \frac{y_I}{\varepsilon}\right]$$

The parameter $\frac{V_I}{[gy_I S]^{\frac{1}{2}}}$ is a type of inception Froude number.

Keller, Lai and Wood (1974) showed that by combining Eqs. 11.1 and 11.2, the inception Froude number is given by

$$\frac{V_I}{[gy_I S]^{\frac{1}{2}}} = 8.9 \left[\frac{y_I}{\epsilon}\right]^{.091}$$

For a concrete spillway with roughness ϵ = 1.5 mm, this is almost constant, varying from 13.0 - 18.6 for the range of depths y_I = 0.1 - 5 m.

The aerated flow region is highly turbulent. Small changes in the magnitude of the inception Froude number are unlikely to have a large effect on the aerated flow. It is therefore reasonable to neglect its influence.

The parameter $\frac{V_I\, y_I}{\nu}$ is an inception Reynolds number, which may also be interpreted as a dimensionless expression for the water discharge per unit width q. Analogy with non-aerated flows would suggest the inception Reynolds number will not be an important variable in these very high Reynolds number flows. This is supported by the air concentration distributions measured at Aviemore and by Lai (1971) and reported in the next Section. It is therefore reasonable to neglect its influence also.

In general therefore, the air concentration may be expressed as

$$C = f_3\left[\frac{x}{y_I}, \frac{y}{y_I}, S, \frac{y_I}{\epsilon}\right] \qquad 11.3$$

The velocity downstream of the point of inception can be expressed in terms of the significant parameters as

$$V = f_4(V_I, y_I, x, y, g, \nu, S, \epsilon)$$

Using the same arguments as before, the ratio $\frac{V}{V_I}$ may be expressed as

$$\frac{V}{V_I} = f_5\left[\frac{x}{y_I}, \frac{y}{y_I}, S, \frac{y_I}{\epsilon}\right] \qquad 11.4$$

Eqs. 11.3 and 11.4 indicate a basis for plotting the measurements of air concentration and velocity. Namely, values of C and $\frac{V}{V_I}$ plotted on $\frac{x}{y_I}$, $\frac{y}{y_I}$ axes for various slopes and spillway roughnesses.

The air concentration measurements from Aviemore (adjusted for variations in gate opening) have been plotted in Fig. 11.4. The data is that which was used to plot Fig. 10.50 but the axes are now the non-dimensional parameters $\frac{x}{y_I}$ and $\frac{y}{y_I}$. The scatter of the points about the smooth curves is caused by errors in the air concentration data and possibly errors in the observed positions of the point of inception. The small scatter of the points supports the contention that the inception Reynolds number (range 2.1 - 3.1 x 10^6) has little effect on the distribution of air. One interesting observation is that the line C = 0.5 remains at depth $\frac{y}{y_I}$ = 1.0 over the entire range of $\frac{x}{y_I}$. The distribution of air at $\frac{x}{y_I}$ = 0 shows that upstream of the point of inception, the vortex induced aeration is indeed restricted to a thin surface layer. The flow is non-uniform even at the largest values of $\frac{x}{y_I}$.

Some of the regions of flow previously defined can be identified in Fig. 11.4 and have been reproduced in Fig. 11.5. The line C = 0.1 (S) has been used to represent the lower limit of aeration for this discussion, and the line C = 0.9 (T) the upper limit of aeration. These boundaries were chosen as they are common to the other measurements which will later be compared with those measured at Aviemore. The line U has been sketched as a broken line to indicate that its position is only approximate. As previously mentioned, it is constructed as the continuation of the mirror image of the line S.

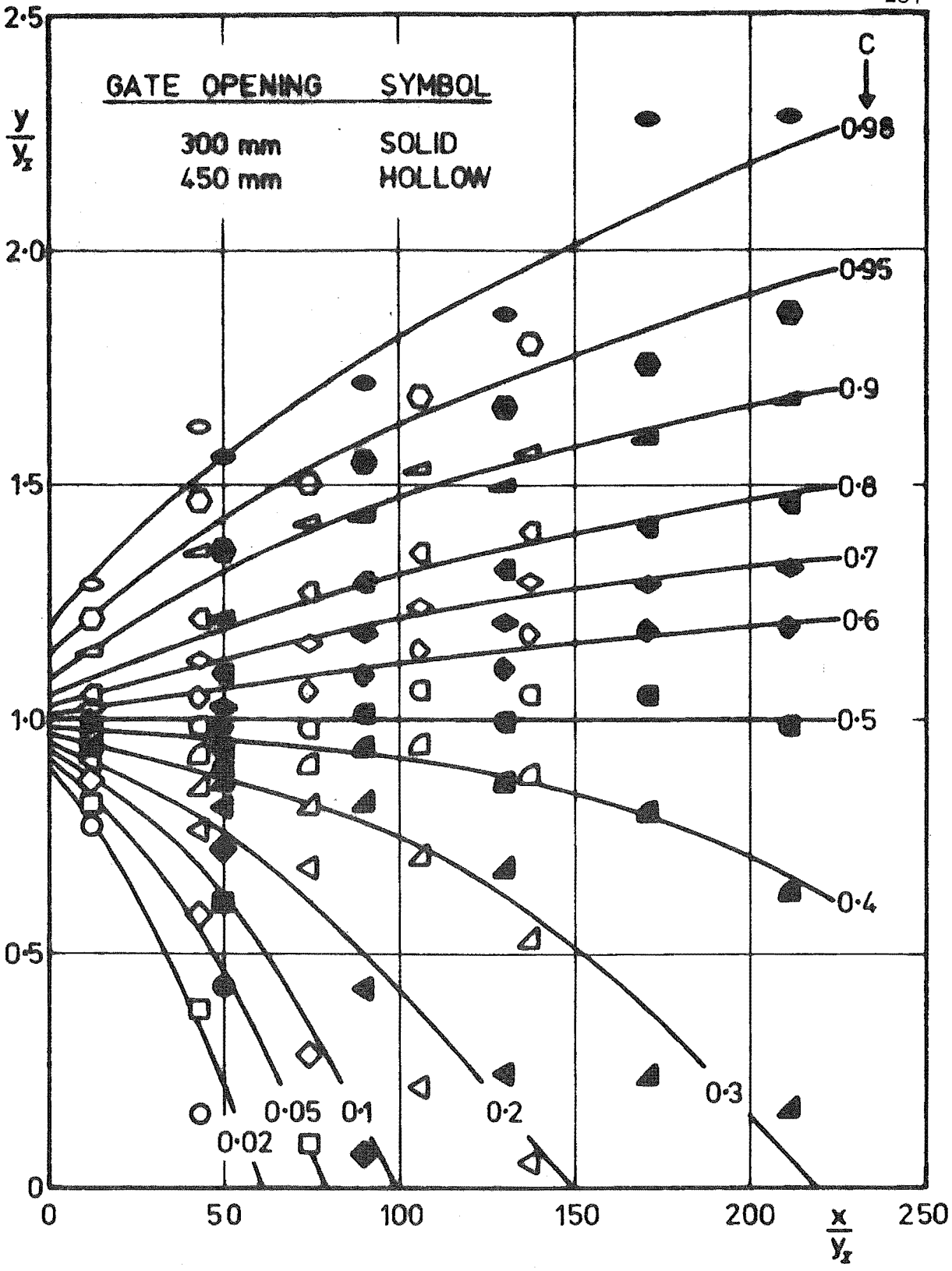

Fig. 11.4 Air Concentration Distribution, Aviemore.

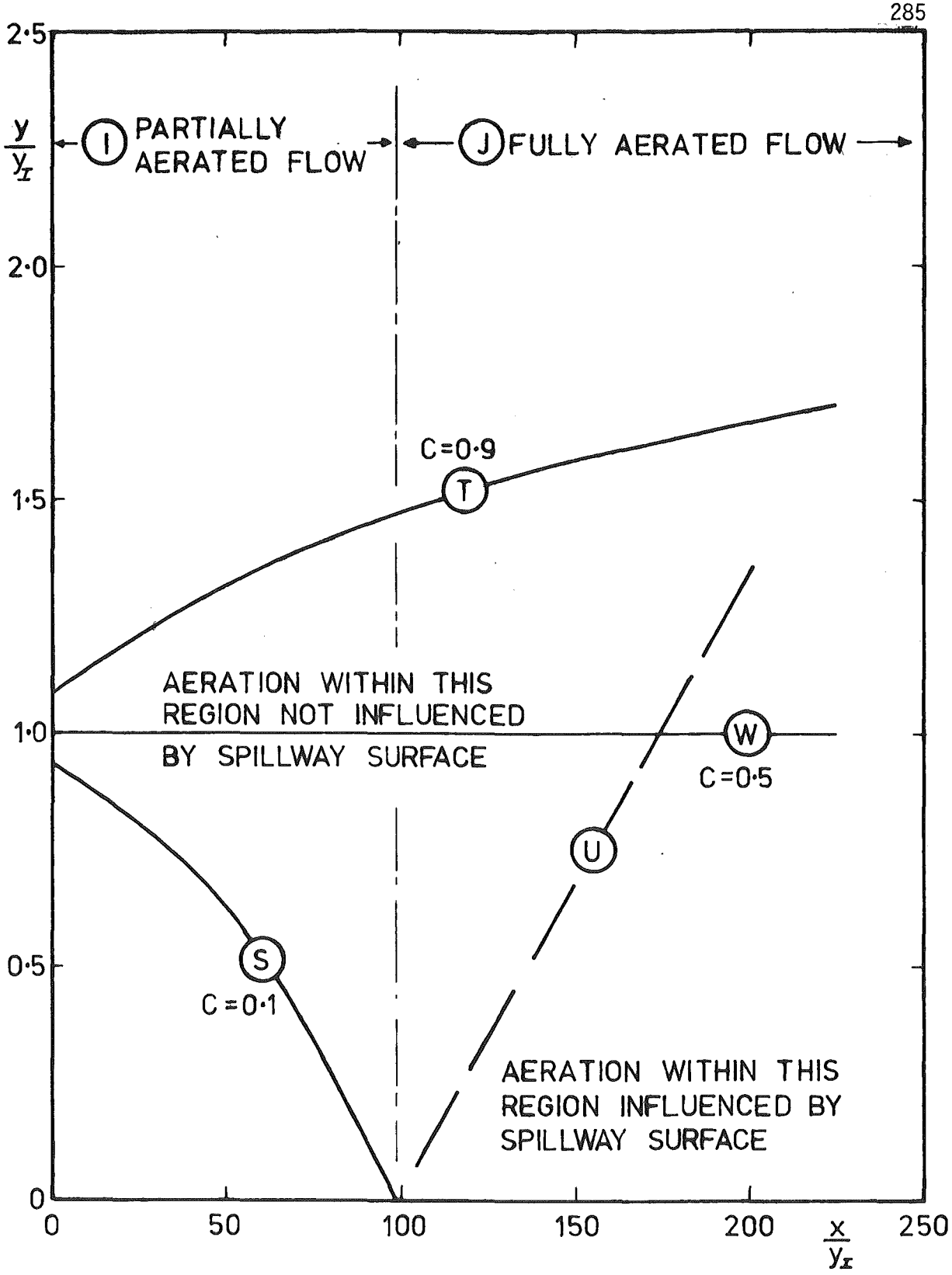

Fig. 11.5 Regions Within the Aerated Flow.

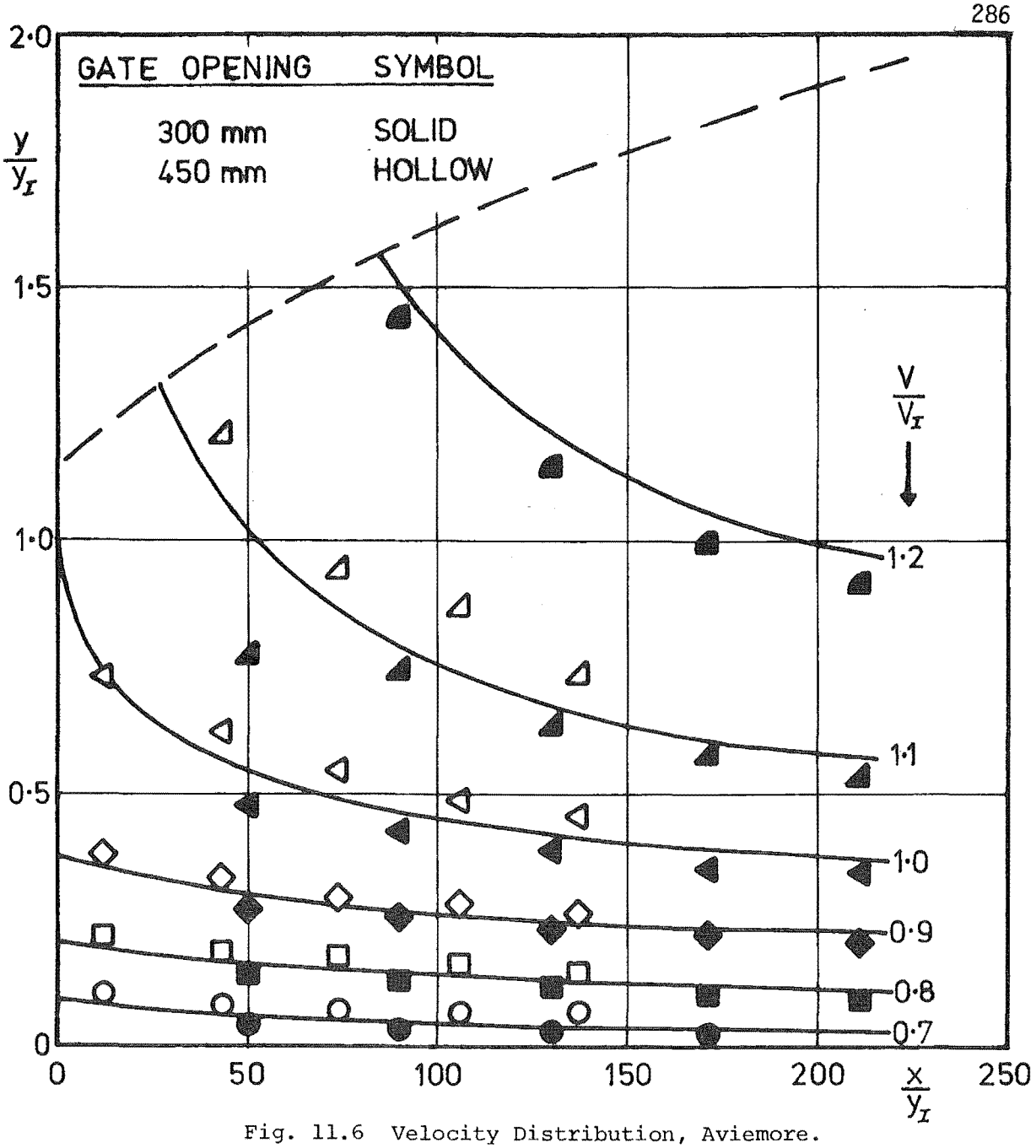

Fig. 11.6 Velocity Distribution, Aviemore.

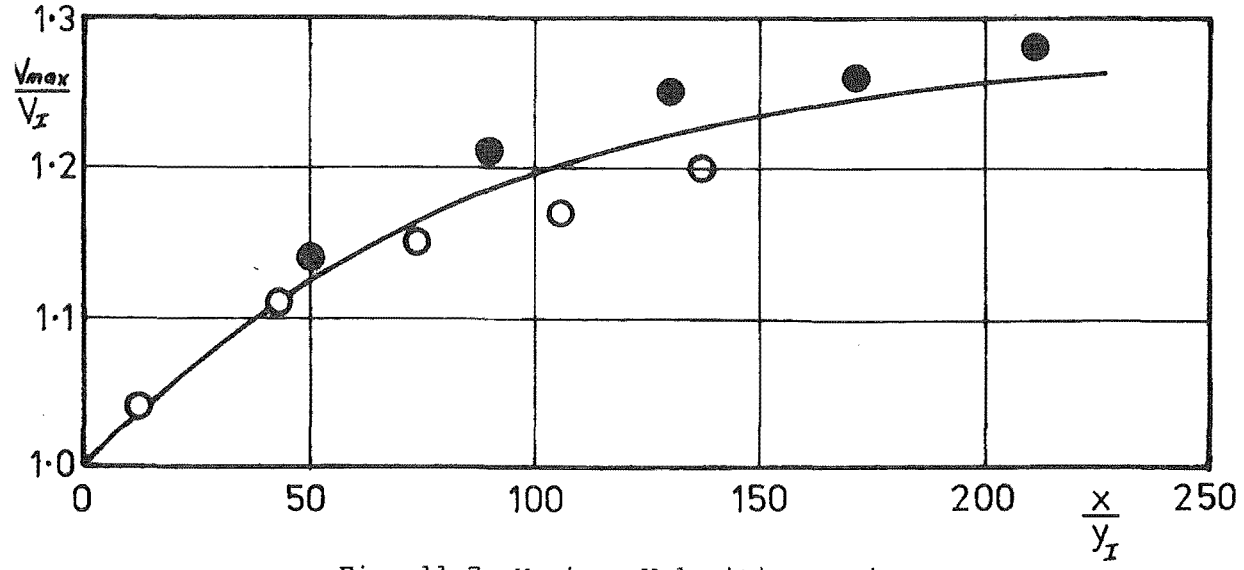

Fig. 11.7 Maximum Velocities, Aviemore.

The velocity measurements from Aviemore are plotted in Fig. 11.6 as ratios $\frac{V}{V_I}$. The values of V_I are those in Table 11.1. The velocity data was that obtained with the correlation technique (Fig. 10.20). The data for the 300 and 450 mm gate openings falls below and above the curves respectively. This suggests an error in the observed positions of the point of inception.

For each profile, the maximum velocity V_{max} occurred at the upper limits of the flow. These are poorly represented in Fig. 11.6 and have therefore been plotted in Fig. 11.7 as the non-dimensional parameter $\frac{V_{max}}{V_I}$. Together, Figs. 11.6 and 11.7 allow the original velocity profiles to be reconstructed.

The measurements of air concentration and velocity from Aviemore therefore support the conclusions from the dimensional analysis.

11.5 PARTIALLY AERATED REGION

11.5.1 Aviemore Measurements

It was previously stated that the distribution of air within the partially aerated region is unlikely to be influenced by the spillway surface. If we ignore the non-uniform velocity distribution in this region, then it is reasonable to test for self-similarity of the air concentration profiles.

Only three of the air concentration profiles measured at Aviemore are within the partially aerated region. These have been plotted non-dimensionally in Fig. 11.8 in which y is the normal distance from the spillway surface; $y_{.1}$ is the distance to the point at which C = 0.1, and $y_{.9}$ is the distance to the point at which C = 0.9. Thus when C = 0.1,

$y = y_{.1}$ and the vertical ordinate equals 0. When C = 0.9, $y = y_{.9}$ and the vertical ordinate equals 1.0. The limiting values of C = 0.1 and 0.9 were chosen as they are common to the other measurements which will be compared with these.

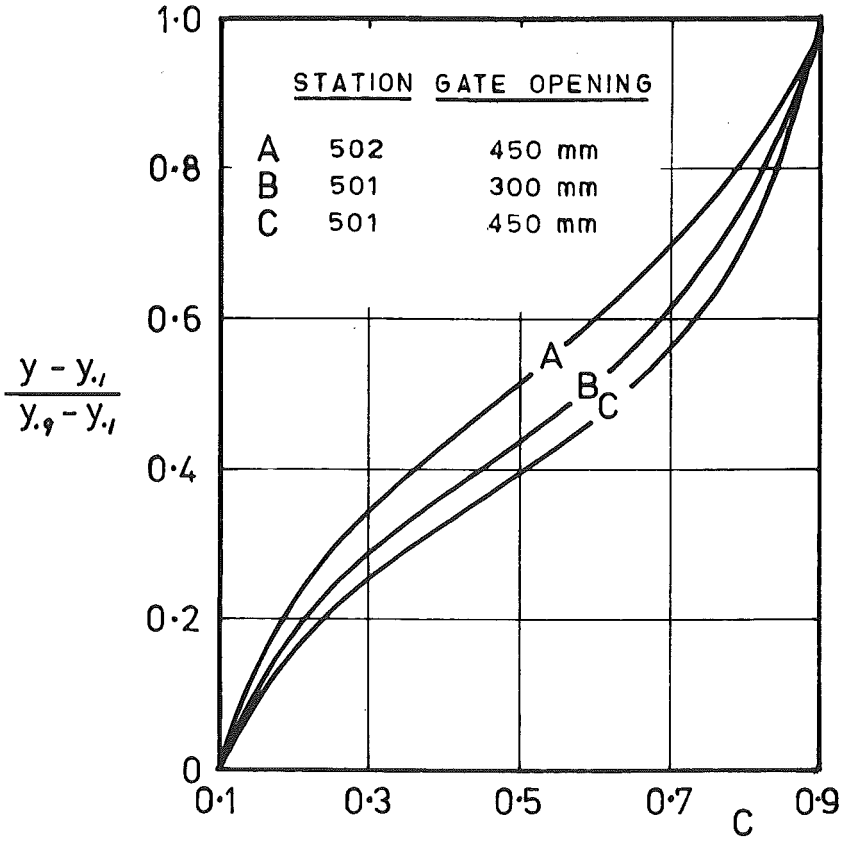

Fig. 11.8 Air Concentration Profiles in Partially Aerated Region

Curve C (measured at station 501 with a 450 mm gate opening) is very possibly in error because the corresponding velocity predictions were grossly underestimated (see W, Fig. 10.42). Curve C will therefore be excluded from all further discussions within this Chapter.

Vortex induced surface aeration is the major source of aeration upstream of the point of inception. The volume of air entrained by vortices increases with distance downstream. The air concentration

profiles A and B (Fig. 11.8) which are just downstream of the point of inception are therefore likely to be influenced by the distribution of air within the vortex induced surface aeration. (In most instances, vortex induced aeration will be unimportant in the centre of laboratory flumes).

Curves A and B are in fact the curves M - N and K - L in Fig. 10.49. Their vertical scale has been significantly increased in Fig. 11.8. Inaccuracies in the original measurements will therefore be exaggerated.

11.5.2 Comparison With Other Measurements

Very few measurements have been obtained within the partially aerated region. Lai (1971) reported some measurements in a laboratory flume, which were all within this region. The flume was glass bottomed, 8.2 m long and 457 mm wide. Measurements were obtained with three water discharges 0.074, 0.105 and 0.136 m^2/s for each of two flume slopes, 18^o and 24^o.

The air concentration was measured with a mechanical probe, similar to that described in Section 3.3. His measurements have been plotted in Fig. 11.9. The accuracy of these has been limited by the small size of the original profiles from which these were derived. The depth y_I ranged from 19 - 32 mm, and is noted on each plot.

None of Lai's flows became fully aerated even though his values of $\frac{x}{y_I}$ were as large as 300. By comparison, the flows at Aviemore were fully aerated at values of $\frac{x}{y_I}$ larger than about 50 (ref. Fig. 11.4). Unlike the Aviemore measurements, Lai's curves for C = 0.5 are not horizontal straight lines at $\frac{y}{y_I} = 1.0$.

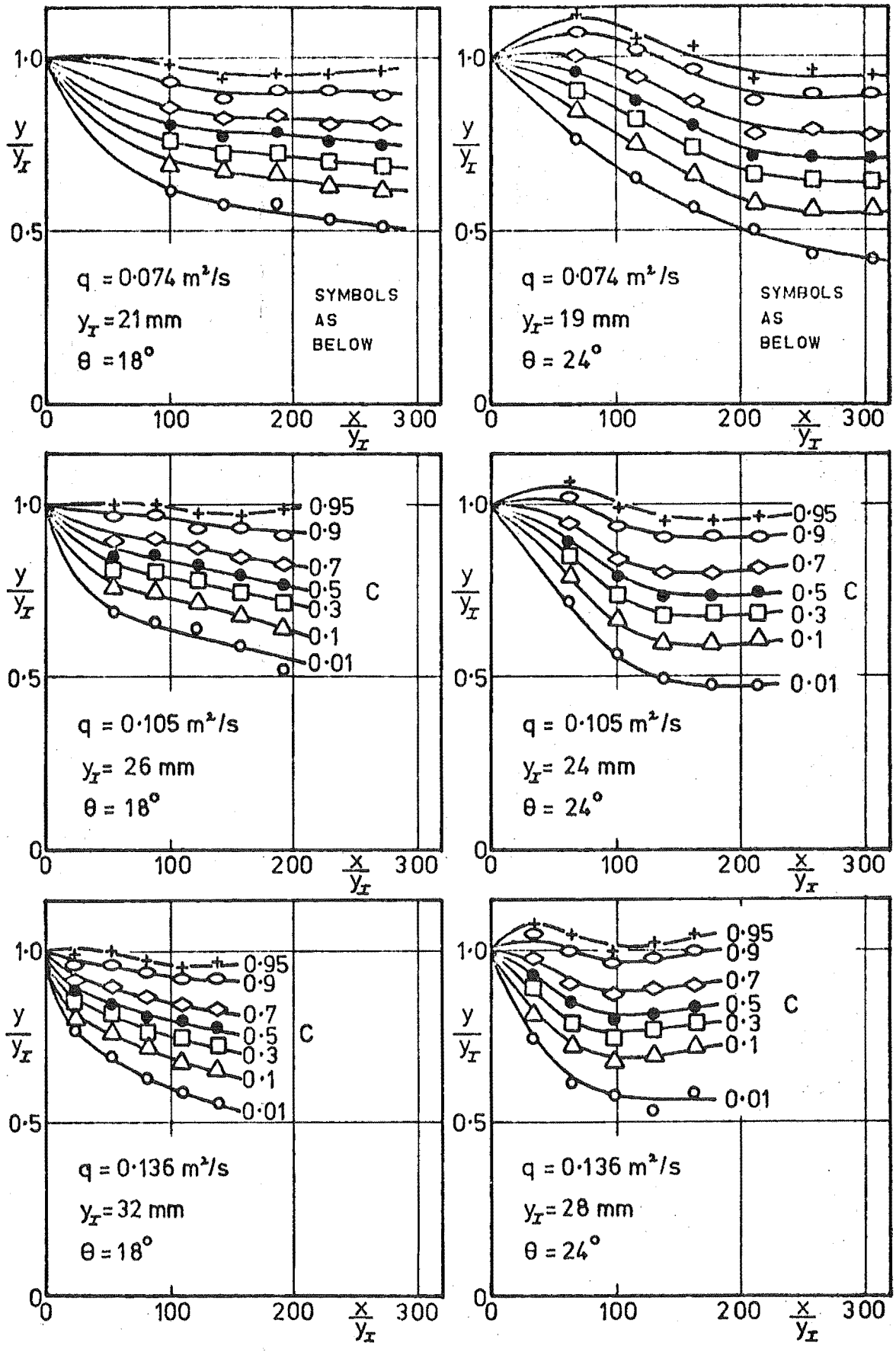

Fig. 11.9 Air Concentration Distribution, Following Lai (1971).

The air concentration distributions suggest that some of the flows approached uniform conditions at the maximum values of $\frac{x}{y_I}$ (for example q = 0.105 m^2/s, $\theta = 24^\circ$). This is not supported by the corresponding velocity profiles in the non-aerated flow (discussed below) which in all cases show increasing velocity with distance downstream.

The measurements at different discharges have been superimposed in Fig. 11.10. The small differences between these shows that the inception Reynolds number (range 0.7 - 1.3 x 10^5 for both flume slopes) is not important, and supports the dimensional analysis.

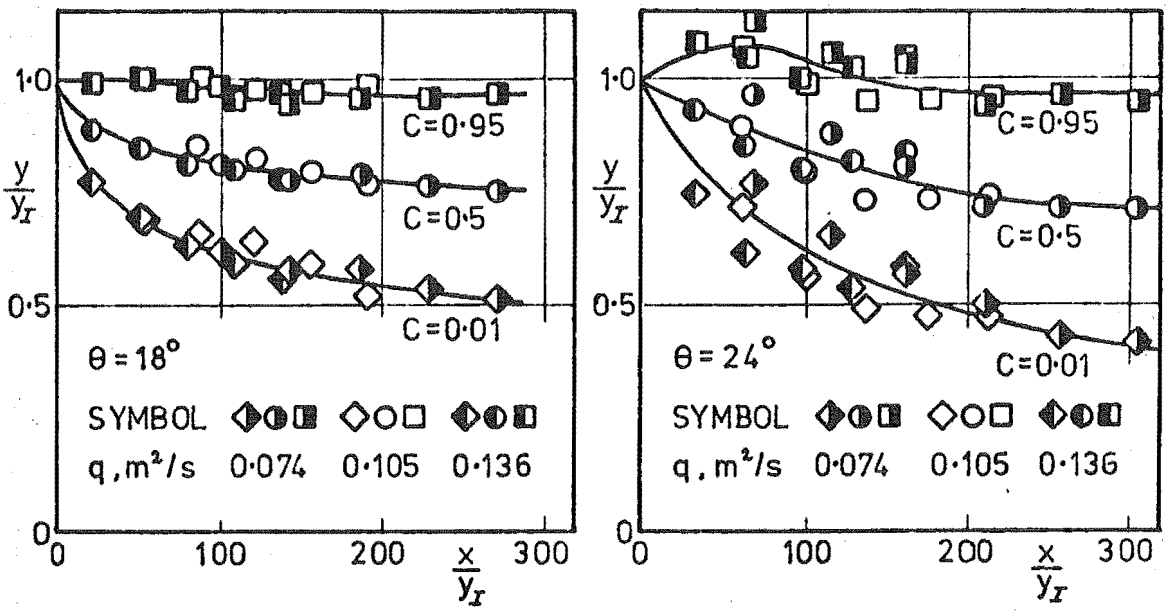

Fig. 11.10 Air Concentration Distribution, Following Lai (1971)

The writer considers that Lai's velocity measurements in the aerated flow are unreliable. To understand why, it is necessary tc consider his measurement technique in detail.

His probe was a sharp edged pitot tube with which he could either measure the stagnation pressure or sample the flow to measure the air concentration. From these measurements, he calculated the velocity as

$$V = \left[\frac{2P_s}{\rho_w\ (1-\lambda C)}\right]^{\frac{1}{2}}$$

where λ is a tapping coefficient which accounts for the non-homogeneous behaviour of air-water flows approaching the stagnation point. λ was determined by calibrating the probe in an aerated flow. The mean air concentration and velocity of this flow were calculated independently from volume flow rates of the air and water phases prior to mixing. Using the value of stagnation pressure measured with the probe, λ was found to vary from 0.91 to 1.09 for air concentrations from 0.4 - 0.8, (Fig. 11.11).

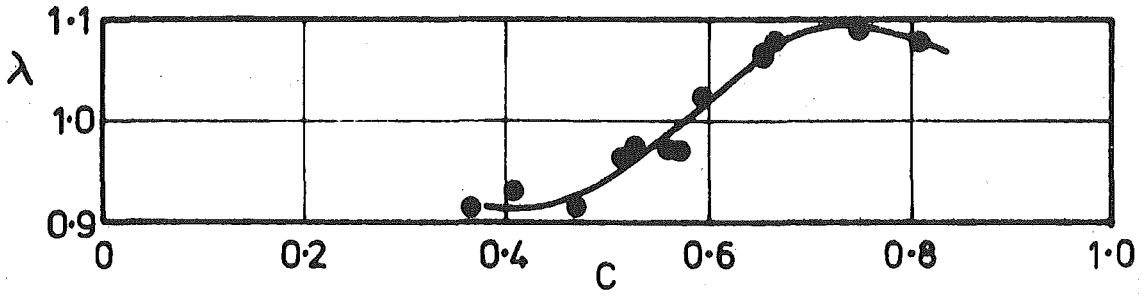

Fig. 11.11 Tapping Coefficient, Following Lai (1971)

Lai took λ = 1.0 for all his self-aerated flow measurements, incorrectly assuming this value of λ would have little effect on the accuracy of his velocity predictions. To illustrate the effect of this, his velocity profiles for a 24^{o} slope with a discharge of 0.105 m^2/s are shown in Fig. 11.12. In the top plot, λ has been assumed equal to 1.0.

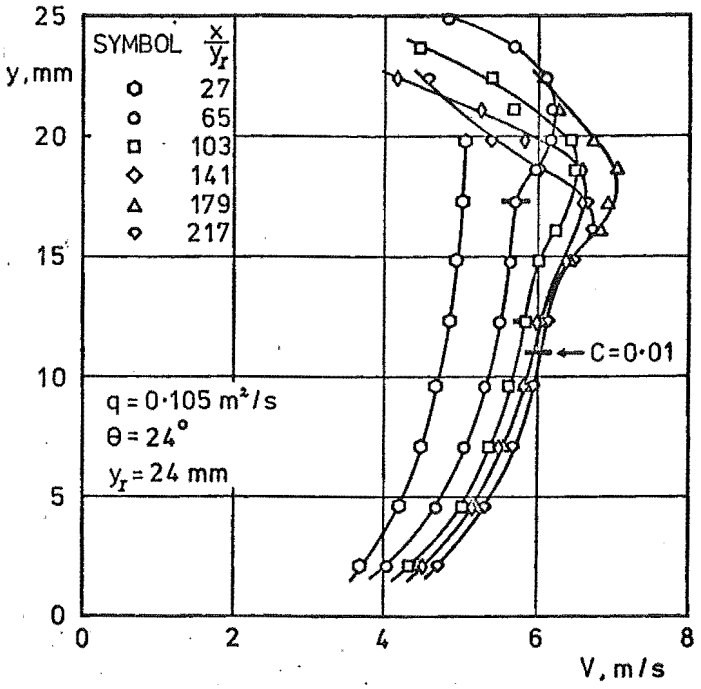

VELOCITY PROFILES WHEN $\lambda = 1$.

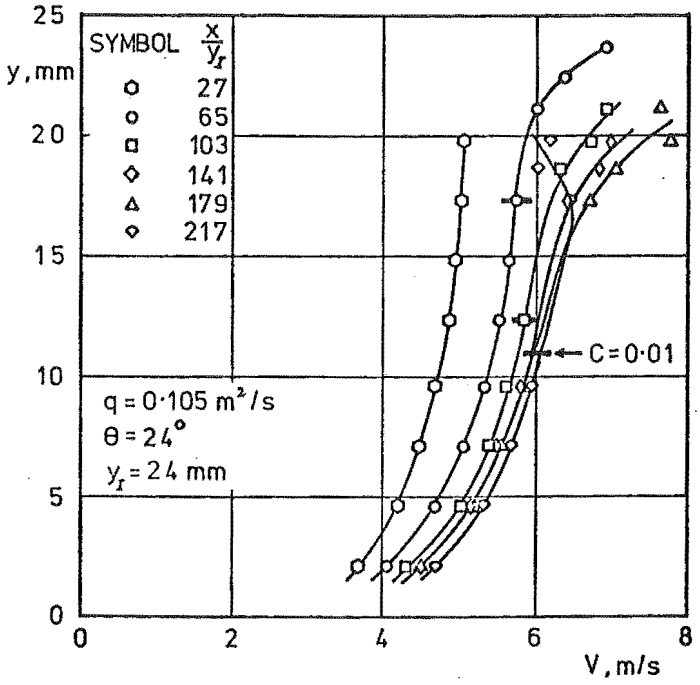

VELOCITY PROFILES WHEN
λ IS GIVEN BY FIG. 11.11 .

Fig. 11.12 Effect of Tapping Coefficient on

Lai's (1971) Velocity Calculations

In the lower one, the value of λ from Fig. 11.11 has been used. The lower limit of aeration (C = 0.01) has been indicated on each profile. The aerated regions are seen to be markedly different. A similar trend is to be expected for Lai's other five sets of velocity profiles which are not presented here.

This fault with Lai's velocity profiles was not detected by Keller, Lai and Wood (1974) in their analysis of the developing region in self-aerated flows.

Even if Lai's measurements of λ are reliable, it would be unwise to place too much confidence in the velocity predictions in the aerated region. The accuracy of the velocity predicted is too sensitive to errors in P_s, C or λ when the air concentration tends to 1.0. Lai's results in the non-aerated region are reliable, and have therefore been plotted in a non-dimensional form in Fig. 11.13.

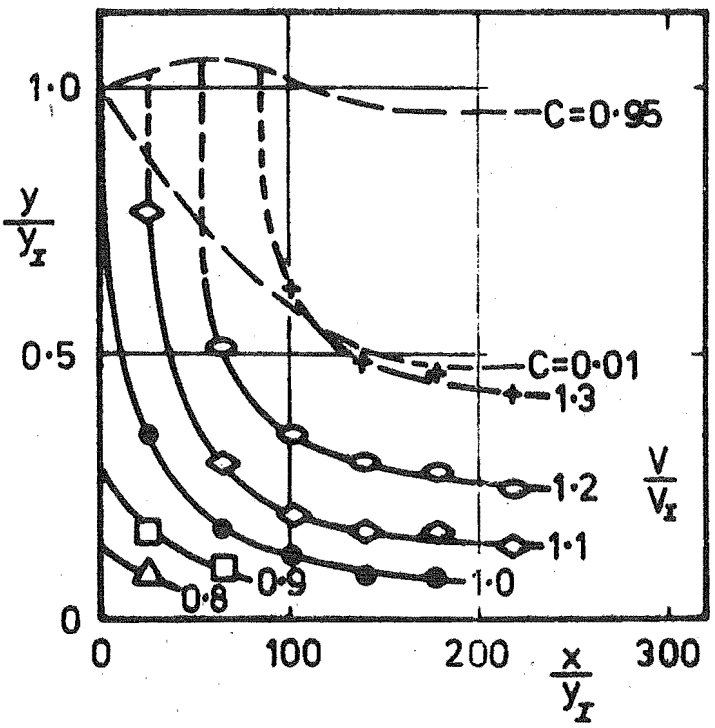

Fig. 11.13 Velocity Distribution, Following Lai (1971)

$q = 0.105\ m^2/s$, $\theta = 24^\circ$, $y_I = 24$ mm.

Comparison with the data from Aviemore (Fig. 11.6) shows similar trends but no direct correlation.

Rao et al (1970) also report some measurements of air concentration and velocity in a laboratory flume. It would appear that their measurements were within both the partially and fully aerated regions. The flume was 13.7 m long and 457 mm wide. The bottom of the flume was lined with sand grains with a mean diameter of 0.9 mm. They used a flume slope of 32^{o}, publishing measurements for a water discharge of 0.095 m^2/s.

The air concentration was measured with a mechanical probe similar to that described in Section 3.3. Fig. 11.14 illustrates a peculiarity of their measured air concentration profiles. This shows a relatively large air concentration at the flume surface compared with the overlying fluid. This behaviour has not been reported by any other researchers.

In spite of this peculiarity their measurements have been plotted non-dimensionally in Fig. 11.15. The flow was in fact aerated at the spillway surface at each station. It has not been possible to illustrate this clearly because of the shape of the profiles.

For $\frac{x}{y_I} = 38$, the air concentration at the spillway surface is only about 0.01. It is therefore reasonable to assume that at this station, the flow is in the partially aerated region.

The accuracy of Fig. 11.15 has been limited by the small size of the original profiles from which this was derived. The curves are different from those measured at Aviemore (Fig. 11.4) and by Lai (Fig. 11.10). It would appear that the flow does not become uniform even though the values of $\frac{x}{y_I}$ are as large as 400.

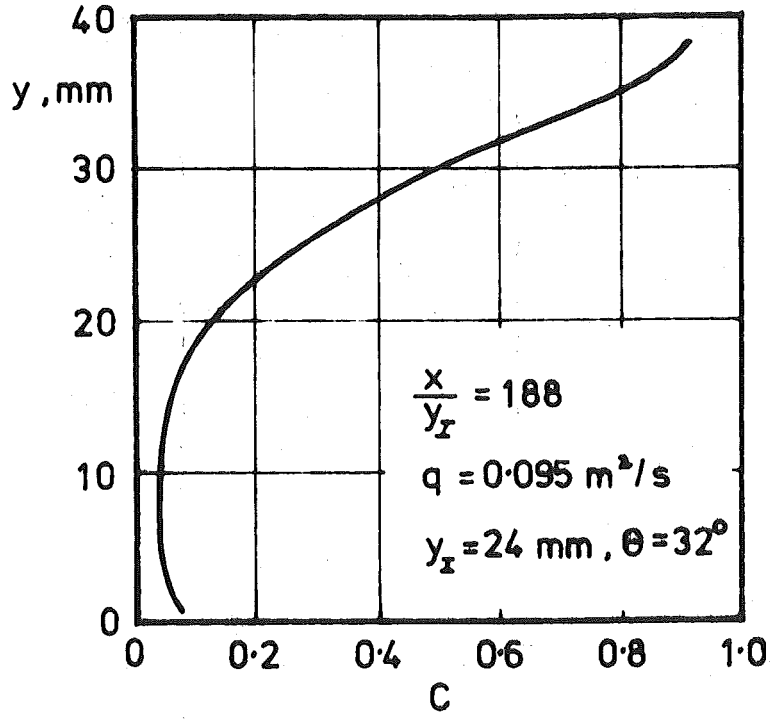

Fig. 11.14 Air Concentration Profile, Following Rao et al. (1970).

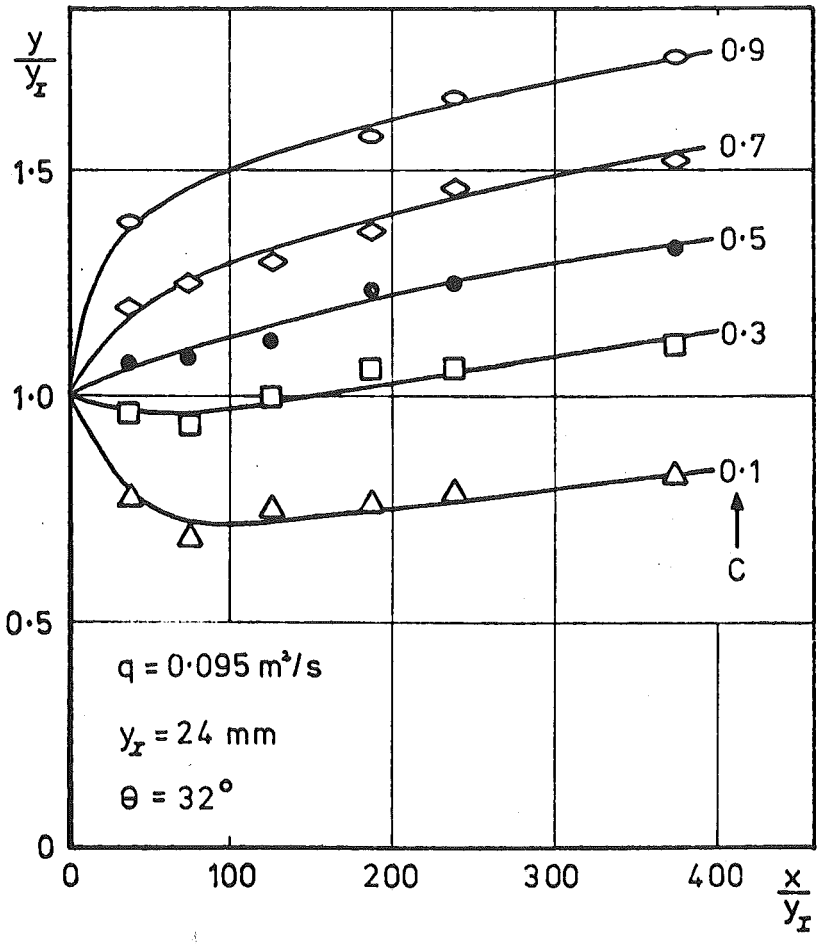

Fig. 11.15 Air Concentration Distribution, Following Rao et. al. (1970)

To obtain velocity profiles, Rao et al used the same probe to measure (separately) the stagnation pressure and air concentration. From these, they calculated a "mixture velocity" V_m which they defined as

$$V_m = (1-C)V + C\ V_a$$

where V is the water velocity,

V_a is the air velocity.

The concept of a "mixture velocity" has been strongly criticized by Viparelli and Pica (1970) because it is only a mathematical value and does not represent a physical quantity. From equations given by Rao and Kobus (21) it can be shown that the water velocity is related to the "mixture velocity" according to

$$\frac{V}{V_m} = \frac{1-C}{(1-\lambda C)^3}$$

where λ is a "tapping coefficient" for the probe, which accounts for the non-homogeneous behaviour of air-water flows approaching the stagnation point. For their pitot tube, Rao et al. (1970) measured $\lambda = 0.74$.

The difference between the "mixture velocity" and water velocity is shown in Fig. 11.16(a) for $\frac{x}{y_I} = 375$. The profiles of water velocity for all stations is shown in Fig. 11.16(b). Their accuracy has been severely limited by the small scale of the published profiles from which these were derived. They are therefore unsuitable for exact comparison.

Straub and Anderson (1958) reported measurements of air concentration and velocity for a very wide range of flume slopes and discharges. In each case, the flow was fully aerated. For a flume slope of 7.5^o, the air concentration at the spillway surface was only 0.02. It is therefore reasonable to assume that these measurements were in a partially aerated region.

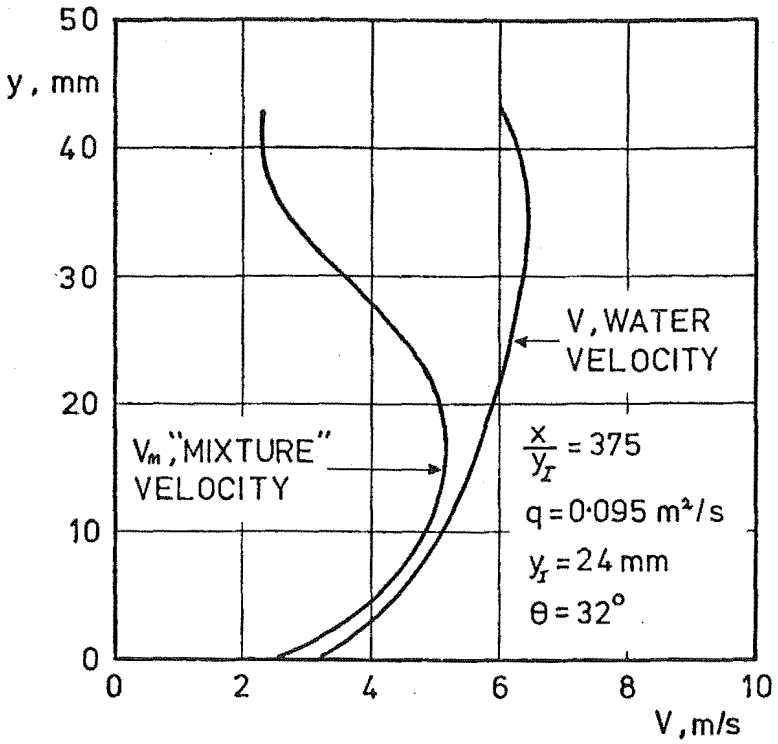

(a) "Mixture" and Water Velocity Profiles.

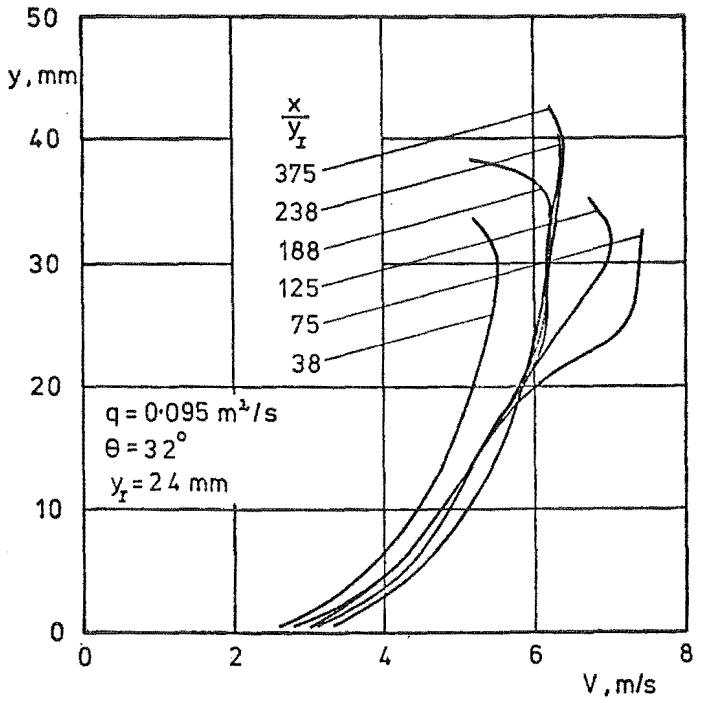

Fig. 11.16 (b) Velocity Profiles, Following Rao et al. (1970).

They measured air concentration with the resistance probe developed by Lamb and Killen (1950) and discussed in Section 3.3. The corresponding velocity profiles were not published.

Some other laboratory measurements within the partially aerated region of self-aerated flow have been published. These will not be presented here because the writer has little confidence in the instrumentation used.

All the air concentration profiles within the aerated region have been plotted non-dimensionally in Fig. 11.17. The vertical ordinates are identical to Fig. 11.8. The horizontal scale refers to curves A and B. Curves D, E and F have been displaced by 0.2, 0.4 and 0.6 respectively. Information about each curve is given in Table 11.2.

Curves A and B were measured at Aviemore and are reproduced from Fig. 11.8. These were measured at stations 502 and 501 respectively, with gate openings 450 and 300 mm. Curve D was measured by Rao et al (1970) at $\frac{x}{y_I} = 38$, for which the air concentration at the spillway surface was about 0.01. Curve E is based on Lai's (1971) measurements with a discharge of 0.105 m^2/s and a flume slope of 24^o. It is an average of all 5 profiles, which are all within ± 0.03 (vertical ordinate) of the curve shown. Keller, Lai and Wood (1974) have shown that all of Lai's (1971) profiles (for both flume slopes and all discharges) were in fact self-similar. Curve F was measured by Straub and Anderson (1958) with a 7.5^o flume slope.

In view of the accuracy of these results and the likely influence of vortices on curves A and B, these profiles can all be considered self-similar.

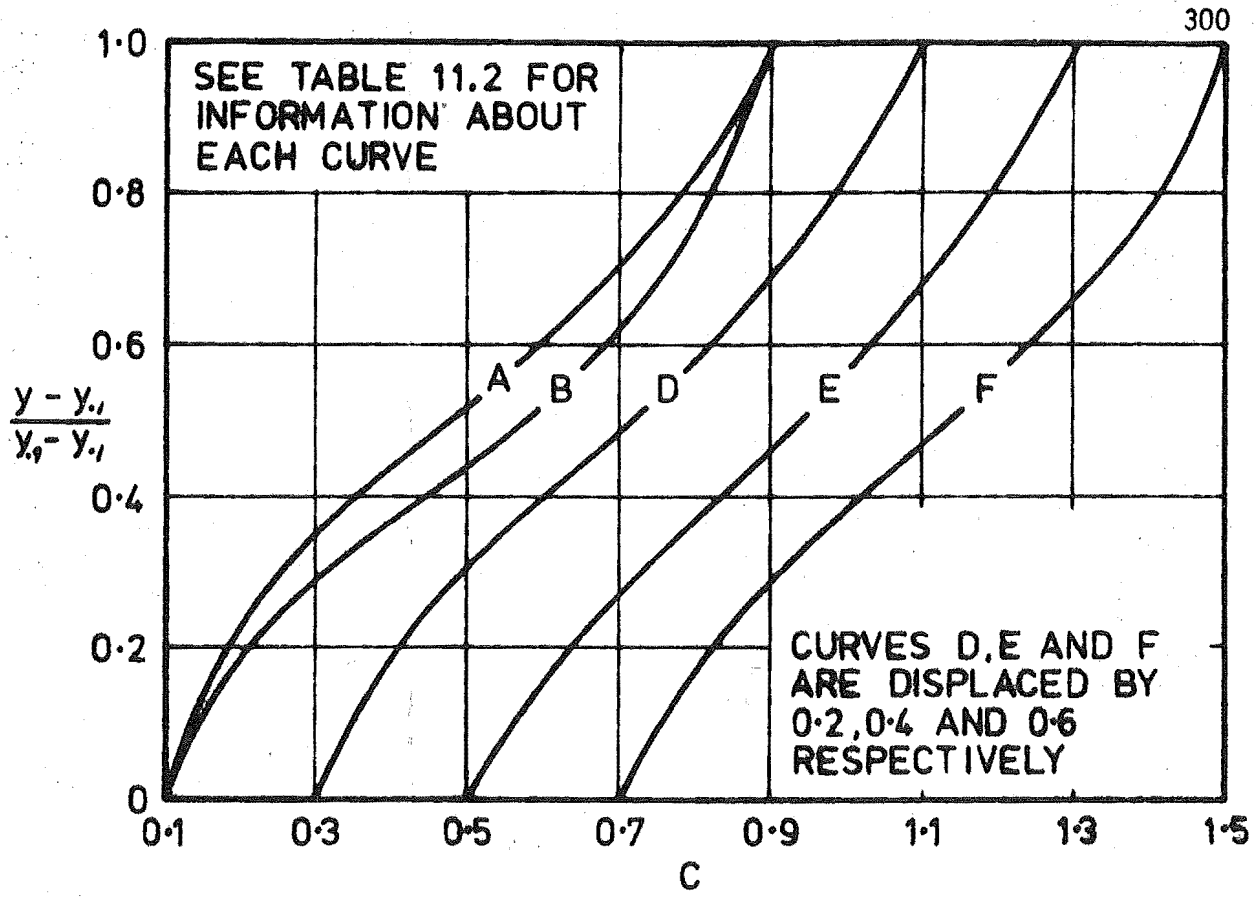

Fig. 11.17 Comparison of Air Concentration Profiles in Partially Aerated Flow.

Table 11.2 Data for Curves in Fig. 11.17

Curve		Spillway slope θ^{o}	Discharge q, m^2/s
A	Aviemore	45	3.16
B	Aviemore	45	2.23
D	Rao et al (1970)	32	0.095
E	Lai (1971)	24	0.105
F	Straub & Anderson (1958)	7.5	0.595

11.5.3 Growth Rate of Partially Aerated Region

The growth rate of the partially aerated region of flow has been plotted non-dimensionally in Fig. 11.18 in which $y_{.1}$ is the distance from the spillway surface to the point at which C = 0.1; and $y_{.9}$ is the distance to the point at which C = 0.9. The limiting values of C = 0.1 and 0.9 were chosen as they are common to all the measurements.

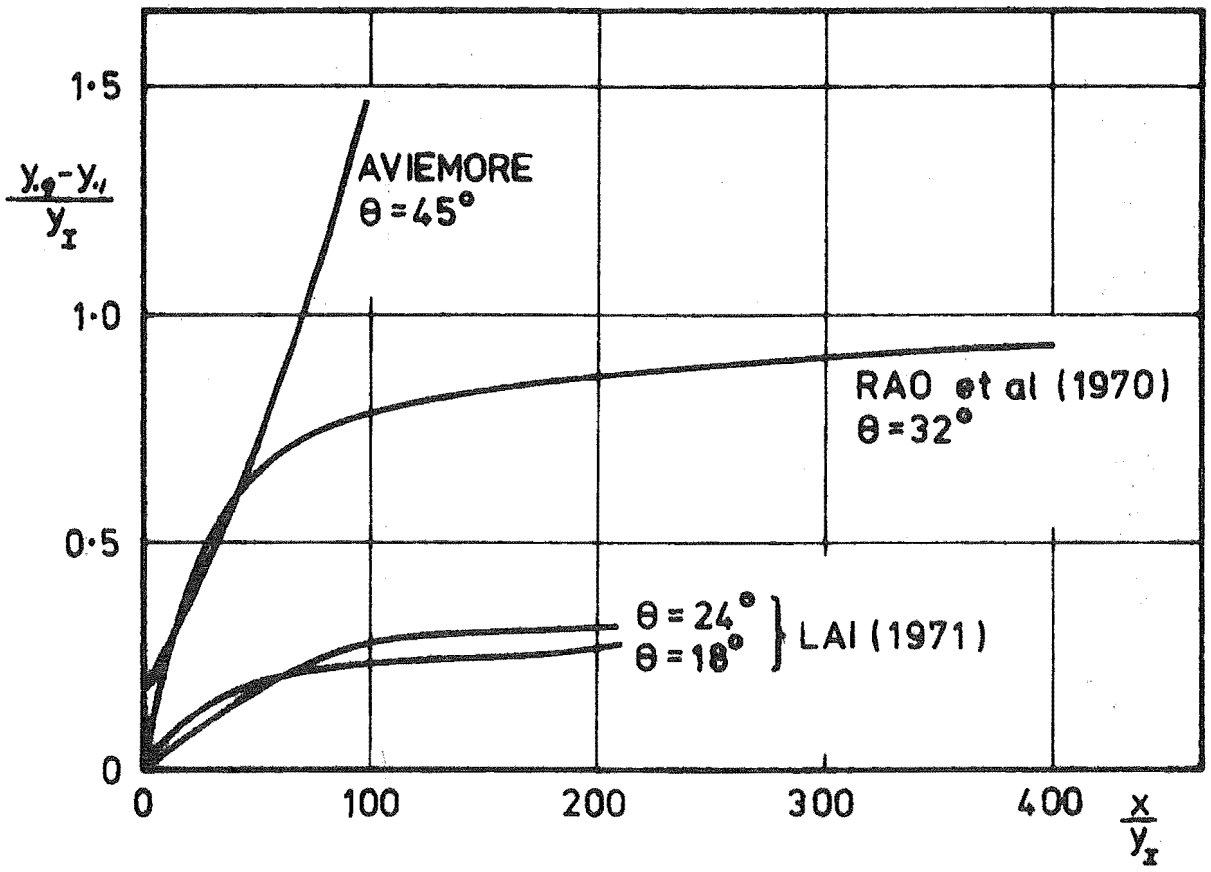

Fig. 11.18 Comparison of Growth Rates of Partially Aerated Regions.

The data for Aviemore was taken from Fig. 11.5. This data only covers the partially aerated region of flow I (Fig. 11.5). Lai's (1971) data was taken from Fig. 11.9 for q = 0.105 m^2/s and Rao et al's (1970) data was taken from Fig. 11.15. For this comparison of growth rates,

it was considered best to treat Rao et al's flows as being partially aerated, and to ignore the aeration at the spillway surface.

The different growth rates in Fig. 11.18 show that Keller, Lai and Wood's (1974) tentative design procedure for partially aerated flow, based only on Lai's (1971) measurements, was not in fact general.

By considering Rao et al's flow to be partially aerated, no growth rate measurements in fully aerated flow are available for comparison with the measurements from Aviemore.

11.5.4 Spillway Shear Stress in Partially Aerated Flow

The shear stress on the Aviemore spillway has been calculated as a mean value between adjacent spillway stations. Only one of these is within the region of partially aerated flow; between stations 501 and 502 with a 450 mm gate opening.

The momentum change M per unit time and per unit width in the flow enclosed between Sections 1 and 2 (Fig. 11.19) is

$$M_2 - M_1 = \mathbb{P}_1 - \mathbb{P}_2 + W\sin\theta - F$$

Each term is described below:

M, the momentum passing a section, is given by

$$M = \int_{y=0}^{y=d} \rho_w (1-C_y)\ V_y^{\,2}\ dy$$

$\mathbb{P}$ is the force at a section due to the static pressure distribution. The static pressure P_z at height z is given by

$$P_z = \int_{y=z}^{y=d} \rho_w (1-C_y)\ g\ \cos\theta\ dy$$

$$P_z = \rho_w\ g\ \cos\theta \int_{y=z}^{y=d} (1-C_y)\ dy$$

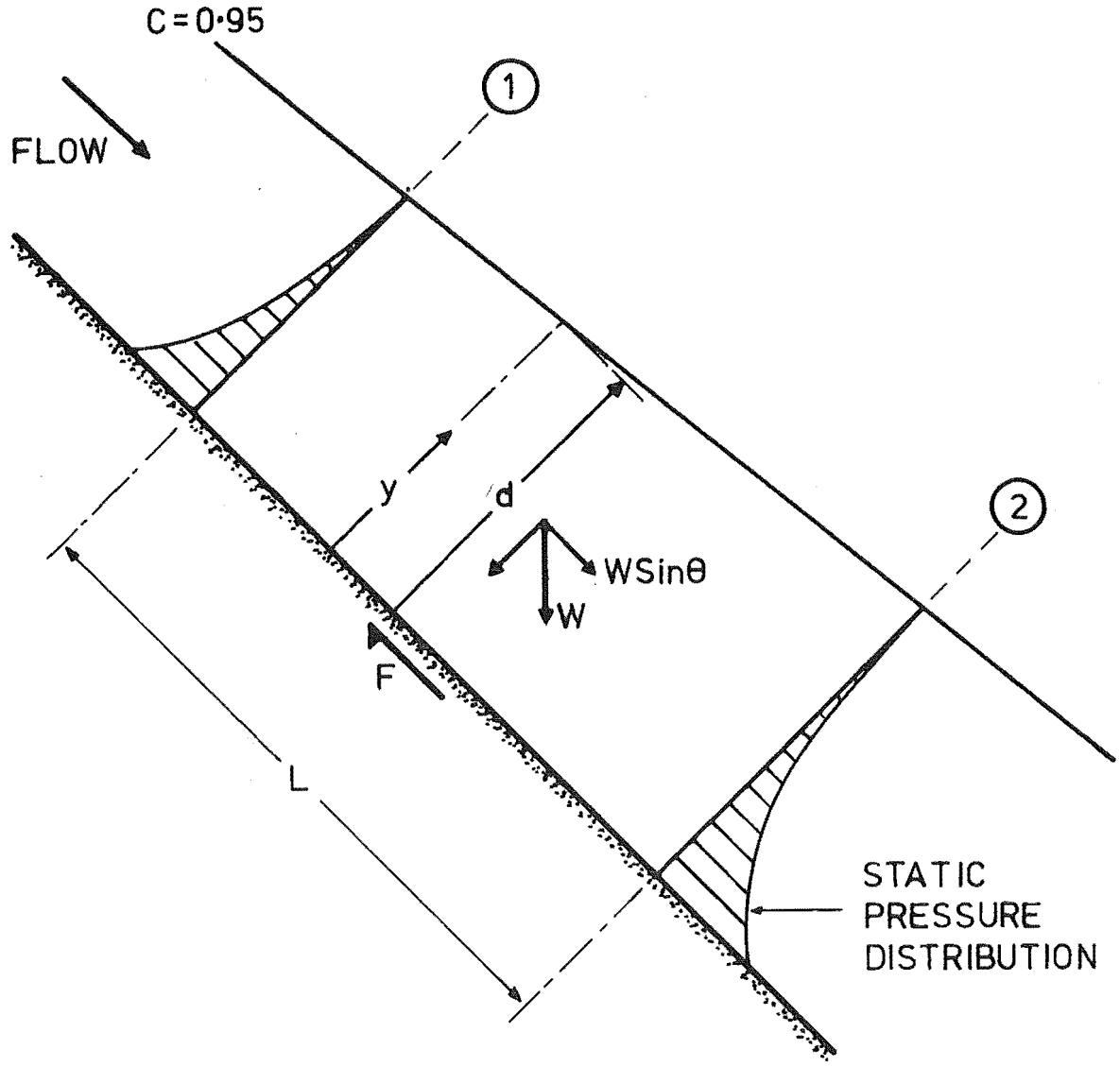

Fig. 11.19 Definition Sketch for Shear Stress Calculations.

The force $\mathbb{P}$ is therefore

$$\mathbb{P} = \int_{y=0}^{y=d} P_z \, dy$$

WSin θ is the component of the weight of water in the direction of the spillway. This can be calculated as

$$W\sin\theta = \left[\left[\frac{h_1 + h_2}{2}\right] \rho_w \, g \, L\right] \sin\theta$$

where $$h = \int_{y=0}^{y=d} (1-C_y) \, dy$$

F is a friction force equal to τL where τ is the mean shear stress between the two sections, and is the only unknown variable.

The shear stress τ has been calculated using the "adjusted" air concentration profiles (Fig. 10.49) and the measured velocity profiles (Fig. 10.20). For the partially aerated flow between stations 501 and 502 with a 450 mm gate opening, the mean shear stress was $\tau = 900$ N/m^2.

The only comparable measurements known to the writer are those of Bauer (1954). These were obtained in non-aerated flow in a laboratory flume, with slopes of 20, 40 and 60°. They closely followed the relationship

$$\frac{1}{[C_f]^{\frac{1}{2}}} = 4.06 \log\left[\frac{\delta}{\epsilon}\right] + 8.56$$

where δ is the boundary layer thickness at the section,

ϵ is the surface roughness,

C_f is a drag coefficient which is related to the shear stress τ' by

$$\tau' = C_f \frac{\rho_w V^2}{2}$$

where V is the potential velocity at that section and is given by Eq. 10.2, i.e.

$$V = [2gH]^{\frac{1}{2}}$$

These have been used to predict the shear stresses that would occur at Aviemore between stations 501 and 502. The value of δ used was that predicted by Keller and Rastogi (14) (Fig.11.3) at a point midway between stations 501 and 502. The roughness was taken as $\epsilon = 1.5$ mm.

The predicted shear stress was 680 N/m^2. The measured shear stress (900 Nm/^{2}) is 30% larger than that predicted. It is considered this difference is real and that it is not due to the inaccuracy of the measurements.

11.6 FULLY AERATED REGION

11.6.1 Aviemore Measurements

It was shown that in the region of partially aerated flow (I, Fig. 11.5) all the air concentration profiles were self-similar. In the region of fully aerated flow (J, Fig. 11.5) the air concentration profiles above and upstream of the line U (Fig. 11.5) should also be self-similar.

This hypothesis was tested by plotting the data in a non-dimensional form in Fig. 11.20, in which y is the normal distance from the spillway surface; $y_{.5}$ is the distance to the point at which C = 0.5 (W, Fig. 11.5), and $y_{.9}$ is the distance to the point at which C = 0.9. Thus, when C = 0.5, the vertical ordinate equals 0 and when C = 0.9, the vertical ordinate equals 1.0.

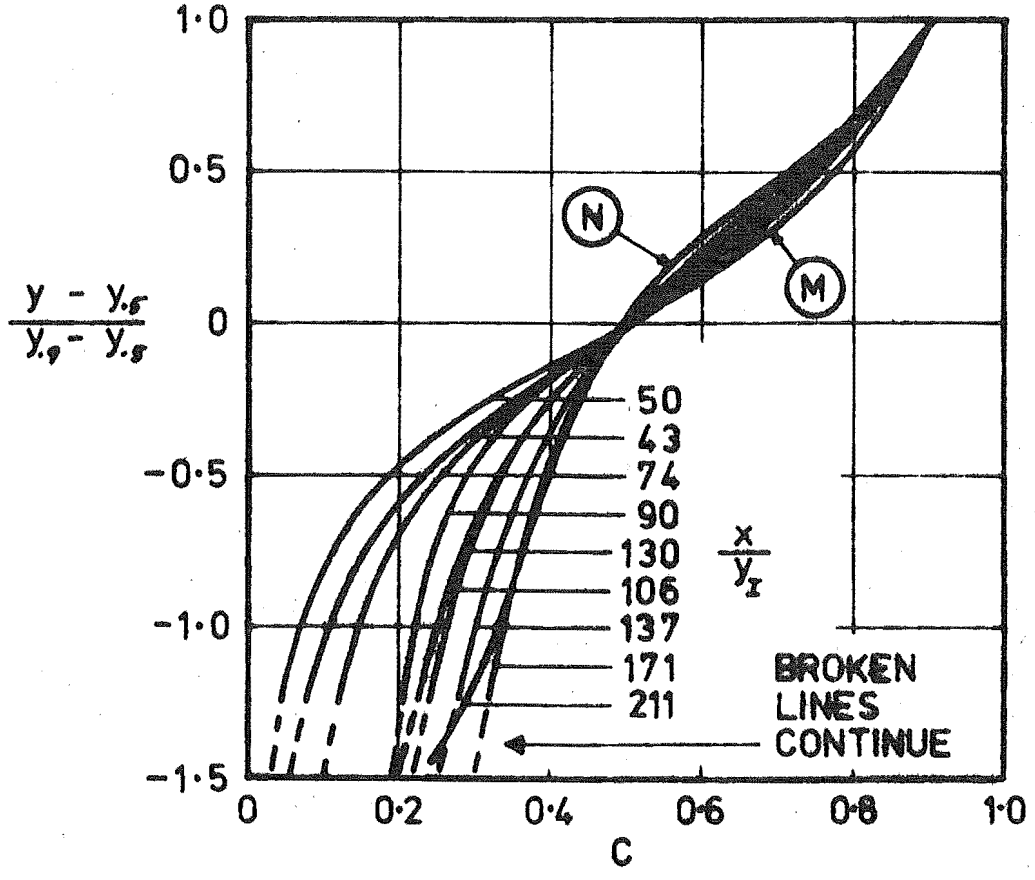

Fig. 11.20 Comparison of Air Concentration Profiles, Aviemore.

In the lower region for which C < 0.5, there is a definite trend with increasing values of $\frac{x}{Y_I}$. This indicates the increasing influence of the spillway surface on the aerated flow.

In the upper region for which C > 0.5 there is a similar though less pronounced trend with increasing values of $\frac{x}{y_I}$. Curve M was measured at station 501 with a 300 mm gate opening. It was suggested previously that this air concentration profile could have been influenced by the vortex induced surface aeration. Curve N has a value of $\frac{x}{y_I} = 211$. This is most likely within the region of influence of the spillway surface, even at the flow surface.

11.6.2 Comparison With Other Measurements

It was previously shown that in partially aerated flow, the air concentration profiles of Rao et al. (1970), Lai (1971) and Straub and Anderson (1958) plus those from Aviemore were self-similar from C = 0.1 to 0.9. It follows that from C = 0.5 - 0.9, these profiles are the same shape as in Fig. 11.20. The scale of Rao et al's published profiles is too small to allow any trends to be accurately observed at air concentrations less than C = 0.5.

It was earlier mentioned that all of Straub and Anderson's measurements were within the fully aerated region. All their measurements were at 13.72 m from the flume inlet in what they considered to be uniform flow. To achieve this, they adjusted the inlet velocity and depth until the air concentration profiles were "similar" at 10.67 and 13.72 m from the inlet.

The writer would suggest that their measurements are difficult to interpret because the parameter $\frac{x}{y_I}$ can not be calculated. They did not publish any information on the point of inception. Nor did they publish either the inlet velocity or depth, from which the position of the point of inception could be predicted.

The writer would also suggest that most if not all of their measurements were in a slowly developing region of flow. This statment is based on values of $\frac{x}{y_I}$ estimated as follows. A value of y_I can be associated with each discharge and slope if it is assumed that the flume was in fact an overflow spillway. y_I can then be calculated using Bauer's (1954) method. (Ref. Section 11.3.2). x can be taken as the length of the flume so that the calculated values of $\frac{x}{y_I}$ may well be overestimated. $\frac{x}{y_I}$ was found to range from about 100 - 500, and was typically about 200. These values are very similar to the maximum values of Figs. 11.4, 11.10 and 11.15 for which uniform flow was not established.

It is interesting to compare the velocity profiles reported so far with those obtained at St. Anthony Falls. Straub, Killen and Lamb (1954) developed a sophisticated velocity instrument for use in self-aerated flows. This injected small slugs of salt solution into the flow. Their passage was electronically timed between two probes which were aligned in the direction of flow, and spaced 76 mm apart. This method of velocity measurement requires the measurement of only one parameter, time, and should therefore be more reliable than the use of stagnation pressure and air concentration measurements to predict velocity.

The velocity and air concentration profiles of Fig. 11.21 were obtained by Straub and Lamb (1956) for a 45^{o} slope with a painted steel flume surface and a discharge of 0.4 m^2/s. The velocity profile is

typical of the few that were published. It shows a definite decrease in velocity at distances larger than 12 mm from the flume surface. Straub and Lamb attributed this to the drag of the overlying air. The writer considers this explanation unlikely.

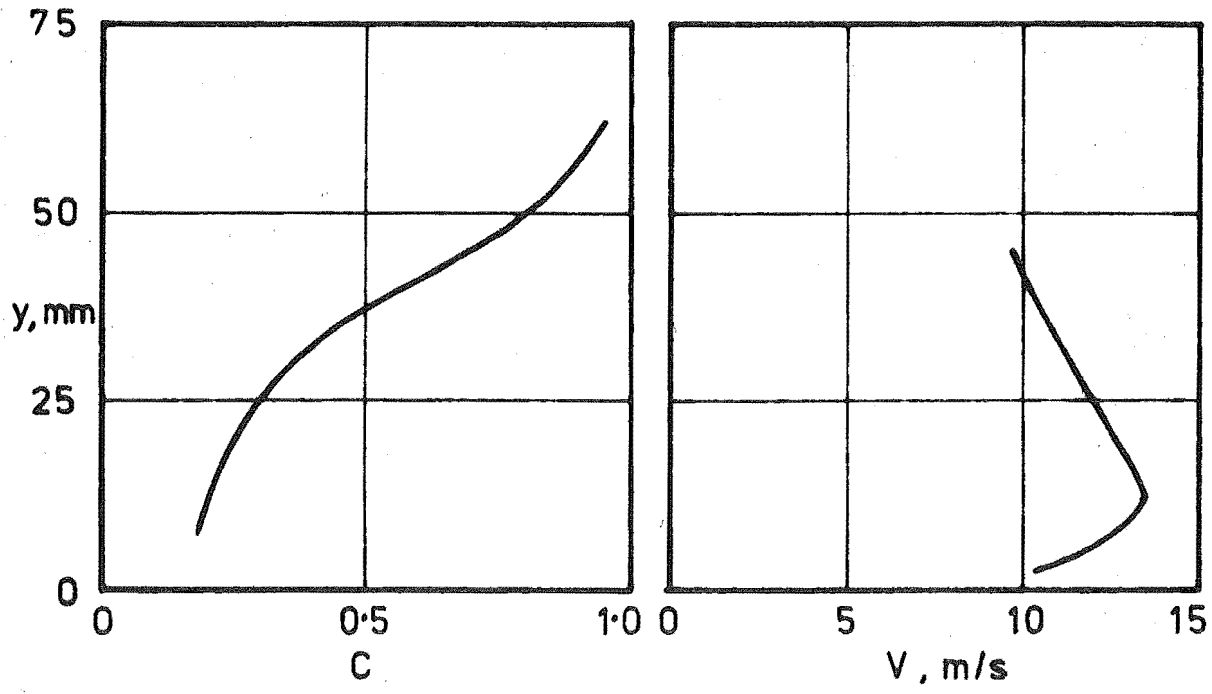

Fig. 11.21 Velocity and Air Concentration Profiles, Following Straub and Lamb (1956). $q = 0.40\ m^2/s$, $\theta = 45^\circ$, Smooth Flume Surface.

11.6.3 Prediction of Air Concentration Distribution in Fully Aerated Flow

An attempt was made to explain the air concentration distribution measured in fully aerated flow at Aviemore by assuming an image flow below the spillway surface. As mentioned earlier an image flow satisfies the requirement that there should be no flow of air ($\frac{\partial C}{\partial y} = 0$) through the spillway surface. This analysis assumes incorrectly a uniform velocity distribution.

Because of the self-similarity of the air concentration profiles in partially aerated flow, a "standard" profile can be constructed, which is shown in Fig. 11.22. This is an average of all the profiles in Fig. 11.17 which were all measured in partially aerated flow. It has been extended to the range of air concentrations 0.02 - 0.1 by reference to the profiles measured at Aviemore.

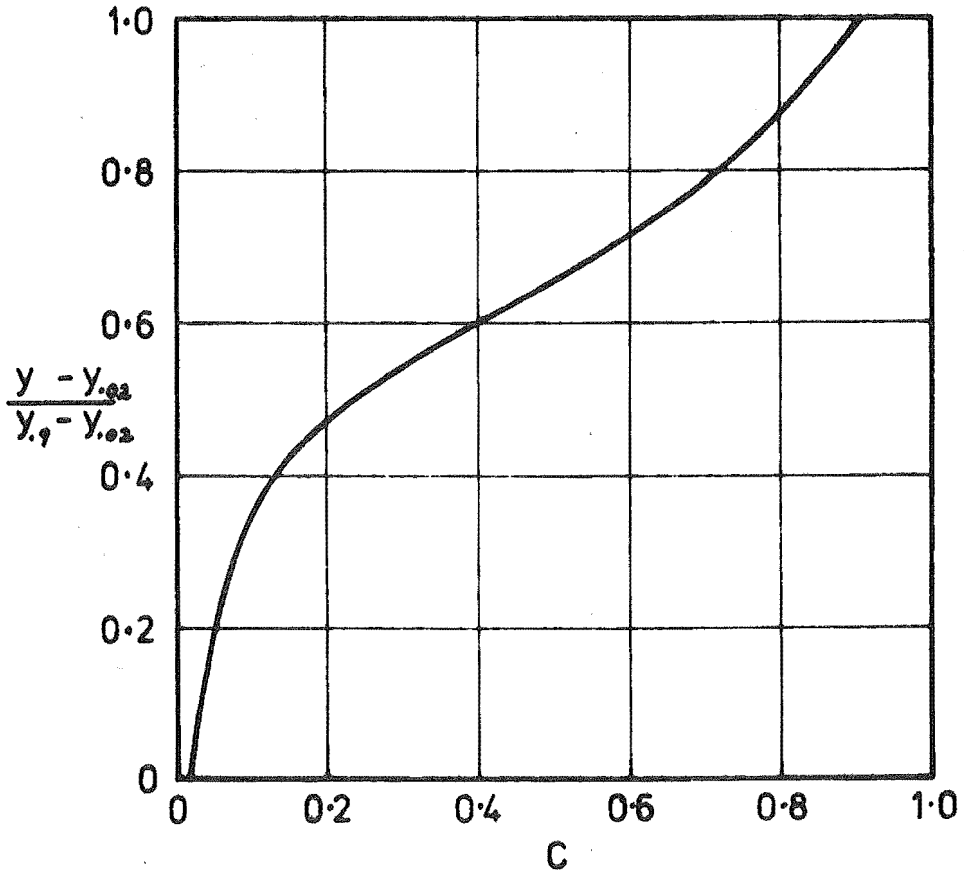

Fig. 11.22 "Standard" Air Concentration Profile.

To predict the distribution of air using this "standard" profile (Fig. 11.22) requires knowledge of the distribution of air along two lines in the direction of flow. Two distributions are shown in Fig. 11.23 constructed using the principle of mirror images. In each case, the very wide lines are those along which the air concentration was initially

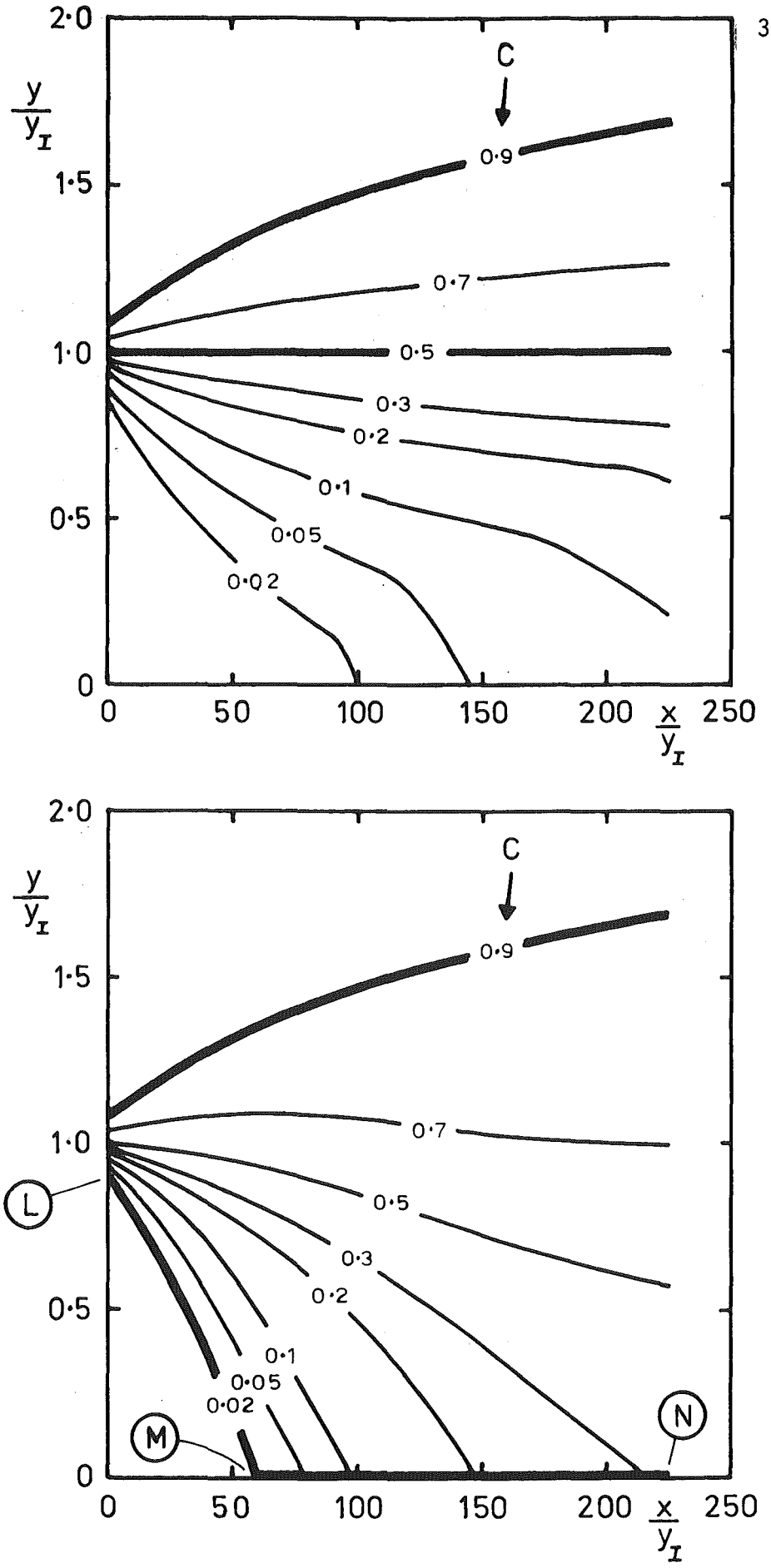

Fig. 11.23 Predicted Air Concentration Distributions.

assumed. In the top case, these are the curves for which $\bar{C} = 0.9$ and $\bar{C} = 0.5$, taken from Fig. 11.4. In the lower case these are $\bar{C} = 0.9$, $\bar{C} = 0.02$ (L - M) and the distribution of air along the spillway surface (M - N), again taken from Fig. 11.4.

Comparison with the measured distribution of air (Fig. 11.4) shows both predicted distributions agree qualitatively. It is considered that the differences are caused by the assumption of a uniform velocity distribution. It may be possible to improve this analysis by taking the measured velocity distribution into account. Such an analysis was considered beyond the scope of this project.

11.6.4 Spillway Shear Stress in Fully Aerated Flow

It was shown in Section 11.5.4 that the mean shear stress on the spillway surface could be calculated from momentum considerations. The complete set of calculated shear stresses is given in Table 11.3. This includes the value in partially aerated flow at station 501 - 502 with a 450 mm gate opening. In each case, it was found that the term $P_1 - P_2$ could have been ignored with less then 1% effect on the calculated shear stress.

The writer is not aware of any measurements with which the measurements in fully aerated flow can be compared.

Table 11.3 Measured Spillway Shear Stress, N/m^2

Section	Gate Opening	
	300 mm	450 mm
501 - 502	775	900 *
502 - 503	820	1040
503 - 504	720	970
504 - 505	740	930

* Partially aerated flow.

CHAPTER 12

SUMMARY AND CONCLUSIONS

12.1 SUMMARY

The instrumentation used at Aviemore is appraised. The results are summarised and proposals for future research are given. These include specific proposals for future tests at Aviemore plus suggested instrumentation.

12.2 INSTRUMENTATION APPRAISAL AND CONCLUSIONS

12.2.1 Introduction

The performance of the instruments used at Aviemore is discussed below and conclusions drawn as to their suitability for measurements within self-aerated flows. The use of resistivity probes for future research is also discussed, and a probe suggested for future measurements within self-aerated flows.

12.2.2 Air Concentration Measurement

The air concentration was measured with a resistance technique as described in Chapter 3. To obtain adequate resolution of the measured profiles, the dimensions and spacing of the electrodes were made small compared with the depth of flow. The dimensions were made larger than the 1 - 3 mm bubble size initially expected. All the aerated flow beneath the water surface was then expected to appear as a homogeneous air-water mixture.

Bubbles as large as 20 mm were later measured at Aviemore, much larger than the electrodes. For the flow to appear homogeneous, the electrodes' dimensions and spacing should therefore have been about 25 - 30 mm (i.e. larger than the largest bubbles). This would have significantly simplified the analysis and interpretation of the data and possibly increased the accuracy of the measurements.

As the depth of the flow at Aviemore was typically 300 mm, such large electrodes would seriously reduce the resolution of the measured air concentration profile. It must therefore be concluded that resistance type probes are not suited to field measurements within self-aerated flows on spillways.

Other drawbacks of this type of probe are:

(1) they do not provide any information on bubble sizes and

(2) they will not respond to spray smaller than the electrodes.

By comparison, the recently developed resistivity probes (ref. Chapter 5) have none of these disadvantages. They detect the presence (or absence) of air at a point. They can detect spray, bubbles and gaps between waves, the dimensions of which can be simply calculated if the velocity is known. Herringe and Davis (1974), Serizawa et al (1975) and White and Hay (1975) report the use of resistivity probes for measuring mean air concentration. This can be calculated with a simple electronic averaging circuit. Alternatively, the air concentration can be calculated from the cumulative probability density function of the signal. This can be formed by a computer or with a commercial device such as the Hewlett-Packard Correlator model 3721A.

Recent development of resistivity probes has been stimulated by applications such as nuclear reactor coolers. Their suitability for use

within self-aerated flows was demonstrated by the measurements reported here.

12.2.3 Velocity Measurement

An initial aim of this project was to calculate velocity from measurements of stagnation pressure and air concentration. It was hoped a velocity signal could be generated which had a flat frequency response to 1 kHz. This would then allow turbulent velocity parameters to be calculated.

It was shown that the velocity of self-aerated flows could not be accurately predicted because the theoretical expressions could not account for the behaviour of an air-water mixture approaching a stagnation point.

It was also shown that at high air concentrations, small errors in either the stagnation pressure or air concentration cause large errors in the calculated velocity.

In view of the recent developments of resistivity probes for velocity measurements, the writer would recommend no further attempts be made to calculate the velocity of self-aerated flows from measurements of stagnation pressure and air concentration.

The best method of measuring velocity presently available is with resistivity probes such as the one developed for this research (ref. Section 5.3). Herringe and Davis (1974) and Serizawa et al (1975) report similar probes used to measure bubble velocities. The instruments' electronics can be very simple but a cross-correlator (or a computer) is needed to process the output signals. This method allows only the mean velocity to be calculated. No turbulence measurements are possible.

The writer would in fact now question the meaning of turbulence measurements within self-aerated flows.

This velocity measuring technique will only work in aerated flows. Stagnation pressure measurements can be used to calculate the velocity in non-aerated flows if these are required.

12.2.4 Stagnation Pressure Measurement

Stagnation pressure measurements within self-aerated flows are complicated by the transient nature of the flows. Because most (if not all) commercial pressure transducers are undamped, they will resonate continually in self-aerated flows. Suitable dynamic response characteristics can only be obtained by connecting the pressure transducer and the measurement region with an appropriate pressure inlet tube.

The frequency response of the probe used in the final field tests at Aviemore was flat to less than 1 Hz. It was shown in Appendix G that this response could theoretically have been increased to larger than 1 kHz by using a small high frequency pressure transducer and a much shorter pressure inlet tube. To prevent air entering the inlet tube and altering the dynamic response, the inlet tube is oil filled, with a very small internal diameter. It was also shown to be very difficult to determine the dynamic response, either analytically or experimentally.

Stagnation pressure measurements can be used to calculate velocity and turbulence parameters within non-aerated flow. This application does not require the use of a pressure inlet tube.

The writer sees little need for stagnation pressure measurements within self-aerated flows.

12.2.5 Proposed Instrumentation for Future Measurements in Self-Aerated Flows

The writer considers the most important parameters within self-aerated flows are mean (time-wise) air concentration and mean velocity. These can be simply obtained with a single resistivity probe similar to the one used at Aviemore (ref. Fig. 5.7) and to those used by Herringe and Davis (1974) and Serizawa et al (1975). If carefully designed, this should enable measurements accurate to about 3% without the need for calibration.

Fig. 12.1 shows a schematic of the suggested probe for future research. The two probes B and C are electrically insulated except for about 0.02 mm at the tips. The tips are sharpened with diameters about 0.02 mm so that bubbles as small as 0.1 mm can be detected. The sharpened rods A and D provide a very short electrical path through the water to the probe tips.

The signal from the upstream probe can be used to calculate the mean air concentration plus details of bubble size, spray size and the spacing of the waves.

The signals from both probes can be used to calculate the velocity using a cross-correlator. Because the two probes are not aligned exactly in the direction of flow, bubbles will often be detected by only one of the probes. This is not important, as was demonstrated in Section 5.3.6

The spacing of the two probes in the direction of flow is shown as 35 mm. For the 12 - 22 m/s velocities at Aviemore, this would correspond to time delays from 1.6 - 2.9 ms. If a Hewlett-Packard correlator model 3721A (about $10,000) was used with a delay range of

3.33 ms, it would take about 18s to form a cross-correlogram using the same number of samples as for the 14s EAI analyses reported here.

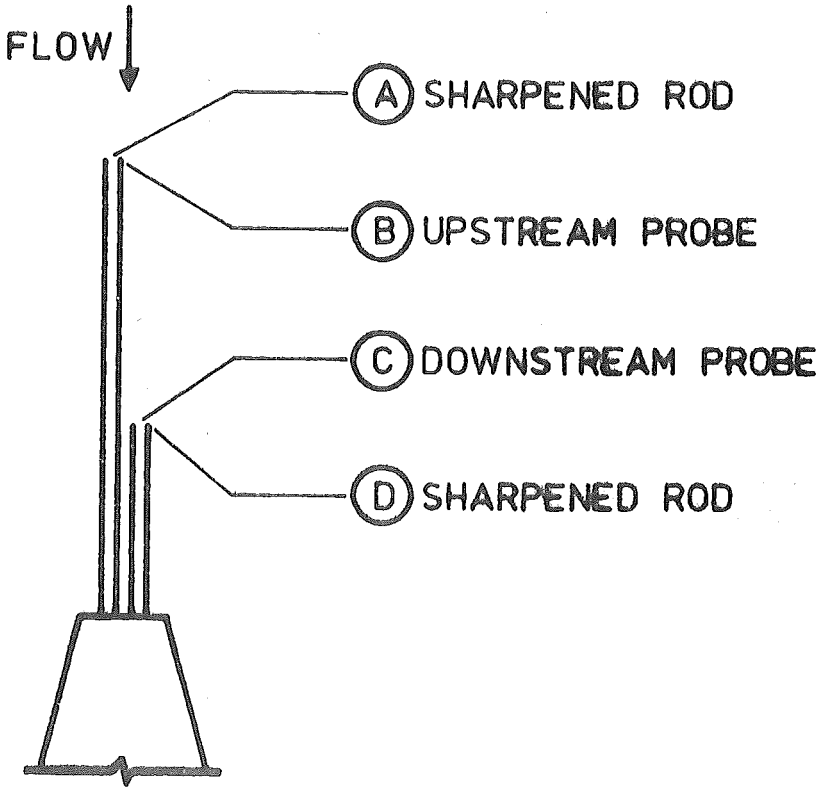

Fig. 12.1 Schematic of Proposed Velocity Air Concentration Probe

If the probe spacing was reduced to 10 mm and the correlators 1 ms delay range used, the same number of samples and calculations would take about 6s.

Electronic circuits and construction details for the probe are reported in Chapter 5 plus by Herringe and Davis (1974) and by Serizawa et al (1975).

For any future tests at Aviemore, a fail safe gate opening indicator should be devised, and well regulated mains power supply should be used.

(Ref. Sections 9.3 and 9.4). It is also suggested that the data analyses should be performed on line and plotted simultaneously to reduce the possibility of error.

12.3 SUMMARY OF RESULTS

Profiles of air concentration, velocity and stagnation pressure were measured on the spillway of Aviemore Dam. Measurements were obtained at each of five stations for two different water discharges. These represent the most comprehensive results yet obtained on a prototype structure.

It was shown that for analysis purposes, the flow down a spillway could be divided into various regions.

The non-aerated region of flow from the spillway gate to the point of inception has previously been analysed by several methods. These were shown to predict the point of inception with reasonable accuracy.

A dimensional analysis was used here to indicate the important parameters effecting the air concentration and velocity distributions downstream of the point of inception. Two of the parameters, an inception Reynolds number and an inception Froude number were shown to have little if any influence. It was not possible to determine the effect of the spillway slope and a roughness parameter.

The air concentration profiles were shown to be self-similar in the aerated region not directly influenced by the spillway surface (E, Fig. 11.1). This was supported by measurements from laboratory flumes.

Shear stress measurements on the spillway surface were also reported. These were in both partially and fully aerated flows.

12.4 PROPOSALS FOR FUTURE RESEARCH

(i) It was stated in Section 11.6.2 that the writer was unable to calculate $\frac{x}{y_I}$ values for Straub and Anderson's (1958) measurements. It is possible that these could be calculated either from existing unpublished data or by recreating the flows in the original flume. The measurements cover such a large range of slopes (7.5 - 75°) and discharges (0.136 - 0.93 m^2/s) that they ought to be analysed in the same way as the Aviemore measurements. The writer has written to the St. Anthony Falls Hydraulic Laboratory to pursue this matter.

(ii) The writer attempted to predict the distribution of air measured at Aviemore by using the principle of mirror images. This analysis relied on the initial self-similarity of the air concentration profiles plus an assumption of uniform velocity distribution. It required the distribution of air to be known along two lines in the direction of flow. For example, along the spillway surface and at a depth $y = y_I$, or along the curve for which the air concentration $C = 0.9$. This gave qualitative agreement with the measured distribution of air. It may be possible to improve this analysis by taking the measured velocity distribution into account.

(iii) It would be of interest to obtain a series of good quality high speed photographs of the surface of self-aerated flow on large structures. This would clarify the air entrainment mechanism and the structure of the flow. Appendix A details an unsuccessful attempt to photograph self-aerated flow on Aviemore spillway.

(iv) The writer considers that the measurements of air concentration and velocity obtained at Aviemore are sufficiently accurate for analysis purposes, and that there would be little point in repeating them to improve their accuracy. It would be of interest to obtain measurements with a gate opening about 150 mm. This would give very large values of

$\frac{x}{y_I}$ (about 500 at station 505) so that the flow should approach uniform conditions. Such a small gate opening may not be practical. As the gate is opened, the shape of the gate seal causes the water to leave the spillway surface as shown in Fig. 1.10. To make it flow down the spillway, it may be necessary to first open the gate to say 300 mm and then close it to 150 mm.

It would also be of interest to obtain measurements with a gate opening about 900 mm. This would provide information on the vortex-induced surface aeration upstream of the point of inception.

Measurements of side wall induced aeration could be obtained on the Aviemore spillway. This would require a different probe traversing mechanism.

Proposed instrumentation and improvements for any future tests at Aviemore are discussed in Section 12.2.

If a complete analysis describing the development of air entrainment is to be obtained, it will be necessary to obtain further field measurements on at least one other prototype structure. This should be much longer than the Aviemore spillway so that the effect of large flow depths can be investigated.

REFERENCES

1. Bauer, W. J., Turbulent Boundary Layer on Steep Slopes, Transactions, ASCE, Vol. 119, Paper No. 2719, 1954, pp 1212-1233.

2. Bryer, D. W., Pankhurst, R. C., Pressure Probe Methods for Determining Wind Speed and Flow Direction, London, 1971.

3. Cimorelli, L., Evangelisti, R., The Application of the Capacitance Method for Void Fraction Measurement in Bulk Boiling Conditions, Int. J. Heat Mass Transfer, Vol. 10, 1967, pp 277-288.

4. Eddington, R. B., Investigation of Supersonic Shock Phenomena in a Two-Phase (Liquid-Gas) Tunnel, TR 32-1096, NAS 7-100, Jet Propulsion Lab., Pasadena, Calif., 1967.
   Also published in : AIAA J., Vol. 8, No. 1, 1970, pp 65-74.

5. Elliot, D. G., Private Correspondence, Jet Propulsion Lab., Pasadena, Calif., November 1974.

6. Gangadharaiah, T., Rao, N.S.L., Seetharamiah, K., Inception and Entrainment in Self-Aerated Flows, Journal of the Hydraulics Division, Proc. ASCE, Vol. 96, No. HY7, 1970, pp 1549-1565.

7. Gouse, S. W., Brown, G. A., Some Remarks on the Velocity of Sound for Two-Phase Mixtures and Flows, TR 8040-1, Engineering Projects Laboratory, Dept. Mechanical Engineering, Massachusetts Inst. Tech., 1963.

8. Halbronn, G., Discussion of Bauer (1954) (Reference 1), Transactions, ASCE, Vol. 119, Paper No. 2719, 1954, pp 1234-1242.

9. Herringe, R. A., Davis, M. R., Detection of Instantaneous Phase Changes in Gas-Liquid Mixtures, Journal of Physics E : Scientific Instruments, Vol. 7, 1974, pp 807 - 812.

10. Hewitt, G. F., The Role of Experiments in Two-Phase Systems with Particular Reference to Measurement Techniques, Progress in Heat and Mass Transfer, Vol. 6, Proc. International Symposium on Two-Phase Systems, Haifa, Pergamonn Press, 1971, pp 295-343.

11. Keller, R. J., Field Measurement of Self-Aerated High Speed Open Channel Flow, PhD. Thesis, University of Canterbury, New Zealand, 1972.

12. Keller, R. J., Lai, K. K., Wood, I. R., Developing Region in Self-Aerated Flows, Journal of the Hydraulics Division, ASCE, HY4, 1974, pp 553-568.

13. Keller, R. J., Rastogi, A. K., Prediction of Flow Development on Spillways, Journal of the Hydraulics Division, ASCE, HY9, 1975, pp 1171-1184.

14. Keller, R. J., Rastogi, A. K., Design Chart for Predicting the Critical Point on Spillways, to be published.

15. Killen, J. M., The Surface Characteristics of Self-Aerated Flow in Steep Channels, Phd. Thesis, University of Minnesota, St. Anthony Falls Hydraulic Laboratory, 1968.
Also : Killen, J. M., Anderson, A. G., A Study of the Air-Water Interface in Air-Entrained Flow in Open Channels, IAHR, 13 Congres Kyoto, Vol. 2, Subject B, 1969.

16. Lai, K. K., Studies of Air Entrainment in Steep Open Channels, Phd. Thesis, University of New South Wales, Sydney, Australia, 1971.

17. Lamb, O. P., Killen, J. M., An Electrical Method for Measuring Air Concentration in Flowing Air-Water Mixtures, University of Minnesota, St. Anthony Falls Hydraulic Laboratory, Technical Paper Number 2, Series B, 1950.

18. Maxwell, J. C., A Treatise on Electricity and Magnetism, Oxford, Clarendon Press, 1873.

19. Neal, L. G., Bankoff, S. G., AIChE Journal, 1963, pp 490-494.

20. Neubert, H. K. P., Instrument Transducers, Oxford, Clarendon Press, 1963.

21. Rao, N. S. L., Kobus, H. E., Characteristics of Self-Aerated Free-Surface Flows, Water and Waste Water, Current Research and Practice, Vol. 10, Erich Schmidt Verlag, Berlin.

22. Rao, N. S. L., Seetharamiah, K., Gangadharaiah, T., Characteristics of Self-Aerated Flows, Journal of the Hydraulics Division, ASCE, HY2, 1970, pp 331 - 355.

23. Schrock, V. E., Radiation Attenuation Techniques in Two-Phase Flow Measurements, Two-Phase Flow Instrumentation, 11th National Heat Transfer Conference, Minneapolis, 1969, pp 24-35.

24. Serizawa, A., Kataoka, I., Michiyoshi, I., Turbulence Structure of Air-Water Bubbly Flow - 1. Measuring Techniques, Int. J. Multiphase Flow, Vol. 2, 1975, pp 221 - 233.

25. Sterlini, J., Trotignon, M., A Technique of Local Velocity and Void Fraction Measurement in High Velocity Two Phase Gas-Liquid Flows, Int. Symposium on Two-Phase Systems, Haifa, 1971.

26. Straub, L. G., Anderson, A. G., Experiments on Self-Aerated Flow in Open Channels, Journal of the Hydraulics Division, ASCE, Vol. 84, No. HY7, 1958.

27. Straub, L. G., Killen, J. M., Lamb, O. P., Velocity Measurement of Air-Water Mixtures, Trans. ASCE, Vol. 119, pp 207-220.

28. Straub, L. G., Lamb. O. P., Studies of Air Entrainment in Open Channel Flows, Trans. ASCE, Vol. 121, 1956, pp 30-44.
Also published in: Proc. Minnesota International Hydraulics Convention, Minneapolis, 1953.

29. Thomas, A. S. W., Brown, G. L., Large Structure in a Turbulent Boundary Layer, 6th Australian Hydraulics and Fluid Mechanics Conference, Adelaide, Australia, 1977.

30. Viparelli, M., Pica, M., Discussion of Rao et al. (1970) (Reference 22), Journal of the Hydraulics Division, ASCE, HY12, 1970, pp 2622-2627.

31. Wad, G., Pressure Transducers in Liquid Filled Pressure Systems, DISA Information, No. 7, 1969, pp 25-29.

32. White, P. R. S., Hay, N., A Portable Air Concentration Meter, IAHR, 16th Congress, Sao Paulo, Subject C.d., 1975, pp 541-548.

APPENDIX A

PHOTOGRAPHS OF FLOW SURFACE

It was considered desirable to obtain some photographs of the surface of self-aerated flows on the spillway of Aviemore dam. These would assist in understanding the mechanism of air entrainment and be of value in interpreting measurements.

Because of the high speed of the flow, the film exposure must be limited to about $\frac{1}{10\ 000}$ s (maximum) if good resolution is to be obtained. This requires either a camera with a very fast shutter speed or a very short duration flash unit. Alternatively, a longer exposure, say $\frac{1}{250}$ - $\frac{1}{2\ 000}$ s would be satisfactory providing the camera is "panned" in the direction of the flow.

A high speed movie camera (40 μs exposure at 10 000 frames/s maximum speed) was available but it required very powerful lighting; would take several days to set up and photograph; the photographs would be of limited definition; and it would be very expensive.

Panning a single frame 35 mm camera was chosen in preference because it was not restricted in these ways. The photographs were taken from the spillway side wall as indicated in Fig. A.1. The camera was mounted on a rotating fixture on top of a tripod. A system of pointers fixed to the side spillway wall appeared along the bottom of each photograph. These indicated the orientation of the camera when the shutter was released. A rectangular grid was placed on the spillway surface (Fig. A.1) and photographed at various camera orientations. In this way the grid could be accurately superimposed on the photographs of the aerated flow.

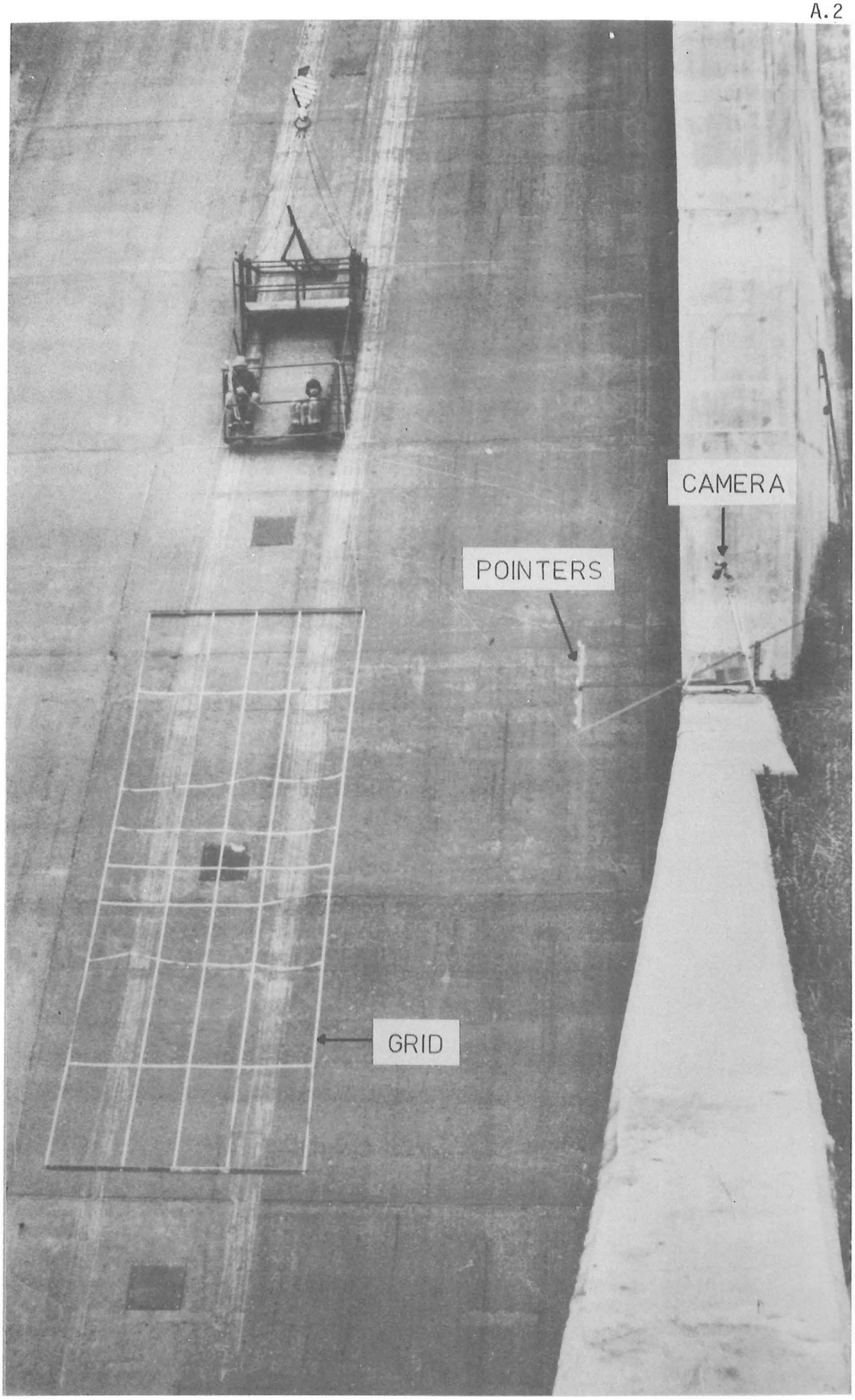

Fig. A.1 Photographing Grid on Spillway Surface

About seventy photographs were taken of the flow surface, with three different telephoto lenses. Unfortunately, these were all blurred because the camera was panned too fast.

The best photograph, Fig. 1.4,was obtained with a hand held camera which was panned much slower. The flow direction and dimensions indicated are approximate only. These are based on the small part of the dexion pointer system appearing in the bottom right hand corner.

APPENDIX B

DERIVATION OF VELOCITY RELATIONSHIPS IN AIR-WATER MIXTURES

B.1 Isothermal Speed of Sound

The speed of sound in an air-water mixture is derived below for a homogeneous mixture which can be considered an isothermal continuum for the propagation of pressure waves.

The speed of sound in a continuum is

$$S = \left[\frac{dP}{d\rho}\right]^{\frac{1}{2}} \qquad \text{B.1}$$

where P = static pressure,

ρ = continuum density

For an air-water mixture

$$\rho = \rho_w(1-C) + \rho_a C$$

where ρ_w = water density

ρ_a = air density

C = air concentration.

When $C < 0.99$, $\rho_a C \ll \rho_w(1-C)$ so that

$$\rho = \rho_w(1-C) \qquad \text{B.2}$$

To derive the isothermal equation of state, consider a control volume containing air and water. If the volume of air is Ψ_a and the volume of water is Ψ_w, then the air concentration within the control volume is

$$C = \frac{\Psi_a}{\Psi_a + \Psi_w}$$

This can be rearranged as

$$\Psi_a = \Psi_w \left[\frac{C}{1-C}\right]$$

The isothermal equation of state for this air is

$$P \Psi_a = \text{constant} \qquad \text{so that}$$

$$P \Psi_w \left[\frac{C}{1-C}\right] = \text{constant.}$$

$$\frac{PC}{1-C} = k \quad \text{(constant)} \qquad \text{B.3}$$

which is in the required form.

Combining Eqs. B.2 and B.3 so as to eliminate C gives

$$P = \frac{k}{\left[\frac{\rho_w}{\rho} - 1\right]}$$

Differentiating this and combining with Eqs. B.2 and B.3 gives

$$\frac{dP}{d\rho} = \frac{k\,\rho_w}{\rho^2\left[\frac{\rho_w}{\rho} - 1\right]^2}$$

$$\frac{dP}{d\rho} = \frac{P}{\rho_w\, C\, (1-C)}$$

So, from Eq. B.1 we get the isothermal speed of sound

$$S = \left[\frac{P}{\rho_w\, C\, (1-C)}\right]^{\frac{1}{2}} \qquad 2.1$$

B.2 Normal Shock Relationships

The following relationships are derived for isothermal flow of a homogeneous air-water mixture through a normal shock structure.

Let subscript 1 denote the region ahead of the shock and subscript 2 the region behind the shock. Then from Eqs. B.2 and B.3

$$\rho_1 = \rho_w\,(1-C_1)$$

$$\rho_2 = \rho_w\,(1-C_2) \qquad \text{B.4}$$

$$\frac{P_1\, C_1}{1 - C_1} = \frac{P_2\, C_2}{1 - C_2} \qquad \text{B.5}$$

and from Eqs. B.1 and B.2

$$M_1 = V_1 \left[\frac{\rho_w C_1 (1 - C_1)}{P_1} \right]^{\frac{1}{2}} \qquad \text{B.6}$$

$$M_2 = V_2 \left[\frac{\rho_w C_2 (1 - C_2)}{P_2} \right]^{\frac{1}{2}} \qquad \text{B.7}$$

The continuity equation across the shock is

$$\rho_1 V_1 = \rho_2 V_2 \qquad \text{B.8}$$

and the momentum equation is

$$P_2 - P_1 = \rho_1 V_1^2 - \rho_2 V_2^2 \qquad \text{B.9}$$

Combining Eqs. B.8 and B.9 to eliminate V_2 gives

$$P_2 - P_1 = \rho_1 V_1^2 \left[1 - \frac{\rho_1}{\rho_2} \right]$$

and eliminating P_1 between this and Eq. B.5 gives

$$\frac{P_2}{C_1} \left[\frac{C_1 - C_2}{1 - C_2} \right] = \rho_1 V_1^2 \left[1 - \frac{\rho_1}{\rho_2} \right]$$

Substitute Eq. B.4 into this to eliminate ρ_1 and ρ_2

$$P_2 = V_1^2 \rho_w C_1 (1 - C_1)$$

Combining this with Eq. B.6 gives

$$P_2 = M_1^2 P_1 \qquad 2.3$$

Eliminating P_1 and P_2 between Eqs. B.5 and 2.3 gives

$$M_1^2 = \frac{C_1}{C_2} \left[\frac{1 - C_2}{1 - C_1} \right] \qquad \text{so that}$$

$$C_2 = \left[1 + \left[\frac{1 - C_1}{C_1} \right] M_1^2 \right]^{-1} \qquad 2.4$$

Combining Eqs B.4 and B.8 to eliminate ρ_1 , ρ_2 and ρ_w gives

$$V_2 = \left[\frac{1 - C_1}{1 - C_2} \right] V_1$$

Combining this with Eq. 2.4 to eliminate C_2 gives

$$V_2 = V_1 \left[1 - C_1 + \frac{C_1}{M_1^2} \right] \qquad 2.5$$

By following the same method used to derive Eq. 2.3, it can be shown that

$$P_1 = M_2^2 P_2$$

Combining this with Eq. 2.3 gives

$$M_1 M_2 = 1 \qquad 2.6$$

B.3 Derivation of Eq. 2.8

Consider the shock-free isothermal deceleration of a homogeneous air-water mixture between two points denoted 1 and 2. The momentum equation at each point is

$$-VdV = \frac{dP}{\rho}$$

Substituting $VdV = \frac{dV^2}{2}$

and $\rho = \rho_w (1 - C)$ gives B.2

$$-dV^2 = \frac{2\, dP}{\rho_w (1 - C)}$$

Integrating this over the pressure rise from 1 to 2 gives

$$V_1^2 - V_2^2 = \frac{2}{\rho_w} \int_{P_1}^{P_2} \frac{dP}{1 - C} \qquad B.10$$

where subscripts 1 and 2 denote points 1 and 2.

From the isothermal equation of state (Eq. B.3) we have

$$\frac{1}{1 - C} = 1 + \frac{k}{P}$$

Substituting this into Eq. B.10 gives

$$V_1^2 - V_2^2 = \frac{2}{\rho_w} \int_{P_1}^{P_2} \left[1 + \frac{k}{P} \right] dP$$

$$V_1^2 - V_2^2 = \frac{2}{\rho_w}\left[P + k \ln P\right]_{P_1}^{P_2}$$

$$V_1^2 - V_2^2 = \frac{2}{\rho_w}\left[P_2 - P_1 + k \ln\left[\frac{P_2}{P_1}\right]\right]$$

From Eq. B.3, k can be expressed as

$$k = \frac{P_1 C_1}{1 - C_1} \qquad \text{so that}$$

$$V_1^2 - V_2^2 = \frac{2}{\rho_w}\left[P_2 - P_1 + \frac{C_1}{1 - C_1} P_1 \ln\left[\frac{P_2}{P_1}\right]\right]$$

If point 1 is in undisturbed flow and point 2 is a stagnation point, then

$$V_1 = \left[\frac{2}{\rho_w}\left[P_2 - P_1 + \frac{C_1}{1 - C_1} P_1 \ln\left[\frac{P_2}{P_1}\right]\right]\right]^{\frac{1}{2}}$$

where P_2 is the stagnation pressure P_s.

Substituting P_s for P_2 and dropping the subscript 1 which denotes the undisturbed flow, then

$$V = \left[\frac{2}{\rho_w}\left[P_s - P + \frac{C}{1 - C} P \ln\left[\frac{P_s}{P}\right]\right]\right]^{\frac{1}{2}} \qquad 2.8$$

B.4 Derivation of Eq. 2.10

Referring to Fig. 2.4 for the case of a detached normal shock in front of a probe, if the flow is isothermal and if the shock relaxation processes are completed at 2 before the flow decelerates to the stagnation point at 3, then from Eqs. 2.3 and 2.4

$$\left[\frac{C_2}{1 - C_2}\right] P_2 = \left[\frac{C_1}{1 - C_1}\right] P_1 \qquad B.11$$

where subscripts 1, 2 and 3 denote points 1, 2 and 3.

Eq. 2.8 can be applied between points 2 and 3 as

$$V_2 = \left[\frac{2}{\rho_w}\left[P_s - P_2 + \frac{C_2}{1 - C_2} P_2 \ln\left[\frac{P_s}{P_2}\right]\right]\right]^{\frac{1}{2}} \qquad B.12$$

Substituting Eqs. 2.3, B.11 and B.12 into Eq. 2.5, rearranging, and dropping the subscript 1 gives

$$V = \frac{\left[\frac{2}{\rho_w}\left[P_s - M^2P + \frac{C}{1 - C} P \ln\left[\frac{P_s}{M^2P}\right]\right]\right]^{\frac{1}{2}}}{\left[1 - C + \frac{C}{M^2}\right]} \qquad 2.10$$

where M^2 is given by Eqs. 2.1 and 2.2 as

$$M^2 = \frac{V^2 \rho_w C (1 - C)}{P}$$

the unsubscripted variables now referring to the undisturbed flow upstream of the shock.

APPENDIX C

RANGE OF FLOW PARAMETERS

C.1 Summary

The magnitude of various flow parameters are estimated so as to indicate the range of flow conditions for which self-aeration will occur on large spillways. These estimates are most likely accurate to within 20%. The static pressure within self-aerated flows is discussed.

C.2 Magnitude of Parameters at the Point of Inception

The magnitude of the most important flow parameters at the point of inception can be estimated from the work of Bauer (1954) and Halbronn (1954), discussed in Section 11.3.2. Three parameters will be considered:

(i) V_I , the velocity at the point of inception.

(ii) y_I , the depth of flow at the point of inception.

(iii) x_I , the distance down the spillway from the free surface to the point of inception, (see Fig. 11.2).

The depth y_I given by Halbronn's expression for the boundary layer thickness (Eq. 11.2) is

$$y_I = 0.0447\ \epsilon^{0.154}\ x_I^{0.846} \qquad C.1$$

where ϵ is the equivalent sand grain roughness.

The velocity V_I is given by Eq.11.1

$$V_I = \left[2g\ x_I\ \sin\theta \right]^{\frac{1}{2}} \qquad 11.1$$

where θ is the spillway slope.

Following Bauer, the boundary layer displacement thickness can be taken as $\frac{1}{10}$ the boundary layer thickness. It follows that the discharge per unit width q is given by

$$q = \frac{V_I \, y_I}{1.1} \qquad C.2$$

Eqs. C.1, 11.1 and C.2 can be combined to give the required expressions,

$$V_I = 12.15 \; \varepsilon^{-0.0572} \; S^{0.314} \; q^{0.372} \qquad C.3$$

$$y_I = 0.131 \; \varepsilon^{0.0572} \; S^{-0.314} \; q^{0.629} \qquad C.4$$

$$x_I = 3.58 \; \varepsilon^{-0.114} \; S^{3.71} \; q^{0.743} \qquad C.5$$

Eqs. C.3 to C.5 have been plotted in Fig. C.1, assuming ε = 1.5 mm. This value is representative of concrete spillways. Relatively large variations in ε will in fact have very little effect on the values of V_I, y_I and x_I predicted.

Most spillways are likely to have slopes ranging from 10 - 60°, with maximum discharges on large spillways about 100 m^2/s. From Fig. C.1, the maximum likely values of V_I, y_I and x_I are therefore about

$$V_I = 50 \text{ m/s}$$

$$y_I = 2 \text{ m}$$

$$x_I = 200 \text{ m}$$

C.3 Static Pressure in Self-Aerated Flows

Because of the small depths of self-aerated flows, the static pressure within them can often be assumed equal to atmospheric pressure.

For the measurements at Aviemore, the maximum depths of aerated flow were about 350 mm. The maximum static pressure in a non-aerated

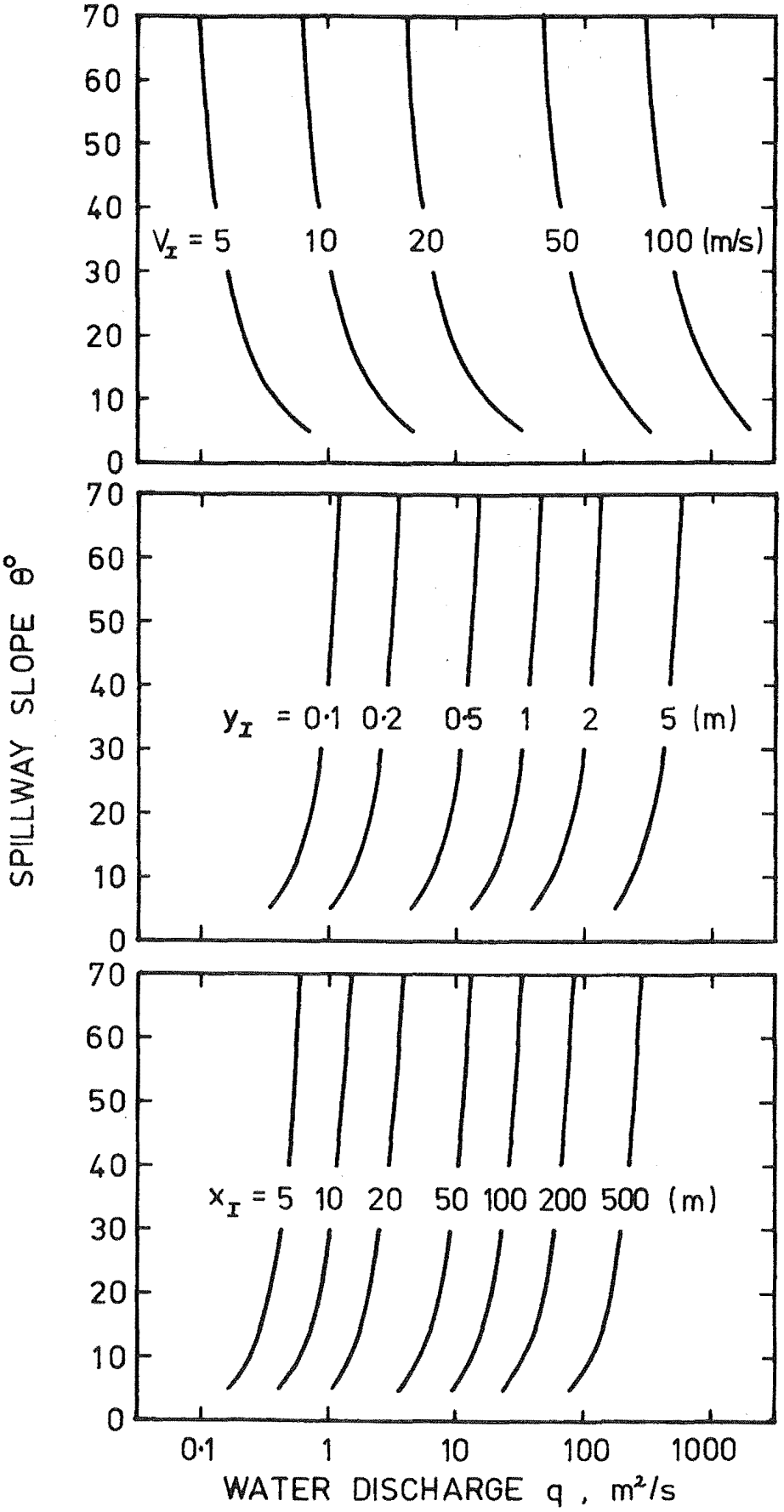

Fig. C.1 Magnitude of V_I , y_I , x_I at the Point of Inception (ε = 1.5 mm)

flow 350 mm deep would be 2.4 kN/m^2. In general, the static pressure in the aerated flow at Aviemore would be much less than this. For the analysis of Aviemore measurements it is therefore reasonable to assume the static pressure equals the atmospheric pressure.

APPENDIX D

FREQUENCY RESPONSE OF ELECTRODES

The response of the air concentration probe to the frequency of air concentration variations (ref. Section 3.5) can be related to the velocity V and the length of the measurement region L by assuming:

(i) the electric field between the electrodes is uniform and of length L in the flow direction, (see Fig. D.1a),

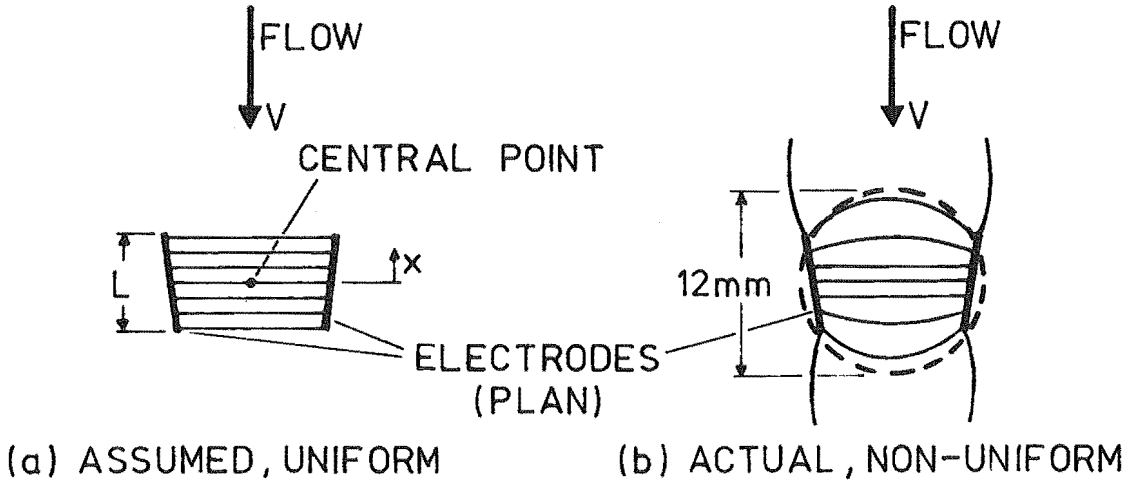

Fig. D.1 Schematic of Electric Field

(ii) the air concentration varies in the flow direction, but at any instant is constant on planes normal to this direction. In practice this could be caused by an appropriate distribution of bubbles that are much smaller than the electrodes.

Consider a variation in air concentration at the central point of the measurement region (see Fig. D.1a) given by

$$C = a \sin (2 \pi ft) + b$$

This is a sinusoidal input signal of frequency f as illustrated in Fig. D.2.

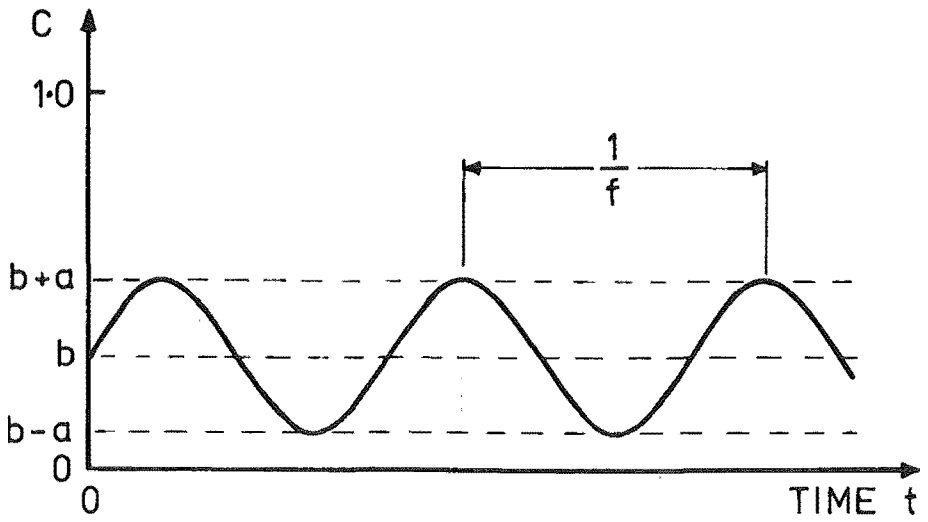

Fig. D.2 Input Signal

At a distance x upstream of this point, the air concentration will be given by

$$C_x = a \text{ Sin } (2 \pi f(t - \tau)) + b$$

where $\tau = \frac{x}{V}$, a time difference.

Now the output signal at any instant will be the mean value of C_x from $x = -\frac{L}{2}$ to $\frac{L}{2}$ and is given by

$$C_{meas} = \frac{V}{L} \int_{\tau = -\frac{L}{2V}}^{\tau = \frac{L}{2V}} (a \text{ Sin } (2 \pi f (t - \tau)) + b) \, d\tau$$

which reduces to

$$C_{meas} = \frac{Va}{\pi fL} \text{ Sin } (2 \pi f t) \text{ Sin } \left[\frac{\pi fL}{V}\right] + b$$

The frequency response is therefore given by

$$\% = \frac{C_{meas} - b}{C - b} = \frac{V}{\pi f L} \quad \text{Sin} \left[\frac{\pi f L}{V} \right] \qquad 3.2$$

The electric field between the electrodes is not uniform, but is mainly contained within a volume about 12 mm diameter as shown in Fig. D.1b. An estimate of the frequency response can therefore be obtained by taking L = 12 mm.

APPENDIX E

ELECTRICAL SPECIFICATIONS

E.1 Frequency Response of Electronic Circuit for Air Concentration Probe.

The frequency response of the electronics was measured by replacing the probe with the electronic circuit in Fig. E.1, which creates a sinusoidally varying resistance. The measured frequency response is shown in Fig. E.2

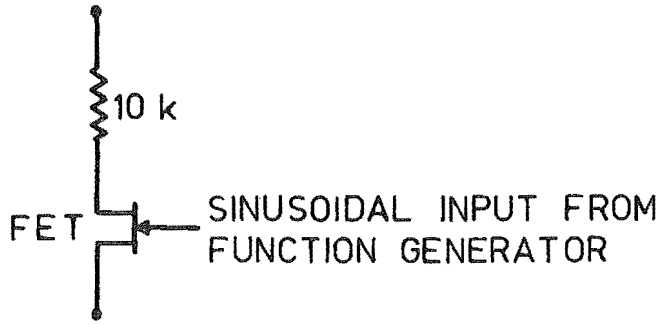

Fig. E.1 Variable Resistance Test Circuit

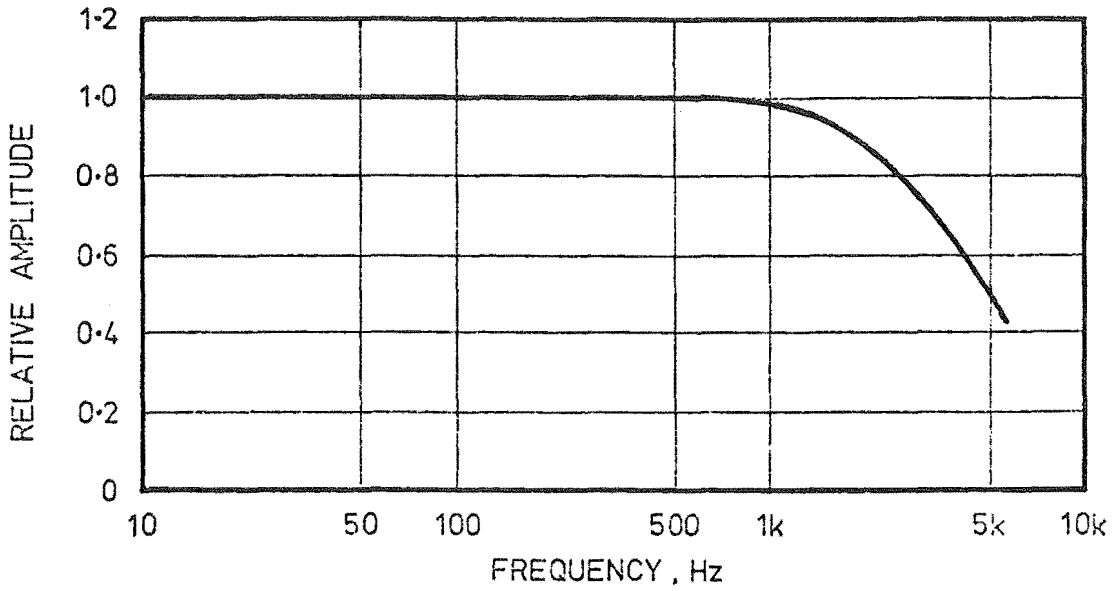

Fig. E.2 Frequency Response of Electronic Circuit

E.2 Pressure Transducer Specifications

National Semiconductor:

Type	LX1610GF
Pressure Range	0 - 415 kN/m^2
Combined Linearity and Hysteresis	± 0.75% FS

Kyowa:

Type	PS - 5 KB
Description	Full bridge bonded strain gauge
Pressure Range	0 - 490 kN/m^2
Non Linearity	1% FS
Hysteresis	1% FS
Natural Frequency	20 kHz

E.3 High Frequency Response Chart Recordings

A technique used to obtain high frequency response recordings was to record data on the FM tape recorder at 381 mm/s tape speed. This was replayed 8 times slower at 47.6 mm/s, the output signal being recorded on a Hewlett Packard chart recorder at its maximum paper speed of 125 mm/s. This effectively increases the time base of the chart recorder by 8 times. The resultant frequency response is shown in Fig. E.3

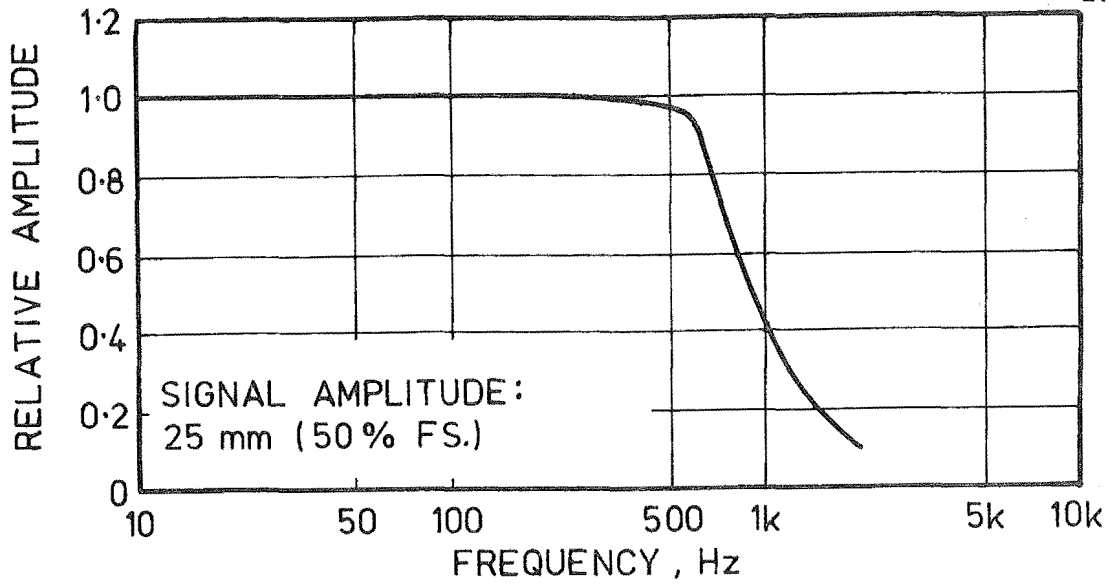

Fig. E.3 Frequency Response of Chart and Tape Recorders

E.4 Tape Recorder Specifications

Type	CEC Datatape VR-3300
Description	A 6 speed 7 track FM tape recorder.
Output Signal Noise Level	< 0.7% FS (as measured)
Drift	Typically 1% FS over 5 hours. (as measured)
Frequency Response	Proportional to tape speed. Fig. E.4 shows the response at 381 mm/s.

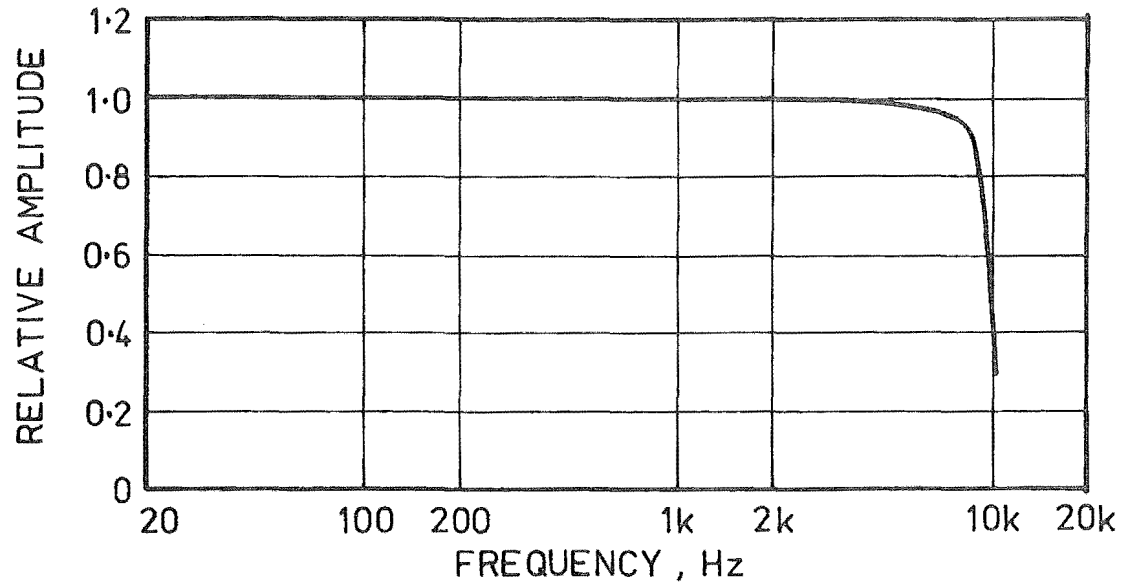

Fig. E.4 Tape Recorder Frequency Response

APPENDIX F

SOURCE FREQUENCY

It is desirable to evaluate δ (ref. Section 3.6) for source frequencies other than the 126×10^3 rad/s used here. This is of interest in assessing the sensitivity of δ, but more importantly is useful for the future design of electronic circuits for similar instruments

Table F.1 lists values of δ for angular frequencies $w = 25.1$, 126 and 628×10^3 rad/s. (These correspond to frequencies of 4, 20.2 and 100 kHz). These were calculated using the measured values of C_E and R_E listed in Table 3.1, and were evaluated from Eqs. 3.6, 3.7 and 3.8. (The values for $w = 126 \times 10^3$ rad/s were taken from Table 3.1). When w is decreased to 25.1×10^3 rad/s (as used by Lamb and Killen, 1950) δ reduces to <0.001. However, when w is increased to 628×10^3 rad/s, δ increases to a maximum of -0.12. The source frequency is therefore a very important parameter in the design of the electrical measuring circuit that is to operate on the principle used here.

Table F.1 Evaluation of δ

R_R = 10 kΩ

Depth Electrodes Submerged (approx.) mm	Measured Data R_E kΩ	Measured Data C_E pF	δ w=25·1 x10^3 rad/s	δ w=126 x10^3 rad/s	δ w=628 x10^3 rad/s
75	15.8	351	0.0	0.0	0.0
10	16.1	311	0.001	0.010	0.035
6.4	18.1	265	0.0	0.012	0.036
4.8	22.6	233	0.0	0.007	-0.017
3.2	28.9	195	0.0	0.005	-0.046
1.6	41.0	157	0.0	0.002	-0.076
just touching	62.5	135	0.0	-0.004	-0.122
in air	63 700	13.3	0.0	-0.001	-0.006

APPENDIX G

INLET TUBE DESIGN FOR OPTIMUM DYNAMIC RESPONSE

The theoretical analysis (ref. Section 4.4) of the dynamic response of pressure transducers and fluid filled inlet tubes can be used for design purposes. It must be realised that the analysis is not strictly correct, but does allow the dynamic response to be predicted reasonably well. It is preferable that such an instrument be tested dynamically if dynamic measurements are important. However, the difficulties of testing pressure instruments may well prevent this.

Eqs. 4.10 and 4.11 can be used to predict the resonant frequency and damping ratio. It was shown that for optimum dynamic response, the damping ratio should be h = 0.75. The three parameters that can be varied to achieve this are the length of the inlet tube L, the internal cross-section area A, and the viscosity of the fluid in the inlet tube μ.

Consider for example that it was desired to achieve a flat frequency response to 1 kHz, and that a damping ratio h = 0.75 was desirable because of the transient nature of the input pressures. These are the design requirements initially sought for the measurements at Aviemore. It will be assumed that a small transducer such as the Kyowa is available. The writer does not know the value of the ratio $\frac{\delta\Psi}{\delta P}$ for this transducer. For this exercise, $\frac{\delta\Psi}{\delta P}$ will be estimated as $\frac{\delta\Psi}{\delta P} = 1 \times 10^{-15}\ m^5/N$.

If the length of the inlet tube is 10.9 mm and its internal diameter is 1 mm and it is filled with SAE 30 oil, then the resonant frequency f_o = 1220 Hz and the damping ratio h = 0.75. From Fig. 4.1a this would give an almost flat frequency response to 1000 Hz.

APPENDIX H

PRESSURE WAVE ANALYSIS

(Ref. Section 4.5.2)

The velocity of a pressure wave in a fluid in a pipe is given by

$$c \simeq \frac{\left[\frac{K}{\rho}\right]^{\frac{1}{2}}}{\left[1 + \frac{KD}{Et}\right]^{\frac{1}{2}}}$$

where K = bulk modulus of elasticity of fluid,

ρ = density of fluid,

D = diameter of pipe,

E = elastic coefficient of pipe,

t = thickness of pipe.

For the copper tube $c_t = 1.24 \times 10^3$ m/s

and for the cylinders $c_c = 1.08 \times 10^3$ m/s

where subscript t denotes tube, and c denotes cylinder.

For a pressure wave in the tube, the transmission factor s and the reflection factor r are given by

$$s = \frac{2\,\frac{A_t}{c_t}}{\frac{A_t}{c_t} + \frac{A_c}{c_c}} = 3.8 \times 10^{-3} \simeq 0$$

$$r = s - 1 = -0.996 \simeq -1.0.$$

For a pressure wave in a cylinder

$$s = \frac{2\,\frac{A_c}{c_c}}{\frac{A_c}{c_c} + \frac{A_t}{c_t}} = 1.998 \simeq 2.0$$

$$r = s - 1 = 0.998 \simeq 1.0$$

APPENDIX I

VELOCITY INSTRUMENT CIRCUIT DIAGRAM

Identical electrical circuits were provided for the upstream and downstream probes, as shown below.

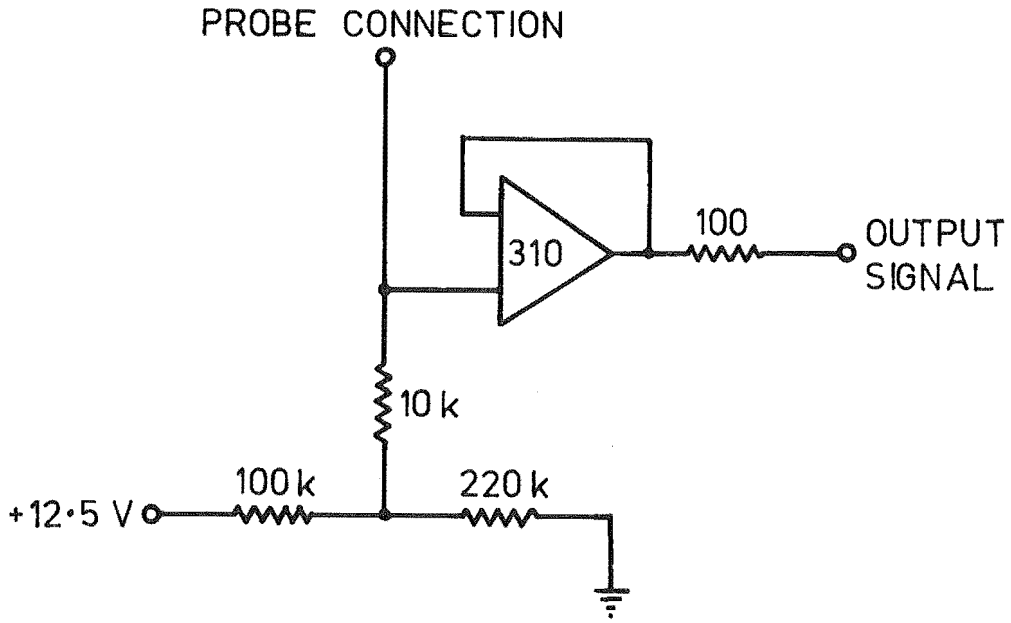

Fig. I.1 Velocity Instrument Circuit Diagram

APPENDIX J

DESCRIPTION OF EAI 590 HYBRID COMPUTER

This is a user operated mini-computer installation comprising an EAI 580 analogue computer, an EAI 640 digital computer and various peripherals. (See Fig. J.1). The components used in the analysis of Aviemore data are shown in Fig. J.2 and are described briefly below.

The EAI 640 digital computer has 16000 16 bit words of core storage. Software is written in either FORTRAN IV or EAI assembler. Programs are stored external to the computer on paper tape. These are read into the computer and transferred to the disc which is used for storage during editing and compiling of programs. Operator control is via the console or either of two keyboards, with output on a line printer or visual display unit. The visual display unit is a storage oscilloscope which can be used for plotting. A xerox-type copy of the display can be obtained from another unit.

The EAI 580 analogue computer was used to condition the analogue signals from the tape recorder and to digitise them. Each analogue component is ± 10 volt FS input with better than 0.1% accuracy. The various analogue components are interconnected on a patch panel, depending on what signal conditioning is required (see Fig. 10.27). A single analogue to digital converter is connected to a 20 channel multiplexor. The multiplexor and analogue to digital converter were controlled by software generated interrupts and by externally generated interrupts (from a function generator).

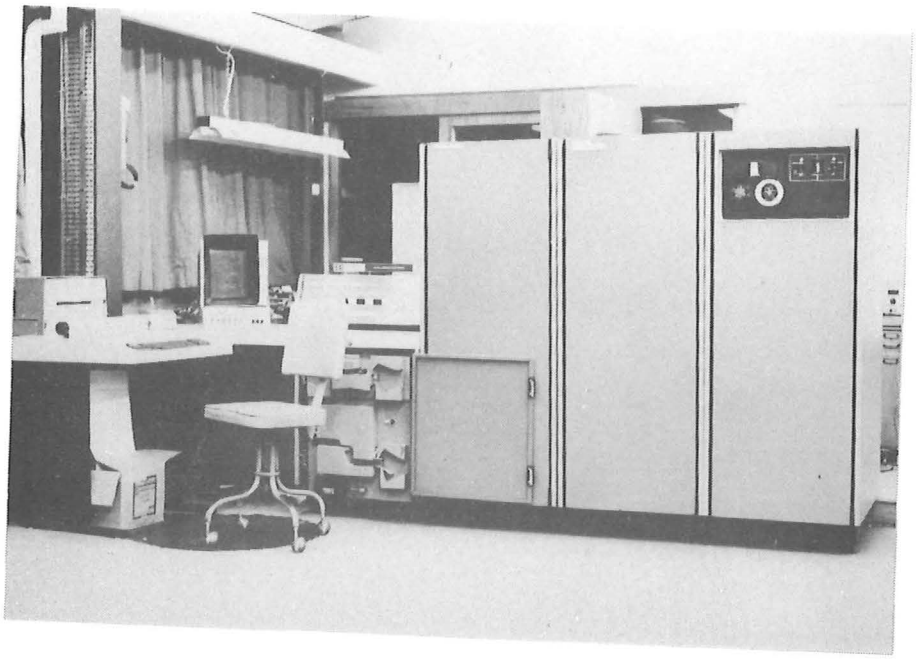

DIGITAL COMPUTER

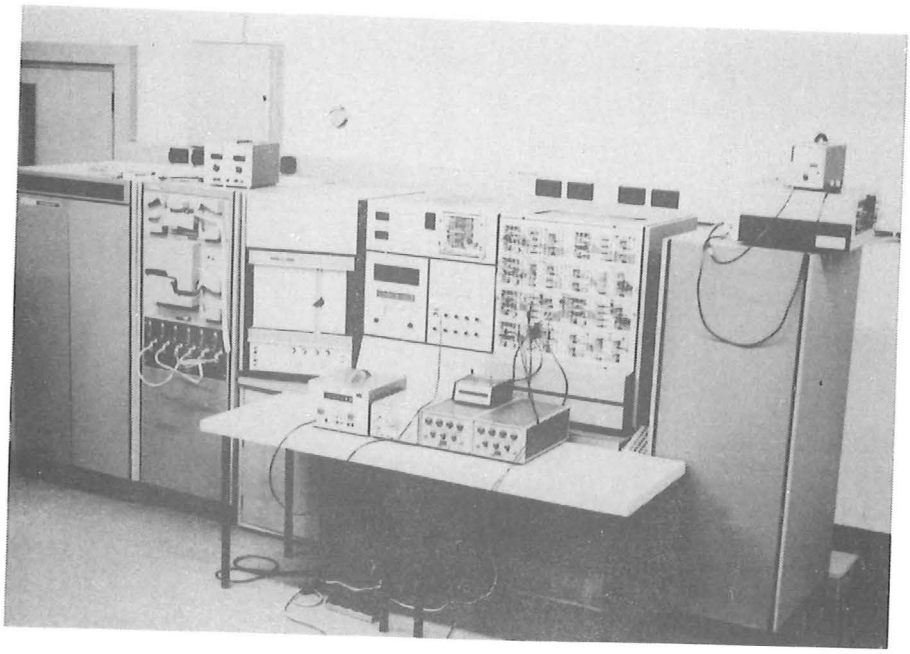

ANALOGUE COMPUTER

Fig. J.1 EAI 590 Computer

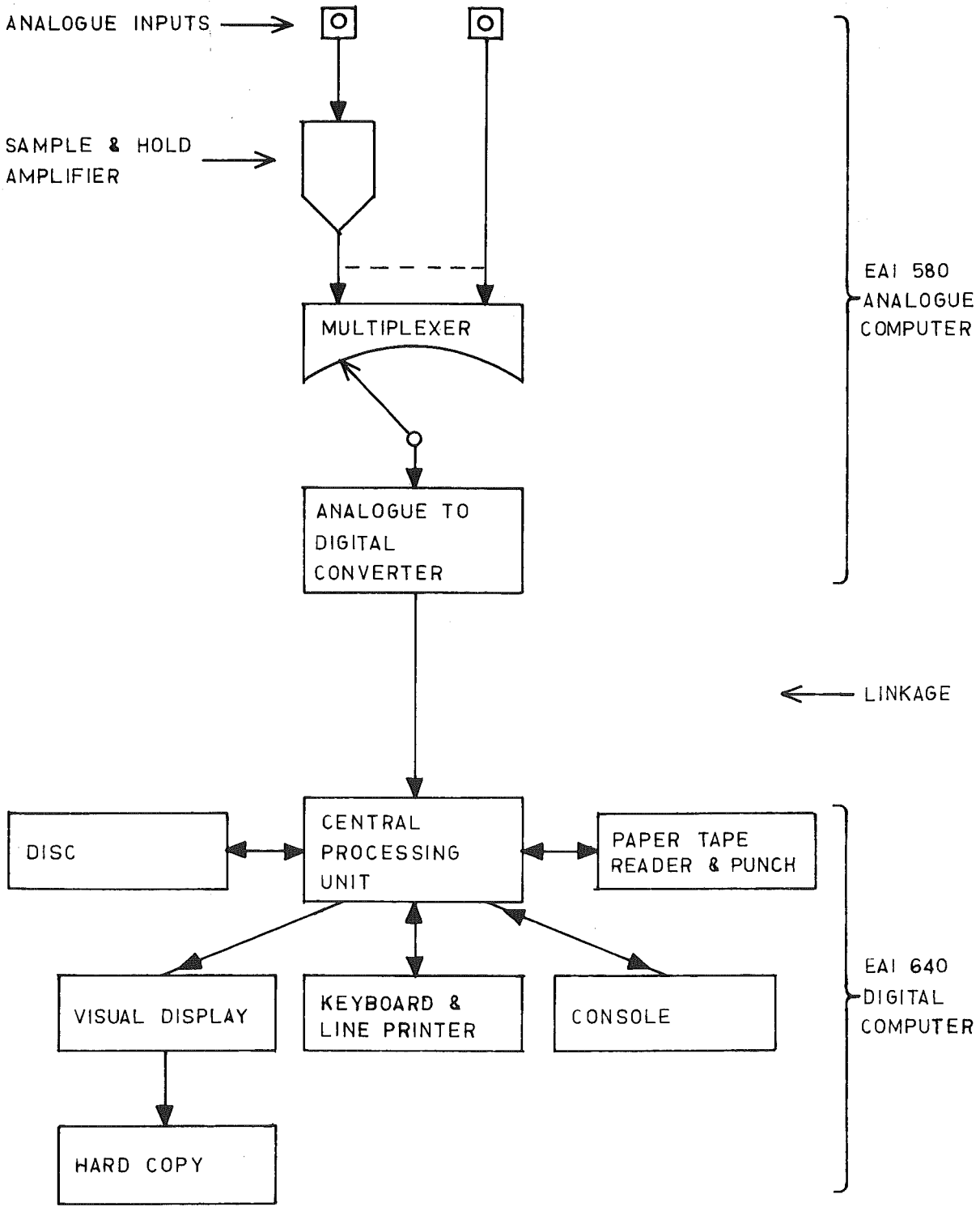

Fig. J.2 The Components of the EAI 590 Computer used for Data Analysis

APPENDIX K

CROSS-CORRELATION PROGRAM

This program calculates the cross-correlation function as described in Section 5.4.2.

```
001: C     ************************************************************
002: C     *  CROSS CORRELATION ANALYSIS FOR VELOCITY CALCULATION     *
003: C     *  AVIEMORE SPILLWAY DATA                                  *
004: C     *  CAIN,DEPT CIVIL ENG,UNIV OF CANT,CHCH NZ,1976           *
005: C     ************************************************************
006: C
007:       INTEGER POS,STN,IGOP,ST,D5(103),I,J,K,G,H,TIME
008:       REAL GOP,E(97),F,E1(97),E5(93),E9(89),ED(97),MAX,MIN,SPAN
009:       COMMON/ARRAY/D5,TIME
010:       COMMON/SUB/POS,STN,IGOP,ST,E1,E5,E9
011: C
012: C     SET HYBRID INTERUPTS
013:       CALL INIT
014: C
015: C     MAIN ITERATION LOOP
016:       DO 29 L=1,1000
017: C
018: C     INPUT DATA IDENTIFICATION FROM TELETYPE
019:     1 TYPE 2
020:     2 FORMAT(99H******************')
021:       TYPE 3
022:     3 FORMAT(99HPOS  STN  GOP'/)
023:       ACCEPT 4,POS,STN,GOP
024:     4 FORMAT(I3,I5,F5.1)
025:       TYPE 5
026:     5 FORMAT(99HSAMPLE TIME (SECS)'/)
027:       ACCEPT 6,ST
028:     6 FORMAT(I2)
029:       IGOP=10.*GOP
030:       IF(ST.EQ.15)GO TO 8
031:       IF(ST.EQ.60)GO TO 9
032:       TYPE 7
033:     7 FORMAT(99HINCORRECT,RE ENTER')
034:       GO TO 1
035:     8 TIME=1
036:       GO TO 10
037:     9 TIME=-1
038: C
039: C     CALL ASSEMBLER SUBROUTINE TO OBTAIN CCF DATA
040:    10 CALL SAMPLE
041:       DO 11 I=1,97
042:       K=I+3
043:       E(I)=D5(K)
044:    11 ED(I)=E(I)
045: C
046: C     SCALE UNAVERAGED DATA
047:       G=97
048:       H=1
049:       GO TO 22
050:    12 DO 13 I=1,97
051:    13 E1(I)=ED(I)
052: C
```

```
053: C      FORM 5 POINT MOVING AVERAGES AND SCALE
054:        ED(1)=0.
055:        DO 14 I=1,5
056:     14 ED(1)=ED(1)+E(I)
057:        DO 15 I=2,93
058:        J=I-1
059:        K=I+4
060:     15 ED(I)=ED(J)-E(J)+E(K)
061:        G=93
062:        H=2
063:        GO TO 22
064:     16 DO 17 I=1,93
065:     17 E5(I)=ED(I)
066: C
067: C      FORM 9 POINT MOVING AVERAGES AND SCALE
068:        ED(1)=0.
069:        DO 18 I=1,9
070:     18 ED(1)=ED(1)+E(I)
071:        DO 19 I=2,89
072:        J=I-1
073:        K=I+8
074:     19 ED(I)=ED(J)-E(J)+E(K)
075:        G=89
076:        H=3
077:        GO TO 22
078:     20 DO 21 I=1,89
079:     21 E9(I)=ED(I)
080:        GO TO 28
081: C
082: C      SCALING ROUTINE FOR PLOTTING
083:     22 MAX=ED(1)
084:        MIN=ED(1)
085:        DO 26 I=2,G
086:        IF(MAX-ED(I))23,24,24
087:     23 MAX=ED(I)
088:     24 IF(ED(I)-MIN)25,26,26
089:     25 MIN=ED(I)
090:     26 CONTINUE
091:        SPAN=250./(MAX-MIN)
092:        DO 27 I=1,G
093:     27 ED(I)=SPAN*(ED(I)-MIN)
094:        GO TO (12,16,20),H
095: C
096: C      OUTPUT DATA TO CRT PLOTTER
097:     28 CALL FPLOT
098: C
099:     29 CONTINUE
100:        STOP
101:        END
102: @
103:
103: _
```

```
001: ************************************************
002: * ASSEMBLER SUBROUTINE                         *
003: * CROSS CORRELATION FOR VELOCITY CALCULATION *
004: ************************************************
005: *
006:          NAME      INIT,SAMPLE
007:          COMMON    ARRAY
008: D5       BSS       103
009: TIME     BSS       1
010:          REL       0
011: *
012: ************************
013: * SET HYBRID INTERUPTS
014: ************************
015: *
```

```
016: INIT    ADR       0
017:         RMI
018:         LA        ='77        RESET ALL CONSOLES
019:         DO        '54
020:         LA        ='40        SET CONSOLE 1
021:         DO        '53
022:         LA        ='176000    DISABLE ALL CONSOLE INTERUPTS
023:         DO        '53
024:         LA        ='100000    ENABLE CONSOLE 1 TO INTERUPT
025:         DO        '54
026:         LA        ='177777    DISABLE ALL HYBRID INTERUPTS
027:         DO        '40
028:         LA        ='100000    ENABLE GPI 0
029:         DO        '46
030:         LA        ='1000      ENABLE INTERUPTS ON DATA CH 0
031:         ES
032:         J,I       INIT
033: *
034: ************************
035: * SAMPLING SEQUENCE
036: ************************
037: *
038: SAMPLE  ADR       0
039: *
040: * SET INITIAL ZERO VALUES
041:         LX        MIN103
042:         CLR
043: ZERO    STA,X     D1+103
044:         STA,X     D2+103
045:         STA,X     D3+103
046:         STA,X     D4+103
047:         STA,X     D5+103
048:         ICX       1
049:         J         ZERO
050: *
051: * SET SUMMATION LOOP COUNTERS
052:         LA        NEG8
053:         STA       L1
054:         STA       L2
055:         LA        NEG4
056:         STA       L3
057:         LA        NEG5
058:         STA       L4
059:         LA        NEG4
060:         STA       L5
061: *
062: * ADDRESS OF SERVICING ROUTINE FOR SAMPLING CHANNEL 1
063: LOOP    LA        AD1
064:         STA       '705
065: *
066: * SAMPLE CHANNEL 1 5 TIMES.(FIRST SAMPLE NOT USED)
067:         LX        MIN5
068: *
069: WAIT1   SMI
070:         NOP
071:         P         0
072: *
073: SAMP1   ADR       0
074:         ADR       0
075:         LA        =1
076:         DF        '64
077:         DI        '65
078:         STA,X     A+5
079:         ICX       1
080:         J         WAIT1
081: *
082: * ADDRESS OF SERVICING ROUTINE FOR SAMPLING CHANNEL 2
083:         LA        AD2
084:         STA       '705
085: *
086: * SAMPLE CHANNEL 2 100 TIMES
087:         LX        MIN100
088: *
```

```
089: WAIT2   SMI
090:         NOP
091:         P          0
092: *
093: SAMP2   ADR        0
094:         ADR        0
095:         LA         =2
096:         DF         '64
097:         DI         '65
098:         STA        B
099:         M          A+1          FIRST PRODUCT/SUMMATION
100:         A,X        D1+103
101:         STA,X      D1+103
102:         LA         B
103:         M          A+2          SECOND PRODUCT/SUMMATION
104:         A,X        D1+102
105:         STA,X      D1+102
106:         LA         B
107:         M          A+3          THIRD PRODUCT/SUMMATION
108:         A,X        D1+101
109:         STA,X      D1+101
110:         LA         B
111:         M          A+4          FOURTH PRODUCT/SUMMATION
112:         A,X        D1+100
113:         STA,X      D1+100
114:         ICX        1
115:         J          WAIT2
116: *
117:         AOM        L1           LOOP 1 SUMMATIONS
118:         J          LOOP
119: *
120:         LX         MIN103       LOOP 2 SUMMATIONS
121: LOOP2   LA,X       D1+103
122:         ARS        3
123:         A,X        D2+103
124:         STA,X      D2+103
125:         CLR
126:         STA,X      D1+103
127:         ICX        1
128:         J          LOOP2
129:         LA         NEG8         RESET COUNTER L1 = -8
130:         STA        L1
131:         AOM        L2
132:         J          LOOP
133: *
134:         LX         MIN103       LOOP 3 SUMMATIONS
135: LOOP3   LA,X       D2+103
136:         ARS        2
137:         A,X        D3+103
138:         STA,X      D3+103
139:         CLR
140:         STA,X      D2+103
141:         ICX        1
142:         J          LOOP3
143:         LA         NEG8         RESET COUNTER L2 = -8
144:         STA        L2
145:         AOM        L3
146:         J          LOOP
147: *
148:         LX         MIN103       LOOP 4 SUMMATIONS
149: LOOP4   LA,X       D3+103
150:         ARS        3
151:         A,X        D4+103
152:         STA,X      D4+103
153:         CLR
154:         STA,X      D3+103
155:         ICX        1
156:         J          LOOP4
157:         LA         NEG4         RESET COUNTER L3 = -4
158:         STA        L3
159:         AOM        L4
160:         J          LOOP
161: *
```

```
162:          LA          TIME
163:          SKN
164:          J           OUT
165: *
166:          LX          MIN103      LOOP 5 SUMMATIONS
167: LOOP5    LA,X        D4+103
168:          ARS         2
169:          A,X         D5+103
170:          STA,X       D5+103
171:          CLR
172:          STA,X       D4+103
173:          ICX         1
174:          J           LOOP5
175:          LA          NEG5        RESET COUNTER L4 = -5
176:          STA         L4
177:          AOM         L5
178:          J           LOOP
179: *
180:          J,I         SAMPLE
181: *
182: OUT      LX          MIN103      STORE D4 IN D5
183: LOOP6    LA,X        D4+103
184:          STA,X       D5+103
185:          ICX         1
186:          J           LOOP6
187: *
188:          J,I         SAMPLE
189: *
190: ************************
191: NEG2     DEC         -2
192: NEG4     DEC         -4
193: NEG5     DEC         -5
194: NEG8     DEC         -8
195: MIN5     DEX         -5
196: MIN100   DEX         -100
197: MIN103   DEX         -103
198: D1       BSS         103
199: D2       BSS         103
200: D3       BSS         103
201: D4       BSS         103
202: L1       OCT         0
203: L2       OCT         0
204: L3       OCT         0
205: L4       OCT         0
206: L5       OCT         0
207: B        OCT         0
208: A        BSS         5
209: AD1      ADR         SAMP1
210: AD2      ADR         SAMP2
211: ************************
212:          END         0
213: @
214:
214: _
```

```
001: C     ************************************************************
002: C     * PLOTTING SUBROUTINE VELOCITY CORRELATION CAIN CIVIL *
003: C     ************************************************************
004: C
005:       SUBROUTINE FPLOT
006:       INTEGER POS,STN,IGOP,ST
007:       REAL E1(97),E5(93),E9(89)
008:       COMMON/SUB/POS,STN,IGOP,ST,E1,E5,E9
009: C
```

```
010:        CALL AINIT
011:        CALL AGRID(750,340,-14,-270,50,1,1)
012:        CALL AGRID(750,610,-14,-270,50,1,1)
013:        CALL AGRID(750,880,-14,-270,50,1,1)
014:        CALL ASIZE(0,800,0,1023,1)
015:        CALL AGRID(50,70,70,810,10,1,3)
016:        CALL ALAB(50,1000,27HCROSS CORRELATION FUNCTION.,27,1)
017:        CALL ALAB(50,970,32HVELOCITY DATA,AVIEMORE,JAN 1976.,32,1)
018:        CALL ALAB(50,940,33HCAIN.CIVIL ENG.ILAM UNIV.CHCH.NZ.,33,1)
019:        CALL ALAB(50,890,32HPOS=       STN=       GOP=   FT.,32,1)
020:        CALL ALAB(635,899,1H.,1,0)
021:        CALL ASCA(72,890,0,0,POS,0,1,1)
022:        CALL ASCA(314,890,0,0,STN,0,1,1)
023:        CALL ASCA(534,890,0,0,IGOP,0,1,1)
024:        CALL ALAB(50,10,32HTIME DELAY,MSECS  (   SECS DATA),32,1)
025:        CALL ASCA(380,10,0,0,ST,0,1,1)
026:        CALL ASCA(-70,40,70,0,0,1,10,1)
027:        CALL ASCA(640,40,0,0,10,0,1,1)
028:        CALL ALINEX(7.,E1,97,78.,-620.,100.,100.,4,0)
029:        CALL ALINEX(7.,E5,93,92.,-350.,100.,100.,4,0)
030:        CALL ALINEX(7.,E9,89,106.,-80.,100.,100.,4,0)
031:        RETURN
032:        END
033: @
034:
034: _
```

APPENDIX L

GAMMA RADIATION ABSORPTION

L.1 Introduction

This Appendix supplements Section 6.5.4 on the gamma radiation absorption technique for measuring the air concentration in an air-water mixture. It is divided into six sections: Beam attenuation, statistical uncertainty, test apparatus, coincidence loss, linearity test and the calibration tests. The beam attenuation analysis presented here is given in various references of which Schrock (1969) is recommended. The analyses of statistical uncertainty and coincidence loss were derived by the writer for the experimental procedure used here.

L.2 Beam Attenuation

A monoenergetic collimated beam of γ-rays (photons) is attenuated in a homogeneous material according to

$$I = I' e^{-\mu x} \qquad \text{L.1}$$

where I is the local intensity of the beam,

I' is the incident intensity of the beam,

x is the absorber thickness,

μ is the linear absorption coefficient.

When used with the flow simulators, the beam is attenuated by the perspex walls and the air-water mixture as shown in Fig. L.1.

Applying Eq. L.1 we get

$$I = I' e^{-\mu_p x_p} \; e^{-\mu_f x_f} \; e^{-\mu_p x_p}$$

where subscript p denotes perspex and f denotes fluid.

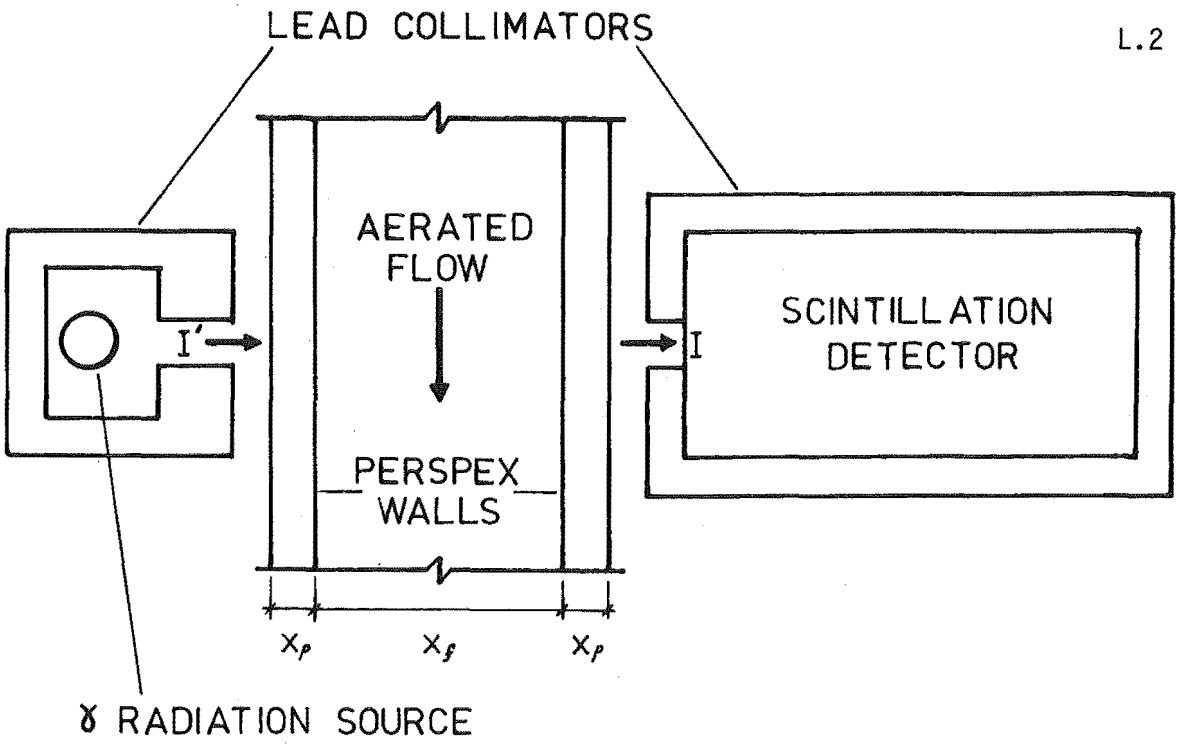

Fig. L.1 Schematic of γ Radiation Test Apparatus

For a homogeneous air-water mixture

$$\mu_f = C\,\mu_a + (1 - C)\,\mu_w$$

where subscript a denotes air and w denotes water.

When C = 1.0 the measured intensity is then given by

$$I_1 = I' e^{-2\mu_p x_p}\, e^{-\mu_a x_f}$$

When C = 0.0 the measured intensity is given by

$$I_0 = I'\, e^{-2\mu_p x_p}\, e^{-\mu_w x_f} \qquad \text{so that}$$

$$\frac{I_1}{I_0} = e^{(\mu_w - \mu_a) x_f} \qquad \text{and} \qquad \text{L.2}$$

$$\frac{I}{I_0} = e^{C(\mu_w - \mu_a)\, x_f} \qquad \text{L.3}$$

Combining Eqs. L.2 and L.3 we get

$$C = \frac{\ln\left[\frac{I}{I_0}\right]}{\ln\left[\frac{I_1}{I_0}\right]} \qquad \text{L.4}$$

Thus C can be determined by simply measuring I, I_1 and I_0

L.3 Statistical Uncertainty

There is a statistical uncertainty ΔI associated with any measurement of intensity I which is given by

$$\frac{\Delta I}{I} = \frac{1}{N^{\frac{1}{2}}} \qquad \text{L.5}$$

where N is the number of γ rays counted.

The scatter of results from a series of 340 tests with the apparatus used here showed that the results were in agreement with this equation. Each of these tests used $N = 4 \times 10^4$. They were conducted at $10^{\circ}C$ and $20^{\circ}C$ with no observable temperature effects.

If I_1 and I_0 are known exactly then from Eq. L.4 the error in C caused by an error ΔI is given by

$$\Delta C = \frac{\frac{\Delta I}{I}}{\ln\left[\frac{I_1}{I_0}\right]}$$

Combining this with Eq. L.5 we get the relationship between ΔC and N as

$$\Delta C = \frac{1}{N^{\frac{1}{2}} \ln\left[\frac{I_1}{I_0}\right]}$$

This equation can be used to determine the number of γ rays that must be counted to achieve a given accuracy ΔC.

L.4 Test Apparatus

γ radiation source	-	Cobalt 60
δ radiation strength	-	about 35μ Curie
scintillation detector	-	Philips PW 4111
detector power supply	-	Philips PW 4022
counter	-	Philips PW 4032
timer	-	Advance timer counter

Technical note: A serious factory design fault prevented the detector operating correctly. Resistor R19 was increased from 1k6 to 10 kΩ with two improvements:

(i) the measured intensity was insensitive to variations in the detector operating voltage from 1100 - 1150 volts,

(ii) the output pulse widths decreased from about 50 μs to 2 μs thus allowing much higher radiation intensities.

This fault most likely reduced the accuracy of Keller's (1972) calibration tests.

L.5 Coincidence Loss

If two γ rays arrive at the detector within 2 μs of each other (the "dead time" of the detector), only one pulse will be generated for counting. This is called a coincidence loss and is proportional to the radiation intensity. For I = 90 000 cpm (counts per minute) this causes about 0.3% underestimation of the true intensity. The following analysis shows that the coincidence loss can in fact be ignored because it does not effect the calculation of air concentration.

If $I = I''(1 + k)$

where I is the true intensity at the detector,

I" is the indicated intensity at the detector,

k is the proportion of dead time per unit time,

then when C = 1.0 the true intensity is

$$I_1 = I_1''(1 + k) \qquad \text{L.7}$$

and when C = 0.0 the true intensity is

$$I_0 = I_0''(1 + k) \qquad \text{L.8}$$

Eqs. L.7 and L.8 can be substituted into Eq. L.4 to give

$$C = \frac{\ln\left[\frac{I''(1 + k)}{I_0''(1 + k)}\right]}{\ln\left[\frac{I_1''(1 + k)}{I_0''(1 + k)}\right]}$$

therefore

$$C = \frac{\ln\left[\frac{I''}{I_0''}\right]}{\ln\left[\frac{I_1''}{I_0''}\right]}$$

L.6 Linearity Test

The linearity of the gamma radiation apparatus was verified in a test in which two pieces of perspex were glued to each end of a 69.85 mm length of PVC tube. (See Fig. L.2). This was placed between the source and the detector as in Fig. L.3 and the intensities I_1 and I_0 were measured as 36145 and 24310 cpm respectively. The perspex end pieces were then glued to each end of a 35.04 mm length of PVC. This was water filled and the intensity I was measured as 29650 cpm. After subtracting the 70 cpm background radiation from I, I_0 and I_1 , Eq. L.4 predicts the simulated air concentration C = 0.501 whereas the difference in length

of the PVC tubes indicates C = 0.498. The 0.0024 difference is in excellent agreement with the statistical uncertainty in C given by Eq. L.6 as

$$\Delta C = 0.0040 \quad (N = 4 \times 10^5)$$

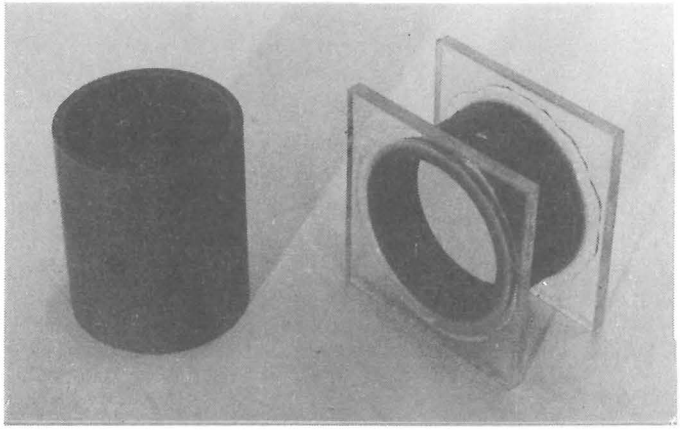

Fig. L.2 PVC Tubes with Perspex End Plates

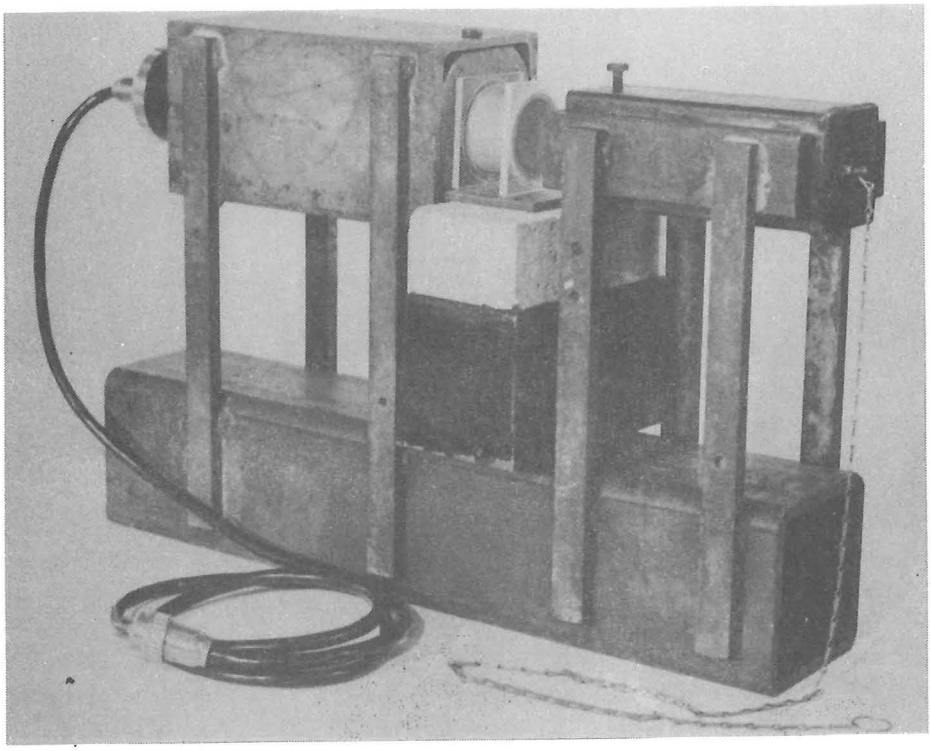

Fig. L.3 Linearity Test Apparatus

L.7 Calibration Tests

For the calibration tests in the B flow simulator, $N = 8 \times 10^5$ for I_1 and I_0 and 4×10^5 for I. From Eq. L.2 the statistical uncertainty $\Delta C = 0.006$. The radiation intensities are listed in Table L.1. The background radiation intensity of 67 cpm was subtracted from these values before the air concentration was calculated using Eq. L.4.

Table L.1 Radiation Intensity (cpm)

		Test		
I_1	I_0	D	E	F
91562	70916	73959	73753	73670

APPENDIX M

MAINS FREQUENCY VARIATIONS

M.1 Introduction

The effect of mains frequency variations on the output signals from the tape recorder will be discussed firstly with respect to stagnation pressure and air concentration measurements and then the velocity measurements.

M.2 Calculation of Stagnation Pressure P and Air Concentration C

The magnitudes of P and C are determined by the output voltage of the tape recorder. To predict the variation in output voltage with variation in mains frequency requires a knowledge of the operating principles of this tape recorder. In brief, an input voltage is converted to a frequency which is recorded onto the tape. On playback this frequency is converted back to a voltage.

Because the tape is driven by a synchronous motor, an increase in the mains frequency MF will cause a proportionate increase in the tape speed TS. This is represented by

$$\frac{\Delta TS}{TS} = \frac{\Delta MF}{MF} \qquad M.1$$

where Δ refers to a change.

An increase in tape speed during recording results in an expansion of the time base during playback at the correct speed. Thus a frequency f (corresponding to a given input voltage) recorded onto the tape will decrease on playback at the correct speed according to

$$\frac{\Delta f}{f} = -\frac{\Delta TS}{TS} \qquad M.2$$

At 381 mm/s tape speed, the relationship between this frequency and the output voltage Y is given by

$$f = 27\,000 + 7640\,Y$$

A decrease in this frequency will result in a decrease in the output voltage given by

$$\frac{\Delta f}{f} = \frac{7640\,\Delta Y}{27\,000 + 7640\,Y} \qquad M.3$$

Combining Eqs. M.1, M.2 and M.3 and rearranging, gives

$$\underbrace{\left[\frac{\Delta Y}{2.83} \times \frac{100}{1}\right]}_{\text{\% FS output voltage change}} = -\alpha \underbrace{\left[\frac{\Delta MF}{MF} \times \frac{100}{1}\right]}_{\text{\% mains frequency change}} \qquad M.4$$

where $\alpha = 1.25 + \frac{Y}{2.83}$

The magnitude of α is shown in Table M.1 for the output voltage a minimum; zero; and maximum.

Table M.1 Magnitude of α

Y (volts)	- 1.41	0	1.41
α	0.75	1.25	1.75

Consider the output voltage Y = 0.0. With reference to Fig. 9.5, it is seen that most variations in these signals are bounded by the broken lines which correspond to ± 1% variation in mains frequency as predicted by equation M.4. This compares well with the 49.5 - 51 Hz indicated by the New Zealand Electricity Department.

Because the radiation in mains frequency is about ± 1%, the uncertainty of any output voltage will be about ± α%. The uncertainty of a stagnation pressure measurement must be related to the range of the pressures measured. This was about 60% of the tape recorder's full scale range. The uncertainty of a stagnation pressure measurement will therefore range from about 1 - 3% FS, depending on the voltage. Similarly, the air concentration full scale range was about 80% of the tape recorder's. The uncertainty of an air concentration measurement will therefore range from about 1 - 2% FS.

M.3 Calculation of Velocity (By Cross-Correlation)

The magnitude of the velocity is calculated from the time delay τ between two signals recorded on the tape. The variation of this time delay with mains frequency is predicted below.

As stated previously, an increase in the mains frequency during recording results in an effective expansion of the time base during playback at the correct mains frequency. Consider two "events" with a time delay τ between them. If recorded onto the tape at an increased tape speed, the time delay will increase upon playback at the correct speed, i.e.

$$\frac{\Delta\tau}{\tau} = \frac{\Delta TS}{TS} \qquad \text{so}$$

$$\frac{\Delta\tau}{\tau} = \frac{\Delta MF}{MF}$$

Now the variation in velocity with change in time delay is given by

$$\frac{\Delta V}{V} = -\frac{\Delta\tau}{\tau} \qquad \text{so}$$

$$\frac{\Delta V}{V} = -\frac{\Delta MF}{MF}$$

The ± 1% variation in mains frequency will therefore cause a ± 1% uncertainty in the magnitude V.

APPENDIX N

DATA ARRAYS

The most important measurements from Aviemore are tabulated below. The air concentration data in Tables N.1 and N.5 has been truncated from 3 to 2 decimal places for presentation here. This will only cause minor differences between this data and the figures and calculations within Chapters 10 and 11.

Table N.1 Measured Air Concentration Profiles (Fig. 10.12)

		STATION									
		GATE OPEN 300 mm					GATE OPEN 450 mm				
I	y	501	502	503	504	505	501	502	503	504	505
1	6	0.00	0.07	0.13	0.21	0.25	0.00	0.00	0.03	0.11	0.18
2	18	0.04	0.10	0.18	0.26	0.28	0.00	0.00	0.06	0.16	0.21
3	30	0.05	0.12	0.21	0.28	0.30	0.00	0.01	0.07	0.18	0.23
4	43	0.06	0.15	0.22	0.29	0.32	0.00	0.01	0.09	0.20	0.24
5	55	0.06	0.17	0.24	0.31	0.33	0.00	0.02	0.11	0.21	0.25
6	68	0.07	0.18	0.25	0.32	0.35	0.00	0.03	0.12	0.23	0.25
7	80	0.08	0.19	0.27	0.33	0.36	0.00	0.04	0.13	0.24	0.27
8	93	0.10	0.20	0.29	0.35	0.38	0.00	0.06	0.14	0.25	0.28
9	105	0.14	0.21	0.33	0.37	0.39	0.00	0.08	0.16	0.26	0.29
10	118	0.26	0.25	0.37	0.38	0.41	0.01	0.09	0.17	0.28	0.30
11	130	0.47	0.30	0.42	0.40	0.43	0.02	0.12	0.20	0.29	0.32
12	142	0.64	0.37	0.48	0.42	0.46	0.06	0.15	0.25	0.31	0.33
13	155	0.76	0.46	0.55	0.46	0.49	0.11	0.21	0.30	0.33	0.35
14	167	0.85	0.56	0.63	0.50	0.52	0.26	0.29	0.37	0.36	0.37
15	180	0.91	0.66	0.71	0.57	0.57	0.57	0.38	0.45	0.39	0.39
16	192	0.95	0.74	0.79	0.64	0.62	0.78	0.48	0.53	0.43	0.43
17	205	0.96	0.81	0.84	0.72	0.69	0.86	0.58	0.61	0.49	0.47
18	217	0.98	0.88	0.89	0.78	0.75	0.91	0.67	0.68	0.57	0.51
19	230	0.98	0.92	0.92	0.84	0.80	0.95	0.76	0.74	0.65	0.56
20	242	0.99	0.95	0.95	0.88	0.85	0.97	0.82	0.79	0.71	0.62
21	255	0.99	0.96	0.96	0.91	0.88	0.99	0.87	0.84	0.77	0.68
22	267	1.00	0.97	0.97	0.94	0.91	0.99	0.90	0.88	0.82	0.75
23	279	1.00	0.98	0.98	0.95	0.94	1.00	0.93	0.92	0.86	0.81
24	292	1.00	0.98	0.99	0.97	0.95	1.00	0.96	0.95	0.89	0.86
25	304	1.00	0.99	0.99	0.97	0.96	1.00	0.97	0.96	0.91	0.89
26	317	1.00	0.99	0.99	0.98	0.97	1.00	0.98	0.97	0.93	0.91
27	329	1.00	0.99	1.00	0.98	0.98	1.00	0.99	0.97	0.95	0.92
28	342	1.00	1.00	1.00	0.98	0.98	1.00	0.99	0.97	0.97	0.94
29	354	1.00	1.00	1.00	0.98	0.98	1.00	0.99	0.98	0.98	0.95

Table N.2 Measured Velocity Profiles (Cross-Correlation), m/s (Fig. 10.20)

		STATION									
		GATE OPEN 300 MM					GATE OPEN 450 MM				
I	y	501	502	503	504	505	501	502	503	504	505
1	6	11.0	11.1	11.2	11.3	11.7	11.1	11.2	11.3	11.4	11.5
2	18	12.4	12.7	12.8	12.9	13.3	12.4	12.8	12.9	13.1	13.2
3	30	13.5	13.8	14.1	14.2	14.4	13.5	14.0	14.2	14.4	14.6
4	43	14.5	14.7	15.1	15.3	15.4	14.5	15.0	15.2	15.5	15.7
5	55	15.2	15.5	15.8	16.1	16.3	15.3	15.8	16.1	16.3	16.5
6	68	15.8	16.1	16.4	16.8	16.9	16.0	16.4	16.8	17.0	17.2
7	80	16.3	16.6	17.0	17.3	17.6	16.6	16.9	17.3	17.6	17.8
8	93	16.8	17.0	17.5	17.8	18.1	16.9	17.4	17.9	18.1	18.2
9	105	17.2	17.4	17.9	18.2	18.5	17.3	17.7	18.2	18.5	18.7
10	118	17.7	17.8	18.3	18.5	18.8	17.6	18.1	18.6	18.9	19.2
11	130	17.8	18.1	18.6	18.8	19.1	17.9	18.4	18.9	19.2	19.6
12	142	17.9	18.3	18.9	19.2	19.4	18.2	18.7	19.2	19.5	20.0
13	155	18.0	18.6	19.1	19.4	19.6	18.4	19.0	19.5	19.8	20.3
14	167	18.1	18.9	19.2	19.5	19.8	18.5	19.2	19.8	20.0	20.5
15	180	18.2	19.1	19.4	19.7	20.0	18.6	19.5	20.0	20.2	20.8
16	192	18.2	19.1	19.5	19.9	20.2	18.7	19.7	20.2	20.4	20.9
17	205	18.3	19.2	19.6	20.0	20.3	18.8	19.3	20.3	20.6	21.1
18	217		19.3	19.7	20.1	20.3	18.9	19.9	20.5	20.8	21.2
19	230		19.3	19.8	20.1	20.4	18.9	20.0	20.6	20.9	21.3
20	242		19.3	19.8	20.2	20.4	19.0	20.1	20.6	21.0	21.4
21	255		19.3	19.9	20.2	20.4	19.0	20.1	20.7	21.1	21.5
22	267			19.9	20.2	20.4	19.0	20.2	20.7	21.2	21.6
23	279			20.0	20.2	20.4	19.0	20.3	20.8	21.2	21.6
24	292			20.0	20.2	20.4	19.0	20.3	20.8	21.3	21.7
25	304			20.0	20.2	20.4		20.3	20.9	21.3	21.7
26	317					20.4		20.3	20.9	21.3	21.7
27	329					20.4			21.0	21.4	21.7
28	342								21.0	21.4	21.8
29	354									21.4	21.8

Table N.3 Measured Stagnation Pressure Profiles, kN/m^2 (Fig. 10.4)

		STATION									
		GATE OPEN 300 MM					GATE OPEN 450 MM				
I	y	501	502	503	504	505	501	502	503	504	505
1	6	59	57	62	53	59	62	63	64	52	59
2	18	79	76	83	74	78	78	81	83	76	81
3	30	94	93	96	91	93	92	98	100	96	99
4	43	108	107	109	105	103	105	112	115	112	114
5	55	119	119	122	116	114	117	125	127	124	125
6	68	129	129	131	125	121	129	136	138	135	136
7	80	138	138	138	131	124	138	146	148	143	145
8	93	143	145	140	136	127	145	153	156	150	153
9	105	143	150	141	138	129	150	160	164	155	160
10	118	129	154	138	141	129	153	165	169	159	165
11	130	100	152	129	142	129	154	171	172	163	168
12	142	65	140	119	141	128	153	174	174	165	169
13	155	41	121	103	134	126	148	171	169	167	170
14	167	26	99	88	126	121	134	162	156	167	170
15	180	16	76	69	112	114	76	143	140	165	167
16	192	10	55	54	93	101	31	121	121	155	164
17	205	6	38	41	76	81	14	98	109	138	155
18	217	5	26	32	60	64	3	76	79	117	143
19	230	4	17	24	46	50	0	57	64	99	131
20	242	3	14	17	32	38	0	43	52	83	116
21	255	3	10	14	25	30	0	31	40	69	99
22	267	2	8	12	19	23	0	22	30	53	78
23	279	2	7	10	14	17	0	15	22	41	57
24	292	0	6	8	12	13	0	12	14	32	40
25	304	0	5	7	8	9	0	9	9	25	32
26	317	0	4	6	6	7	0	8	7	21	25
27	329	0	3	4	5	6	0	7	5	16	21
28	342	0	0	3	4	5	0	6	4	12	16
29	354	0	0	3	3	4	0	6	3	8	12

Table N.4 Measured Intermittency Parameter Profiles (Fig. 10.26)

		STATION									
			GATE OPEN 300 MM					GATE OPEN 450 MM			
I	y	501	502	503	504	505	501	502	503	504	505
1	6	1.00	1.00	1.00	1.00	1.00	1.00	1.00	1.00	1.00	1.00
2	18	1.00	1.00	1.00	1.00	0.99	1.00	1.00	1.00	1.00	1.00
3	30	1.00	1.00	1.00	0.99	0.99	1.00	1.00	1.00	1.00	1.00
4	43	1.00	1.00	1.00	0.99	0.98	1.00	1.00	1.00	1.00	1.00
5	55	1.00	1.00	1.00	0.98	0.98	1.00	1.00	1.00	1.00	1.00
6	68	1.00	0.99	0.99	0.97	0.98	1.00	1.00	1.00	1.00	0.99
7	80	1.00	0.99	0.98	0.96	0.97	1.00	1.00	1.00	0.99	0.99
8	93	1.00	0.98	0.96	0.95	0.96	1.00	1.00	0.99	0.99	0.98
9	105	0.98	0.98	0.93	0.93	0.94	1.00	1.00	0.99	0.98	0.98
10	118	0.92	0.97	0.89	0.92	0.92	1.00	1.00	0.99	0.98	0.97
11	130	0.75	0.93	0.84	0.90	0.89	1.00	0.99	0.98	0.97	0.97
12	142	0.55	0.88	0.77	0.86	0.86	1.00	0.98	0.95	0.95	0.96
13	155	0.35	0.78	0.69	0.82	0.81	0.97	0.95	0.91	0.93	0.94
14	167	0.22	0.64	0.58	0.74	0.76	0.80	0.91	0.85	0.91	0.92
15	180	0.13	0.51	0.43	0.63	0.69	0.57	0.81	0.76	0.87	0.90
16	192	0.07	0.37	0.28	0.50	0.61	0.33	0.68	0.66	0.82	0.86
17	205	0.03	0.24	0.18	0.37	0.50	0.13	0.56	0.57	0.75	0.81
18	217	0.01	0.14	0.13	0.27	0.41	0.04	0.44	0.48	0.65	0.76
19	230	0.01	0.08	0.09	0.18	0.31	0.02	0.32	0.38	0.54	0.68
20	242	0.00	0.05	0.06	0.13	0.22	0.01	0.22	0.29	0.44	0.60
21	255	0.00	0.03	0.04	0.09	0.14	0.01	0.15	0.20	0.34	0.50
22	267	0.00	0.02	0.02	0.05	0.09	0.00	0.11	0.13	0.24	0.38
23	279	0.00	0.01	0.02	0.03	0.06	0.00	0.07	0.06	0.17	0.27
24	292	0.00	0.01	0.01	0.02	0.04	0.00	0.04	0.02	0.13	0.18
25	304	0.00	0.00	0.01	0.01	0.03	0.00	0.02	0.01	0.09	0.14
26	317	0.00	0.00	0.01	0.01	0.02	0.00	0.01	0.01	0.07	0.11
27	329	0.00	0.00	0.00	0.00	0.02	0.00	0.00	0.01	0.05	0.09
28	342	0.00	0.00	0.00	0.00	0.02	0.00	0.00	0.01	0.03	0.07
29	354	0.00	0.00	0.00	0.00	0.01	0.00	0.00	0.01	0.02	0.06

Table N.5 Adjusted Air Concentration Profiles (Fig. 10.49)

		STATION									
			GATE OPEN 300 MM					GATE OPEN 450 MM			
I	y	501	502	503	504	505	501	502	503	504	505
1	6	0.00	0.09	0.11	0.22	0.26	0.00	0.01	0.02	0.11	0.19
2	18	0.00	0.12	0.16	0.27	0.29	0.00	0.01	0.05	0.16	0.22
3	30	0.00	0.15	0.19	0.29	0.31	0.00	0.02	0.07	0.18	0.24
4	43	0.01	0.17	0.21	0.31	0.33	0.00	0.03	0.09	0.20	0.25
5	55	0.01	0.19	0.22	0.32	0.35	0.00	0.03	0.10	0.21	0.26
6	68	0.02	0.20	0.24	0.34	0.36	0.00	0.04	0.11	0.23	0.27
7	80	0.03	0.22	0.26	0.35	0.38	0.00	0.06	0.12	0.24	0.28
8	93	0.05	0.22	0.28	0.36	0.40	0.00	0.07	0.14	0.25	0.29
9	105	0.08	0.24	0.31	0.38	0.41	0.00	0.09	0.15	0.26	0.30
10	118	0.14	0.27	0.35	0.39	0.43	0.00	0.11	0.17	0.28	0.32
11	130	0.27	0.33	0.39	0.41	0.45	0.00	0.14	0.19	0.29	0.33
12	142	0.50	0.40	0.45	0.44	0.48	0.00	0.17	0.23	0.31	0.35
13	155	0.69	0.51	0.52	0.48	0.51	0.03	0.24	0.29	0.33	0.37
14	167	0.80	0.61	0.59	0.53	0.55	0.09	0.32	0.36	0.36	0.39
15	180	0.88	0.70	0.67	0.59	0.59	0.24	0.41	0.43	0.39	0.42
16	192	0.93	0.78	0.76	0.68	0.66	0.57	0.52	0.52	0.43	0.46
17	205	0.95	0.84	0.82	0.75	0.72	0.81	0.61	0.59	0.49	0.50
18	217	0.96	0.90	0.87	0.81	0.78	0.88	0.69	0.66	0.57	0.55
19	230	0.98	0.94	0.91	0.86	0.83	0.93	0.77	0.73	0.65	0.60
20	242	0.98	0.96	0.93	0.90	0.87	0.97	0.83	0.78	0.71	0.66
21	255	0.99	0.98	0.95	0.93	0.90	0.99	0.88	0.83	0.77	0.72
22	267	1.00	0.99	0.97	0.95	0.93	0.99	0.91	0.88	0.82	0.78
23	279	1.00	0.99	0.98	0.96	0.94	1.00	0.94	0.91	0.86	0.84
24	292	1.00	0.99	0.99	0.97	0.96	1.00	0.96	0.95	0.89	0.87
25	304	1.00	0.99	0.99	0.98	0.97	1.00	0.98	0.96	0.91	0.90
26	317	1.00	0.99	0.99	0.98	0.97	1.00	0.98	0.97	0.93	0.92
27	329	1.00	0.99	1.00	0.98	0.98	1.00	0.99	0.97	0.95	0.93
28	342	1.00	1.00	1.00	0.98	0.98	1.00	0.99	0.97	0.97	0.94
29	354	1.00	1.00	1.00	0.98	0.98	1.00	0.99	0.98	0.98	0.96

Table N.6 Depth (mm) to the Curves of Constant Air Concentration Down the Spillway (Fig. 10.50)

AIR CONCENTRATION	STATION 501	GATE OPEN 300 MM 502	503	504	505	501	GATE OPEN 450 MM 502	503	504	505
0.02	66					150	30			
0.05	93					159	74	19		
0.10	110	11				169	113	55		
0.20	124	64	37			177	148	132	42	10
0.30	132	124	103	36	25	182	165	157	136	102
0.40	137	142	131	122	96	186	179	174	183	171
0.50	143	154	151	160	150	190	191	190	206	204
0.60	149	166	168	181	182	194	203	206	222	230
0.70	156	179	184	196	201	199	218	225	240	251
0.80	167	196	201	215	222	204	236	247	262	271
0.90	185	218	228	243	255	222	263	275	297	304
0.95	207	236	253	267	284	236	284	291	328	349
0.98	237	261	283		348	250	315			

Table N.7 Depth (mm) to the Streamlines Down the Spillway (Fig. 10.51)

PROPORTION OF WATER	STATION 501	GATE OPEN 300 MM 502	503	504	505	501	GATE OPEN 450 MM 502	503	504	505
0.20	30	33	34	39	40	42	42	43	48	51
0.40	60	69	70	79	81	81	83	86	96	101
0.60	89	103	106	119	123	118	122	127	142	150
0.80	117	139	146	161	169	153	165	173	193	204
0.90	136	165	174	190	201	172	195	207	228	241
0.95	153	186	197	215	227	185	219	234	257	272
0.98	172	206	221	240	254	202	244	260	288	308
1.00	205	242	255	279	292	242	279	304	329	354

APPENDIX P

INTERMITTENCY PARAMETER, PLOTS

Figs P.1 and P.2 show the profiles of the intermittency parameter calculated as the integral of the probability density functions from C = 0 - 0.6 and from C = 0 - 0.8 respectively. (Ref. Section 10.3.4). Figs P.3 and P.4 show the percentage overestimation of velocity calculated with Eq. 2.14 using the intermittency parameter profiles of Figs. P.1 and P.2 respectively. (Ref. Section 10.4.2)

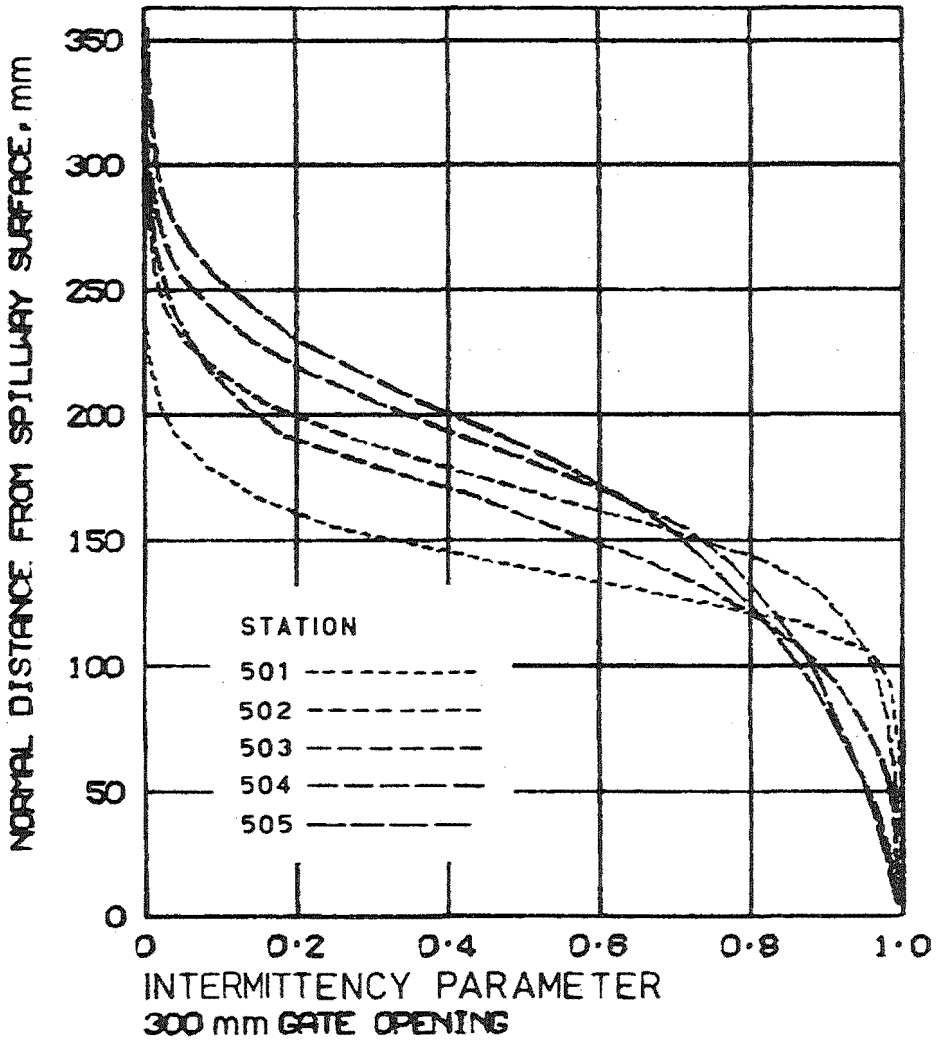

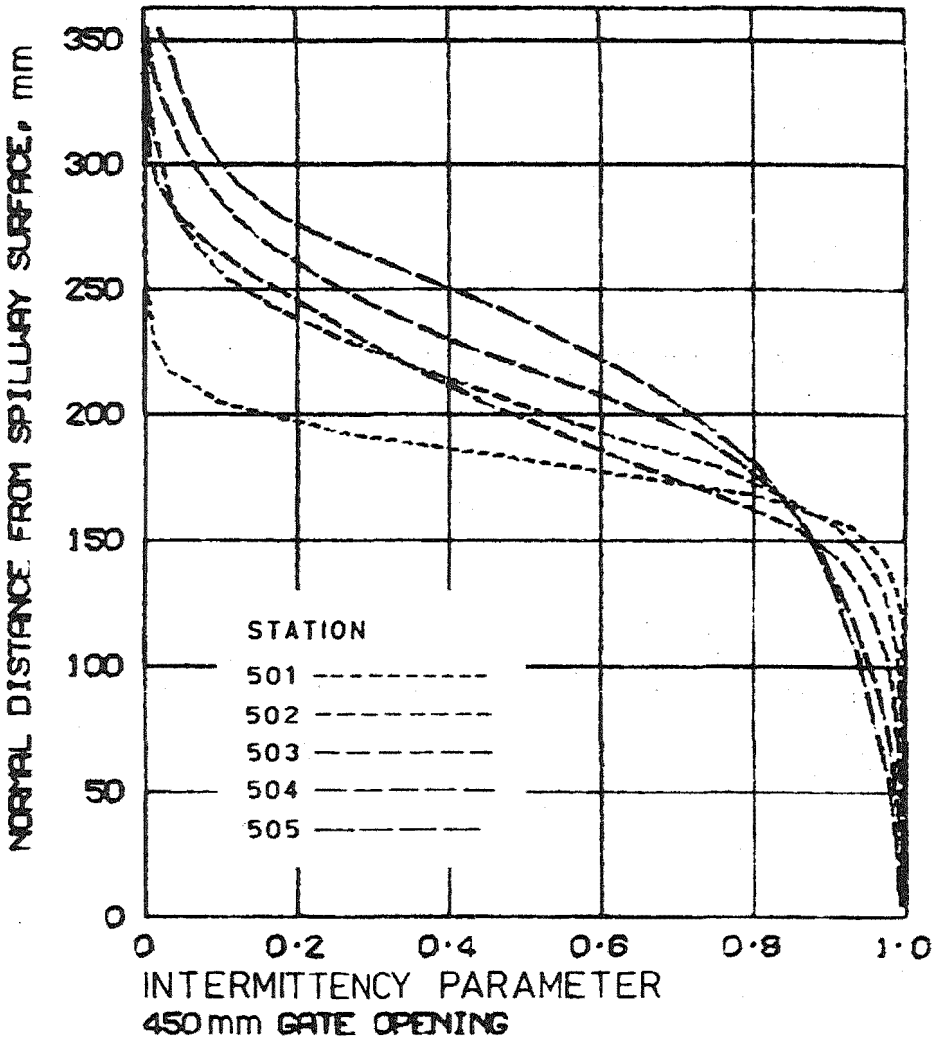

Fig. P.1 Measured Intermittency Parameter Profiles
Calculated as the Integral from C = 0 - 0.6.

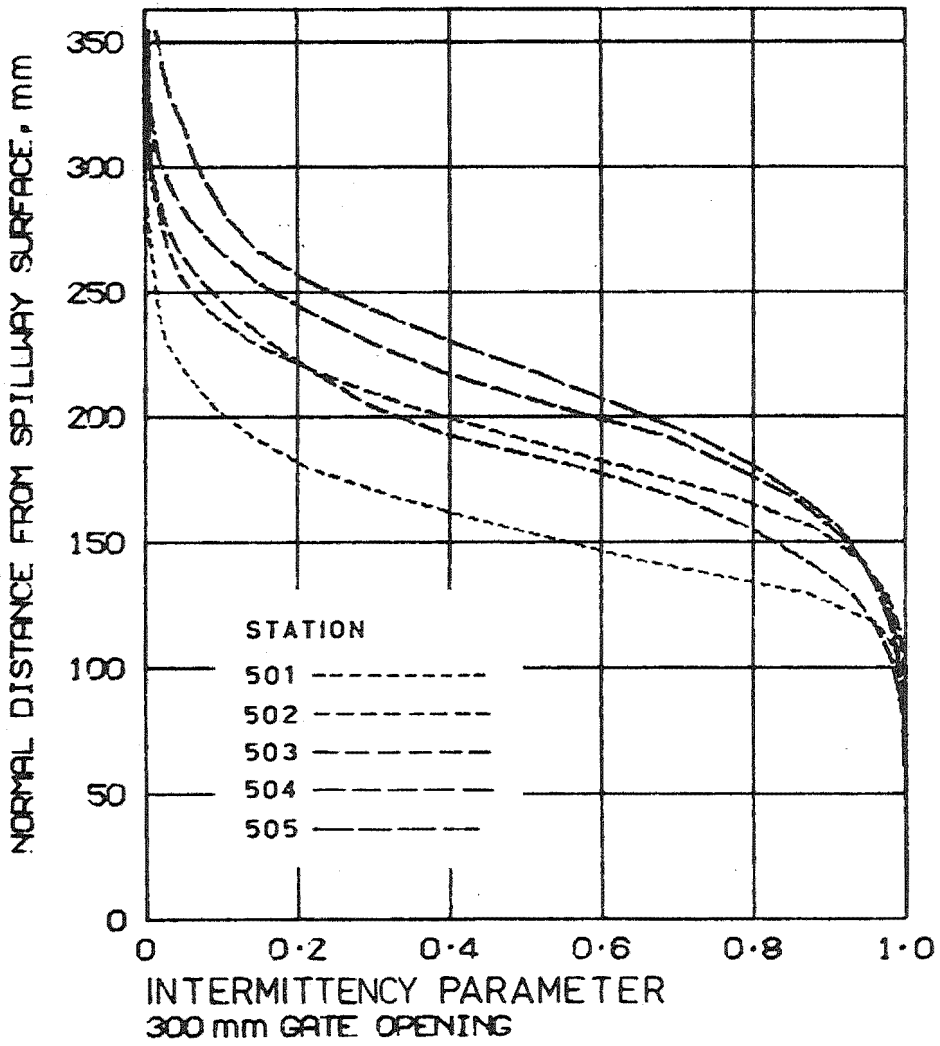

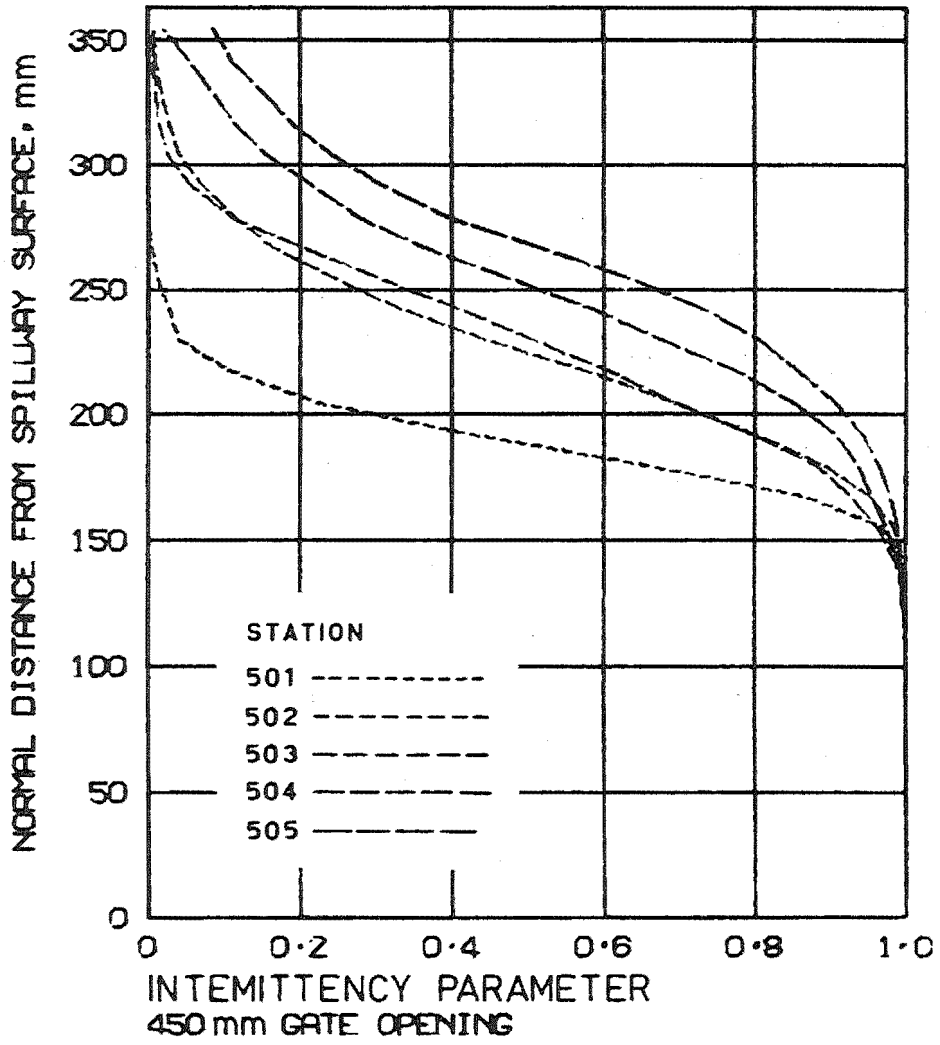

Fig. P.2 Measured Intermittency Parameter Profiles
Calculated as the Integral from C = 0 - 0.8

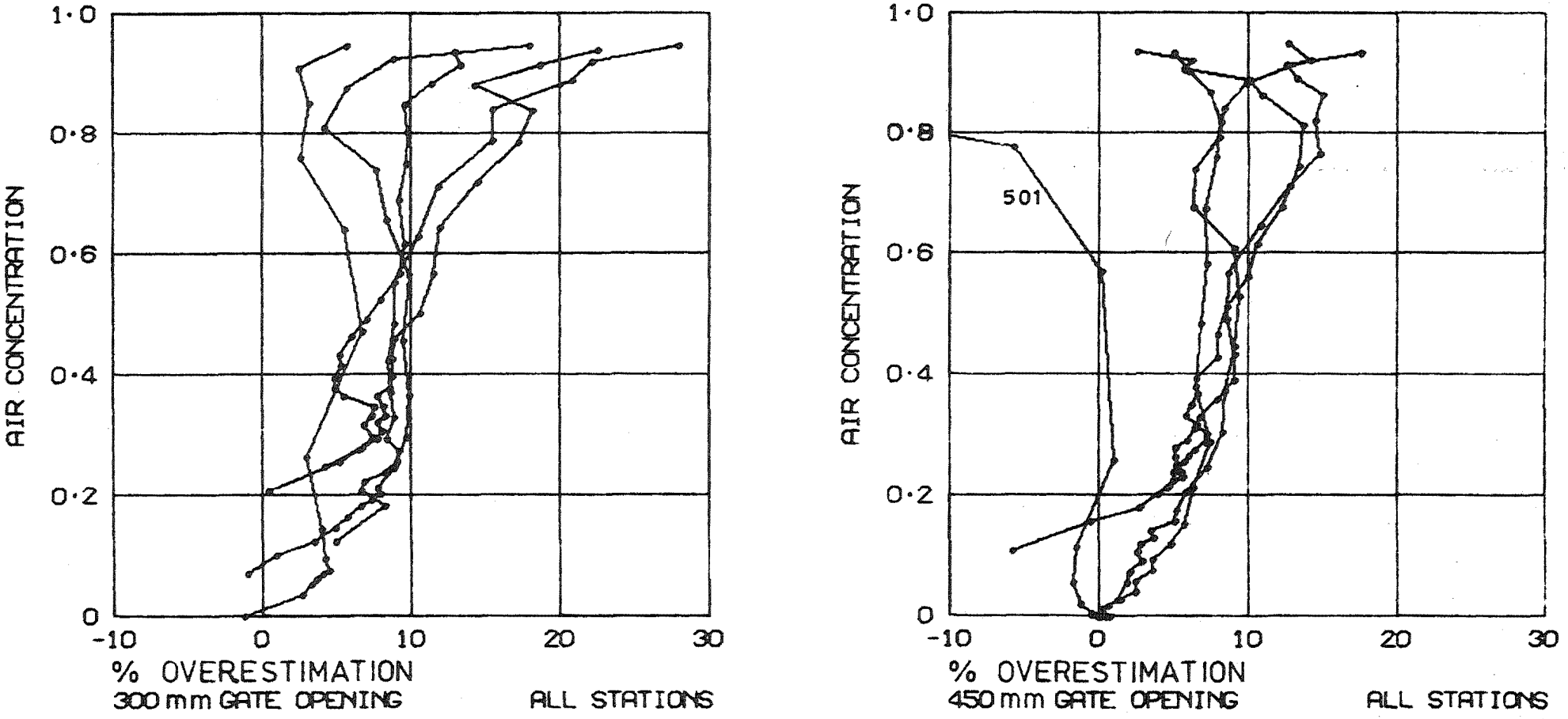

Fig. P.3 Percentage Overestimation of Calculated Velocity.
Based on Intermittency Parameters Calculated as the Integral from C = 0 - 0.6.

Classn:
MEASUREMENTS WITHIN SELF-AERATED FLOW ON A LARGE SPILLWAY
P. Cain.
ABSTRACT: Instruments were developed for use in self-aerated flows. These were used to measure profiles of velocity, air concentration and stagnation pressure on the spillway of Aviemore Dam. These are the most comprehensive and detailed measurements yet obtained on a large structure.

U. of Cant. C. Eng. Dept. Res. Report No. 78/18